Electronic Attack of a Dual Band Radar

Prepared by:

Aadil Valli Essop

ESSAAD001

Department of Electrical Engineering

University of Cape Town

Prepared for:

Professor Michael Inggs

Radar Remote Sensing Group

Department of Electrical Engineering

University of Cape Town

March 2014

Submitted to the Department of Electrical Engineering at the University of Cape Town in partial fulfilment of the academic requirements for a

Master of Engineering *specialising in Radar and Electronic Defence*

Declaration

I know that plagiarism is wrong. Plagiarism is to use another's work and pretend that it is one's own.

I have used the IEEE convention for citation and referencing. Each contribution to, and quotation in, this final year project report from the work(s) of other people, has been attributed and has been cited and referenced.

This minor dissertation project report is my own work.

I have not allowed, and will not allow, anyone to copy my work with the intention of passing it off as their own work or part thereof.

Name: ******AADIL VALLI ESSOP******

Signature: **Date:** 3 February 2014

Terms of Reference

A modelling and simulation environment to represent and test the Electronic Attack (EA) of a Dual Band Radar (DBR) should be developed. Specific outcomes of the research must be:

- Realistic target models should be simulated.

- The primary functions of the radar with respect to target parameter measurement and estimation should be simulated. These simulated primary functions must be easily adaptable to model and simulate different radars.

- The interception of the radar signal and its parameter estimation, by the Electronic Support (ES) system must be modelled and simulated. The efficiency of the signal interception and processing techniques should be assessed.

- EA techniques must be proposed, modelled and simulated.

- The efficiency of the EA techniques should be assessed with respect to radar performance impact, and jammer efficiency. This assessment must be done in “single-plot” mode as well as “multiple-plot (track)” mode.

- Throughout the radar-target-jammer “engagement”, extensive use must be made of visual representations to visualise and understand the applicable physical phenomena.

- Hardware architecture for the jammer can be proposed.

- Electronic Protection (EP) techniques to harden or defend a DBR against current EA techniques must be recommended.

Acknowledgements

"All Praise and Gratitude is for the Initiator and Maintainer of:

The Visible and Invisible;

The Known and Unknown;

The Apparent and Hidden;

The Obvious and Subtle;

To the True Master!"

Sincere appreciation is due to the sponsors, mentors and reviewers of this dissertation:

Chris Mocke (CSIR Defence Peace Safety and Security)

Christo Cloete (CSIR Defence Peace Safety and Security)

Pieter-Jan Wolfaardt (Reutech Radar Systems)

Ralph Mills (Denel Integrated Systems Solutions)

Schalk Verwey (Denel Integrated Systems Solutions)

Special mention must certainly be made, of the uncompromising "Chief Programme Manager"
and
the three tough "Project Managers" for this work:

My Amazing Wife and Fantastic Daughters for their exceptional support and incredible patience!

Abstract

Radars are required as sensors for Ground Based Air Defence System's (GBADS's). The GBADS is used for point or area defence against aerial attack by aerial platforms (reference [13]).
Radars of a GBADS are used in the following roles:

1. Air Surveillance and Target Acquisition
2. Tracking

In the "Air Surveillance and Target Acquisition" role, the radars provide "Early Warning" to the effectors so that the hostile target/targets can be engaged. The effectors used in the GBADS Battery are generally:

1. Short Range Air Defence (SHORAD) Missiles
2. Very Short Range Air Defence (VSHORAD) Missiles
3. Anti-Aircraft Guns

In the "Target Tracking" role, the radar provides target designation information to the effector, which uses the information to locate and engage the target.
It is therefore logical that any radar used in a GBADS must be robustly protected against Electronic Attack (EA), to ensure it is able to provide the functions of Air Surveillance, Target Acquisition and Target Tracking. A potential candidate for radar with these functions, within a GBADS is a novel Dual Band Radar (DBR). *Simultaneous transmission of dual band* ("X" and "L") radar pulses in a *single radar*, are used to determine target range, speed, direction and height. This type of radar has inherent design features such as dual band operation, multiple frequency pulse transmission and "digital beam-forming on receive" technology, which make it "difficult to jam".
The objective of this thesis is to determine if this radar can be attacked electronically, what techniques would be most suitable, determine the effectiveness thereof and then propose electronic protection (EP) measures.
The "radar-ES-EA" interaction was modelled as having a "signal" level dimension and a "system" level dimension. The system-level approach analysed and modelled radar performance (Signal to Noise Ratio (SNR) vs. Range, P_d vs. Range) and radar performance degradation (Jammer Power vs. Radar Power, Burn-through Range, etc.). The signal-level approach allowed possible EA techniques to be determined through visualisation of the radar signal interactions. Following the above-mentioned methodology showed that the DBR can be electronically attacked effectively, proposed ES and EA algorithms that would be most useful and also suggested an EA system architecture that can be used for testing EA of a DBR. The latter outcome was an additional optional outcome of the study. Finally, EP measures were proposed, to reduce or eliminate the effects of EA proposed in this study.

Table of Contents

List of Figures

List Tables

1 Introduction

1.1 Background to the study

1.1.1 Definitions

This study is a research project in the field of Radar and Electronic Defence (ED). ED is the "use of Electromagnetic (EM) and directed energy to control the EM spectrum", Schleher [4]. There are three branches of ED as shown in Figure 1. Also indicated in the figure are the new and old names for the ED branches and their definitions. The old names are shown in italics and the new names are shown in normal font.

The primary functions of an advanced Air Surveillance, Acquisition and Tracking Radar were modelled and simulated. Together with this, primary functions of an Electronic Support (ES) and Electronic Attack (EA) system were also modelled and simulated.

Regarding Electronic Protection (EP), recommendations from literature were proposed but not modelled.

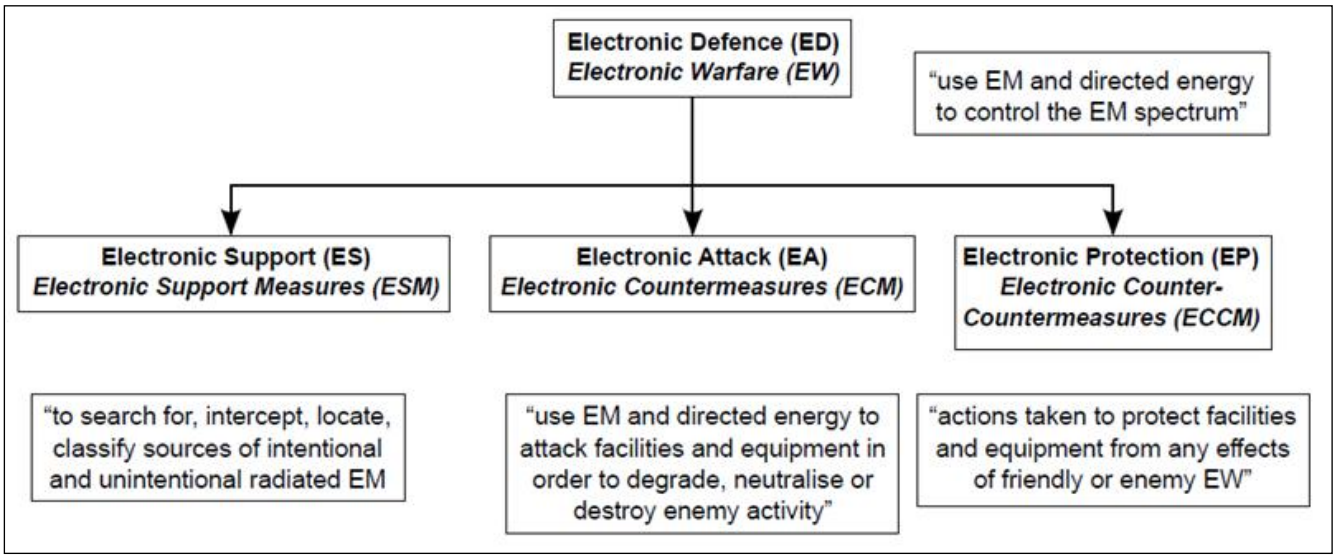

Figure 1: Electronic Defence Terminology (Schleher [4])

1.1.2 Why Simulate the "Scenario"?

The "Scenario" is an Electronic Warfare (EW) scenario of an attack on a Ground Based Air Defence System (GBADS). "A GBADS is used to provide "point or area defence" of a "strategic" asset against aerial attack", AV Essop (reference [13]). The "aerial attacking platform" is classified as either "Fixed wing", "Rotary wing" or "Missile" and the defended asset might be an airbase, stadium, bridge etc. It can be seen that testing an actual GBADS with an actual airborne Jammer System is complex and expensive. Due to this, modelling and simulation is used to reduce the development risk, before physical testing.

All of the information in this section is described in detail in reference [13].

The GBADS operated by an Army, in the broader system context is one pillar of the Joint Air Defence (JAD) System. The other two Air Defence pillars are the first line of defence, the Airborne Air Defence System (ABADS), operated by the Air Force and the Surface Based Air Defence System (SBADS), operated by the Navy. All three Air Defence pillars when combined, provide a complete defensive air defence layer through the use of an integrated network of sensors (radars, Electro-optic (EO)/Infrared (IR)), effectors (missiles, anti-aircraft guns) and aCommand, Control, Computers and Intelligence (C4I) system.

The concept of integrated multi-layer air defence is shown in Figure 2 below. The ranges and altitudes indicated, are governed by effector engagement and not sensor detection. The Inner Defence Layer persists typically to an altitude of 4km and a range of 6km. The engagement range of the Very Short Range Air Defence (VSHORAD) effectors, governs this layer while the Middle Air Defence Layer is defined by the Very Short Range Air Defence (SHORAD) effector's engagement "envelope". An effector could be a missile or anti-aircraft gun.

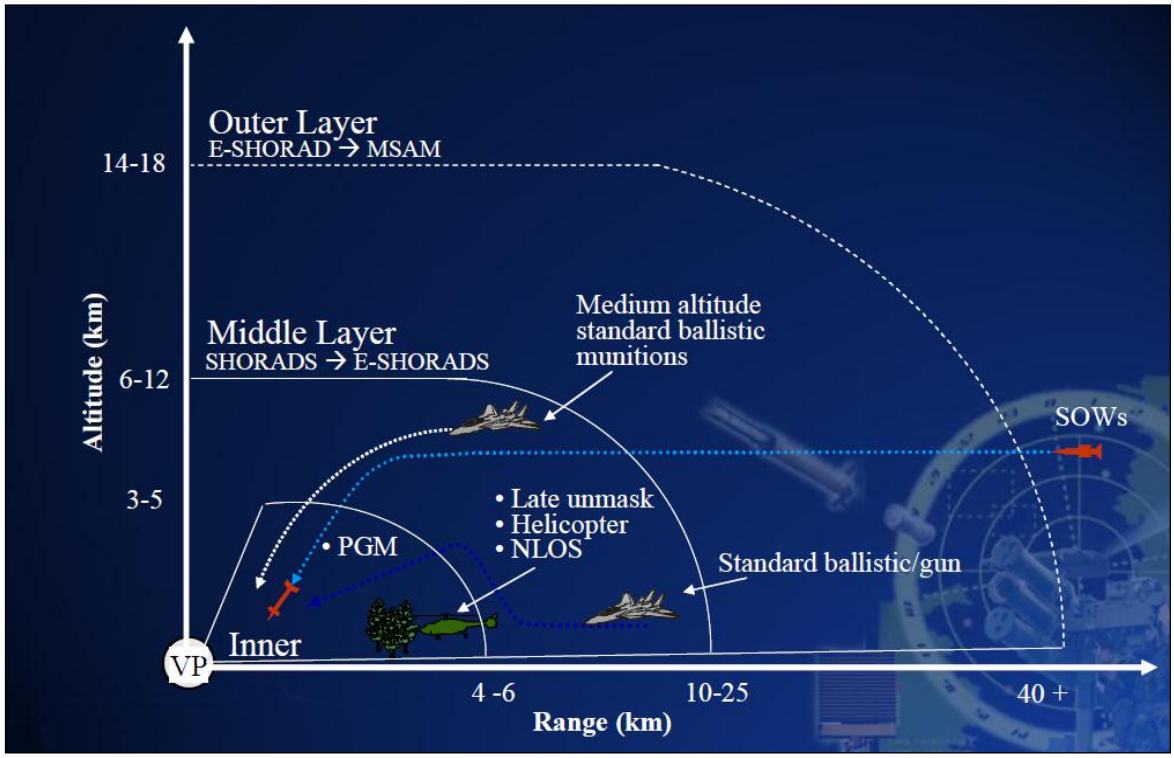

Figure 2: Air Defence Layers (Verwey [38])

The basic functionality of the GBADS is depicted by the schematic shown in Figure 3. The physical system elements providing the "Sense, Decide, Act" functions are also shown in the figure. These three primary System functions have effect in the operating environment. The operating environment includes the Area of Responsibility (AOR) as well as higher authority C4I Centres. The AOR is the area allocated to the battery over which an Air Defence function is

to be provided, and/or over which sensor coverage is required. It is represented by the blue oval in Figure 3.

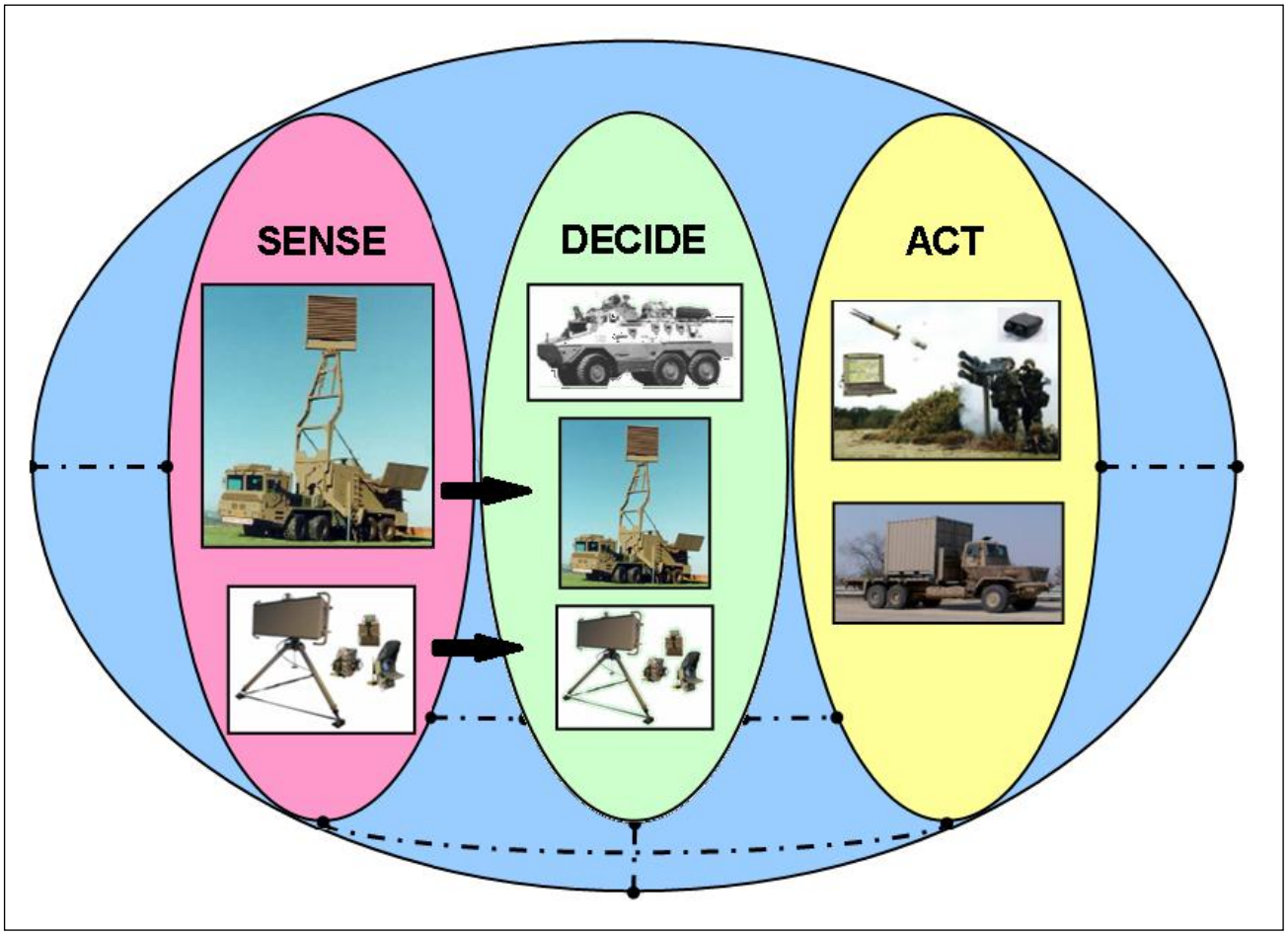

Figure 3: GBADS Functions (Essop [13])

The "Sense" functions in a GBADS are typically carried out by radar. EO/IR sensors could also be used to supplement and complement the sensor data received from radars. The radars are used in Air Surveillance, Target Acquisition and Tracking roles. In the "Air Surveillance and Target Acquisition" roles, the radars provide "Early Warning" to the effectors so that the hostile target/targets can be timeously engaged.

In the "Target Tracking" role, the radar provides target designation information to the effectors, which use the information to locate and engage the target or targets.

It is therefore logical that radars used in a GBADS must be robustly protected against Electronic Attack (EA) to ensure they are able to provide the functions of Air Surveillance and Target Tracking without interference. A potential candidate for an Air Surveillance, Acquisition and Tracking Radar in a GBADS, is a novel Radar called the "Dual Band Radar (DBR)". It is novel since it uses *simultaneous transmission of dual band* ("X" and "L" frequency band) radar pulses to determine target range, speed, direction and height. Conventional radar either transmits pulses in the X-Band or L-Band, but not in *both bands simultaneously*.

The L-Band frequencies start at 1 GHz and end at 2 GHz, while X-Band frequencies are defined from 8 GHz to 12 GHz, as described by Richards in reference [6].

The DBR has inherent design features that make it "difficult to jam. The dual band operation, multiple centre frequency Linear Frequency Modulated (LFM) pulses and the use of digital beam forming on receive are some of the non-typical EP features of the DBR.

1.2 Scope and Limitations

The scope and limitations of the study are described in the context of an "Actual EW scenario" vs. a "Simulated EW scenario", in this section. The extent, to which the scenarios, radar, targets and jammers are modelled are discussed in this section. All the assumptions made in the simulation and justification for adopting them is explicitly stated in this chapter.

1.2.1 Scenario Definition

The complete "radar-target-EW system" engagement cycle simulated in this report, can be depicted by the scenario definition shown in Figure 4.

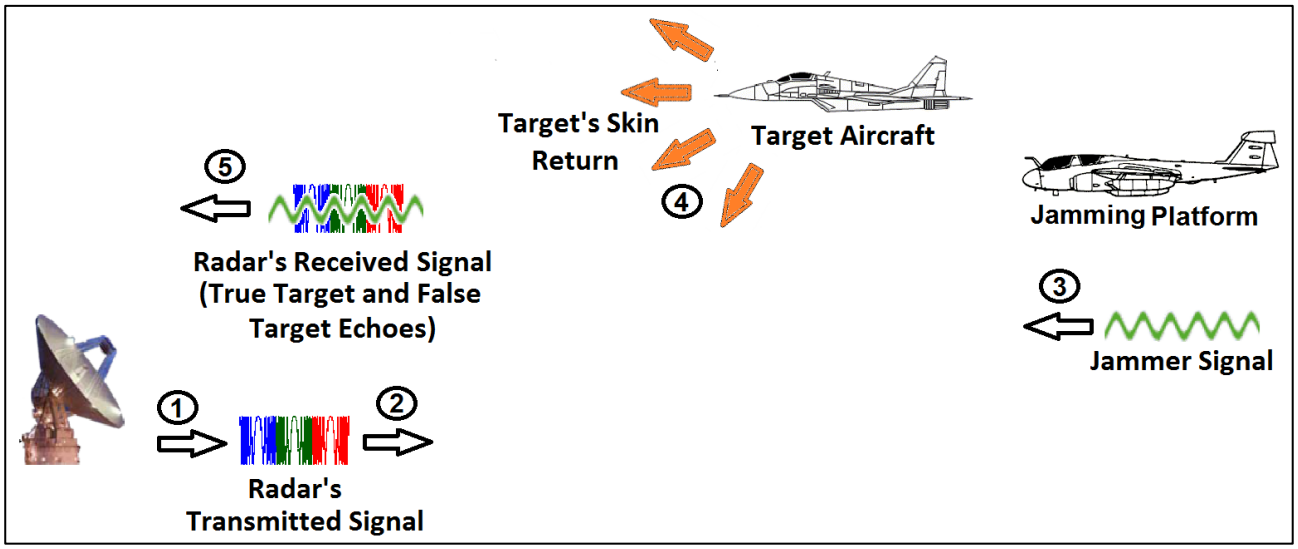

Figure 4: Radar-EW Engagement Scenario Definition

The cycle starts at the point of radar transmission (Step 1), with the transmitted pulse simulated on a signal-level. The pulse propagates through free space and it is assumed that no volume clutter (rain, hail, snow, etc.) is present in the environment.

Generally, the effects of clutter in the radar-EW jamming engagement were not simulated. To induce a realistic false target into the radar to deceive it, was one of the primary goals of this simulation. For this to occur, the false target signal-level must be stronger than the clutter power, for detection by the radar. The target would need to be even stronger than the true target skin return signal, in order to mislead the radar to track the false target.

For this reason, it was assumed that modelling the effects of clutter would not add substantial value to the simulation, but would substantially increase computational processing. This assumption was also made in a full-scale fighter jet radar-EW system simulation developed by D. DiFilippo, et. al, in reference [16].

The ES system then intercepts the radar's transmitted signal as indicated by step 2 in Figure 4. It is assumed in the context of this study that the ES subsystem and EA subsystem are combined into one "Jammer" system that is fitted to the jamming platform, which is not detected by the radar. The term "DBR Jammer" therefore refers to the combined ES and EA subsystems used to attack the DBR.

The "jamming platform" could usually be an aircraft, ship or ground based system. The key point is that the jammer platform is not detectable by the radar. This situation would arise in one of two situations. Either the jammer platform is at a range outside maximum radar detection range ("stand-off" range) or the true target masks the platform carrying the jammer. This would occur if the jammer platform is a supporting aircraft or towed decoy in the same "Range-Doppler-Angle" cell as the true target. The overall scenario was kept as generic as possible to allow the DBR EA techniques to be developed without restricting application to a specific set of limited scenarios. Obviously, this assumption has an impact on jammer receiver sensitivity, response time and transmitted power (amongst other requirements). However, the jammer requirements considered both a worst case (stand-in jammer) and best case (stand-off) for the simulation.

At step 2, the radar's signal parameters are estimated so that it can be replicated by a DRFM based Jammer. The transmitted signal also interacts with the true target and reflects off its surface. In other words, the true target detection process has commenced.

The jammer on the jamming platform then transmits the false target signal (step 3) to electronically attack the DBR. Simultaneously (or slightly before) this event, the true target is detected by the radar (step 4). While the ES subsystem is analysing and processing the intercepted signal, the radar enters its "Search and Acquisition Mode" and before it enters its "Track Mode" for tracking of the true target, the false target is transmitted to the radar. The radar then receives the combined true and false target returns as indicated by step 5.

It is important to note that this report structure follows the sequence of events described in this section. For example, the literature review describes the research conducted on subjects relevant to the radar, then research on the ES system and target models are presented, followed by jamming techniques. Thereafter "Electronic Protection" of the radar was presented. In a similar manner, the overall document structure follows the radar-EW system-target interaction described in this section.

Single Plot Mode Scenarios

One of the main reasons for developing the "Single Plot" mode was to visualise radar and EW interaction for a single detection inside the smallest radar signal-processing block, so that DBR-specific EW techniques could be developed and tested, from a fundamental level.

This "radar signal processing block" is a single "range-Doppler-elevation angle" bin in this simulation. Similarities and differences between radar detection of true and false targets could be test on a single building block, using the "Single Plot" simulation mode. The single-plot scenarios were therefore selected to test the capability of the simulation in single-plot mode.

X-Band and L-Band single-plot scenarios are shown in Table 1 and Table 2. The "worst case" scenario in terms of SNR was selected with range to one of the furthest bins used to set the amplitude functions. This range is called "Range to Bin" and is also shown in Table 1 and Table 2. If the "range to bin" is selected as large as possible within the radar's maximum detection range, then the SNR would be as small as possible. The signal amplitude is related to power, according to the following relationship (reference [6]):

$$V \propto \sqrt{P} \tag{1}$$

If the furthest range bin is selected, the signal amplitude or voltage would be as low as possible and present a challenge to the radar's target estimation algorithms. The above relationship between signal voltage and RF power is described in detail in section 1.2.3.

False targets in both the "Single Plot" and "Multiple Plot" modes were selected to be close to the true target, in order to simulate the "masking" of the true target for its self-protection.

	Target Type	Range to Bin [m]	Bin Range [m]	Unfolded Velocity [m/s]	Folded Velocity [m/s]	Unwrapped Elevation Angle [deg	Wrapped Elevation Angle [deg]
True Target 1	Fixed Wing	44025	200	102.5	20	23.2	7
True Target 2	Missile	44025	-100	432.5	20	18.2	2
False Target 1	Missile	44025	200	240	20	21.2	5

Table 1: X-Band, Single Plot Mode Scenarios

	Target Type	Range to Bin [m]	Bin Range [m]	Unfolded Velocity [m/s]	Folded Velocity [m/s]	Unwrapped Elevation Angle [deg	Wrapped Elevation Angle [deg]
True Target 1	Rotary Wing	100000	4000	124	15	19.2	3
True Target 2	Missile	100000	15	471	35	28.3	4
False Target 1	Rotary Wing	100000	3900	119	10	21.2	5
False Target 2	Missile	100000	0	466	30	31.3	7

Table 2: L-Band, Single Plot Mode Scenarios

The ambiguous or folded ranges and Doppler frequencies listed in Table 1 and Table 2 are calculated using the following equations from reference [6]:

$$R^a(t) = R(t) - k_R \frac{c\tau}{2} \tag{2}$$

$$f_d{}^a = f_d - k_f \, PRF \tag{3}$$

The folded Doppler frequency is then converted to velocity using equations (118), (119) and (120) (listed in section 3.1.1), while the ambiguous elevation angles are calculated using the equation (4):

$$\phi_{amb} = k_\phi \sin^{-1}\left(\frac{\hat{\lambda}}{d}\right) \tag{4}$$

Range and Doppler folding, as well as elevation angle wrapping are described in detail in section 9.1.

Multiple Plot Mode Scenarios

Multiple-plot mode, was developed to simulate the measurement of a true or false target *trajectory* that is changing in range, velocity and elevation angle. The next priority for the multiple-plot mode development was to simulate the effects of false target injection into the radar receiver, to determine whether the radar could *distinguish* between true and false target *tracks*. In multiple-plot mode, the capability to inject various types of false target profiles ("Range Gate Pull Off/Range Gate Pull in etc.") has been "built-in" to the simulation. Therefore, in order to test the full capability of the "Multiple Plot" mode *over all possible ranges, velocities and elevation angles*, in X and L-Band, the scenarios listed in Table 3 and Table 4 were developed. In general, the missile target was selected in the majority of multiple-plot scenarios, since the missile covers a larger distance and travels at a higher velocity than the other targets. The radar target estimators are therefore tested over a larger sequence of range, velocity and elevation angle values.

	Target Type	Range to Target [m]	Velocity [m/s]	Acceleration [m/s^2]	Elevation Angle [deg]
True Target 1	Rotary Wing	0 - 45000	60	9.81	0
True Target 2	Missile	0 - 5000	150-1000	98.1	0-40
False Target 2	Missile	0 - 5000	150-1000	98.1	1-41

Table 3: X-Band, Multiple Plot Mode Scenarios

	Target Type	Range to Target [m]	Velocity [m/s]	Acceleration [m/s^2]	Elevation Angle [deg]
True Target 1	Missile	0 - 187000	800	98.1	0
False Target 1	Missile	15 -187015	800	98.1	0
True Target 2	Missile	0 - 5000	150-1000	98.1	0
False Target 2	Missile	0 - 5000	160-1010	98.1	0

Table 4: L-Band, Multiple Plot Mode Scenarios

1.2.2 Radar

Basic description

The DBR is a mono-static radar that uses three LFM Pulses *per* frequency band, for detection. It transmits the three signals one after the other, in the L and X Bands, but the L and X Band transmissions can be simultaneous. The radar also uses "Digital Beam-forming on Receive" processing, in the X-Band only, to determine target elevation angle and hence its height.

It is not practical to implement the digital beam-forming on receive processing for the L-Band subsystem, since it would require the antenna spacing to be too large to be practically useful, in this radar application. The DBR is a *mobile* "Air Surveillance, Acquisition and Tracking" Radar. There are therefore, practical limitations for antenna size. This can be explained by inspecting equation (5) for the maximum positive unambiguous angle measured using the phased interferometry technique:

$$\phi_{\max} = \frac{\sin^{-1}\frac{\lambda}{d}}{2} \tag{5}$$

The quantity λ/d must be less than ±1, because the "sin" function is always greater than or less than one. However, antenna element spacing "*d*" is typically 2 to 4 times larger than the wavelength in a phased interferometry application. The wavelength corresponding to the centre frequency at L-Band is 0.272m. If "*d*" is 2 times larger than the wavelength it should be 0.544m! If six elements are used, the total height of the L-Band digital beam-forming on receive elements of the antenna would be 3.26m, which is too large to be of practical use in this application.

Multi-frequency operation

The "multi-frequency dual-band" signal transmission and processing, together with the "Digital Beam-forming on Receive" elevation angle estimation capability are the distinguishing features of the DBR. To the author's knowledge, this type of radar is a completely new development and has never been fielded. Because the radar transmits in both L and X Bands, it benefits from the advantages in transmitting in both bands but does not suffer the disadvantages of radar transmission in either band. For example long-range target detection is realised with the L-Band signals because of the longer wavelength while good range resolution for smaller RCS target detection is possible with the X-Band signal. In this simulation, a maximum practical detection range of a rotary wing target was calculated as 50.6 km in the L-Band and 36.4 km at X-Band (this result is presented and discussed in section 4.1).

Using the expression for range resolution from reference [6], it was found that the X-Band range resolution was 10m, while the L-Band resolution was 50m (described in section 4.1). Therefore, the radar would be able to distinguish between two targets if they are greater than 10m apart! This implies that in a support-jamming scenario, the *jamming aircraft* has to be less than 10m from the *"attacking" aircraft* (true target).

As stated earlier, three signals are transmitted by either the L-Band or X-band Transmitters. These signals are shown expanded in the bottom half of Figure 5. The signals are transmitted sequentially at three different frequencies, as shown in the figure.

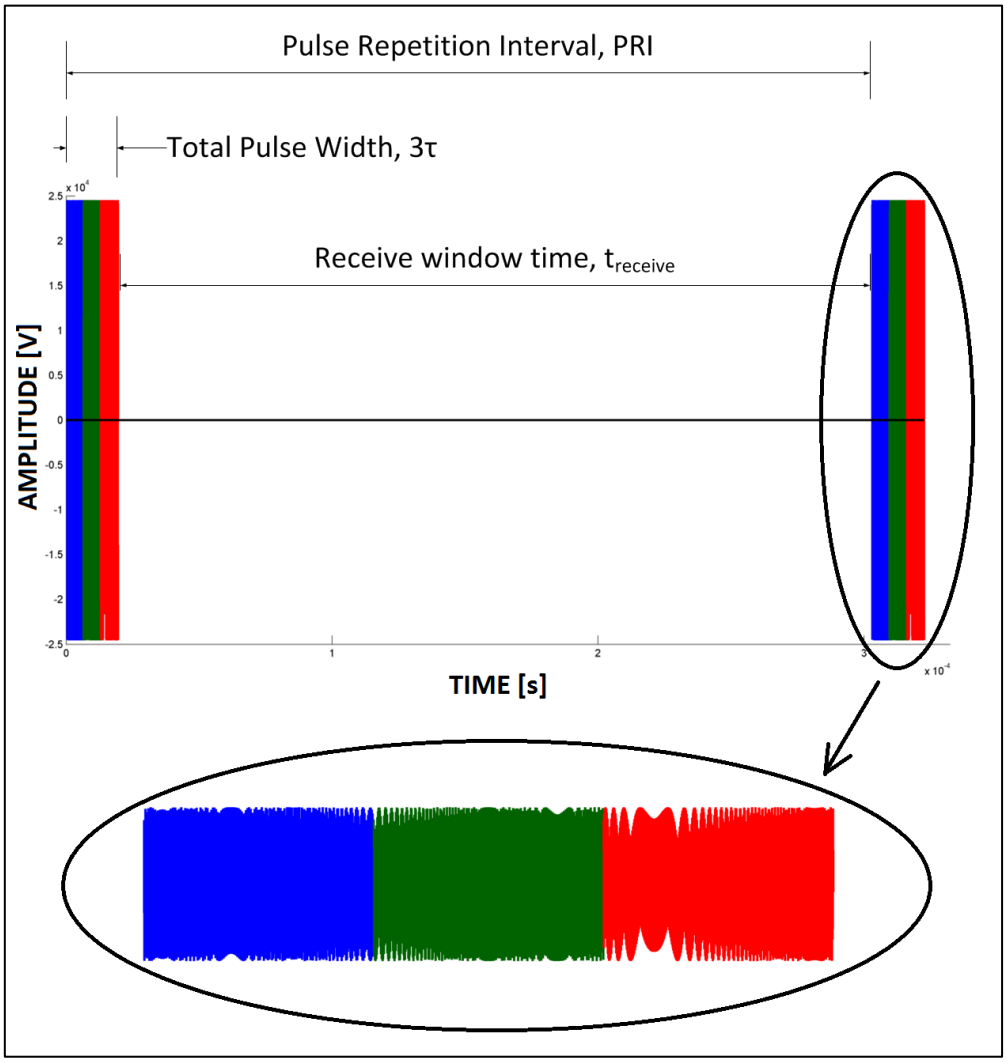

Figure 5: DBR Transmitted Signal definitions

After the three pulses are transmitted, the radar receives return signals during the "Receive Window" interval between transmitted pulses. This receive window interval defines the theoretical maximum range during which the radar can receive pulses before transmission of the next batch of pulses, after a "Pulse Repetition Interval (PRI)". Because the radar transmits three consecutive pulses, the receive window time is defined as:

$$t_{receive} = PRI - 3\tau \qquad (6)$$

According to the fundamental radar equation, relating signal time delay to range, the distance measurable by the radar is ([6]):

$$R_{recieve} = \frac{ct_{receive}}{2} \quad (7)$$

Because of the three-frequency operation, the Receive window interval is reduced by four pulse widths, which effectively reduces the "usable" range measured by the radar (processing of echoes from at all the three different frequencies per band, is done independently in separate processing channels).

Nevertheless, the use of three multi-frequency pulses increases the number of return echo samples by a factor three. In other words, three times more information is available for target parameter estimation. For the DBR X- Band subsystem the number of pulses transmitted per "Coherent Processing Interval (CPI)" is 31 x 3 = 93 pulses. The L-Band transmitter transmits 20 x 3 = 60 pulses. In total in a single CPI, 93 + 60 =153 samples of information can be processed. This substantially more data available for target detection and estimation compared to conventional radar. This DBR feature presents a challenge to a deception jammer, that has to simultaneously jam all three pulses per frequency per band, in order to deceive the radar.

Since three times more information is available for processing compared to a standard "single pulse" PD radar, full coherent processing is not completely necessary for all detection scenarios. Additional gain offered by coherent processing would be beneficial in long-range detection or small RCS detection; however, this capability adds complexity and cost to the radar hardware and processing.

For these reasons the DBR uses non-coherent integration for signal processing This processing capability is simpler to implement and computationally less intensive compared to coherent processing, but offers less processing gain. The non-coherent processing gain is proportional to the square root of the number of pulses integrated "$\sqrt{n_p}$" and is shown mathematically in equation (8):

$$SNR_{burst} = \sqrt{n_p} SNR_{single} \quad (8)$$

Besides the advantages offered by the large number of pulses, the three pulses are also modulated linearly at a different frequencies. Thus, a typical ES system would have difficulty in estimating the DBR signal parameters, since these frequencies would appear over a large bandwidth in the ES Receiver.

The L-Band PRF is classified to be in the "Low PRF" category. Because of this, the L-Band subsystem is more ambiguous in Doppler frequency estimation and less ambiguous in range

estimation compared to the X-Band Receiver. The use of dual bands therefore adds more flexibility for resolving ambiguous range and velocities even without the use of PRF agility.

Radar architecture

A radar functional block diagram representing core DBR architecture is shown in Figure 6. The architecture was developed to ensure efficient transmission and processing of the three-frequency signal information. The processing chains are duplicated per frequency and *per "Digital Beam forming on Receive" antenna element.* Since the DBR has 6 elements (See Table 6) this means that there 3 x 6 = 18 processing channels per band and 32 in total for both bands.

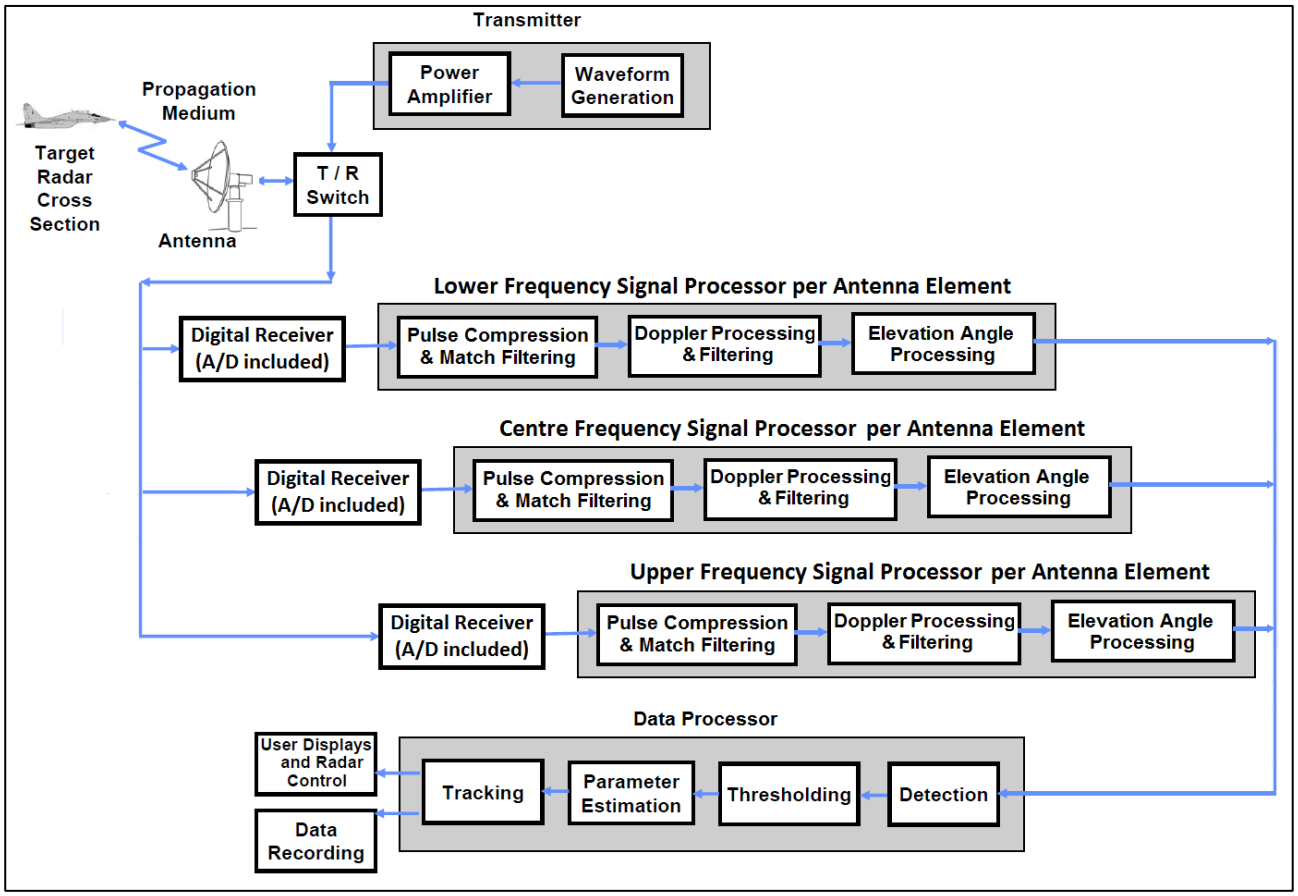

Figure 6: Radar Architecture (adapted from R.M. O'Donnell [8])

The structure shown in Figure 6 is duplicated for both L and X band processing chains.

The radar signal processor was simulated in detail in this study. Pulse compression (with match filtering), Doppler Processing and Elevation angle processing are some of the signal processing functions performed by the DBR signal processor depicted in Figure 6. Besides this processing, clutter rejection is also performed in the radar's signal processor. Once target information has been detected and clutter been rejected, candidate target "plots" are generated as an output of the signal processing stage. This information is then passed to the

"Data Processor", which performs target detection, thresholding and estimates detected target parameters. Eventually the Data Processor forms tracks from the confirmed plots and continues to track the targets. This information is then sent to the User by means of visual information displayed on a Human Machine Interface (HMI) display and the information is recorded. In a GBADS system, the output of the DBR would be used for Air Surveillance or Fire Control of Effectors as already described in section 1.1.2.

Radar model, Limitations and Assumptions

In this simulation, the transmitter signal is modelled. Transmit antenna losses are taken into consideration but internal transmission path losses and transmitter duty cycle effects were not. Parameter estimation and basic track formation was modelled but other data processing functions (detection, thresholding and track filtering) were not modelled on a signal-level. The system-level model considered Constant False Alarm Rate (CFAR) losses. Pulse Compression Gain, Non-Coherent Integration Gain, and Doppler Processing Gain, were accounted for. Antenna losses, Doppler windowing losses, Doppler straddling losses, Range straddling losses, Elevation angle straddling losses, Azimuth angle straddling losses and Azimuth beam shape losses were also taken into account.

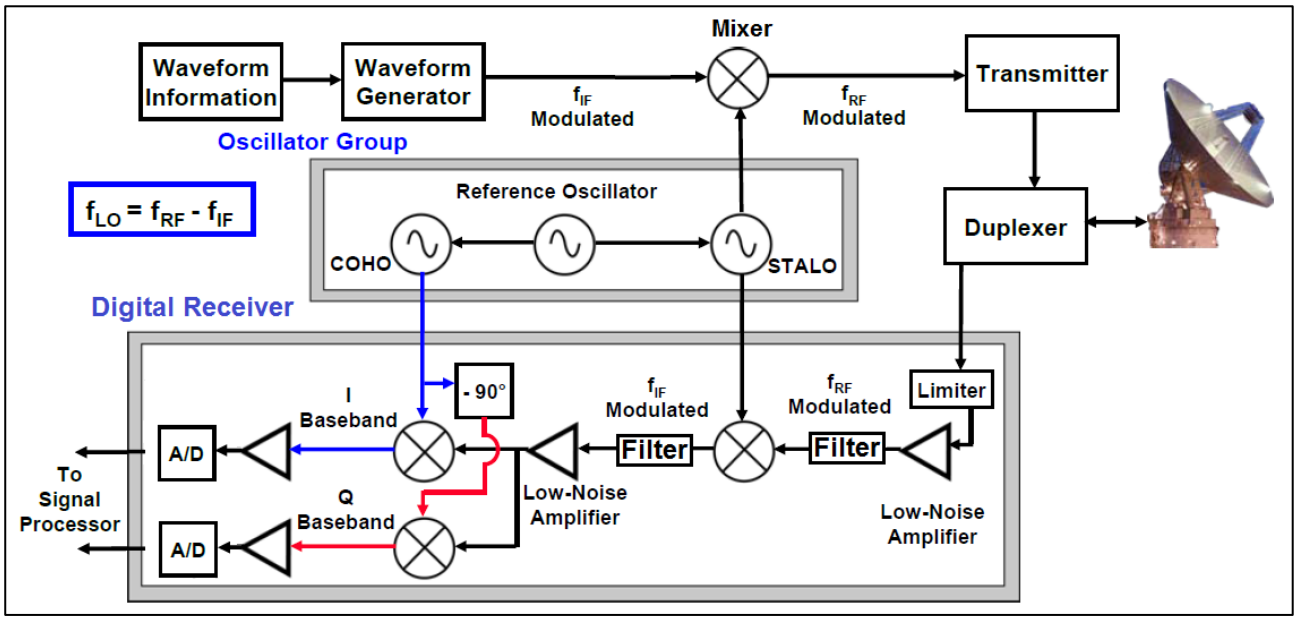

Figure 7: Detailed Schematic of Radar Receiver (adapted from R.M. O'Donnell [8])

The DBR digital receivers shown in the DBR architecture diagram of Figure 6 are shown in more detail in Figure 7. The diagram shows the DBR Digital Receiver schematic for a single processing channel at either L-Band or X-Band. A "Stable Local Oscillator (STALO)" and "Coherent Local Oscillator (COHO)" are used to ensure phase coherency between transmitter

and receiver. They are also used to supply the "Local Oscillator (LO)" frequency in the up and down conversion chains in the radar.

A DBR receiver has a "limiter" for receiver protection against close returns and other large returns such as close-in clutter. The signal is then processed using solid-state low noise amplifiers, mixers and filters followed by a Coherent Demodulator. The RF processing gain in X-Band was calculated as:

$$\begin{aligned} G_{r,proc} &= G_{LNA} - L_{Filter} - L_{Mixer} + G_{LNA} - L_{Mixer} + G_{LNA} \\ &= 30\,dbW - 3\,dBW - 8.5\,dbW + 30\,dbW - 8.5\,dbW + 30\,dbW = 70\,dBW \end{aligned} \quad (9)$$

The RF component gains and losses were assumed from a standard Low Noise Amplifier (LNA) and Mixer product specification. A representative loss of 3 dBW was assumed for the filter insertion loss at either the DBR X or L band frequencies. The product sheets for the "CTT Incorporated" LNA (AMX/00518-3522) and "Hittite Microwave Corporation" X-Band Mixer (HMC141C8) is included in Appendix 14.5 and 14.6, for the X-Band components.

The L-Band receiver RF processing gain was calculated in a similar manner and the same LNA and filters were used in the L-Band RF processing chain. However, the L-Band mixer is a different type (HMC423MS8/423MS8E). This product data sheet was also included in Appendix 14.7. The L-Band RF processing gain was calculated as shown below:

$$\begin{aligned} G_{r,proc} &= G_{LNA} - L_{Filter} - L_{Mixer} + G_{LNA} - L_{Mixer} + G_{LNA} \\ &= 30\,dbW - 3\,dBW - 8\,dbW + 30\,dbW - 8\,dbW + 30\,dbW = 71\,dBW \end{aligned} \quad (10)$$

After the received RF echo is finally down converted to baseband in the coherent demodulator it is passed to the DBR signal processor.

Throughout the simulation, it was assumed that the target approaches the radar from a single azimuthal direction, therefore azimuth measurement and estimation process was not modelled. However, the elevation angle measurement and estimation process was fully modelled. The reason for this seeming "inconsistency" is quite simple; Prioritization was given to simulating the functions of the DBR that are unique to it and then to simulate the jamming of those unique functions. Azimuth angle deception jamming is very difficult in practice, to achieve with a single jamming platform. However, if range, Doppler frequency and elevation angle are jammed, a single radar cannot track a target for fire control (to direct effectors). Exact target coordinates are therefore unknown.

The "three frequency dual band" operation, with "Digital Beam-Forming on Receive" for elevation angle measurement are the unique DBR capabilities and to the author's knowledge, the jamming of a radar with these functions *has never been done or documented before*.

1.2.3 Stochastic Signal Components

In order to simulate the true and false target signals or "target echoes" as accurately as possible some randomly behaved (stochastic) "real world" phenomena was simulated. Signal noise, "RCS fluctuation" dependent amplitude and measurement uncertainty were included to simulate the corresponding real world phenomena.

Signal Amplitude Modelling

Transmit signal amplitude "A_t", intercepted radar signal amplitude "A_{jr}", false target signal amplitude transmitted by the jammer "A_j", true target signal amplitude reflected off the target "A_{rr}" and false target signal amplitude received at the radar "A_{rr}" were all modelled using the "Signal Amplitude–RF Power Relationship". This relationship enabled the use of the *power forms* of the relevant *radar range* and *jammer performance* equations to be used to model the different signal amplitudes. The various signal amplitude models described above were not modelled in any of the textbooks or technical papers reviewed and are original derivations by the author.

In other words, the power forms of the radar range equation and jammer performance equations provided the basis for the definition of the various signal amplitudes. The following assumption was made regarding the relationship between signal voltage and RF power, from the textbook by Richards ([6])):

$$V \propto \sqrt{P} \tag{11}$$

In addition, inspection of Equation 18.2 in Richards [6] indicated that the power form of the radar range and jammer equations could be used to formulate the various signal amplitudes.

The relationship between signal voltage and RF power was then finalised using Blake [7]:

$$V_{rms} = \sqrt{P Z_o} \;\; \therefore V_{peak} = \sqrt{2}\sqrt{P Z_o} = \sqrt{2}\sqrt{50}\sqrt{P} = 10\sqrt{P} \tag{12}$$

Where

$$V_{peak} = \sqrt{2} V_{rms} \text{ and } Z_o = 50\Omega \tag{13}$$

Since the units of signal amplitude are "Volts", equation (12) is re-written as follows:

$$A = 10\sqrt{P} \tag{14}$$

By applying the simple relationship between signal amplitude and RF power, shown in equation (14), the useful system-level power forms of the radar and jammer performance could be harnessed for the signal-level modelling. The system-level radar and jammer performance models are discussed in sections 4.1 and 4.2, while signal level models are described in chapters 5, 6, 7, 8 and 9.

Noise

Signal noise is modelled as "zero mean white noise" with a Gaussian PDF. Complex noise samples are generated using following function:

$$noise(t) = \frac{U_{NR}(t) + jU_{NC}(t)}{\sqrt{2}} \tag{15}$$

Both U_{NR} and U_{NC} are zero mean random variables generated from a Gaussian PDF. The normalisation of the noise by $\sqrt{2}$ ensures the variance of the noise remains at 1, so that amplitude only is used to scale the signal SNR. This method of generating the noise was obtained from input received from Chris Mocke at the Council for Scientific and Industrial Research (CSIR), Radar department.

The noise is simulated as a function of time, so that a noise sample can be added to the relevant signal *per simulation time step* for NRT processing.

In this simulation, noise is included at both the signal level as well as system levels to mimic "real world" receiver noise effects. However, in the application of noise in the "signal-level" case, the signal amplitude functions did not make use of the radar or jammer receiver noise power in their amplitude functions. This is relevant since the amplitude functions are derived from the power form of the radar range and jammer performance expressions, where noise *power (in units of watts)* is explicitly defined. Therefore, the noise modelled using equation (15) is added to the signal models and has *units of volts*.

In the system-level simulation ("Radar System Model", section 4.1 and "Jammer System Model", section 4.2), noise power is included as a factor in the denominators for determining "maximum detection range" or "jammer burn-through range".

The use of noise power at both the signal and system levels is defined by M.A Richards et. al in reference [6].

Measurement Uncertainty

The error between *true* target coordinates in range, velocity and angle, and the *measured* target coordinates is randomly distributed. It is assumed that this radar measurement error is normally distributed according to a standard Gaussian distribution, with a standard deviation and mean (average). Measurement uncertainty is the "standard deviation" of the target measurement. The measured target coordinate is therefore normally distributed about the true target coordinate, which is assumed to be the mean of the distribution. The measurement uncertainty or "standard deviation" has been was modelled using equations developed by D.K.

Barton in his famous textbook "*Modern Radar Systems Analysis"* (reference [2]). In all of these expressions, measurement uncertainty is inversely proportional to SNR. Therefore, the radar measurement of the target coordinate becomes more inaccurate as the SNR decreases (or range increases). It is important to note, that the SNR in this context is the SNR *before mixer pre-amplification* (i.e. before RF processing gain is applied). Target range measurement uncertainty is defined from Barton [2] as:

$$\sigma_R = \frac{\Delta R}{\sqrt{2\,SNR_{burst}}} + 0.35\,L_r \tag{16}$$

Also from Barton [2], the velocity estimation standard deviations are:

$$\sigma_V^{centre} = \frac{\Delta v_{centre}}{\sqrt{2\,SNR_{burst}}} \tag{17}$$

$$\sigma_V^{lower} = \frac{\Delta v_{lower}}{\sqrt{2\,SNR_{burst}}} \tag{18}$$

$$\sigma_V^{upper} = \frac{\Delta v_{upper}}{\sqrt{2\,SNR_{burst}}} \tag{19}$$

Each frequency component of the DBR signal at L or X-bands has its own velocity measurement uncertainty. This is because velocity resolution "ΔV" is dependent on signal wavelength and the DBR has three wavelengths per frequency component at L and X-Bands.
This relationship between DBR velocity resolution and wavelength is shown in the expressions below:

$$\Delta v_{centre} = \frac{\Delta f_d\ \lambda_{centre}}{2} \tag{20}$$

$$\Delta v_{upper} = \frac{\Delta f_d\ \lambda_{upper}}{2} \tag{21}$$

$$\Delta v_{lower} = \frac{\Delta f_d\ \lambda_{lower}}{2} \tag{22}$$

Elevation angle standard deviation is given in the technical report by R. McAulay [33] as:

$$\sigma_\phi = \frac{1}{2\pi\left(\frac{d}{\lambda}\right)\sqrt{SNR_{pulse}}} \tag{23}$$

The measurement uncertainties described above are used in the "Radar Receiver Track Model", to randomize the range, velocity or elevation angle measurement before "*Range and Doppler folding*" and "*Angle wrapping*". These concepts and detailed application of the measurement uncertainty equations are described in detail in section 9.4.

1.2.4 Targets

Target parameters used in this simulation, are listed in Table 5. The DBR would be deployed to detect targets similar to these, in an actual deployment, which are examples of fixed wing and rotary wing aircraft and a missile.

	Fixed Wing	Rotary Wing	Missile
Swerling Model	1	1	3
Average RCS [m^2]	3	6	0.2
Speed Range [m/s]	20 - 400	0 - 200	150 - 1000
Elevation Range [deg]	0 - 40	0 - 40	0 - 40

Table 5: Target Parameters

Targets are modelled in the electromagnetic spectrum, as accurately as possible using the Swerling models as described by M.A Richards et. al in reference [6]. It was assumed that the target Radar Cross Section (RCS) decorrelation is on a "Scan-to-Scan" basis and not a "Pulse to Pulse" basis. Therefore, Swerling 1 and 3 models are applicable.

A Swerling 1 target type is selected for the fixed wing and rotary wing targets since one or two dominant scatterers are expected from these targets. A scatterer is an electromagnetically reflective section of the target. One target would have multiple scatterers.

The Swerling Type 1 model assumes that the target RCS is distributed exponentially ([6]):

$$p_\sigma(\sigma) = \frac{1}{\sigma_{average}} e^{-\frac{\sigma}{\sigma_{average}}} \tag{24}$$

For the missile target, a Swerling 3 RCS fluctuation is assumed, since multiple target scatterers are expected from the missile, with none of them dominant. In the Swerling Type 3 model, the target RCS is distributed according to the 4th Degree Chi Square Distribution as shown below ([6]):

$$p_\sigma(\sigma) = \frac{4\sigma}{\sigma_{average}^{\ 2}} e^{-\frac{2\sigma}{\sigma_{average}}} \tag{25}$$

The average RCS's "$\sigma_{average}$" for the three different targets, were used as inputs to the probability models described by equations (24) and (25), to obtain the random RCS's "σ" or "σ_f". The random RCS's values were used in the "Radar System" model as well as the "Signal Amplitude" models, to simulate target RCS fluctuations for the fixed wing, rotary wing and missile targets. Signal amplitude models use the RCS estimate in NRT processing.

Actual targets deviate from the standard Swerling models under certain conditions and present combinations of Swerling model types in some cases. This deviation of actual targets from the Swerling idealisations was not modelled.

1.2.5 Jamming Techniques and Methods

The manner in which jamming is carried out by the jammer has been categorised into "Techniques" and "Methods". Jamming techniques answer the question: "*what EA weapon is used?*", while jamming methods answer the question: *"how is the EA weapon used?"*

In a broad sense, primary *EA techniques* are categorised as follows:

- Active
  - Anti-Radiation Missiles (ARM's)
  - High Power Microwave (HPM) Devices
  - Electromagnetic Pulse (EMP) Weapons
  - Deception Jamming
  - Noise Jamming
  - Coherent Source Jamming
- Passive
  - Chaff
  - Decoys (Towed and "Droned")

It can be firstly seen, that the techniques can be divided into "Passive" and "Active" techniques i.e., those that require energy to operate and those that use the radar emitter's energy.

The "Active" techniques such as ARM's, HPM's, EMP's and "Passive" techniques such as Chaff and Decoys are assumed to have a similar effect on all radars, i.e. no unique DBR characteristic makes it more or less vulnerable to these techniques. This study therefore focuses on noise jamming, deception jamming and coherent source jamming techniques, whose effect on the radar varies greatly, with radar type and processing capability.

Noise jamming involves the transmission of either narrowband or wideband noise by the jammer to the victim radar, in order to raise the radar receiver noise floor level, sufficiently high enough to prevent detection of the target.

Deception jamming on the other hand induces false targets at "jammer specified" ranges and velocities, while coherent source jamming techniques such as "Cross-Eye" Jamming make use of "out of phase" coherent repeater signals to disrupt the radar's waves phase front, at the victim radar's antenna. Then any radar measurement mechanism that uses return echo phase information to estimate target parameters (such as elevation angle) is degraded by the jammer. These jamming techniques are discussed in detail in subsequent chapters.

To carry out the jamming techniques, a device called the "Digital Radio Frequency Memory" (DRFM) is used in the modern context. A DRFM-based jammer employing digital jamming techniques is the current "state of the art" for jamming platforms. It was deemed the highest priority radar threat in this study. This decision was based on a review of the EW suites on the international market, extensive "Institute for Electrical and Electronics Engineers (IEEE)" research in this area and recent advances in digital processing technology.

From the survey on ES systems shown in Appendix 14.4, it can be seen that 53 out of 62 ES systems from the major manufacturers of EW suites, are "digital" systems. The survey was conducted by members of the "Association of Old Crows (AOC)", and reported in the "Journal of Electronic Defence", reference [49].
New efficient Analog-to-Digital (A/D) and corresponding Digital-to-Analog (D/A) converters have enabled the DRFM ES and EA concept to be feasible and practical as discussed in detail by D. Schleher in reference [4].
Also, in the words of D. Adamy in reference [50]:
"The DRFM is an important development supporting electronic countermeasures. It allows the rapid analysis of complex received waveforms and generation of countermeasure waveforms. In can increase the effectiveness of a jamming system against complex waveforms by many dB".

According to the "World Defence Almanac 2013", (reference [53]), weapons used by African armies are generally less expensive and of a lower technological complexity compared to West or East European, Asian or Middle Eastern countries. For this reason, in the African context, noise jamming is also a high threat priority to the DBR, since this form of jamming can usually be carried out by a "low-technology" jamming platform that is cheap to field and easy to operate. The DBR would be fielded in the "African Battle-space".
However, the some of the advantages offered by noise jamming have been reduced, by recent signal, processing advances in radar such as Coherent Integration, Pulse Compression (PC) and Doppler Processing (DP).

The EA techniques discussed (deception jamming, coherent source jamming and noise jamming), can be employed using a variety of different "Jamming Methods". As stated in a similar way earlier; jamming methods answer the question: *"how is the EA weapon used?",* while jamming techniques answer the question: "*what EA weapon is used?*"

The primary *"EA methods"* are listed below:

- Rotary Wing, Fixed Wing and Ground Based
- Self-Protection Jamming (SPJ)
- Support Jamming (SJ)
- Stand-off Jamming (SOJ)
- Stand-in Jamming (SIJ)

Firstly, the platform carrying the EA weapon can be either airborne or ground based. The airborne platforms can be manned or unmanned, fixed wing or rotary.

Then the EA system can be on the attacking platform ("Self-Protection Jamming") or carried on "Escort" aircraft ("Support Jamming"). Figure 8 illustrates the difference between self-protection jamming and support jamming.

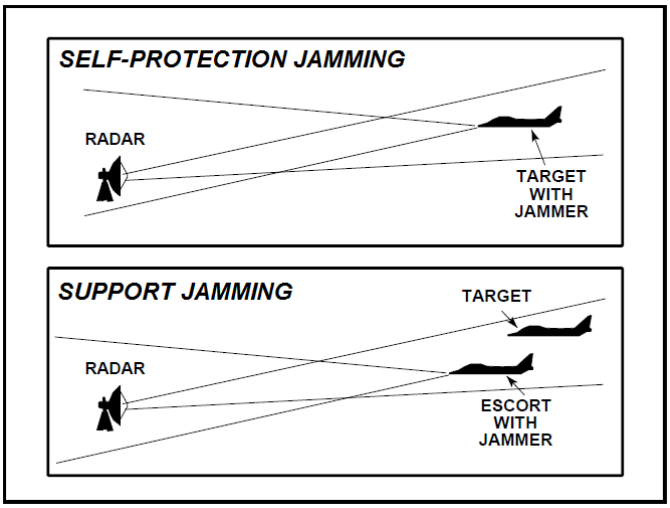

Figure 8: Self-Protection vs. Support Jamming [10]

The jamming can be either outside radar detection range ("Stand-off Jamming"), or within, ("Stand-in Jamming"). This difference is shown in Figure 9. In the stand-in jamming method, UAV's or ground-based jammers are usually employed.

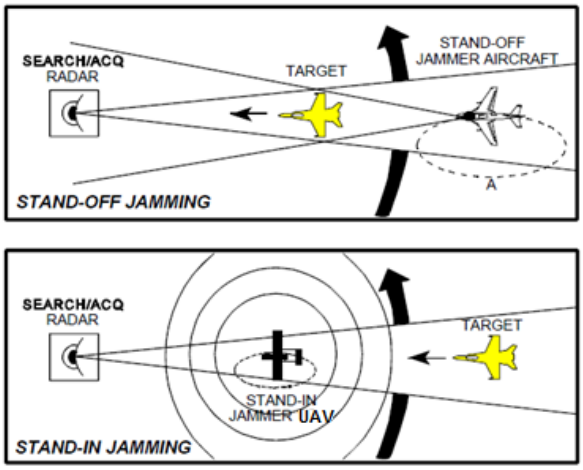

Figure 9: Stand-in Jamming vs. Stand-off Jamming [10]

The jamming methods considered in this study were focussed on simulating jamming methods used to carry out jamming techniques *against a GBADS Battery*. Therefore, the focus was on "stand-in", "stand-off" and "self-protection" jamming from airborne platforms. The simulation can be easily adapted to a specific jamming method easily, by selecting appropriate jammer parameters for the "Jammer Setup" file.

1.2.6 Jammer Architecture

Digital channelized receiver jammer architecture was developed in this study. The concept is illustrated in Figure 10. The jammer would use an array of "Sinuous Antennas" to intercept a radar signal of any polarisation in any direction over the entire radar frequency band. The sinuous antenna is shown in Figure 12. This antenna type is selected in ES applications, for its very wide 3dBi beam-width that allows signals from a wide range of Angle of Arrival's (AoA's) to be intercepted. The antenna gain pattern showing the broad 3dBi beam-width is shown in the top right of Figure 12. The large 3dBi beam-width feature of the antenna is the reason the antenna has been used broadly in practical EW systems such as the Saab Electronic Defence Systems Tactical ELINT and ES Systems for Submarines (see reference [52] and Appendix 14.8).

A microwave lens would be used to "mechanically" determine the AoA of the radar signal. A microwave lens is shown in Figure 11. It can also be used to replace the power divider shown in Figure 10 and perform exactly the same function as the power divider.

Multiple channels allow for multiple frequency signals across the 0.1 -18 GHz band, to be received and digitized. The proposed digital receiver is the "Delphi ADC3295". The datasheet for the device is included in Appendix 14.3. The receiver is well suited to implement the DRFM-based EA concept, against the DBR, since it has a wide bandwidth that is larger than the DBR signal bandwidths, if a channelized architecture that uses multiple digital receivers in parallel is used. The combination of full azimuth and elevation angle antenna coverage with large bandwidth, give the proposed DBR ES system a 100% Probability of Intercept (POI) range. As stated mathematically by J.B. Tsui in reference [5], the POI for azimuth angle is:

$$POI_{\theta}^{AOA} = \frac{\theta_{3dB}}{\theta_T} \tag{26}$$

$$POI_{\phi}^{AOA} = \frac{\phi_{3dB}}{\phi_T} \tag{27}$$

The DBR Jammer "Spiral Cavity Backed" antenna array covers the entire 360° azimuthal and elevation angular area of interest. Therefore both the azimuth angle POI "POI_{θ}^{AOA}" and elevation angle POI, "POI_{θ}^{AOA}" are 100%. The wide instantaneous bandwidth of 2GHz per ES receiver channel ensures that the entire frequency range of interest is covered, which means

the bandwidth POI "POI_{BW}" is also 100%. The expression for the bandwidth POI is shown in equation (28).

$$POI_{BW} = \frac{B_j}{B_r} \tag{28}$$

Then, individual POI values are multiplied to obtain the overall ES system POI:

$$POI = POI_{\theta}^{AOA} POI_{\phi}^{AOA} POI_{BW} \tag{29}$$

In the DBR Jammer configuration proposed it is assumed the POI would be 100%. This assumption is a reasonable one, based on inspection of an actual POI from the Saab product specification for a submarine Tactical ELINT and ESM system, included in Appendix 14.8.

The proposed jammer architecture shown in Figure 10 was derived from descriptions of the digital channelized receiver in the textbooks written by Schleher [4], Tsui [5] and P. Tang's technical report (reference [41]). The DBR Jammer architecture shown in Figure 10, would allow radar signals to be intercepted and processed in near real time (NRT) by an actual ES system. However, computer processor limitations on the author's commercial laptop (Dell Latitude E6500 Commercial Laptop) do not allow the ES signal interception simulation to be run in NRT. Because of this limitation, the ES simulation model simulates the processing and parameter estimation of the intercepted radar signal "off-line". Once the parameters have been estimated, a false echo signal injection (false range, velocity and height) is injected into the simulated radar receiver in NRT.

Clutter was not simulated, since the false target signal must be greater than the received clutter power at the radar in order to be detected above the CFAR threshold. If this was not the case, the false target would not be detected by the radar, thus defeating the purpose of this simulation. In fact, the false target amplitude should be even larger than the true target amplitude, to deceive the radar. Therefore, the detection of the false target in clutter would be better than detection of the true target in clutter. Modelling clutter would therefore add substantial complexity to the model without adding substantial benefit.

An assumption made was that the simulated false target amplitude was similar to the true target echo magnitude in this simulation. In an actual jammer, the ES system constraint of determining the correct false target echo power in order to mimic accurately the true target would be overcome by knowledge of the AOA, range to the target radar, radar frequency band and obviously received signal amplitude. The required magnitude of the false target signal level was investigated and discussed in section 4.2.

A concluding remark on the DBR Jammer is that it is *critical* for its ES subsystem to estimate intercepted radar signal parameters as accurately as possible, in order for EA subsystem to mimic the true target signal as accurately as possible. These two EW subsystems must therefore by "tightly integrated" in order for them to interoperate effectively.

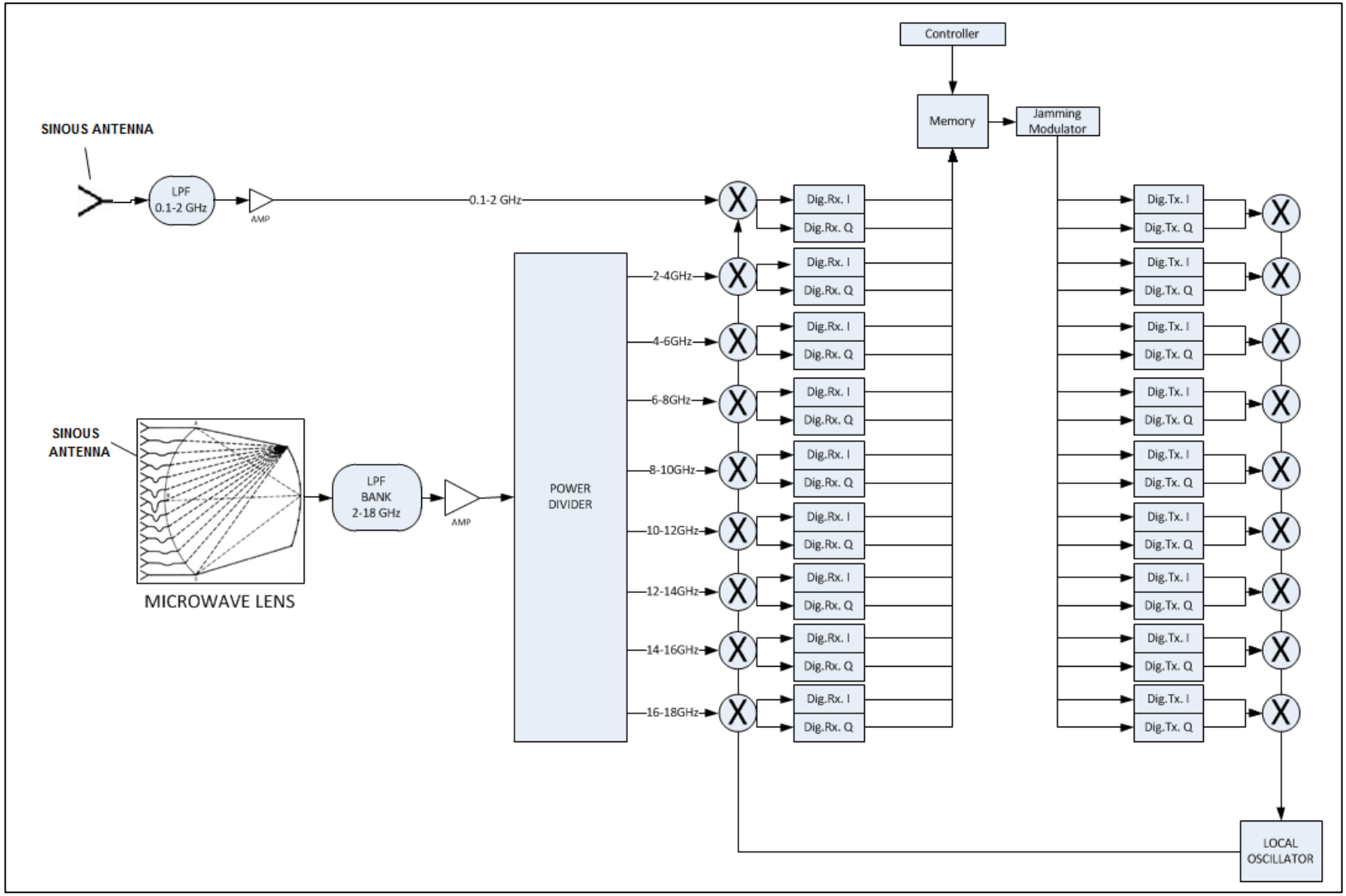

Figure 10: Jammer Architecture, Digital Channelized Receiver

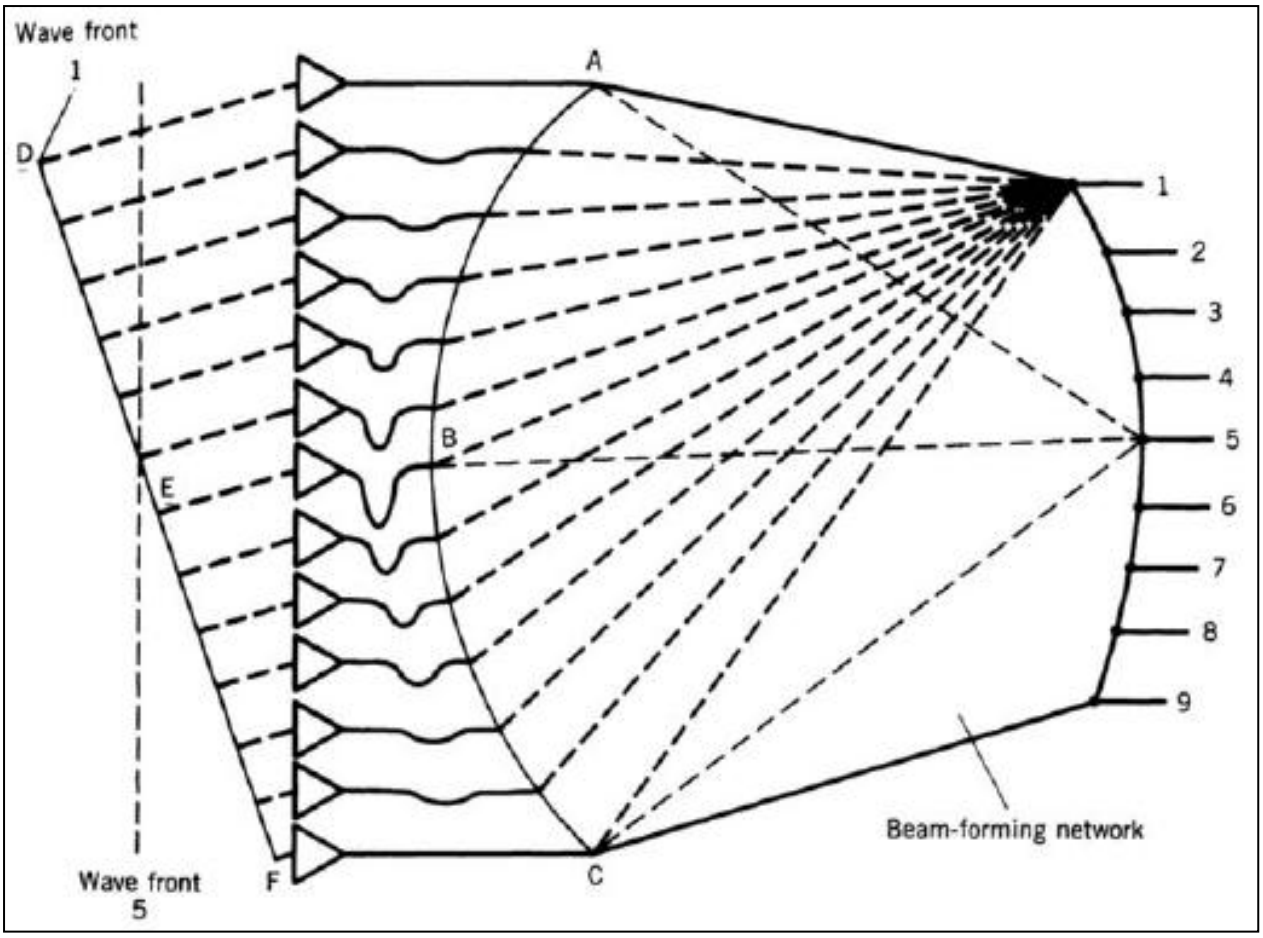

Figure 11: Microwave Lens [5]

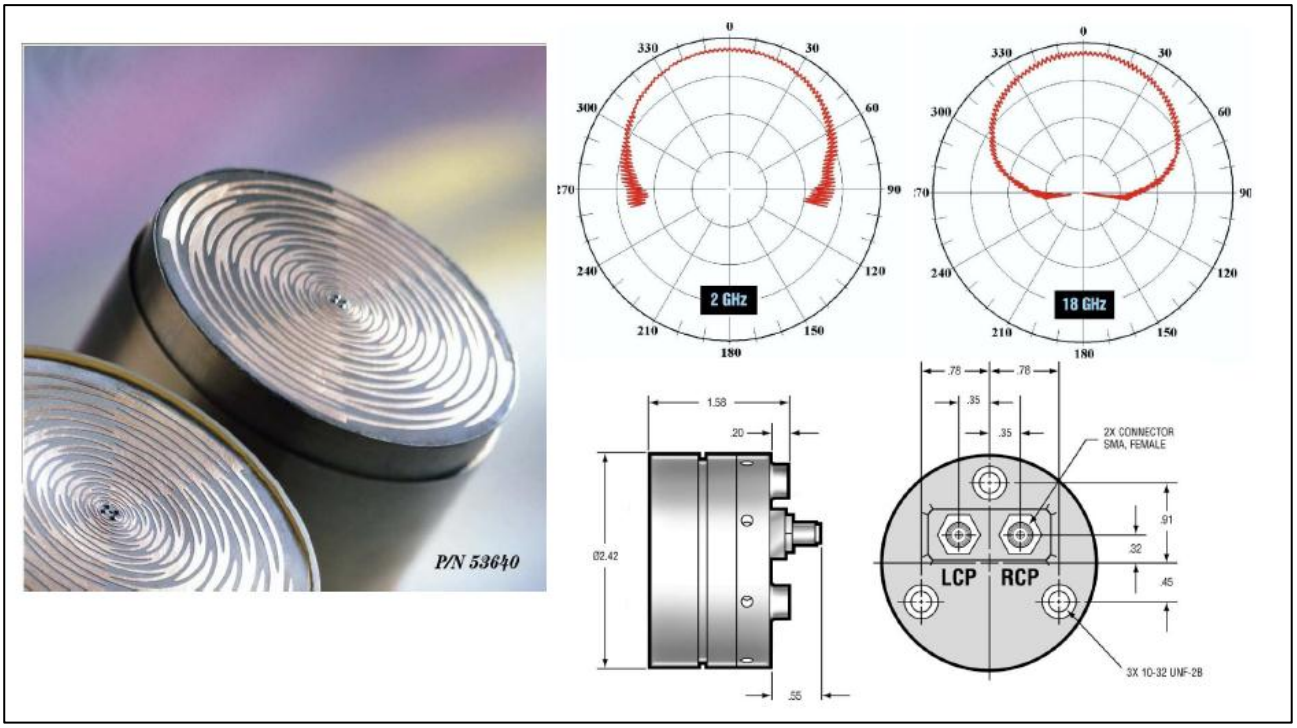

Figure 12: Sinuous Antenna [48]

1.3 Overview

The EW techniques required to effectively jam an advanced Air Surveillance, Acquisition and Tracking Radar was simulated in this study.

The radar is called the "Dual Band Radar (DBR)". It is capable of dual band operation in the X and L Bands simultaneously. Frequency diverse time-shared LFM pulses are used as radar signals. The radar is a "3D" radar, since it is capable of estimating target height through measuring and estimating multiple target elevation angles. The radar can also measure target azimuth angle and range.

Two "views" on the finding solutions to the problem were taken, to reduce complexity. The problem was examined from both a "signal-level" perspective, and from a "system-level" view. This principle of partitioning a complex problem into two abstract levels in order to solve it is called the "System Approach".

Typically, the "Signal (or Analytic) Approach" to problem solving is usually applied to individual elements of the problem without any regard for their interaction. This approach typically leads to an overall solution that is not streamlined or impractical to implement.

The System approach, on the other hand considers links and interactions of subsystems to one another *as well as* the environment, while the "Signal/Analytic" approach analyses the subsystems or system partitions only without regard to the interactions between partitions. A combination of the two thinking philosophies and balance between them is generally the best method to solving complex problems. This approach to problem solving is a fundamental principle in a thinking process called the "Systems Thinking Process". It is a well-documented principle in the theory of Systems Engineering and described in the "Systems Engineering Handbook" (reference [11]).

The signal-level dimension is intended to assist in visualisation of the various radar phenomena and measurement mechanisms. Generally, it is only once this visualisation of a problem is complete, can it be understood properly, described mathematically and then solved. The signal-level visualisation allowed insight into the EA techniques that are best suited to jamming the DBR. Extensive research into EA techniques and algorithms was also done. The selected EA algorithms were then, modelled and simulated on a "signal-level". The effect on the DBR for a single-plot was then tested. Thereafter, the simulation was extended to include multiple-plots to form a track so that true and false target trajectories could be simulated and tested.

Concurrent with the signal-level simulation, the system-level simulation was developed. This level of abstraction was used to simulate radar and jammer performance. Some interaction between signal-level and system-level models was necessary. For example, the signal amplitude modelling and measurement uncertainties, required system-level parameters as inputs. For example, consider the following equation from Barton [2]:

$$\sigma_R = \frac{\Delta R}{\sqrt{2\,SNR_{burst}}} + 0.35\,L_r \qquad (30)$$

From equation (30), it can be seen that signal-level range measurement uncertainty "σ_R" is dependent on the system-level "SNR_{burst}". On the other hand, in the system-level models, requirements such as "maximum DBR detection range", "Jammer Burn-through range" and "maximum ES system intercept range" were determined. These requirements then provided higher-level constraints to which the signal models must comply.

The "System vs. Signal" simulation philosophy selected was successful in that, it exposed the DBR vulnerabilities to EA, which was the intent in adopting the philosophy. This is a positive development, because possible EP measures were thereafter recommended to counter the simulated EA techniques.

The structure of all the individual chapters within this report is shown in Figure 17 and the contents of the chapters are summarized below.

Chapter 1

Introductory remarks and background information for the study is provided in this chapter. The DBR operational environment is described initially. Thereafter, important points on the simulation test scenarios are discussed. The extent to which the radar, jammer, targets and signals are modelled is also described in this chapter. Important fundamental information for understanding the simulation is provided here.

Chapter 2

A literature review of research material used in this study is described in this chapter. The research material consisted of standard radar textbooks, a Matlab toolbox and IEEE technical reports. The topics researched were:

- Radar Modelling
- Digital Beam forming
- Electronic Support Measure Algorithms
- Low Signal to Noise Ratio Electronic Support Measure Algorithms

- Electronic Attack Algorithms
- ES and EA System Architecture
- Electronic Protection Methods

Summaries of the research on the relevant topics listed are presented in the logical order in which the "radar-target-jammer" engagement naturally occurs.

At the end of every section, a summary *comparing* and *contrasting* the key points in all the technical reports researched is provided. "Coherent sense" is made of all the references researched in a particular section of the chapter (using "Systems Thinking"), explaining the applicability of the research to this study.

Chapter 3

In this chapter, the structure of the simulation software program as it was coded in Matlab is discussed. In addition, the information necessary to run the simulation is also included in this chapter, which consists of the inputs and outputs from the simulation as well as simulation controls or features. A list of all the files used in this simulation and their basic function within the simulation is included in Appendix 14.1.

Chapter 4

System-level performance aspects of both the radar and the jammer are investigated, simulated and discussed in this chapter. Extensive use is made of the "Radar Range Equation" and Jammer "One way Link" equations to analyse radar and jammer performance.

The system performance simulation of both the radar and jammer generate lower level requirements in terms of required power output, antenna gains, and equipment losses necessary to achieve a particular detection or burn-through range.

Maximum radar detection range, burn-through range, maximum ES Intercept range, jammer response time and jammer transmit power requirements are all investigated and discussed in this chapter.

Chapter 5

All the information necessary to simulate the DBR transmitted signal are described in this chapter. A logical simulation flow, following the actual transmission path of the signal, from when it is transmitted, interacts with the jammer and true target and is finally returned to the radar was followed in this study. The start of the process for the signal is described in this chapter. Mathematics describing the transmitter signal model is initially presented, followed by the "Simulation Functional Flow (SFD)" block diagram. The SFD is a visualization tool to aid the reader into understanding the implementation of the mathematics in the software. This is

followed by presentation and analysis of results obtained from the implemented mathematics. An important result showing the transmitted pulses, as they would be transmitted by the DBR is shown in Figure 13. It can be clearly seen from this figure that the signals at the three frequencies per band are transmitted consecutively.

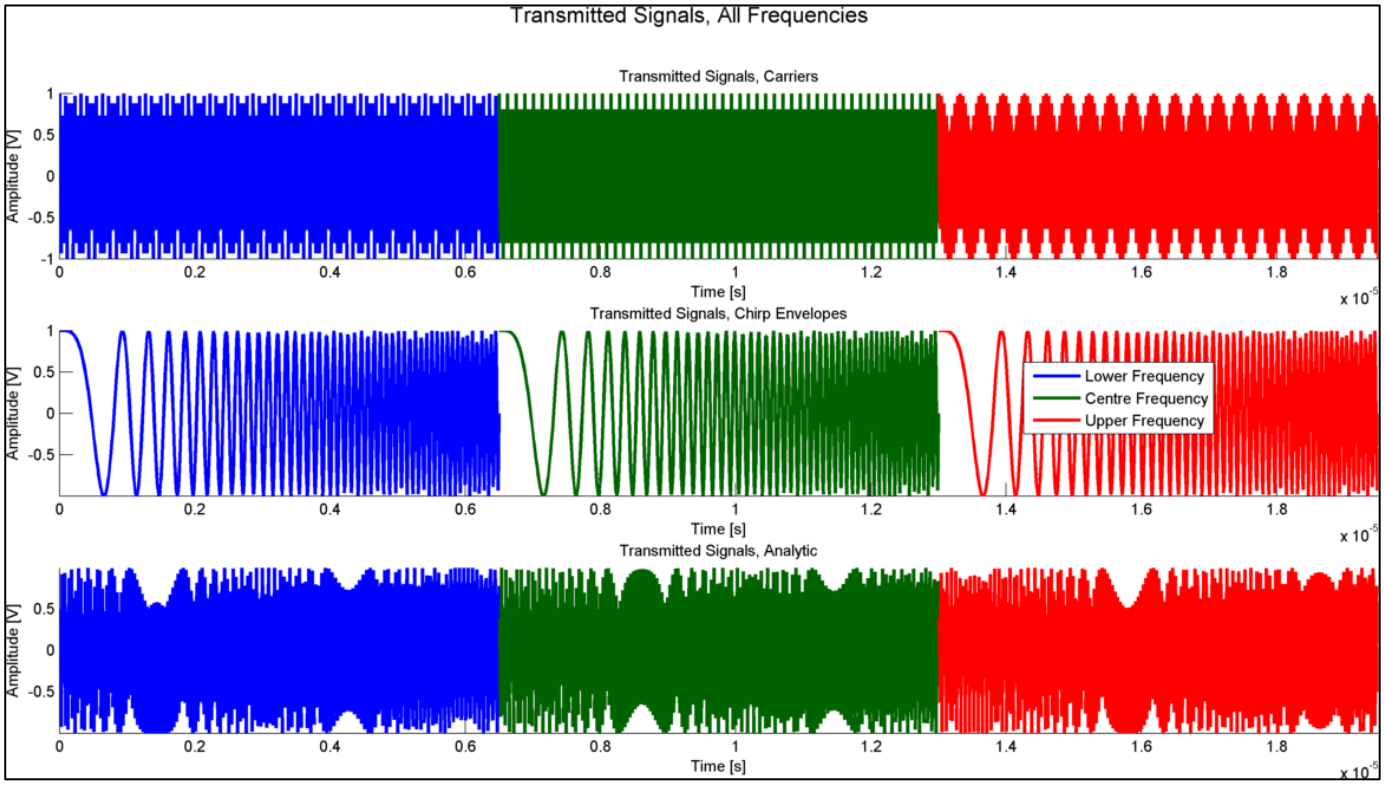

Figure 13: Transmitted Signals, X-Band

Chapter 6

The signal parameter estimation of the intercepted radar signal by the DBR Jammer's ES subsystem is described in this chapter. The effectiveness of the entire jamming process is highly dependent on the capability of the ES system to estimate *accurately* the victim radar's signal, without being detected by the radar. If the intercepted signal parameters are estimated, accurately and quickly, then the replicated false target would closely resemble a true target, and the radar would be deceived. The radar would then be jammed, even before it detects the presence of the jammer or tracks the true target in order to attack it, by means of fire control of effectors.

This chapter follows a similar structure to all of the "Signal Model" chapters. The fundamental mathematics describing the intercepted signal parameter estimation is initially described.

Then the ES algorithms and methods used and tested are presented. The process to estimate intercepted transmitted signals was made clear by using the favourite ES algorithm for intercepted *LFM* signals, namely the "Wigner-Ville Distribution". An example of the Wigner

Ville Distribution (WVD) output is shown in Figure 14 below. The time-frequency (TF) relationship of the intercepted signal is visible, immediately. This TF relationship is exploited by the ES subsystem, to obtain the radar signal parameters.

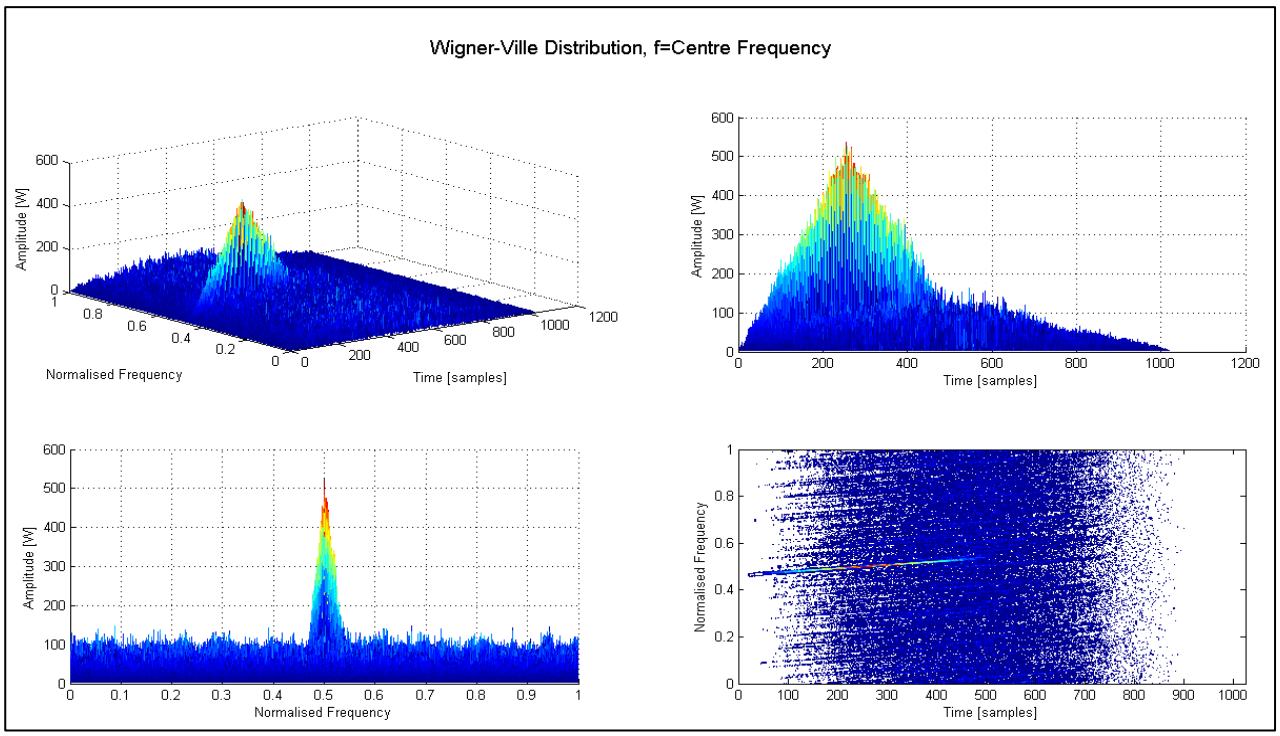

Figure 14: WVD of Intercepted Signal

The parameter estimation results are presented *and discussed* and efficiency of the methods and their practicality is discussed thereafter at length. Use was made of "Monte Carlo" analysis methods, to analyse practically, the performances of the proposed algorithms against older, conventional methods.

Chapter 7

The synthesis of the false target signal by the Jammer is described in this chapter. Mathematics defining the false signal definitions is described in detail. The chapter builds up the signal model with increasing complexity from a basic level, in order to aid understanding. For example, the signal definitions are presented in the following order of increasing complexity:

- False Stationary Target Echo
- False Moving Target Echo
- False Moving Target Echo with Elevation Angle
- False Moving Target Echo with Cross-Eye Jamming

All of the information necessary to generate a false target signal and a description of the process developed to inject the false signal into the radar is described in this chapter.

Chapter 8

In this chapter the estimation of "*single-plot"* target parameters for true and false target detection by the radar receiver are discussed and analysed. Chapter 9 is the second chapter on radar receiver operation, but the estimation of true and false target parameters from "*multiple-plots" (or "tracks")* is discussed there. A "plot" is a single radar measurement point, containing target coordinates in range, Doppler, azimuth and elevation angle. However, in this simulation the targets are assumed to approach along a single azimuthal direction. This assumption has been explained in section 1.2.2.

In other words, the analysis of target information from a single "Range-Doppler-Elevation Angle" bin is discussed in this chapter, while the analysis of "Range-Doppler-Elevation Angle" information over multiple bins is discussed in Chapter 9. Target echoes from the true target metallic surface and synthetic false signals from the DRFM Jammer on the Jammer Platform are received at the radar and processed. The aim of this portion of the simulation is to determine target range, velocity and elevation angle at a fixed azimuthal angle relative to the radar.

The mathematics describing the signal model is discussed initially followed by the SFD and simulation results. An example of the output of the Range Estimator module of the DBR receiver is shown in Figure 15. The true target echo of a rotary wing aircraft and missile is jammed by the DBR Jammer, which uses two similar false targets slightly offset in range and higher in amplitude to deceive the radar. After all the range estimator results are presented, a *detailed discussion* of the results is provided per subsection.

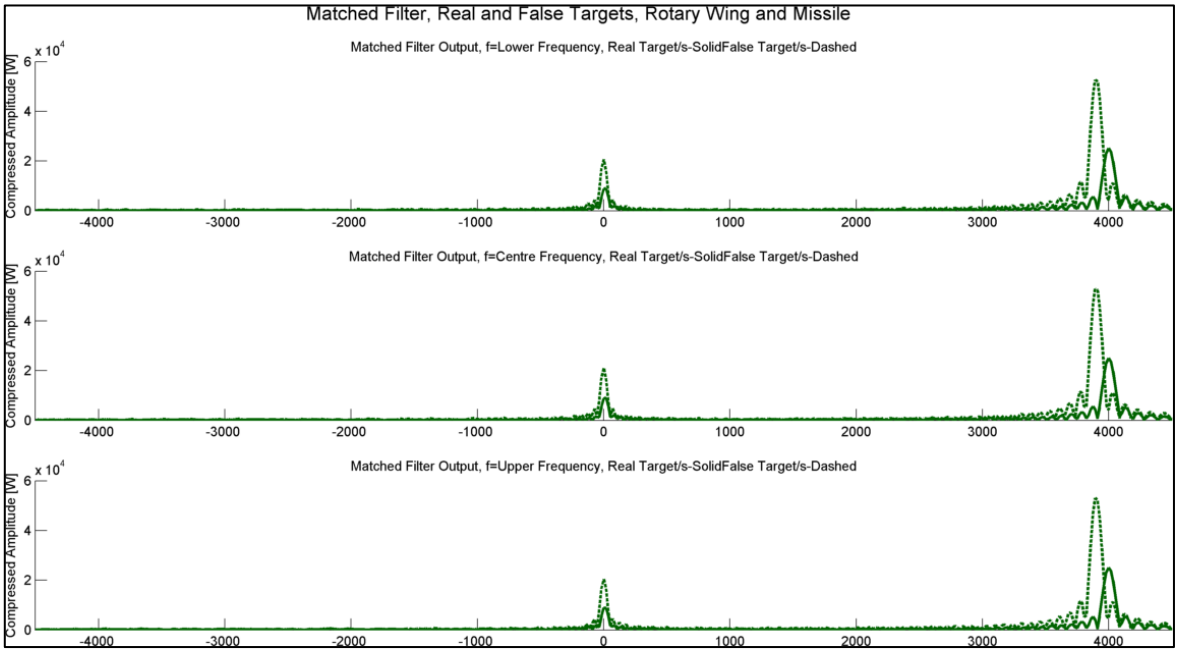

Figure 15: L-Band Range Match Filtered Response, Cover Pulse Jamming

Chapter 9

The Radar Model in "Multiple Plot" or "Track Mode" is discussed in this chapter. Radar receiver models for simulating the measurement and estimation of target range, velocity and elevation angle as described in Chapter 8 are used in this section of the simulation. However, in "multiple-plot" mode, the radar receiver's "single-plot" estimation models are "called" repeatedly over the entire vector of target ranges, velocities and elevation angles. Simulating the radar operation in this manner provides an estimated target coordinate per simulation time step. One major advantage of simulating the radar operation in this manner is that any error in the single-plot implementation is made apparent over the numerous simulation cycles necessary to generate the target track. Another feature of the "multiple-plot" mode simulation is that the single-plot mode figures can be run dynamically, as the track is generated. For example if the range match filter switch is activated in multiple-plot mode as the track is being generated and estimated, the functioning of the match filter per plot is visible. The user can therefore dynamically visualise the exact process at the single-plot level in NRT.

In this chapter, the mathematical foundation to the simulation multiple-plot mode is initially described, followed by presentation of results. An important result simulated in this chapter was the "range estimation variance comparison". The range estimation variance calculated by *repeatedly running the simulation in "single-plot"* mode (multiple-plot mode in other words) is shown in Figure 16. The simulated range estimation error was compared to the theoretical range estimation error defined by Barton in reference [2] and shown in equation (16). By comparing the trend line of the simulated (or measured) range estimation variance to the theoretical variance, it can be concluded that this DBR simulation model is of the correct fidelity. This is because both trend lines are closely spaced. At the end of the chapter, all of the results are collectively interpreted for the range, velocity and elevation angle estimators and *conclusions are drawn* from the results.

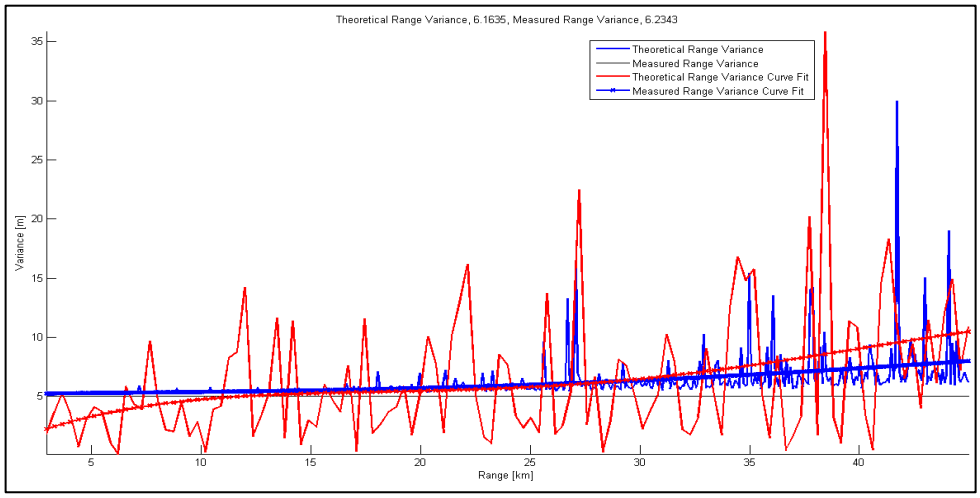

Figure 16: X-Band Theoretical Range Measurement Variance

Chapter 10

Overall conclusions made from the entire study are discussed in this chapter. The primary conclusion from this study is that the DBR can be effectively electronically attacked, if a modern EA system is used. Modern in this context, is classified as "digital EA", with a particular focus on digital "Deception Jamming" and "Cross Eye Jamming" using a DRFM. DRFM's can be built from COTS hardware that is available commercially.

It is concluded that the DBR Jammer proposed can effectively jam the DBR's range, velocity and elevation angle estimators, *in theory*. The azimuth angle estimator cannot be jammed using only one DBR jammer, however target azimuth angle information alone, cannot be used by the radar to track the target, in order to engage it with anti-aircraft weapons. Practical design constraints on the jammer would reduce the jamming effectiveness.

The conclusions are followed by recommendations for implementing EP on the DBR and improving the simulation model. For example, the importance of using "Pulse Diversity" to counter the effects of DRFM based jammers, simulating a wider range of EA techniques and optimizing the simulation for complete NRT processing are all discussed in this section of Chapter 10.

Chapter 11

The abbreviations list of all of the acronyms used in this report are described in this section. The list is arranged in alphabetical order, with abbreviations starting with a different alphabet, separated for "ease of readability".

Chapter 12

Every symbol used in this report is listed in Chapter 12. Where applicable, the symbols from all of the references researched *were standardized* to reduce complexity in understanding the mathematical formulations. The "List of Symbols" in Chapter 12 is organised into the "English Symbol" section as well as "Greek Symbol" section in order to simplify organisation of the list. To further simplify presentation to reduce complexity, the symbols are arranged in alphabetical order in both the "English" and *"Greek"* sections with descriptions and units.

Chapter 13

All of the references used in this document are listed in chapter 13. General information on the topics was contained in textbooks. Detailed and specific information was described in the form of "IEEE Technical Reports". For example, no textbook describes in detail, the Electronic Attack algorithms applicable to the DRFM deception jamming techniques, but this information was contained in various IEEE technical reports. Applicable subjects described in the *textbooks* were emphasized in this literature review only and not summarized in detail. This was done for the sake of brevity.

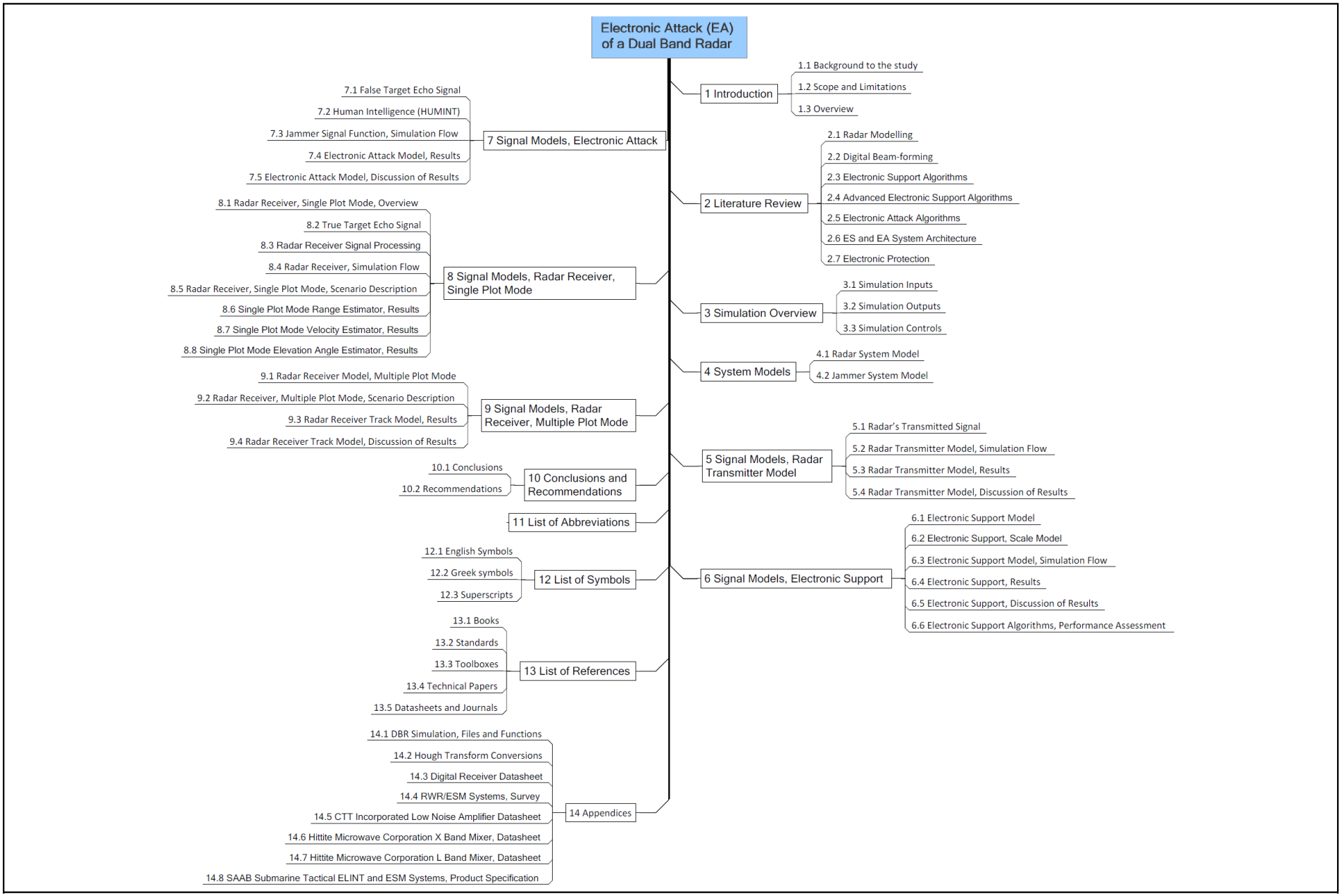

Figure 17: Dissertation Structure

2 Literature Review

Research material consisted of standard radar textbooks, a Matlab toolbox and IEEE technical reports. The topics researched were:

- Radar Modelling
- Digital Beam forming
- Electronic Support Measure Algorithms
- Low Signal to Noise Ratio Electronic Support Measure Algorithms
- Electronic Attack Algorithms
- ES and EA System Architecture
- Electronic Protection Methods

Summaries of the research on the relevant topics listed are presented in the logical order in which the "radar-target-jammer" engagement naturally occurs.

At the end of every section, a summary comparing and contrasting the key points in all the technical reports researched is provided.

General information on the topics was contained in textbooks, while the detailed and specific information was described in the form of "IEEE Technical Reports". For example, no textbook describes in detail the Electronic Attack algorithms applicable to the DRFM deception jamming techniques, but this information was contained in various IEEE technical reports. Applicable subjects described in the *textbooks* were emphasized in this literature review only and not summarized in detail. This was done for the sake of brevity. All of the references described in this chapter are listed in chapter 13.

2.1 Radar Modelling

The radar textbooks mentioned in this section provided most of the necessary information on the subject of radar modelling. The three papers on radar modelling provided interesting information, not found in the standard texts.

2.1.1 Textbooks

B Mahafza [1] explained the LFM signal models clearly and in detail.

The basic definition of the LFM signal, relationships between LFM variables and LFM signal processing is described. The theory regarding range "Match Filtering" is also well described. In particular, match filtering of a target echo from a transmitted LFM pulse is analytically defined. The dependency of a match filter of a LFM pulse on an uncompensated target echo Doppler frequency is described.

The simulations of all the common radar functions are well described in this textbook by B. Mahafza [1]. Numerous supplementary Matlab simulations are included to complement the theory.

Barton, in reference [2] describes fundamental equations on radar system performance and radar measurement uncertainty. These equations are easy to understand and implement. A big advantage of this book is that it is a well-established text on radar, whose methods and algorithms have been used successfully, over many years, by numerous radar engineers.

Valuable theory regarding the specific implementation of the Discrete Fourier Transform (DFT) in Matlab is described by D. Hanselman [3]. This book is a good basic user guide for Matlab implementation of the radar algorithms.

The IEEE Radar System Engineering Course Notes by R. M. O'Donnell [8] gives an excellent concise overview of radar, from the fundamental equations to advanced techniques such as Pulse Compression and Doppler Filtering. Basic radar architectures are well described in this text.

For this study, the prime radar textbook has been the book by M.A. Richards [6]. Basic to intermediate level radar theory, is described in this book. Fundamental radar relations are clearly explained. Doppler processing techniques and frequency fold-over effects are also described. The textbook also describes DFT sampling limitations and nuances clearly.

2.1.2 Technical Reports

Brief summaries of the technical reports researched are included in this section. If the technical report was an emphasis or corroboration of work summarized before it, its summary was made compact for the sake of brevity. At the end of the technical report summary, the relevance of the material researched, was emphasized.
The following technical reports are summarized in this section:

- *"Universal Equations for Radar Target Detection",* reference [18]
- *"Target Velocity Estimation with FM and PW Echo Ranging Doppler Systems Part I: Signal Analysis",* reference [22]
- *"Target Velocity Estimation with FM and PW Echo Ranging Doppler Systems Part II: Systems Analysis",* reference [23]

Universal Equations for Radar Target Detection

D. K. Barton [18] presents an interesting simplified model for target RCS modelling. The theory originates from research conducted by Russian scientists. In the paper he states that all the Swerling Models can be represented by a single Probability Density Function (PDF), instead of the different types ("Exponential", "Chi-Square", etc.), usually used to represent RCS target fluctuations per Swerling Model.

The universal equations represent the four *fluctuating* Swerling targets by a Chi-Square Distribution:

$$f(x,d) = \frac{1}{\Gamma(d/2)} e^{-x/2} \left(\frac{x}{2}\right)^{(d/2)-1} \tag{31}$$

A single set of expressions for the Probability of Detection "P_d" and *required* Signal to Noise Ratio or Detectability Factor "D", for all four Swerling targets were developed. In these equations the integral of the Chi-Square Distribution "K_m" or its inverse "K_m^{-1}" was the core function. The equations are:

$$P_d(SNR_{pulse}, P_{FA}, n_p, n_e) = K_m \left[\frac{K_m^{-1}(P_{FA}, 2n_p) - 2(n_p - n_e)}{\frac{n_p}{n_e} SNR_{pulse} + 1} \right] \tag{32}$$

$$D(P_d, P_{FA}, n_p, n_e) = \left[\frac{K_m^{-1}(P_{FA}, 2n_p) - 2(n_p - n_e)}{K_m^{-1}(P_{FA}, 2n_p)} - 1 \right] \frac{n_e}{n_p} \tag{33}$$

The integral of the Chi-Square distribution "K_m" is related to the "Incomplete Gamma Function" as follows:

$$K_m(x,d) = 1 - \Gamma\left(\frac{d}{2}, \frac{x}{2}\right) \tag{34}$$

Both "K_m" and the incomplete Gamma Function "$\Gamma(a,b)$" are functions that are easy to solve, particularly since these are built-in functions implemented in programmes such as Matlab or Mathcad. Equations (32) and (33) can thus be used easily to find "P_d" and "D", without the typical equation solving, root finding, integrations or double summations that are usually required in the traditional sense. The performance curves obtained using equations (32) and (33) were compared to the curves obtained using the traditional methods, as described in references [1], [2], [6] and [8]. These curves from reference [18] are shown in Figure 18. Performance curves generated using traditional methods are shown by the solid lines, while performance curves generated using the new method are depicted by dotted lines.

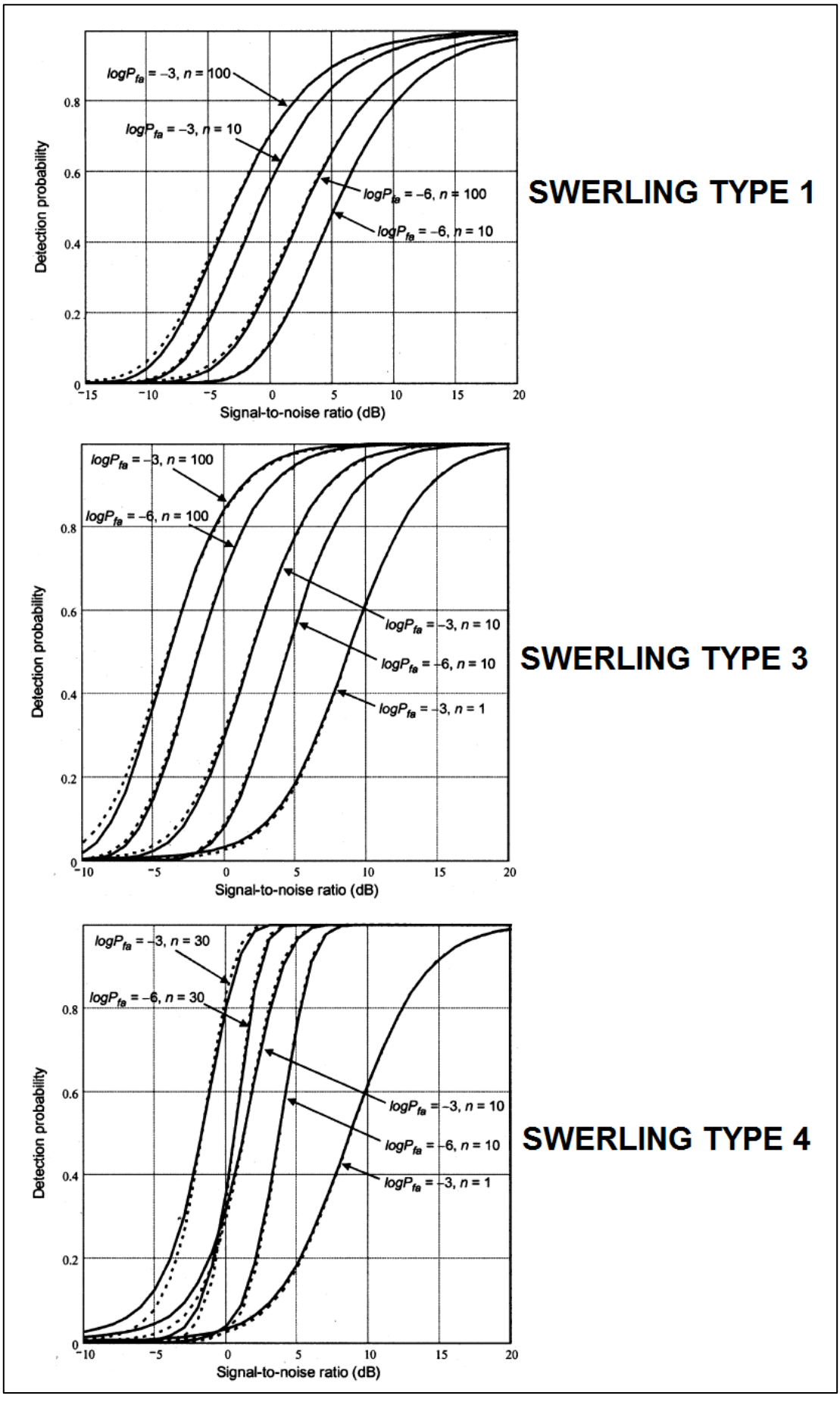

Figure 18: Detection Probability Comparisons for Swerling Target Types, 1, 3 and 4

Small differences between the two methods are noticeable in Figure 18; however, these differences were not significant. Equations (32) and (33) are far easier to compute, compared to the traditional definitions for "P_d" and "D". The material in this technical was included for information only and not implemented in this study. Nevertheless, D.K. Barton highlights a set of equations describing RCS fluctuations that can be used to *easily* generate the Radar's Operating Curves (ROC's).

Target Velocity Estimation with FM and PW Echo Ranging Doppler Systems Part I: Signal Analysis

In this first of two papers by J. E. Wilhjelm [22], the signal-level modelling of a Pulse Doppler (PD) radar using a LFM signal for non-invasive blood velocity estimation in humans, is presented. An interesting derivation of the "Doppler frequency-target velocity" relationship from first principles is included in this paper. This particular derivation was obtained in a Biomedical Engineering context and not the traditional field of Radar. An important result is the derivation describing the effect of a Doppler shift on a LFM signal in the TF Domain. Many of the equations used in this report were derived from first principles, which are unnecessary, since these equations have already been derived and simplified for use in the radar field.

Nevertheless, the shift of the LFM waveform in time and frequency on the TF plane is shown graphically in this technical report. This information assisted in visualising the effect of true target reflection and required false target signal characteristics on the LFM waveform in this study.

Target Velocity Estimation with FM and PW Echo Ranging Doppler Systems Part II: Systems Analysis

In his second paper on blood velocity measurement, J. E. Wilhjelm [23] describes the operation and performance of the PD radar used to measure blood velocity, from a system-level. The first paper (reference [22]) focuses on the signal-level modelling for visualisation while, the second paper focussed on modelling system performance and operation. The problem solving philosophy of using a combination of the "Systems Approach" and "Analytic (or Signals)" approach observed in this paper was applied in this study.

2.2 Digital Beam-forming

2.2.1 Technical Reports

Use of technical reports only was made to study the subject of Digital Beam-forming.

The following technical reports that were researched are summarized in this section:

- *"A Primer on Digital Beam-forming", Spectrum Signal Processing",* reference [40]
- *"Interferometer Design for Elevation Angle Estimation",* reference [33]

A Primer on Digital Beam-forming", Spectrum Signal Processing

T Haynes in reference [40] defines beam forming as a "combination of radio signals from a set of small non-directional antennas to simulate a large directional antenna". The paper gives an overview of microwave and digital beam-forming for transmission and receipt of radio signals. Radiation patterns and different types of antennas are described. The half-wave Dipole Antenna is discussed initially.

Directional antennas, Linear Array Antennas and Electronically Steered Arrays are then discussed. Directional antennas and Linear Array Antennas allow antenna gain to be maximized in a particular direction. This direction is fixed for these types of antennas. The antenna has to be mechanically rotated to ensure the maximum gain portion of the transmitted beam or main beam is pointed at the target.

An electronically steered array is able to "steer" electronically the main beam by means of phase shifters that alter the phase of the signal.

In beam-forming both the amplitude and phase of the transmitted or received signal is changed by means of "complex weights" which are defined as:

$$w_i = a_i e^{j\psi_i} \tag{35}$$

Digital beam forming uses digital technology to perform the beam-forming instead of microwave devices. The structure of a "Radio Frequency (RF) Translator" and "Digital Down-Convertor" of the signal applied prior to beam-forming is discussed. These devices are also discussed in the radar textbooks (references [1], [6] and [8]).

The use of a Fast Fourier Transform (FFT) in a digital beam-former is then described. A "spatial FFT" is performed whose outputs are a set of samples separated in space. Usually the output of the FFT is a set of samples separated in frequency. Finally, the measurement of target AoA is described using digital beam-forming on receive. Such a device is called a "phase interferometer". It is depicted in Figure 19.

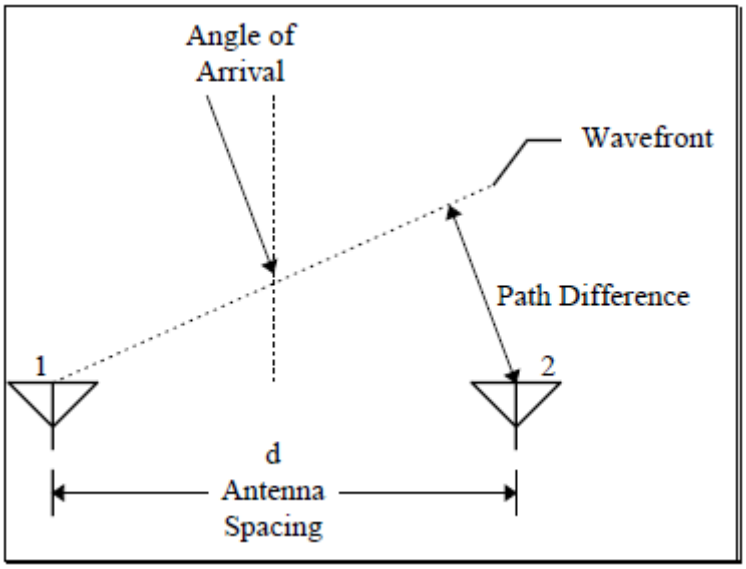

Figure 19: Interferometer for Direction Finding

If the target echo signal in the form of a plane EM wave arrives at the antenna aperture at an angle, the antenna elements would relay signals of different relative phases. This is because the signals arriving at the different elements travel difference path lengths compared to one another. Because of this phenomenon, the phases of the signals in the antenna elements are measured and used to estimate target AoA. Target AoA is related to the antenna element phase and interferometer parameters according to:

$$\phi = \sin^{-1}\left(\frac{\Delta\psi_i \lambda}{2\pi d}\right) \tag{36}$$

The spacing between antennas "*d*" and signal wavelength influence the angular resolution of the device.

The basic principle of operation behind the DBR elevation angle estimation was obtained from this paper. In addition, this paper was used as input to the antenna configuration development of the proposed DBR Jammer.

Interferometer Design for Elevation Angle Estimation

R McAulay in reference [33] presents, in detail the technique of using phased interferometry to measure the Angle of Arrival (AoA) of a target signal using an Air Traffic Control radar interferometer. The interferometer *passively* measures the aircraft's azimuth and elevation angle with sufficient resolution in order to conduct air traffic control using the transmitted signal power from the aircraft transponder to determine its direction.

An optimal solution for a fundamental interferometer design trade-off is found. Antenna element aperture width is traded off against interferometer baseline width (spacing between antenna elements) in order to obtain a specified elevation angle estimation error. This is done while minimizing the overall height of the interferometer configuration.

The equations described herein, model the interferometry phenomena as well as accuracy and precision metrics of the proposed method. The sources of error in the elevation angle measurement process are the antenna front-end noise error, hardware errors, multipath effects and antenna pattern effects. These errors are modelled in detail and used to form a design equation for the interferometer. The design equation is shown below:

$$\sigma_{\phi} = (2\pi d)^{-1}\left\{\frac{1}{SNR(Q;\bar{a})} + \sigma_{\psi}{}^{2} + \left[\frac{\delta_s}{(1-\delta_p)\rho_m(\phi_{\min})}\right]^2\right\}^{1/2} \tag{37}$$

For design purposes, the required elevation angle error "σ_{ϕ}" and minimum detectable elevation angle "$\phi_{\min}$" is specified. Once the hardware is selected the phase noise error parameter "σ_{ψ}" is known. If the intended deployment site is a fixed installation, the multipath ratio "ρ" can be estimated by measurements of the deployment site. Then the equation can be used to determine an optimum antenna spacing "d" and antenna taper ("δ_s" and "δ_p"). The antenna's gain pattern of the interferometer antenna is similar to the Finite Impulse Response (FIR) filter, since a low gain antenna without directionality is required for this "passive" radar application. This gain pattern is similar to the profile of the FIR filter. The antenna pattern was therefore optimised based on the FIR filter synthesis method.

By analysing equation (36), it can be seen that a phase of 2π only can be measured. An ambiguous measurement would therefore result if:

$$\sin\phi > \frac{\lambda}{d} \tag{38}$$

Therefore, an ambiguous angle would result at "n" multiples of "λ / d". As a result of this problem, R. McAulay in reference [33] uses a multiple hypothesis test based on Bayes theorem to determine the most likely value of the integer "n", to resolve angle ambiguity.

2.2.2 Digital Beam-forming, Contextual Summary

The "Digital Beam-forming on Receive" principle of the DBR was obtained in detail from R. McAulay's technical report ([33]). The error definitions for the interferometer and ambiguous angle information were also obtained from this technical report. The work done by T Haynes

in reference [40], on the other hand, gives a basic view on the "digital beam-forming on receive" principle which complements the R. McAulay report ([33]) and does not contradict it.

2.3 Electronic Support Algorithms

2.3.1 Toolboxes

The Time-Frequency Toolbox [12], developed by F. Auger et. al. provides an excellent overview of fundamental TF algorithms and processing, that can be used by an ES System. It consists of the Matlab TF functions, a tutorial as well as a useful reference guide. The ES system uses these algorithms to estimate intercepted radar signal parameters.

The Time Frequency Toolbox Matlab tutorial, as a visualisation tool, is excellent. It shows the performances of the various complicated TF algorithms in a clear and easy to understand manner. The associated reference guide describes in detail, the fundamental mathematics governing the algorithms.

In particular, this reference clearly explains the suitability of the "Wigner-Ville Distribution" and "Hough Transform" for the time frequency analysis of a LFM signal.

The tutorial commences with an explanation into the need for signal analysis tools that are able to show the combined "time-frequency" history of signal, as opposed to separate time or frequency representations. A fundamental point made is that *frequency information* is not visible in the *time domain* signal and *time dependent information* is not visible in the *frequency domain* representations. However, time-frequency domain representations allow signal frequency modulations, bandwidths and durations to be estimated directly.

An example, illustrating this point, is included here from reference [12]. The time domain echo of a bat sonar signal is shown in Figure 20. It can be seen from this figure, that the frequency content at each time instant cannot be seen by looking at this time domain representation of the signal. The "Energy Spectrum (Squared Modulus of Fourier Transform)" of the signal (Figure 21), does not show at what times the signal frequencies of 38 kHz and 40 kHz occur. "Thus, the spectrum essentially tells us which frequencies are contained in the signal, as well as their corresponding amplitudes and phases, but does not tell us at which times these frequencies occur", F Auger, [12].

However, the time-frequency representation (Figure 22) clearly shows the spectral content in the signal varying with time. It can been from this plot that the signal is narrowband, with decreasing frequency content from 55kHz to 38kHz and it has a non-linear (hyperbolic) modulation.

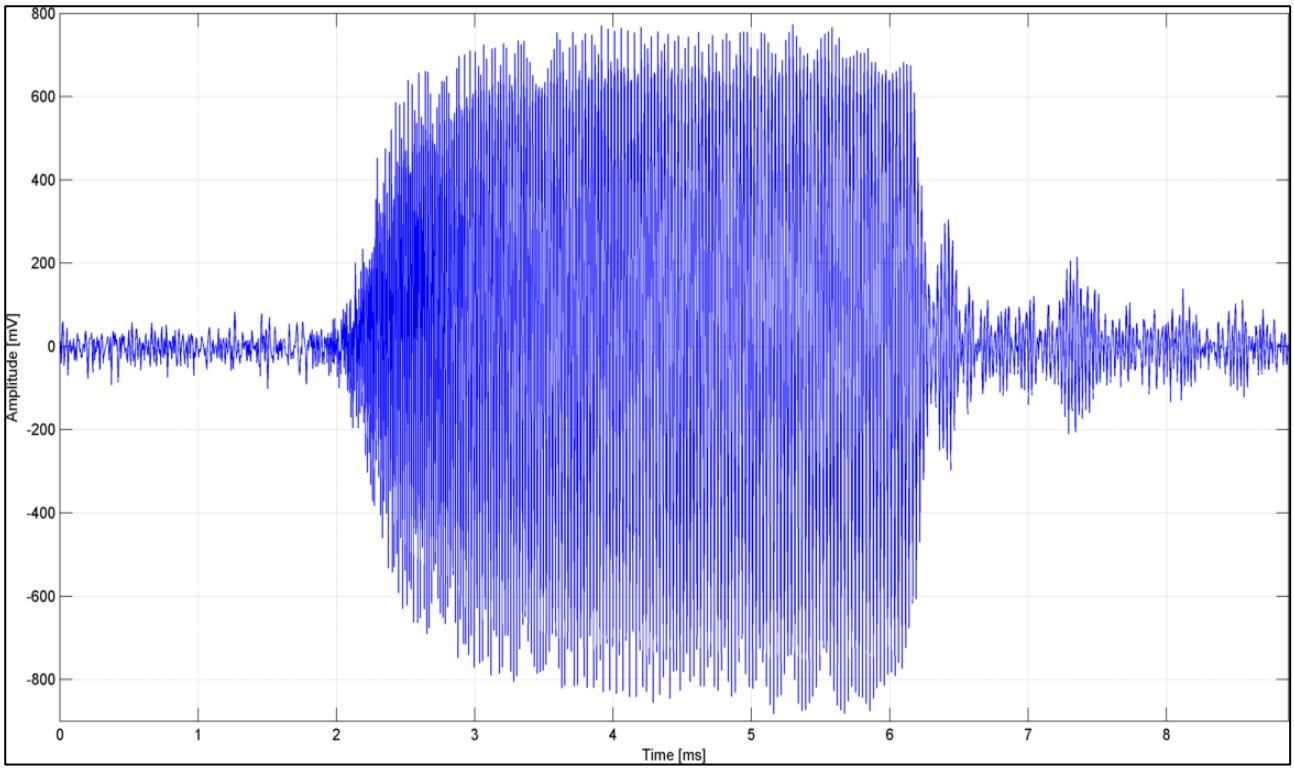

Figure 20: Sonar Signal from bat (reference [12])

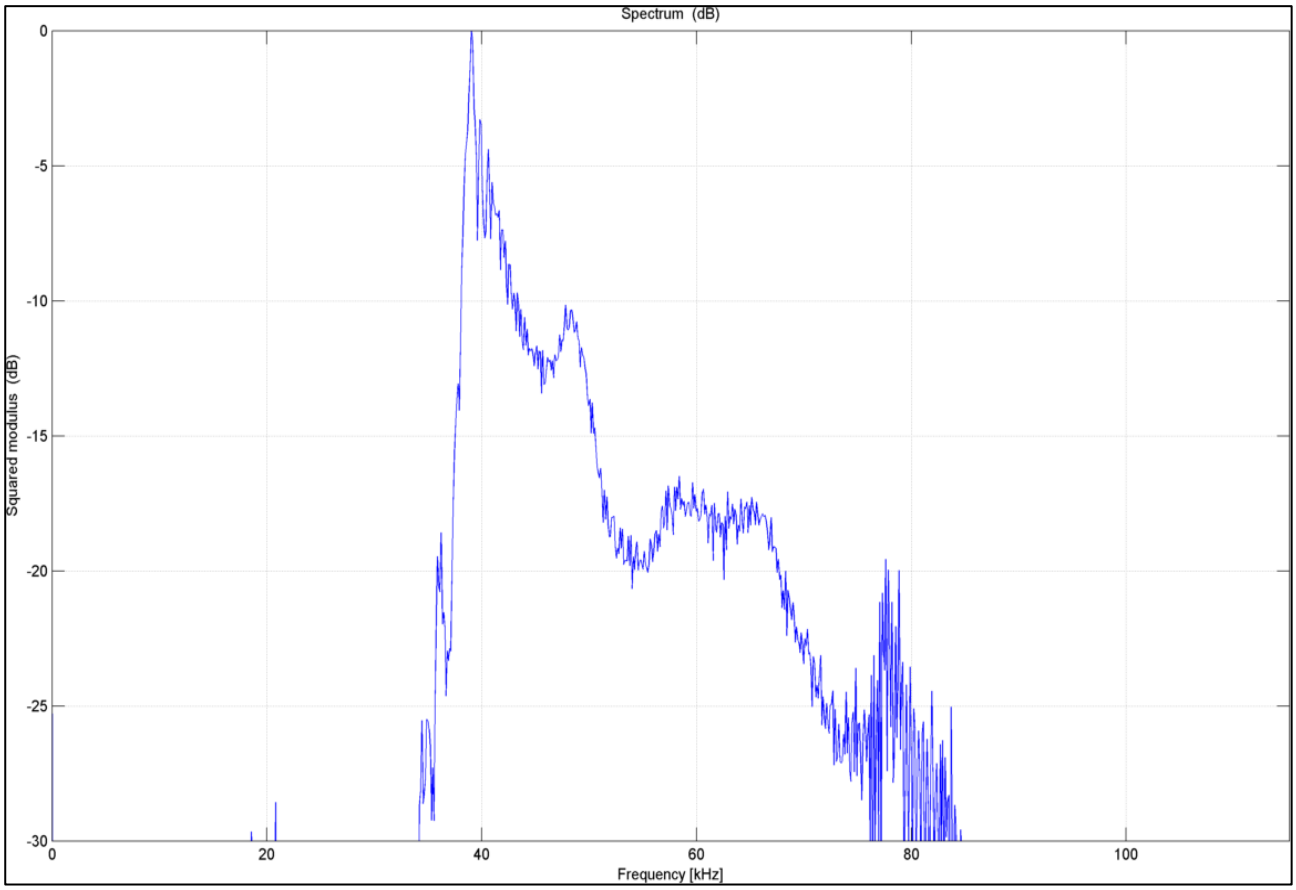

Figure 21: Energy Spectrum of Bat Sonar Signal

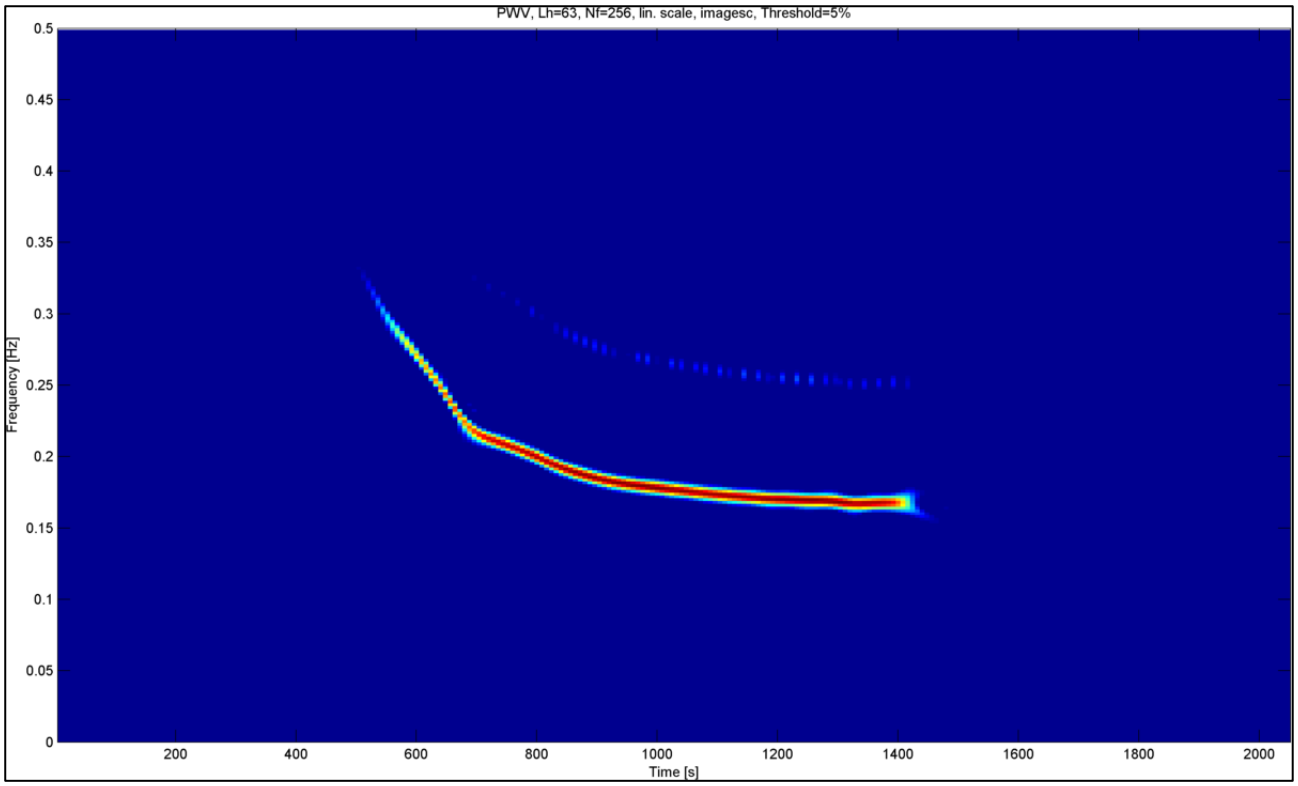

Figure 22: Time-Frequency plot of the bat sonar signal

Different methods of describing a signal in time and frequency are then discussed.

The time and frequency averages and standard deviations can be used to characterize the signal. Signal pulse widths and bandwidths can also be used.

A fundamental constraint to TF domain representations is the "Heisenberg-Gabor Inequality" which states that the signal duration and bandwidth are constrained according to:

$$\tau\beta \leq 1 \tag{39}$$

This constraint forces a trade-off on the time-frequency representations between time resolution and frequency resolution. The "instantaneous frequency" and "group delay" of a signal are the basic methods of representing a non-stationary signal. A "non-stationary" signal is one whose frequency content changes with time such as a LFM signal. "Instantaneous frequency" as a function of time is defined as:

$$f(t) = \frac{1}{2\pi}\frac{d\left(\arg x(t)\right)}{dt} \tag{40}$$

While "Group Delay" as a function of frequency is defined as:

$$t_g(f) = \frac{1}{2\pi}\frac{d\left(\arg X(t)\right)}{dt} \tag{41}$$

Group delay measures the average time of arrival of the signal frequency.

When the time-bandwidth "$\tau\beta$" product of a signal is large, instantaneous frequency and group delay TF plots are identical, since the instantaneous frequency is the inverse transform of the group delay. However, this is not the case when the time-bandwidth product is small.

Another limitation of both methods for representing non-stationary signals on the TF plane occurs when the signal has "multiple components". A "multi-component" signal is made up of many signals, each with a different frequency or frequency/amplitude modulation. The different "component" signals are added to obtain the multi-component signal.

A multi-component signal might occur under the following conditions:

- When transmissions from more than one DBR are received or,
- Interference in the DBR band is also simultaneously received. The interference might be caused by another radar operating in either the "L" or "X" Bands.

A "multi component, non-stationary" signal can be formed by adding two LFM signals as shown in Figure 23. Using the "Instantaneous Frequency" and "Group Delay" equations to obtain the TF plot for the signal does not represent the actual TF relationship of the signal components. This incorrect TF representation is shown in Figure 24.

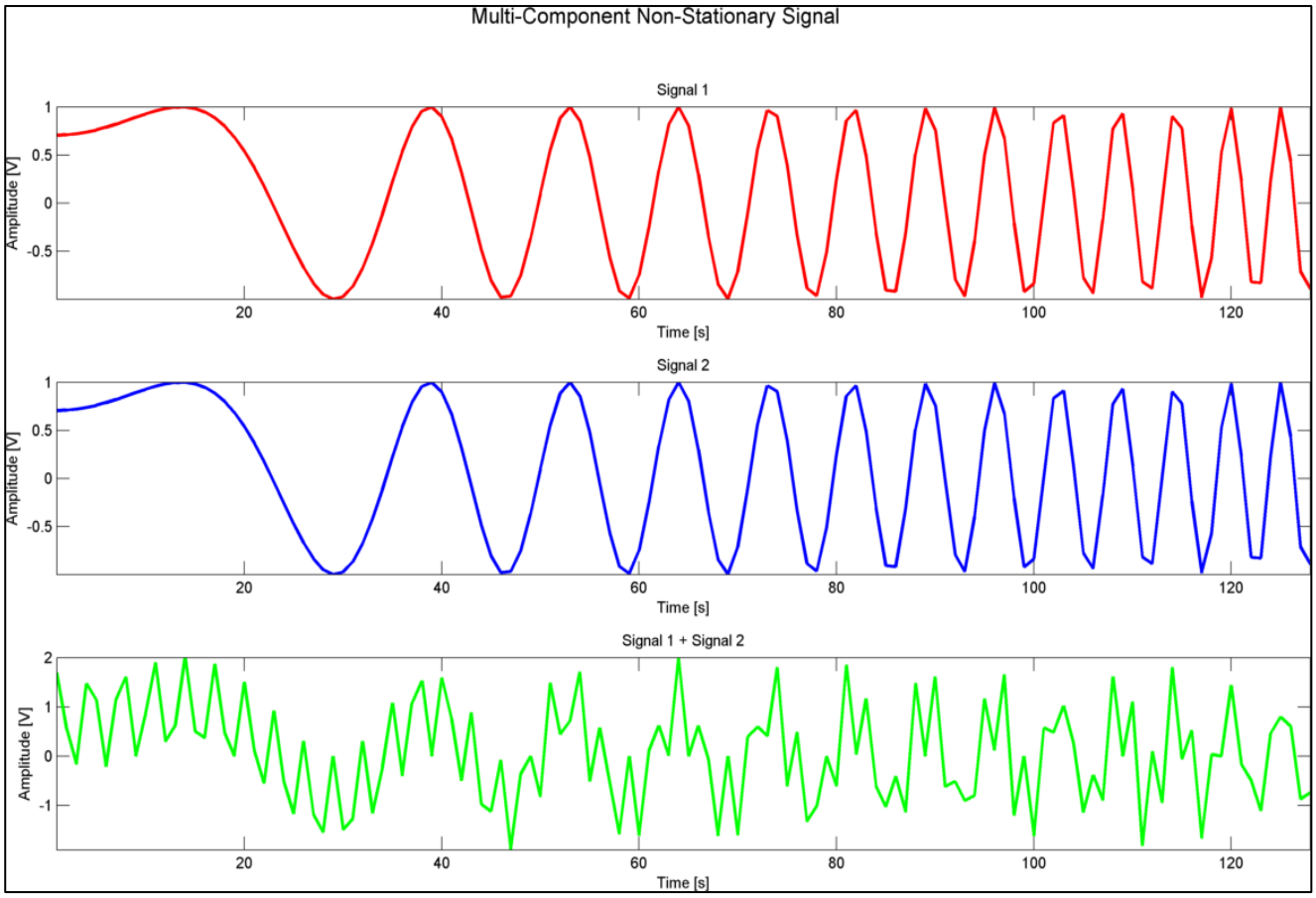

Figure 23: Multi component, Non-stationary Signal

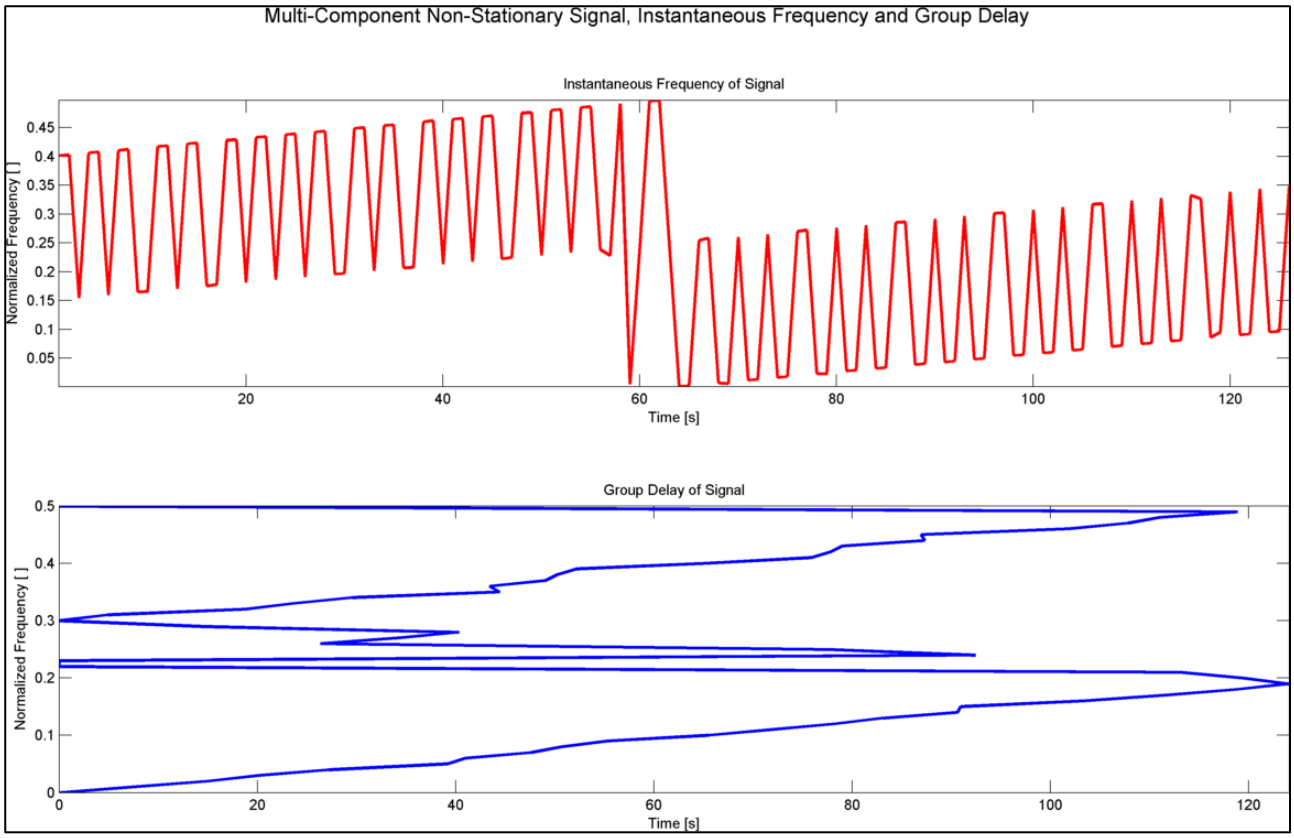

Figure 24: Instantaneous Frequency and Group Delay Discrepancy (reference [12])

The "one-dimensional" representations of instantaneous frequency and group delay are therefore not sufficient to represent all the non-stationary signals. Rather a "two dimensional" approach to the TF representation that couples time and frequency is needed for these types of signals.

Atomic Decompositions

The first class of two-dimensional representations are called the "atomic decompositions" or "linear time frequency representations". They are based on the "Short Time Fourier Transform (STFT)" and "Continuous Wavelet Transform (CWT)". The STFT is defined as:

$$F_x(t, f; h) = \int_{-\infty}^{+\infty} x(u)h^*(u-t)e^{-j2\pi f u}du \qquad (42)$$

It can be seen that a "short time" sliding window ($h^*(u-t)$) is applied to the data that suppresses the signal outside the neighbourhood of the window. The STFT is then the "local" spectrum of the signal. A short time sliding window is shown in Figure 25.

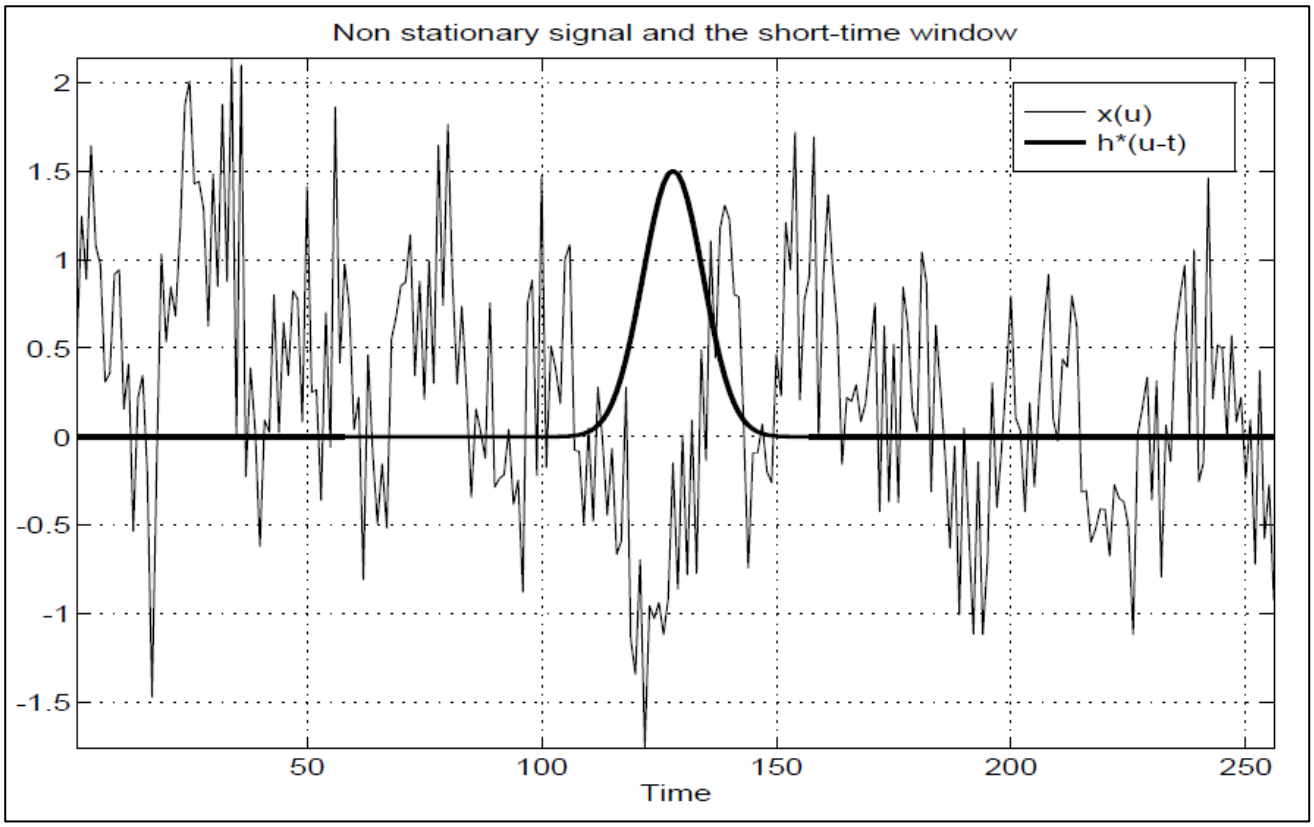

Figure 25: Non Stationary Signal and the short time window (reference [12])

Any type of window can be applied to the signal. Some typical windows used are the, "Blackman", "Harris", "Hamming", and "Gaussian" window. It is important to note that the time and frequency resolutions in the TF image are dependent on both the *type of window* as well the *window size*. A disadvantage of the STFT method is exactly this problem. A short window would result in perfect time resolution (Figure 26) but poor frequency resolution, while a long window would cause perfect frequency resolution but poor time resolution (Figure 27). This time frequency resolution trade-off results because of the fundamental "Huisenberg-Gabor inequality", shown in equation (39).

The time domain signal and its spectrum are also shown in the TF representations plotted using the TF Toolbox. For example, in Figure 26 and Figure 27, the time domain signal is shown in blue in the subplot above the TF representation. The envelope of the function is also shown in green in the time-domain plot. Then the spectrum of the signal is shown in the subplot to the left of the TF image. The time domain representation is plotted so that it corresponds with the time axis of the TF plot. In a dual manner, the spectrum is plotted so that it corresponds to the TF frequency axis. Arranging the plots in this configuration allow and easy and intuitive understanding of the time-frequency relationship for the signal. This method of representating the signal is a built-in feature of the F. Auger's TF Toolbox.

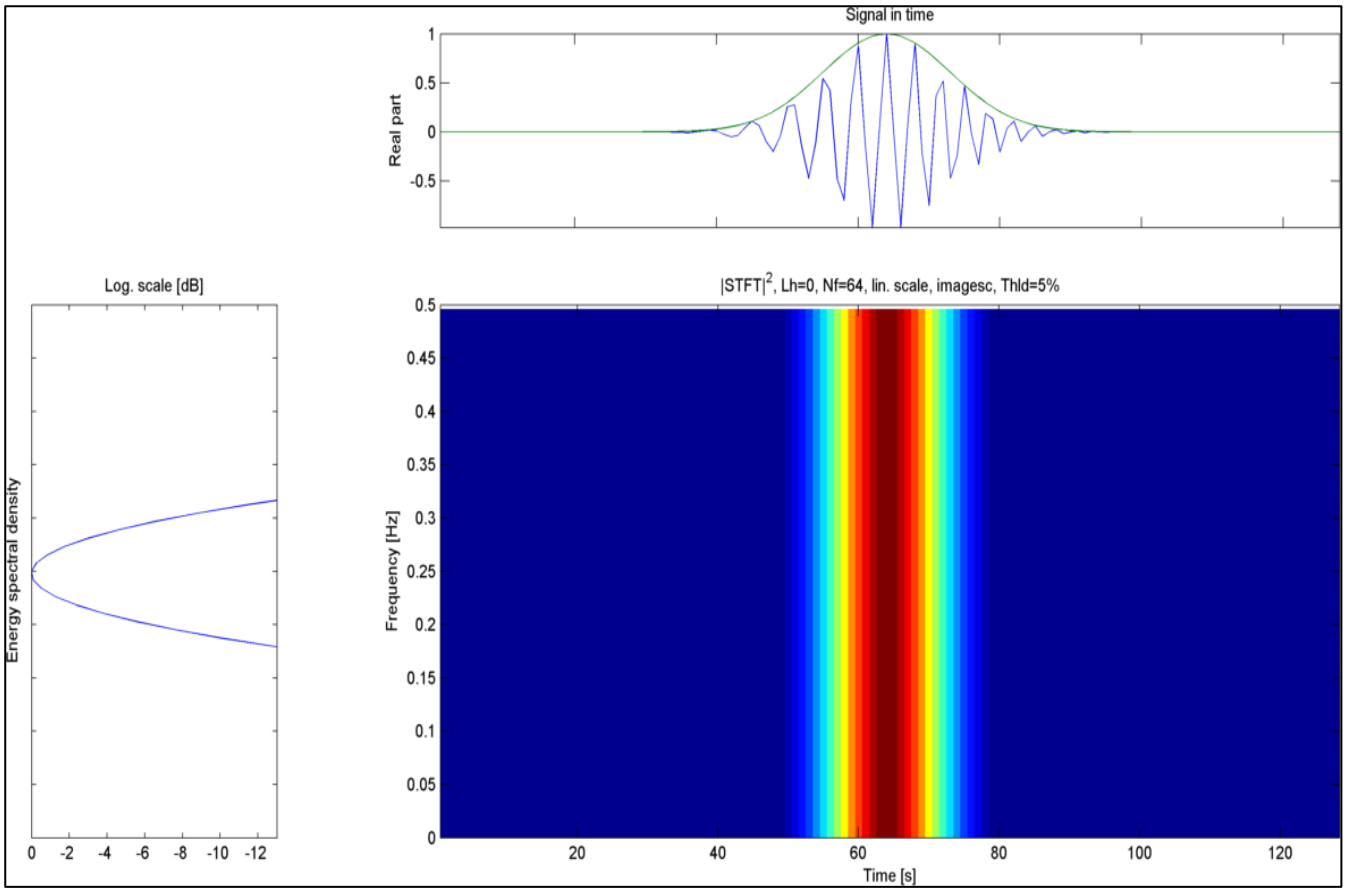

Figure 26: Perfect Time Resolution with the STFT (reference [12])

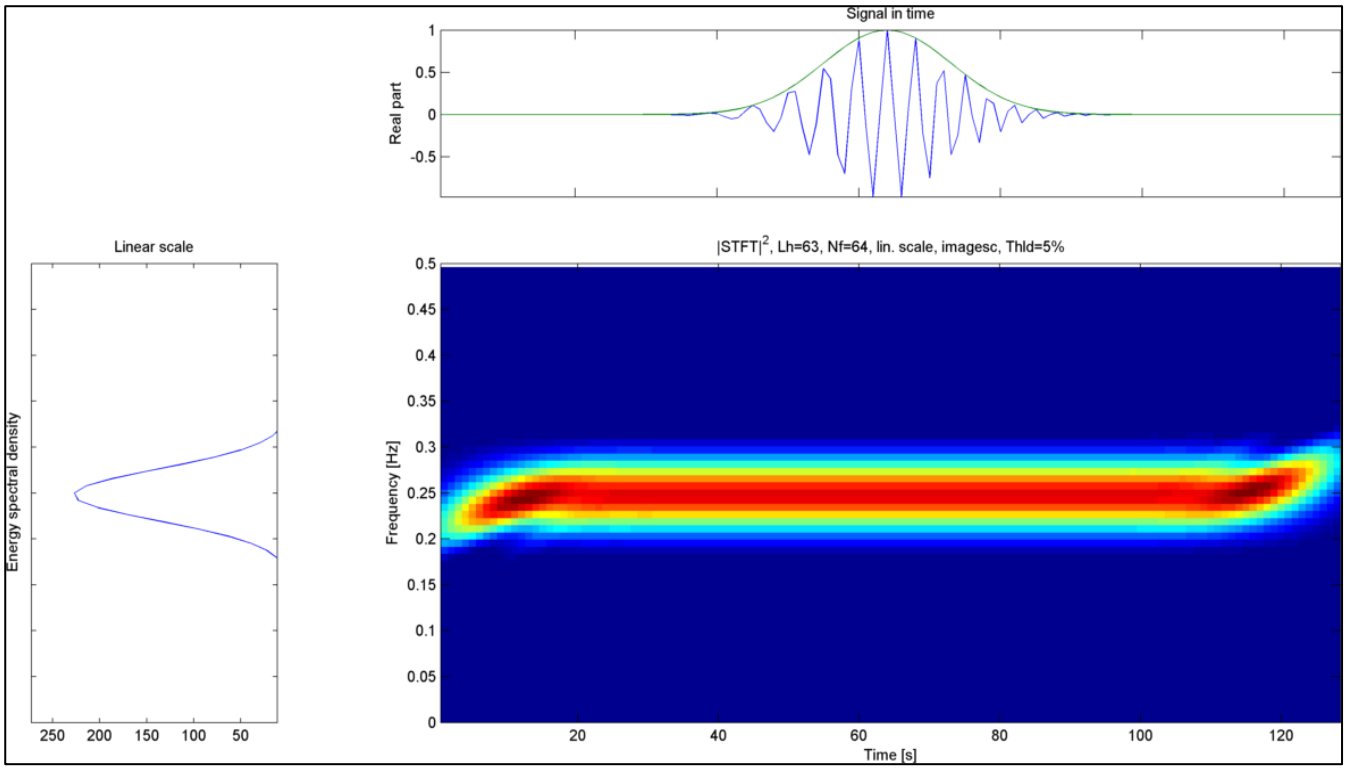

Figure 27: Perfect Frequency Resolution with the STFT (reference [12])

The dependency of time-frequency resolution on window length was partially eliminated by means of the CWT. It was defined as:

$$T_x(t,w;\Psi) = \int_{-\infty}^{+\infty} x(s)\Psi_{t,w}{}^{*}(s)ds \tag{43}$$

Where the "Wavelet Function" is defined as:

$$\Psi_{t,w}{}^{*}(s) = |w|^{-1/2}\,\Psi\left(\frac{s-t}{w}\right) \tag{44}$$

The main difference between the STFT and CWT are that the CWT wavelet is adaptable in terms of duration and bandwidth with the scale factor, while the STFT uses a fixed shape window. It is therefore possible for the CWT to use short windows at high frequencies and long windows at low frequencies, which partially overcomes the resolution limitation of the STFT. However, a deficiency of the CWT is that the frequency resolution still depends on the signal frequency. In the CWT, the frequency is related to the scale parameter by:

$$f = \frac{f_o}{w} \tag{45}$$

The resolution limitations CWT are also constrained by the "Heisenberg-Gabor Inequality Principle" shown earlier (equation(39)).

Energy Decompositions

A different approach to the linear transformation of the signal compared to the "Atomic Decomposition" methods is to use the distribution of the *signal energy* in the TF plane to represent it. The squared modulus of the STFT, which is the "Spectrogram", is the first of these "energy decomposition" methods to be discussed by F. Auger, in reference [12]. It is:

$$S_x(t,f) = \left|\int_{-\infty}^{+\infty} x(u)h^{*}(u-t)e^{-j2\pi f u}du\right|^2 \tag{46}$$

The squared modulus of the *CWT* is called the "Scalogram" which is defined as:

$$Sc_x(t,w) = \left|\int_{-\infty}^{+\infty} x(s)\Psi_{t,w}{}^{*}(s)ds\right|^2 \tag{47}$$

Both the Spectrogram and Scalograms suffer from the same time-frequency resolution deficiencies of the STFT and CWT. However, the interference between multiple signal components rapidly decreases with increased component spacing, which are advantages of the STFT and CWT based methods. This effect can be compared by inspection of the TF plots of the "two chirp component signal" shown in Figure 28 and Figure 29. TF resolution is traded off against multi-component interference suppression for all the energy based TF representations.

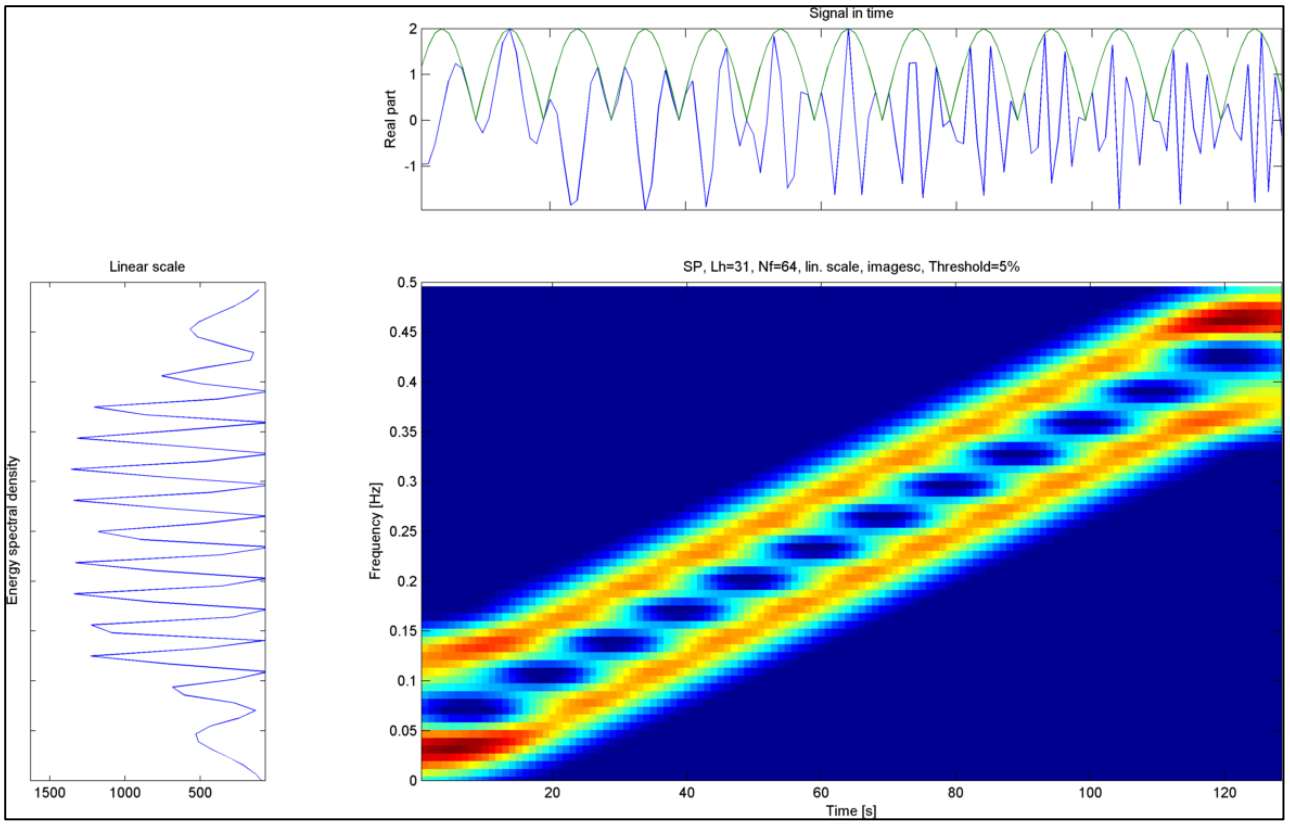

Figure 28: Spectrogram of two closely spaced parallel LFM signals (reference [12])

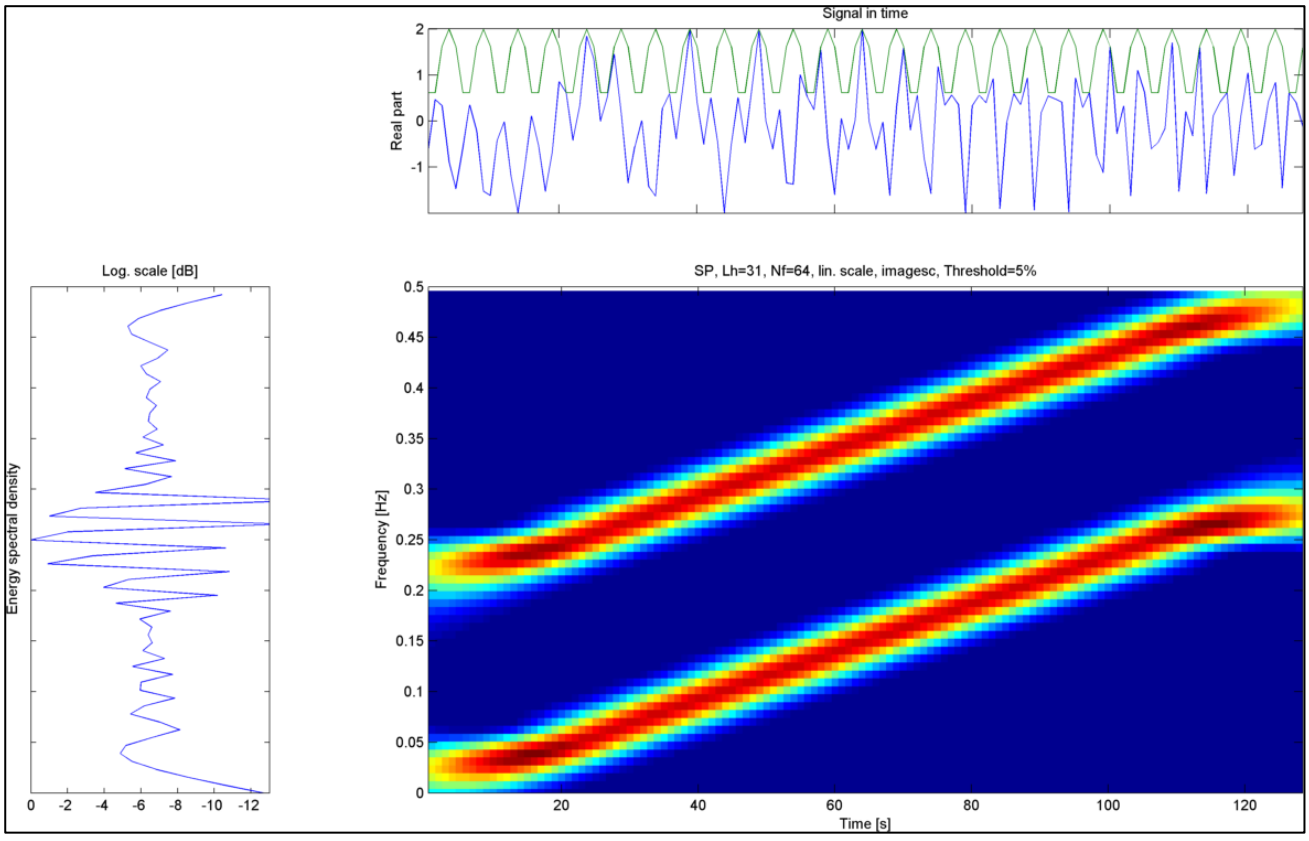

Figure 29: Spectrogram of two more distant parallel LFM signals (reference [12])

Cohen Class

A second class of energy distributions in the TF plane are called the "Cohen" class. An important feature of these distributions is that they are time and frequency covariant. This property is important because it ensures that a time or frequency shift of the signal in the time domain or frequency domain is translated by the same amount in the TF domain.

Cohen class energy distributions are generalized as:

$$C_x(t, f; g) = \int\int\int_{-\infty}^{+\infty} e^{j2\pi\xi(s-t)} g(\xi,\eta) x(s+\eta/2) x(s-\eta/2) e^{j2\pi f\eta}\, d\xi ds d\eta \tag{48}$$

Where $g(\xi,\eta)$ is a two dimensional function called the "Parameterization Class", that varies per Cohen Distribution sub-class.

A particularly important distribution in this class is called the "Wigner-Ville Distribution (WVD)". It is most useful for estimation of LFM signals and is defined as:

$$W_x(t, f) = \int_{-\infty}^{+\infty} x\left(t + \tau_d/2\right) x^*\left(t - \tau_d/2\right) e^{j2\pi f\tau_d}\, d\tau_d \tag{49}$$

This distribution is important since it satisfies a large number of mathematical properties that make it suitable for use as a TF signal estimation algorithm. Some useful properties are:

1. Energy contained in the signal $x(t)$ can be obtained in the TF plane by integrating the WVD over the time-frequency plane.
2. Marginal Distributions of the WVD yield the energy spectral density and instantaneous power which are defined as:

$$\int_{-\infty}^{+\infty} W_x(t, f) dt = |X(f)|^2 \tag{50}$$

$$\int_{-\infty}^{+\infty} W_x(t, f) df = |x(t)|^2 \tag{51}$$

3. The WVD is always "real-valued".
4. Supports translation covariance in time and frequency
5. Supports dilation covariance in time and frequency
6. Compatibility with filtering, which expresses the fact that if a "signal y is the convolution of x and h the WVD of y is the time-convolution between the WVD of h and the WVD of x", F Auger (reference [12]).
7. Compatibility with modulations, which expresses the fact that "if y is the modulation of x by a function m, the WVD of y is the frequency-convolution between the WVD of x and the WVD of "m" F Auger (reference [12]).

8. "Wide sense support conservation" states that if a signal has a compact support in time or frequency, then its WVD also has the same compact support in time or frequency. It mathematics the "support of a function" is defined as that set of points for which the function is not zero-valued.
9. The "Unitarity" property expresses the "conservation of the energy" as scalar product from the time-domain to the time-frequency domain.
10. The Instantaneous frequency of a signal "x" can be recovered from the WVD, as its first order moment (or "Centre of Gravity") in frequency.
11. Group delay of "x", in a dual way to instantaneous frequency, can be obtained as the first order moment in time of its WVD:
12. The WVD offers *perfect Localization of LFM signals*. For example if the LFM signal is defined as:

$$x(t) = Ae^{j(2\pi f_c + \pi\mu t^2)} \tag{52}$$

Then its WVD is:

$$W_x(t, f) = \delta\left(f - (f_c + \mu t)\right) \tag{53}$$

From equation (53), it can be seen that the WVD of a LFM signal causes a large peak to be formed in the distribution at a frequency equal to "$f_c + \mu t$" where the "Dirac's Delta" function "δ" represents the WVD peak at "$f_c + \mu t$".

"The WVD therefore ideally concentrates the LFM Signals in the TF plane. Thus, the problem of detection and estimation of a LFM signal, which is not easily recognizable in the time domain, is reduced to the problem of detection and estimation of a line in an image, which is a well-known and easy-to-solve problem in pattern recognition." F. Auger ([12]). The recognition of the LFM line in a TF image, can be done by using the "Hough transform (HT)". The WVD and HT are collectively termed "Wigner Hough Transform (WHT)" and the WHT *of a chirp signal* is defined as:

$$\begin{aligned} WH_x(f_c, \mu) &= \int_{-\infty}^{+\infty} W_x(t, f_c + \mu t)dt \\ &= \iint_T x\left(t + \tau_d/2\right) x^*\left(t - \tau_d/2\right) e^{-j2\pi(f_c + \mu t)\tau_d}\, dt\, d\tau_d \end{aligned} \tag{54}$$

In the above equation, $x(t)$ is observed or measured over a sampling time interval "T", so the WHT is calculated for this time.

The "WHT based detection test" for a LFM is "asymptotically the optimum detector (i.e. optimal when "T" tends to infinity)" and "asymptotically efficient (i.e. they asymptotically reach the Cramer-Rao lower bounds)", F Auger ([12]). A classic decision test, which is usually used to detect the presence of a intercepted radar signal, is the Generalized Likelihood Ratio Test (GLRT). However, the WHT based detection method presents the following advantages over the GLRT.

- "It is free from the estimation of the initial phase and amplitude of each component, which usually do not bring any information, and
- Its complexity does not increase with the number of components unlike the GLRT whose complexity increases linearly with the number of components in the signal."
  F Auger (reference [12]).

These advantages are also valid for the special case of the TF representation of a multi component signal, only.

Unfortunately, the WVD does suffer from interference when estimating a multi-component signal in the TF plane, which is because it is "quadratic" distribution. This interference is caused by a "cross WVD" term formed in the calculation. An example of this interference is shown in Figure 30, for a multi-component signal that is made up of two chirps.

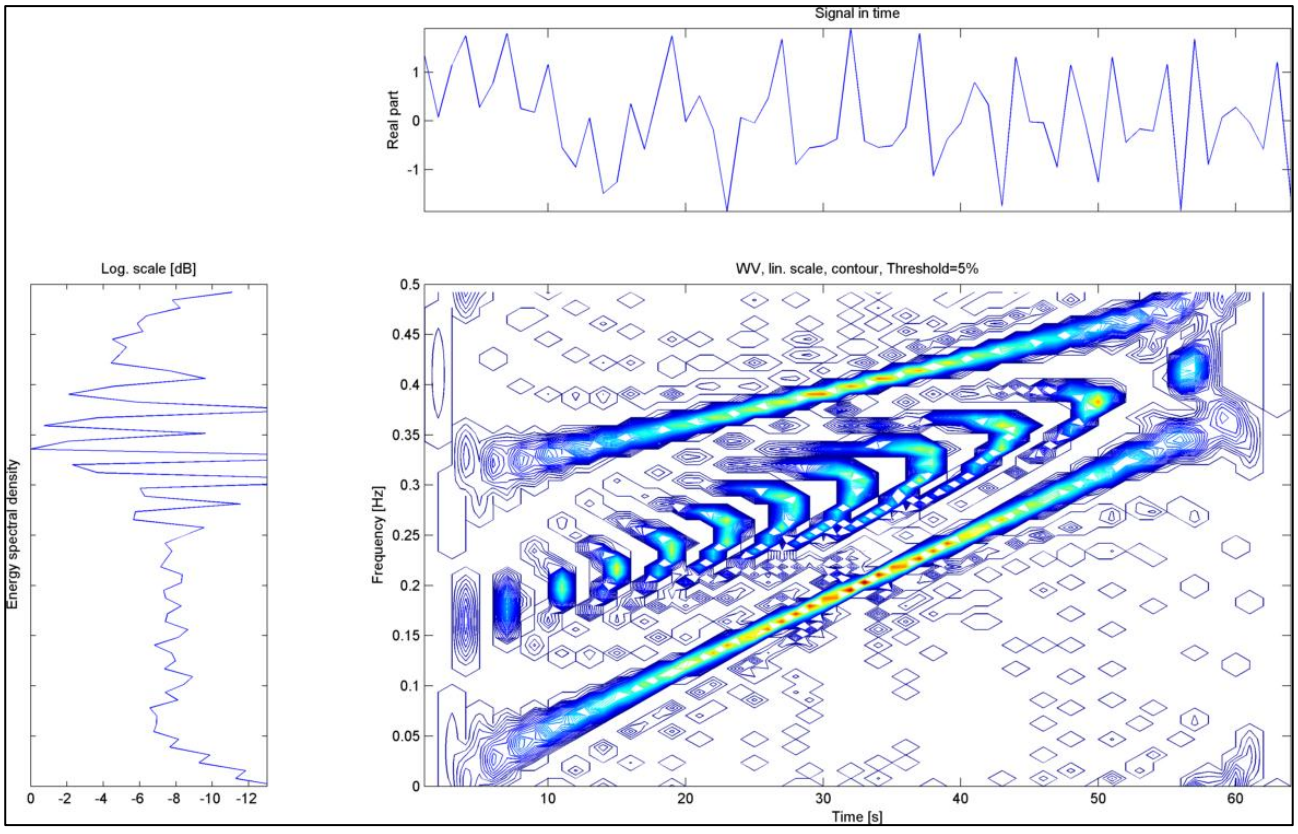

Figure 30: WVD of two simultaneous LFM signals in noise (reference [12])

However, applying the HT after the WVD, effectively suppresses the cross term interference as shown in the WHT image in Figure 31.

The coordinates of peaks in the image correspond to the centre frequency and chirp rate of the two LFM signal components of the multi-component signal shown in Figure 30. The cross WVD term peak shown in the WVD plot does not form

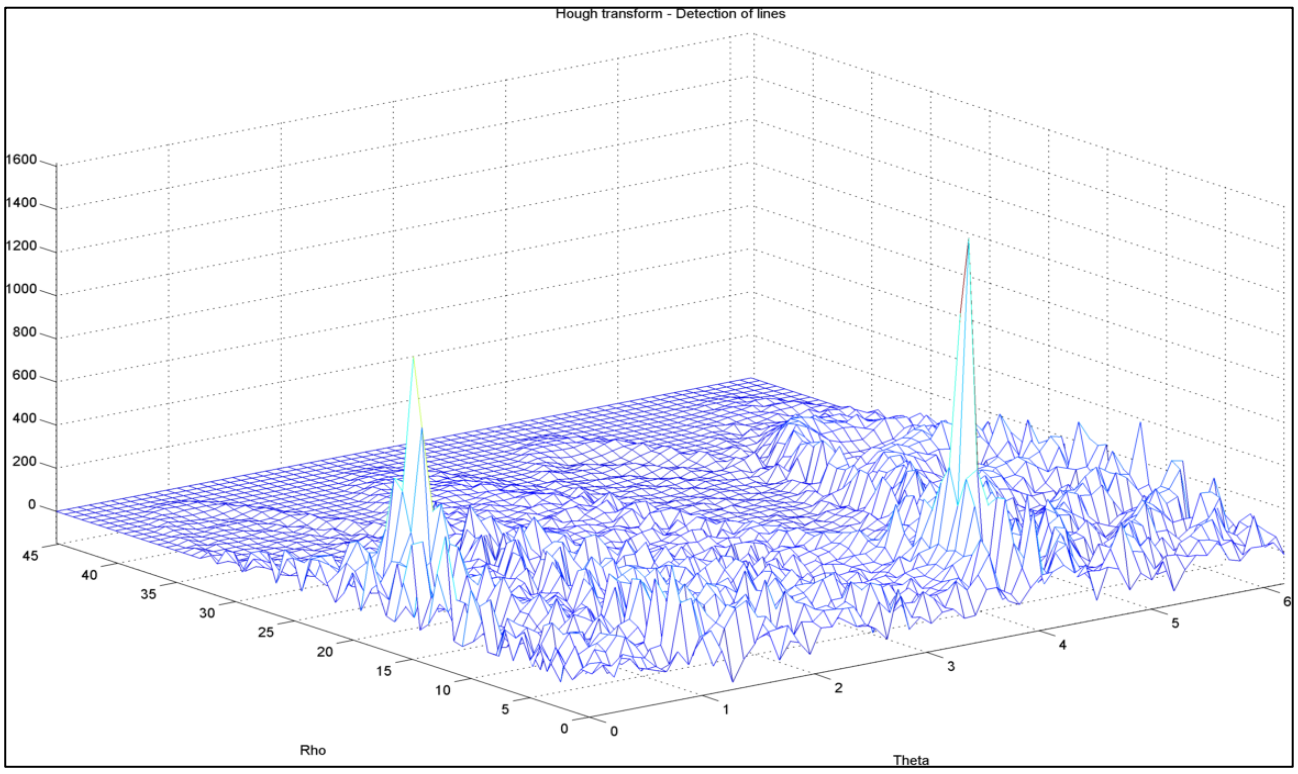

Figure 31: WHT of the two simultaneous LFM signals in noise (reference [12])

In order to suppress the interference terms in the WVD for multi-component signals the "Pseudo-Wigner-Ville-Distribution (PWVD)" was derived which uses a "short-time" window to reduce the effects of the cross terms.

The expression for the PWVD is:

$$PW_x(t,f) = \int_{-\infty}^{+\infty} h(\tau_d)\, x\left(t + \tau_d/2\right) x^*\left(t - \tau_d/2\right) e^{j\cdot 2\pi\cdot f\cdot \tau_d}\, d\tau_d \qquad (55)$$

The WVD algorithm was further improved by the use of a separable smoothing window to reduce interference. The window is separable in time and frequency and thus allows, "independent progressive control in both time and frequency" (F Auger (reference [12])), of the interference suppression of the WVD. This distribution is called the "Smoothed Psuedo Wigner Ville Distribution (SPWVD)". It is:

$$SPWV_x(t,f;g,h) = \int_{-\infty}^{+\infty} h(\tau_d) \int_{-\infty}^{+\infty} g(s-t)\, x\left(s + \tau_d/2\right) x^*\left(s - \tau_d/2\right) e^{j\cdot 2\pi\cdot f\cdot \tau_d}\, ds\, d\tau_d \qquad (56)$$

An important point made by F. Auger was that the "Ambiguity Function" of a signal is the Fourier Transform of the signal's WVD.

Other energy distributions in the Cohen class were the:

- Rihaczek Distribution
- Margenau-Hall Distribution
- Page Distribution
- Choi-Williams Distribution
- Born-Jordan Distribution
- Zhao-Atlas-Marks Distribution

All of these distributions and their characteristics are defined in detail in reference [12]. None of these distributions outperform the WVD for the detection of a LFM signal, and estimation of its parameters. In Figure 32, a comparison from reference [12], of TF representations for the main Energy Decomposition methods is shown.

It can be seen that the WVD gives the best TF resolution for the LFM signal, while the Spectrogram has the poorest TF resolution. However, the Spectrogram presents the least amount of cross term interference for the multi-component signal.

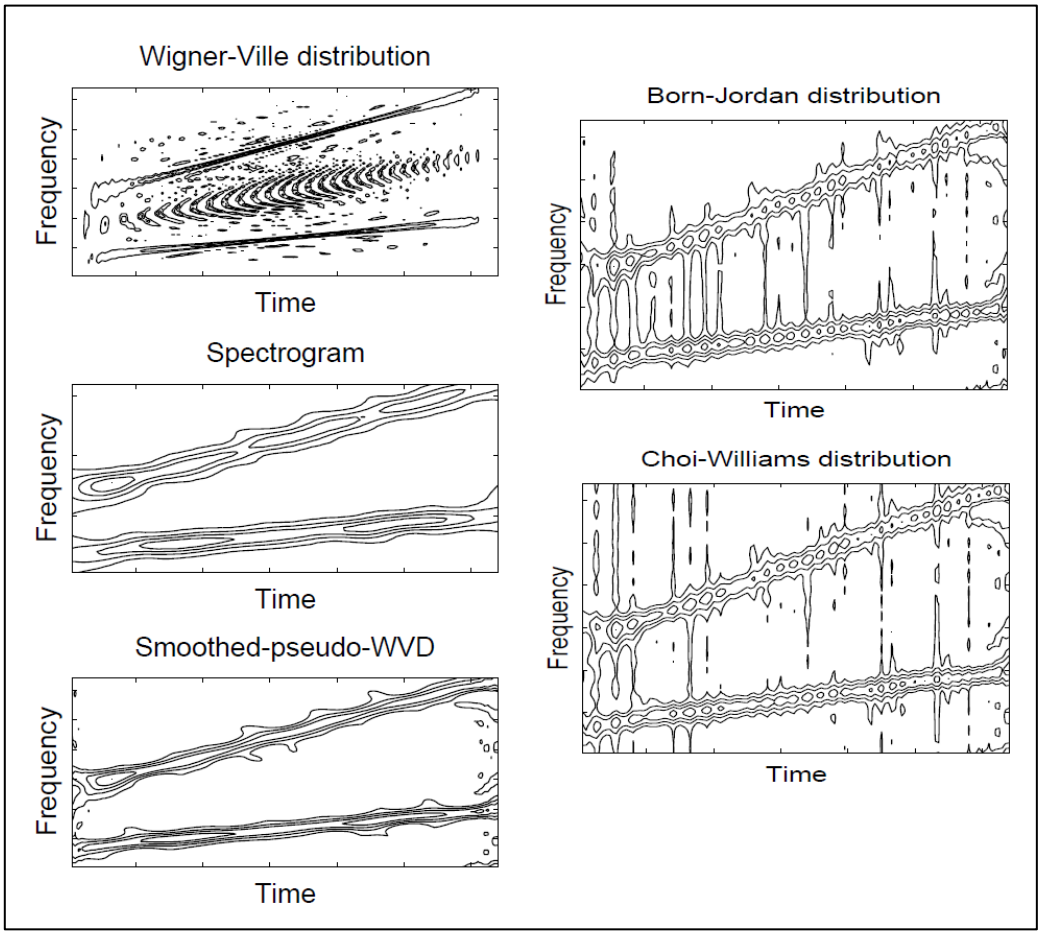

Figure 32: Energy Decompositions, Comparison (reference [12])

Affine Class

The second class of energy decompositions are the "Affine Class" TF representations. These TF representations allow time and frequency covariance to be scaled between the time/frequency domain and TF domain. In the Cohen class, the time and frequency covariance was fixed between the domains. This scalable covariance is an advantage for detection and estimation of non-linear modulated signals. For example, the Affine Class "Bertrand Distribution" perfectly represents a hyperbolic modulated signal as shown in Figure 33. Other distributions in this class are the "D-Flandrin Distribution" and "Unterberger Distributions". Each of these distributions perfectly localises a particular type of hyperbolic modulated signal.

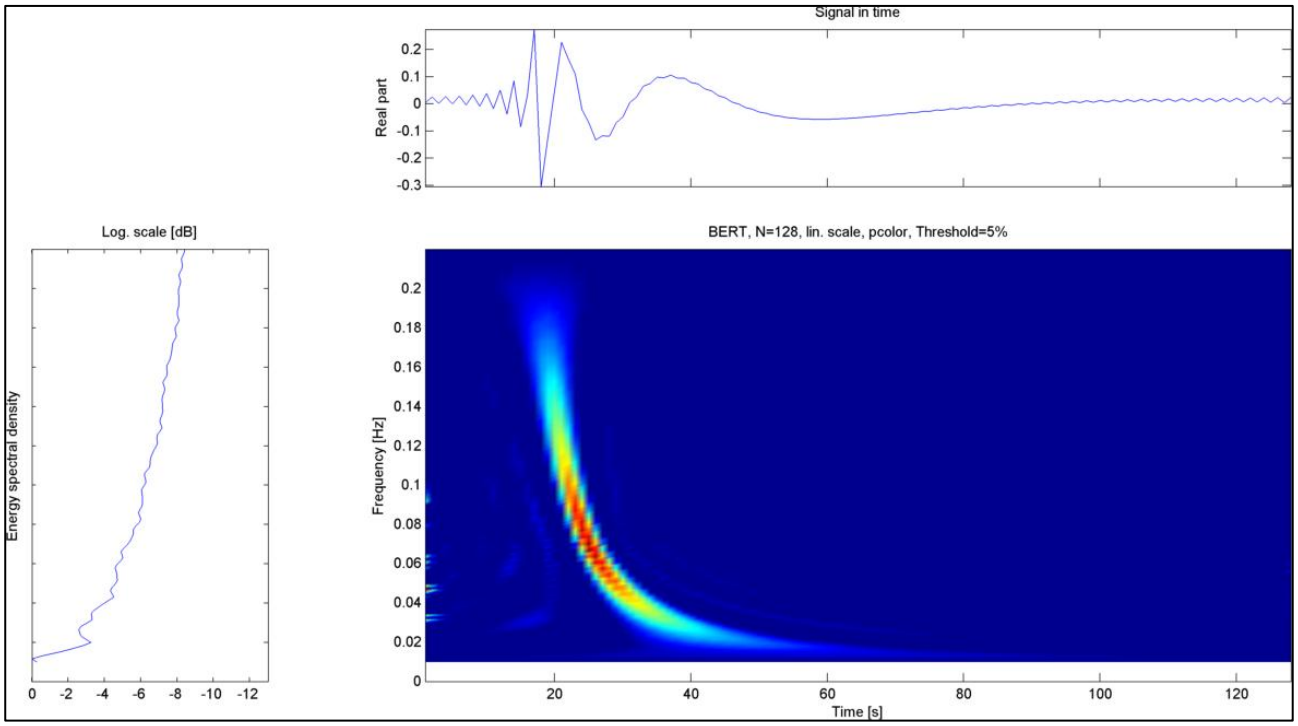

Figure 33: Bertrand distribution of a hyperbolic modulated signal (reference [12])

Reassignment method

This method was developed to either reduce, or eliminate the effects of interference in the energy decompositions. This is done by reassigning the TF representation values inside the smoothing windows, which substantially improve interference suppression without increased computational complexity.

As an example, consider the Spectrogram distribution. Recall that a sliding short time window is used to calculate the STFT of the signal, whose magnitude is then squared to calculate the Spectrogram (see equation (46)).

The key principle in the "Reassignment" method is to redistribute the average value of the WVD within the window. The average value is assigned to the *centroid* inside the window as opposed to its *geometrical centre*. Recall that the coordinates of the centroid or geometrical centre are time-frequency measures. The PWVD and SPWVD smoothing windows averages can also be reassigned to substantially improve readability of the TF image for a non-stationary multi-component signal. The reassigned time and frequency coordinate for the SPWVD TF image is calculated using equations (57) and (58).

$$\hat{t}\left(x;t,f\right)=t-\frac{SPWV_x\left(t,f;\left(t\cdot h(t)\right),h\right)}{2\pi\cdot SPWV_x\left(t,f;g,h\right)} \tag{57}$$

$$\hat{f}\left(x;t,f\right)=f+j\frac{SPWV_x\left(t,f;g,\frac{dh}{dt}(t)\right)}{2\pi\, SPWV_x\left(t,f;g,h\right)} \tag{58}$$

The expression for the "Reassigned Smoothed Psuedo Wigner Ville Distribution (RSPWVD)" is shown in equation (59) below.

$$RSPWV_x\left(t',f';g,h\right)=\int_{-\infty}^{+\infty}\int SPWV_x\left(t,f;g,h\right)\,\delta\left(t'-\hat{t}\left(x;t,f\right)\right)\,\delta\left(f'-\hat{f}\left(x;t,f\right)\right)dt\,df \tag{59}$$

The improvements in terms of interference suppression are clearly visible in Figure 34. The upper right subplot in Figure 34 shows the TF relationships for the three signal components. Then the WVD, SPWVD and RSPWVD representations are shown. The effectiveness of the "Reassignment Principle" is clearly visible in the RSPWVD plot, by the good TF resolution and absence of interference.

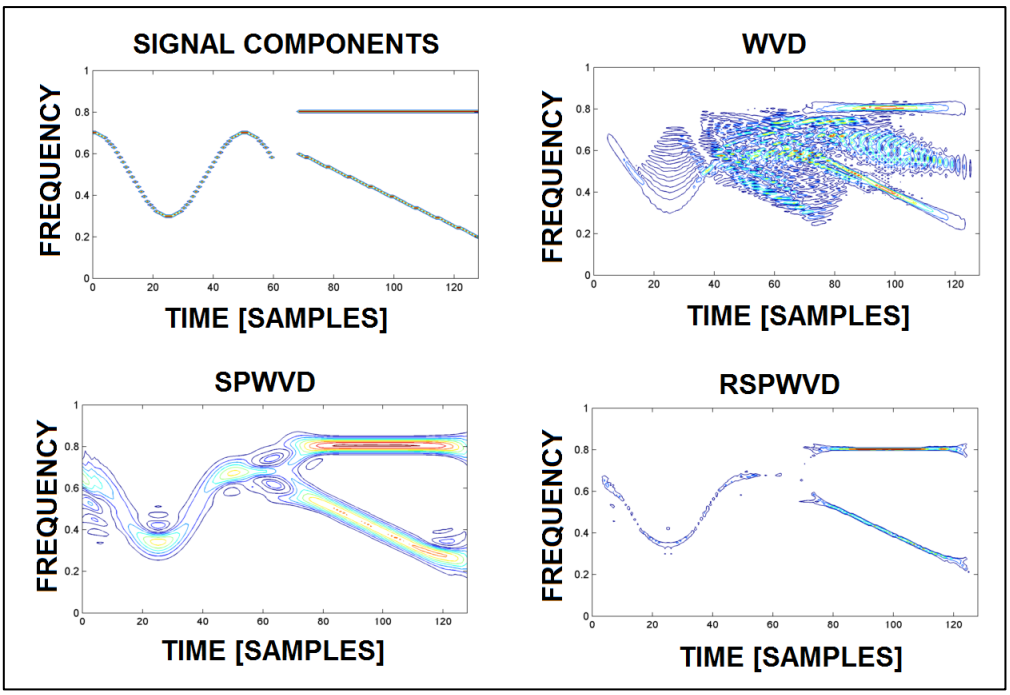

Figure 34: Reassignment Principle, Interference Comparison (reference [12])

Besides the WVD, the reassignment method can be applied to any of the energy distributions already discussed. This includes the Spectrogram, other Cohen Class distributions as well as the Affine Class distributions.

Extraction of information from Time-Frequency image

The Hough Transform mentioned earlier is one of the tools that can be used to detect the straight line TF representation of a LFM signal in noise. Other outputs of analysing the TF images interference patterns are information on the phase of the signal and rate of phase jumps. "Renyi Information" can be used to determine the number of components in multi-component signal and local singularities in the signal can be analysed using the "Lipschitz exponent" on a Scalogram or Unterberger Distribution.

The "family tree" shown in Figure 35 shows all the distributions described by F. Auger in reference [12] as well as their classes.

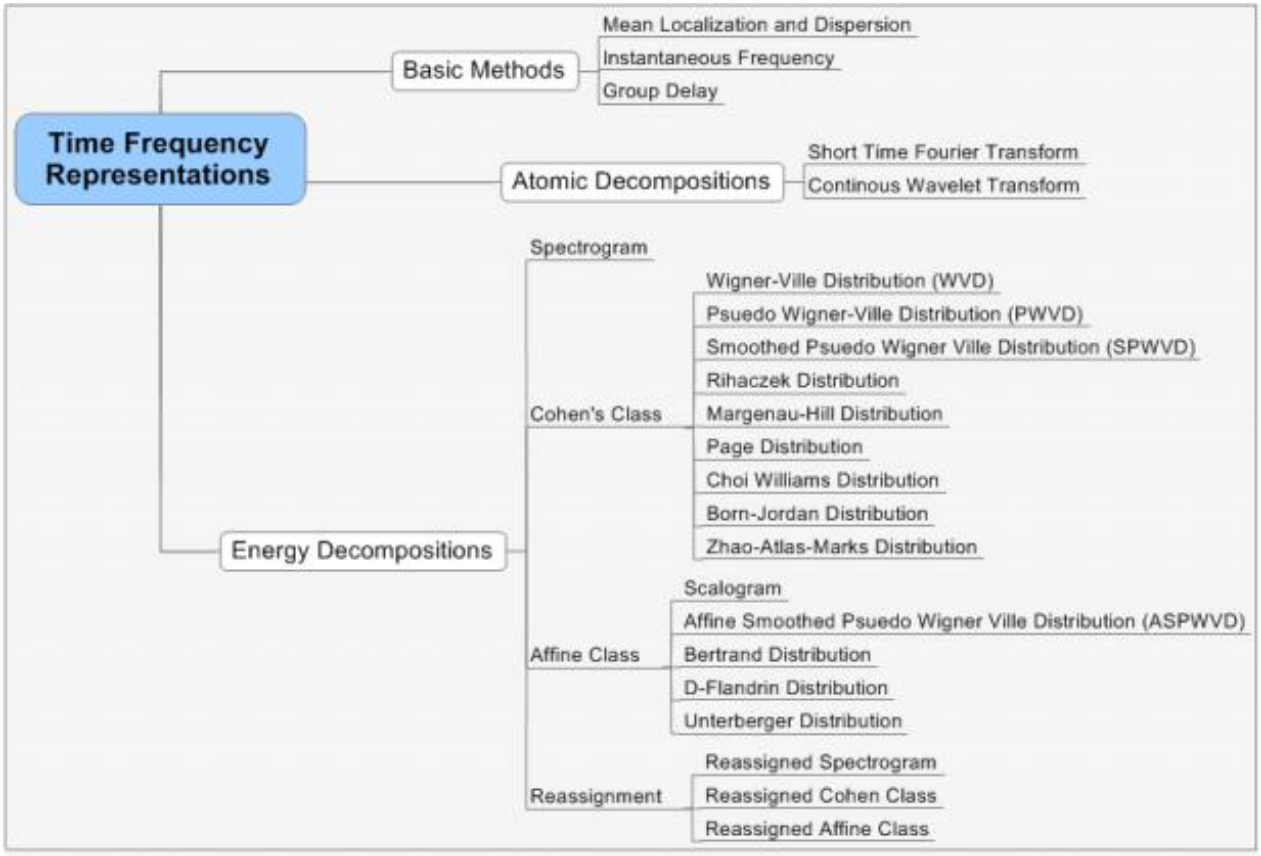

Figure 35: Summary of Time Frequency Representations, TF Toolbox

2.3.2 Technical Reports

The following technical reports that were researched are summarized in this section:

- *"On the Concept of Instantaneous Frequency",* reference [30]
- *"Hough Transform for Straight Lines",* reference [21]
- *"Combined Wigner-Ville and Hough Transform for Cross Term Suppression and Optimal Detection and Parameter Estimation",* reference [35]
- *"Analysis of Multi-component LFM Signals by a Combined Wigner-Hough Transform",* reference [34]
- *"An Efficient Real Time Implementation of the Wigner-Ville Distribution"*, reference [15].
- *"Smart Repeater for a Weapon Location Radar Based on Time-frequency Analysis",* reference [24]

On the Concept of Instantaneous Frequency

In reference [30], P Oliveira and V Barriso describe the problems associated with the basic definition of "Instantaneous Frequency", particularly with respect to multi-component signals. They propose a new definition that is based on the "*Instantaneous Auto-Correlation*" of the signal.

The report commences with a definition of the typical radar signal as:

$$x(t) = a(t)e^{j\psi(t)} \tag{60}$$

Where "$\psi(t)$" is some arbitrary signal phase.

The traditional definition of instantaneous frequency is:

$$f(t) = \frac{d\psi}{dt} \tag{61}$$

This definition is not valid for multi-component signals as shown by the example in Figure 36.

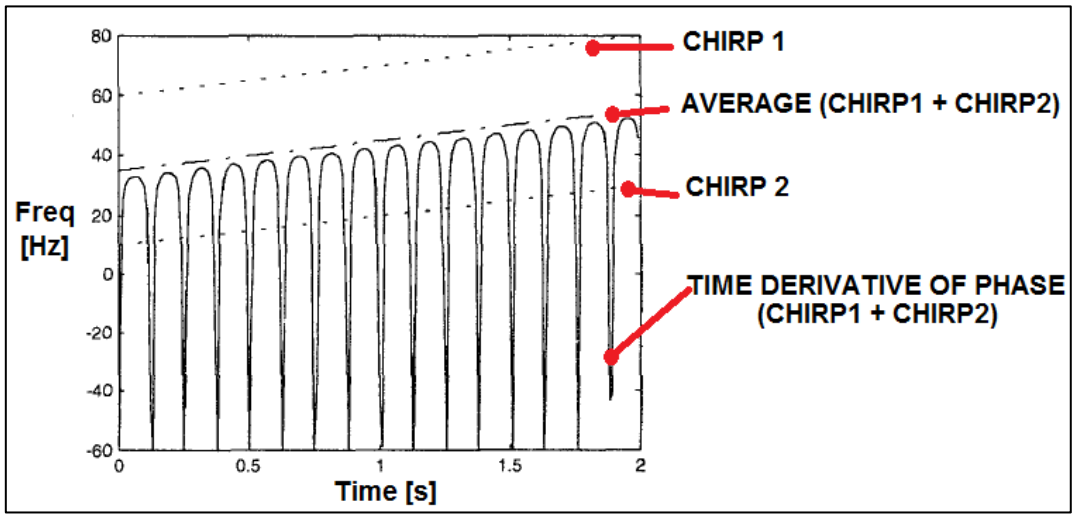

Figure 36: Instantaneous Frequency of Two Chirp Signals (reference [30])

It can be seen that the traditional definition of instantaneous frequency does not represent the individual TF relationships of the individual chirps or even their average. This result corroborates similar statements in reference [12], made with respect to the unsuitability of instantaneous frequency for representing multi-component signals on the TF plane (see Figure 24).

According to P Oliveira and V Barriso in reference [30], the problem resides with symmetry of the signal's amplitude spectrum. The instantaneous frequency " $f(t)$" is usually the *central frequency of the spectrum of the amplitude function* of the signal "$a(t)$". However since "$a(t)$" is a real function; it must have a symmetric spectrum. So the instantaneous frequency is actually the frequency about which the spectrum of $a(t)$ is symmetric and not necessarily the central frequency. If the spectrum of $a(t)$ is not symmetric, the definition (61) does not yield the true instantaneous frequencies of the multi-component signal. An alternative definition of " $f(t)$" is:

$$f(t) = \frac{\Omega'(0)}{2\pi} \tag{62}$$

Where "$\Omega'(0)$" is the derivative of the phase of the Instantaneous Auto-correlation function at "$t = 0$". The Instantaneous Auto-correlation function is defined below:

$$R_t(\tau) = \int_{-\infty}^{\infty} x\left(t + \tau_d/2\right) x^*\left(t - \tau_d/2\right) \gamma\left(t - \tau_d\right) d\tau_d \tag{63}$$

The kernel function "$\gamma\left(t - \tau_d\right)$" in equation (63) is selected based on the TF representation required. In this report the WVD, the Instantaneous Power Spectrum and Choi-Williams distribution kernels were used.

From the definition of instantaneous frequency in equation (62), it can be concluded that multi-component signals cannot be represented by the traditional instantaneous frequency definition. Rather the instantaneous frequency definition of a multi-component signal is only sensible when it is defined in terms of the Instantaneous Autocorrelation function which is in turn defined in terms of the TF representations discussed in reference [12] i.e. WVD distribution, Choi-Williams distribution etc.

This report therefore corroborates and emphasizes the conclusions made by F. Auger with respect to the instantaneous frequency TF representations.

Hough Transform for Straight Lines

J. Jensen [21] describes the Hough Transform (HT) and provides images to visualise easily the HT conversion. The HT is an image processing technique used to detect shapes in digital images. It is used to detect any shape that can be described mathematically. A line is typically represented, using the following equation:

$$f_{line}(x,y) = y = m_{line}\,x + c_{line} \tag{64}$$

However, the line can also be expressed by an angle "$\hat{\theta}$" and distance "ρ" coordinate, as shown in Figure 37. The equation for the straight line then becomes:

$$f_{line}(x,y) = y = -\frac{\cos\hat{\theta}}{\sin\hat{\theta}}x + \frac{\rho}{\sin\hat{\theta}} \tag{65}$$

Equation (65) is rearranged to give equation (66):

$$g(\rho,\theta) = \rho = x\cos\theta + y\cdot\sin\theta \tag{66}$$

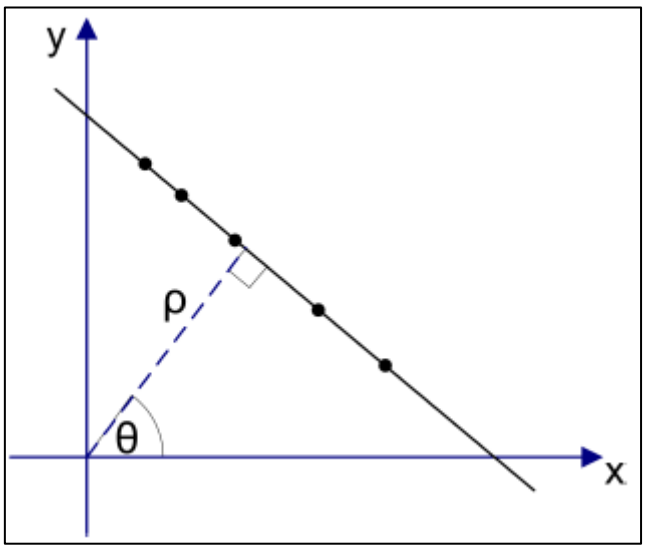

Figure 37: Hough Transform of straight line (reference [21])

The values of "$\hat{\theta}$" are limited to $[0, 2\pi]$ and the value of "ρ" is limited to $[D, -D]$, where "D" is the diagonal length of the sample image. In this case, a single point in the HT space represents the straight line.

However, if an picture is converted to HT space, the edges of the images must be detected initially. Then the pixels in the picture are converted to sinusoids in the HT space. Each pixel has a unique sinusoid curve based on its position in the digital image. This conversion of the pixels to sinusoids is done for all pixels in the image and the sinusoids (per pixel) in the HT domain intersect one another at a single point. This intersected point represents a line joining the two pixels in "picture" space.

An example of the HT processing of a digital image of a bridge is shown in Figure 38. The sinusoids per pixel from the "Edge detected" image of the bridge are clearly visible in the "Hough Transform". The large number of dark red points, indicate large number of "intersections". A large number of intersections are visible around 90°, indicating the presence of many horizontal lines in the original picture.

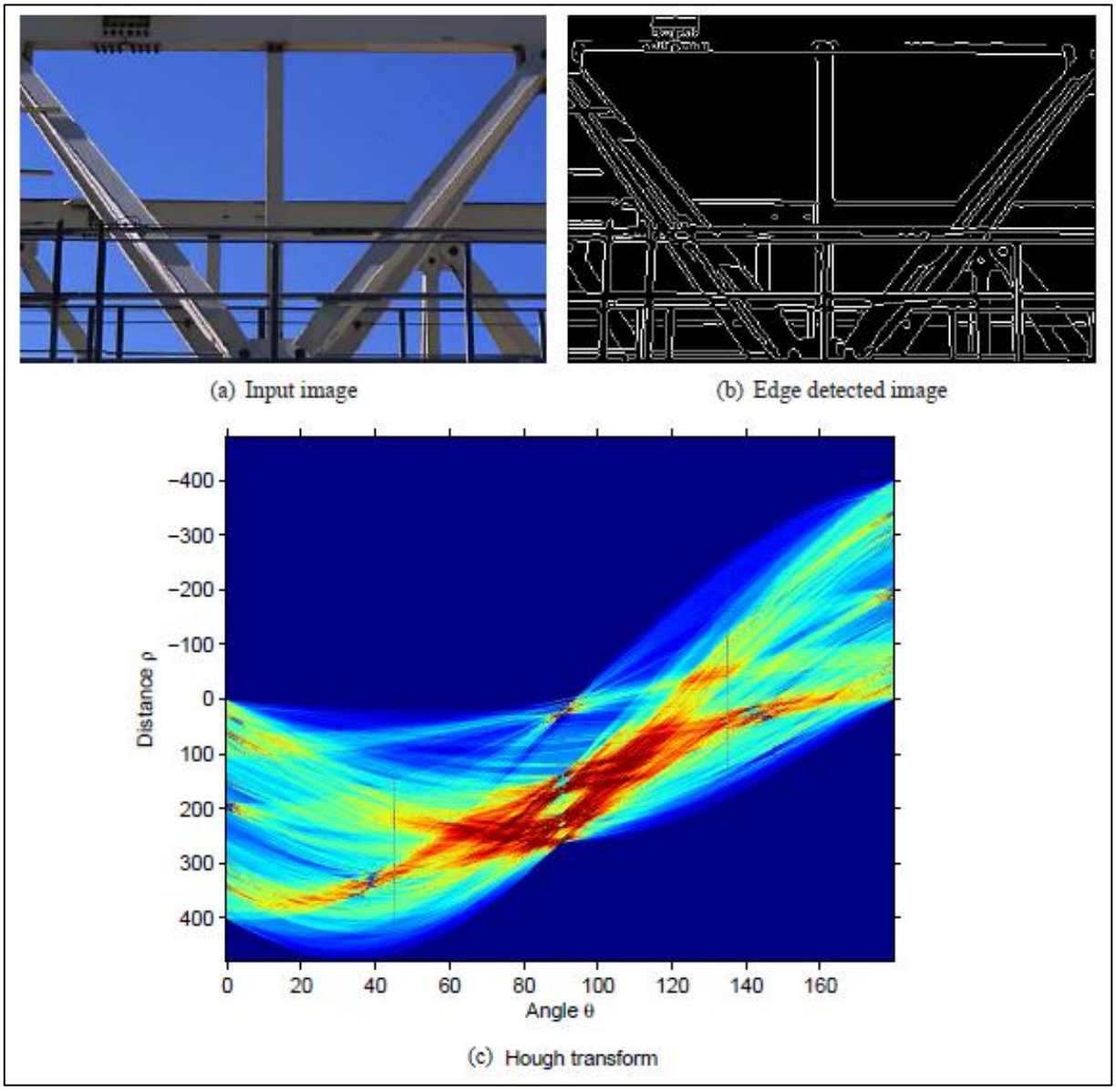

Figure 38: HT of a digital image (reference [21])

From this paper, the theory on the HT processing of a straight line in an image is applicable to this study (not HT of an image), since the LFM signal is represented as a straight line in the TF plane after two dimensional TF processing.

Combined Wigner-Ville and Hough Transform for Cross Term Suppression and Optimal Detection and Parameter Estimation

S Barbarossa [35] describes the suppression of cross-term interference caused by multi-component signals in the WVD using the HT, in detail. More information on the combined use of the HT with the WVD for multi-component signals is included in this paper. This report corroborates reference [12] with respect to the advantage of using the HT to suppress effectively the WVD interference terms that originate, if the WVD TF representation of a multi-component non-stationary signal is generated.

Analysis of Multi-component LFM Signals by a Combined Wigner-Hough Transform

In another paper by S Barbarossa [34], the WHT is presented in a continuous, as well as a discrete form. A statistical analysis of the WHT in terms of SNR and estimation efficiency was discussed in this report. The report commences with the following definition of the WVD:

$$WH_x(f_c,\mu)=\int_{-\infty}^{\infty}\int_{-\infty}^{\infty}x\left(t+\tau_d/2\right)x^*\left(t-\tau_d/2\right)e^{-j2\pi(f_c+\mu)\tau_d}\,d\tau_d\,dt \tag{67}$$

The WVD as defined in reference (67) can be interpreted as either a line integral of the WVD or as the FT of slices of the Ambiguity Function of the signal "$x(t)$". A discrete form of the WHT is given in this report as:

$$\begin{aligned}WH_x(f_c,\mu)=&\sum_{n=0}^{(M/2)-1}\sum_{k=-n}^{n}x(n+k)\,x^*(n-k)e^{-j4\pi k(f_c+\mu n)}\\&+\sum_{n=M/2}^{M-1}\sum_{k=-(M-1-n)}^{M-1-n}x(n+k)\,x^*(n-k)\,e^{-j4\pi k(f_c+\mu n)}\end{aligned} \tag{68}$$

$$n=0,1,\ldots,M-1 \tag{69}$$

The most important property of the WHT transformation is that it assumes an absolute maximum at the coordinates corresponding to the centre frequency and chirp rate of the chirp signal being analysed. This statement corroborates the conclusion with respect to suitability of the WHT for chirp signal detection and estimation as stated in reference [12].

An expression was derived by Barbarossa, for the output SNR as function of input SNR and number of signal samples "n_p". It is:

$$SNR_{out}=\frac{\frac{n_p^2}{2}SNR_{in}^2}{n_p\,SNR_{in}+1} \tag{70}$$

Equation (70) shows that a threshold exists ($SNR_{in} \ll 1$) at which the output SNR would be worse or lower than the input SNR for a signal processed using the WVD. The threshold value is derived as:

$$threshold_{WHT} = \frac{1}{n_p} \tag{71}$$

This states that in spite of the threshold effect, the WHT accuracy threshold can be lowered by increasing the number of signal samples. The "coherent integration" effect is also visible when analysing the centre frequency and chirp rate estimation variances. The expressions for them are shown below:

$$\sigma_{f_c}^2 = \frac{3\left(7+8n_p\right)n_p}{\pi^2 n_p{}^2\left(n_p{}^2-4\right)\left(n_p-1\right)}\left(\frac{1}{SNR}+\frac{2}{n_p\,SNR^2}\right) \tag{72}$$

$$\sigma_{\mu}^2 = \frac{90\,n_p}{\pi^2 n_p{}^2\left(n_p{}^2-4\right)\left(n_p^2-1\right)}\left(\frac{1}{SNR}+\frac{2}{n_p\,SNR^2}\right) \tag{73}$$

A simulation result from reference [34] for testing equations (72) and (73) is shown in Figure 39. The WHT estimation standard deviation for chirp rate "σ_{μ}" is shown for 16 pulses. The line with circular markers shows measured values, while the solid line shows the theoretical standard deviation. It can be seen that the theoretical standard deviation deviates from the measured one at low SNR, because, "perturbation assumptions" used by S. Barbarossa in the derivation are not valid at low SNR.

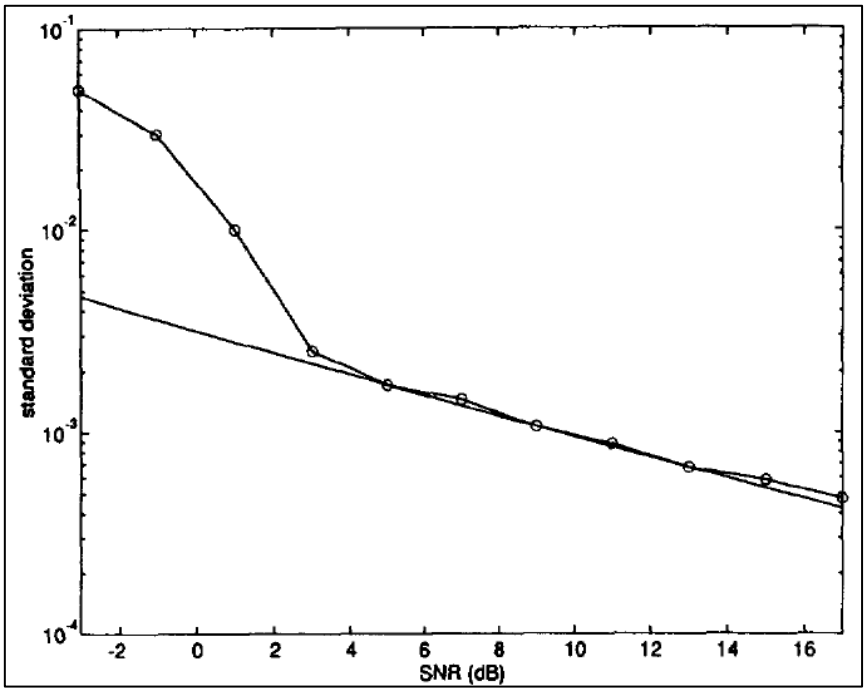

Figure 39: WHT standard deviation for chirp rate vs. SNR for 16 pulses (reference [34])

The variances derived (equations(72) and (73)) were then normalised by the "Cramer-Rao Lower Bounds" to obtain the following efficiencies for the WVD algorithm:

$$\varepsilon_{f_c} = \varepsilon_{\mu} = 1 + \frac{2}{n_p\, SNR} + O\left(\frac{1}{n_p{}^2}\right) \tag{74}$$

It was concluded from equation (74), that:

- The WHT method is asymptotically efficient,
- The WHT benefits from coherent integration, in spite of the SNR threshold limit,
- It offers advantages over a similar ES algorithm (Polynomial Phase Transform) because of a lower SNR threshold and closer approach to the Cramer-Rao Lower Bound for the variances.

The variances given in this paper were used to determine the theoretical WHT estimation variances of the chirp centre frequency and rate of the DBR, in this simulation.

An Efficient Real Time Implementation of the Wigner-Ville Distribution

In the technical report written by B. Boashash and P. Black [15], a practical implementation model for the WVD is presented. A modification of the algorithm, to improve efficiency and decrease processing time by capitalising on the "symmetrical properties of the WVD kernel", (B. Boashash) is derived and presented. The Discrete Wigner Ville Distribution (DWVD) definition is shown in reference [15]. It is:

$$W_x(nT,\, f) = 2T \sum_{l=-L}^{L} x(nT + lT)\, x^*(nT - lT)\, w(l)\, w^*(l)\, e^{-j4\pi fl} \tag{75}$$

Where

$$w(lT) = 0 \quad for \ \ |l| > L;\ L \in \mathbb{Z}^+ \tag{76}$$

And

$$n = 0, 1, 2, \ldots N \tag{77}$$

Equation (75) can be expressed in terms of its "Kernel" or "Core" sequence:

$$W_x(nT,\, f) = 2T \sum_{l=-L}^{L} K(l)\, e^{-j4\pi fl} \tag{78}$$

Where the Kernel " $K(l)$ " is defined as:

$$K(l) = x(nT + lT)\, x^*(nT - lT)\, w(l)\, w^*(l) \tag{79}$$

Sampling considerations are presented in the technical report. Thereafter the optimization of the WVD of a signal is done by taking advantage of its symmetrical or quadratic nature. The symmetry properties of the Kernel can be expresses as:

$$K(l) = K^{*}(-l) \tag{80}$$

The number of operations for calculation of the DWVD is substantially reduced as result of this optimization strategy.

In this study, the DWVD was used pre-programmed as part of the TF toolbox (reference [12]). Nevertheless, the technical report by B. Boashash and P. Black [15] presents other optimization methods that could be used in a practical DBR jammer.

Smart Repeater for a Weapon Location Radar Based on Time-frequency Analysis

J. Hu et al. [24] describe developing a radar simulator that simulates the radar return from ballistic targets for testing of a "Counter Battery" Radar called the European Counter Battery Radar (COBRA). The COBRA is an Active Electronically Scanned Array (AESA) radar, used to detect enemy Rockets, Artillery, Mortars and small arms fire in order to launch countermeasures. Besides the tracking of the incoming rounds, the radar also calculates the launch position for the rounds.

In order to reduce development costs, a DRFM-based repeater was developed which negated the need to fire live rounds for testing of the COBRA. The repeater receives the radar signal, digitizes and pre-processes it, estimates the COBRA's emitted signal parameters, applies time delay, Doppler shift and RCS amplitude to the false signal and retransmits it to the radar. The repeater thus simulates a false projectile echo trajectory to the radar. Once the COBRA signal is received at the repeater, "blind de-convolution is used to pre-process the signal in order to separate the radar signal from other interference sources in the repeater's "electromagnetic" neighbourhood", J. Hu et al. [24].

Then the WVD algorithm is used to estimate the COBRA's LFM signal parameters. The WVD was chosen in this case (as opposed to other TF representations) despite its cross term interference for the multi-component signals. This decision was made, since the blind de-convolution separates the received signal into signal interferences and mono-component signals. The WVD cross terms that usually obscure a TF image of multi-component signal, are therefore not generated and the mono-component signals only are processed separately.

Once the WVD was calculated, a 10 dBW threshold on the WVD was set to eliminate noise from the WVD, which allowed the radar pulse parameters (LFM centre frequency, and rate) to be easily estimated. The application of the 10 dBW threshold on the signal is indicated in Figure 40.

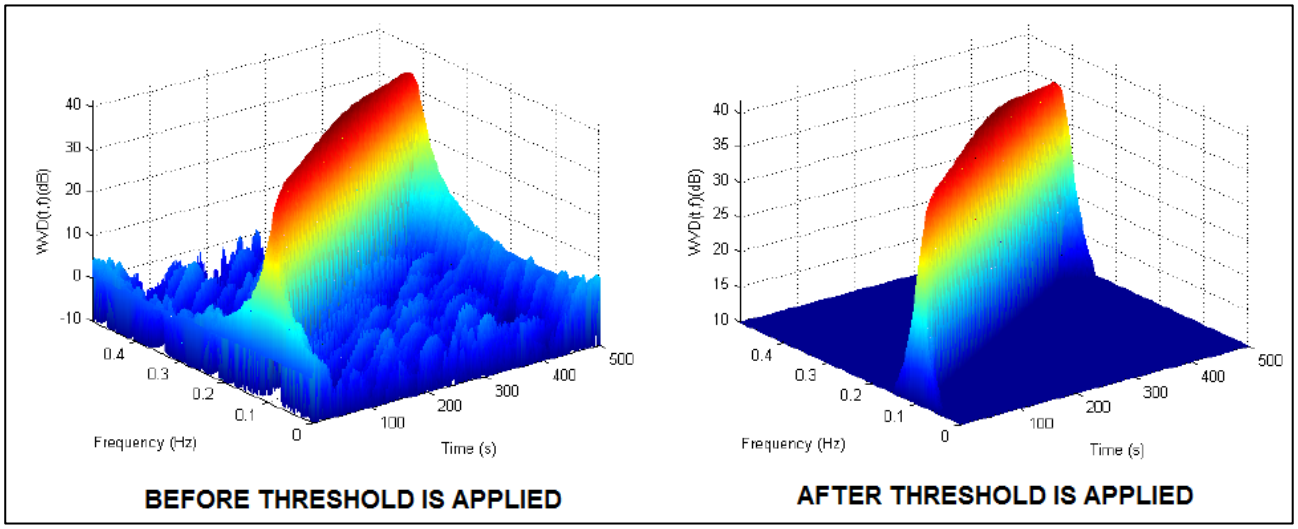

Figure 40: WVD of COBRA signal

Once the centre frequency of the chirp and its rate are estimated, signal amplitude and phase are estimated using "Psuedo Pulse Compression". The received signal used for the Psuedo Pulse Compression is:

$$x(t) = \text{Rect}\left(\frac{t}{\tau}\right) a(t) \cos\left(2\pi(\hat{f}_c \cdot t + \frac{\hat{\mu}t^2}{2}) + \psi\right) \tag{81}$$

The COBRA centre frequency and chirp rate in equation (81) were found using the WVD TF representation stated earlier. These quantities must be found before the radar signal amplitude and phase can be estimated.

This signal "$x(t)$" is then low pass filtered, using a low pass finite impulse response filter. This process is described analytically by:

$$x_I(t) = x(t) \cos\left(2\pi(f_c \cdot t + \frac{\mu t^2}{2}) + \psi\right) \otimes h(t) = a(t)\frac{\cos\psi}{2} \tag{82}$$

$$x_Q(t) = x(t) \sin\left(2\pi(f_c \cdot t + \frac{\mu t^2}{2}) + \psi\right) \otimes h(t) = -a(t)\frac{\sin\psi}{2} \tag{83}$$

The amplitude is then found from the magnitude of the I and Q components:

$$x(t) = \sqrt{x_I^{\,2}(t) + x_Q^{\,2}(t)} = \frac{a(t)}{2} \tag{84}$$

Moreover, signal phase can then be found using the result from equation (84), with equation (82) or (83) to solve for the instantaneous phase "ψ". The digitised test signal is then re-

transmitted to the radar with the appropriate time delay, Doppler shift, amplitude and phase to simulate correctly, an actual projectile trajectory.

This paper presented a method of pre-processing the repeater's return to obtain the radar signal only, using blind de-convolution. It also confirmed suitability of the WVD for estimation of LFM signal parameters. A threshold on the WVD was set in order to improve the TF representation. Then pseudo PC was used to estimate amplitude and phase of the signal. These methods are directly applicable to this study. However, this repeater was developed to test a single radar at a range that would allow sufficient SNR for the WVD to be optimal. These exact methods would not be completely valid for an ES system that must estimate target radar signal parameters outside detection range. This implies that the signal would be intercepted at long range (or low SNR).

2.3.3 Electronic Support, Contextual Summary

The report provided by F. Auger in reference [12] is the primary reference used in this study for modelling of ES techniques. The selection of the WVD as the signal estimation "tool of choice" for this study was made easy by studying the advantages and disadvantages of the numerous TF representations discussed in this paper. The toolbox summarized and classified all the TF representations that were current at that point in time.

The specific advantage of using the WVD with the HT for LFM signal detection was well described in this paper. This algorithm was selected over others, such as the Spectrogram, based on the trade-offs and constraints discussed in the toolbox.

The unsuitability of using the "Instantaneous Frequency" of a multi-component signal to represent it in the TF domain was another important point made by F. Auger that was used in this report. This fact was also corroborated by P Oliveira and V Barriso in reference [30]. They in fact redefine the "Instantaneous Frequency" of a signal in terms of the WVD and other "Cohen Class" TF representations.

Detailed information on the HT described by F. Auger in reference [12] was provided by J. Jensen in his technical report "*Hough Transform for Straight Lines*", reference [21]. This definition of the HT was used in this simulation.

In the first paper by S. Barbarossa (reference [35]), he confirms what was stated by F. Auger [12] with respect to the advantage of using the HT to suppress cross term interference generated by WVD processing of a multi-component signal. S. Barbarossa's second paper (reference [34]) provides expressions for performance measures in terms of SNR and

estimation efficiency of the combined WHT algorithm. The expressions were used in this simulation for the DBR Jammer.

B. Boashash and P. Black [15] provided interesting information on programming of the WVD and optimization of the WVD for future implementation, of the DBR Jammer.

Finally, the paper by J. Hu et al. [24] was included to identify a "real world" example of using blind de-convolution, followed by WVD processing to estimate a radar's signal parameters.

2.4 Advanced Electronic Support Algorithms

2.4.1 Technical Reports

Key points of the following technical reports on "Advanced Electronic Support Algorithms" that were researched are summarized in this section:

- *"A Detection and Parameter Estimation Algorithm of Multi-component Chirp Signals Based on Generalized S-Transform"*, reference [19]
- *"A Parameter Estimation Method for Linear Amplitude Modulated Chirp Signals Based on Discrete Fractional Fourier Transform"*, reference [39]
- *"A Fast Algorithm for Parameter Estimation of Multi-Component LFM Signal at Low SNR",* reference [42]
- *"A New Method of Detecting Multi-component LFM Signals Based on Blind Signal Processing"*, reference [43]

A Detection and Parameter Estimation Algorithm of Multi-component Chirp Signals Based on Generalized S-Transform

D. Wang et al. [19] describes an improved method of LFM signal detection and estimation in low SNR called the "Generalized S-Transform". A distinguishing future of this algorithm is that it is designed to work at a low SNR. Many TF representations including the WVD suffer from interference in the TF Plane when a multi-component signal is processed. This interference, as stated by F Auger in reference [12], is caused by the cross WVD terms formed during the calculation. Because of this problem with the TF representations, the "S-Transform" was developed. It was derived from the STFT and CWT and defined as:

$$S_x(\tau_d, f) = \int_{-\infty}^{\infty} x(t) \frac{|f|}{\sqrt{2\pi}} e^{\frac{-f^2(\tau_d - t)^2}{2}} e^{-j2\pi ft} dt \tag{85}$$

With the window function being

$$w(\tau_d - t, f) = \frac{|f|}{\sqrt{2\pi}} e^{\frac{-f^2(\tau_d - t)^2}{2}} \tag{86}$$

The advantage of the S-Transform is that the window function changes width, with frequency, which allows a variable resolution to be applied to the signal. This is a characteristic of the CWT TF representations. However, despite this, the S-Transform still suffers from poor time and frequency resolution compared to the WVD. Nevertheless, an advantage of the S-Transform, is that, there is no multi-component cross term interference generated.
In order to improve the resolution of the S-Transform a "Generalized S-Transform" was then developed. The equation for it is shown below:

$$GS_x(\tau_d, f) = \int_{-\infty}^{\infty} x(t) \frac{|p_1||f|^{p_2}}{\sqrt{2\pi}} e^{\frac{-p_1^2 f^{2p_2}(\tau_d - t)^2}{2}} e^{-j2\pi ft} dt \quad (87)$$

Where

$$p_1, p_2 \in \left[\frac{1}{2}, \frac{3}{2}\right] \quad (88)$$

The "Generalized S-Transform" exhibits better time and frequency resolution than the S-Transform and no cross term interference. However, its resolution is still worse than the WVD. Using the Generalized S-Transform together with the Hough Transform nevertheless, does produce better overall results. A comparison of the WHT, S-Transform and HT and Generalized S-Transform and HT are shown in Figure 41. The poor TF resolution of both the S-Transform and Generalised S-Transform compared to the WVD can be seen in the subplots on the left of Figure 41. However, the improved performance of the Generalised S Transform with the HT over the other two algorithms can be inferred by the distinct peaks formed per single component.

A deficiency of this paper was that the performance of the Generalized S Transform algorithm in low SNR was not clearly stated. In addition, no comparison was made between the Generalized S-Transform and RSPWVD, which is the "flagship" of the WVD distributions. This was despite D. Wang et al. acknowledging the advantages of the RSPWVD in reference [19].
The RSPWVD does not suffer from cross term interference as much as the WVD and it also offers better time and frequency resolution compared to the Generalized S-Transform. The RSPWVD is also easier and faster to calculate compared to the S-Transform and is therefore still the best candidate for a two dimensional TF based LFM signal representation.

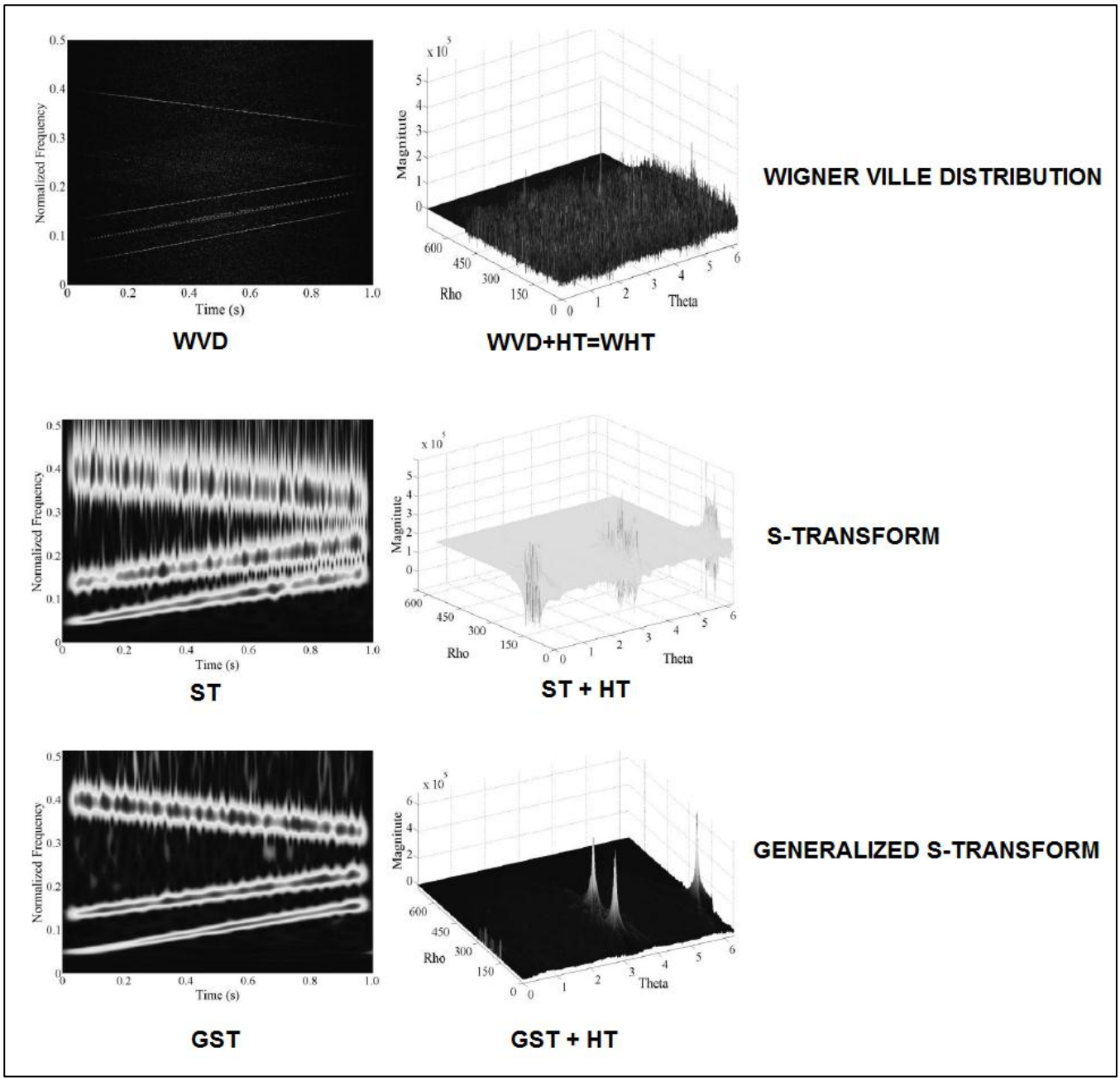

Figure 41: Generalized S-Transform with HT, Comparison, three component signal

A Parameter Estimation Method for Linear Amplitude Modulated Chirp Signals Based on the Discrete Fractional Fourier Transform

S. Z. K. Sajib and A. Mostayed [39] present a practical ES algorithm to estimate the parameters of multi-component non-stationary signals. The method uses the WVD and Radon Transform (RT) to obtain the LFM chirp rate and centre frequency. Then, the Fractional Fourier Transform (FrFT) is used to estimate amplitude and phase of the intercepted radar signal. An advantage of using these methods is that all the signal parameters can be estimated using the three methods (WVD, Radon Transform and FrFT).

An important result was the low SNR performance of the method, which can operate in SNR,'s as low as -10dBW.

The Radon Transform is an image-processing tool that operates similarly to the Hough Transform. In this paper, an analytic expression is found for the peak coordinates of the LFM signal using the RWT. Nevertheless, the performance of the RWT is similar to the WHT and the LFM centre frequency and rate are found in a similar manner.

The FrFT used to estimate signal amplitude and phase is defined as:

$$F^{\alpha}\left[x(t)\right] = X_{\alpha}(u) = \int_{-\infty}^{\infty} x(t) K_{\alpha}(t,u)\,dt \tag{89}$$

Where

$$K_{\alpha}(t,u) = \begin{cases} \sqrt{\dfrac{1-j\cot\alpha}{2\pi}}\; e^{j\frac{(t^2+u^2)\cot\alpha}{2} - j\frac{tu\ \mathrm{cosec}\,\alpha}{2}} & ; \quad \alpha = 0, n\pi \\ \delta(t-u) & ; \quad \alpha = 0, 2n\pi \\ \delta(t+u) & ; \quad \alpha = \pi, (2n\pm 1)\pi \end{cases} \tag{90}$$

A big advantage of using the FrFT for estimating unknown LFM signal parameters is that it is computationally faster, since it involves a "*one dimensional"* processing for a peak parameter as opposed to a "*two dimensional"* processing used in the TF representations (Spectrogram, WVD, etc.). The accuracy of the FrFT method for obtaining signal amplitude and phase is high despite operating at low SNR's.

A Fast Algorithm for Parameter Estimation of Multi-Component LFM Signal at Low SNR

In the paper written by P. Wang et al. [42], an ES signal intercept model that is both fast in terms of processing overhead, and capable of working at low SNR is described. Measurement uncertainty metrics are presented for the algorithm operating at SNR's as low as -13 dBW. The algorithm applies the FrFT on the multi-component chirp signal, to determine the LFM chirp rate using fast one-dimensional processing. The FrFT is calculated for each angle "$\alpha_n = 1, 2, \ldots M$". Then, a detection statistic based on the squared magnitude of the FrFT is used to calculate the "Fractional Autocorrelation (FA)". This quantity is defined as:

$$R_{\alpha}(\rho) = e^{j\pi\rho^2\cos\alpha\sin\alpha} \int x(t)\, x(t-\rho\cos\alpha)\, e^{-j2\pi t\rho\sin\alpha}\,dt \tag{91}$$

However, the FA can be easily found, once the FrFT of the signal is calculated from the "Inverse Fast Fourier Transform (IFFT)" of the squared magnitude of the FrFT:

$$R_{\alpha}(\rho) = IFFT\left\{\left|X_{\alpha}(u)\right|^2\right\} \tag{92}$$

Once the FA has been calculated, a detection statistic for the LFM signal can be calculated using:

$$L(\alpha) = \int_{-\infty}^{\infty} \left| R_{\alpha}(\rho) \right| d\rho \tag{93}$$

The peak of this function "$L(\alpha)$" corresponds to the estimate chirp rate, i.e. "$\hat{\alpha} = \tan^{-1} \hat{\mu}$".

When the chirp rate has been estimated, the centre frequency and signal amplitude can be found using the following equations:

$$\hat{f}_c = \hat{\mu} \operatorname{cosec} \hat{\alpha} \tag{94}$$

$$\hat{A} = \max \frac{\left| X_{\hat{\alpha}}(u) \right|}{\sqrt{\frac{1 - j \cot \alpha}{2\pi}}\ \Delta t} \tag{95}$$

Once the LFM signal parameters have been estimated, the "Clean" algorithm is used to find all the components of the multi-component signal, using the following steps:

- The signal is reconstructed using the estimated parameters.
- It is then subtracted from the total multi-component signal.
- The process is repeated until no signals can be detected in the observed signal using the "FrFT based" detector.

The method described in this report is both fast and practical. The amplitude of the pulse can also be estimated easily. The "Clean" algorithm implemented to detect all multi-component signals is a quick and easy method to process the multi-component signal without the complications related to the cross term interference – resolution trade-off inherent to many 2D TF representations.

Nevertheless, the FrFT method for multi-component LFM signal detection is optimised for LFM signals only but other two dimensional TF representations can be used to visualize a signal with many different types of modulations, besides linear.

A New Method of Detecting Multi-component LFM Signals Based on Blind Signal Processing

Q Guo et al. in reference [43] presents a method of multi-component LFM signal detection that uses Fast Independent Component Analysis (FastICA) for pre-processing of a multi-component non-stationary LFM signal embedded in noise. The FastICA algorithm separates

the radar signal components from noise at the outset of the signal processing. This FastICA algorithm is a type of Blind Source Separation processing.

Q Guo et al. [43] then use the "Second Central Moment of FrFT" to identify the noise component in the signal after the radar signals have been separated using FastICA. Once this has been done the FrFT algorithm is run *separately per signal component* identified in the observed multi-component signal.

The method uses "Independent Component Analysis" (ICA) with the FrFT and provides a large improvement over the standard FrFT, in low SNR. A "two order-of-magnitude" improvement is shown at an SNR of -15 dBW by using the FastICA with FrFT, compared to using the FrFT alone.

2.4.2 Advanced Electronic Support Algorithms, Contextual Summary

The performance advantages of using the Generalized S-Transform with the HT (D. Wang et al. reference [19]), was not sufficient to justify its use in this simulation. As a two-dimensional TF representation, it does not significantly outperform the WVD. No comparison was made against the RSPWVD in D. Wang's paper, which outperforms the Generalised S-Transform.

The FrFT offers distinct advantages in terms of processing speed over any of the two-dimensional TF representations, including the WVD. S. Z. K. Sajib and A. Mostayed [39] present a method that utilises both two-dimensional (WVD and Radon Transform) as well as a one dimensional TF representation (FrFT) to estimate all the intercepted radar's LFM signal parameters.

Improvements to the methods used by S. Z. K. Sajib and A. Mostayed [39] are those proposed by P. Wang et al. [42], and Q. Guo et al. in reference [43]. These methods are faster since they make use of a one-dimensional TF representation only (FrFT), to estimate *all* of the signal parameters.

Using the methods described by Q Guo et al. [43], the interference, resolution and processing problems associated with two-dimensional TF representations such as the WVD can be avoided, since the FrFT is run per LFM signal component. The method described by P. Wang et al. in reference [42] is similar to Q Guo's except the "Clean" algorithm is used at the end of the detection and estimation process to "separate" or eliminate identified signal components. Using FastICA reduces or eliminates noise and other interference sources from the signal *before* processing, which allows a larger SNR signal to be processed.

However, a disadvantage of using the FrFT, is that signals other than a LFM signal would not be detected and characterised, whereas the two-dimensional TF representations visually

show the signal modulation type clearly. This is done whether the signal is amplitude or frequency modulated. The type of modulation can be linear, non-linear, or coded. All of this information will be visible on the 2D representation of the signal's TF relationship.

The optimal and most robust solution for detecting an unknown multi-component signal would be to perform the FastICA algorithm on the signal. Thereafter the low interference RSPWVD or conventional WVD is applied. The WVD can be used despite the raw signal having multiple components since the FastICA algorithm separates the components, and therefore a single signal component can be processed. If the signal is classified as a LFM signal, either the HT or FrFT should be used to estimate the LFM parameters. In general, multiple TF representations can be used to process the signals if sufficient time is available.
The algorithm choice, once the LFM pulse has been confirmed also depends on the integration time available, as well as SNR. Thus, it can be seen that an actual ES system would have to process the intercepted radar signal with multiple detection and processing algorithms in order to classify and optimise parameter estimation.
The conclusions drawn in this chapter on "Advanced Electronic Support Algorithms" were not simulated but rather recommended for future versions of this simulation.

2.5 Electronic Attack Algorithms

2.5.1 Textbooks

The fundamental textbook used to model EW system performance is the textbook, "*Electronic Warfare in the Information Age"*, by D. Schleher [4]. Repeater and noise jammer theory, LFM signal definitions and general theory on EW is described in this textbook. Useful information and simulations on cross-eye jamming is also described in this textbook.
The Electronic Warfare and Radar Systems Engineering Handbook [10] describe the fundamental system-level Radar-EW considerations, such as jammer techniques and methods, fundamental radar-jammer Radio Frequency (RF) power relationships and basic descriptions of the physical radar phenomena.

2.5.2 Technical Reports

The following technical reports that were researched are summarized in this section:

- *"Solid-state Multiple Deception Jamming System For ECM Applications", reference* [14]
- *"ECM Modelling for Assessment of Target Tracking Algorithms"*, reference [32]

- "*Benchmark Problem for Beam Pointing Control of Phased Array Radar Against Manoeuvring Targets in the Presence of ECM and False Alarms"*, reference [44]
- *"DRFM Linear Range Gate Stealer Spectrum"*, reference [36]
- "*Study on Frequency-shifting Jamming to Linear Frequency Modulation Pulse Compression Radars",* reference *[45]*
- *"Simulated Study of Jamming of LFM PC Radar Signal", reference* [46]
- *"Denial Jamming Technique Development against Pulse-Doppler Radars using the Genetic Algorithm"*, reference [37]

Solid-state Multiple Deception Jamming System for ECM Applications

A. Madni and H. M. Endler in reference [14] describe solid-state devices for multi-technique deception jamming. The "Solid-state, phase-shifting serrodyne techniques are discussed as a high performance, light-weight, high reliability and low cost alternative to the medium power Traveling Wave Tube Amplifier (TWTA) generated deception jamming", A. Madni and H. M. Endler (reference [14]).

Amplitude modulation is achieved by voltage control of "Positive-Intrinsic-Negative" (PIN) Diodes or Gallium Arsenide (GaAs) Field-Effect Transistors (FET). These components are built into integrated circuits called Microwave Integrated Circuits (MIC) or Monolithic MIC (MMIC).

RF frequency translation is achieved using "serrodyning". This technique is a means of frequency translation that is used to induce frequency shifts into a signal by exploiting the fact that frequency is proportional to the rate of change of signal phase albeit for a mono-component signal.

Serrodyning is implemented in solid-state devices using three techniques; "Digital Phase Shifters", "Single Sideband Suppressed Carrier up converter" techniques and "Vector Modulators". The principle of operation of these devices, their structure, as well as their performances is described in detail in this technical report. Some deception jamming techniques that can be generated by the solid-state digital phase shifters were then discussed. Velocity Gate Stealing, Repeater Swept Amplitude Modulation, Velocity Gate Stealing with angle deception, Gate Stealing, Narrow Band Repeater Noise, Random Doppler, Multiple Frequency Repeating, and Psuedo Random Noise are the techniques discussed. These techniques are intended to be used against a tracking radar. An example of the application for this device is a self-protection jammer, used by a fighter jet, against an attacking radar guided missile.

The Velocity Gate Stealer "pulls off" a radar's velocity tracking gate from the actual target. An example of the radar spectrum after Velocity Gate Stealing is shown in Figure 42. The false velocity is represented by the second peak in the spectrum. Velocity Gate Stealing is also known as Velocity Gate Pull Off (VGPO)/Velocity Gate Pull In (VGPI).

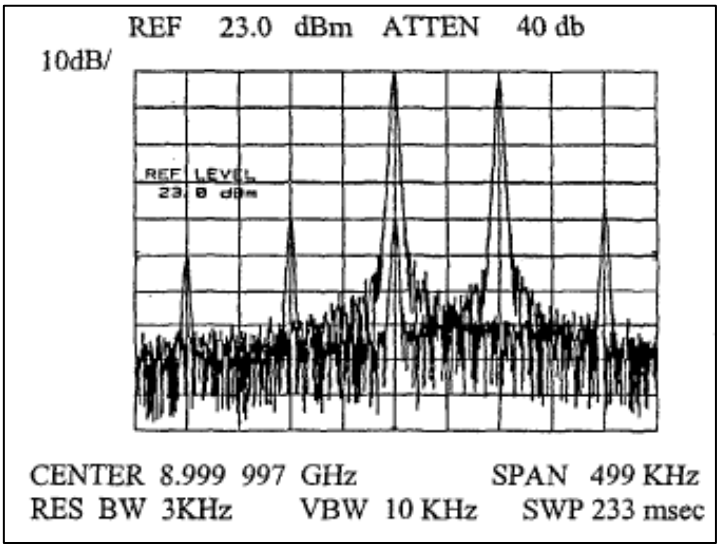

Figure 42: Velocity Gate Stealer Spectrum

"Repeater Swept Amplitude Modulation" is generated by amplitude modulation of the repeated radar signal at a frequency that is linearly varied in a sawtooth pattern. The result in terms of radar spectrum is shown in Figure 43. It can be seen that spectrum of the false signal masks the true target.

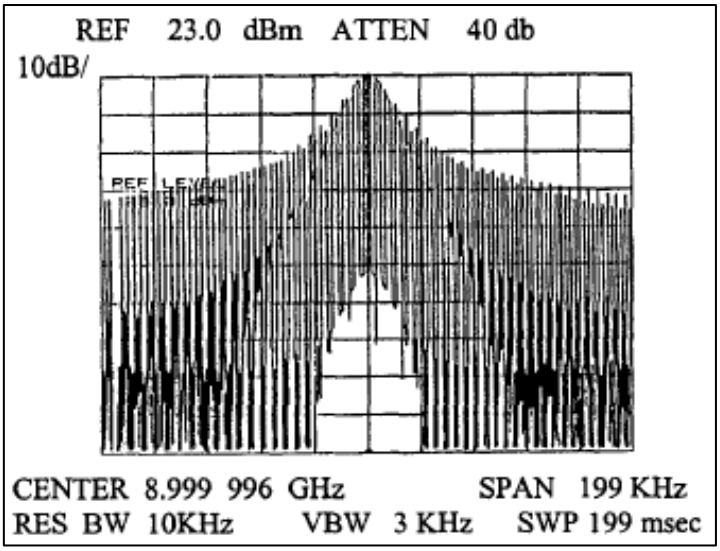

Figure 43: Repeater Swept Amplitude Modulation Spectrum

Combining Velocity Gate Stealing with Repeater Swept Amplitude Modulation allows the jammer to simulate a false target in velocity and angle. See Figure 44 for the radar spectrum of these combined jamming techniques. The true target is shown by the darker spectrum.

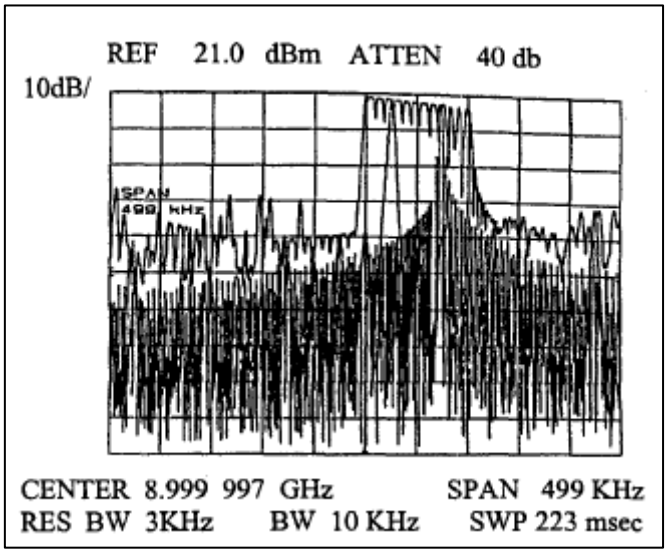

Figure 44: Velocity Gate Stealer with Angle, Spectrum

Generating Narrowband Repeater Noise has the effect of "smearing" the repeater spectrum as shown in Figure 45.

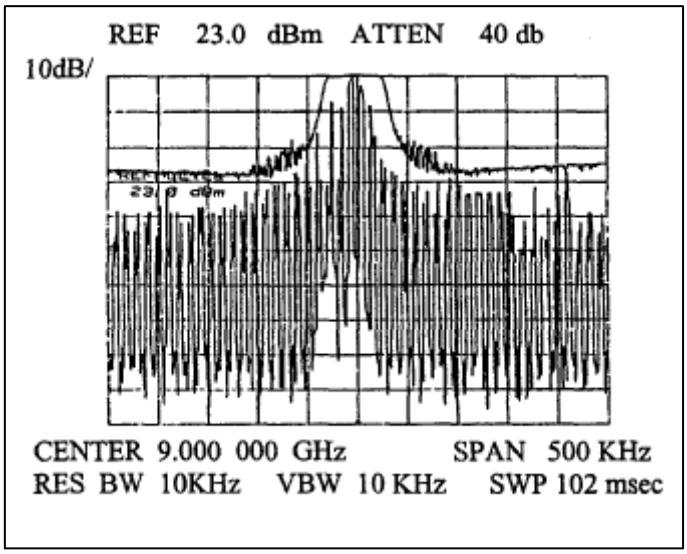

Figure 45: Narrowband Repeater Noise

Inducing multiple false targets by generating many random Doppler frequencies masks the true target as shown in the spectrum in Figure 46.

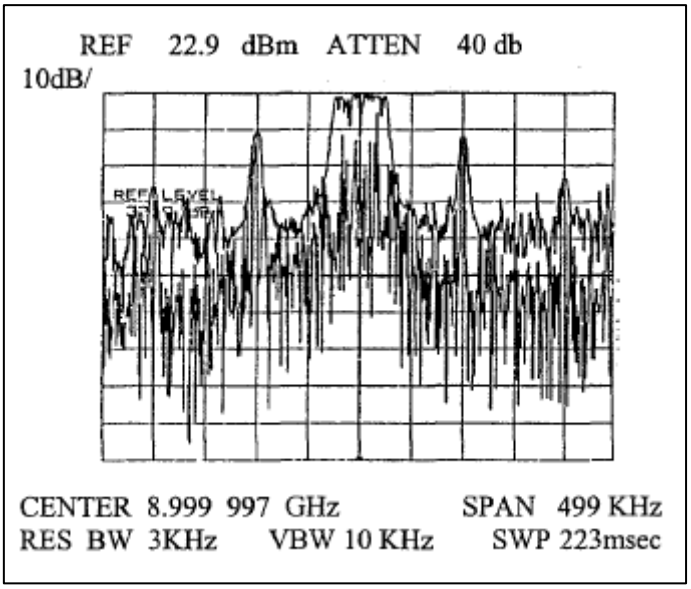

Figure 46: Random Doppler

Multiple frequency jamming is also known as "cover pulse" jamming or "blanket" jamming. This technique also masks the true target as shown in Figure 47.

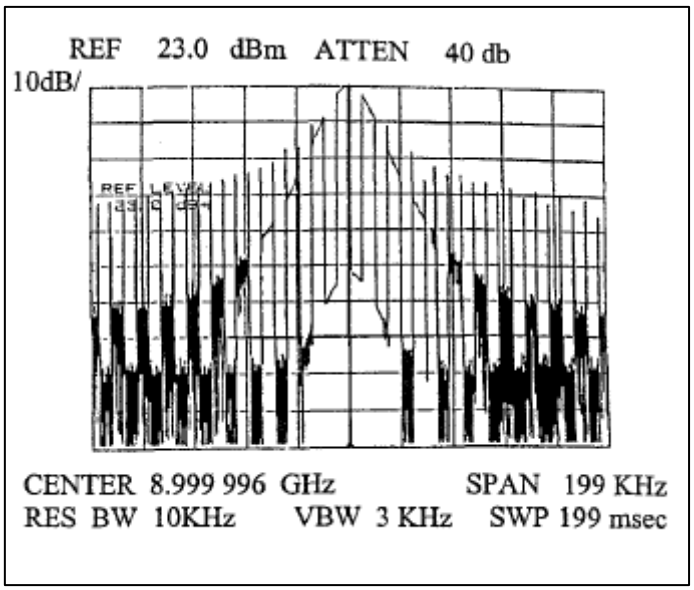

Figure 47: Multiple Frequency Jamming

"Smearing" of the spectrum to mask the true target can also be done by generating "Pseudorandom Noise", by serrodyning the phase shifter with a random saw tooth frequency. The effect on the repeater spectrum is shown in Figure 48.

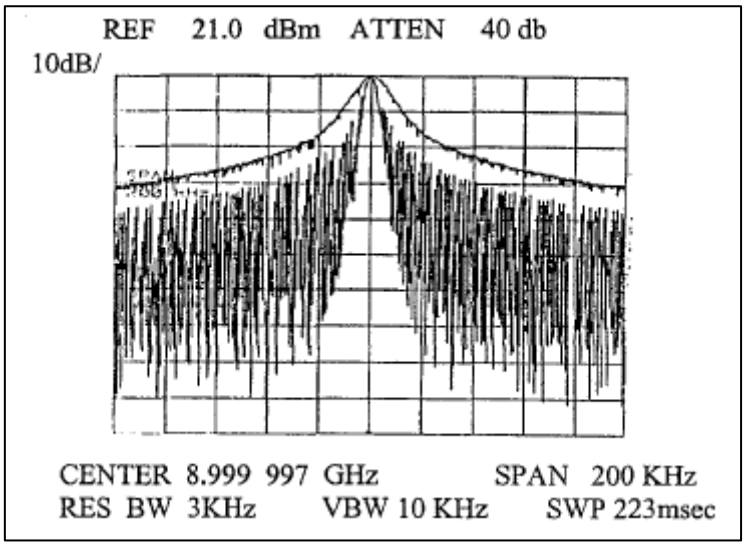

Figure 48: Psuedo Random Noise

Although the jamming techniques discussed in the report by A. Madni and H.M. Endler were developed using serrodyning in digital phase shifters they can still be implemented digitally in a DRFM. However, it is probable that the devices as described would not be effective against a multi-component signal if they were directly applied (without blind de-convolution techniques). This is because the devices use the definition of instantaneous frequency as the rate of change of phase, which is not valid for multi-component signals, as already discussed in section 2.3.3. Nevertheless, useful spectrums of the jamming on the radar that allow visualization of the process have been provided in this technical report. These spectrums will guide the DRFM technique generation in this study.

ECM Modelling for Assessment of Target Tracking Algorithms

In this research paper by P. West and B.J. Slocomb [32], EA models for testing target tracking algorithms on a radar termed the "Benchmark Radar Model" are presented. The Benchmark Radar Model was developed by radar engineers to provide a radar standard, on which to test radar algorithms as well as EW algorithms that were developed by different engineers. The goal was to provide the same basis for comparison of different EA and EP algorithms.

This model describes a "beam-agile electronically scanned phased array, track-while-scan radar" (reference [32]). The radar uses a single pulse phase coded waveform for target detection and processing. Angle tracking is done using monopulse processing.

Because of these features, the radar is difficult to jam and EA techniques are limited to a small class of possibilities. Two types of jamming would nevertheless still be effective against this radar. These would be range deception jamming which includes induce targets at false ranges and "Range Gate Pull Off" (RGPO). This is a technique to steadily "pull off" a tracking radar's

range gates (or designation window) from the true target in order to "break lock". This type of situation would naturally occur, if two actual aircraft that were flying initially in the same radar RD cell suddenly separate. These deception jamming techniques could be implemented in a repeater jammer such as the DRFM.

Two EP measures used by the Benchmark Radar restrict jamming possibilities even further. The radar uses a single pulse and its update rate is asynchronous. Therefore inducing a false target at a range closer to the radar than the true target would be ineffective. Because of this, "Range Gate Pull *In*" as a technique is not considered at all.

An additional technique that might be effective is the "range denial" of the true target. This could be implemented using a transponder-based wideband or narrowband noise jammer. The effectiveness of this technique depends on numerous factors such as radar transmitter vs. jammer power and antenna gain, range between radar and jammer, etc.

Since the Benchmark Radar did not have Doppler processing, no velocity deception jamming techniques were necessary or simulated in this technical report.

An algorithm that simulates false ranges for a constant acceleration false target is:

$$\tau_d(t) = \frac{a_o}{c} t^2 \quad ; \quad t \le T_{ca} \tag{96}$$

$$\tau_d(t) = \frac{a_o}{c} T_{ca}{}^2 + \frac{2v_o}{c}(t - T_{ca}) \quad ; \quad t > T_{ca} \tag{97}$$

These time delays are inserted into replicas of the radar's transmitted signal as follows:

$$x^f(t) = A\sum_{n=0}^{M} x(t - \tau_d{}^n) \tag{98}$$

RGPO profiles for three false targets are shown in Figure 49. The separation between true and false trajectories is clearly visible in the figure. In addition, a "hook pulse" is shown at the end of the false trajectory. The hook pulse is a strong amplitude (higher than true target skin return) pulse that tries to ensure radar does not reacquire the true target.

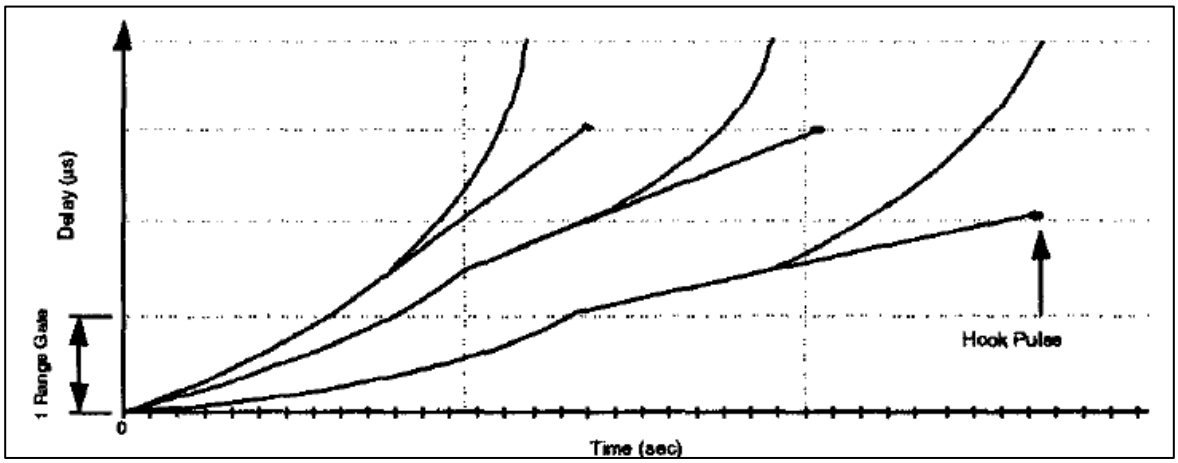

Figure 49: RGPO profiles for three false targets (reference [32])

Cover pulses that mask the true target return could also be effective at the start of the jamming cycle. A specific condition to RGPO effectiveness is that the RGPO be stopped after the false target is further than one range Doppler cell away from the true target. This is because, if the radar continues to track the false target, the radar's angle tracking would still be effective in its "track-while-scan" mode, which would allows the true target to be detected and tracked.

A possible EP measure recommended by the author against the EA proposed is for the radar to de-prioritize targets further than the closest detection. All targets are compared pairwise and the monopulse angle discriminant is then used, to discriminate between the targets. However, an EP based on this method would then be vulnerable to close-in clutter returns.

This technical report, despite describing EA of an electronically phase array antenna still includes RGPO algorithms that would be useful against the DBR. Practical, applicable electronic protection measures of the radar have also been mentioned.
An additional EP of the DBR is that it uses Doppler processing, so it is important for the EA system to coordinate the RGPO carefully with velocity deception jamming in order to avoid detection by the radar of the false deceptive targets.

Benchmark Problem for Beam Pointing Control of Phased Array Radar Against Manoeuvring Targets in the Presence of ECM and False Alarms

W.D. Blair et al. [44] describe the parameters and operation of the "Benchmark Radar Model" in detail. This is the same radar model used by P. West and J. Slocomb in reference [32].
Both the system performance equations and signal definitions for the electronically scanned phased array radar are provided. The signal definitions include expressions for the monopulse tracking signal and error. W.D. Blair et al. in reference [44] also provide two simple expressions for RGPO. The first equation describes a linear RGPO model, equation (99) and the second equation describe a parabolic RGPO trajectory.

$$R_o{}^f(t) = R_o(t) + v_o{}^f(t - t_i{}^f) \tag{99}$$

$$R_o{}^f(t) = R_o(t) + \frac{1}{2} a_o{}^f(t - t_i{}^f)^2 \tag{100}$$

The equations above can be used to simulate RGPO against the DBR and are not limited to a radar of similar type to the Benchmark Radar Model.

DRFM Linear Range Gate Stealer Spectrum

S. D. Berger [36] derives an analytic equation describing the DRFM spectrum of a PD sinusoidal signal. The effect of digitization of the intercepted radar signal on the DRFM spectrum is also derived. False target velocity is simulated by inserting a false Doppler frequency into the signal. Thereafter an analytic expression for the spectrum is found.

The author also emphasizes the need to coordinate "Range Gate Pull Off" (RGPO)/"Range Gate Pull In" (RGPI) with "Velocity Gate Pull Off" (VGPO)/"Velocity Gate Pull In" (VGPI), in order to present a consistent false target to the radar, by the EA system. RGPO/RGPI refers to the "pulling off" or "pulling in" of a radar's range tracking gates away from the true target. The false range increases either closer to the radar (RGPI) or moves further away from the target (RGPO). VGPO and VGPI refer to the "pulling off" or "pulling in" of a radar's velocity tracking gates.

It is important for the jammer to coordinate range deception jamming with velocity deception because some PD radars perform consistency checks on their velocity measurements.

The target velocity calculated from the "range rate (time derivative of range)" and velocity obtained through Doppler processing are compared to one another. If the target velocities obtained from two methods are different, then this discrepancy is indicative of a false target.

Easy to use analytic expressions for the magnitude of the DRFM digitization spurs, their spacing and shift due to induced frequency were also derived by S.D. Berger in this paper.

The DBR uses a LFM signal and not a pure sinusoid. Therefore, the expressions for the derived false signal spectrum in reference [36] would therefore not be valid for the LFM signals used by the DBR.

The effect of spurs as result of the "A/D – D/A" digitization of the radar signal was done for a sinusoidal signal sampling at a rate of *10 kHz*. Modern A/D's and D/A's sample at *"GHz"* rates. Because of this "two order of magnitude", improvement in digitization technology, compared to the A/D simulated by S. Berger in 2003, the DRFM sampling period is much smaller. Therefore, the magnitude of the spurs would be much smaller than predicted by S. Berger. Because of this, the EP method of designing the radar to detect the false target spurs or spectral lines in the received signal would not be effective in the current age of "GHz" digitization.

For the Jammer in this study, the spectrum of the signal is found using the "fft.m" Matlab function of the signal. An analytic expression for the spectrum was therefore not necessary, in this simulation.

Study on Frequency-shifting Jamming to LFM Pulse Compression Radars

Y. Yang in reference [45] describes three methods of "frequency-shift" jamming to induce targets at false ranges into the radar. The method would be easy to implement in DRFM algorithms or even in the Digital Phase Shifters described by A. Madni and M. Endler in reference [14]. The basic principle is that the frequency be inserted into a sinusoidal replica of the intercepted radar signal. Y. Yang describes the various permutations of the method as "Single False Target Jamming", "Multiple False Target Jamming" and Multiple Cover Jamming. The signal model for Single False Target Jamming is shown below:

$$x^f(t) = e^{j2\pi f_j t + j\pi\mu t^2} \quad ; \quad |t| < \frac{T}{2} \tag{101}$$

The signal shown above is the baseband jammer signal before up conversion and repeat transmission to the radar, by the DRFM. Upon up-conversion at the DRFM, the induced frequency " f_j " is added to the carrier estimate frequency.

The model for the multiple false target signal is shown in equation (102):

$$x^f(t) = e^{j2\pi f_{jm}(n_s)t + j\pi\mu t^2} \quad ; \quad |t| < \frac{T}{2} \tag{102}$$

$$f_{jm}(n_s) = f_{jo} + (n_s - 1)\Delta f_j \tag{103}$$

Multiple targets are generated by the multiple frequencies inserted into the signal model using equation (103).

The signal model for "Multiple Cover" jamming is shown in equation (104):

$$x^f(t) = e^{j2\pi f_{jc}(n_s)\,t + j\pi\mu t^2} \quad ; \quad |t| < \frac{T}{2} \tag{104}$$

$$f_{jc}(n_s) = f_{jo}(t) + (n_s - 1)\Delta f_j \tag{105}$$

In this case, the constituent signal components are linearly frequency modulated. The TF relationship of the multi-component non-stationary signal " $f_{jc}(n_s)$ " is shown in Figure 50.

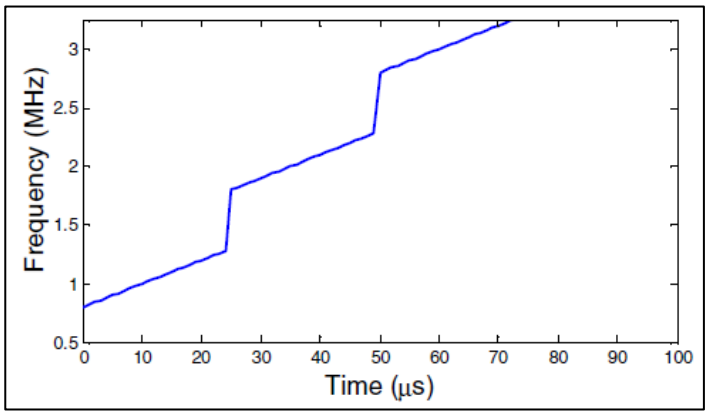

Figure 50: "Multiple Cover Pulse " Frequency Shift Jamming (reference [45])

Analytic expressions were found by Y. Yang for the match-filtered responses of the false signals at the radar. Thereafter the analytic expressions were tested through simulation. The radar match filter outputs for all three proposed jamming methods (single target, multiple target and multiple cover pulse) are shown in Figure 51. It can be seen that the false targets can be induced into the radar using the frequency shift method proposed. In addition, the false targets can deceive the radar, provided that the radar's signal is estimated accurately and that the correct amplitude modulation is applied to the false signals.

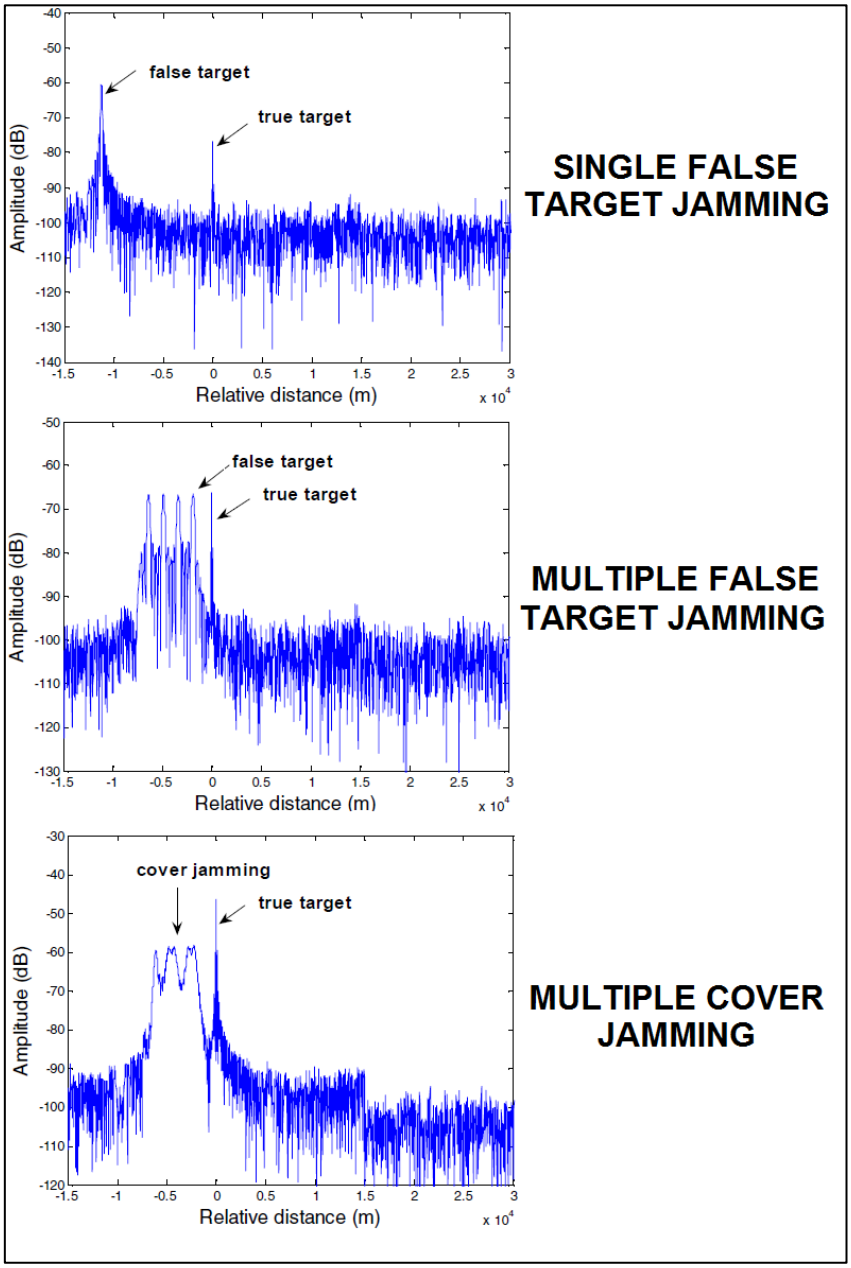

Figure 51: Matched Filter response for Frequency Shift Jamming (reference [45])

.

Simulated Study of Jamming of LFM PC Radar Signal

Z. Bin [46] in this paper describes important deception jamming techniques for radar that use LFM signals. Interestingly this paper was originally written in Chinese! "Google Translate" was used to translate the report.

Analytic expressions for the LFM signal and its spectrum are shown initially. Then deception jamming signal models that could be easily implemented in a DRFM are presented. An important expression for a smart noise signal generated by a DRFM is shown. It is:

$$J_1(t) = U_n(t) \cdot \cos\left(2\pi \cdot f_j \cdot t + \varphi(t)\right) \tag{106}$$

Where the signal phase is a random number sampled from a "Uniform Distribution" with:

$$\varphi(t) \in [0\,;\,2\pi] \tag{107}$$

Thereafter signal models for cover pulse jamming and frequency shift jamming to induce false ranges and Doppler shifts are shown. These expressions are identical to those shown in reference [45] and corroborate that work done by Y Yang. The effect of the deception jamming Models, on a radar's match filter response were simulated and included in this report.

The technical report presents the deception jamming signal models in clear and straightforward manner. These simple equations were not explicitly stated in any textbook or most of the technical reports reviewed in this study. These methods also operate on the assumption that the victim radar's signal parameters are accurately estimated so that the DRFM can use the signal for deception jamming.

Denial Jamming Technique Development against Pulse-Doppler Radars using the Genetic Algorithm

S. Kristoffersen and H. J. F. Meon in reference [37] describe an advanced DRFM based jamming technique that uses the "Genetic Algorithm (GA)" to mask true target detection by radar. The effect on the radar is similar to coordinated conventional "cover pulse jamming" that obscures the true target. In this case, however the DRFM uses the GA algorithm to simultaneously manipulate the radar's range and Doppler signal power in the CFAR guard band. This is done in order to manipulate the radar's "Cell Averaging Constant False Alarm Rate" (CA-CFAR) mechanism. In a radar, the CA-CFAR is used to set the detection threshold for target detection. The signal power for a true target has to be above the detection threshold before it is recognized. By manipulating the CA-CFAR, the jammer is able to manipulate the radar into erroneously raising its threshold, so that the true target is not detected. Signal power in the guard cells around the target is altered, without the radar detecting the jammer.

A “radar-jammer engagement” generally occurs in a complex electromagnetic environment (clutter, interference, noise etc.). Because of this conventional RD cell power optimization methods are complex since it is “hard to obtain continuous and differentiable mathematical descriptions of the system” S. Kristoffersen, H. J. F. Meon (reference [37]). The GA algorithm was selected by them, because solutions to problems with a large number of states can be solved for and the algorithm does not require that system description functions be differentiable.

The GA algorithm operates on the Range-Doppler map as shown in Figure 52.

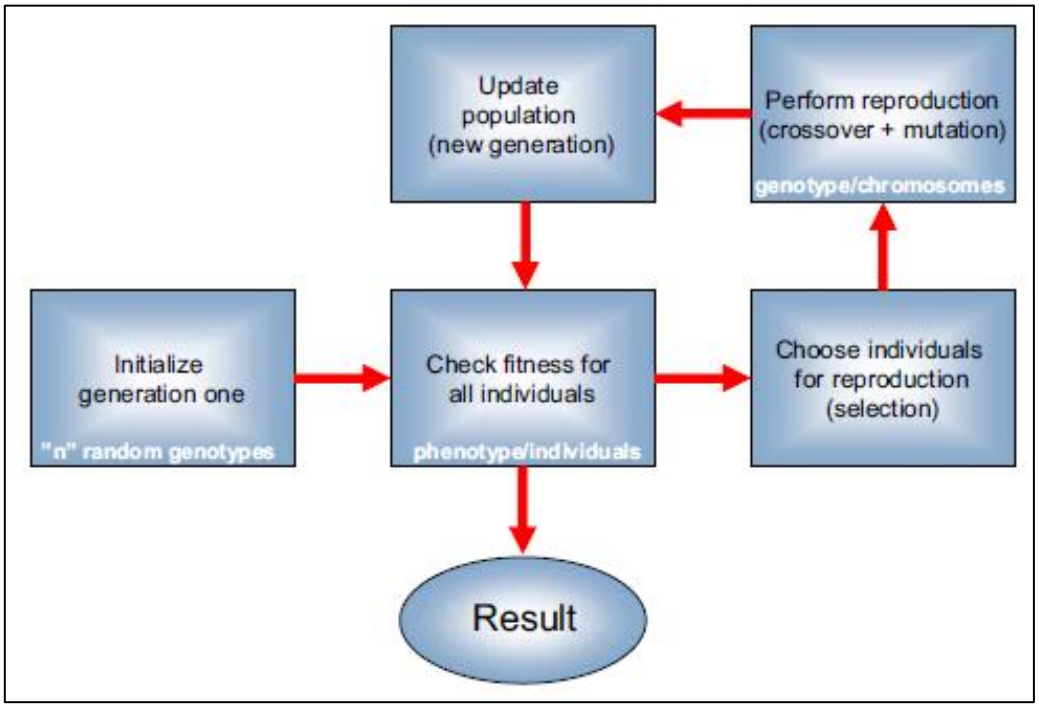

Figure 52: GA algorithm, Principle of Operation (reference [37])

In this context, the “Genetic Engineering terms” for the GA algorithm are related to the radar-jammer elements as follows:

- The “genotype” or “chromosome” is the bit string used to program an instance of the false RD map. A “gene” is an element of the chromosome that codes an individual RD cell.
- The “phenotype” or “individual” that the chromosome codes, is the manipulated RD-matrix
- The fitness or quality evaluation of each individual is the CFAR ratio.
- The environment on which to evaluate fitness is the CFAR ratio matrix.

The bit strings used to program the individual cells in the RD map are shown in Figure 53. Individual bit strings defined by the “genes” in the “chromosome” control the signal power levels in the RD cells.

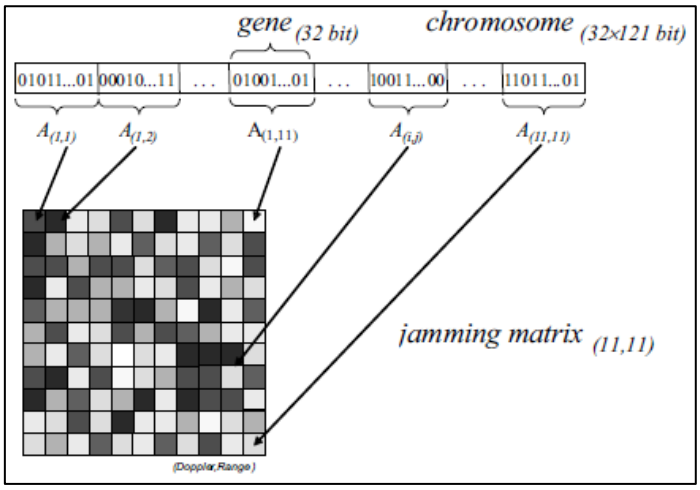

Figure 53: GA Chromosome relationship to Range Doppler Map

The effect of the jamming on the radar is shown in Figure 54. This result was obtained with a known target RCS. The true target is shown in the centre of the radar's RD map (or matrix). The CFAR ratio matrix is shown adjacent to the RD Matrix. The last image in the row is the output of the CA-CFAR processor showing 100 detections on a scan. When GA jamming is active the true target is not detected, nor is the jammer detected. This detection failure of the radar is due to the GA Jamming method's subtle manipulation of signal power in the RD map.

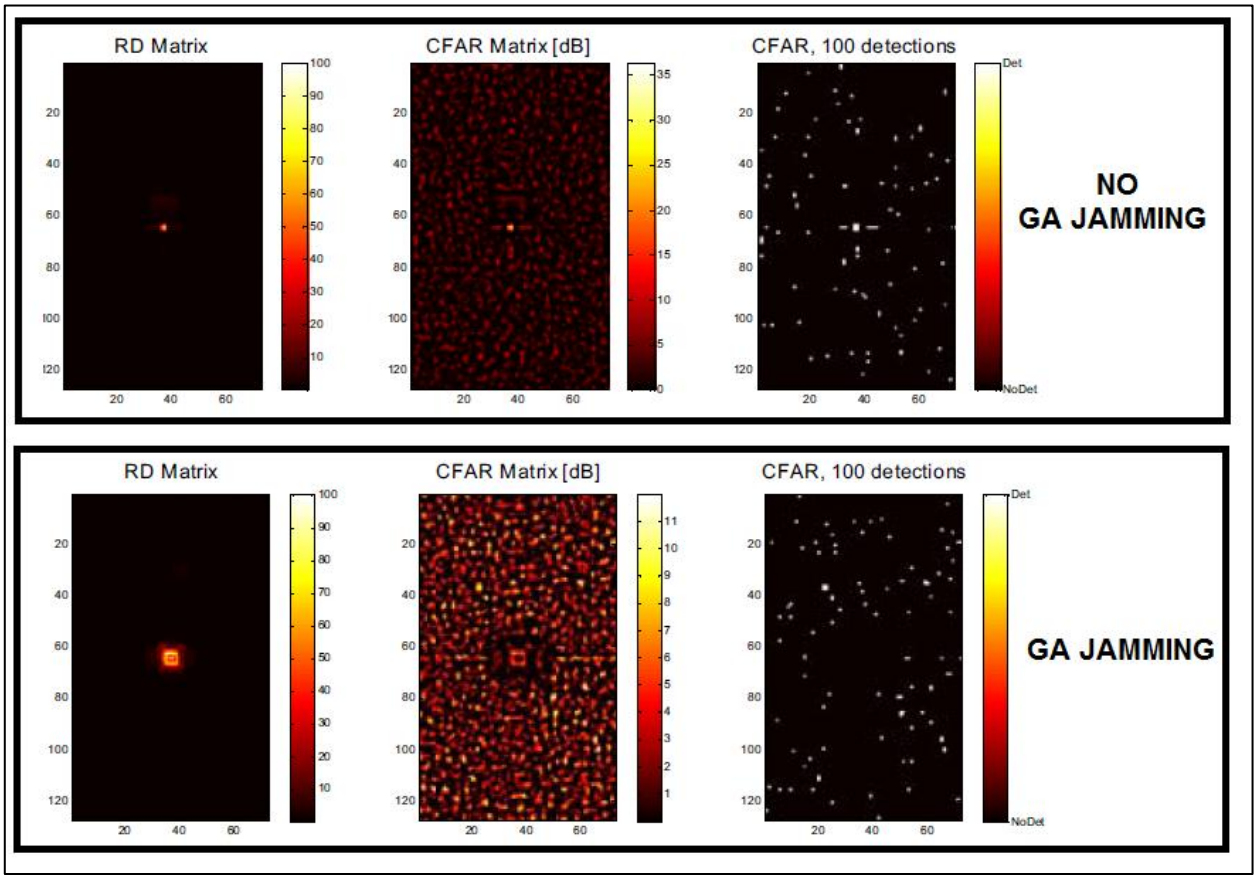

Figure 54: GA Jamming Effects on Radar's RD Map

It was found that the difference between radar-jammer range and Doppler resolutions degraded the effects of the GA Jamming algorithm. Further testing was required in order to overcome this problem, as reported by authors of this technical report.

This algorithm is an example of an advanced DRFM based jamming technique that is quite an effective means of providing cover pulse jamming which would not be detectable by the radar. However, the technique needs more to be developed and tested further, before it can be used as practical EA technique.

2.5.3 Electronic Attack Algorithms, Contextual Summary

A fundamental constraint to success of all of the DRFM deception jamming EA algorithms is the accuracy to which the victim radar's signal parameters are estimated. This is important because the DRFM has to use these signal parameters to generate false targets that would deceive the radar.

This fundamental constraint to the EA subsystem does not apply to the digital phase shifting repeater jammers developed b A. Madni and HM Endler (reference [14]) that apply EA signal modulations without estimating signal parameters.

Although the jamming techniques discussed in the report by A. Madni and H.M. Endler were developed using serrodyning in digital phase shifters they can still be implemented digitally in a DRFM. It is probable however, that the devices as described would not be effective against a multi-component signal if they were applied directly (without blind de-convolution techniques). This is because the devices use the fundamental definition of instantaneous frequency as the "rate of change of phase", which is not valid for multi-component signals as already discussed in section 2.3.3.

P. West and B.J. Slocomb [32], present two important jamming techniques to be used against a theoretical advanced AESA radar called the "Benchmark Radar Model". Useful expressions for RGPO profiles are provided and expressions for hook and cover pulse jamming. The generation of narrowband or wideband noise from a DRFM was also proposed as a viable EA against an AESA radar such as the "Benchmark Radar". These EA techniques are not restricted to the jamming of an AESA radar only, but would also be applicable to the DBR. Both P. West and B.J. Slocomb [32], and W.D. Blair et al. [44] emphasis the need to coordinate range deception with velocity deception to prevent the radar from identifying the false target . W.D. Blair et al. [44] also provided expressions for RGPO profiles, but these are different to those given by West and B.J. Slocomb in reference [32].

In the work done by S. D. Berger as documented in reference [36], the poor SFDR and low sampling rates of DRFM's is suggested as a potential weakness that can be exploited for identification of the false target, by the radar. However, modern DRFM's sampling rates are fast enough to ensure high SFDR's. This point is discussed in more detail in the summary of reference [27] in section 2.6.2.

Y. Yang in reference [45] describes three simple methods of "frequency-shift" jamming to inject a false range target to radar. The signal models for cover pulse jamming and frequency shift jamming were identical to those shown by Z. Bin et. al, in reference [46] and corroborate the work done by Y Yang.

It was interesting to note that cover pulse jamming can be generated using a variety of different methods, each having the same effect on the radar i.e. they obscure the true target. A. Madni and HM Endler ([14]), apply phase shifts to the signal; P. West and B.J. Slocomb [32], recommend inserting multiple time delays into multiple false targets and Y. Yang in reference [45] suggests frequency shifting the false signal carrier term. In section 2.7.1, two advanced DRFM based deception jamming methods called "Chopping and Interleaving (C&I)" and "Smeared Spectrum (SMSP)" are also used to generate the cover pulses. These methods are introduced by G. Lu et. al, in reference [20].

In this simulation, range was inserted into the false target signal as a time delay as discussed by P. West and B.J. Slocomb [30]. Doppler frequency for a DBR Jammer false target was inserted into the signal model using an approach similar to that proposed by Y. Yang [43] and Z. Bin et. al, in reference [43].

2.6 ES and EA System Architecture

In order to develop realistic wideband architecture for the ES subsystem of the DBR Jammer, various textbooks and technical reports were researched.

2.6.1 Textbooks

In the book by J.B. Tsui [5], fundamental limitations and trade-offs of EW system hardware are described. Current microwave receiver performance and architecture is described herein.

Important and useful information with respect to "Microwave Lenses" was found in this book.

The book by L. Blake [7] is an excellent text on the latest antenna technology and theory. Basic "Transmission Line" Theory is also described in it. Operation and performance of various antennas for EW applications are also explained.

2.6.2 Technical Reports

The following technical reports on ES and EA architecture, that were researched, are summarized in this section:

- *"Design and performance of wideband DRFM for radar test and evaluation",* reference [27]
- *"Advances in DRFM technology during the past decade and its importance as part of an EW suite",* reference [26]
- "*Phase Performance of DRFM's*", reference [31]
- *"Simulator for advanced fighter radar EPM development",* reference [16]
- *"Design and Simulation of DRFM System Based on Digital Channelized Receiver and Transmitter",* reference [41]

Design and performance of wideband DRFM for radar test and evaluation

K Olivier et al. in reference [27], describe the development of a wideband DRFM from "Commercial-off-the-Shelf (COTS)" components, for radar testing purposes. The DRFM was built onto a "Printed Circuit Board" (PCB) using COTS components. This was done, instead of building the device into a single "Integrated Circuit (IC)" in order to keep cost and device complexity down.

As operating frequencies increase in microwave circuits, it becomes more important to keep the circuit's "electrical length" as short as possible. In order to do this, PCB circuits must be built in close proximity to one another, which could cause electromagnetic interference problems. To mitigate or eliminate this problem, the following principle must be utilized in the design: "*return currents at high frequencies follow the path of least inductance*", K Olivier et al. [25].

A second important design aspect to prevent is to ensure good separation of analog and digital components to avoid grounding problems and further interference problems. The "moat and bridge" approach to separating analog and digital components is a viable design to prevent grounding problems between analog and digital components and this design principle is shown in Figure 55, for a wideband DRFM built by the CSIR. "The key to success of the moat and bridge approach is to route all the signals that cross between the analogue and digital partitions, over the bridge", K. Olivier et al. reference [27].

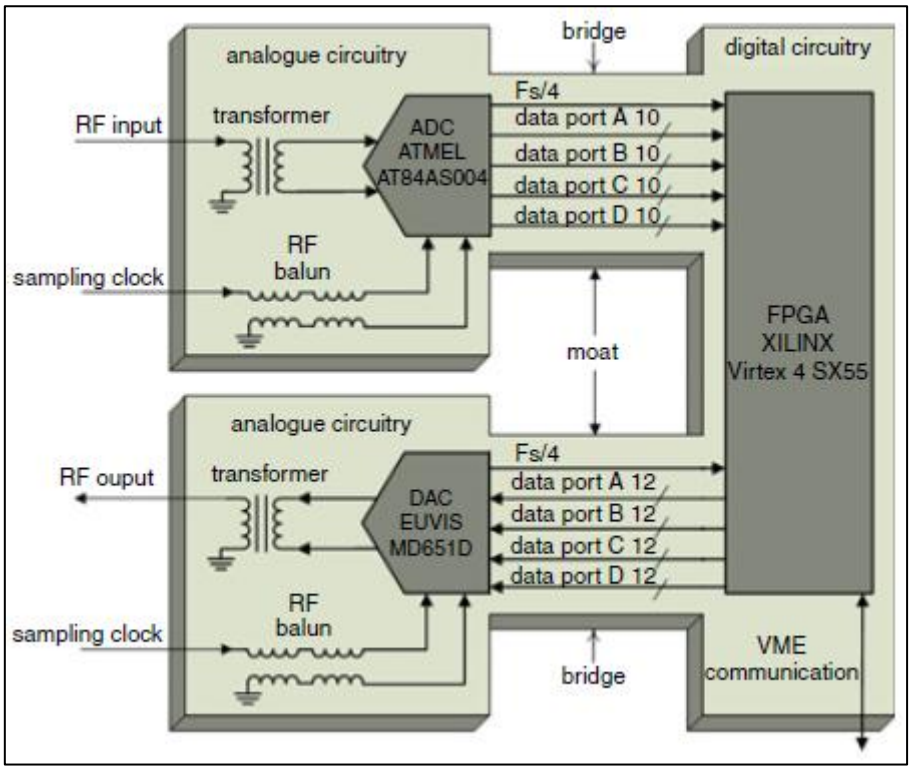

Figure 55: CSIR Wideband DRFM Design

The COTS components that were used in the CSIR DRFM are also shown in Figure 55. The DRFM has a bandwidth of 800 Mhz and a "Spurious Free Dynamic Range (SFDR)" of -47 DBc. This specification is a large improvement to the DRFM tested by S Berger in reference [36] who measured a SFDR of 17DBc. The CSIR DRFM was built and tested against a Pulse-Doppler radar. It was also found that the target generated by the DRFM was almost identical to a true test target. In K. Olivier's opinion: "The test against the pulse-Doppler radar showed that, even though quantisation effects of the DRFM are evident, the spurious levels are so low that it is unlikely that advanced electronic counter countermeasures (ECCMs) in the radar will be able to distinguish between a physical target return and one generated by the DRFM."

Advances in DRFM technology during the past decade and its importance as part of an EW suite

In another study by K. Olivier, in reference [26], he describes the actual advances in DRFM hardware and architectures, until the 14 September 2011.

An important statement made was that the use of Field Programmable Gate Arrays (FPGA's) in place of the standard computer memory in the DRFM was the current "state of the art". The FPGA is an IC, designed to be customized by the designer. Therefore, customized DRFM algorithms can be programmed into the IC to allow optimized processing for EW applications.

A useful forecast of future DRFM performances is also made by K. Olivier in reference [26] and is shown in Figure 56.

Performance Description	Performance Specifications			
	2nd Generation '99 – '03	3rd Generation '04 – '06	4th Generation '07- '11	5th Generation '12 – '16
Sampling Rate	1 GSPS	1.2 GSPS	2 GSPS	5 GSPS
Resolution	8 bits	10 bits	ADC = 10 bits DAC = 12 bits	ADC = 10 bits DAC = 12 bits
IBW	400 MHz	500 MHz	800 MHz	2000 MHz
Range Delay Resolution	16 ns (2.4 m)	13.3 ns/3.3 ns (2 m)/(0.5 m)	0.5 ns (75 mm)	0.2 ns (30 mm)
Memory Depth	1 ms	1.7 ms	8.3 ms	3 ms
SFDR	30 dBc	36 dBc	45 dBc	> 45 dBc
DIFM	No	No	Yes	Yes
Digital EQ for flatness	No	No	Yes	Yes
Arbitrary Modulation	No	No	Yes	Yes
Range Update Phase Correction	No	No	Yes	Yes
Typical Latency	120 – 250 ns	120 – 250 ns	70 – 280 ns	From < 70 ns
Carrier Modulation Range	100 MHz	20 MHz	800 MHz	2000 MHz

Figure 56: DRFM Performance (reference [26])

The CSIR DRFM development capabilities are also described in reference [26]. These capabilities include inserting "Micro-Doppler" effects onto the false target, such as "Helicopter Rotor Blade Modulation (RBM)" and "Jet Engine Modulation (JEM)". These signal modulations are naturally added to the true target RCS, by a helicopter or jet engined aircraft. The CSIR DRFM can also simulate multi-component non-stationary signals.

This reference gives an excellent overview of DRFM technology that was the "state of the art" in 2011. The DRFM capability prediction since 2011 has proven to be accurate as shown in the digital receiver performance survey conducted in this study.

Phase Performance of DRFM's

PCJ. Pring et al. [31] describe and show the various basic hardware configurations for DRFM's in this informative paper. The configurations analysed were the "Amplitude DRFM", the "Phase DRFM" and the "Cartesian DRFM". In the deception jamming of a modern Pulse Doppler and Angle Tracking radar, preservation of the phase information between input and

output of the DRFM is important. For this reason an investigation into the phase errors introduced by the DRFM during sampling and signal reconstruction was done by PCJ Pring.

In the "amplitude DRFM", the input is mixed to the Intermediate Frequency (IF) and then band pass filtered. A limiter is used to maintain the phase of the signal over a wide range of signal levels. The IF signal is mixed and band pass filtered to baseband before being digitized and stored in memory. While in memory, it is modulated before being reconstructed in the DAC at the same clock rate rates at which the signals were sampled. Instantaneous bandwidth of the device is constrained by the clock rate. The amplitude DRFM is shown in Figure 57 below.

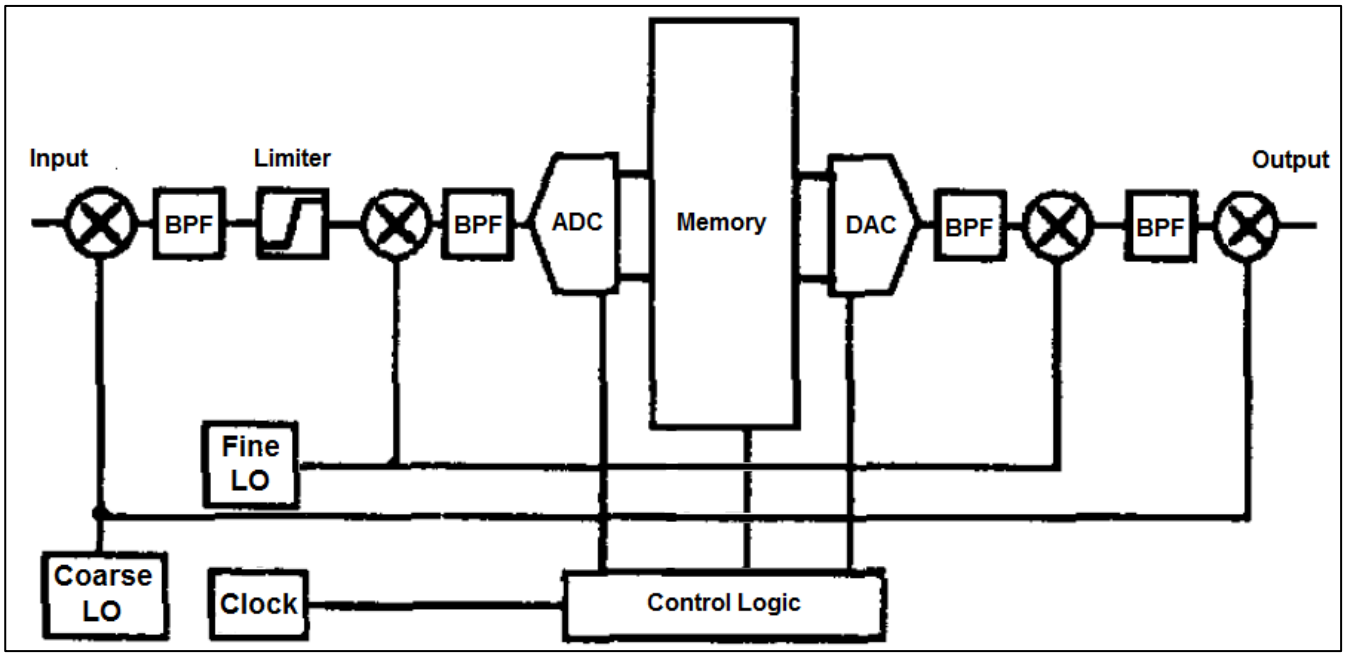

Figure 57: Amplitude DRFM

A schematic of the "Phase Configuration DRFM" is shown in Figure 58. The signal at baseband is converted to "I" and "Q" signals by mixing the signal with the "fine Local LO" signal and its 90° phase shifted version.

Analogue comparators are then used to obtain the signs and relative magnitudes of the signals before they are stored in memory. Thus, enough information is stored in order to identify the signal phase. A vector modulator is used to apply modulation to the signal before it is reconstructed.

The instantaneous phase is obtained from the "I" and "Q" samples of the signal. A key advantage of using the "Phase Configuration" is that, there is no unwanted sideband formed in the conversion back to the IF signal, which is the case in the "Amplitude DRFM".

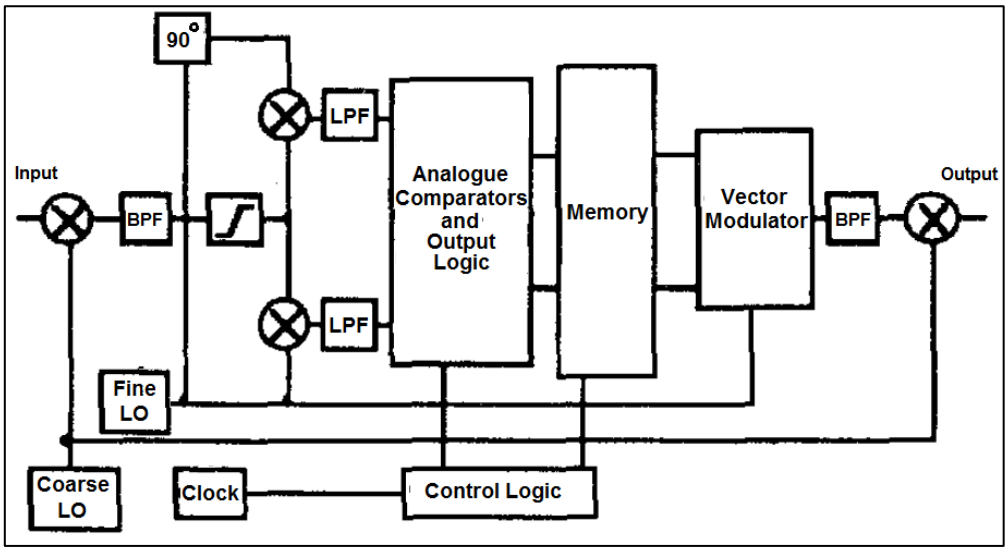

Figure 58: Phase DRFM

In Figure 59, the Cartesian DRFM is shown. This configuration is a combination of the amplitude DRFM and phase DRFM's. But in this case, the "stored IQ components are used to directly reconstruct the output IQ components" reference [31].

It was found by P. Pring that the phase accuracy of both the amplitude DRFM and Cartesian DRFM converge to the phase DRFM. It was also stated that the Cartesian and Phase DRFM operate at twice the bandwidth of the amplitude DRFM, however the amplitude DRFM is simpler and more robust against phase imbalance errors. Increasing the number of bits in the DRFM improves the phase preservation performance of DRFM's.

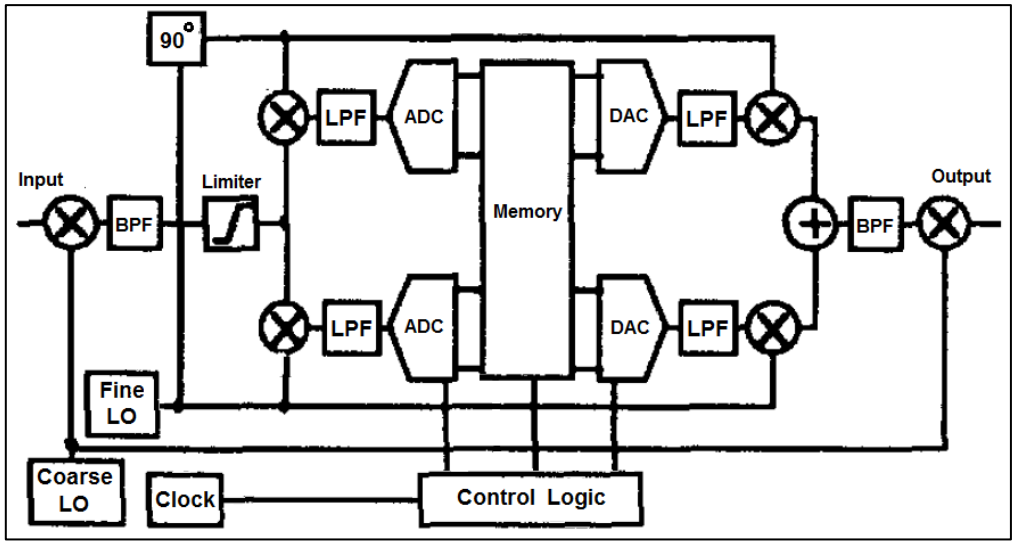

Figure 59: Cartesian DRFM

Three basic architectures for DRFM's were shown and their operation was explained. These configurations have been replaced by more modern types, as discussed by K Olivier et. al in references [26] and [27].

Simulator for advanced fighter radar EPM development

D. DiFilippo, et al. [16] describes the development of a simulator for testing a fighter aircraft EP suite. The simulator was called "Software Based Simulator for Advanced Fighter Radar (SAFIRE)". The high-level architecture of this ES and EA simulators are described. Important and useful design principles were also described. The SAFIRE was developed to ensure accurate testing of EA techniques and EP protection principles could be also be tested without the need for expensive flight trials.

The simulated radar has multiple "Air-to-Air" modes that include "Velocity Search", "Range-while-Search", "Track-while-Search" and "Single Target Track". A combination of waveform encoding, varying PRF regimes and sidelobe cancellation are used in the various radar operating modes to provide EP. The radar modes are simulated as well as various targets, and clutter. An assumption was made in the SAFIRE simulation with respect to modelling the effects of jammer EP measures that exploit jammer hardware imperfections. This is usually done in order to detect the jammer or discriminate true targets from false ones.

The jammer hardware imperfections were not modelled in SAFIRE, since the "DRFM technology development rapidly evolves and hardware is improved", D. DiFilippo, et al. [16]. Therefore EP measures based on identification of the jammer imperfections would quickly become obsolete and unreliable.

The SAFIRE EA model is based on a DRFM, whose generic structure is shown in Figure 60. Incoming signals are mixed to a frequency that is within the A/D converters. The pulse is then digitized at a sampling rate high enough to ensure a Frequency Hopping (FH) signal can be properly captured. Both positive and negative ranges can be inserted into the false target model. Doppler frequencies can also be inserted into the false target models using "Direct Digital Synthesizers (DDS's)". With this architecture, the number of false signals that can be generated is limited to the number of up-conversion channels for signal reconstruction at the radar's carrier frequency.

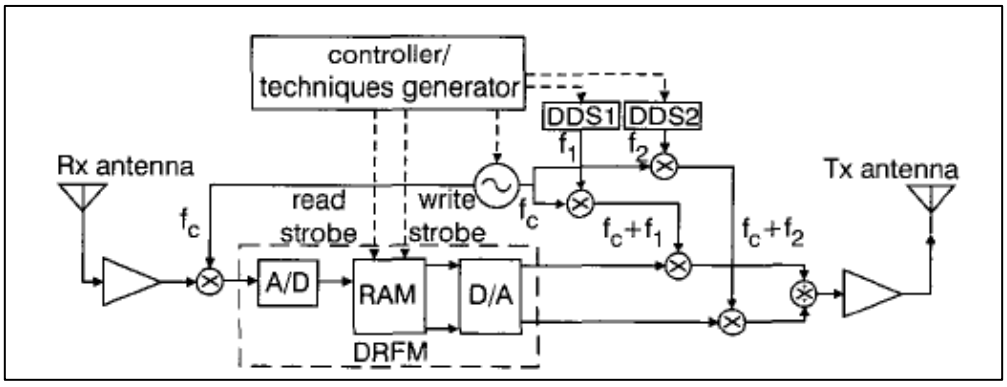

Figure 60: SAFIRE DRFM Structure

VGPO, RGPO, RGPO with VGPO, smart noise and multiple cover pulse jamming can be generated by the SAFIRE DRFM. An example of coordinated RGPO and VGPO profiles for a false target is shown in Figure 61.

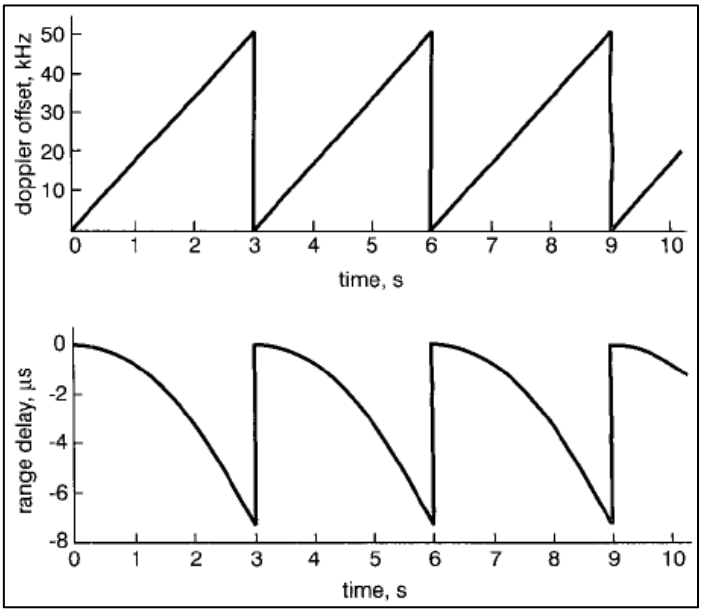

Figure 61: Coordinated RGPO/VGPO Profiles

Much work was done to improve the computational efficiency of the SAFIRE Simulation.
One of the measures made was to allow the clutter model to be deactivated during deceptive EA technique testing. The reason this is done was "since in general, false target signals would be strong enough that their detection in clutter is not an issue", reference [16].
The SAFIRE has been proven to be a cost effective tool for the R&D of EA techniques and methods to provide EP for the fighter aircraft radar for which it was developed.

The SAFIRE simulation is restricted to a single radar type, which reduces its flexibility or applicability for testing of other radars. Nevertheless, this technical report provides insight into some of the important simulation design decisions necessary for developing a realistic radar-EW system simulator.
Two assumptions are made in this publication that justify simplifications made in this DBR simulation. The decision to not model DRFM sampling effects and clutter were also made for SAFIRE. These assumptions were made for the SAFIRE simulation, since they would significantly slow down the simulation without adding significant value.

Design and Simulation of DRFM System Based on Digital Channelized Receiver and Transmitter

P. Tang, et al. [41] list different architectures to cater for multi-channel (different frequencies, multiple radars) ES and EA. The ES system has to digitize the radar signal over a broad bandwidth since the radar signal's carrier frequency, modulation; instantaneous phase and amplitude are unknown. The radar signal could therefore be located anywhere in the radar portions of frequency spectrum. Because of this, the ES receiver has to operate over a very wide bandwidth. In order to achieve this design constraint, while still remaining within the sampling rate limits of A/D and D/A converters, a multi-channel digital receiver architecture has been proposed.

The EA system applies modulations to the signal in order to simulate the false target. In order to do this, the sampling rate must be low enough to ensure memory and processing resources are not overburdened, when the false target signal is generated. For this purpose, P Tang et al., in reference [41], have proposed "downsampling" and "upsampling" of the signals, to allow signal modulations to be applied efficiently using standard COTS hardware. The structure proposed allows high speed A/D's and D/A's to be used without data losses and is shown in Figure 62.

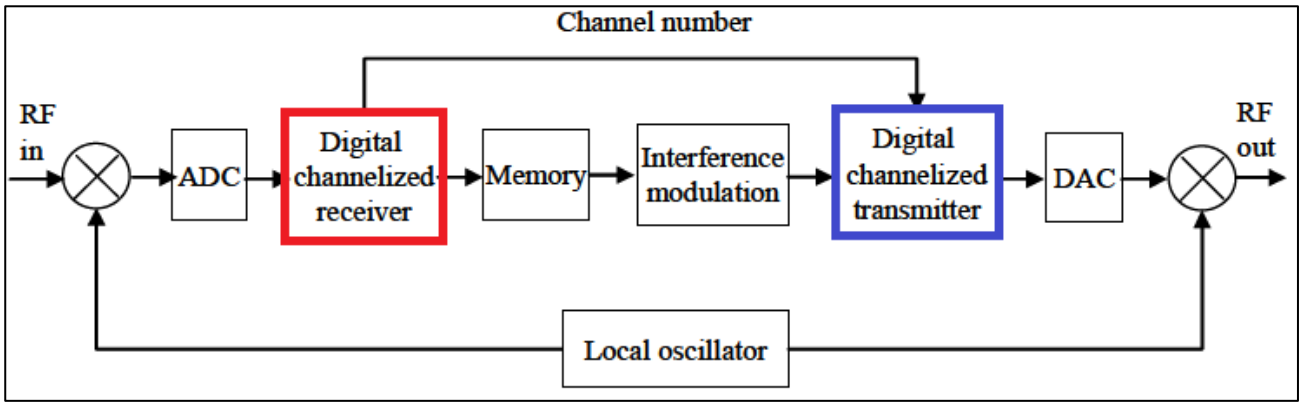

Figure 62: Digital Channelized Receiver, Overall structure

An important feature of this DRFM is that channel information with respect to detected signals is sent to the "digital channelized" transmitter" from the ES receiver.

The channelized digital *receiver* architecture block highlighted in red in Figure 62 is shown in detail in Figure 63. The signal "$x(n)$" is received through the antenna system. The downsampling decimation factor is then applied before low pass filtering of the signal. The downsampling process is completed by application of a delayed decimation factor after low pass filtering. Finally, an IFFT is applied to the received signal, which by now has been

digitized, channelized and downsampled. Signal parameters can now be accurately estimated and modulations for deception jamming can be efficiently applied to the false target signal.

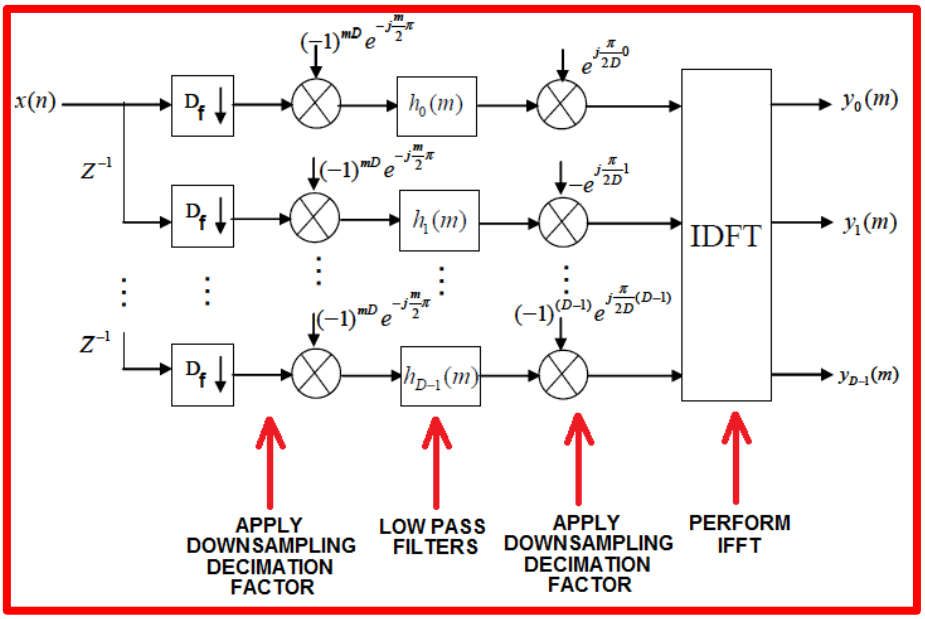

Figure 63: Digital Channelized Receiver

The digital channelized *transmitter* architecture is shown in detail in Figure 64. It was shown in blue in the overall DRFM structure in Figure 62. The signal with modulations already inserted into it, is input into an IFFT module. Thereafter the signals are upsampled with a delayed version of the decimation factor and low pass filtered once again. The output of the transmitter is converted to analogue in the D/A converter (shown in Figure 62), up-converted using the LO signal and re-transmitted to the radar.

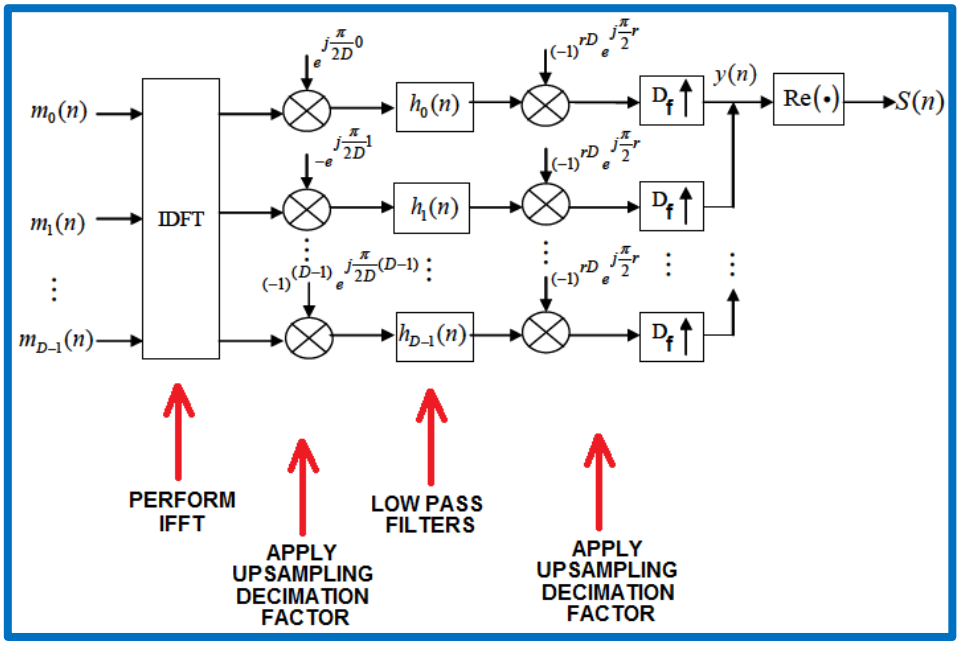

Figure 64: Digital Channelized Transmitter

Y. Yang et. al., provided simulation results for digitally channelizing two LFM signals. Signal 1 had a carrier frequency of 25 MHz and bandwidth of 10 MHz, while signal 2 had a carrier frequency of 245 MHz and bandwidth of 15 MHz. The spectrum of the signal received and transmitted by the DRFM, over the entire channelized bandwidth, is shown in Figure 65. It can be seen that the two spectrums are almost identical.

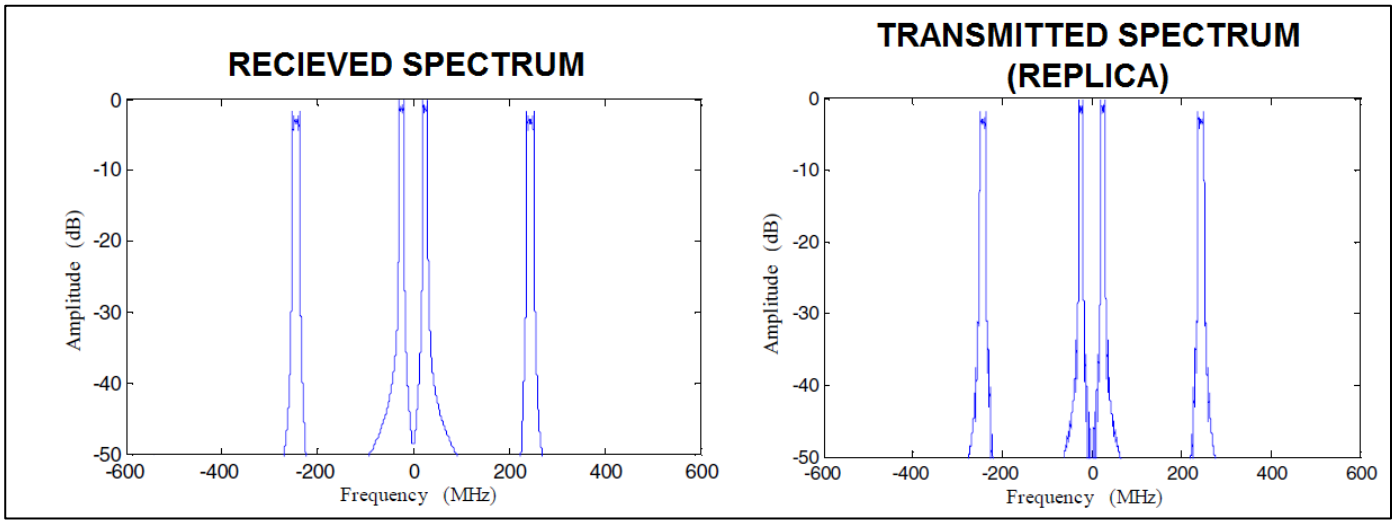

Figure 65: Received and Transmitted Spectrum Comparison

In Figure 66, the spectrums of signal 1 and 2 only, are shown. The signals are detected in channels 8 and 11.

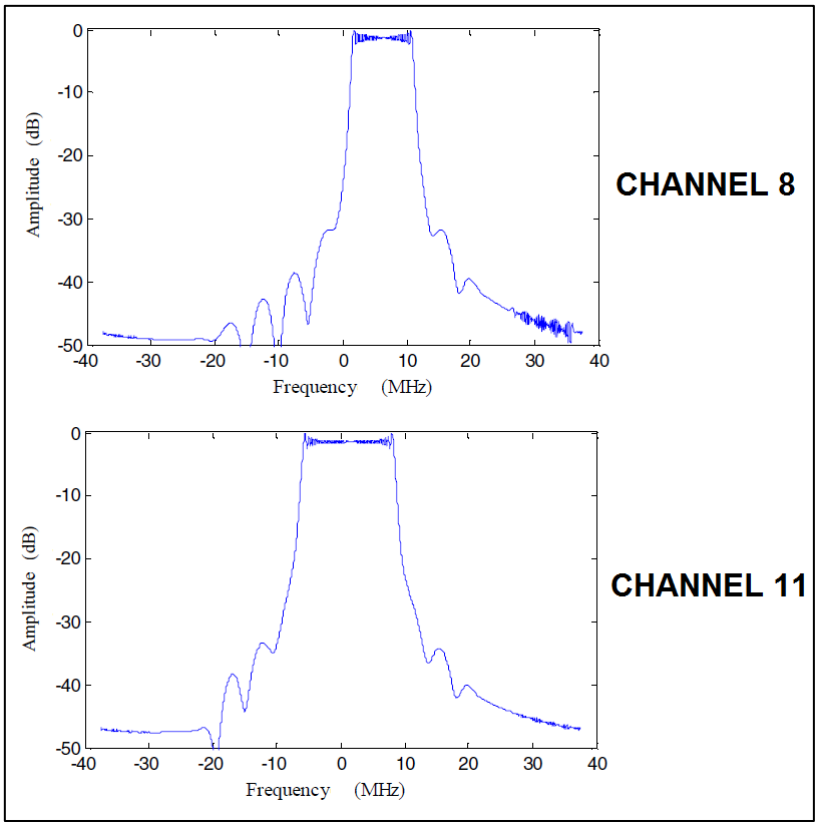

Figure 66: Close up of Channel 8 and 11 Spectrums

2.6.3 ES and EA System Architecture, Contextual Summary

By comparing the work done be S. Berger [36] in 2003 and K. Olivier et. al [27], in 2011, it can be concluded that substantial improvements have been made to DRFM hardware in terms of digitization efficiency. Since 2011, even further improvements have been made to DRFM technology for improved bandwidth, better resolution and faster sampling rates. These advances indicate the excellent viability of DRFM technology for deception jamming applications in EW, which is one of the primary reasons the DRFM was selected as the "deception jamming weapon of choice", in this simulation. In another technical paper by K Olivier (reference [26]), DRFM performance is predicted to have a sampling rate of 5 GHz, with an SFDR greater than 45 dBc. S. Berger in reference [36] tested a DRFM with a sampling rate of 10 kHz and SFDR of -16dBc, which is why he concluded that spurious effects due to DRFM sampling are sufficient to allow detection of the false target signal by the radar.

In the reports written by K Olivier (references [26] and [27]), PCJ. Pring et al. [31] and D. DiFilippo, et al. [16], a *single channel* wideband DRFM receiver and transmitter architecture is proposed. However, this configuration is more suited to radar testing applications, where the radar's frequency band is known.

In the "anti-radar" EW application, the ES system cannot determine what bands, threat radars are operating in. It therefore has to search the entire radar band (from 0.1 GHz to 18 GHz). No single digital receiver has the capability to digitize this entire bandwidth instantaneously. Because of this, the "digital channelized" receiver architecture was investigated. Multiple receivers are used in parallel in this type of system. The ES architecture concept described by P. Tang, et al. [41] for a "Digital Channelized" receiver to split the ES signal intercept bandwidth was used as input to the architecture proposed for the DBR Jammer, in this study.

An assumption made by D. DiFilippo, et al. in reference [16] for the SAFIRE simulation was also used in this simulation. Clutter was not simulated since a false target would be have to be strong enough for the radar to detect it, which is necessary in order to deceive the radar with respect to the true target location and speed. Modelling the clutter was found to be computationally intensive and did not add a significant benefit to the SAFIRE Simulation.

Two assumptions are made by D. DiFilippo, et al. in reference [16] that justifies simplifications made in this DBR simulation. The decision not to model DRFM sampling effects and clutter were also made for SAFIRE. These assumptions were made for the SAFIRE simulation, since they would significantly slow down the simulation without adding significant benefit.

2.7 Electronic Protection

2.7.1 Technical Reports

For the subject of "Electronic Protection", the following technical reports that were researched are summarized in this section:

- *"SAR-ECCM using Phase Perturbed LFM Chirp Signals and DRFM Repeat Jammer Penalization",* reference [29]
- *"Deception Jamming Modelling in Radar Sensor Networks",* reference [25]
- *"Cancellation of Complicated DRFM Range False Targets via Temporal Pulse Diversity",* reference [20]
- *"A Blanket Deception Jamming Rejection Approach Based on Jamming Sample Recognition",* reference [28]

SAR-ECCM using Phase Perturbed LFM Chirp Signals and DRFM Repeat Jammer Penalization

In this technical report by M. Soumekh, (reference [29]) two methods of protecting a radar against a DRFM based repeater jammer false signal are proposed. The radar is an airborne Synthetic Aperture Radar (SAR) that uses LFM pulses. Both EP methods involve modification of the radar's transmitted pulse in the "fast time domain" i.e. within a PRI. The principle is that a DRFM estimates radar signal parameters one pulse *before* the radar's current transmitted pulse. By encoding the radar pulses within the PRI, the DRFM is therefore estimating the *previous* radar signal. The radar on the other hand uses the *current* pulse as the "replica" signal for calculation of its match filter response. The first method of "encoding" the pulse in the fast time is to apply a random Multi-Tone (MT) Phase Modulation (PM) to the pulse. In the SAR application, this causes degradation in the "Point Spread Function (PSF)" by altering the transmitted pulses spectrum. However, M. Soumekh derives a power equalization method that smooth's the transmitted pulse spectrum. The MT-PM is generated for the *m'th* PRI using equation (108):

$$\psi_m(t) = \sum_{n=1}^{M} a_{mn} \cos(2\pi f_{mn} + \psi_{mn}) \tag{108}$$

"Instantaneous Time-Frequency" plots for four LFM pulses modulated using the MT-PM method is shown in Figure 67.

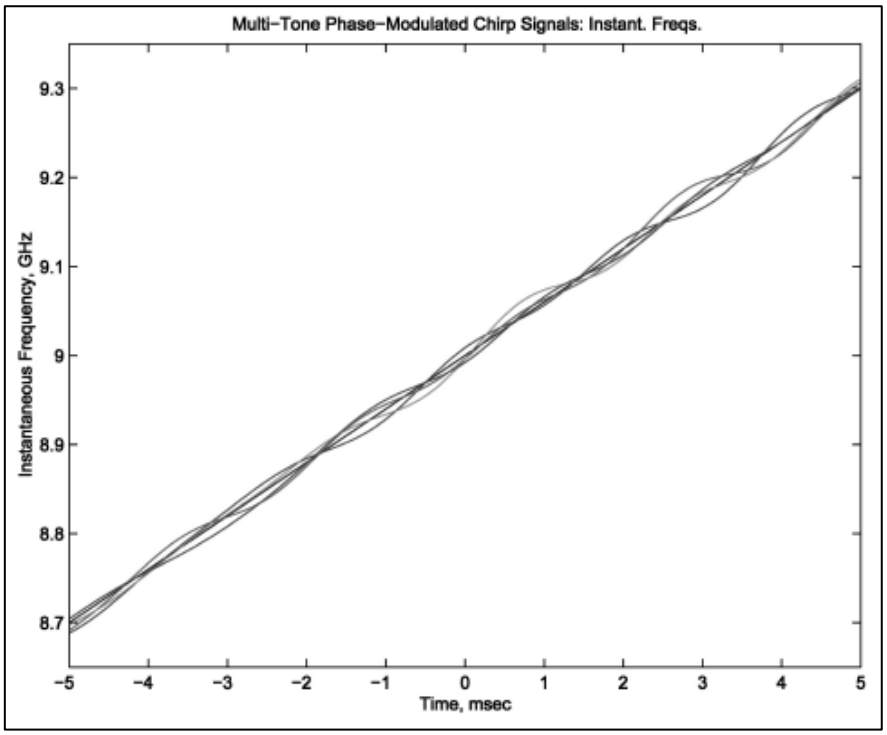

Figure 67: Instantaneous Frequency vs. time for MT-PM LFM pulses (reference [29])

The power spectrum of the four MT-PM pulses is shown in Figure 68. The raw spectrum is shown in dotted lines, while the power equalized spectrum is shown in solid line in Figure 68.

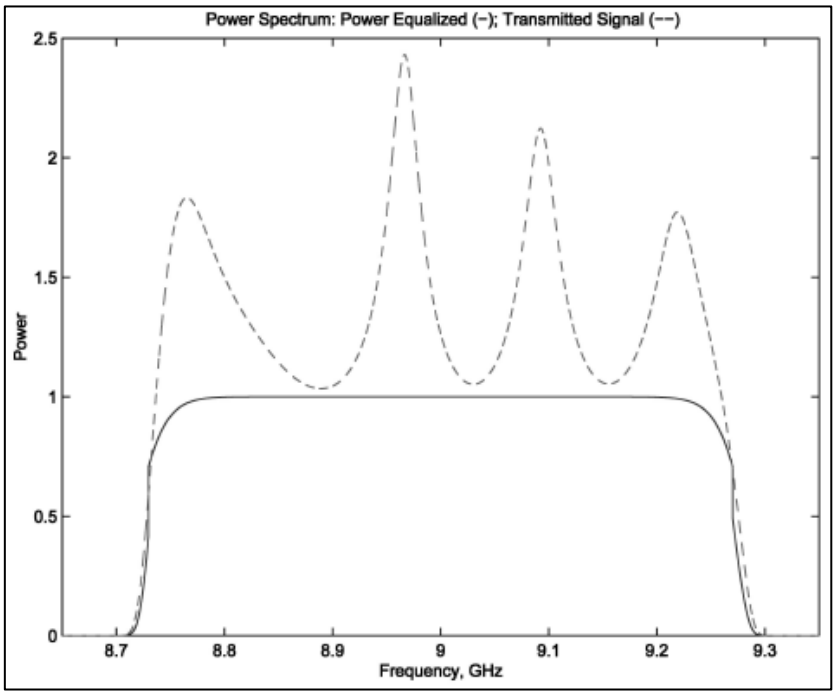

Figure 68: Transmitted MT-PM pulse spectrum (reference [29])

The Autocorrelation function for a single MT-PM pulse is shown in Figure 69 with and without Power equalization. It can be seen that higher side lobes result due to the pulse encoding within the PRI result, if power equalization is not applied.

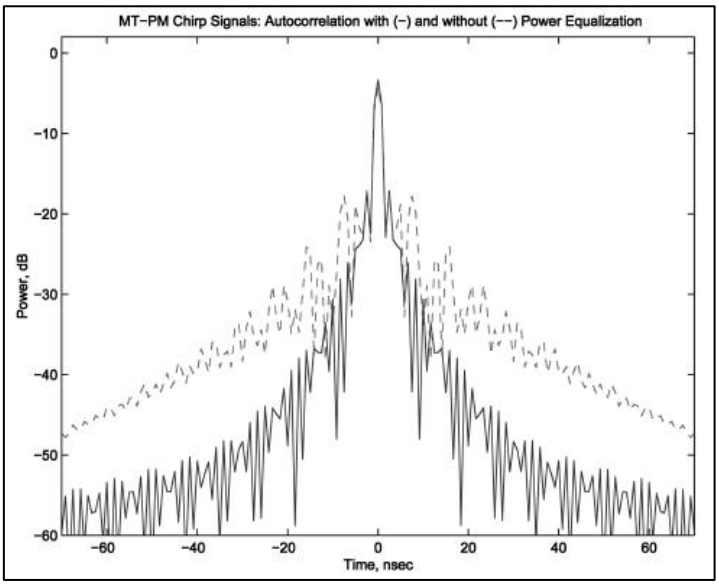

Figure 69: Autocorrelation of MT-PM signal (reference [29])

The second method for applying pulse diversity is called the "Slope Varying (SV)" method. It involves randomly modifying the chirp rate per pulse and is applied using the following equation for the *m'th* PRI:

$$\psi_m(t) = \mu_m t^2 \tag{109}$$

Instantaneous frequency plots for four SV pulses are shown in Figure 70.

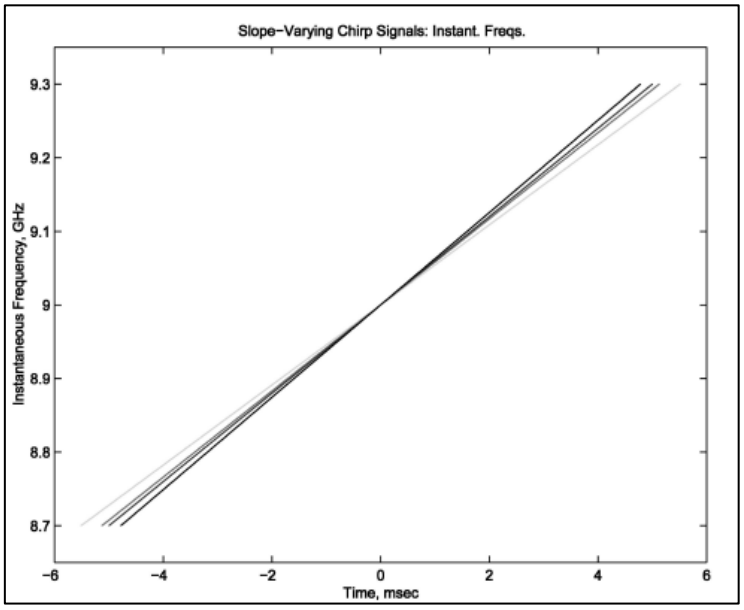

Figure 70: Instantaneous Frequency vs. time for four SV LFM pulses (reference [29])

The MT-PM method would be more difficult for the DRFM to replicate, but requires additional processing for power equalization. The SV LFM on the other hand would be easier for the DRFM to replicate, however it requires no power equalization. Autocorrelation of both the MT-PM and SV LFM pulse are similar with similar side-lobe magnitudes.

After the radar pulses are transmitted *with* pulse diversity, jammer penalization is applied to the signals, by match filtering both true and false target echoes with a replica of the *current* pulse. The *previous* pulse is not used since it would have the incorrect modulation applied to it. The radar keeps track of the random or pseudo-random sequences used to generate the pulses and is able to use the correct replica signal in its match filter. Final output after jammer penalization for the LFM signal is shown in Figure 71. It can be seen that the jammer's return spectrum is "smeared" and more importantly, *40dB below the true target spectrum*!

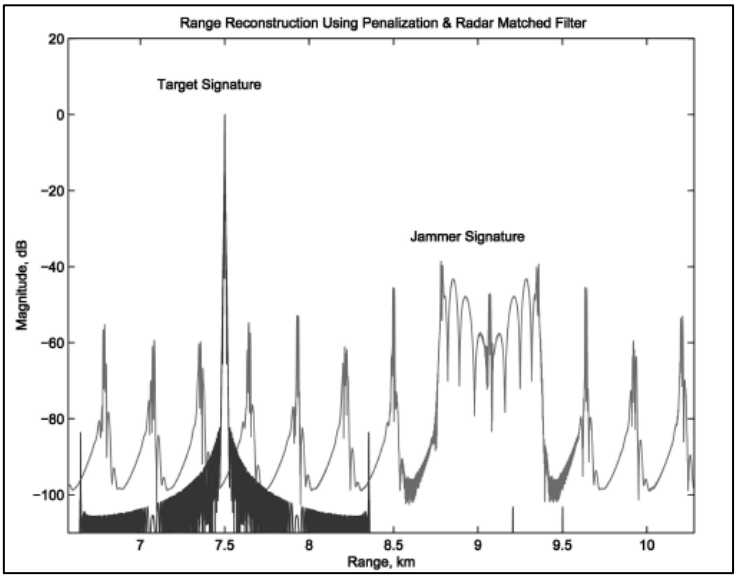

Figure 71: Matched filtered output, after Jammer Penalization (reference [29])

A similar (albeit 2D) jammer penalization processing is applied to a SAR image. The result is shown in Figure 72. The false target is highlighted by the red circle in the figure on the left.

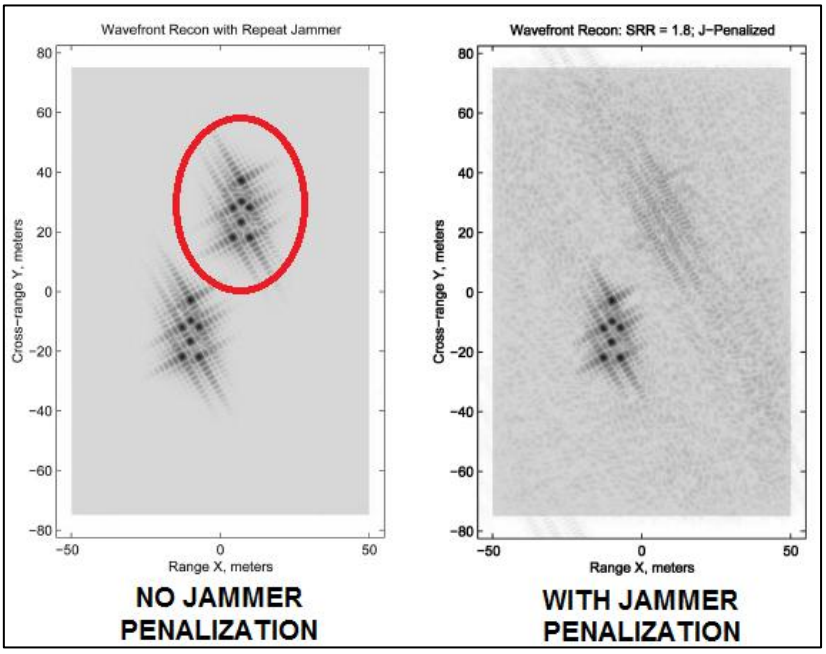

Figure 72: SAR Image, before and after Jammer Penalization (reference [29])

Deception Jamming Modelling in Radar Sensor Networks

J. Schuerger and D Garmatyuk [25] developed a simulation environment to test the robustness of an Ultra-Wideband (UWB) Orthogonal Frequency Division Multiplexing (OFDM) signal as an EP measure on an airborne SAR. The UWB OFDM signal is compared to a LFM signal and a Gaussian frequency hopped signal. The results of the comparison are presented in the form of SAR images.

The EP method proposed, transmits different OFDM pulses in every CPI similar to the way pulse diversity was applied by M Soukmekh in reference [29]. In this case, the deception jammer determines the radar signal parameters in a PRI. However, using those parameters to induce the false target in the radar is not effective since the radar's next set of transmitted pulses is encoded differently from the last set. In other words, the jammer's signal lags the radar signal. The jammer's false target then does not mimic the true target and becomes easily distinguishable. The OFDM waveform has already been used in the communications industry to send multiple packets of data in the same frequency band, without interference. In the radar application, the UWB OFDM waveform exhibits good potential, because of its excellent pulse diversity and wide bandwidth. In radar sensor networks with multiple radars in the same band, the OFDM would also reduce interference between the radars in the network, which is currently a problem in these types of systems.

An OFDM signal is defined as:

$$x(t) = \sum_{n=1}^{M} a_n e^{j2\pi n\Delta f t}; 0 < t < T \tag{110}$$

Where "$a_n = [a_1, a_2, \ldots, a_n]$" are the amplitudes of the individual pulses. The signal "$x(t)$" is the sum of all the individual pulses which are known as sub-carriers. Each sub-carrier has a centre frequency of "$n\Delta f$" where "$\Delta f = 1/T$" is the sub-carrier frequency separation. Each "n^{th}" sub-carrier has a corresponding sub-band that is a "sinc" function with its centre at "$n\Delta f$". The sub-bands overlap, however the peak of one sub-band coincides with the zeros of all other bands. These sub-carriers are thus *orthogonal* to one another.

In reference [25], J. Schuerger and D Garmatyuk compare a deception jammer's effectiveness in generating false replicas of the true radar signal for an OFDM waveform, LFM waveform and a "Frequency Hopping" (FH) Gaussian pulse. An instantaneous frequency jammer and DRFM jammer were considered in the analysis. The result of the waveform comparison is shown in Figure 73. In the figure, the false signal is shown with the "x" marker while the true signal is shown with a solid line. It is clear that the jammer accurately replicates both the LFM

and FH waveforms. In the FH case, it was assumed that the Jammer had obtained the frequency hopping sequence and was "following" the FH radar signal. The actual and false signals for the UWB OFDM signal can be clearly distinguished, which is as result of the orthogonal coding of the transmitted radar pulses.

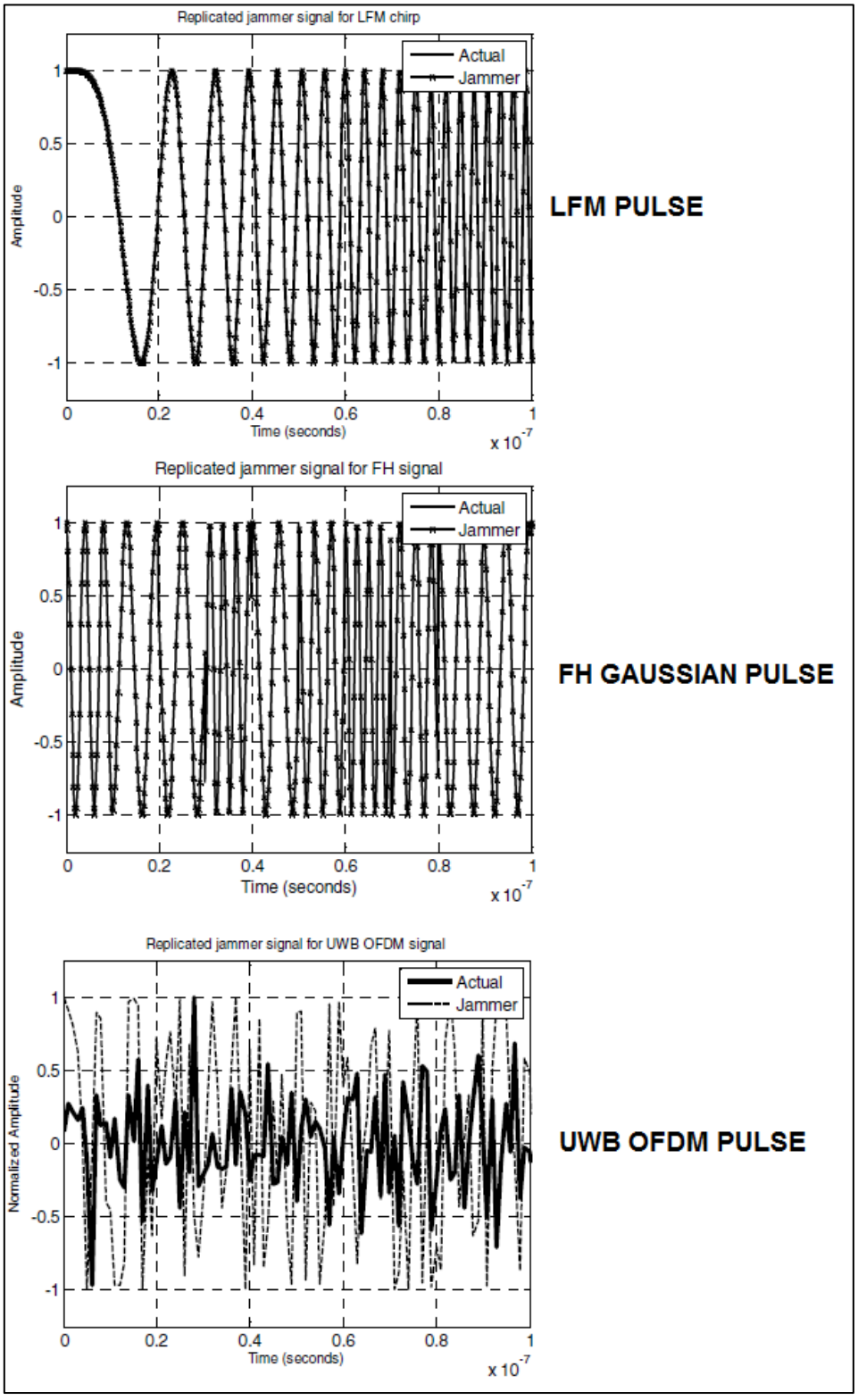

Figure 73: Deception Jammer False Signal Comparison for LFM, FH and OFDM Signals

The comparison between the LFM, FH and UWB OFDM waveforms was extended to SAR images. The result is shown in Figure 74. The OFDM image shows the true target, while the LFM based image shows both the true and false target. In the last case (FH Gaussian Pulse), it was assumed that the jammer had not obtained the frequency hopping sequence, which is why only the true target image is visible in the SAR image.

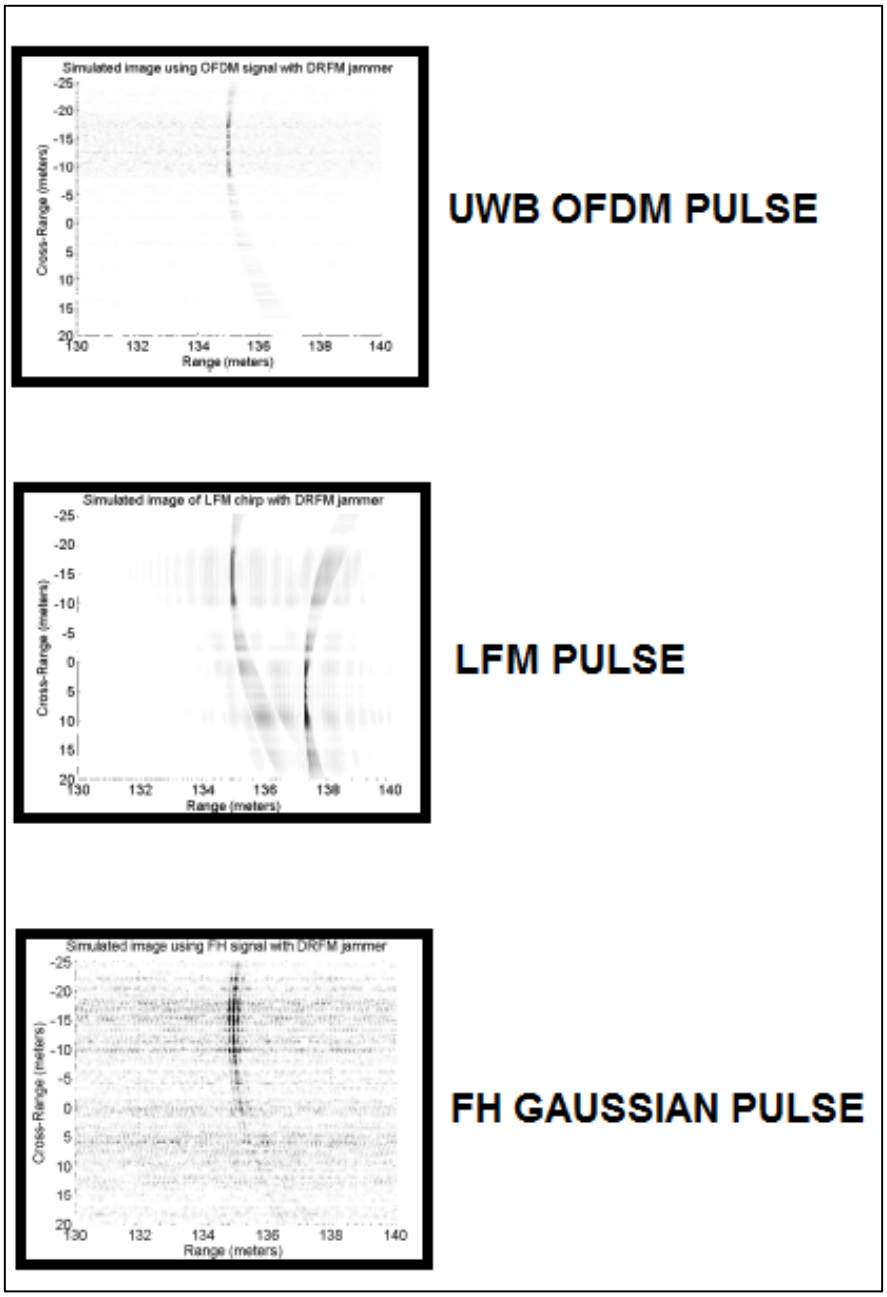

Figure 74: Deception Jammer False Image Comparison for LFM, FH and OFDM Signals

The proposed method is a viable counter-counter measure to DRFM jammers. However, the use of the OFDM waveform in terms of DBR detection performance must be investigated.

Cancellation of Complicated DRFM Range False Targets via Temporal Pulse Diversity

G. Lu et al. [20] present a technique for EP of radars against false target injection by a DRFM, using Temporal Pulse Diversity. In this paper, the author simulates the effect of using his pulse diversity technique, against a DRFM injecting false signals by means of more advanced DRFM signals. Countermeasures against DRFM techniques called "Chopping and Interleaving (C&I)" and "Smeared Spectrum (SMSP)" are simulated in this report. The C&I technique literally chops and interleaves, specific segments of the transmitted radar pulse. By means of this method, the DRFM is able to generate multiple false targets whose effect is similar to "cover pulse" or "blanket" jamming. An example of a C&I jamming signal is shown in Figure 75. The multiple false targets can be seen between -5s to 5s in the matched filter response.

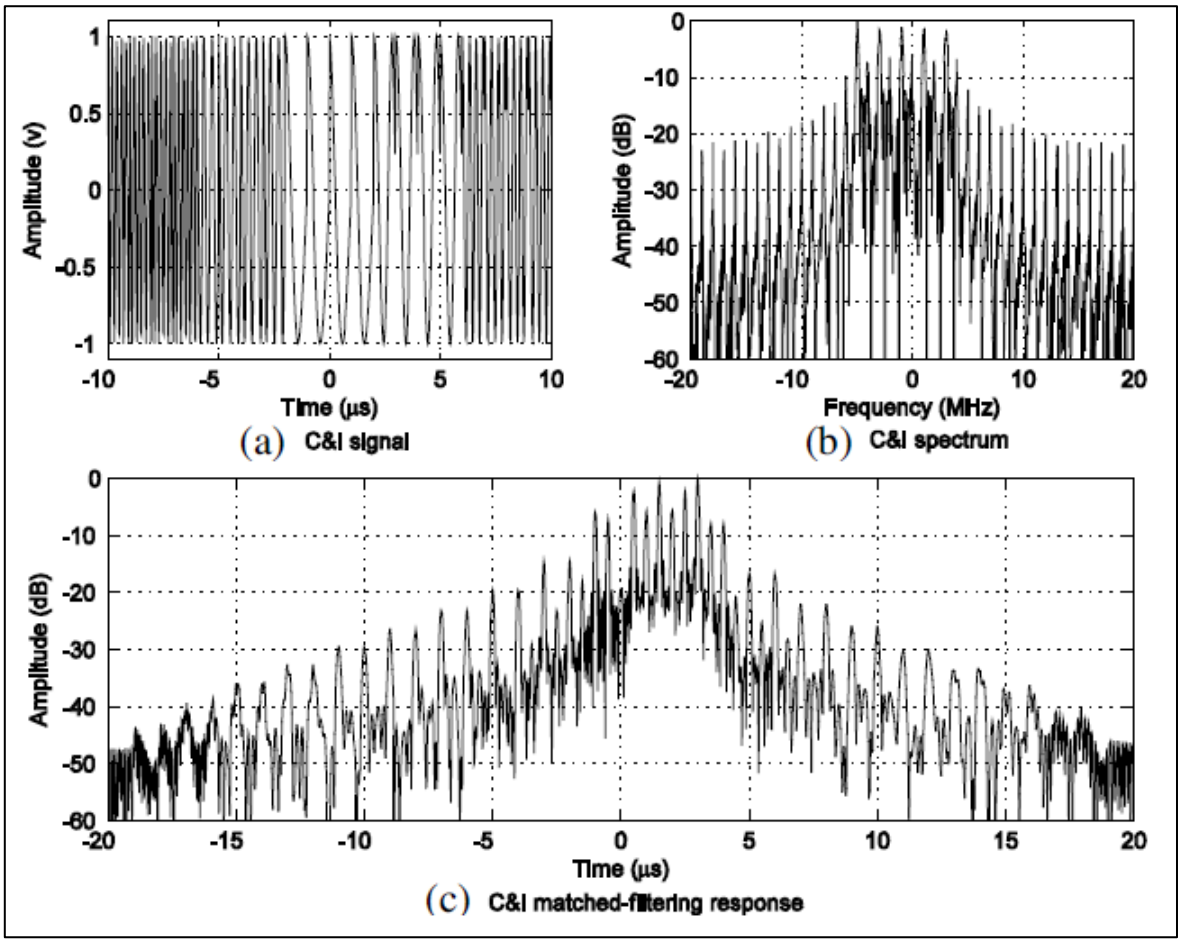

Figure 75: Chopping and Interleaving Jamming

SMSP jamming also generates multiple false targets by repeating a short segment of the transmitted radar pulse multiple times. The effect of SMSP Jamming is shown in Figure 76. Multiple false targets are caused by the "spectrum smearing effect" which is visible in the match filter subplot of Figure 76.

The countermeasure to the C&I and SMSP jamming as well as the conventional false range Doppler target according to the author is to match filter the returned signals with specific pulses in the pulse train. A block of four pulses is selected for the match filtering. The cancellation of the C&I Jamming using the method proposed by G. Lu is shown in Figure 77. The true target only, is visible at 30μs in the match-filtered plot.

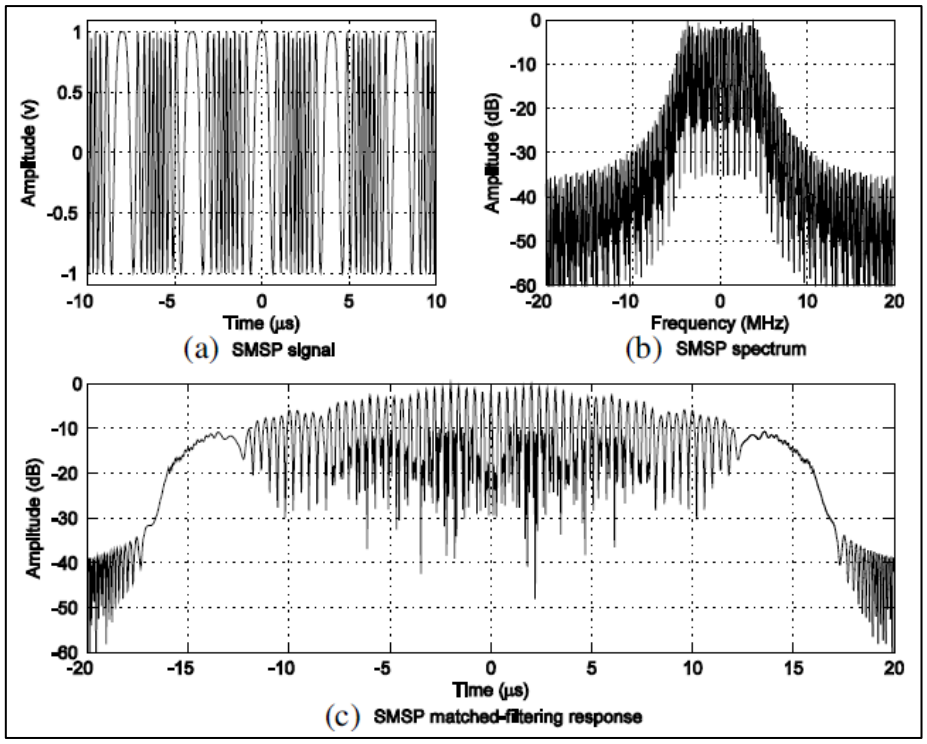

Figure 76: Smeared Spectrum Jamming

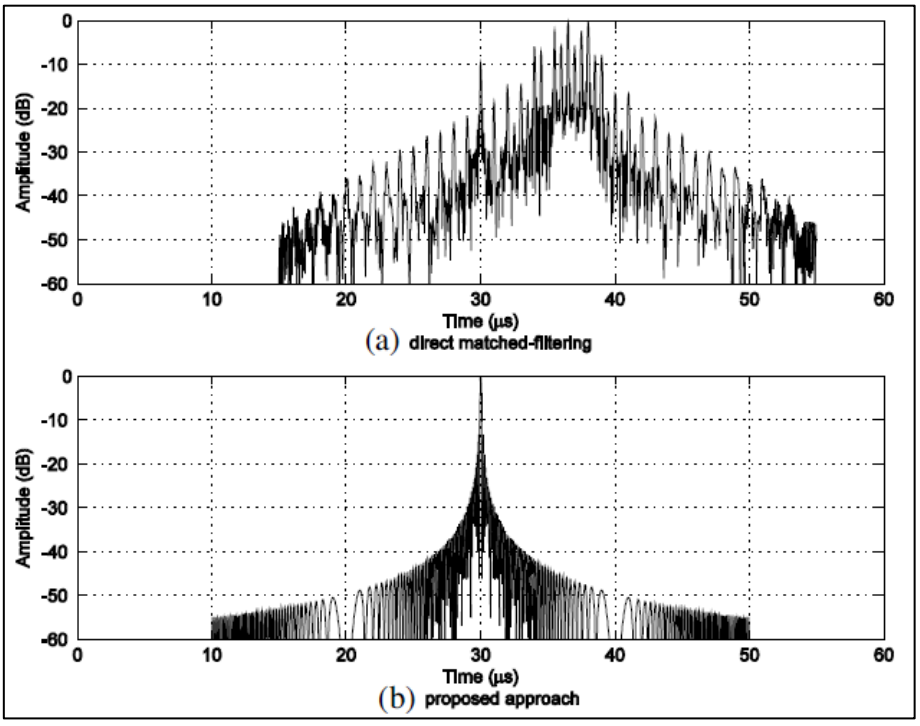

Figure 77: Chopping and Interleaving Jamming Cancellation

A Blanket Deception Jamming Rejection Approach Based on Jamming Sample Recognition

L Dai, in reference [28] describes EP measures against cover pulse or "blanket" jamming using Space Time Adaptive Processing (STAP) and side-lobe cancellation. An important point made is that the number of jammers to be cancelled can be greater than the number of side-lobe canceller channels, using the method presented. This is not the case for traditional sidelobe cancellation systems. The author assumes that a combination of noise jamming and DRFM based deception jamming is used to perform "cover pulse" or "blanket" jamming. This type of jamming generates multiple false targets to obscure the true target. A simulation result from a jamming scenario simulated by L Dai in reference [28] is shown in Figure 78.

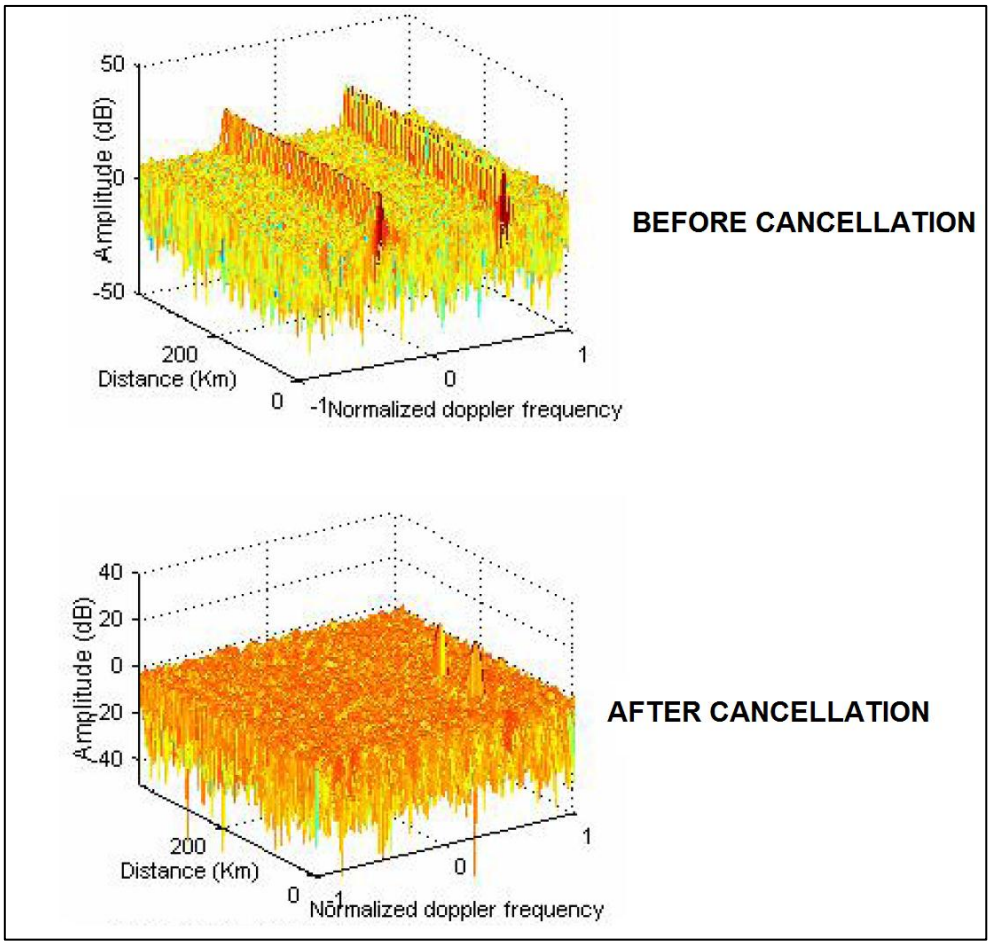

Figure 78: Blanket Jamming Cancellation (reference [28])

The author assumes the DRFM Jammer injects multiple false targets in range only as shown in the upper plot of Figure 78. However, the DRFM can also inject false Doppler frequencies and RCS fluctuations into the radar. The effect of using STAP with side-lobe cancellation against a DRFM Deception Jammer, is therefore not fully tested or simulated in this paper. However, the technique proposed, has merit and should be investigated further for use as an EP measure for the DBR.

2.7.2 Electronic Protection, Contextual Summary

M. Soumekh (reference [29]) describes two methods to encode pulses *within* a PRI for EP of the radar against a DRFM based deception jammer. The anti-DRFM EP proposed by J. Schuerger and D Garmatyuk [25] applies pulse diversity also on a pulse-pulse basis but uses an OFDM waveform to encode the pulses.

The pulse diversity method proposed by G. Lu et al. [20] would only work, if the correct pulse in the pulse block were selected. This would be the case if it were known exactly which pulse the jammer has intercepted and estimated. In an actual radar-EW engagement, this would not be known. The pulse diversity methods proposed by M. Soumekh (reference [29]) and J. Schuerger (reference [25]) are far more practical, since they are not dependent on the radar's jammer identification. Nevertheless, G. Lu's paper gives good insight into advanced DRFM techniques. Any selected DBR pulse diversity technique should also be tested against C&I and SMSP jamming.

L Dai in reference [28] proposed using STAP with sidelobe cancellation to reject DRFM based deception jamming however he does not fully testing the method. The use of STAP with sidelobe cancellation should be further investigated for use as an EP of the DBR, since the method can potentially allow more jammers to be cancelled than the number of sidelobe cancellation channels.

The pulse diversity methods described in references [20], [29], [25] are a capable countermeasure to the DRFM deception jamming techniques. Nevertheless, the effects of the pulse diversity in terms of radar performance must be investigated on the DBR. Specifically the effect on non-coherent integration gain, match filtering, angle estimation accuracy, performance in clutter etc. must be tested before these methods can be adopted by the DBR.

3 Simulation Overview

The structure of the simulation as it was programmed in Matlab is discussed here. In addition, the information necessary to run the simulation is also described in this chapter. This information consists of simulation inputs and controls. The inputs are radar and jammer parameters while "simulation controls" are the means to adjust the simulation for a particular desired output. Simulation outputs are the data and figures that depict radar and jammer performance in a particular EW scenario.

A complete list of all the modules developed and used, in this simulation, is shown in Figure 79. The figure indicates the primary simulation files, developed functions, data files and necessary utility programs. A list of all the files used in this simulation and their basic function within the simulation is included in Appendix 14.1.

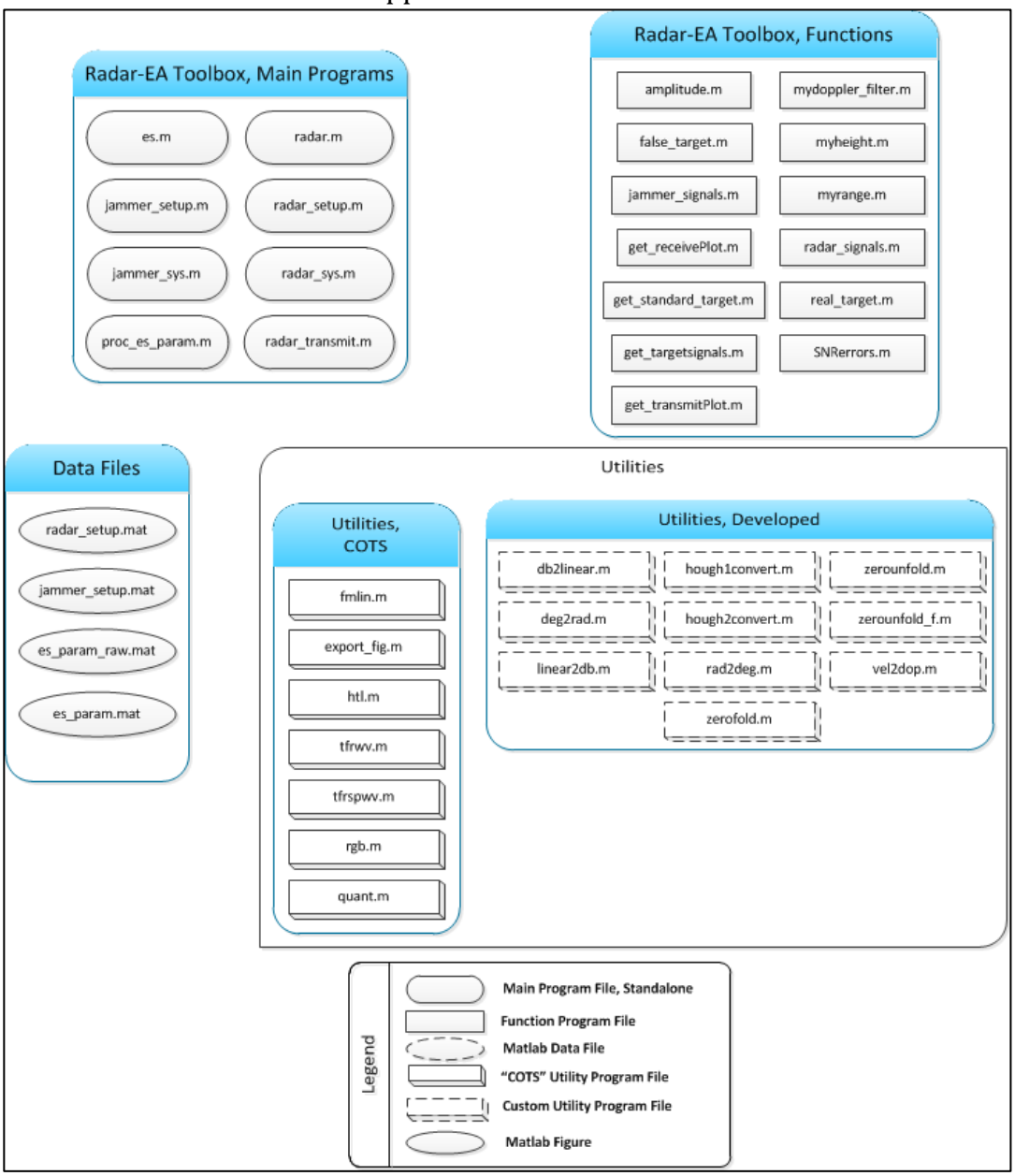

Figure 79: Simulation Files

3.1 Simulation Inputs

In this section, the simulation inputs are described. Inputs to the simulation are the target, radar and jammer parameters. Target parameters were already discussed in section 1.2.4. Only radar and jammer inputs to the simulation are discussed in this section.

3.1.1 Radar Model, Inputs

Radar setup parameters used in the simulation for both X and L Band Simulation Models are listed in Table 6 and Table 7. The parameters are fictitious and *do not represent an actual radar*. Parameters were selected for a selected detection range. Therefore, powers, gains and losses were selected to obtain a particular detection range. The "Radar System Model" was used to determine radar antenna transmit powers, gains and losses after a feasible detection range was selected.

The pulse widths and signal bandwidths were selected to provide a particular pulse compression gain that would be representative of an actual radar.

Resolution cell volume, which is made up of range resolution, Doppler resolution, and 3dB beam-width, was selected. The resolution cell volume, in turn dictated the requirements for antenna scan time and rotational speed.

All of the radar parameters as would be provided by a "Product Specification" are shown on the left side of Table 6 (X-Band) and Table 7 (L-Band). The parameters on the left of the tables were selected while the parameters shown on the right hand side of the table were, calculated using the following basic radar equations:

$$\lambda = \frac{c}{f} \tag{111}$$

$$t_o = \frac{2R_o}{c} \tag{112}$$

$$f_d = \frac{2v}{\lambda} \tag{113}$$

$$f_{d,\max} = \pm\frac{PRF}{2} \tag{114}$$

$$\Delta R = \frac{c}{2B_r} \tag{115}$$

$$\Delta f_d = \frac{1}{n_p \ PRI} = \frac{1}{CPI} \tag{116}$$

$$CPI = n_p \ PRI \tag{117}$$

$$\Delta v_{upper} = \frac{\Delta f_d \ \lambda_{upper}}{2} \tag{118}$$

$$\Delta v_{centre} = \frac{\Delta f_d \ \lambda_{centre}}{2} \tag{119}$$

$$\Delta v_{lower} = \frac{\Delta f_d \ \lambda_{lower}}{2} \tag{120}$$

$$G_{PC} = \tau \ B_r \tag{121}$$

$$R_{rec} = \frac{c\left(PRI - 3\tau\right)}{2} \tag{122}$$

$$R_{\max} = \frac{c \ PRI}{2} \tag{123}$$

$$R_{\min} = \frac{3c\tau}{2} \tag{124}$$

$$n_{Bin} = \frac{R_{\max}}{R_{\min}} \tag{125}$$

$$n_p = \frac{\theta_{3dB} \ PRF}{\dot{\theta}_{scan}} \tag{126}$$

$$T_{scan} = \frac{2\pi \ n_p}{\theta_{3dB} \ PRF} \tag{127}$$

The equations listed above were obtained from Richards [6]. *Every symbol used in this section or anywhere in this report is listed in Chapter 12*. The "List of Symbols" in Chapter 12 is organised into the "English Symbol" section as well as "Greek Symbol" section in order to simplify organisation of the list. To further simplify presentation to reduce complexity, the symbols are arranged in alphabetical order in both the "English" and "Greek" sections with descriptions and units. If an equation was used to calculate a particular parameter in Table 6 or Table 7, a reference to the equation used, was added in the table, next to the calculated radar parameter.

Specified Quantities	
Parameter	**Value**
Transmit Power [dBW]	38
Transmit Antenna Gain [dBi]	31
Receive Antenna Gain [dBi]	32
Pulse Compression Gain [dBW]	20
Doppler Processing Gain [dBW]	7
Sidelobe Ratio [dB]	13
Receiver Noise Temperature [K]	300
Single Pulse P_{fa}	5.77E-04
Multiple Pulse P_{fa}	1.00E-06
Losses [dBW]	6
Loss, Antenna [dBW]	1.2
Bandwidth [Hz]	1.50E+07
Pulse Width [s]	6.50E-06
Chirp rate [$1/s^2$]	2.31E+12
PRF [Hz]	3300
PRI [s]	3.03E-04
Number of Pulses [ ]	31
Element spacing [ ]	0.12
Number of Antenna Elements [ ]	8
Antenna Rotation Speed [rpm]	35
θ_{3db} [deg]	2
ϕ_{3db} [deg]	40
Range Glint [m]	15
Frequency Spacing [Hz]	6.00E+08
Carrier Frequency, Lower [Hz]	9.00E+09
Carrier Frequency, Centre [Hz]	9.60E+09
Carrier Frequency, Upper [Hz]	8.40E+09
Oscillator Frequency, Lower [Hz]	8.30E+09
Oscillator Frequency, Centre [Hz]	8.90E+09
Oscillator Frequency, Upper [Hz]	9.50E+09

Calculated Quantities		
Parameter	**Value**	**Equation**
Integration Time [s]	1.5	(127)
Coherent Processing Interval [s]	9.39E-03	(117)
Receiver RF Processing Gain [dBW]	71	(9)
Range Resolution [m]	10.0	(115)
Doppler Resolution [Hz]	106.5	(116)
Velocity Resolution, Upper [m/s]	1.8	(118)
Velocity Resolution, Centre [m/s]	1.7	(119)
Velocity Resolution, Lower [m/s]	1.9	(120)
Wavelength, Lower [m]	3.33E-02	(111)
Wavelength, Centre [m]	3.12E-02	(111)
Wavelength, Upper [m]	3.57E-02	(111)
Receive Window [m]	42530	(122)
R_{max} [m]	45455	(123)
R_{min} [m]	2925	(124)
n_{Bin} [ ]	44	(125)
Maximum Doppler Frequency [Hz]	±1650	(114)
Unambiguous Velocity , Upper [m/s]	27.5	(118)
Unambiguous Velocity , Centre [m/s]	25.8	(119)
Unambiguous Velocity , Lower [m/s]	29.4	(120)

Table 6: X-Band DBR Parameters

Specified Quantities	
Parameter	**Value**
Transmit Power [dBW]	32
Transmit Antenna Gain [dBi]	22
Receive Antenna Gain [dBi]	22
Pulse Compression Gain [dBW]	22
Doppler Processing Gain [dBW]	7
Sidelobe Ratio [dB]	13
Receiver Noise Temperature [K]	290
Single Pulse P_{fa}	5.77E-04
Multiple Pulse P_{fa}	1.00E-06
Losses [dBW]	4
Loss, Antenna [dBW]	3
Bandwidth [Hz]	3.00E+06
Pulse Width [s]	6.00E-05
Chirp rate [$1/s^2$]	5.00E+10
PRF [Hz]	800
PRI [s]	1.25E-03
Number of Pulses [ ]	20
Element spacing [ ]	2 out 3
Number of Antenna Elements [ ]	1
Antenna Rotation Speed [rpm]	35
θ_{3db} [deg]	5
ϕ_{3db} [deg]	60
Range Glint [m]	15
Frequency Spacing [Hz]	1.00E+06
Carrier Frequency, Lower [Hz]	1.10E+09
Carrier Frequency, Centre [Hz]	1.10E+09
Carrier Frequency, Upper [Hz]	1.10E+09
Oscillator Frequency, Lower [Hz]	1.07E+09
Oscillator Frequency, Centre [Hz]	1.08E+09
Oscillator Frequency, Upper [Hz]	1.08E+09

Calculated Quantities		
Parameter	**Value**	**Equation**
Integration Time [s]	1.5	(127)
Coherent Processing Interval [s]	2.50E-02	(117)
Receiver RF Processing Gain [dBW]	47	(9)
Range Resolution [m]	50.0	(115)
Doppler Resolution [Hz]	40.0	(116)
Velocity Resolution, Upper [m/s]	5.5	(118)
Velocity Resolution, Centre [m/s]	5.4	(119)
Velocity Resolution, Lower [m/s]	5.5	(120)
Wavelength, Lower [m]	2.73E-01	(111)
Wavelength, Centre [m]	2.72E-01	(111)
Wavelength, Upper [m]	2.73E-01	(111)
Receive Window [m]	160500	(122)
Rmax [m]	187500	(123)
Rmin [m]	27000	(124)
nBin [ ]	18	(125)
Maximum Doppler Frequency [Hz]	±400	(114)
Unambiguous Velocity , Upper [m/s]	54.5	(118)
Unambiguous Velocity , Centre [m/s]	54.5	(119)
Unambiguous Velocity , Lower [m/s]	54.6	(120)

Table 7: L-Band DBR Parameters

Radar Inputs, Simulation Flow

The radar setup program saves the parameters listed in Table 6 and Table 7 into a Matlab data file "radar_setup.mat". Two files are used, one for X-Band settings and another for the L-Band settings. This prevents duplication of processing variables for either band, thereby reducing programming complexity substantially.

The "radar_setup.mat" file is then loaded by other simulation models upon request, by the model. A "Simulation Flow Diagram" (SFD) indicating the Matlab structure of the "Radar Setup" file is shown in Figure 80.

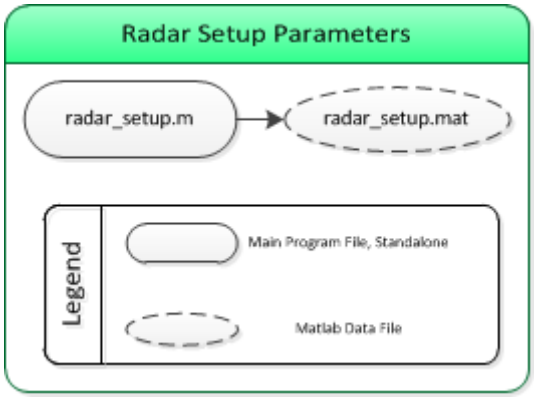

Figure 80: SFD, Radar Setup

3.1.2 Jammer Model, Inputs

Jammer setup parameters are the subject of this section. Jammer specifications listed here, are representative of actual jammers and were obtained through consultation with Christo Cloete (CSIR EW department), who in turn obtained them from a survey of unclassified product literature. Both "Stand-off" and "Stand-in" Jammers were considered, with "Wideband" and "Narrowband" Receivers. Their parameters are listed in Table 4, Table 5, Table 6 and Table 7.

Parameter	Value
Transmit Antenna Gain [dBi]	20
Receive Antenna Gain [dBi]	3
Transmit Power [dBW]	30
Bandwidth [Hz]	1.00E+10
Polarisation Losses [dBW]	3
Losses [dBW]	3
Duty Cycle Losses [dBW]	0

Table 8: Stand-off Jammer Parameters, Wideband

Parameter	Value
Transmit Antenna Gain [dBi]	10
Receive Antenna Gain [dBi]	3
Transmit Power [dBW]	10
Bandwidth [Hz]	1.00E+09
Polarisation Losses [dBW]	3
Losses [dBW]	3
Duty Cycle Losses [dBW]	0

Table 9: Stand-in Jammer Parameters, Wideband

Parameter	Value
Transmit Antenna Gain [dBi]	20
Receive Antenna Gain [dBi]	3
Transmit Power [dBW]	30
Bandwidth [Hz]	5.00E+05
Polarisation Losses [dBW]	3
Losses [dBW]	3
Duty Cycle Losses [dBW]	0

Table 10: Stand-off Jammer Parameters, Narrowband

Parameter	Value
Transmit Antenna Gain [dBi]	10
Receive Antenna Gain [dBi]	3
Transmit Power [dBW]	10
Bandwidth [Hz]	5.00E+05
Polarisation Losses [dBW]	3
Losses [dBW]	3
Duty Cycle Losses [dBW]	0

Table 11: Stand-in Jammer Parameters, Narrowband

Jammer Inputs, Simulation Flow

This jammer setup program functions similarly to the "Radar Setup" program described in the previous section. Jammer parameters listed in Table 8, Table 9, Table 10 and Table 11 were saved as "jammer_setup.mat" files and simulation models that require the jammer setup data, load the appropriate data file. The SFD for the Jammer Setup program is shown below.

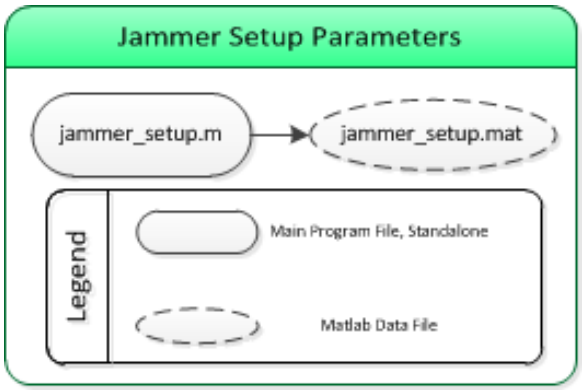

Figure 81: SFD, Jammer Setup

3.2 Simulation Outputs

Figures for scenario visualisation, as well as signal data in the form of Matlab "mat" files can be generated by the simulation models upon user request. The outputs generated by the models are listed below.

a. Radar System Model

- SNR vs. Range Plots
- P_d vs. Range Plots

b. Jammer System Model

- Target power vs. Repeater jammer power Plots
- Radar burn-through range Plots
- Maximum ES Intercept Range Plots

c. Transmitter Model

- Transmit signal amplitude vs. time plots
- Transmit signal spectrum plots
- Transmit signal pulse train plots

d. ES Model

- Estimated intercepted signal parameter data
- Wigner Distribution plots
- Hough Transform plots
- Wigner-Hough transform accuracy plots

e. Radar Model

The radar model is made up of three model components, which are the target range, velocity and elevation angle estimators. The outputs of these models are listed below.

Range Estimator, Single Plot Mode

- Received signal amplitude vs. time plots
- Received signal spectrum plots
- Range matched filter plots

Velocity Estimator, Single Plot Mode

- Doppler spectrum plots
- Doppler "Spectrum of Spectrums" plots

Elevation Angle Estimator, Single Plot Mode

- Received signal, 2 antenna element plot
- Received signal, 6 antenna element plot
- Phase shift height differential plots
- Phase shift height signal plots
- Phase shift height spectrum plots
- Cumulative Fast Fourier Transform (FFT) plots

a. Radar Tracks (Multiple Plot Mode)

- Target range vs. Time plots
- Target velocity vs. Time plots
- Target elevation angle vs. Time plots
- Single bin, error plots
- All bins, error plots

3.3 Simulation Controls

The simulation is designed to allow quick changes to control parameters, enabling specific studies to be carried out per scenario. The following controls can be set:

a. Radar and Jammer parameter setup

A "DBR type" Radar (three pulse LFM signals) and Jammer parameters can be setup as required. A new radar with a different signal type can be easily integrated into the simulation, due to the modular programming structure used to build the simulation.

b. Target type selection

The "target type" can be set. Options are "Fixed Wing", "Rotary Wing", "Missile" or combinations of these target types. Each target type has a fixed "$\sigma_{average}$", which is input to the RCS fluctuation models.

c. Number of targets selection

The number of targets can be set to one, or two of any type per range bin.

d. Noise Control

Noise can be added to the signal when required. The noise is added in the "radar_signals.m" file or "jammer_signals.m" file.

e. Amplitude Control

The appropriate signal amplitude can be incorporated into any signal when required, depending on whether true or false target amplitude at the radar, or intercepted signal amplitude at the jammer is required.

f. Intercepted Signal Model Processing Selection

Parameter estimation can be set to use either the "WVD" estimated or "SPWVD" estimated, parameters per frequency.

g. True and/or False Target Selection

The simulation allows the user to inject a true target only, or a true and false target into the radar receiver.

h. Radar Model, Single Plot Mode

In single-plot mode, any particular figure can be selected for plotting with custom parameters. A processing window for side-lobe reduction in Doppler processing can be also be set. The windows that can be selected are:

- Hamming Window
- Chebyshev Window
- Kaiser Window

i. Radar Model, Multiple Plot Mode

In track mode, the track can be updated with multiple detections for both true and false targets. At this stage, the target trajectory is hard–coded to prove the "multiple-plot" functionality, which repetitively reuses "single-plot" functions. Nevertheless, the simulation can be easily extended to accept any target trajectory. Currently the track can be selected to have:

- Range only varying,
- Elevation angle only varying,
- Range and velocity varying,
- Range, velocity and elevation angle varying simultaneously.

j. Standard Deviation

Standard deviation in range estimation, velocity estimation or elevation angle estimation can be incorporated into the track update mode, for the true echo signal, false echo signal or for both signals.

k. Saving figures and data

Data and any figure can be automatically saved, independently of any other figure or data, if a particular result is required. The figures are cropped and saved to a "Portable Network Graphics File" for reuse within documents. This is usually a tedious manual process. The COTS utility function "export_fig.m" was used for this purpose.

l. Dynamic Plots

A useful visualisation feature is the dynamic plot functionality, which allows any Single Plot Mode output to be *repeatedly generated* as the track is updated with new plots. For example if the "Match Filter Plot" is active in Track mode, the target peak moves in the plot as the track is updated. The function works equally well when a false target is injected. In this way, the effect of RGPO or RGPI on the Range Estimator, over time can be visualized. Using this function, a dynamic plot can be captured in a common video format (AVI, MP4 etc.) for NRT playback of the figure.

m. Automatic Result Generation and Capture

The figures from every model can be saved for every program control option, automatically, without manually changing any of the controls already listed. Therefore, the data and 100+ figures can be generated from the simulation for all target combinations, by activating this switch. In this way, an entire snapshot of a radar and EW system interaction can be obtained with a "switch of the button".

The "Save Data Switch" can be separately activated from the "Automatic Result Generation Switch" to ensure selected pertinent data is saved or not, independently of the automatic generation and display of figures.

4 System Models

In this chapter, the system-level performance aspects of both the radar and the jammer are investigated, simulated and discussed. Extensive use is made of the "Radar Range Equation" and Jammer "One-way Link" equations. The system performance simulation of both the radar and jammer generate lower level requirements in terms of required power output, antenna gains, and equipment losses necessary to achieve certain detection or burn-through ranges. The scenarios developed ensured that all three target types (see section 1.2.4) and signal frequencies in both bands as well as the four jammer categories (see section 3.1.2) were taken into consideration.

The radar system model is presented before the jammer system model in this chapter.

4.1 Radar System Model

The radar system model is placed into context within the overall simulation as depicted in Figure 82. Elements bounded by the red polygon in Figure 82 are relevant to the radar system model.

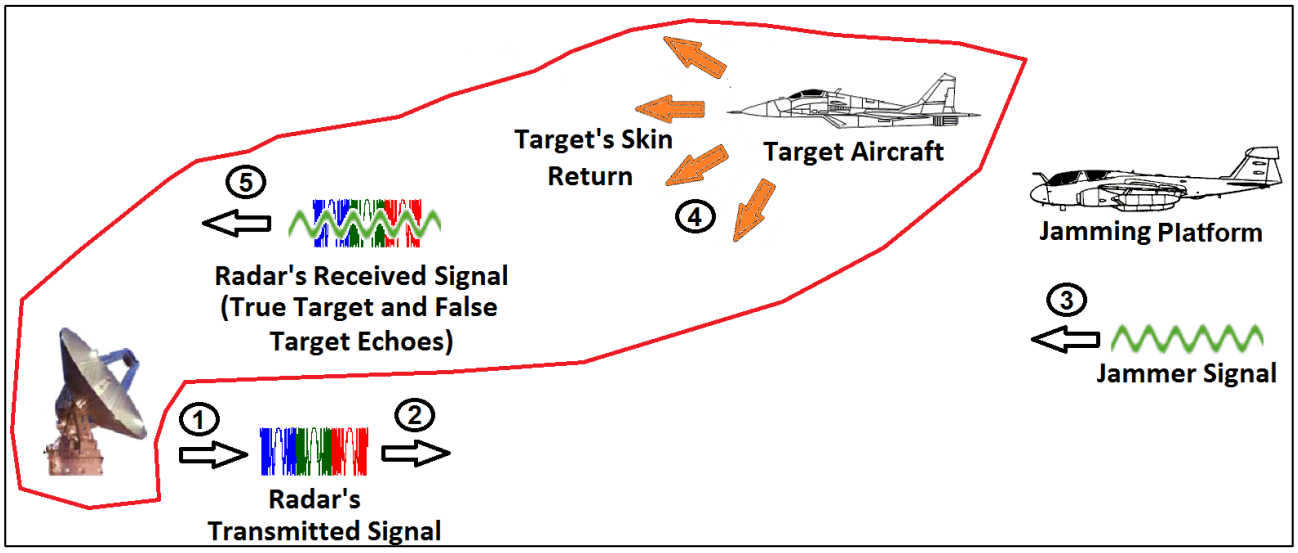

Figure 82: Radar System Model, Simulation Context

The standard Radar Range Equation as defined in Richards [6] was used to predict radar performance. Radar performance in this context is defined by the SNR vs. Range and Probability of Detection plots. These metrics assist in determining the theoretical maximum detection range of the target types specified. The radar range equation is:

$$SNR_{pulse}(t) = \frac{P_{tx}^{r} G_{tx}^{r} G_{rx}^{r} G_{PC} G_{DOP} \lambda^{2} \sigma(t)}{(4\pi)^{3} R_{o}^{4} k_{b} T_{s}^{r} B_{r} L_{radar}} \quad (128)$$

In equation (128), receiver noise is defined as:

$$noise_{radar} = k_b T_s^r B_r \tag{129}$$

Radar losses also used equation (128), are defined as:

$$L_{radar} = L_{other} + 2L_{antenna} \tag{130}$$

An important feature of this simulation is that the "SNR_{pulse}" was made a function of time.

This allows the SNR per time sample to be utilised in the model. The SNR is used to generate the instantaneous measurement errors and target signal amplitudes. In order to generate a SNR value as function of time, target RCS "$\sigma(t)$" is treated as an independent variable and is also made a function of time. For the Swerling Type 1 targets (Fixed and Rotary Wing), an "Exponentially" distributed random variable is generated per time step, whilst a "4th Degree Chi Square" distributed random variable is used to simulate the RCS fluctuation of the Swerling type 3 targets (missile). These distributions and the target RCS fluctuation models were discussed in detail in section 1.2.4.

Once the single-pulse SNR is calculated using equation (128), the multiple-pulse SNR, i.e. "SNR_{burst}" was calculated. Non-coherent integration of pulses was assumed for the multiple-pulse SNR. The SNR of pulses integrated non-coherently was calculated using ([6]):

$$SNR_{burst} = SNR_{single}\sqrt{n_p} \tag{131}$$

In Barton's textbook (reference [2]), the Probability of Detection "P_D" is:

$$P_D^{pulse} = \frac{1}{2} erfc\left(erfc^{-1}(P_{FA}) - \sqrt{\frac{SNR_{pulse}^2}{SNR_{pulse} + 2.3}} \right) \tag{132}$$

In addition, multiple-pulse "Probability of Detection, P_D^{burst}" is found from the binomial theorem ([6]):

$$P_D^{burst} = \sum_{k=r}^{s} \frac{s!}{k!(s-k)!} P_D^{pulse} \left(1 - P_D^{pulse}\right) \tag{133}$$

An example of the SNR plots generated for a two-target scenario is shown in Figure 83. The SNR vs. Range plot for a fixed wing aircraft and missile over the detection range of the radar is shown for the X-Band detection case, in this figure. Effects of the random RCS fluctuation from the Swerling 1 and 3 models for the fixed wing aircraft and missile, can also be seen in the plot. The lower average RCS of the missile causes a lower echo power to be received, at the radar compared to the fixed wing target. The non-coherently integrated multiple-pulse SNR is shown for both targets in the bottom subplot of Figure 83.

In Figure 84, the X-Band "Probability of detection" for the CPI ("P_D^{burst}") against radar detection range is shown, and the L-Band "P_D^{burst}" vs. range is shown in Figure 85. In these plots, the maximum theoretical detection range of the radar can be determined. This is usually calculated at the 80% P_D^{burst} probability. By comparing Figure 84 and Figure 85, the larger maximum detection range of the L-Band subsystem compared to the X-Band is clearly visible. This is shown for the fixed wing target, but is true of all the target types considered in this simulation.

At X-Band, the different maximum detection probabilities at the three X-Band frequencies are clearly visible in Figure 84. This phenomenon is not as visible at L-Band, in Figure 85. The reason for the differences between X and L-Bands "three-frequency" probability of detections for the same target are due to differences in wavelengths of the signals at the two bands. The X-band signals have longer wavelengths (higher frequencies) than the L-Band Signals, which causes the Probability of Detection, plots to show the clearly visible separation between the P_D^{burst} curves in these figures.

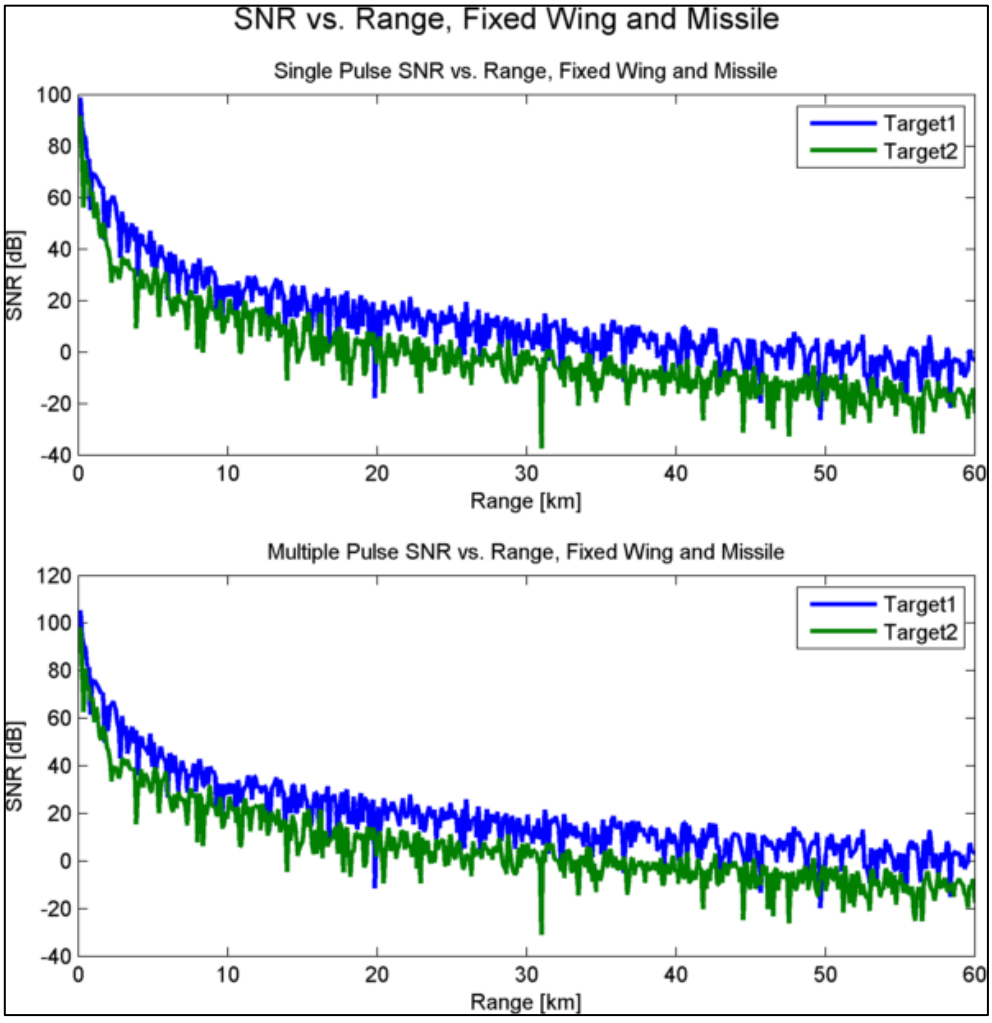

Figure 83: SNR vs. Range, Fixed Wing and Missile, X-Band

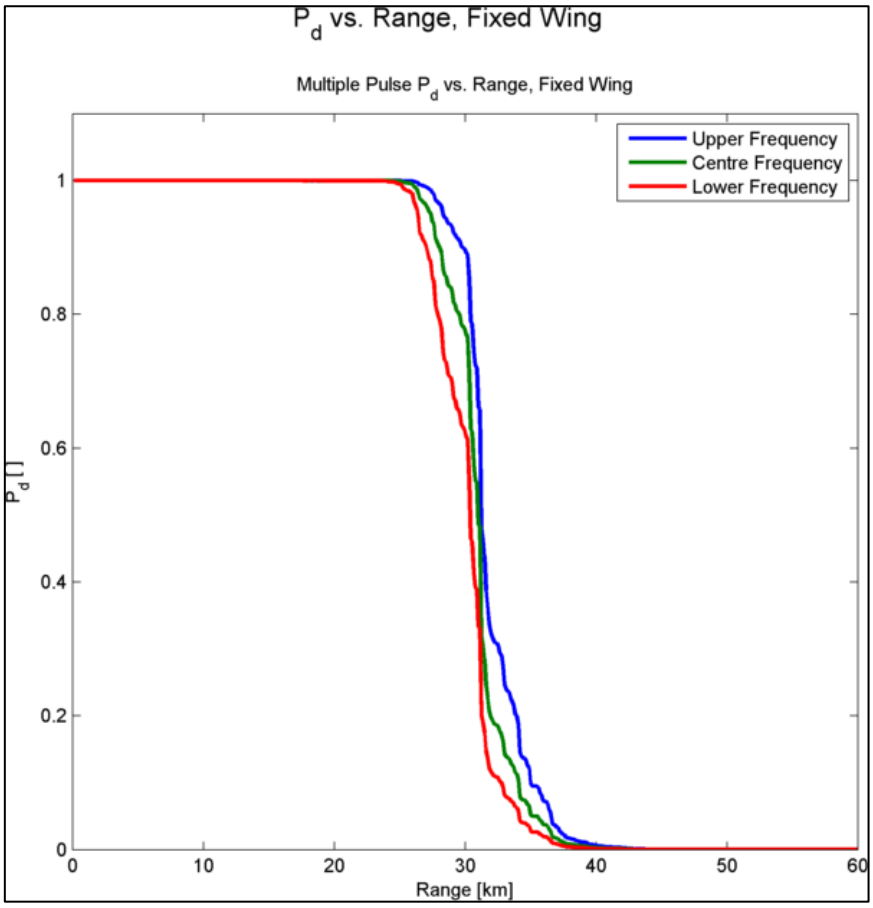

Figure 84: P_d vs. Range, Fixed Wing, X-Band

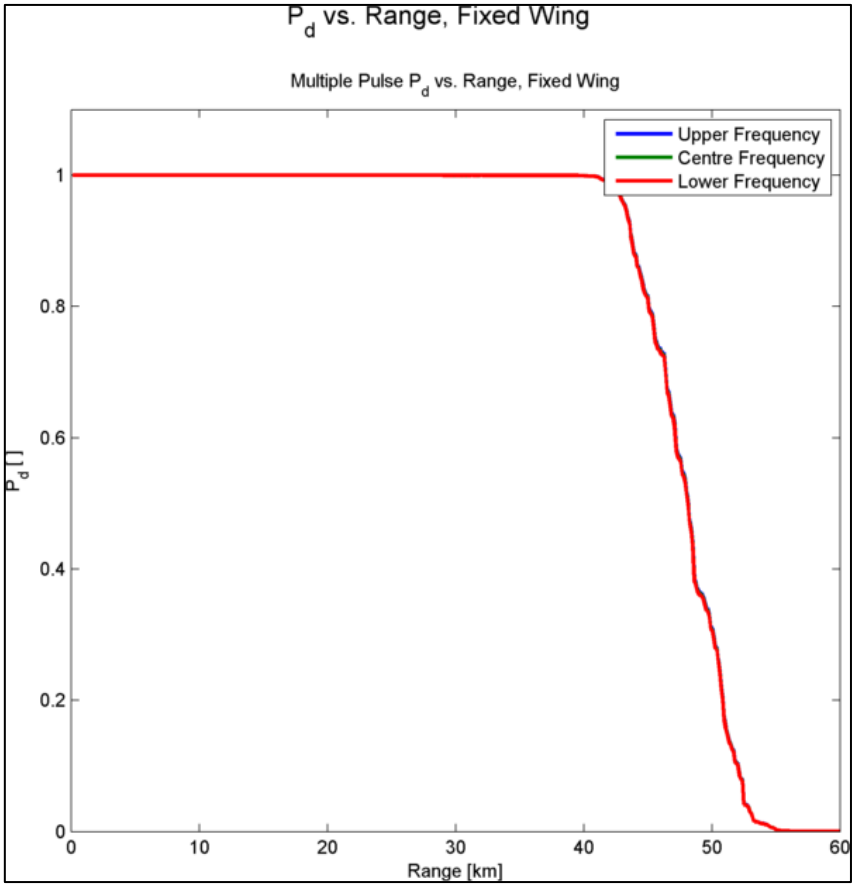

Figure 85: P_d vs. Range, Rotary Wing, L-Band

A summary of the "P_D^{burst}" vs. Range results at X and L Bands for all three target types are shown in Table 12 and Table 13. The longer detection range of the L-Band DBR subsystem mentioned is shown quantitatively in these tables. These results show that the larger RCS targets are detectable at greater ranges than the smaller targets.

Target Type	Radar Detection Range @ 80% P_d [m]
Fixed Wing	29276
Rotary Wing	36360
Missile	15773

Table 12: 80% Detection Range, X-Band

Target Type	Radar Detection Range @ 80% P_d [m]
Fixed Wing	45090
Rotary Wing	50610
Missile	25130

Table 13: 80% Detection Range, L-Band

Radar System Model, Simulation Flow

The radar system model simulation flow, starts with the loading of radar parameters. Two types of radar performance metrics are then output, in the form of figures, i.e. "SNR" vs. Range and "P_D" vs. Range. Various customized programs and COTS utility programs are used to process the data as shown in Figure 86. The radar system model mathematics discussed in this section were implemented in software according to the SFD shown below.

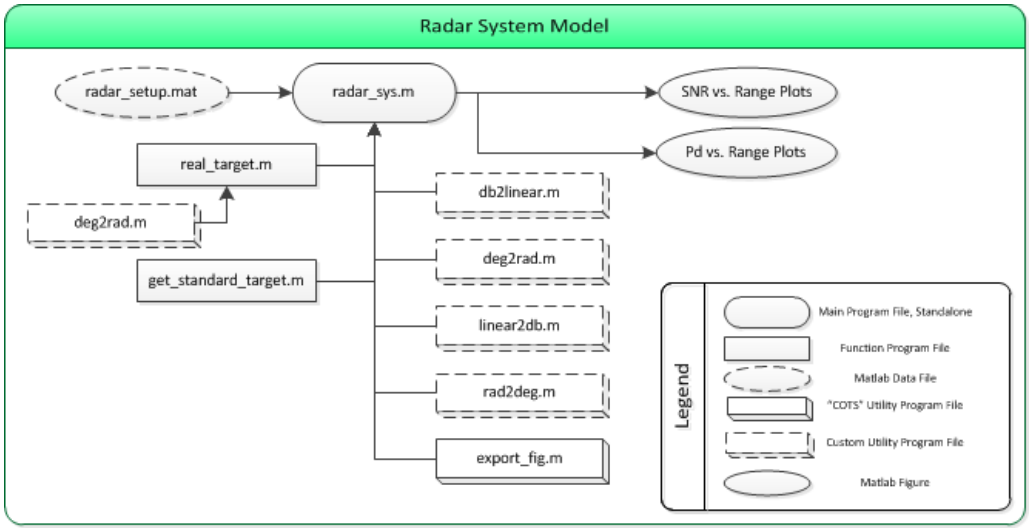

Figure 86: SFD, Radar System

4.2 Jammer System Model

In this system performance model, all of the elements in the simulation scenario shown in Figure 87 are relevant and taken into consideration. Transmitted radar signal power, jammer transmitted power and target echo power are all elements of the Jammer System Model.

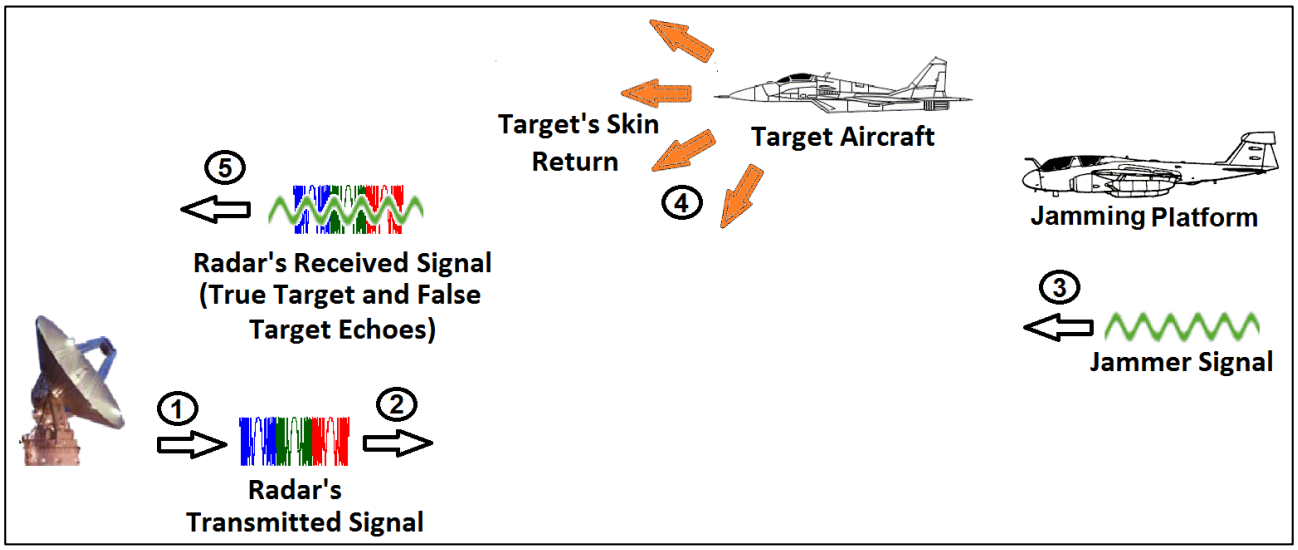

Figure 87: Jammer System Model, Simulation Context

In this section, various system-level constraints on the radar and jammer that result from their interaction are explained. The fundamental concept of "Burn-through Range" is explained initially. This concept gives important insight into the design trade-offs limiting both radar and jammer performance. The advantage of using PC and DP in the DBR is shown graphically.

Then the minimum sensitivity level for the ES Receiver is calculated for typical jammers operating against the DBR, from the "Maximum ES Intercept Range" plots. An interesting electronic protection capability of the DBR, because of its dual X and L band operation was made apparent by this analysis. EW system response time to counter the DBR was thereafter discussed. The inherent limitations to jammer response time are determined by the radar's integration time. Finally, repeater jammer performance against the DBR is discussed.

4.2.1 Burn through Range

The range at which the DBR transmits more signal power than the jammer is able to transmit is called "burn-through range". In other words, the burn-through range is the range at which the radar is able to overcome the jammer, for it to perform its primary role of target detection, in the region that is less than the burn-through range. The radar cannot detect targets at any range greater than the burn-through range, since the jammer's transmitted signal power raises the radar noise power sufficiently enough to prevent detection.

Burn-through range is defined in reference [4] as:

$$R_{burn} = \left(\frac{P_{tx}^{r} G_{tx}^{r} G_{PC} G_{DOP}}{4\pi SJR} \right) \left(\frac{\sigma_{average}}{P_{tx}^{j} G_{tx}^{j}} \right) \left(\frac{B_j}{B_r} \right) \left(\frac{L_{jammer}}{L_{radar}} \right) \quad (134)$$

The radar prefers as large a burn-through range "R_{burn}", as possible, because it should overcome the jammer signal power for target detection at the larger range. If this is achieved further away, it means the radar is able to perform its normal target detection at ranges less than the burn-through range. The jammer on the other hand strives to obtain a smaller burn-through range, so that radar target detection is compromised to the shortest possible range. The radar's transmitted signal power and processing gain competes against the jammer's transmitted signal power and antenna gain in limiting/expanding burn-through range as shown by the first two terms of equation (134).

From the second term, it can be deduced that a narrower jammer bandwidth relative to the radar's signal bandwidth causes a larger burn-through. The jammer has an advantage over the radar because of the shorter path, the false signal would travel compared to the jammer. Received radar power is proportional to "$1/R^4$" as stated by M.A. Richards et. al, in reference [6]). This inversely proportional relationship between radar power to range, is due to the fact that the radar signal has to travel to the target/clutter and back (two-way propagation range). The radar signal received by the ES subsystem of the jammer, on the other hand, has to travel a "one way" distance only from the radar to the jammer. Jammer power therefore varies with range according to a "$1/R^2$" proportion. Because, of the "one way propagation advantage of the jammer, its transmitter power relative to the radar is attenuated far less, over distance.

It is important for the Jammer, that its losses are minimized relative to radar losses, because this also reduces the effective range at which the radar can overcome the jammer.

Burn-through range was calculated for the DBR against the four benchmark jammers described in section 3.1.2 and some of these results are shown in Figure 88 and Figure 89.

This calculation was also repeated for the three target types (Fixed Wing, Rotary Wing and Missile) at a "Signal to Jamming" (SJR) ratios varying from 0dbW to 100dBW. However, in the figures displayed, only the stand-off wideband jammer burn-through range plots are displayed.

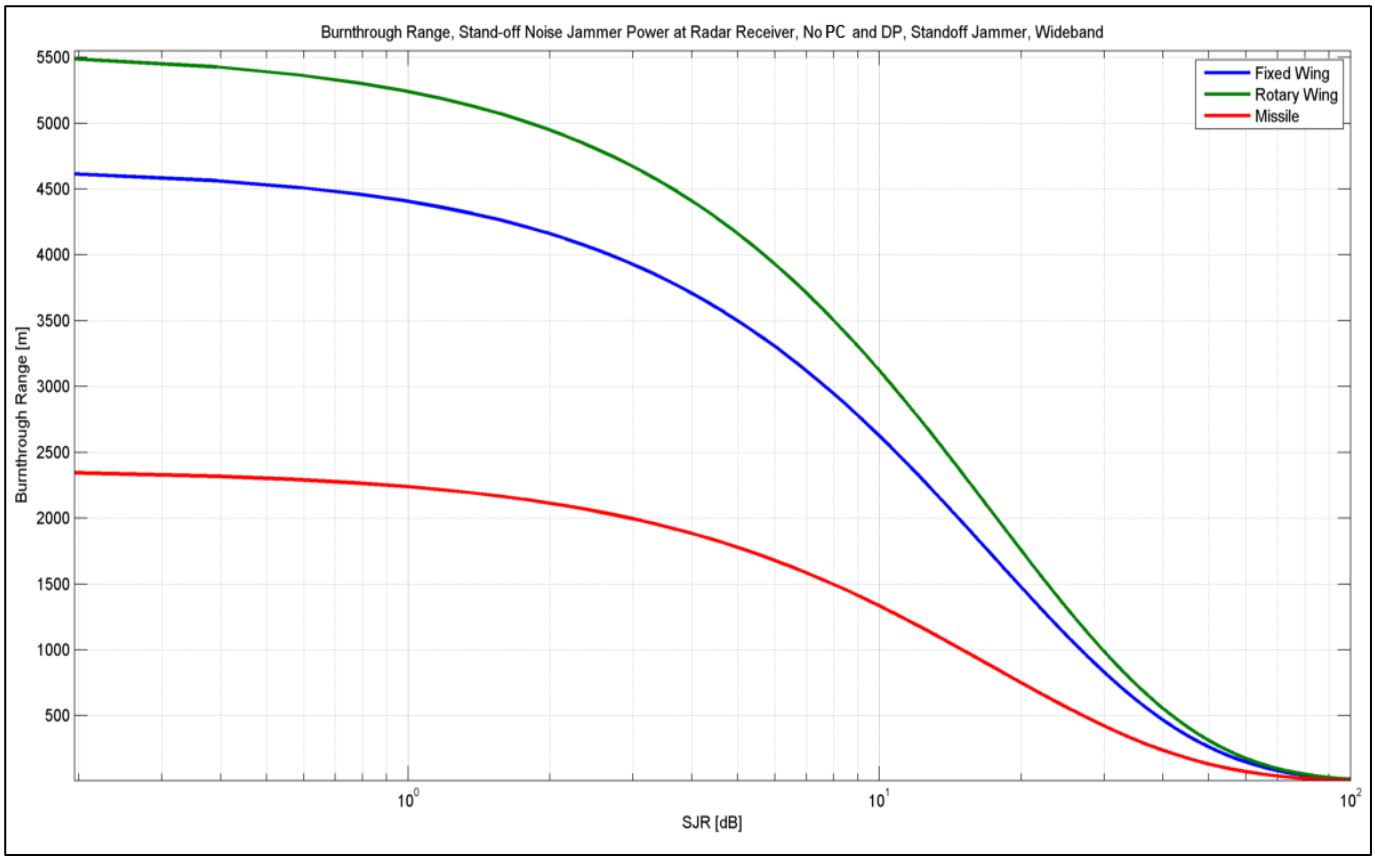

Figure 88: X-Band Burn-through Range with no Pulse Doppler and Doppler Processing

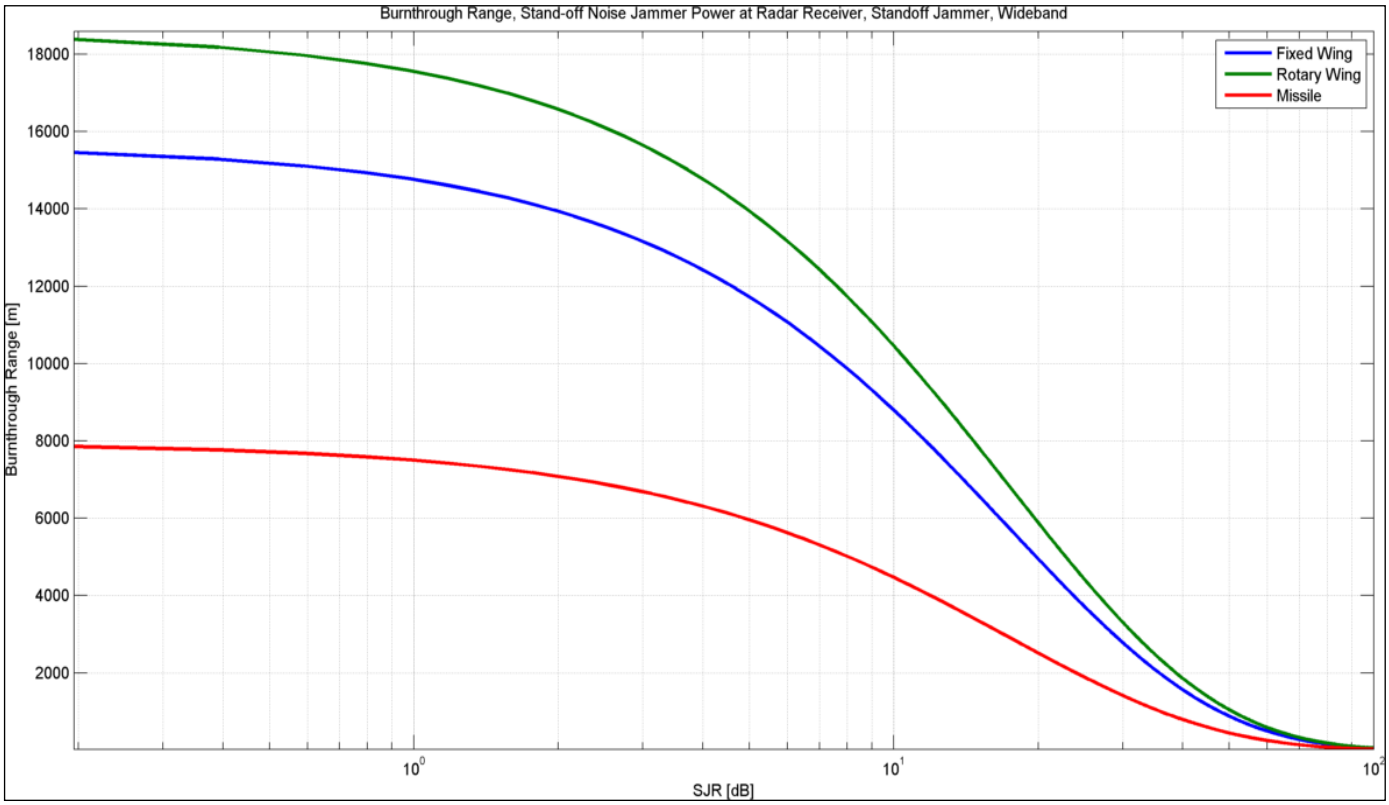

Figure 89: X-Band Burn-through Range with no Pulse Doppler and Doppler Processing

Burn-through ranges for the three standard targets, for the DBR with no PC or DP, are shown in Figure 88. Figure 89 shows the burn-through range for the same targets, for the DBR with PC and DP. A substantial improvement in burn-through range from the radar's perspective (larger burn-through range) is immediately noticeable, for the same target types and jammer parameters.

Another trend that is also visible in the burn-through range plots displayed, is that the noise jammer would induce a smaller burn-through if it were disguising a smaller RCS target (such as the missile). Stated differently, it would be easier for the noise jammer to obscure a smaller RCS target echo than a larger one, which is an intuitive understanding as well.

The results from the burn-through range simulation for all three target types and four jammer types per DBR frequency band are shown in Table 14 and Table 15. The narrowband receiver jammers induce smaller burn-through ranges than the wideband jammer receivers. If the jammer is closer to the radar (stand-in jammer) than this also results in a smaller burn-through range, which is preferred for the jammer.

Target Type	**Jammer Type**	**Radar Burnthrough Range @ 0dbW SJR [m]**
Fixed Wing	Stand-off Jammer, Wideband Receiver	14780
Fixed Wing	Stand-off Jammer, Narrowband Receiver	1478
Fixed Wing	Stand-in Jammer, Wideband Receiver	9781
Fixed Wing	Stand-in Jammer, Narrowband Receiver	219
Rotary Wing	Stand-off Jammer, Wideband Receiver	17580
Rotary Wing	Stand-off Jammer, Narrowband Receiver	1243
Rotary Wing	Stand-in Jammer, Wideband Receiver	13830
Rotary Wing	Stand-in Jammer, Narrowband Receiver	309
Missile	Stand-off Jammer, Wideband Receiver	7510
Missile	Stand-off Jammer, Narrowband Receiver	632
Missile	Stand-in Jammer, Wideband Receiver	2525
Missile	Stand-in Jammer, Narrowband Receiver	56

Table 14: Jammer System Model Burn-through Range Results, X-Band

Target Type	Jammer Type	Radar Burnthrough Range @ 0dbW SJR [m]
Fixed Wing	Stand-off Jammer, Wideband Receiver	14020
Fixed Wing	Stand-off Jammer, Narrowband Receiver	1263
Fixed Wing	Stand-in Jammer, Wideband Receiver	8415
Fixed Wing	Stand-in Jammer, Narrowband Receiver	188
Rotary Wing	Stand-off Jammer, Wideband Receiver	17860
Rotary Wing	Stand-off Jammer, Narrowband Receiver	1502
Rotary Wing	Stand-in Jammer, Wideband Receiver	11900
Rotary Wing	Stand-in Jammer, Narrowband Receiver	266
Missile	Stand-off Jammer, Wideband Receiver	7631
Missile	Stand-off Jammer, Narrowband Receiver	642
Missile	Stand-in Jammer, Wideband Receiver	2173
Missile	Stand-in Jammer, Narrowband Receiver	49

Table 15: Jammer System Model Burn-through Range Results, L-Band

Overall, the burn-through ranges for the L-Band subsystem were smaller than at X-Band. However, differences for the burn-through ranges between X and L-bands are due to the different transmit powers, gains and bandwidths of the two radar subsystems and are not dependent on their frequency bands or signal wavelengths. This fact can also be deduced by inspection of equation (134), where it can be seen that carrier frequency or wavelength is not explicitly included.

A general conclusion that can be drawn from this analysis is that, the burn-through range for the DBR against typical noise jammers is small. This means that the DBR would be vulnerable to this type of jamming unless EP measures are implemented to defend the radar against these types of jammers.

4.2.2 Maximum ES Intercept Range

The maximum intercept range of a radar signal by an ES receiver is defined as:

$$R_{ES}^{\ 2} = \frac{P_{tx} G_{tx} \lambda^2}{4\pi L_{radar}} \frac{1}{L_{jammer}^{pol} MDS} \tag{135}$$

This range is defined as the furthest range from which a radar signal can be detected by the ES receiver. In the above equation the quantity "*MDS*" is the "Minimum Detectable Signal" level or sensitivity of the ES receiver. Typical ES system sensitivities are in the order of -65dBm but the maximum sensitivity of a commercially available ES system was found to be -90dBm. It can be concluded therefore, that a modern military grade ES receiver would use an even more

"sensitive" ES receiver. The greater sensitivity receiver allows radar signals to be detected and intercepted at greater ranges. Major commercially available ES receivers and their specifications are listed in the ES receiver survey displayed in Appendix 14.8.

Equation (135) was derived from the "one way link" jammer equation described by Richards et al. in reference [6]. In this simulation, the DBR transmitter specifications were used as well as the "standard" 3dBW Jammer Polarisation loss. These specifications are shown in sections 3.1.1 and 3.1.2.

The maximum ES system intercept times were simulated using equation (135) at both X-Band and L-Band for the DBR. The results are shown in Figure 90.

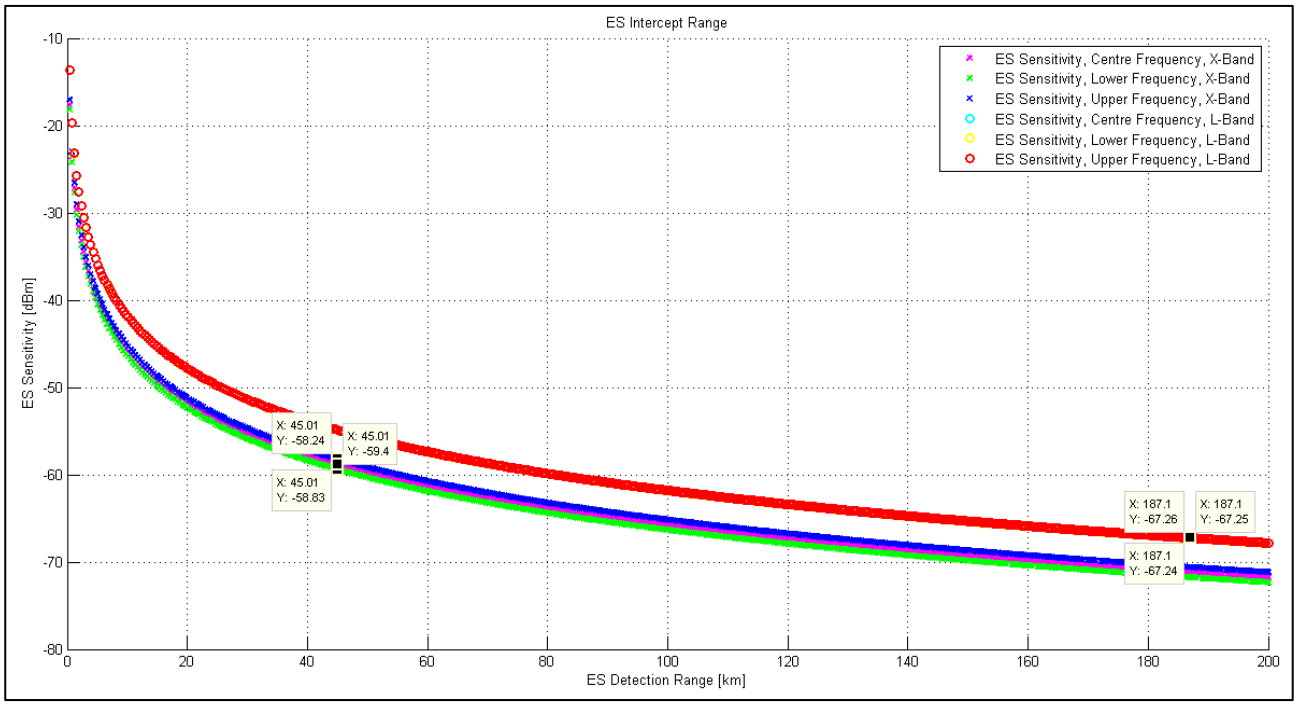

Figure 90: ES Receiver Intercept Range

The maximum ES Receiver intercept range was calculated for ES receiver sensitivities varying from -10 dBm to -80dbm and intercept ranges from 0km to 200km.

From inspection of Figure 90, it is concluded that a more sensitive receiver is required to detect the L-Band DBR signals compared to the L-Band signals because theoretical maximum detection is far greater at L-Band compared to X-Band (187.5km vs. 45.5km).

If the jammer is to achieve "stand-off" relative to the radar, the ES receiver should detect and intercept radar signals at ranges greater than the theoretical maximum detection range of both X-and L Band subsystems. Therefore, the ES receiver sensitivity necessary to obtain standoff from the DBR is dictated by the L-band subsystem. The average sensitivity over the three L-Band frequencies is -67.25 dBm.

Another trend visible in Figure 90 is that the three frequencies at the DBR X and L Bands cause slightly different maximum ES intercept ranges requiring ES receivers with slightly different sensitivities. Practically, the lower frequency at L-Band constrains the minimum ES sensitivity to-67.26 dBm. These small differences in ES receiver sensitivity for the three frequencies are not significant and are slightly larger at X-Band. The differences in MDS for the L-Band and X-Band DBR subsystems are shown in Figure 91 and Figure 92.

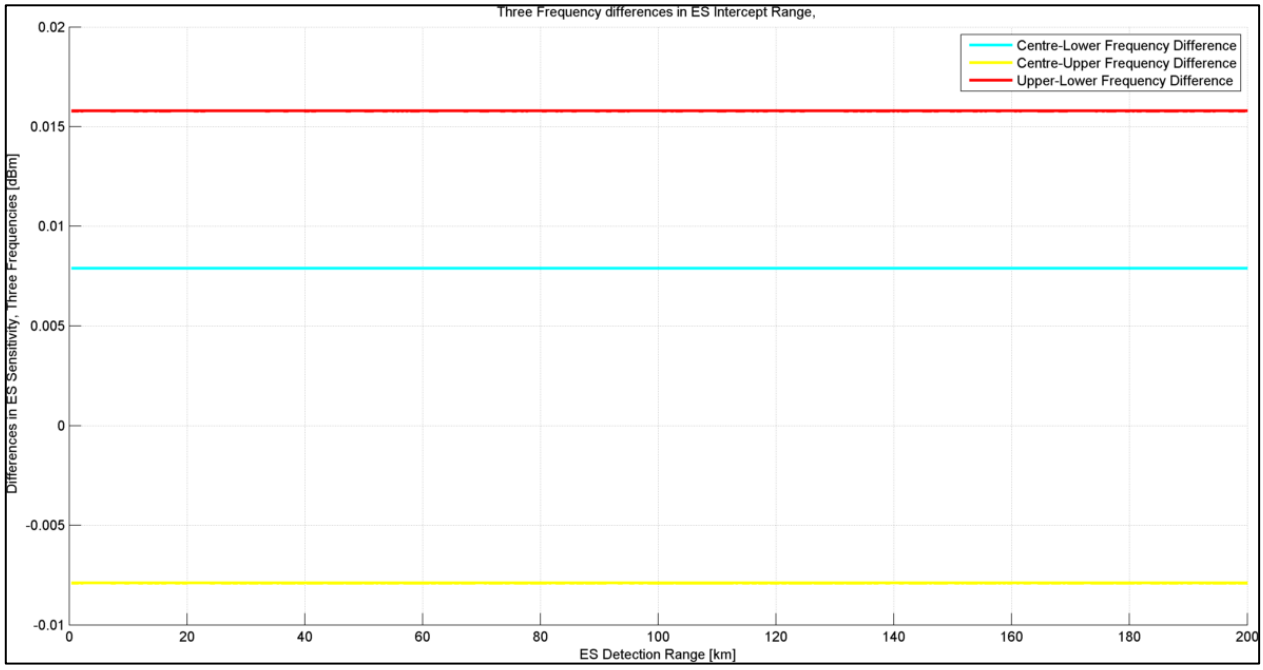

Figure 91: Differences in ES Sensitivities for three L Band frequencies

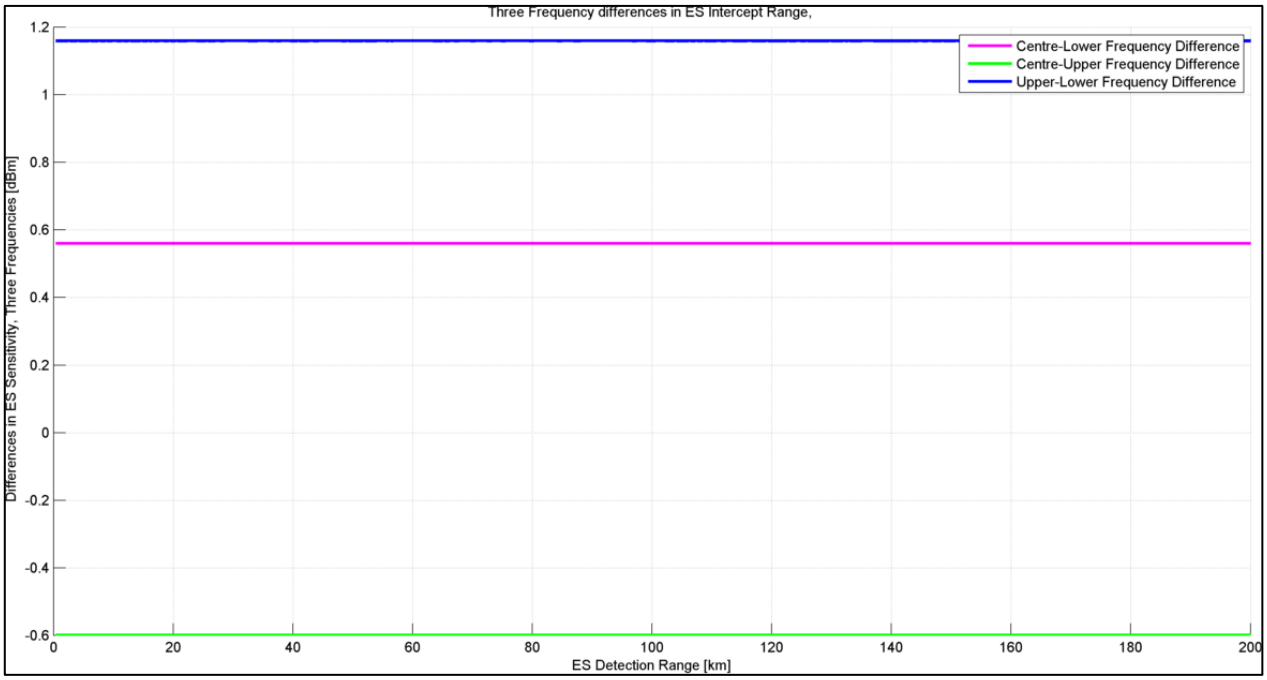

Figure 92: Differences in ES Sensitivities for three X Band frequencies

4.2.3 Response Time

The DBR receive window or "integration" time is shown in Figure 93.

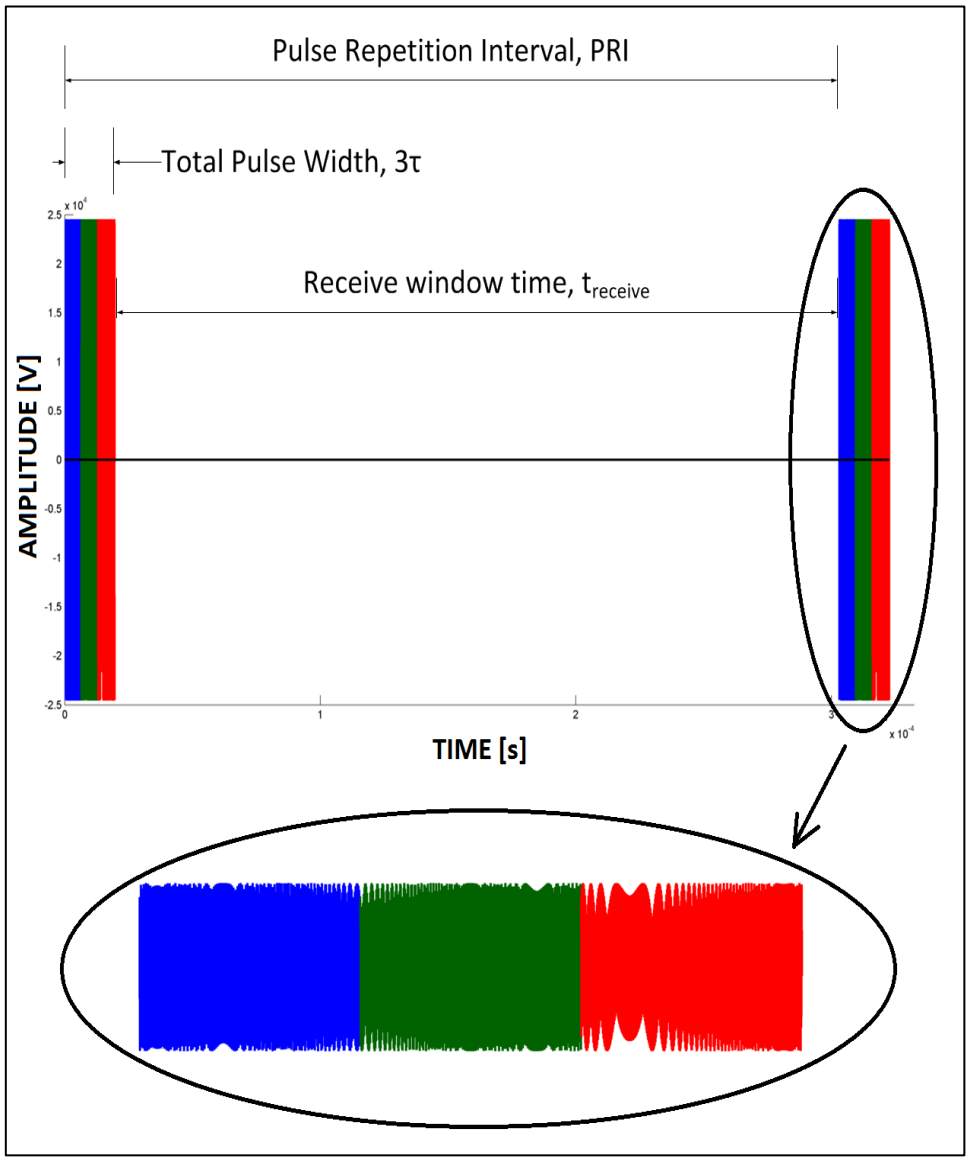

Figure 93: DBR Transmitted Signal definitions

In a mono-static radar configuration such as the DBR, the radar is not transmitting during the receive window time, but is rather processing received echo signals. Therefore, this time period is also the time that the ES system has available to detect and intercept the radar signal, estimate its parameters and generate a false signal; before the true target echo is received by the radar during its next processing cycle.

If the ES system is in either "stand-off" or "stand-in" operation, the jammer's response time is equal to the radar's integration time. In the DBR, this time was defined as:

$$t_{receive} = PRI - 3\tau \tag{136}$$

It was calculated to be 283.5μs at X-Band and 1.07ms at L-Band. These times provide the response time constraint on the ES System. During this time period, the ES system should intercept, interpret and retransmit the appropriately modulated false signal before the radar transmits its next pulse. Typical ES systems have response times in the order of 1 to 2 μs (reference [5]), so the DBR pulses should not be a challenge to the DBR Jammer.

According to the fundamental radar equation, relating signal time delay to range, the distance measurable by the radar is ([6]):

$$R_{recieve} = \frac{ct_{receive}}{2} \tag{137}$$

The X-Band *receive window range* was 42.53km and the L-Band *receive window range* was 160.5km. It can therefore be deduced that the ES system has to be outside L-Band Detection range in order to obtain complete stand-off from the DBR. It therefore has 1.07ms to respond to the radar. However, by this time the intercepted X-Band signal is received at the ES system, is therefore, at least three PRI's later.

Under the hypothesis that the DBR does not use pulse diversity, the ES system would be able to intercept and deceive the X-Band subsystem, from a large standoff range, compared to the L-band. But, the jamming platform would be within detection range of the L-Band system. The DBR Jammer should therefore commence deception jamming of the L-Band system, long before it is within X-band detection range. Only once the jammer is less than 45.5 km away from the DBR would it be able to get within "one PRI's length" to the radar in order to effectively and simultaneously jam both the X-Band and L-Band signals.

However, if the radar were to apply pulse diversity on a pulse-to-pulse basis as described by M. Soumekh in reference [29] and J. Schuerger and D Garmatyuk in reference [25], deception jamming would not be effective against either the L-Band or X-Band subsystems.

It can be therefore be concluded that the dual-band DBR capability is indeed a powerful EP feature that shortens ES receiver required response times and simultaneously ensures long range detection of the jamming platform.

Both equations (136) and (137) as well as Figure 93 were already discussed from the "radar's" perspective in section 1.2.2. However, in this section, this radar measurement time was discussed from the jammer's perspective.

4.2.4 Repeater Jamming

The repeater jamming power equations used in this section were obtained from the textbook written by D. Schleher (reference [4]). Noise jamming is a common subject and is discussed in numerous radar textbooks (see references [1], [2], [5], [6] and [8]). However, an interesting feature of the repeater noise jamming derivation by D. Schleher, not described in the other

radar textbooks researched, was the modelling of *jammer transmitter saturation*. The jammer transmitter has maximum transmit signal power and cannot transmit at a power greater than this level, which is called the "transmitter's saturation level".

The "Main Lobe Target Return" is calculated using equation (128), which was already shown in the "Radar System Model" derivation. This is the standard power form of the radar range equation for a target with a RCS of "σ" at a range of "R_o" to the radar.

The "Repeater Jammer Input Signal" is then calculated using equation (138) as:

$$SNR_{jr} = \frac{P_{tx}^{r} G_{tx}^{r} G_{rx}^{j} \lambda^2}{\left(4\pi \cdot R_j\right)^2 L_{jammer}\, noise_{jammer}} \tag{138}$$

This is the signal power received *by* the jammer *from* the radar. In equation (138), jammer noise is defined as:

$$noise_{jammer} = k_b T_s^{j} B_j \tag{139}$$

If the jammer's available transmitter power "P_{tx}^{j}" is greater than the required jammer to signal ratio as shown below:

$$P_{tx}^{j} \le SNR_{jr} \frac{4\pi JSR\, \sigma L_{jammer}^{pol\ 2}}{G_{rx}^{j} G_{tx}^{j} \lambda^2} \tag{140}$$

Then the jammer transmitter is in an "unsaturated" state. In the above equation, the true target RCS "σ" is used together with the Jammer to Signal Ratio "SNR_{jr}" to set the desired false target RCS "σ_f". Usually the false target RCS is set by amplifying the true target RCS so that the true target can be masked by the false one. The dynamic range of the amplification depends on the jammer receiver and transmitter RF processing and amplification capability. The false target RCS "σ_f" is then written as:

$$\sigma_f = JSR\, \sigma \tag{141}$$

Repeater jammer gain is defined as:

$$G_{REP}^{j} = \frac{4\pi \sigma_f L^{j}}{\lambda^2 \beta^2} \tag{142}$$

Using equations (141) and (142), the jammer transmitter unsaturated condition (equation (140)) can be written as:

$$P_{tx}^{j} > SNR_{jr} \frac{G_{REP}^{j}}{G_{rx}^{j} G_{tx}^{j}} \tag{143}$$

The received signal power at the radar from the jammer is then defined as:

$$SJR = \frac{P_{tx}^{r} G_{tx}^{r} G_{rx}^{r} \left(SNR_{jr} \frac{G_{REP}^{j}}{G_{rx}^{j} G_{tx}^{j}} \right) G_{PC}\, G_{DOP}\, \lambda^2}{\left(4\pi R_j\right)^4 L_{radar}\, L_{jammer}^{pol} noise_{radar}} \tag{144}$$

However, if the required jammer to signal ratio is greater than transmitter maximum signal power capacity, the repeater jammer transmitter is saturated and cannot therefore transmit more power than its maximum limit. This condition is described mathematically as:

$$P_{tx}^{j} > SNR_{jr} \frac{G_{REP}^{j}}{G_{rx}^{j} G_{tx}^{j}} \tag{145}$$

The "Main Lobe Repeater Jammer Signal" power is then given by:

$$SJR = \frac{P_{tx}^{r} G_{tx}^{r} G_{rx}^{r} P_{tx}^{j} G_{PC} G_{DOP} \lambda^{4}}{\left(4\pi R_{j}\right)^{4} L_{radar} L_{jammer}^{pol} noise_{radar}} \tag{146}$$

In saturation mode, the repeater jammer transmitter transmits at its maximum rated power as specified in section 3.1.2.

To calculate the jammer power received in the radar side-lobes the following equations from Schleher [4] are used: If the jammer transmitter is not saturated this condition can be stated as:

$$P_{tx}^{j} > SNR_{jr} \frac{G_{sl}^{r} G_{REP}^{j}}{G_{rx}^{j} G_{tx}^{j} G_{tx}^{r}} \tag{147}$$

Then:

$$SJR = \frac{P_{tx}^{r} G_{tx}^{r} G_{rx}^{r} \left(SNR_{jr} \frac{G_{sl}^{r} G_{REP}^{j}}{G_{rx}^{j} G_{tx}^{j} G_{tx}^{r}} \right) G_{PC} G_{DOP} \lambda^{2}}{\left(4\pi R_{j}\right)^{4} L_{radar} L_{jammer}^{pol} noise_{radar}} \tag{148}$$

However, if the jammer receiver is saturated:

$$P_{tx}^{j} \leq SNR_{jr} \frac{G_{sl}^{r} G_{REP}^{j}}{G_{rx}^{j} G_{tx}^{j} G_{tx}^{r}} \tag{149}$$

Therefore, equation (148) becomes:

$$SNR_{rj} = \frac{P_{tx}^{r} G_{tx}^{r} G_{rx}^{r} P_{tx}^{j} G_{PC} G_{DOP} \lambda^{4}}{\left(4\pi R_{j}\right)^{4} L_{radar} L_{jammer}^{pol} noise_{radar}} \tag{150}$$

The above equations were used to simulate the effects of a repeater noise jammer jamming the DBR Radar when the true target is either a fixed wing, rotary or missile type, while travelling over the entire X-Band and L-Band detection ranges.

In Figure 94, repeater jammer power received from a wideband stand in jammer at the radar is plotted against target detection range, for a fixed wing target. Jammer signal power in the radar main and side-lobes is compared to the true target return and intercepted radar signal power. It can be seen that the main lobe jammer power overpowers the true target power

over the entire range. Side-lobe power exceeds target power at a slightly larger range. The original signal-level of the intercepted signal ("Repeater Input Signal") is also compared to the repeater signal powers ("Main Lobe Repeater Jammer Signal" and "Sidelobe Repeater Jammer Signal").

Jamming power from a wideband stand-off repeater jammer on the DBR is compared against the received target power when the target is a missile, in Figure 95. Due to the small RCS of the missile, its echo power is always below the repeater main lobe and side-lobe jammer power. In Figure 95, the jammers are seen to be transmitting in the unsaturated mode until a range of approximately 5km. Thereafter, the required Jammer to Signal ratio is larger than the jammer transmitter capability and the transmitter saturates.

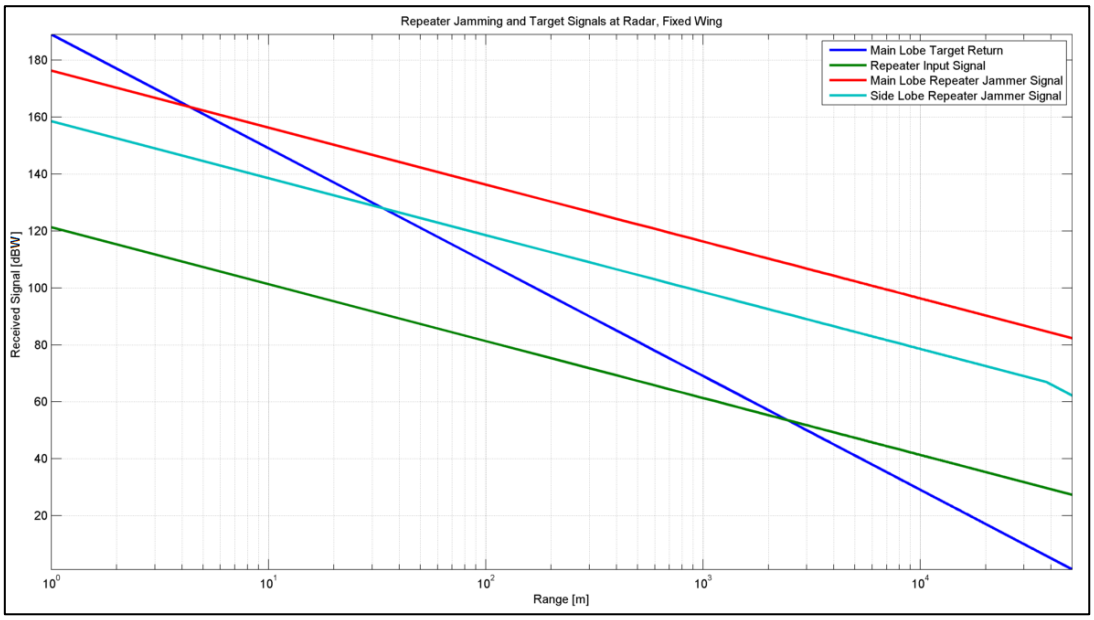

Figure 94: Repeater Jammer Power (Fixed Wing) at Radar Receiver, X-Band

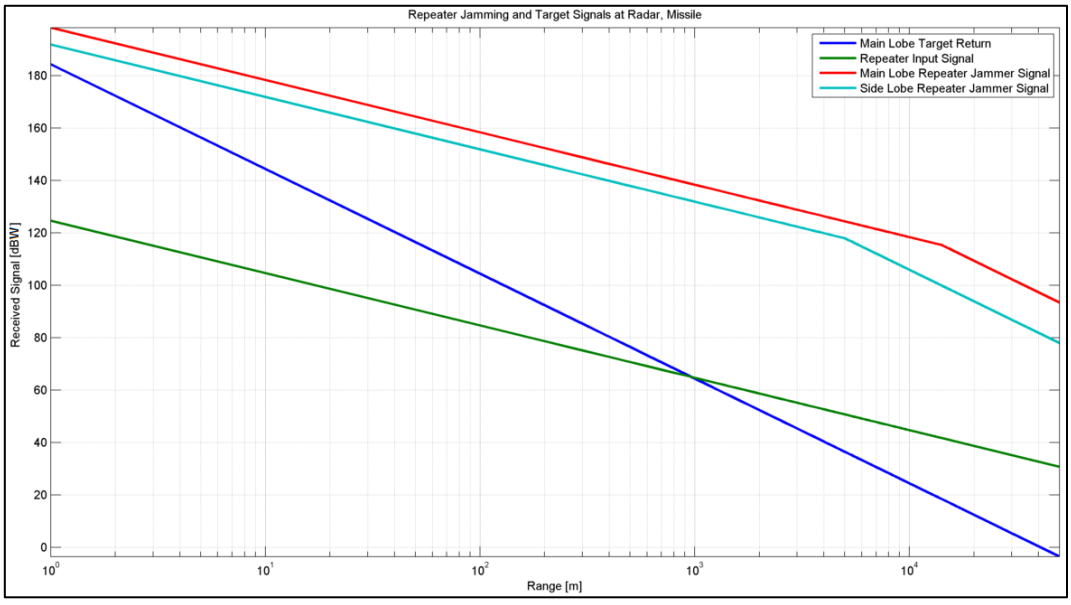

Figure 95: Repeater Jammer Power (Missile) at Radar Receiver, X-Band

From these results, it can be concluded that the advantage is clearly with the Repeater Jammer from a purely "signal power" perspective. The main reason for this, is that the jammer power and intercepted radar power are proportional to "$1/R^2$", while the radar received power is inversely proportional to "$1/R^4$". The radar is therefore more affected by a decrease in signal-level due to varying target range, compared to the jammer.

Clearly, the best results from the jammer's perspective would be obtained with stand-in narrowband jammers in both the X and L bands, against a small RCS target.

This analysis provides the motivation behind fitting a small RCS platform such as an "expendable" Unmanned Aerial Vehicle (UAV), with a stand-in repeater jammer, to perform support jamming for the primary attacking aircraft.

However, the primary benefit of this particular simulation is to determine the correct deception jamming signal-level relative to the true target return measured at the victim radar, in order to deceive the radar. Generally, the false target signal-level is recommended by D. Schleher in reference [4] to be between 7 to 10 dBW relative to the true target return. From this simulation it was found that the selected narrowband or wideband jammer transmitter power outputs and gains (see section 3.1.2) are sufficient to ensure that at fixed wing, rotary or missile target type (as specified in section 1.2.4) is completely masked by the deception jammer.

4.2.5 Jammer System Model, Simulation Flow

The Jammer System Model uses both radar setup parameters and jammer setup parameters as inputs. COTS utility programs as well as custom-built functions are also used in the Jammer System Model. Outputs are the three jammer performance "metrics" benchmarked against the radar, i.e. Target Power vs. Repeater Jammer Power, Burn-through Range Plots and Maximum ES intercept range plots. All of the inputs and outputs to the "Jammer System Model" SFD are shown graphically in Figure 96.

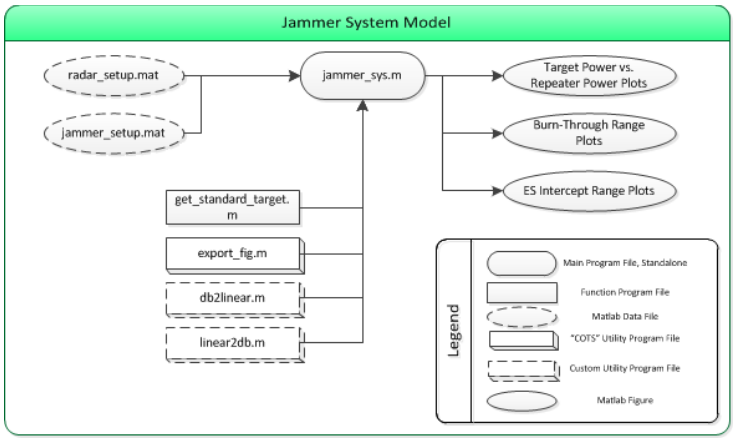

Figure 96: SFD, Jammer System

5 Signal Models, Radar Transmitter Model

All the information necessary to simulate the DBR transmitted signal is described in this chapter, which can be placed into the context of the overall jamming cycle, by referring to Figure 97. The portion of the cycle described in this chapter is bounded by red in Figure 97 below.

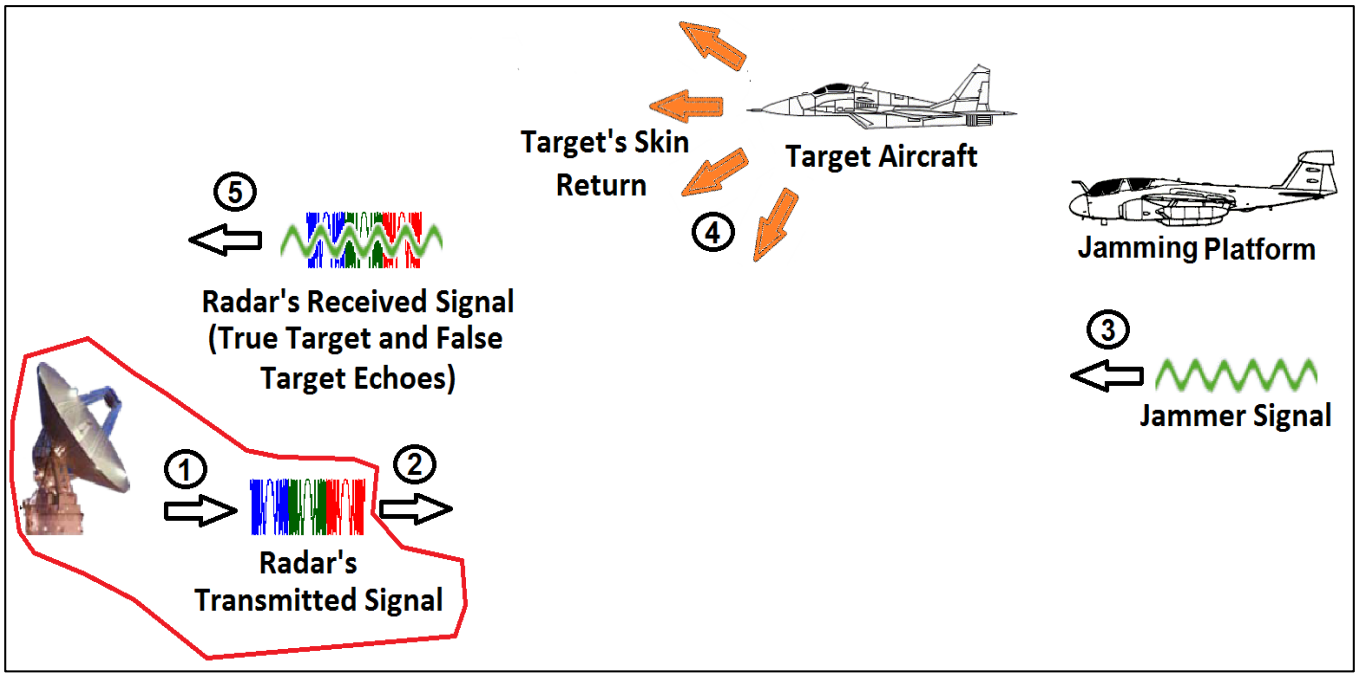

Figure 97: Scenario Definition, "Radar Transmits Signals"

Mathematics describing the transmitter signal model is initially presented, followed by the simulation functional flow block diagram (SFD). The SFD is a visualization tool to aid the reader in understanding the implementation of the mathematics into the software. This is followed by presentation and analysis of results obtained from the implemented mathematics.

5.1 Radar's Transmitted Signal Model

The radar's transmitted signal definition is described in this section. These equations form the basis of all further radar and ES simulation processing in the simulation. A good understanding of these fundamental "signal-level" mathematics are essential in order to understand the "higher-level", more complex signal models and interpret results.

5.1.1 Time Domain Signal

The DBR transmits LFM pulses at three different frequencies per band (L and X Bands). The transmitted LFM pulse is defined in by Mahafza in reference [1] as:

$$\underset{\text{Analytic Signal}}{x(t)} = \underset{\text{Complex Envelope}}{\tilde{x}(t)} \cdot \underbrace{e^{j2\pi f_c t}}_{\text{Carrier Frequency Term}} ; \frac{-\tau}{2} \le t \le \frac{\tau}{2} \tag{151}$$

The complete analytic signal can be written as:

$$x(t) = A_t \cdot \text{Rect}\left(\frac{t}{\tau}\right) e^{j2\pi\left(f_c t + \frac{\mu t^2}{2}\right)} \tag{152}$$

Where the "complex envelope of the signal in equation (151) is defined as:

$$\tilde{x}(t) = A_t \cdot \text{Rect}\left(\frac{t}{\tau}\right) e^{j\pi\mu t^2} \tag{153}$$

In addition, the "rectangular envelope term" is defined as:

$$\text{Rect}\left(\frac{t}{\tau}\right) = \begin{Bmatrix} 1, 0 \le t \le \tau \\ 0, otherwise \end{Bmatrix} \tag{154}$$

The transmitted radar signal (equation (151)) is reflected off the target, and returns, time delayed and Doppler shifted at the radar receiver. The transmitted signal is also intercepted by the ES system. The radar uses coherent demodulation and down-converts the true and false echo signals so that eventually only the complex envelope containing the target information is processed. The "rectangular envelope" ensures the signal pulses are correctly bounded for the simulation.

Please note, that *no noise is added to the transmit signal model*, since "noise" is a characteristic related to the radar receiver. On the other hand, noise on the transmit signal indicates a faulty transmitter. However, signal amplitude "A_t" is still applicable to the transmitted signal and it is modelled using the following equation:

$$A_t = \sqrt{\frac{P_{tx}^r G_{tx}^r}{L_{ant}^r}} \tag{155}$$

Equation (155) was derived using the assumption that the signal is transmitted directly from the radar transmitter through the antenna. No radar processing losses or return signal gains (G_{tx}^r, σ, etc.) are therefore applicable. The equation exploits the following relationship between amplitude (measured in volts) and transmitted power (measured in Watts):

$$V \propto \sqrt{P} \tag{156}$$

This relationship has been explained in detail in section 1.2.3.

5.1.2 Frequency Domain Spectrum

The "Fast Fourier Transform (FFT)" as implemented in the Matlab function "fft.m" was used to form the Fourier Transform (FT) of the transmit signal $x(t)$ (equation (151)). The Discrete Fourier Transform (DFT) as defined in D. Hanselman [3] was implemented in "fft.m". It is:

$$X(k) = FFT\{x(n)\} = \sum_{n=1}^{N} x(n) e^{-j2\pi \frac{(n-1)(k-1)}{N}}, \quad k = 1, 2, \ldots, N-1 \tag{157}$$

Alternatively, an analytic expression for the spectrum can be used [1]:

$$X[k] = \sqrt{\frac{\pi}{2\mu'}} e^{-j\frac{(\pi k)^2}{\mu'}} \left\{ \left[C(Z_2) + C(Z_1) \right] + j \left[S(Z_2) + S(Z_1) \right] \right\}, \quad z_1 < z < z_2 \tag{158}$$

Where

$$\mu' = \pi\mu = \frac{\pi \cdot B}{\tau} \tag{159}$$

$$C(z) = \int_0^z \cos\left(\frac{\pi x}{2} \right)^2 dx \approx \frac{1}{2} + \frac{1}{\pi z} \sin\left(\left(\frac{\pi}{2} z^2 \right) \right), \; z \ll 1 \tag{160}$$

$$S(z) = \int_0^z \sin\left(\frac{\pi x}{2} \right)^2 dx \approx \frac{1}{2} - \frac{1}{\pi z} \cos\left(\left(\frac{\pi}{2} z^2 \right) \right), \; z \ll 1 \tag{161}$$

5.2 Radar Transmitter Model, Simulation Flow

The radar transmitter model, loads radar setup parameters from the "radar_setup.mat" file, which was output from the Radar Setup module (see Figure 80) and obtains the appropriate amplitude ("A_t") for the transmitted signal. This transmit signal amplitude is defined in the Radar Transmitter Model and not in the "Radar Signals" function. This is because the Transmitter model is the only simulation model that uses the "Carrier term" in the signal. All of the other radar receiver signal processing models operate on the complex envelope of the signal where the carrier term would have been removed from the actual signal, through down-conversion and coherent demodulation.

Nyquist's sampling theorem as described in the textbook by B. Mahafza (reference [1]), places the following constraint on the sampling frequency:

$$f_s \geq 2B_r \tag{162}$$

This constraint must be adhered to, for accurately representing the signal in the frequency domain, without aliasing.

For example, the centre frequency at X-Band is 9 GHz and has a bandwidth of 15 MHz. Therefore:

$$\therefore f_s \geq 30E6 \tag{163}$$

The sampling interval for the time domain vector then becomes:

$$dt = \frac{1}{f_s} = 33.333E-9 \tag{164}$$

The duration of the time domain signal is "τ" seconds, if the time domain signal of a single pulse is plotted. Therefore the number of time domain samples necessary to represent the signal, without aliasing in the frequency domain is:

$$M = \frac{\tau}{dt} = \frac{6.5E-6}{33.333E-9} = 195 \tag{165}$$

The transmitter model Matlab implementation is depicted by the "Simulation Flow Diagram" shown in Figure 98. Model inputs, outputs and the utility functions used in the DBR transmitter model, are all indicated in Figure 98. A description of the functions and programs in the SFD below as well as their role in the simulation is listed in Appendix 14.1.

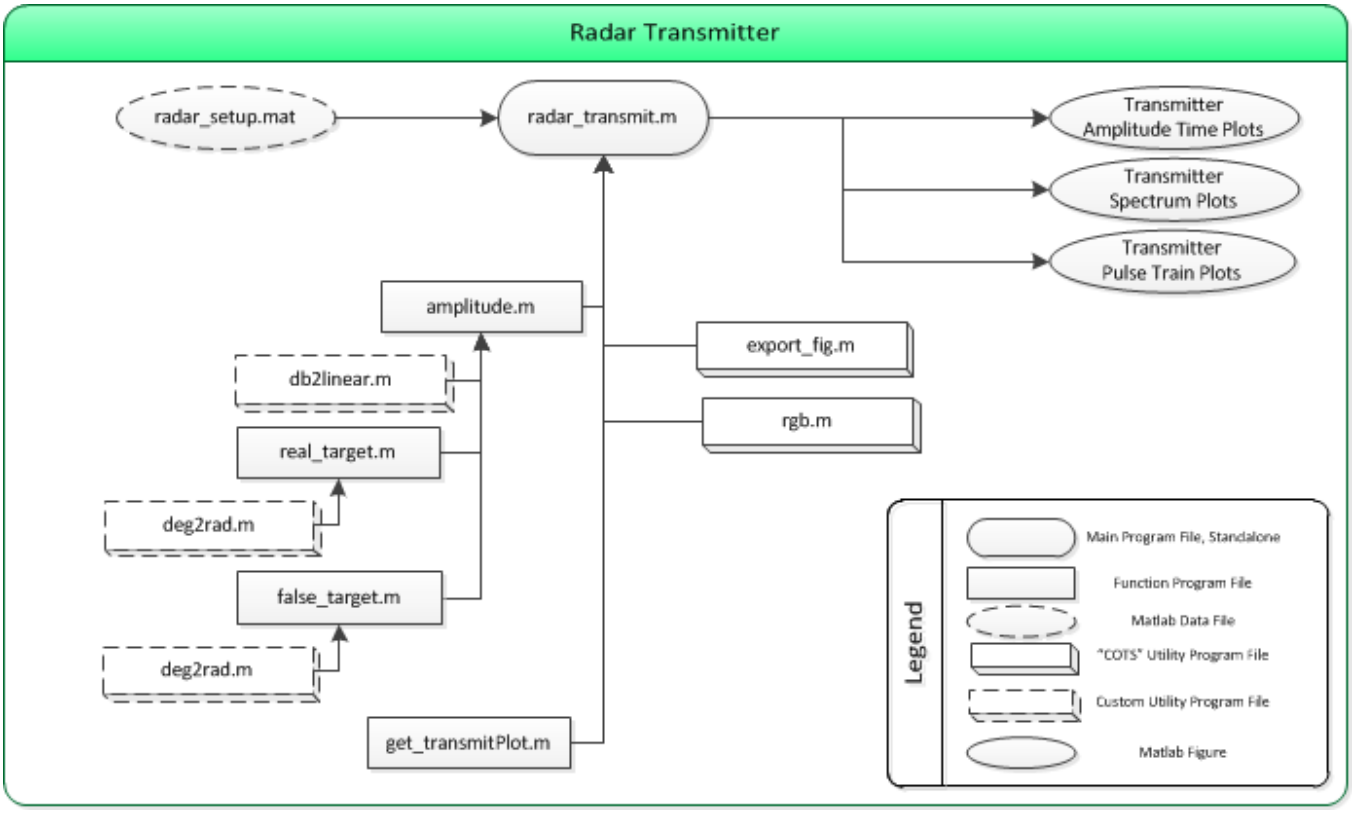

Figure 98: SFD, Radar Transmitter

5.3 Radar Transmitter Model Results

The DBR transmit signal X-Band and L-Band plots are displayed in this section and the reader is advised to inspect the figures and refer to the detailed discussion of results presented after the figures in this section.

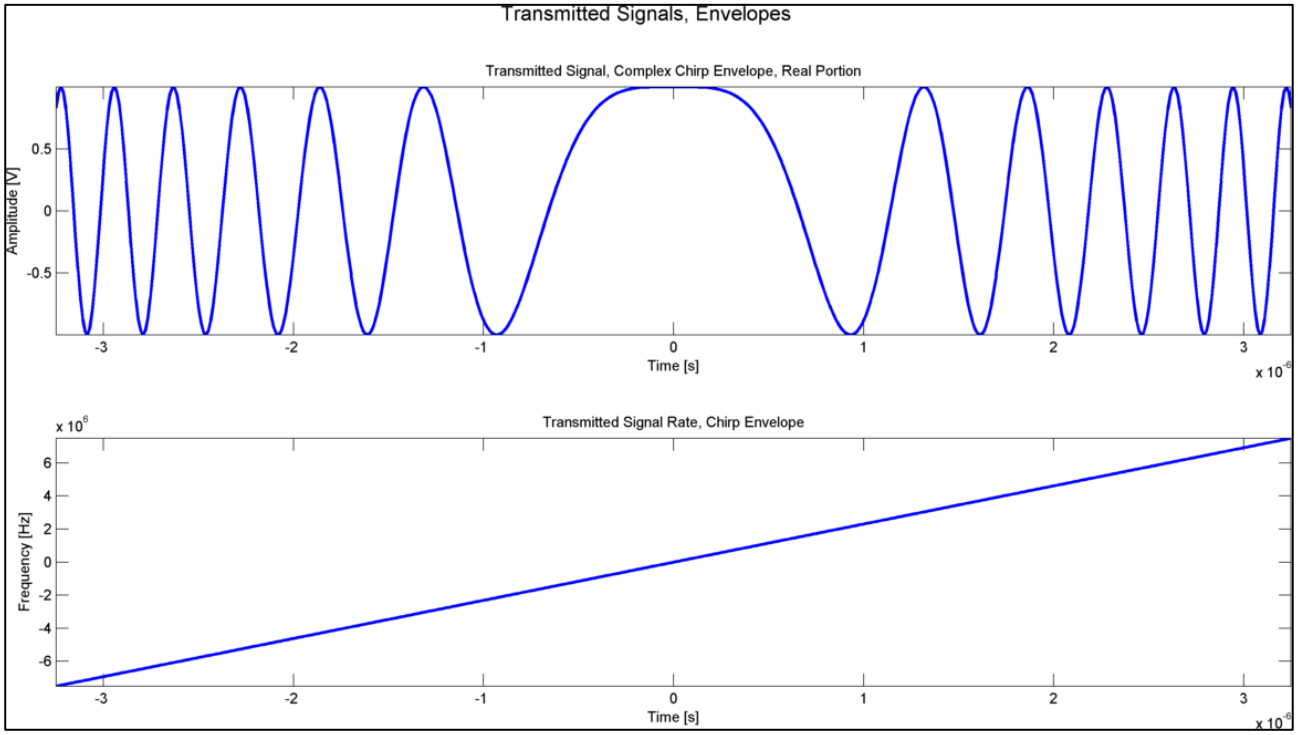

Figure 99: Transmitted Signal Envelope, X-Band

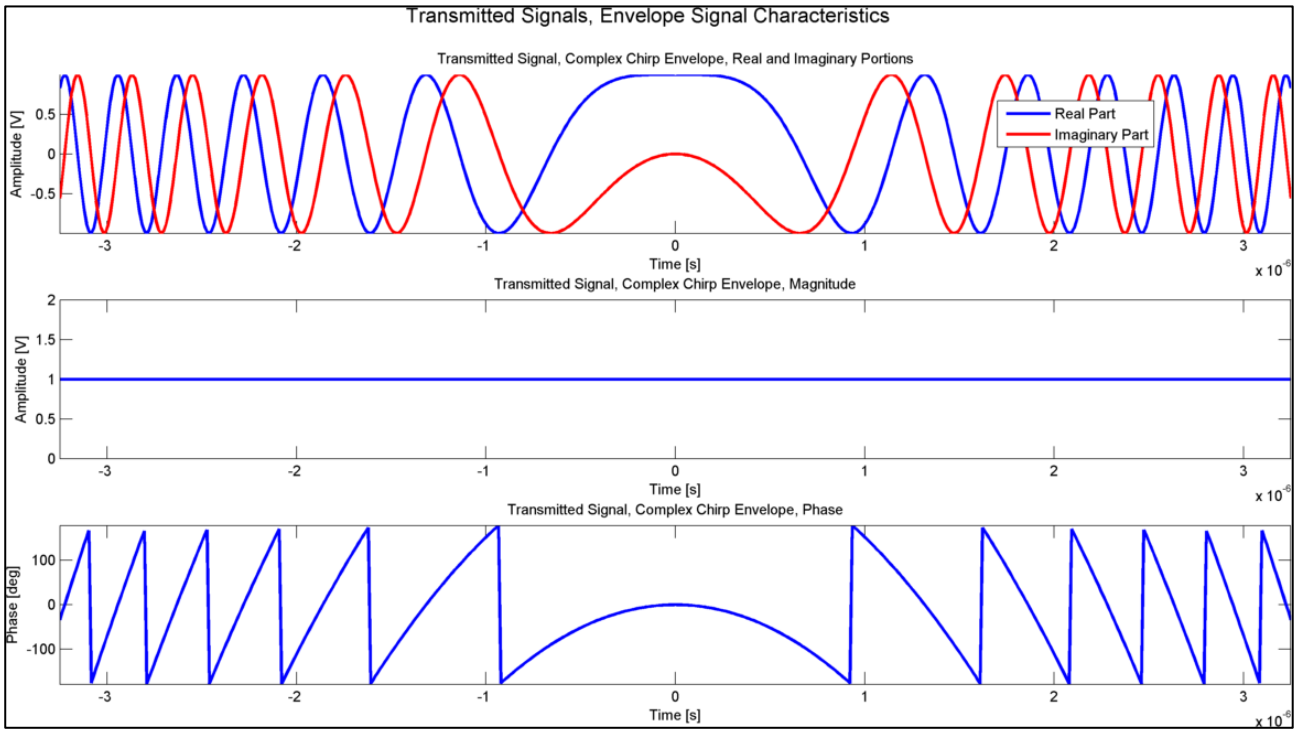

Figure 100: Transmitted Signal Envelope, X-Band, Signal Characteristics

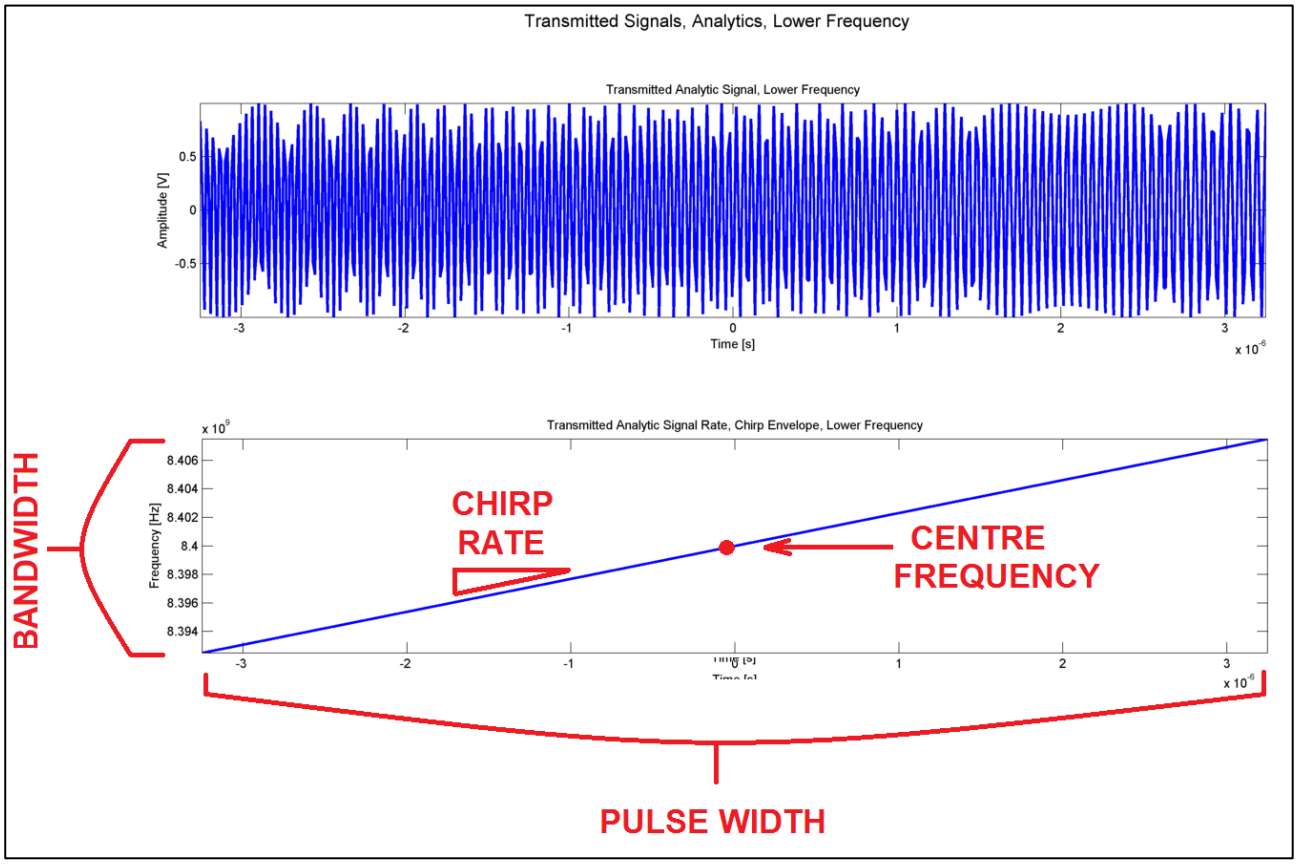

Figure 101: Transmitted Signal, Analytic Signal, X-Band

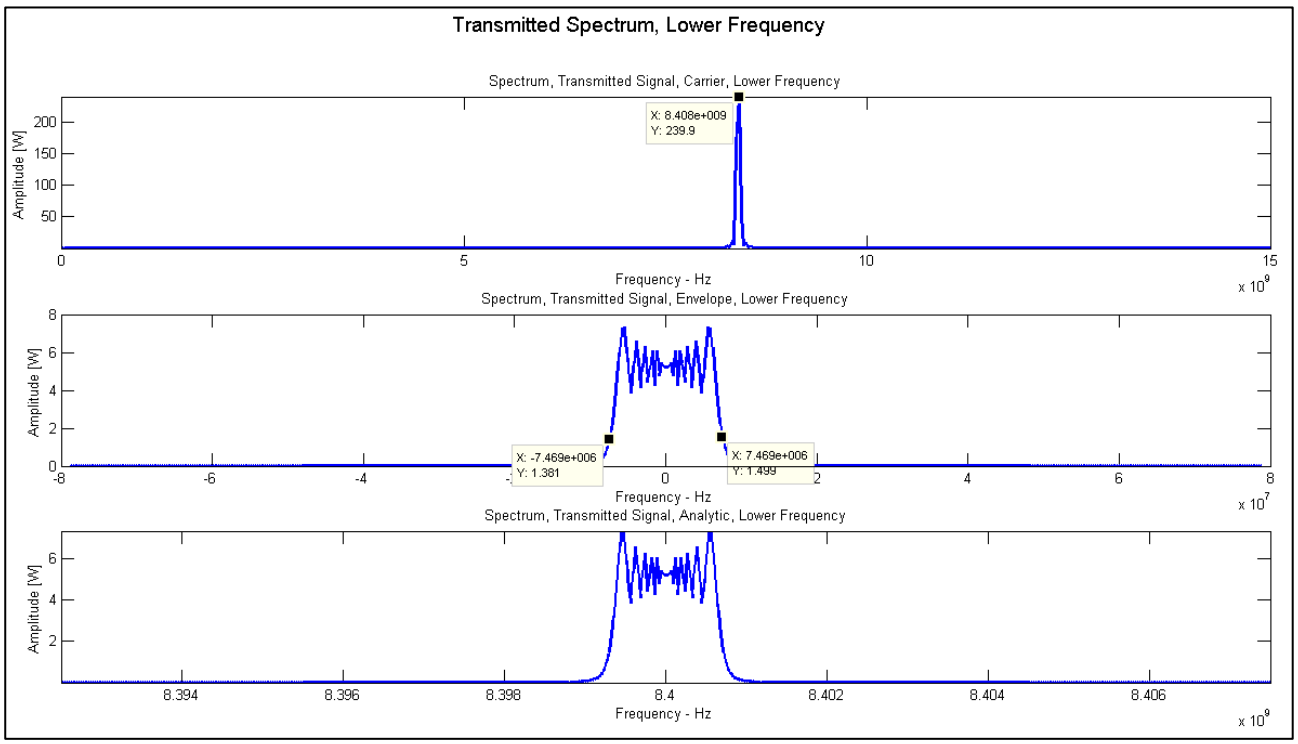

Figure 102: Transmitted Signal, Spectrum, X-Band

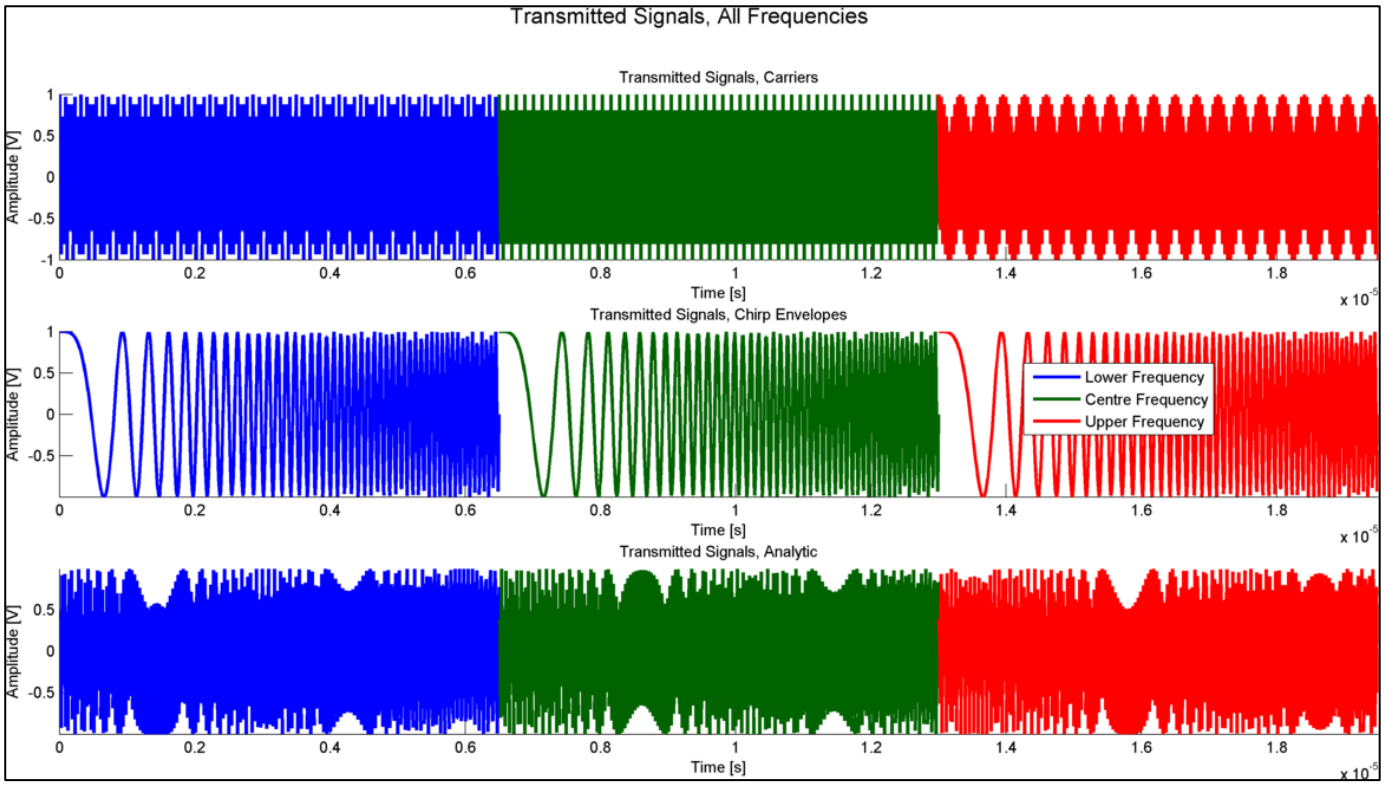

Figure 103: Transmitted Signals, X-Band

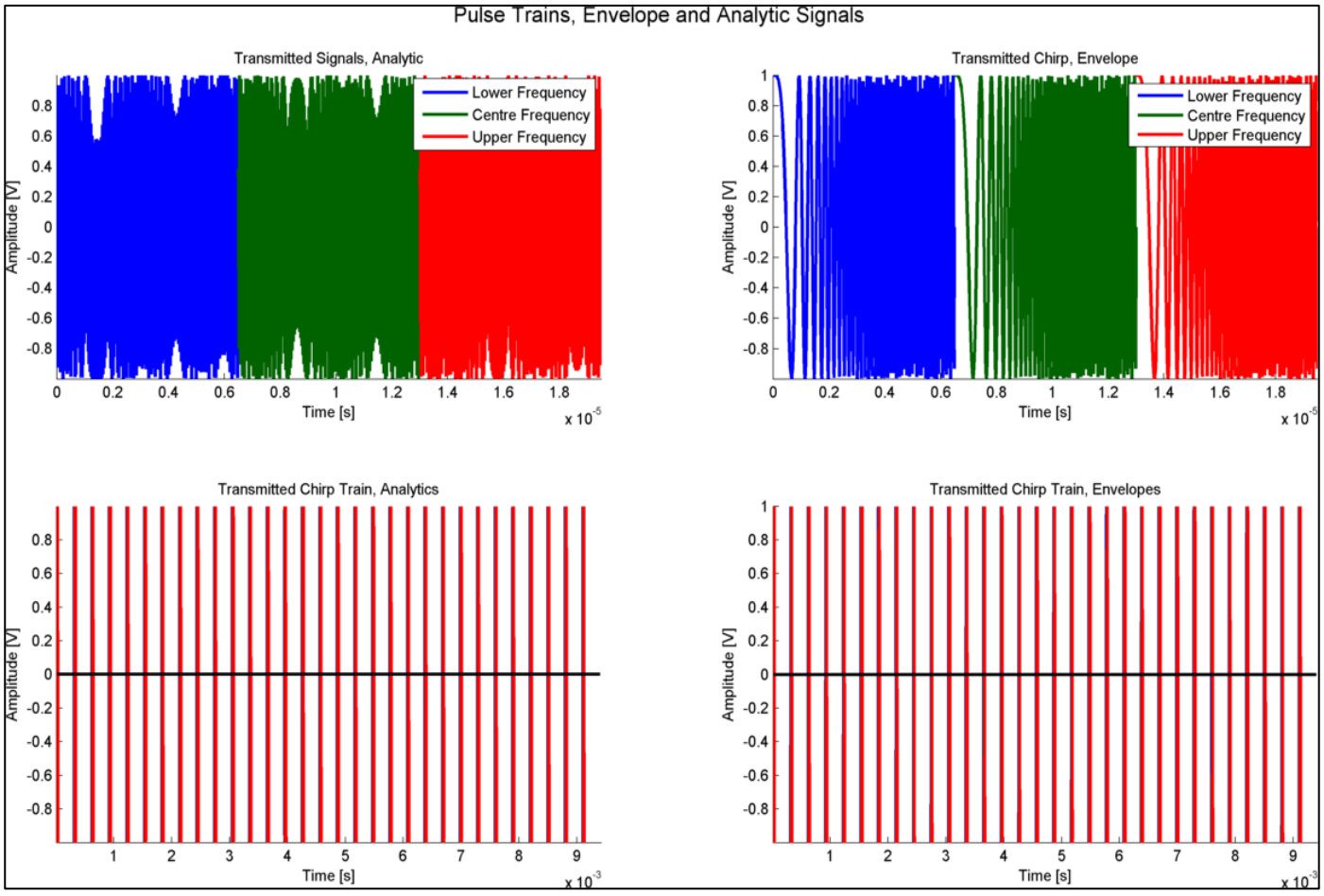

Figure 104: Pulse Trains, X-Band

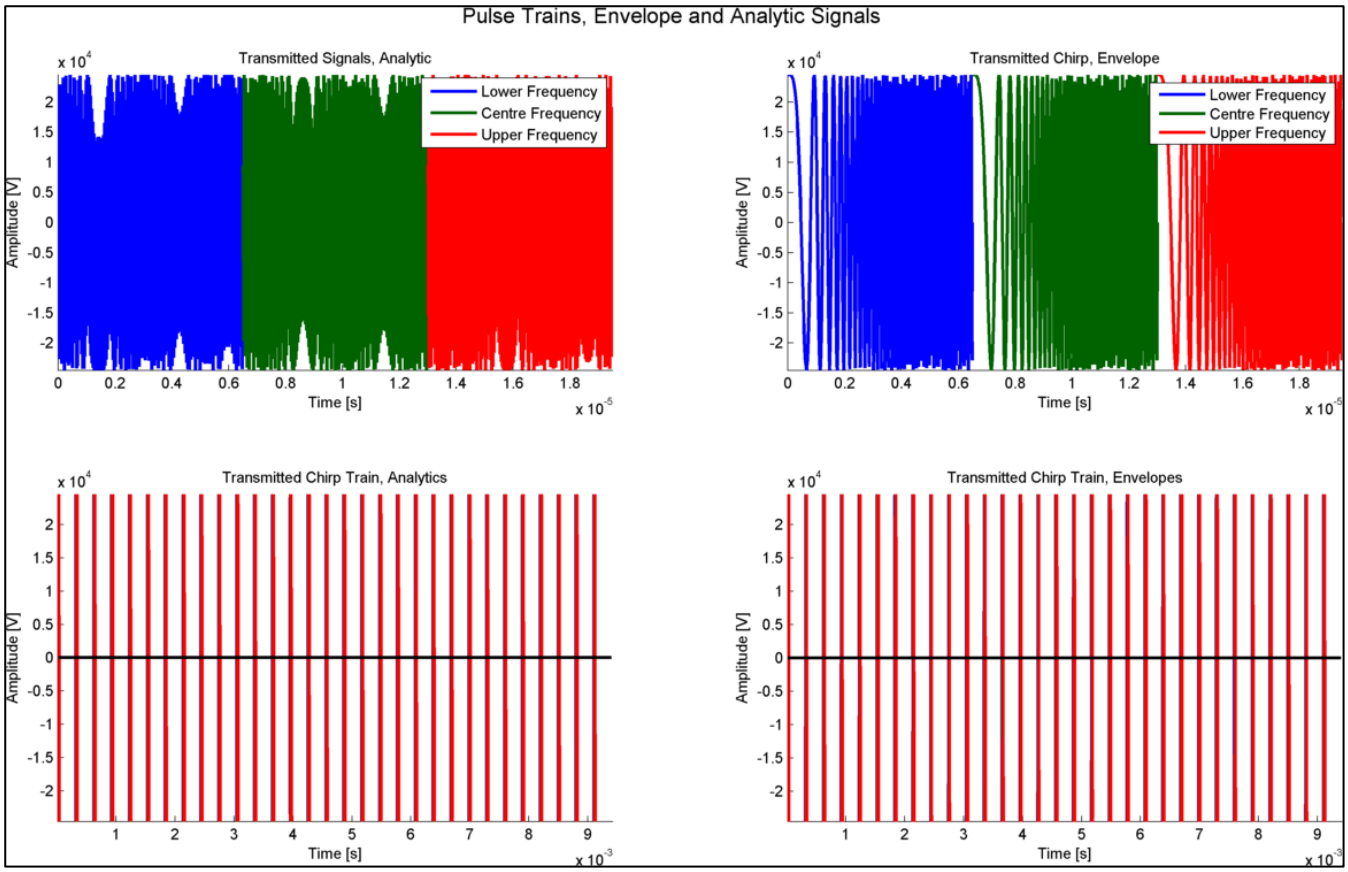

Figure 105: Pulse Trains with Amplitude, X-Band

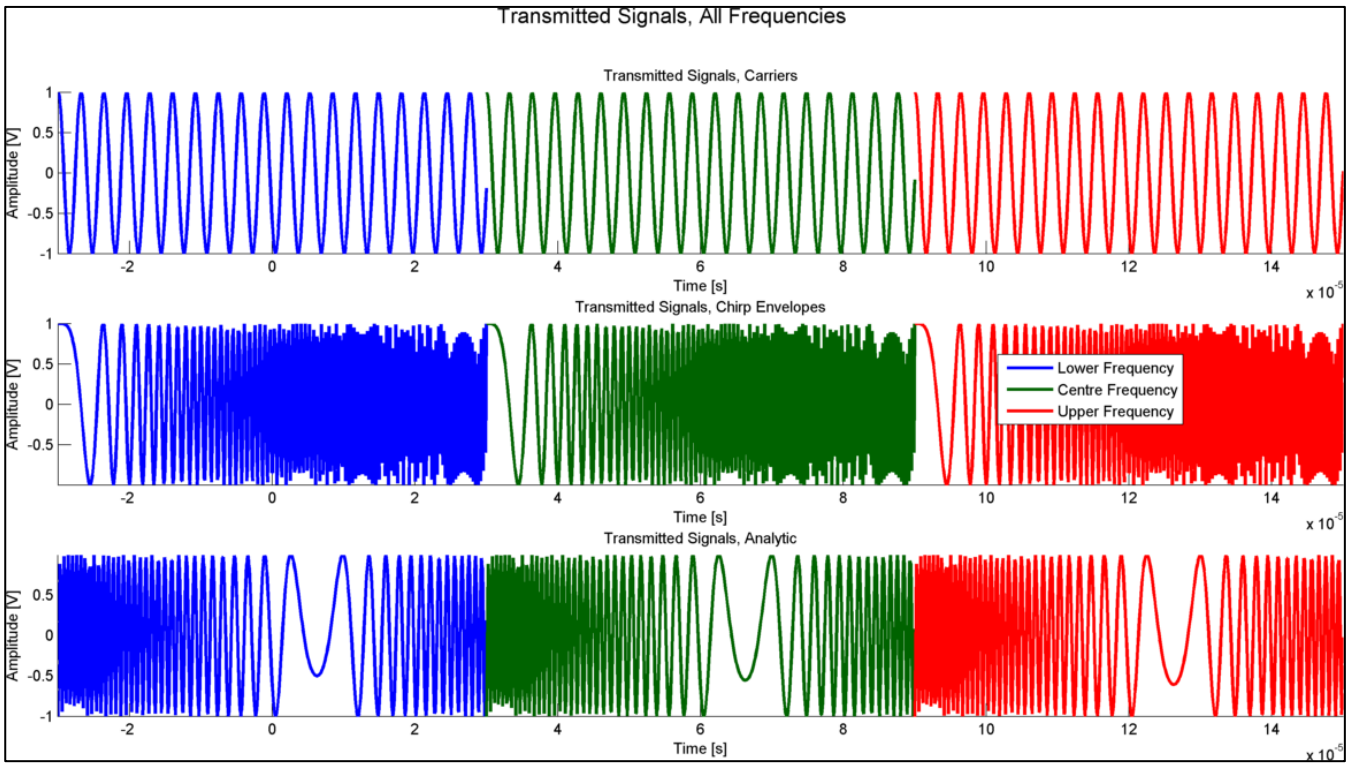

Figure 106: Transmitted Signals, Amplitude, L-Band

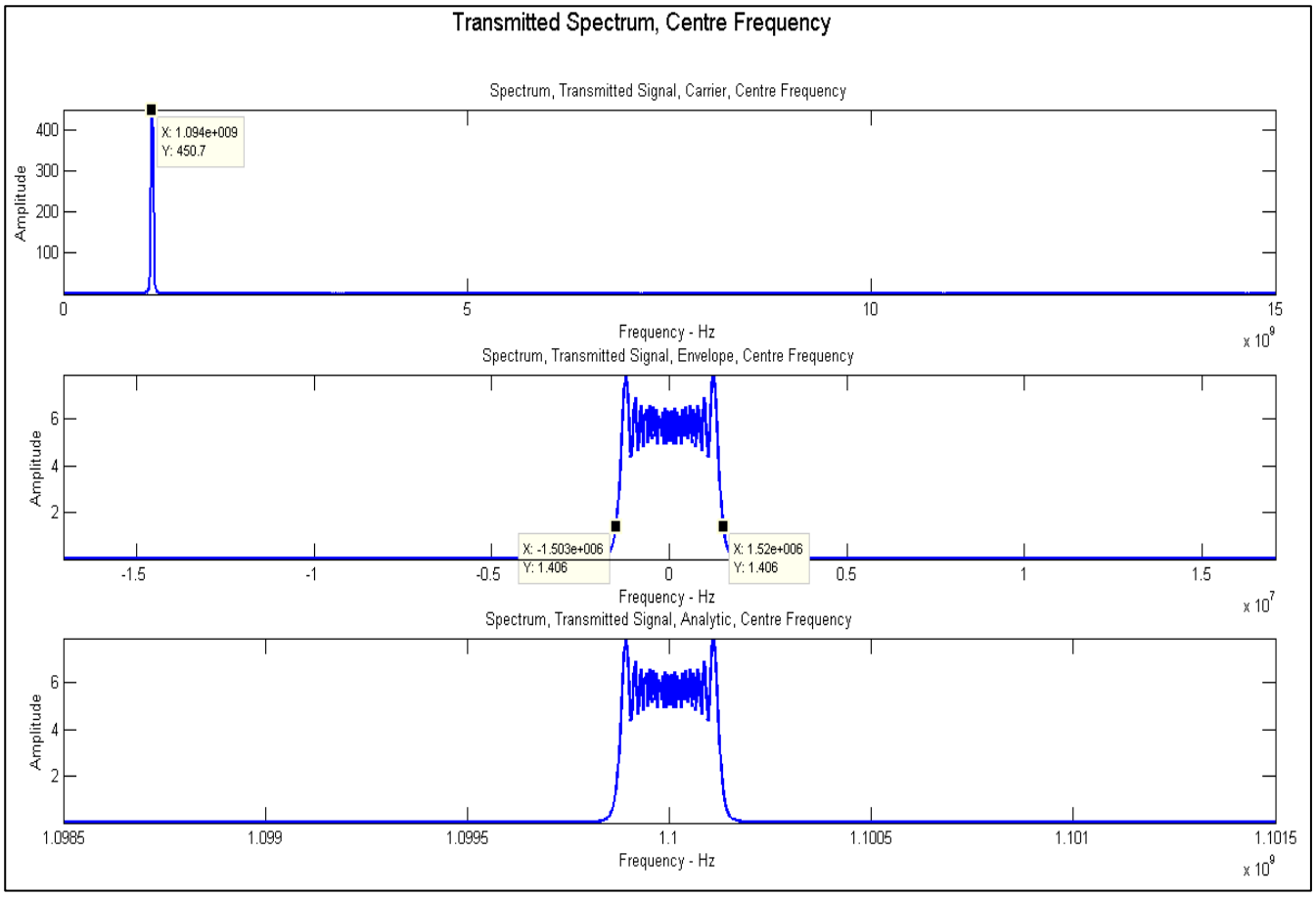

Figure 107: Transmitted Signal, Spectrum, L-Band

5.4 Radar Transmitter Model, Discussion of Results

X-Band Transmitter Signals

The *real* part of the complex envelope of the transmitted signal "$\tilde{x}(t)$" is shown in Figure 99 for a time commencing at negative "half the pulse width $(-\tau/2)$" to positive "half the pulse width $(\tau/2)$". The signal was simulated using these time limits, to show the definition of the LFM signal centre frequency centred at zero, as can be seen in the lower subplot of Figure 99. The middle point of the curve on the "Time-Frequency" plane is the LFM signal's centre frequency, while the lower subplot in the figure shows the "linear change in frequency modulation" with time of the signal, which is why this type of RF signal is called "Linear Frequency Modulation". This linear relationship can be expressed as:

$$f = \mu t + f_c \tag{166}$$

Figure 100 was generated to show all of the "characteristics" of the complex envelope signal in detail. Since "$\tilde{x}(t)$" is a complex signal it has a real and imaginary portion. These portions are shown in the upper subplot of Figure 100. The magnitude of the signal is shown in middle subplot of Figure 100, while the phase of the signal is shown in the lower subplot.

The convention with respect to all of the "Amplitude vs. Time" plots in this simulation is that, they should be interpreted as *the real part of the signal* unless stated otherwise. The amplitude was set to 1V (or 0 dBW) as can be seen by the amplitude of the "Magnitude" subplot in Figure 100. The magnitude of a signal is equal to its amplitude as shown in equation (167):

$$A(t) = \sqrt{\mathrm{Re}(\tilde{x}(t))^2 + \mathrm{Im}(\tilde{x}(t))^2} \tag{167}$$

The phase of the signal varies between "π" to "$-\pi$" radians across the time scale as can be seen in the Figure 100. The signal phase is defined as:

$$\psi(t) = \tan^{-1}\left(\frac{\mathrm{Im}(\tilde{x}(t))}{\mathrm{Re}(\tilde{x}(t))}\right) \quad ; \quad \psi \in [-\pi, \pi] \tag{168}$$

It can be seen that the definition of the signal phase "$\psi(t)$" is related to the inverse tan function "$\tan^{-1}$" and limited to "$-\pi, \pi$" radians. The definition of the limits for the phase is the cause of the periodic discontinuities in the phase as shown in the lower subplot of Figure 100.

The complete analytic form of the transmitted signal "$x(t)$" of duration "τ" seconds is shown in Figure 101. The signal is termed "complete" because it consists of both the carrier frequency term and the complex signal portion. The carrier frequency of the signal in this case ('lower frequency case") was 8.4 GHz with a bandwidth of 15 MHz. All of the signal parameters are shown in Table 6 for the X-Band subsystem and in Table 7 for the L-Band.

Because of the large bandwidth of the signal, a large number of samples is therefore required to represent the signal as per the Nyquist criterion (reference [6]) which is:

$$f_s \geq 2B \tag{169}$$

In order to sample at the frequency required, the time step of the time vector must be spaced according to the following relationship:

$$\Delta t = \frac{1}{f_s} \tag{170}$$

The large frequencies also imply small wavelengths which why the upper subplot of Figure 101 appears very dense. The lower subplot of Figure 101 shows the TF relationship for the

chirp signal. The height of the LFM line corresponds to the signal bandwidth "B" and the width of the plot is its pulse width "τ". The centre point of the line corresponds to the signal's centre frequency "f_c", while the slope of the line is the LFM/chirp rate "μ". It can be seen from the simulation result as shown in Figure 101, how signal parameters can be estimated from the TF representation of a signal.

In Figure 102, the spectrum of the different components of "$x(t)$" are shown. The top subplot shows the spectrum of the carrier frequency term, the middle subplot shows the spectrum of the complex envelope term, while the bottom subplot shows the spectrum of the entire signal i.e. the analytic signal. The spectrum of the carrier signal (which is a complex sinusoid), is theoretically represented by a "Dirac's Delta" function as described by M.A. Richards et. al in reference [6]. In Matlab, Dirac's Delta cannot have an infinite length, so it is limited in the practical "digital world" as a spike at the carrier frequency of 8.4 GHz.
In the middle subplot of Figure 102, the spectrum of the complex envelope LFM signal is shown. The energy in the signal is concentrated between approximately -7.5E6 MHz to 7.5E6 MHz, which corresponds to the bandwidth of the signal. In the bottom subplot, the analytic signal spectrum (spectrum of carrier signal multiplied by complex envelope signal) is shown. Multiplication of the carrier and complex envelope signals in the time domain causes the envelope spectrum to be frequency shifted to the carrier frequency. Therefore, the spectrum of the analytic signal is similar to the complex envelope except that it is shifted to the centre frequency of the carrier.

Figure 103 shows the three parts of the transmitted signal for all three frequencies signals in the X-Band, just as the DBR would transmit them. The three signal components are transmitted one after the other.

In Figure 104, the analytic and complex envelope signals are shown, together with their respective pulse trains over one CPI. The time scales of the pulse (6.50E-06 s) and
CPI (9.39E-03 s) are orders of magnitude apart, which is the reason pulses in the "pulse train" appear as single lines. The magnified individual pulses in the train are identical to individual pulses shown in the upper subplots.

Figure 105 shows the same data as displayed in Figure 104, except that the amplitude of the transmitted pulse has been activated, in this case. If a constant magnitude amplitude is

applied to the signal, then the shape of the waveform is retained, but the maximum and minimum signal levels are “scaled” to the magnitude of the amplitude. If an amplitude that varies with time is applied to a waveform, the waveform is termed “amplitude modulated”.

L-Band Transmitter Signals

The DBR L-Band transmitter signals are shown in Figure 106. The shape and sequence of the three frequency pulses at L-Band are similar to the X-Band pulses shown in (Figure 103). However, larger spacing is noticeable in the upper subplot of Figure 106 compared to the spacing of the X-Band LFM signals shown in Figure 103.

This phenomenon occurs because the L-Band carrier frequency (1.1GHz) is much lower compared to the X-Band carrier frequency of 8.4 GHz. The lower L-Band frequency corresponds to the longer wavelength compared to the X-Band signals, as shown in equation (111). The longer wavelength at L-Band is the reason the spacing in the LFM signal is larger compared to X-Band.

Figure 107 shows the spectrums for the carrier signal, complex envelope and analytic signal at L-Band for the centre frequency pulse. The approximate bandwidth of the plot can be determined from this spectrum plot and the bandwidth of the signal should be exactly 30 MHz. The discrepancy between actual bandwidth and measured bandwidth is caused by small errors introduced during the sampling and DFT processing of the signal.

6 Signal Models, Electronic Support

The signal parameter estimation of the intercepted radar signal by the DBR Jammer's ES subsystem is described in this chapter. The effectiveness of the entire jamming process is highly dependent on the capability of the ES system to estimate *accurately* the victim radar's signal, without being detected by the radar. If the intercepted signal parameters are estimated, accurately and quickly, then the replicated false target would closely resemble a true target, and the radar would be deceived. The radar would then be jammed, even before it detects the presence of the jammer or tracks the true target in order to attack it, by means of fire control of effectors.

In the overall simulation context, the portion of the Jamming cycle highlighted in red in Figure 108 is discussed.

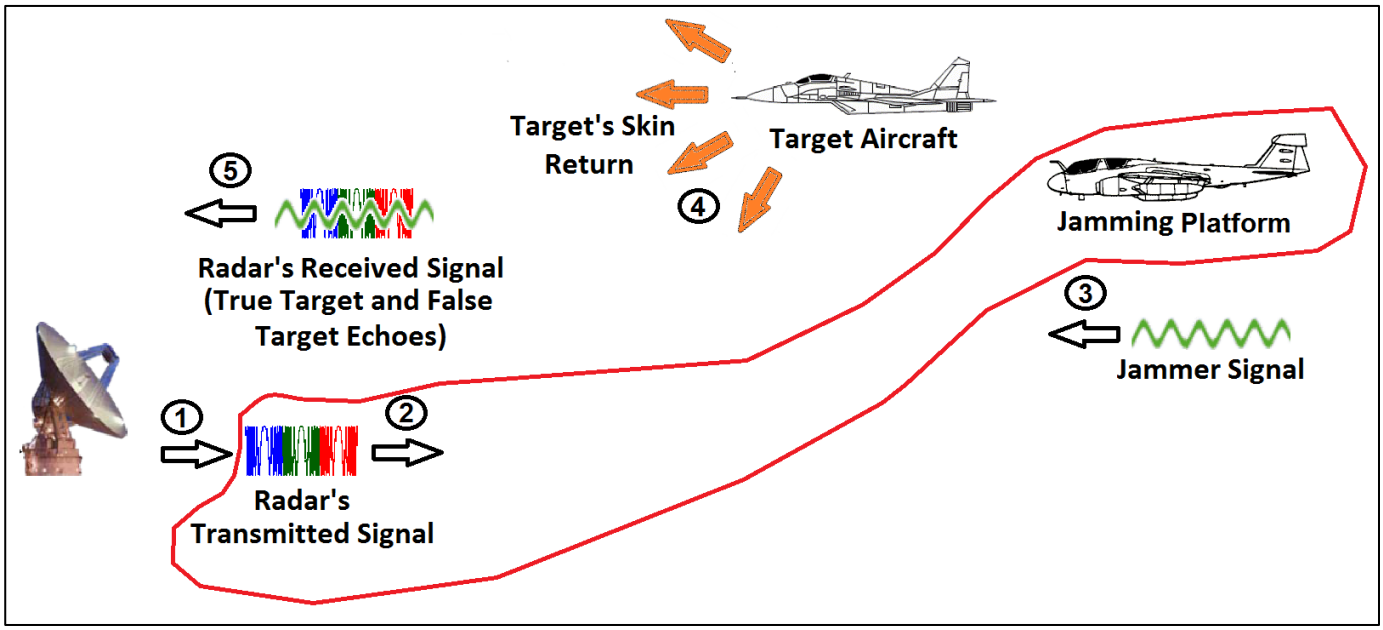

Figure 108: Scenario Definition, "ES System Intercepts Signals"

This chapter follows a similar structure to the previous one. The fundamental mathematics describing the intercepted signal parameter estimation is described initially.

Then the ES algorithms and methods used and tested are presented. Parameter estimation results are presented *and discussed* and efficiency of the methods and their practicality is discussed thereafter, at length. Use was made of "Monte Carlo" analysis methods, to analyse practically, the performances of the proposed algorithms against older, conventional methods.

6.1 Electronic Support Model

The basic definition of the radar signal intercepted at the ES receiver, is identical to the DBR's transmitted signal discussed in 5.1.1. However, the amplitude functions differ between the transmitted signal definition and intercepted signal definitions. As the signal has travelled from the radar to the ES receiver, its signal voltage level has decreased from the radar's transmitted signal amplitude ("A_t"), since the signal power received is proportional to "$1/R^2$".

The received signal amplitude level at the ES receiver was derived from the "One Way Link Equation (Equation 2.34 described by Richards [6])". It is defined as:

$$A_{jr}(t) = 10\sqrt{\frac{P_{tx}^{r} G_{tx}^{r} G_{rx}^{j} \lambda^2}{4\pi^2 R_j^2(t) L_{jammer}^{pol}}} \qquad (171)$$

Besides the decrease in signal power over range, the effects induced by the jammer antenna aperture on the signal are modelled.

The ES Model does not directly process the intercepted radar signal in "Near Real Time (NRT)" due to computational speed limitations (as mentioned in detail in section 1.2.6). Nevertheless, dynamic effects caused by a changing intercept range "R_j" are simulated per time step by varying the Signal to Noise Ratio at the Jammer "SNR_{rj}", *per time step.*

For the ES signal simulation, the TF toolbox by F. Auger (reference [12]) was used extensively, to analyse the intercepted radar signals, in this simulation.

Although the DBR signal is a "multi-component" (multi-LFM centre frequencies) "non-stationary" (linearly varying component frequencies) signal, more common "instantaneous frequency" and "group delay" algorithms can still be used to estimate frequencies of the intercepted signal. This is because the different component frequencies are transmitted in two well-separated frequency bands, i.e. L and X-Bands. The channelized ES receiver is able to separate the transmitted signals in either band, and process them separately. *Still,* any interference in the same frequency band as the intercepted signal would severely degrade the time frequency estimation using "Instantaneous Frequency Measurement (IFM)". This important fact has been discussed by F. Auger in reference [12], P. M. Oliviera and V. Barroso in reference [30] and also discussed in section 2.3.

In the words of F Auger [12]: "The notion of instantaneous frequency implicitly assumes that, at each *time instant*, there exists only a single *frequency component*. A dual restriction applies to the group delay; the implicit assumption is that a given *frequency* is concentrated around a single *time instant*. Thus, if these assumptions are no longer valid, which is the case for multi-

component signals, the result obtained using the instantaneous frequency or the group delay algorithms is meaningless". F. Auger also states in reference [12]: "*The WVD therefore ideally concentrates the LFM Signals in the TF plane*". After researching the TF algorithms described by F. Auger [12], a group of algorithms based on the "Wigner-Ville Distribution" was therefore determined to be the most suitable for estimating the non-stationary LFM signal radiated by the DBR.

Wigner-Ville Distribution (WVD)

The WVD belongs to a class of "Energy Based" TF algorithms called the "Cohen's Class". The fundamental advantage of the using the WVD is for *LFM* signal parameter estimation, as discussed in section 2.3.1. The continuous form of the WVD is defined as ([12]):

$$W_x(t,f)=\int_{-\infty}^{+\infty} x\left(t+\tau_d/2\right)x^*\left(t-\tau_d/2\right)e^{j2\pi f\tau_d}\,d\tau_d \tag{172}$$

It was implemented in the TF Toolbox [12], as the "tfrwv.m" function.

Discrete Wigner-Hough Transform (WHT)

Boashash in reference [15], presented a discrete version of the WVD. Usually, once the Discrete WVD is calculated, the HT is used to estimate the LFM parameters on the TF Plane. Therefore, this is typically a two-step process; first, the WVD of a signal is found and thereafter the WVD "image" is processed using the HT.

A direct "one-step" algorithm has been derived by S. Barbarossa in reference [34]. The "Wigner-Hough Transform (WHT)" algorithm is shown below:

$$\begin{aligned} WH_x(f_c,\mu)=&\sum_{n=0}^{(M/2)-1}\sum_{k=-n}^{n}x(n+k)\,x^*(n-k)e^{-j4\pi k(f_c+\mu n)}\\ &+\sum_{n=M/2}^{M-1}\sum_{k=-(M-1-n)}^{M-1-n}x(n+k)\,x^*(n-k)\,e^{-j4\pi k(f_c+\mu n)} \end{aligned} \tag{173}$$

$$n=0,1,\ldots,M-1 \tag{174}$$

Smoothed Psuedo Wigner-Ville Distribution (SPWVD)

The "standard" WVD suffers from cross term interference if a multi-component signal is estimated. This is a common problem with most standard TF algorithms. Therefore, the SPWVD was developed. A "smoothing" window function is used to reduce multiple signal interference and noise suppression for the SPWVD, compared to the standard WVD.

The continuous form of the SPWVD is ([12]):

$$SPWV_x(t,f;g,h)=\int_{-\infty}^{+\infty}h(\tau_d)\int_{-\infty}^{+\infty}g(s-t)\,x\left(s+\tau_d/2\right)x^*\left(s-\tau_d/2\right)e^{j\cdot2\pi\cdot f\cdot\tau_d}\,ds\,d\tau_d \tag{175}$$

The TF Toolbox implements it as the "tfrspwv.m" function.

Reassigned Smoothed Psuedo Wigner-Ville Distribution (RSPWVD)

Although the SPWVD suppresses cross-term interference over the standard WVD, it suffers a loss of resolution. This is a fundamental problem with TF algorithms in general. It is caused by the constraint on signal pulse width and bandwidth as defined in the "Heisenberg-Gabor" inequality principle, explained in section 2.3 and shown in equation(39).

The "Reassignment" algorithm developed by F. Auger et. al, reassigns the values of the TF distribution to the calculation window centroid, instead of its geometrical centre. This too, has been already explained in section 2.3. The continuous form of the RSPWVD is ([12]):

$$RSPWV_x(t', f'; g, h) = \int_{-\infty}^{+\infty}\int SPWV_x(t, f; g, h)\,\delta\left(t' - \hat{t}(x; t, f)\right)\delta\left(f' - \hat{f}(x; t, f)\right)dt\,df \quad (176)$$

$$\hat{t}(x; t, f) = t - \frac{SPWV_x\left(t, f; (t \cdot h(t)), h\right)}{2\pi \cdot SPWV_x(t, f; g, h)} \quad (177)$$

$$\hat{f}(x; t, f) = f + j\frac{SPWV_x\left(t, f; g, \frac{dh}{dt}(t)\right)}{2\pi\, SPWV_x(t, f; g, h)} \quad (178)$$

It was implemented in the TF Toolbox as the "tfrrspwv.m" function and used in this simulation in the "es.m" function. The best performance of all the WVD variants with respect to multi-component signal interference, noise suppression and good resolution is the RSPWVD. This fact will be shown quantitatively in subsequent sections.

Hough Transform (HT)

Once the LFM signal has been represented on the TF plane, the HT is used to detect the presence of the LFM signal and estimate its parameters. The "htl.m" function from the TF toolbox was used to generate the HT of the WVD, SPWVD, RSPWVD, Spectrogram and IFM representation of the signal. The HT function firstly converts a line into polar coordinates as described in [21]:

$$f_{line}(x, y) = y = m_{line}\,x + c_{line} \quad (179)$$

$$f_{line}(x, y) = y = -\frac{\cos\hat{\theta}}{\sin\hat{\theta}}x + \frac{\rho}{\sin\hat{\theta}} \quad (180)$$

Equation (180) is rearranged as follows:

$$g(\rho, \theta) = \rho = x\cos\theta + y \cdot \sin\theta \quad (181)$$

Then the "htl.m" TF function maps $f(x,y)$, onto the HT function $g(\rho,\theta)$ using the following "accumulator" algorithm ([35]):

$$\forall x_i y_j \Rightarrow g_{line}\left(\rho,\hat{\theta}\right) = g_{line}\left(\rho,\hat{\theta}\right) + f_{line}\left(x_i,y_j\right), \quad for\ all\left(\rho,\hat{\theta}\right) \tag{182}$$

$$\rho = x_i \cos\hat{\theta} + y_j \sin\hat{\theta} \tag{183}$$

The HT parameters (ρ , θ) must then be converted to LFM signal parameters ($\hat{f}_c$, $\hat{\mu}$) using the HT conversion algorithms included in Appendix 14.2. All of the conversion algorithms shown in Appendix 14.2, are an original contribution by the author.

6.2 Electronic Support Scale Model

In an actual ES system that is dedicated to high-speed signal processing of large amounts of data, NRT processing of an actual intercepted radar signal can be done. But, the processing capability of the commercial laptop on which the simulation was run, is limited. For this reason, a "Scale Model" was built to represent the actual TF signal interception domain for a *burst* of intercepted pulses. The interception of an entire CPI duration of signal data represents a very large amount of data. Therefore, in the scale model, the number of samples that were used to model the individual pulses and PRI was representative. If a Digital Receiver such as the Delphi ADC3295, (see Appendix 14.3) is used, the sampling frequency is 2 GHz. Therefore, 2 Gs/s ("Gigasamples a second") are processed by the ES receiver. In this case, the actual intercepted radar pulse width would be represented by:

$$Samples_{\tau}^{X} = \frac{\tau\ 2E9}{1} = 6.5E-6\cdot 2E9 = 13\,000 \tag{184}$$

$$Samples_{\tau}^{L} = \frac{\tau\ 2E9}{1} = 6E-5\cdot 2E9 = 120\,000 \tag{185}$$

And the number of samples per PRI would be:

$$Samples_{PRI}^{X} = \frac{PRI\ 2E9}{1} = 3.03E-4\cdot 2E9 = 606\,000 \tag{186}$$

$$Samples_{PRI}^{L} = \frac{PRI\ 2E9}{1} = 1.25E-3\cdot 2E9 = 2\,500\,000 \tag{187}$$

In addition, the total number of samples over the entire CPI would be:

$$Samples_{CPI}^{X} = \frac{n_P\ PRI\ 2E9}{1} = 31\cdot 3.03E-4\cdot 2E9 = 18\,786\,000 \tag{188}$$

$$Samples_{CPI}^{L} = \frac{n_P\ PRI\ 2E9}{1} = 20\cdot 1.25E-3\cdot 2E9 = 50\,000\,000 \tag{189}$$

This is far more samples than can be simulated, without the actual Digital Processor. For this reason representative number of samples were used, to illustrate the principle behind using the WVD algorithms to estimate signal parameters of intercepted DBR pulses.

6.3 Electronic Support Model, Simulation Flow

The ES model loads radar setup parameters and jammer setup parameters from stored data files as indicated in Figure 109. It then applies the correct signal amplitudes to the intercepted signal when required and also uses the COTS TF functions to generate and process the intercepted signal.

The outputs from this program include figures and the intercepted signal parameter estimates for all frequencies. The "raw" estimated signal parameters are saved to a data file "es_param_raw.mat". This file is then independently processed and finally saved for further use, in an "es_param.mat" file. The "jammer_signals.m" function then uses the saved parameters in "es_param.mat" to generate the simulated false target signals. The "jammer_signals.m" file is also used in the EA Model to generate false targets. In this way, intercepted signal parameters from main ES model "es.m" are use to generate false target signal parameters for the EA "jammer_signals.m" file.

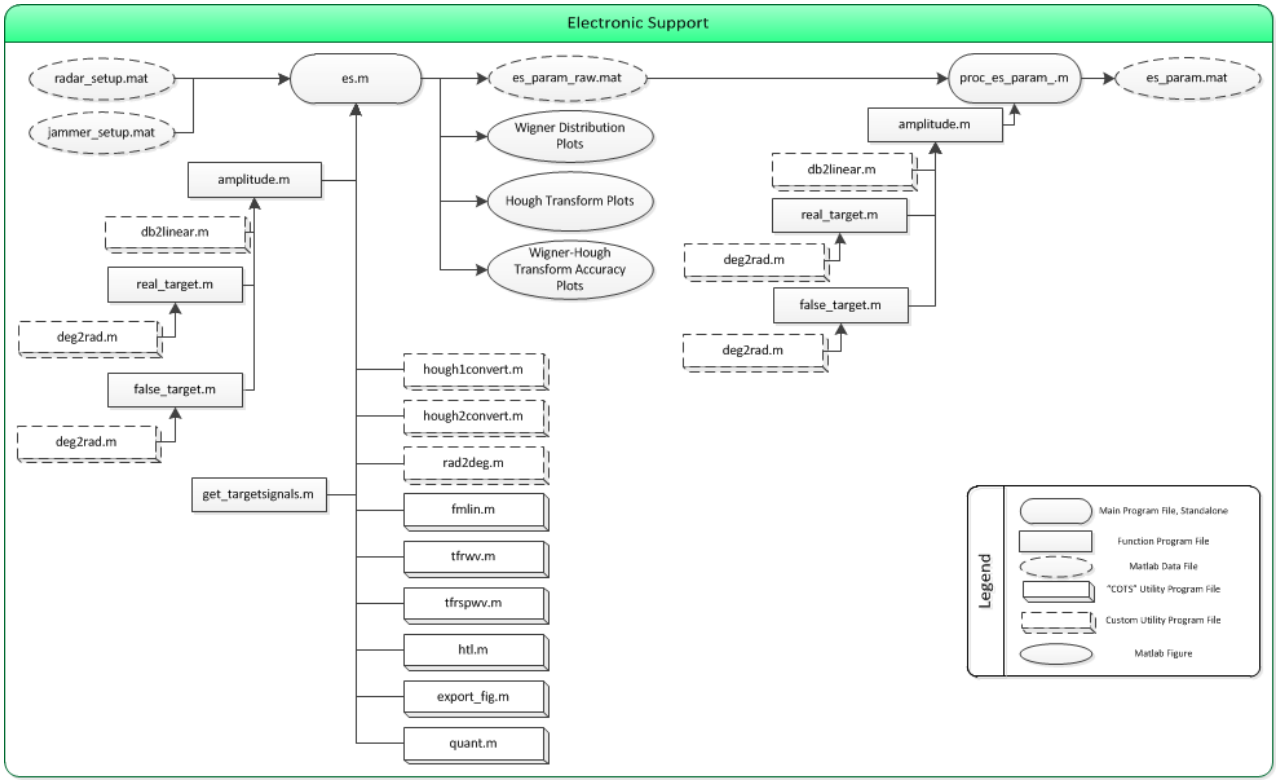

Figure 109: SFD, Electronic Support Module

6.4 Electronic Support Model, Results

The ES model output plots are presented and discussed in this section. The plot outputs are figures illustrating the key principles of signal parameter estimation of the "intercepted" DBR X-Band signals. Plot results for parameter estimation of the DBR LFM carrier frequency and chirp rate are presented initially, followed by "PRI estimation" and "Number of Pulse" results. The reader is advised to inspect the figures and refer to the discussion *after the figures* for observations and conclusions in this section.

6.4.1 Carrier Frequency and Chirp Rate Estimation

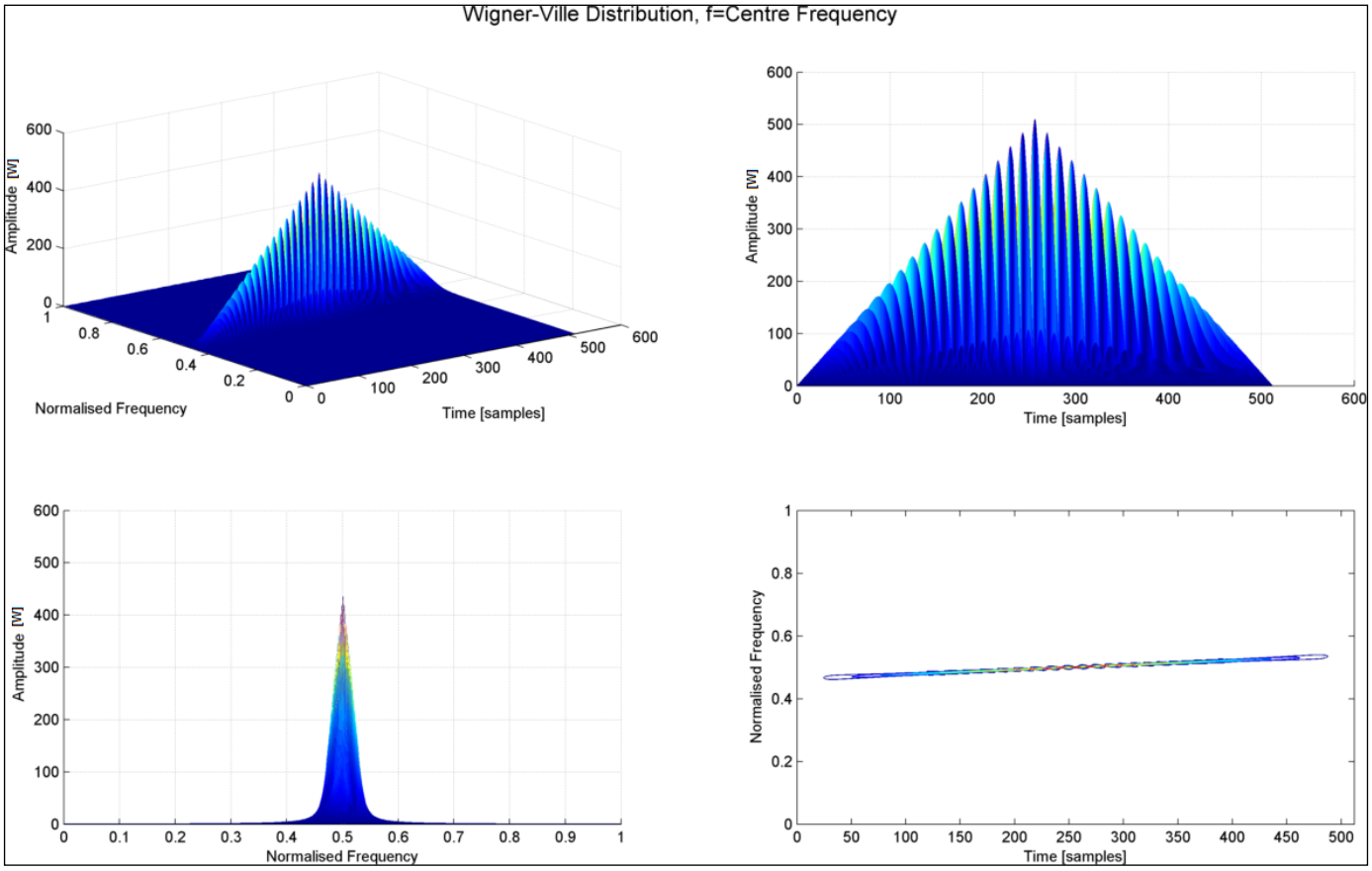

Figure 110: X-Band Single Pulse WVD4 Plot,

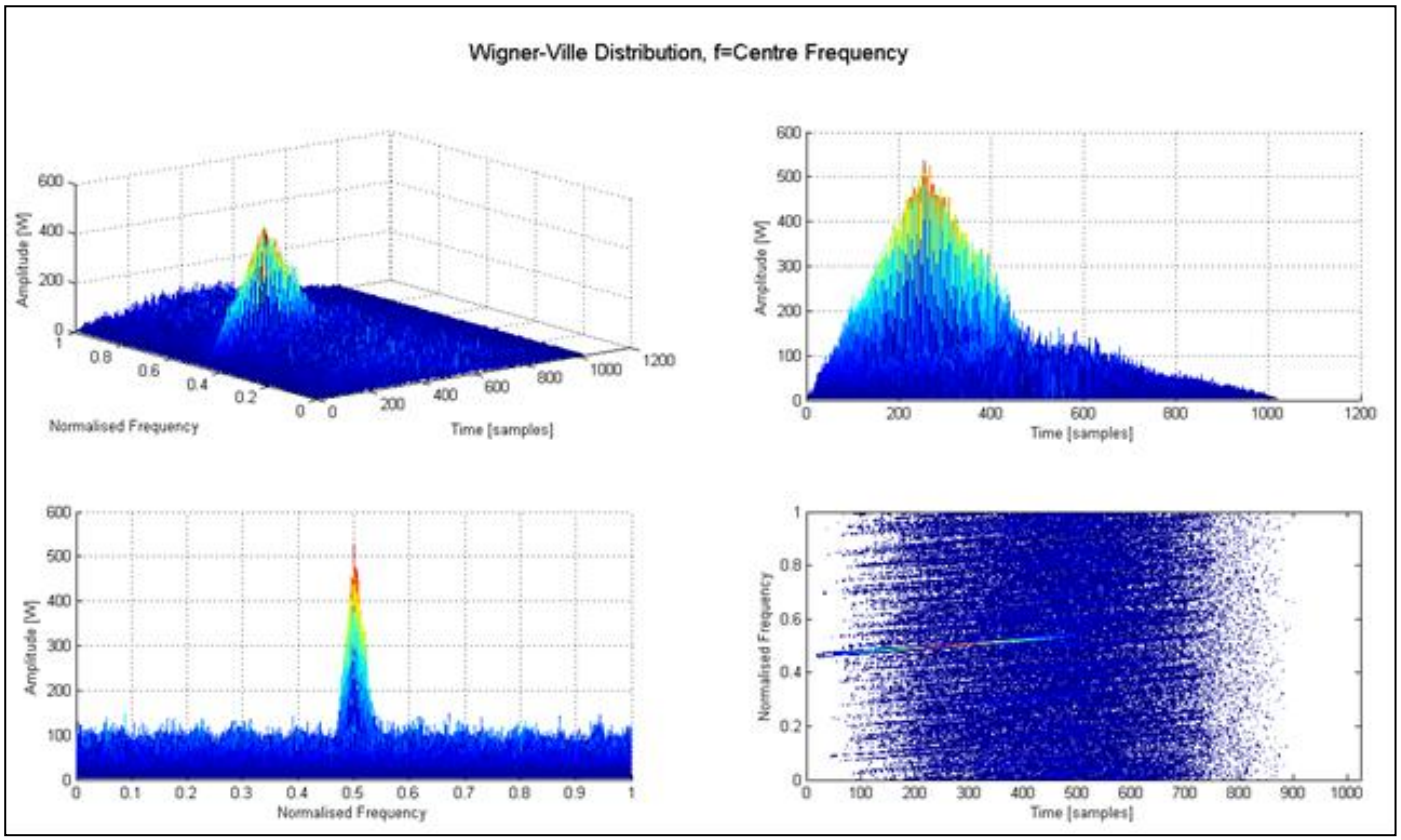

Figure 111: X-Band Single Pulse WVD4 Plot with Noise

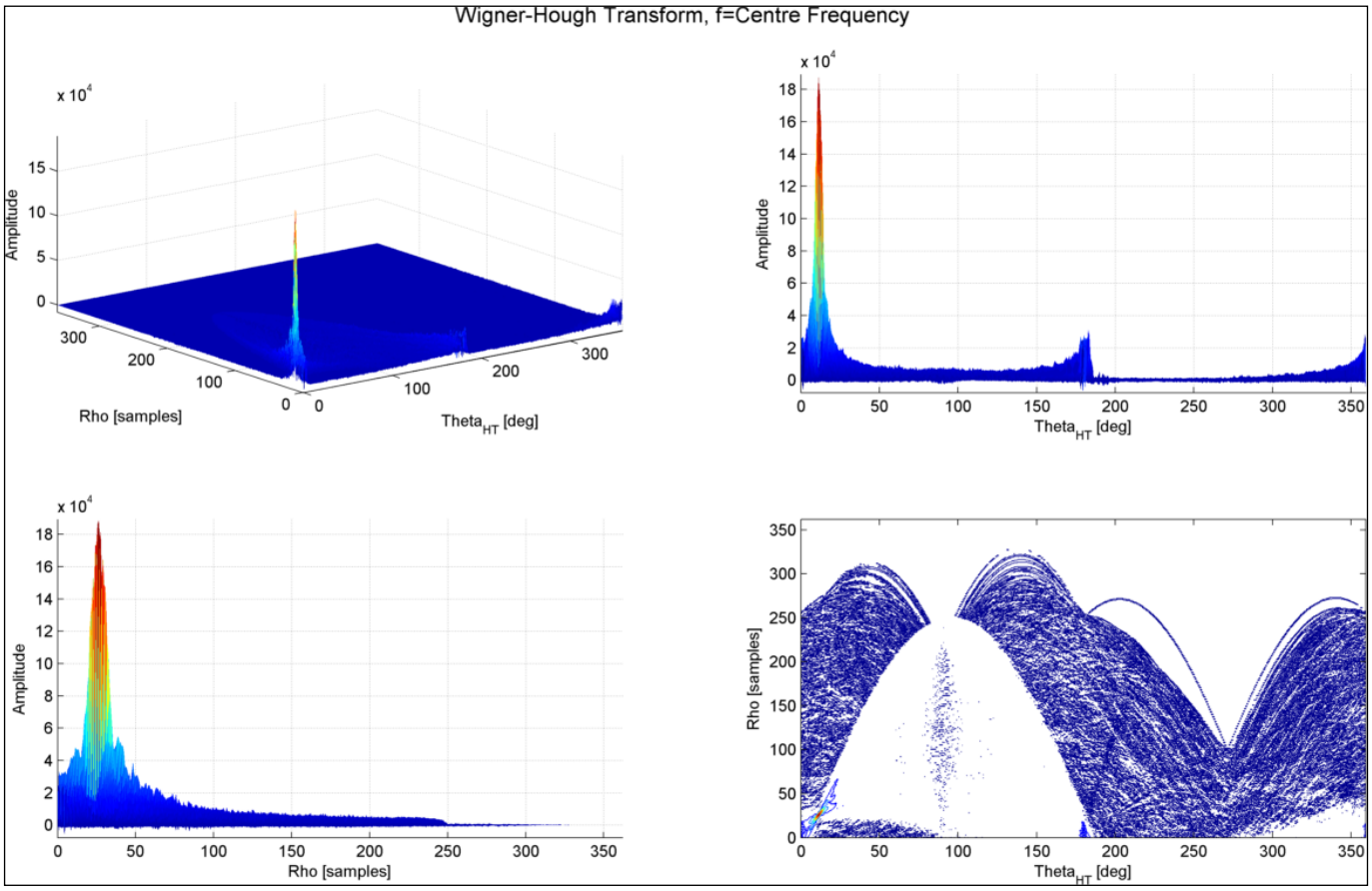

Figure 112: X-Band Single Pulse WHT4 Plot, Noise and Amplitude

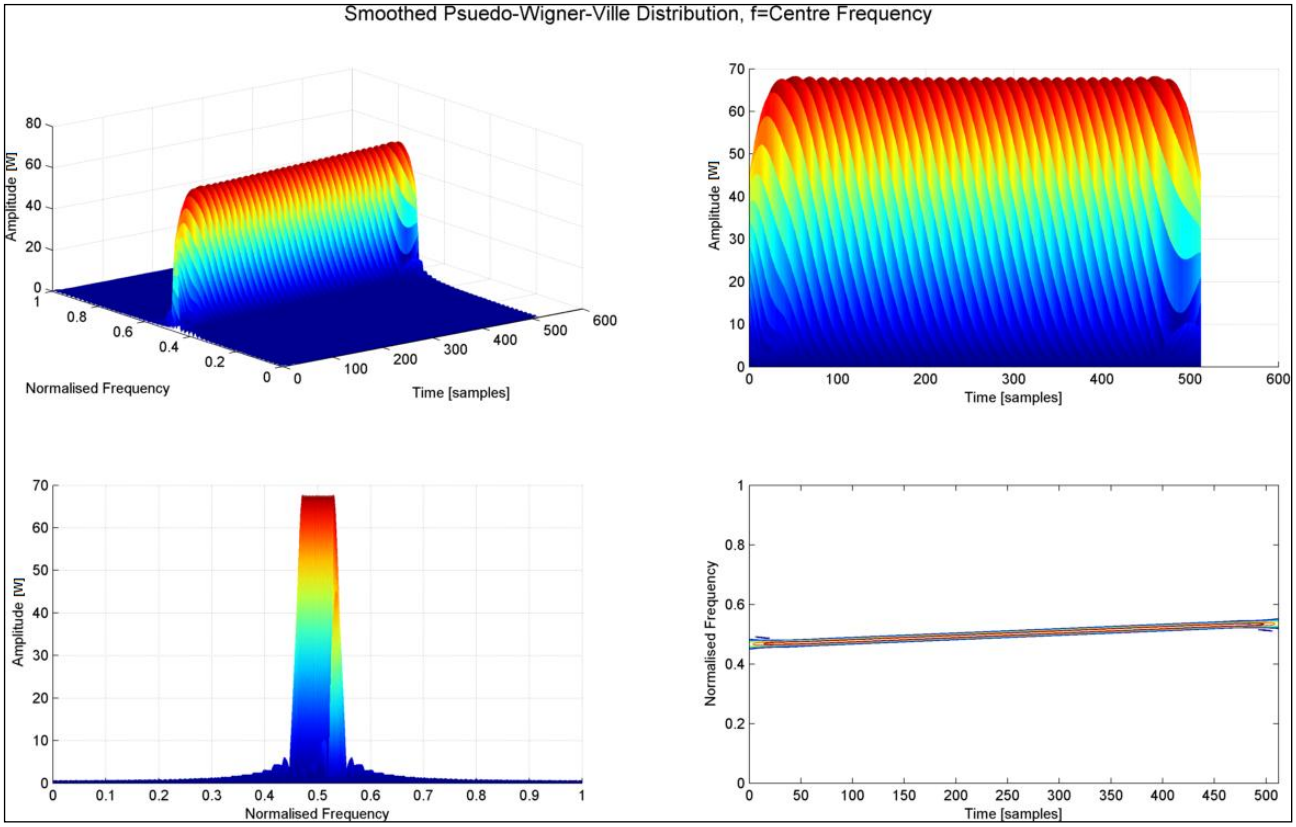

Figure 113: X-Band Single Pulse SPWVD4 Plot

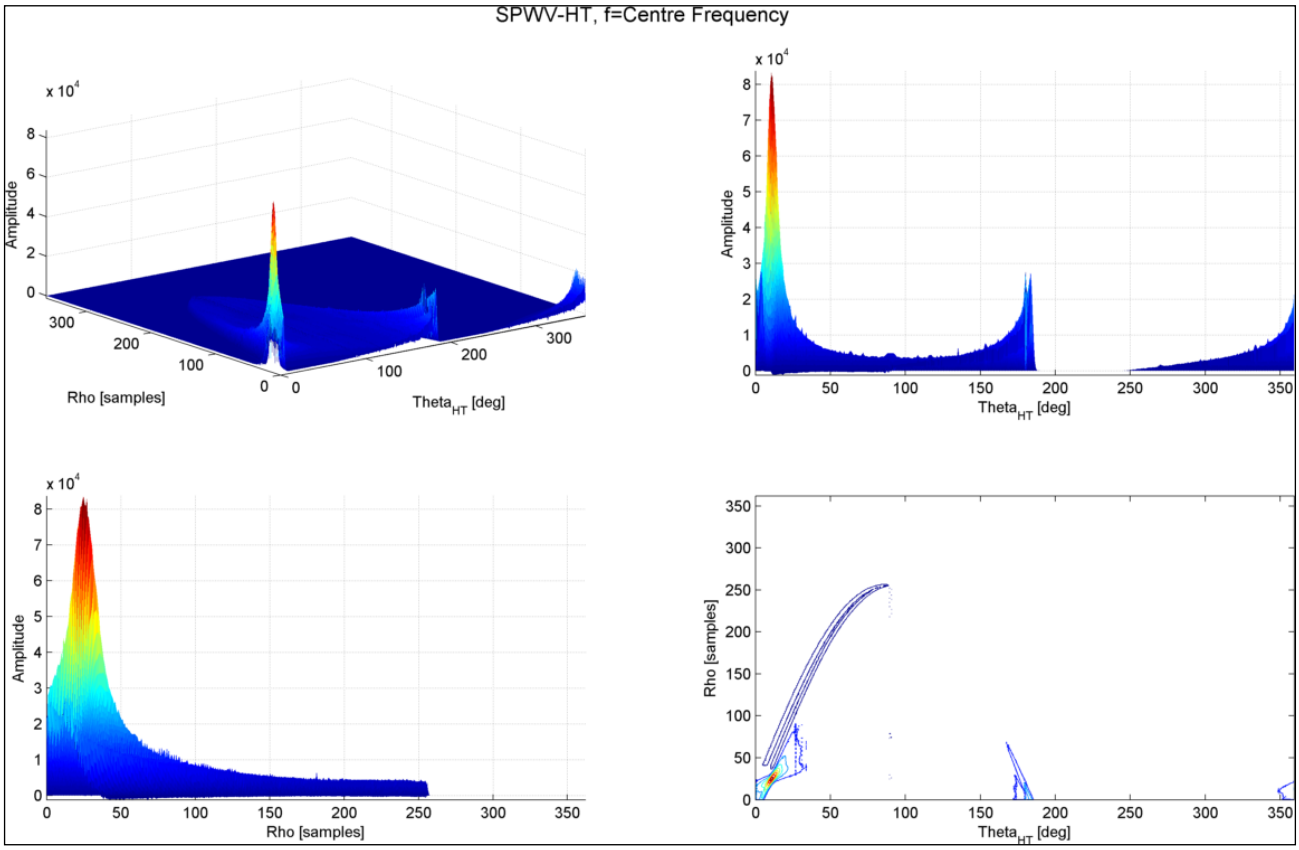

Figure 114: X-Band Single Pulse SPWHT4 Plot with Noise and Amplitude

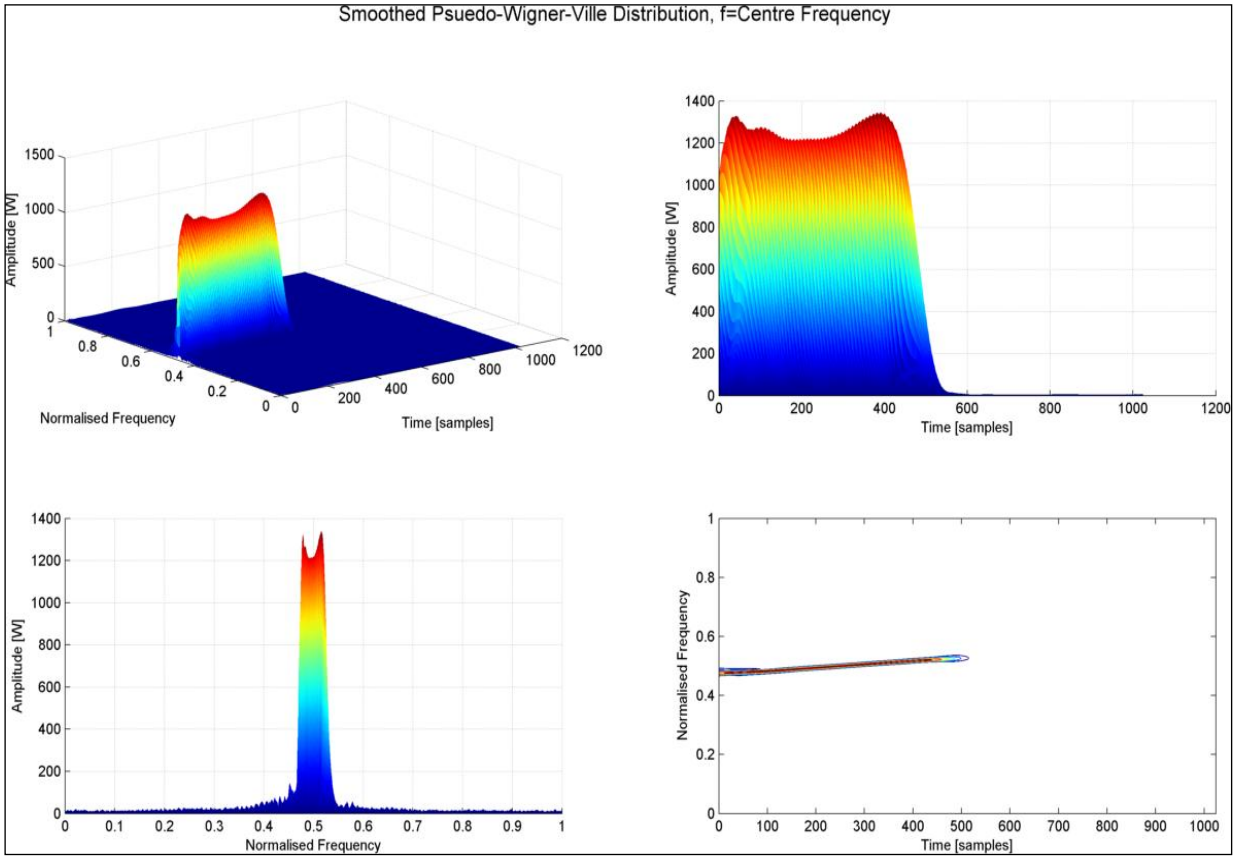

Figure 115: Single Pulse SPWVD4 Plot with Noise and Amplitude, L-Band

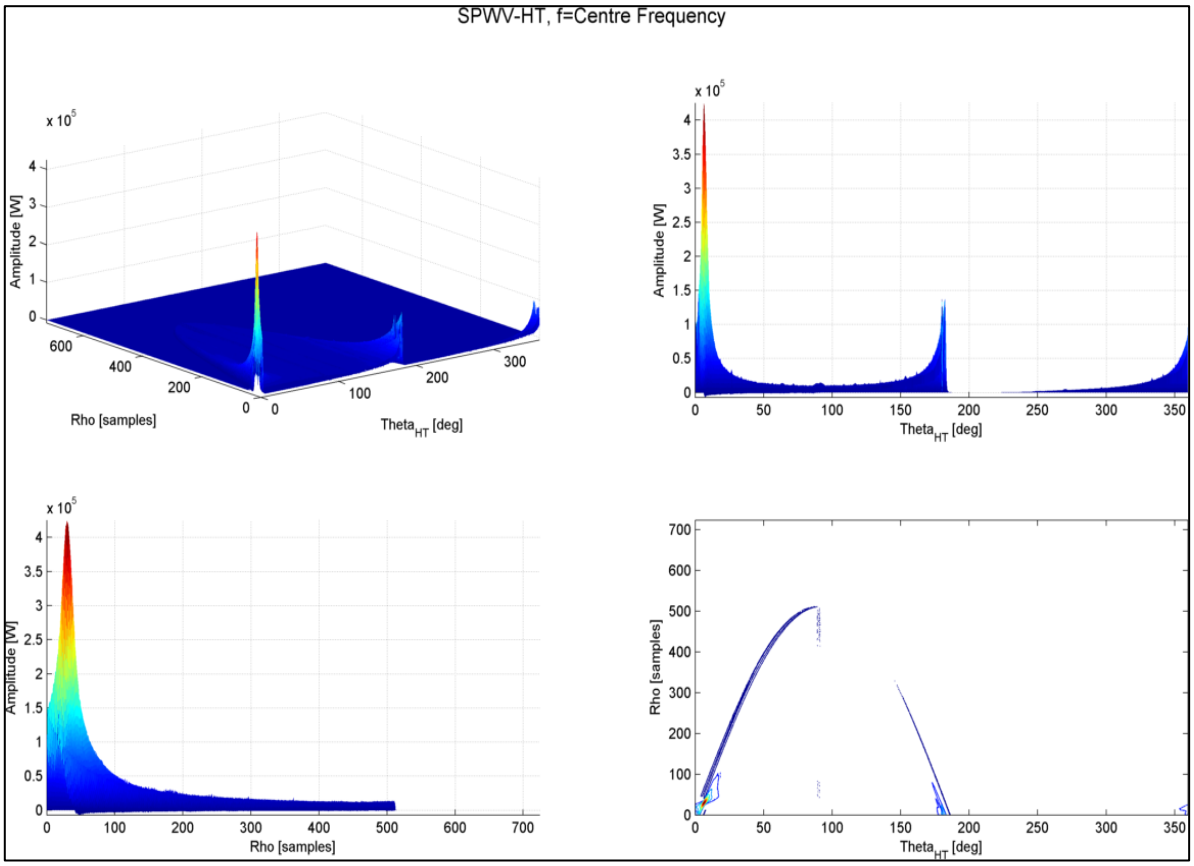

Figure 116: Single Pulse HT4 Plot with Noise and Amplitude, L-Band

6.4.2 PRI and Number of Pulse Estimation

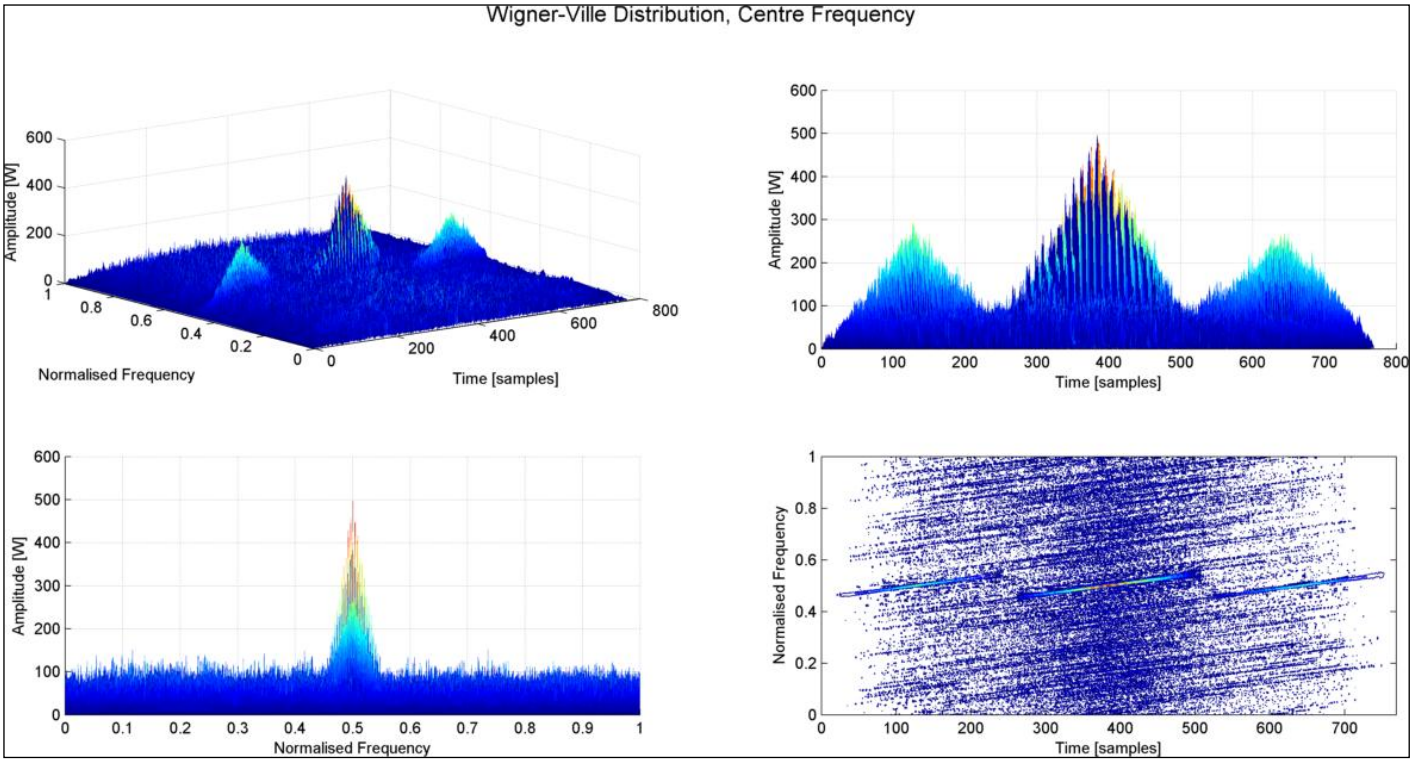

Figure 117: Two-pulse WVD4 Plot with Noise and Amplitude, X-Band

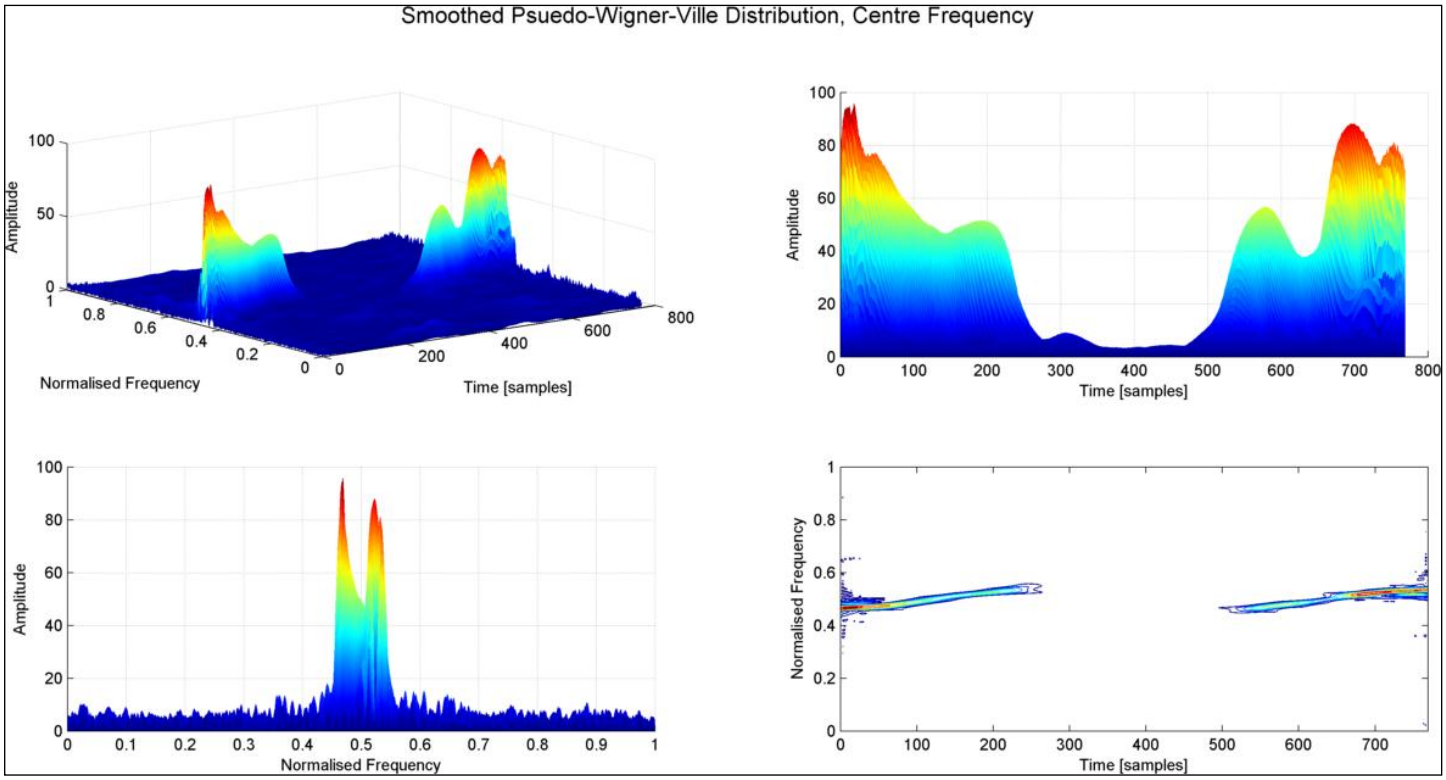

Figure 118: Two-pulse SPWVD4 Plot with Noise and Amplitude, X-Band

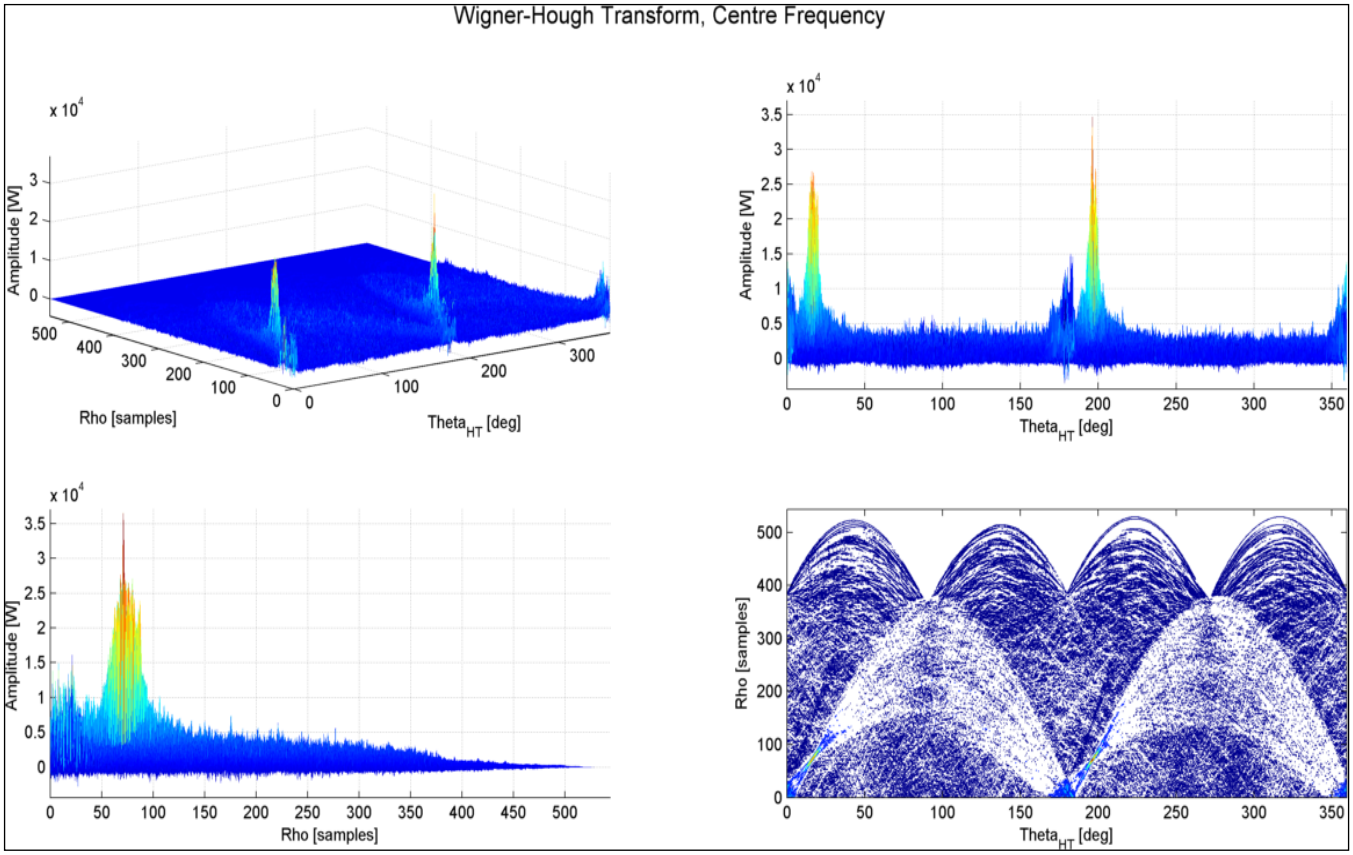

Figure 119: Two-pulse WHT4 Plot with Noise and Amplitude, X-Band

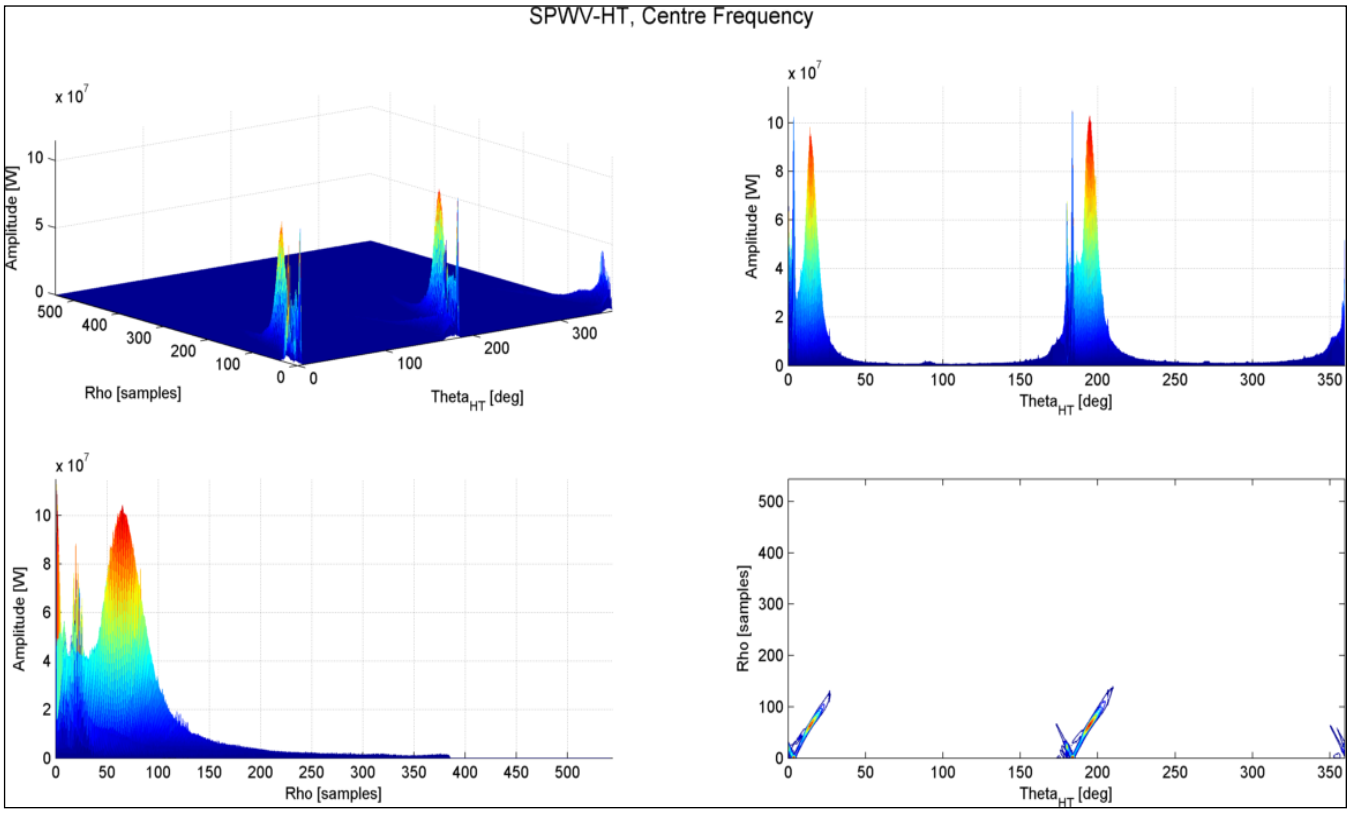

Figure 120: Two-pulse SPWHT4 Plot with Noise and Amplitude, X-Band

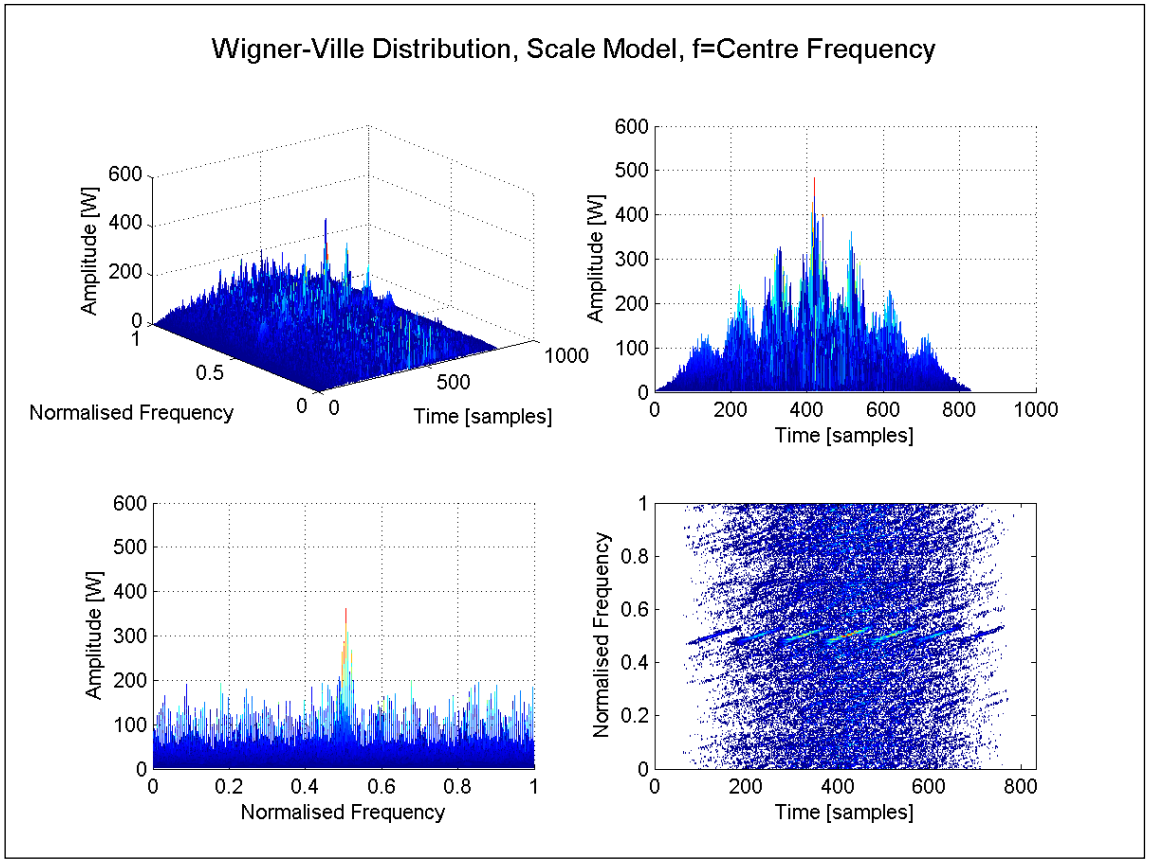

Figure 121: Four Pulse Scale Model, WVD4 with Noise and Amplitude, X-Band

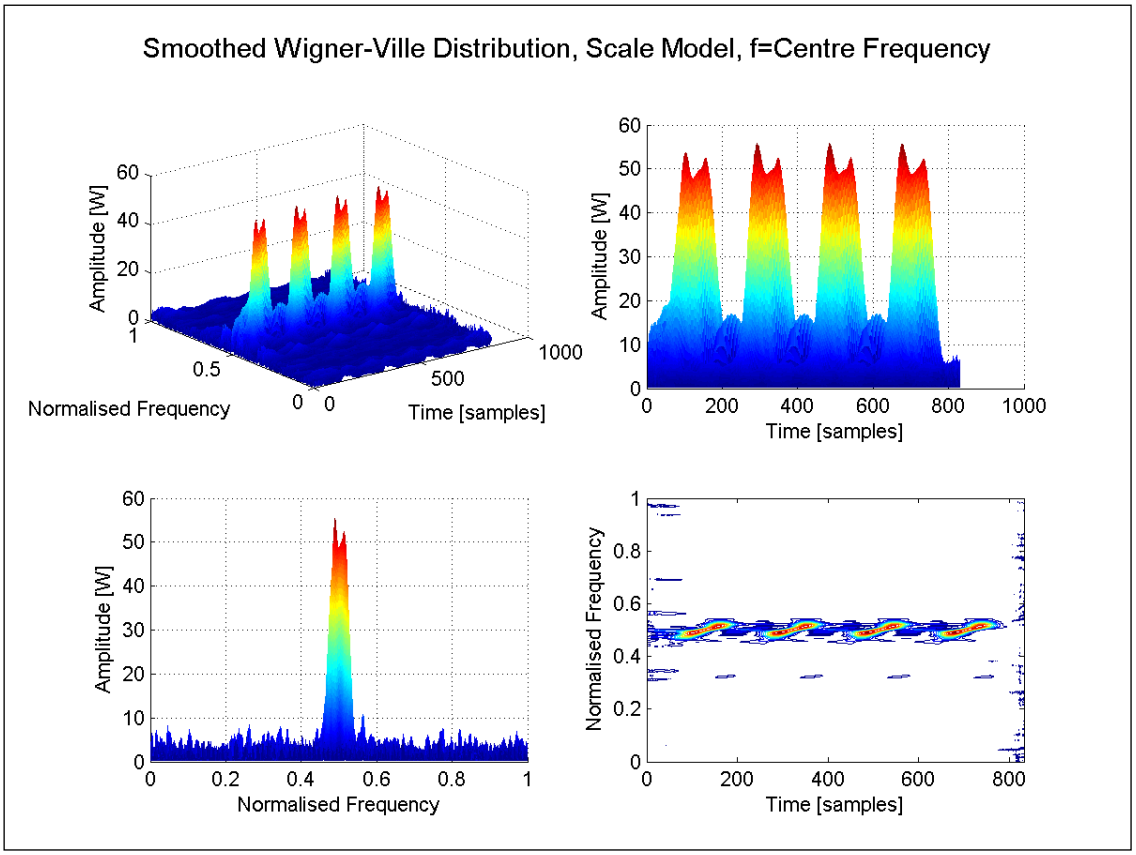

Figure 122: Four Pulse Scale Model, SPWVD4 with Noise and Amplitude, X-Band

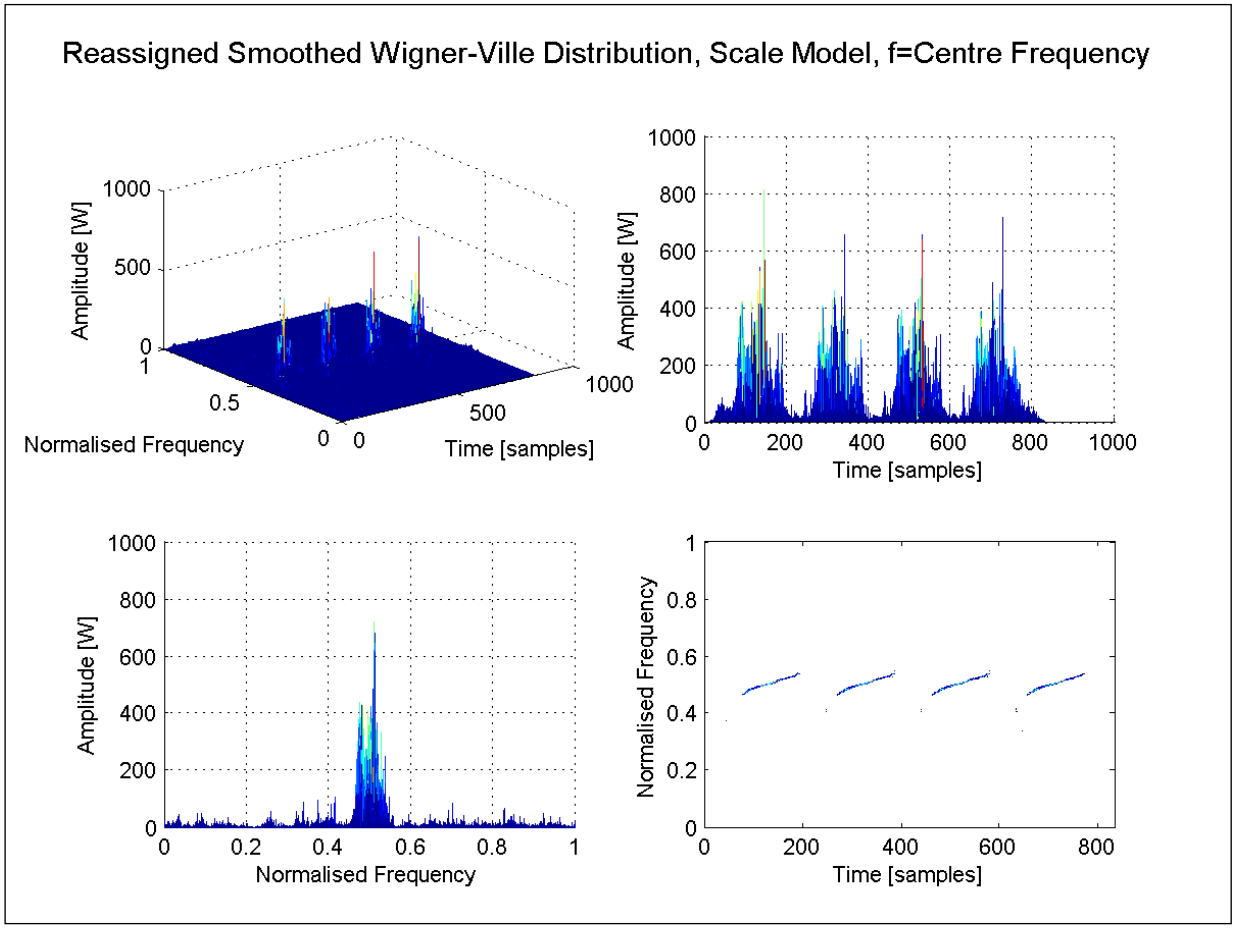

Figure 123: Four Pulse Scale Model, RSPWVD4 with Noise and Amplitude, X-Band

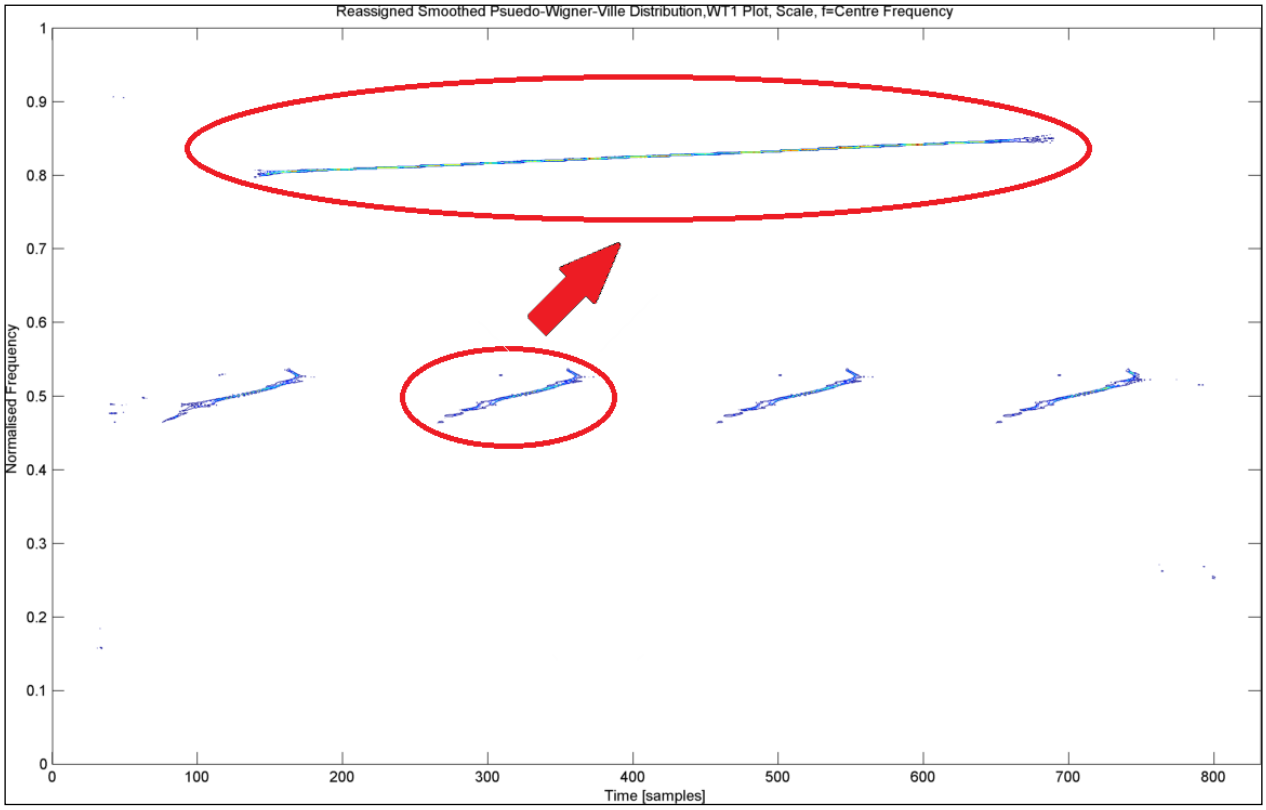

Figure 124: Four Pulse Scale Model, RSPWVD1 with Noise and Amplitude, X-Band

6.5 Electronic Support, Discussion of Results

6.5.1 Carrier frequency Estimation and Chirp Rate Estimation

A contour plot of the WVD ("WVD1" Plot) of the *intercepted signal* without noise and amplitude applied to the signal is displayed in Figure 110. Three-dimensional views of the WVD of the intercepted signal as shown in Figure 110 are called "WVD4" figures. If a figure with a single view of the WVD was generated it was called "WVD1" plot. The same naming convention was applied to to SPWVD and RSPWVD figures as well. The reader is advised to refer to the "List of Abbreviations" in chapter 11 for a description of any abbreviation used in this report.

The relationship between frequency and time can clearly be seen in the bottom right subplot of Figure 110. The bandwidth of the signal can estimated, by its height and the pulse width of the signal can be estimated from its width. In addition, the carrier frequency of the signal " $\hat{f}_c$ " corresponds to the middle point of the line while the gradient of the line is the LFM chirp rate " $\hat{\mu}$ ".

The transmitted signal from the DBR is shown in the upper plot of Figure 125 below (discussed in chapter 5). This is also the basic shape of the signal received at the ES Receiver, except that receiver noise is added to the signal. This noise further obscures the basic shape of the signal in the time domain. It can be seen that the transmitted signal parameters as shown in the bottom subplot of the figure below can certainly be estimated by the WVD.

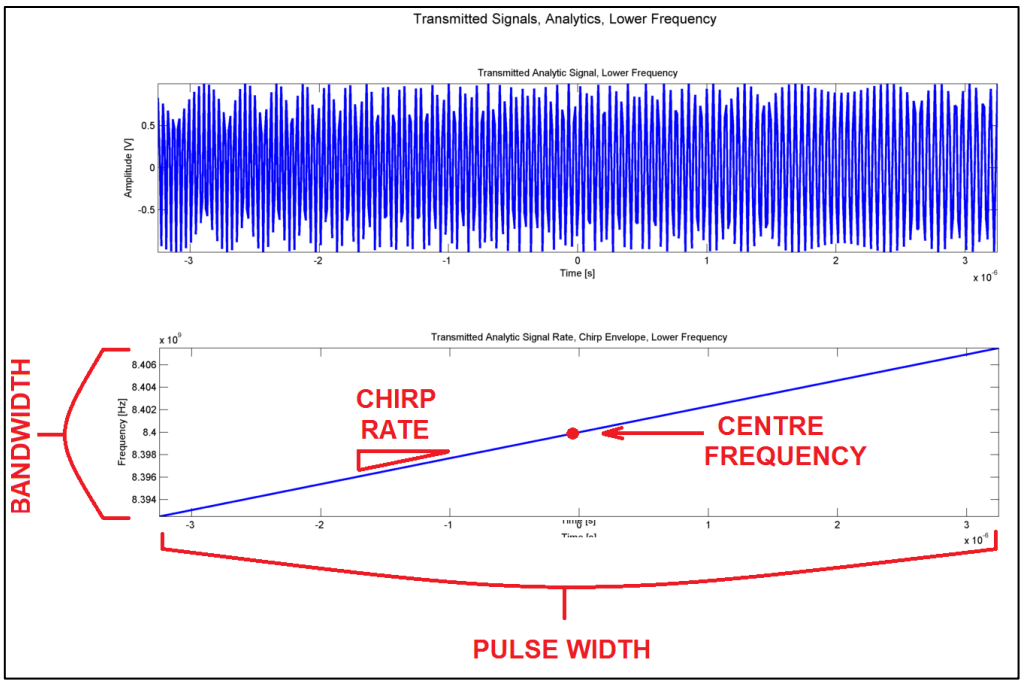

Figure 125: Transmitted Signal, Analytic Signal, X-Band

The WVD output of the signal, as shown in Figure 110, was mixed with noise and processed using the HT. The output of this processing is shown in Figure 111. From this figure it can be concluded that if the SNR is sufficient, the detection of the LFM signal above the noise floor is practically achievable using the WVD. The performance of the WVD in low SNR has been explained in section 6.5.
The HT of the WVD of the intercepted signal with noise and amplitude is displayed in Figure 112. The location of the peak in HT coordinates corresponds to the coordinates of the TF image of the LFM signal shown in the bottom right subplot of Figure 110. From Figure 112, the high peak would only be output from the HT, if a "line" were present in the TF image. The use of the HT to detect a LFM signal in noise can be practically observed by the result shown in Figure 112. This result was discussed by F. Auger ([12]) and summarized in section 2.3.

The improved version of the WVD that reduces cross-term interference caused by multi-component frequencies in the signal is the SPWVD. An SPWVD1 plot of the intercepted DBR pulse, processed with the SPWVD algorithm is shown in Figure 113. The SPWVD TF is clearer than the WVD plots.

In Figure 114, the "HT of the SPWVD four subplot" result or "SPWHT4" plot is shown. The clearer, higher resolution SPWVD TF image (compared to WVD) enables the HT algorithm to be more accurate.

All of the results presented up to now have been for the X-Band DBR signals. The L-Band DBR signal on the other hand is intercepted in a different channel of the digital channelized DBR receiver. The signal is therefore processed independently of the X-Band signals.
The WVD4 of an L-Band signal is shown in Figure 115 and the WHT4 of the same signal is shown in Figure 116. From these plots for the L-Band signals, it can be concluded that there is no difference at the output of the "WHT detector" for the X-band and L band signals. When the L-Band signal has reached the ES signal-processing block, it has already been mixed, down-converted and amplified by the RF processing channel of the Jammer, independently of the X-Band signal.

6.5.2 PRI and Number of Pulse Estimation

In Figure 117, the WVD of a two-pulse signal with noise and amplitude included is shown. The cross-term interference peak generated by the WVD algorithm is clearly visible between the two pulses. This cross term interference is a typical deficiency of the WVD, if the signal components or pulses are close to one another. The interference peak is even higher than the true signal TF representations, as shown in the upper right subplot of Figure 117. The bottom right subplot of the same figure shows the cross-term interference peak as a third line between the two true signal TF images. Using the HT on this image however, suppresses the cross-term interference peak. This advantage of using the HT to process a WVD image, has been reported by F. Auger et. al in reference [12] as well as S. Barbarossa in reference [35].

Nevertheless, the SPWVD offers a substantial improvement over the WVD in terms of interference suppression between adjacent pulses even without the HT. This is shown in Figure 118. The noise level was similar to noise level set in the simulation result shown in Figure 117.

In reality, the pulses from the DBR would be spaced much further apart so that the interference between pulses would not be a problem in any case.

The WHT4 plot and SPWHT4 for the same signal are shown in Figure 119 and Figure 120. The suppression of the cross-term interference peak from the WVD by the HT can be seen in the upper right plot of Figure 119. Also noticeable are the two distinct peaks formed for the two truepulses. The spacing between the peaks in the HT corresponds to the PRI time of the intercepted signal. This information is important since it allows the maximum *unambiguous range* of the radar to be estimated. The inverse of the PRI is the radar's PRF. Information on the PRF allows the radar's maximum *unambiguous Doppler frequency* to be determined. The EW system can then use this information to attack the radar.

6.5.3 Number of Pulse Estimation

To estimate the number of pulses, the number of HT peaks from a particular emitter must be counted. The WVD of a four-pulse signal is shown in Figure 121. Interference between pulses renders the estimate inaccurate, if the *pulses are closely spaced*. The intercepted pulses would typically be separated by a PRI duration, which is a large time (or ES receiver samples) compared to a pulse width. Nevertheless, the SPWVD performs much better than the WVD as can be seen in Figure 122. However, the best performance, from the WVD algorithms is the RSPWVD algorithm as can be seen in Figure 123 and Figure 124. No cross-term interference is visible nor is there any noise distortion visible in the RSPWVD TF images. A single pulse in the pulse train is shown expanded in Figure 124. From this, figure it can be seen that intercepted

signal carrier frequency, chirp rate, PRI, bandwidth and number of pulses can all be estimated using a single TF representation. Older algorithms require different algorithms to estimate all or some of the parameters. A particular advantage of the RSPWVD is the excellent resolution compared to the other ES algorithms. This is important when a radar pulse, with pulse diversity applied is intercepted. The waveform coding applied to the pulse can be determined if the TF image resolution is high enough. In addition, if the TF image is processed over the whole radar bandwidth, the sequence of frequencies or PRF's used by the radar when it is in "frequency agility", "frequency hopping" or "PRF agility" mode can be determined by the ES system. These measures are typically used by the radar to "protect" the radar's signal parameters from being intercepted.

6.6 Electronic Support Algorithms, Performance Assessment

In this section, the analysis into the practicality of the Wigner Ville Based algorithms as well as older algorithms such as the "Spectrogram" and "Instantaneous Frequency Measurement (IFM)" technique is discussed. Performance of the WHT for intercepted signal parameter estimation is initially described. The performance of the WHT in low SNR and its theoretical estimation precision is then discussed. Performance of the ES algorithms in interference is also analysed. Finally, the results of the "Monte Carlo" analysis in an ES algorithm performance comparison is presented and discussed.

6.6.1 WHT Low SNR Performance

The relationship between WHT input and output SNR was derived by Barbarossa in reference [34]. The relationship is shown below:

$$SNR_{out} = \frac{\frac{n_p^2}{2} SNR_{in}^2}{n_p \, SNR_{in} + 1} \tag{190}$$

From equation (190), it can be seen that good performance is achieved at $SNR_{in} > 1$. However, at $SNR_{in} \ll 1$, the output SNR can be worse than the input SNR. Nevertheless, performance in low SNR (i.e. < -2dBW), is a problem common to all the algorithms discussed in reference [12] by F. Auger and the WVD does benefit from coherent integration gain when multiple intercepted pulses are used for signal parameter estimation. This can be concluded by noting the presence of the "$n_p{}^2$" in the numerator of equation (190). The simulation output for the WVD algorithm at a $SNR_{in} = -40 dBW$ is shown in Figure 126. It can be seen that the LFM signal cannot be distinguished from the noise. The obscuring of the signal by noise, on the TF representation, is identical for the WVD, Spectrogram and IFM algorithms.

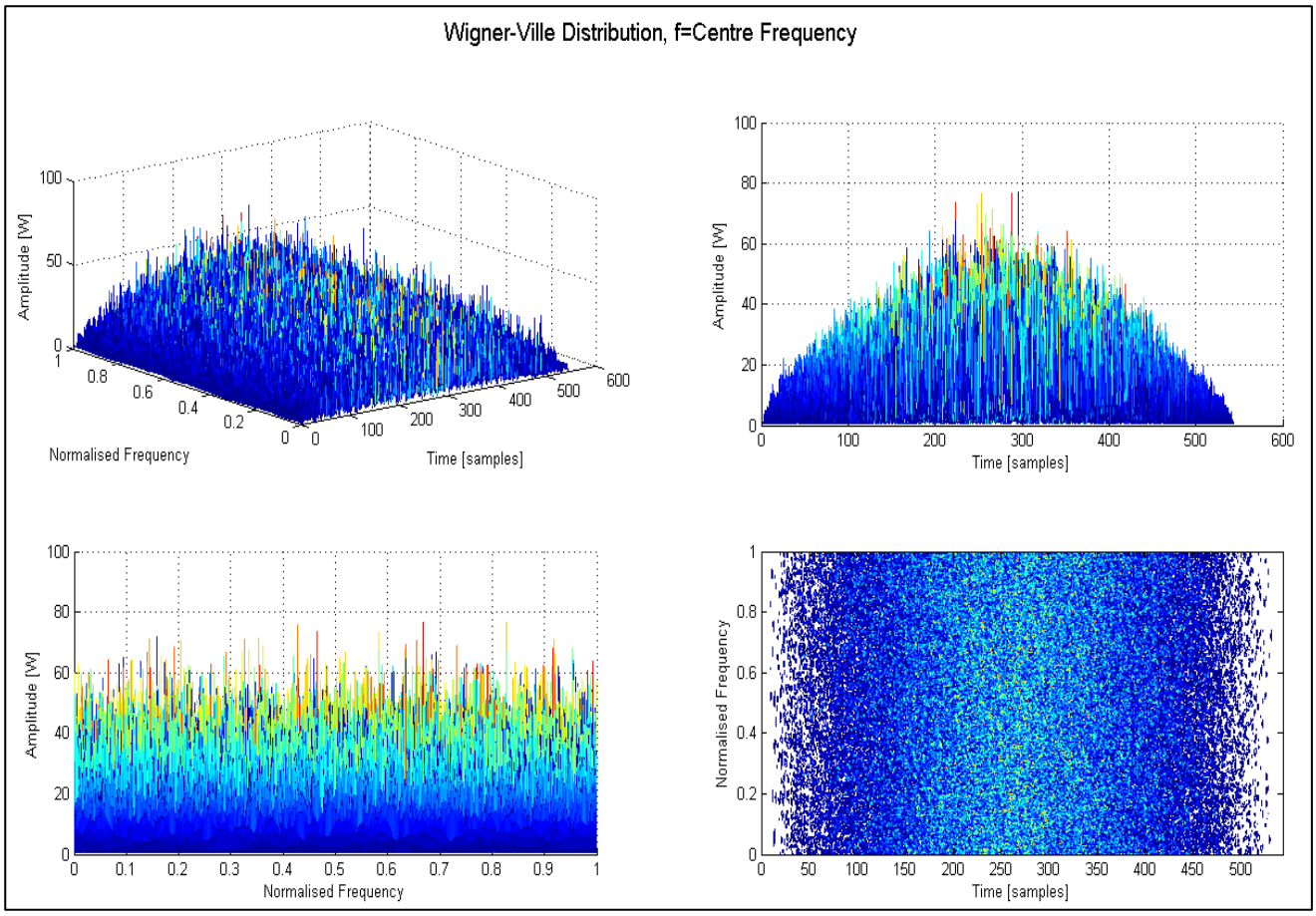

Figure 126: WVD at Low SNR, X-Band

6.6.2 WHT Accuracies

Theoretical expressions for carrier frequency and chirp rate measurement variances were derived by Barbarossa ([34]). The expressions are shown below:

$$\sigma_{f_c}^2 = \frac{3\left(7+8n_p\right)n_p}{\pi^2 n_p{}^2\left(n_p{}^2-4\right)\left(n_p-1\right)}\left(\frac{1}{SNR}+\frac{2}{n_p\,SNR^2}\right) \tag{191}$$

$$\sigma_{\mu}^2 = \frac{90\,n_p}{\pi^2 n_p{}^2\left(n_p{}^2-4\right)\left(n_p-1\right)}\left(\frac{1}{SNR}+\frac{2}{n_p\,SNR^2}\right) \tag{192}$$

Equations (191) and (192) were used to plot "$\sigma_{f_c}^2$" and "σ_{μ}^2" over a range of SNR for the DBR X-Band and L-Band subsystems. The parameter that varied between X and L bands WVD estimation error variance analysis, was the number of pulses with 31 pulses transmitted per CPI at X-Band and 20 pulses transmitted at L-Band. The results of this analysis are shown in Figure 127. The increased number of pulses at X-Band causes a big reduction in both frequency and chirp rate estimation error using the WHT algorithm as shown in Figure 127.

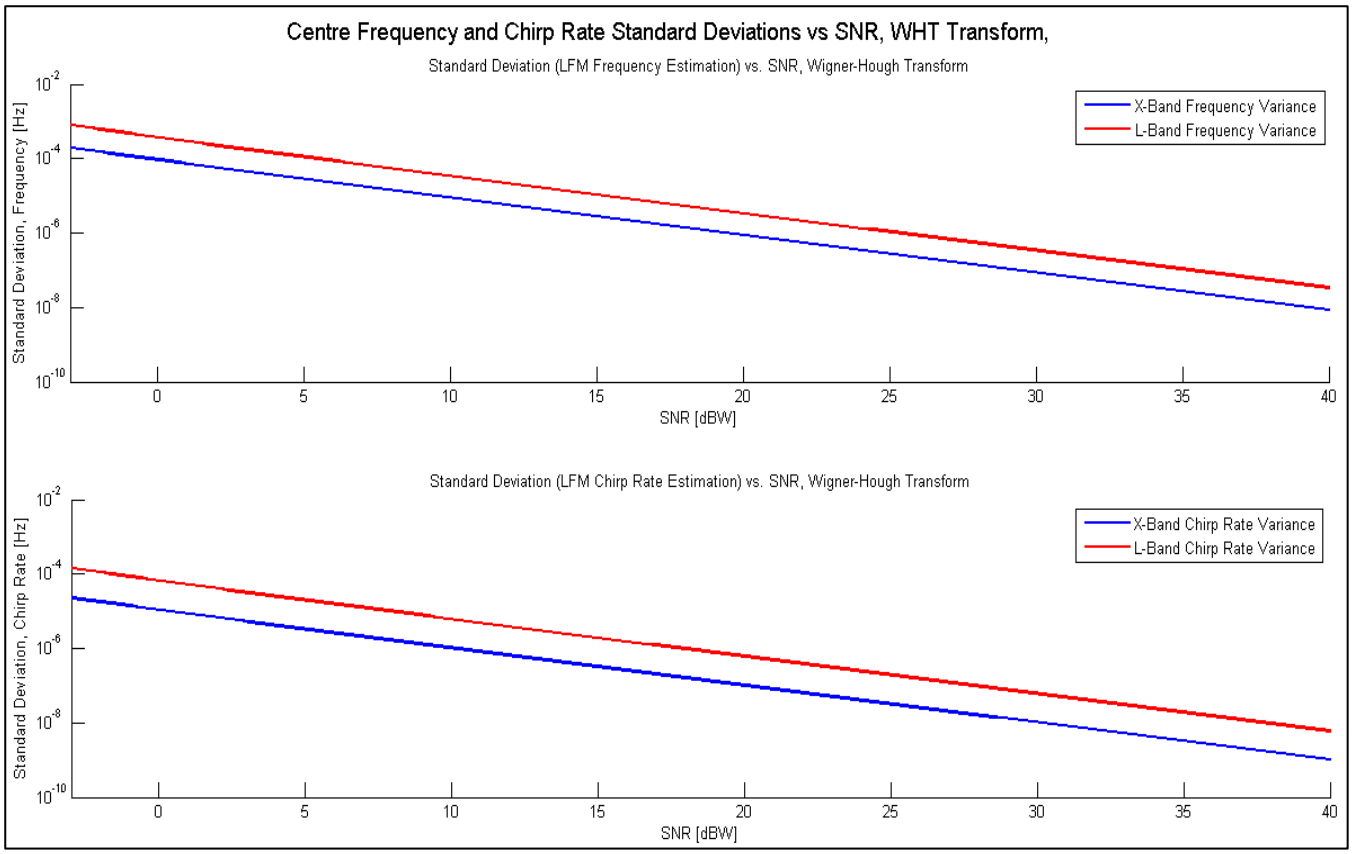

Figure 127: Centre Frequency and Chirp Rate Standard Deviations vs. SNR

At low SNR's the actual chirp rate estimate error, deviates substantially from the theoretical predication as shown in Figure 128. This has been discussed in reference [34] and summarized in section 2.3.2.

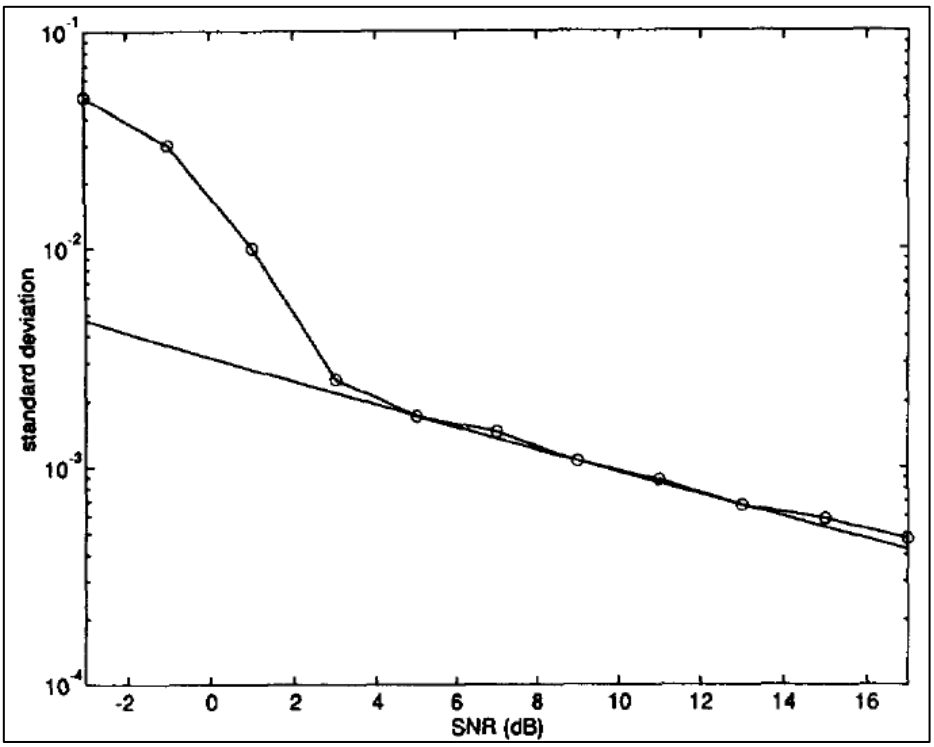

Figure 128: WHT standard deviation for Chirp Rate,16 pulses (reference [34])

6.6.3 Multi component Signal, Interference Effects

A complicated signal was generated with three differently modulated frequency components (sinusoid, linear and no modulation), to test the effects of ES algorithm interference caused processing multi-component signals. The analysis is based on a simulation described by F. Auger in reference [12].

In the multi-component signal simulated, the second and third components are overlapped in time. All three signal components and their composite form is shown in Figure 129.

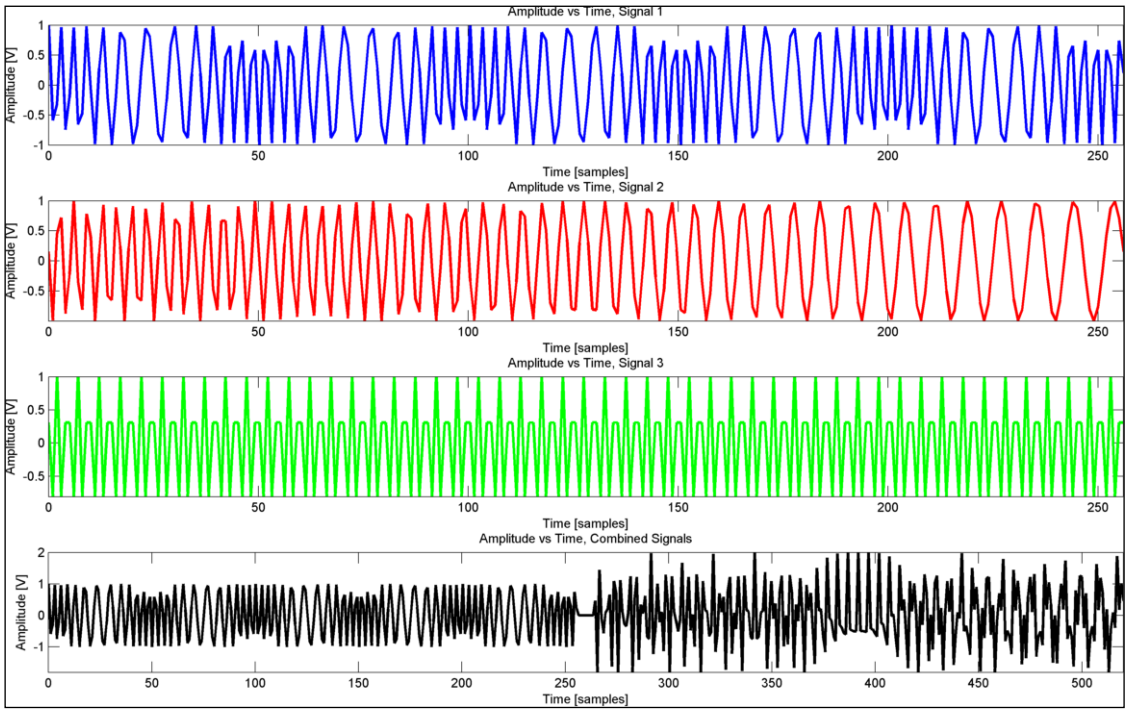

Figure 129: Multi-component Composite Signal

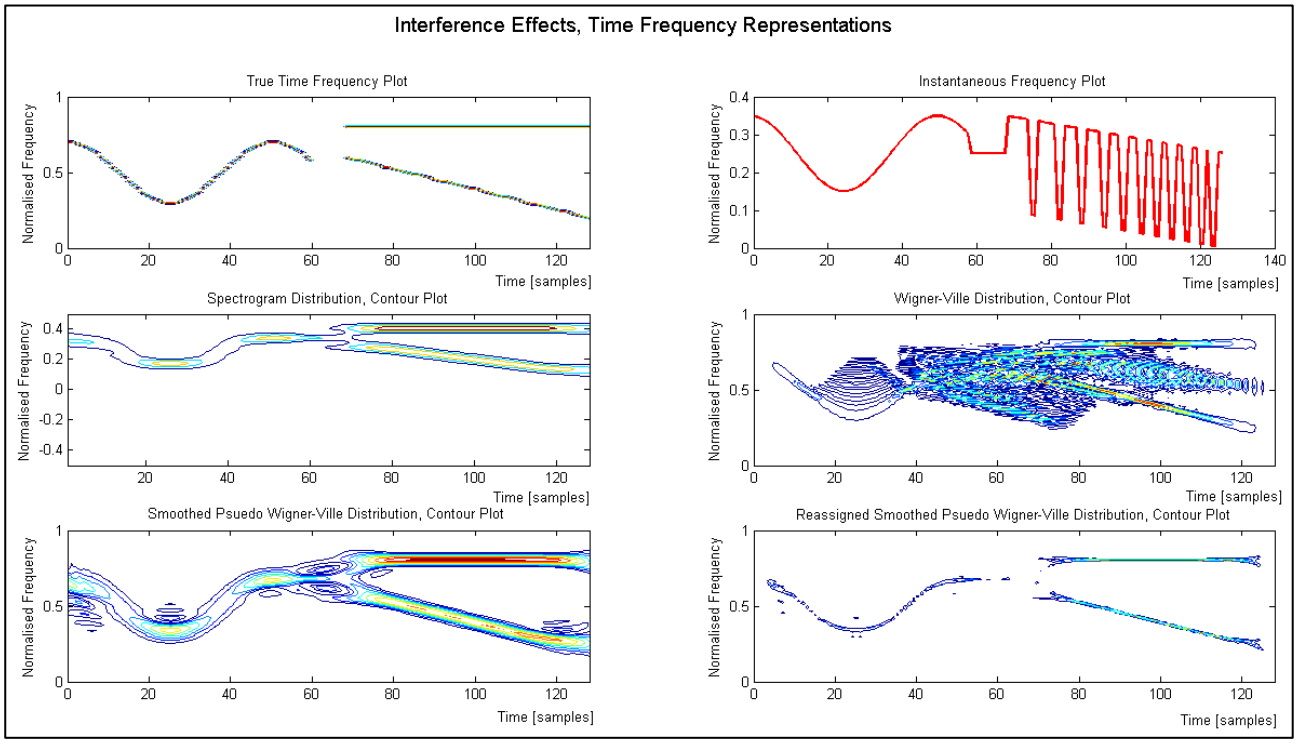

Figure 130: WVD Comparison, Multi-component Composite Signals (reference [12])

In the first subplot on the left of Figure 130, the actual TF relationships of the signal components are shown. The sinusoid modulation of the first component is clearly visible. The overlapped second (LFM) and third component (uniform) are also shown. The signal was processed using the IFM, Spectrogram, WVD, SPWVD and RSPWVD algorithms as shown in the TF representations for the signal. From this figure, the inability of the IFM and WVD algorithms in discriminating between multiple signal components is clearly visible. However, the IFM TF image would be distorted regardless of the separation of the terms in frequency. If the second and third signal components are separated far enough in frequency, the WVD cross term causing the TF image degradation is reduced sufficiently. The HT also suppresses the cross term interference in the WVD in any case. Nevertheless, it can be seen, that the Spectrogram, SPWVD and RSPWVD do not suffer with significant TF image quality degradation due to processing the multi-component signal. Nevertheless, the resolution of the Spectrogram and SPWVD are poor compared to the RSPWVD. Best performance in terms of both multi-component signal estimation and good resolution is the RSPWVD. However, overall estimation accuracy of the ES algorithm, as a function of intercepted signal to noise ratio "SNR_{jr}" must still be compared to determine the best performing ES algorithm for LFM signal parameter estimation. The results of this comparison are presented and discussed in the next section.

6.6.4 Monte Carlo Simulation for ES Algorithm Comparison

A Monte Carlo analysis was done to determine performance of the selected ES algorithms in estimating LFM signal centre frequency and chirp rate.

The frequency estimation error "$f_{c,error}$" calculated using the WVD, SPWVD, RSPWVD, Spectrogram and IFM algorithms to estimate carrier frequency, is shown in equation (193):

$$f_{c,error} = \frac{\left| f_c - \hat{f}_c \right|}{f_c} \cdot 100\% \tag{193}$$

In a dual way the LFM chirp rate estimation error, "μ_{error}" is calculated using equation (194):

$$\mu_{error} = \frac{\left| \mu - \hat{\mu} \right|}{\mu} \cdot 100\% \tag{194}$$

The errors were calculated for SNR's ranging between -18dBW to 5dBW over multiple runs.

In total, the simulation was run 100 times per ES algorithm in either band. In total, this simulation therefore ran for 1000 runs over the selected SNR range. The result of the comparisons for frequency and chirp rate estimation, averaged over 100 runs per ES algorithm at X-Band is shown in Figure 131 and Figure 132. The ES algorithms all show a decrease in performance at SNR's less than zero. However, the minimum SNR at which an

accurate estimate is obtained and the peak error varies from algorithm to algorithm. A similar trend was noted in the simulation results for the intercepted L-Band signals as shown by the estimation errors in Figure 133 and Figure 134.

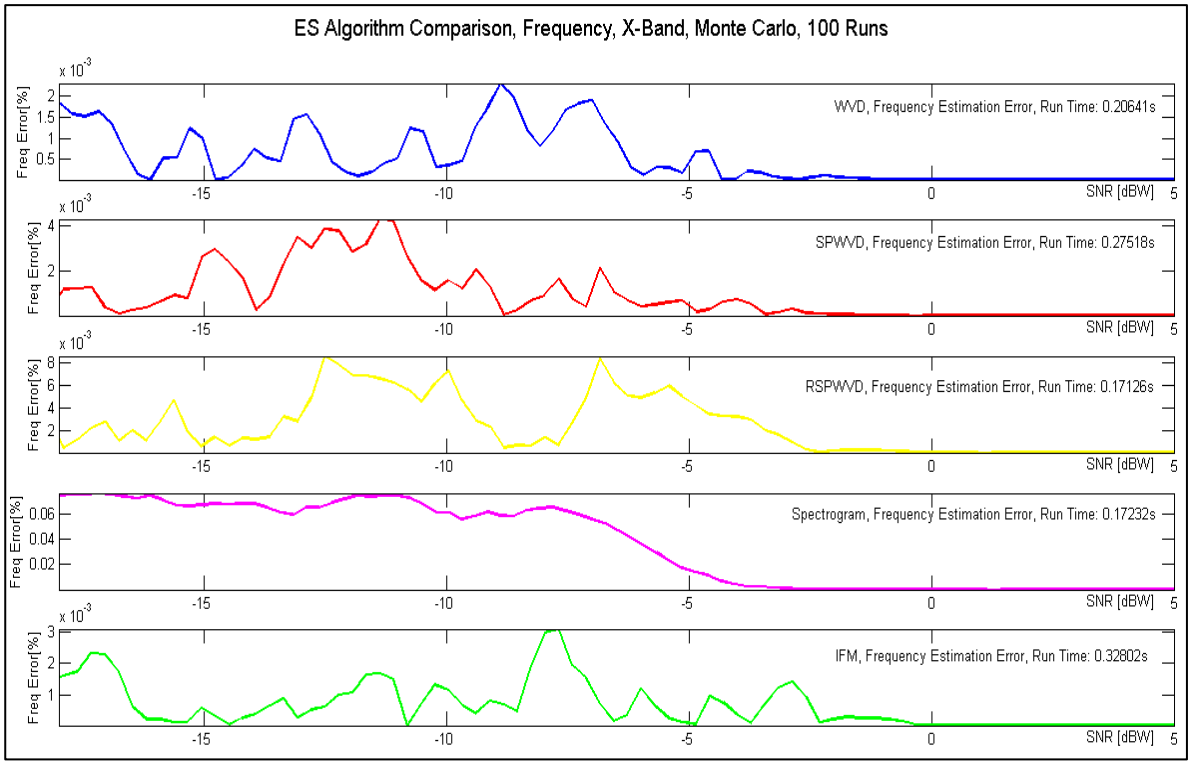

Figure 131: Frequency Estimation Error Comparison, X-Band

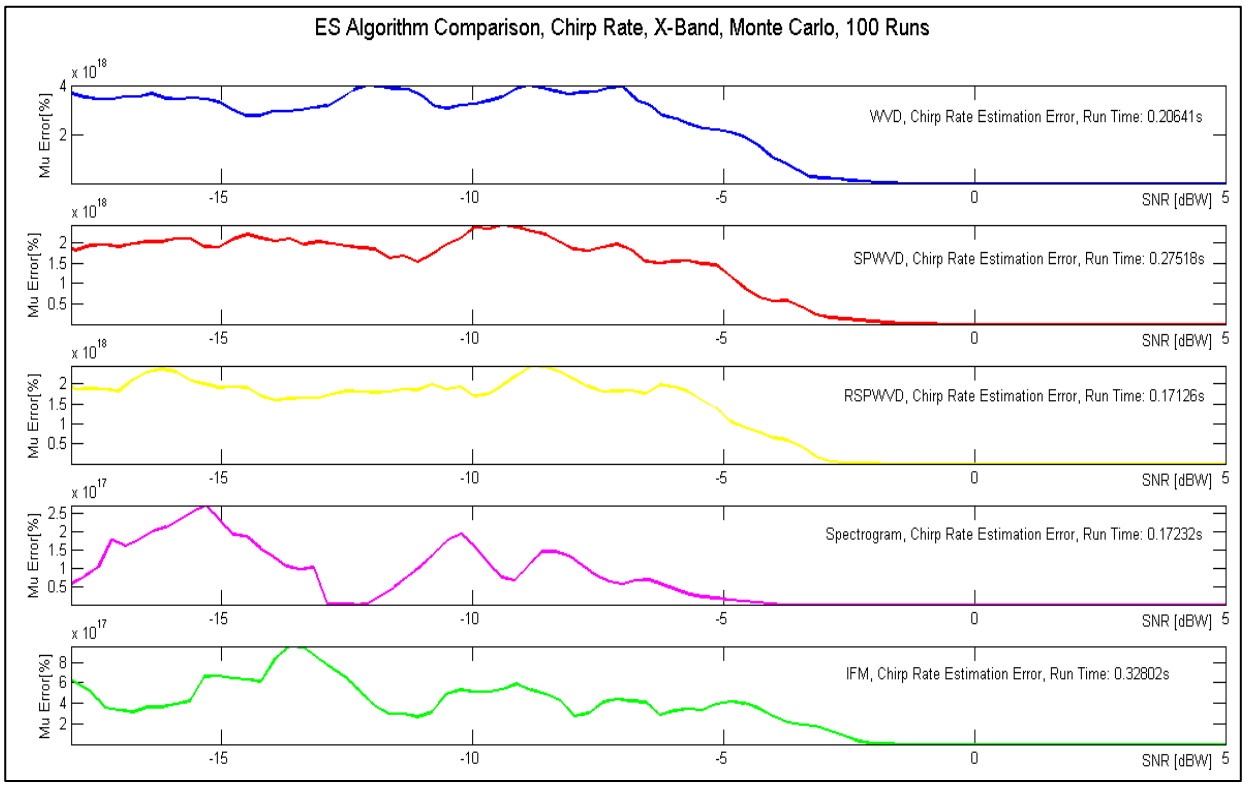

Figure 132: Chirp Rate Estimation Error Comparison, X-Band

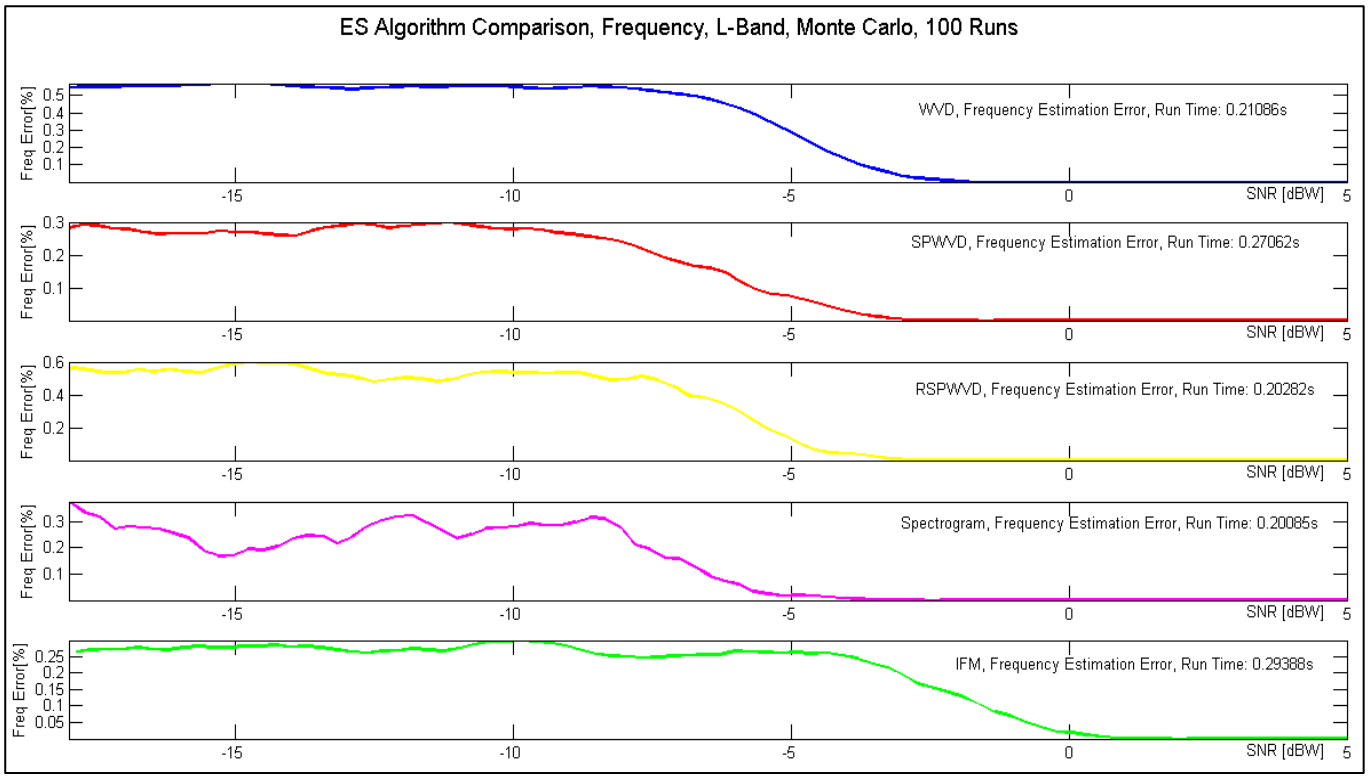

Figure 133: Frequency Estimation Error Comparison, L-Band

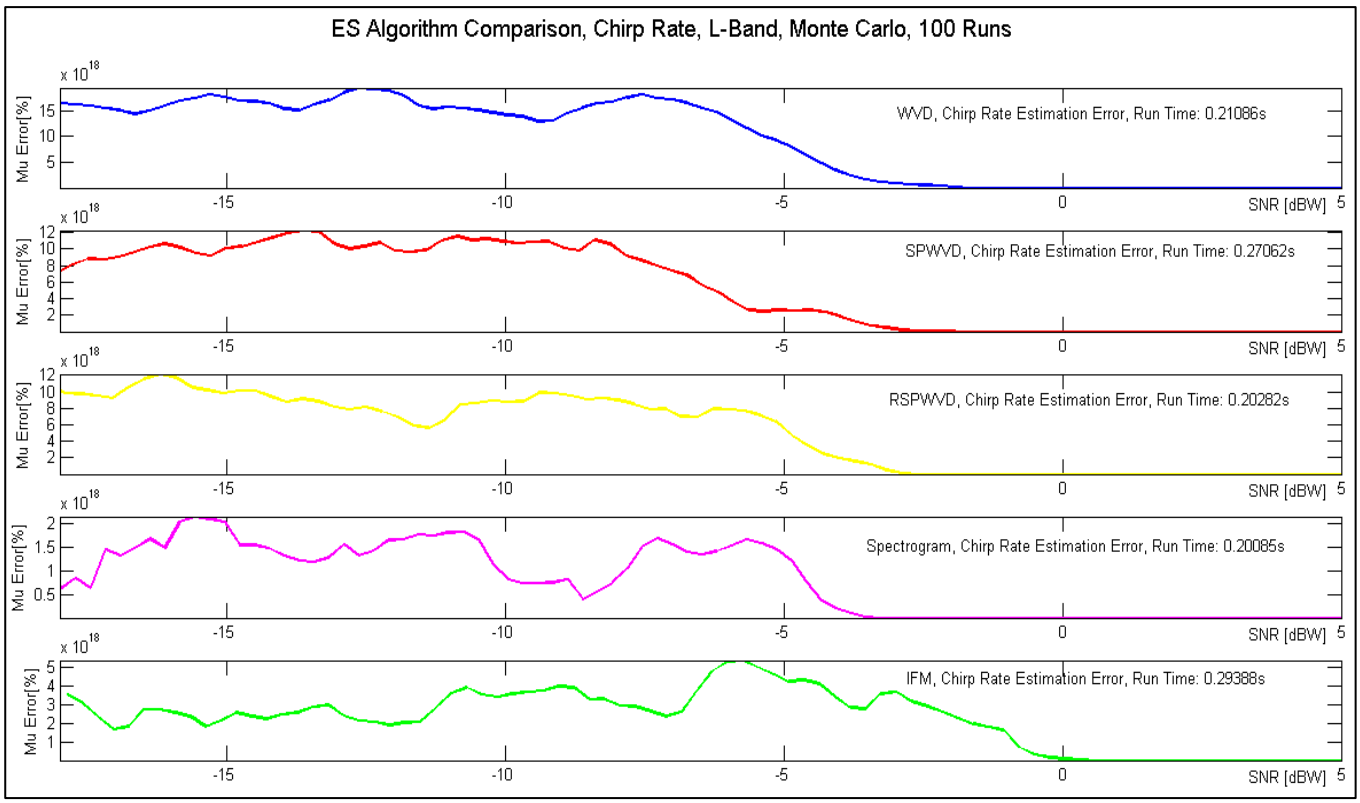

Figure 134: Chirp Rate Estimation Error Comparison, L-Band

A detailed analysis of the information contained in figures was necessary, to determine the actual value of the minimum SNR for accurate estimation and maximum error. The results of this analysis are shown in Table 16 and Table 17.

	Frequency Estimation		Chirp Rate Estimation	
Algorithm	**Maximum Error [%]**	**Minimum SNR [dBW]**	**Maximum Error [%]**	**Minimum SNR [dBW]**
WVD	2.296E-03	-0.583	3.97E+18	-0.583
SPWVD	4.233E-03	0.528	2.33E+18	0.244
RSPWVD	8.594E-03	2.795	2.45E+18	2.795
Spectrogram	7.616E-02	7.449	2.71E+17	7.717
IFM	3.109E-03	-0.039	9.45E+17	-0.039

Table 16: Monte Carlo Run, Error Comparison, X-Band

	Frequency Estimation		Chirp Rate Estimation	
Algorithm	**Maximum Error [%]**	**Minimum SNR [dBW]**	**Maximum Error [%]**	**Minimum SNR [dBW]**
WVD	0.569	-1.654	1.91E+19	-0.315
SPWVD	0.303	0.701	1.21E+19	-1.780
RSPWVD	0.595	-0.606	1.17E+19	-2.024
Spectrogram	0.374	0.756	2.10E+18	-1.386
IFM	0.298	1.701	5.36E+18	0.598

Table 17: Monte Carlo Run, Error Comparison, L-Band

From both the X-Band and L-Band results shown in Table 16 and Table 17, the small size of the maximum frequency estimation error compared to the chirp rate estimation error at low SNR is shown. This trend was noted by S. Barbarossa in reference [34] and discussed earlier in sections 2.3.2 and 6.6.2. Overall, peak frequency estimation error was measured for the RSPWVD algorithm, while the smallest error was noted for the IFM algorithm.

The minimum SNR was defined as the intercepted signal SNR ("SNR_{jr}") at which the error settled to a "steady state" value. From all the algorithms, the WVD showed the best low SNR performance, while the Spectrogram exhibited the worst performance at X-Band. The WVD also performed the best in terms of minimum SNR for chirp rate estimation, while the Spectrogram again was the worst performer. At L-Band, the best performer in terms of low SNR performance was the WVD for frequency estimation and the RSPWVD for chirp rate estimation.

Simulation program run times for the algorithms were also measured during the Monte Carlo simulation and used to compare the algorithms. A summary of the results are shown in Table 18. The two fastest algorithms were the RSPWVD and Spectrogram.

Algorithm	Frequency Estimation Run Time [s]	Chirp Rate Estimation Run Time [s]
WVD	0.208	0.209
SPWVD	0.273	0.273
RSPWVD	0.187	0.187
Spectrogram	0.187	0.187
IFM	0.311	0.311

Table 18: Run Time Comparison, X and L Bands

7 Signal Models, Electronic Attack

The context of this chapter within the complete simulation can be visualised by considering the portion of the jammer cycle bounded by the red polygon in Figure 135.

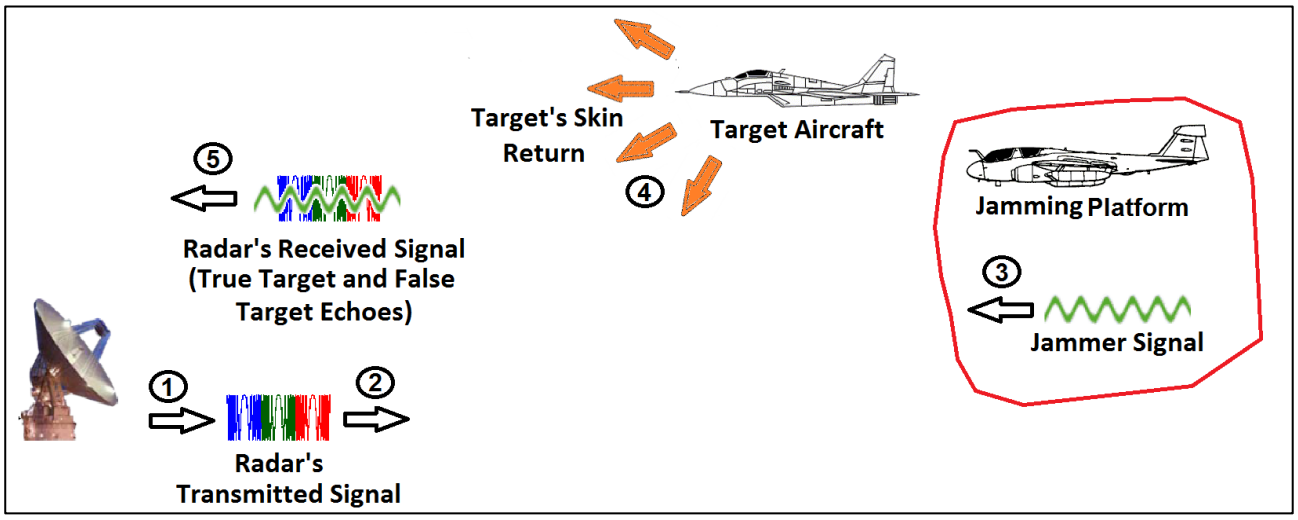

Figure 135: Scenario Definition, "EA System Transmits False Signals"

The synthesis of the false target signal by the Jammer is described in this chapter. Mathematics defining the false signal definitions is described in detail, initially. The SFD showing the implementation of the false signal model in the overall simulation is shown thereafter. Simulation results based on mathematical descriptions of the false signals are then presented, followed by a discussion of the results. Detailed effects of the false signal in comparison to the true signal is analysed at the radar receiver and is discussed in chapter 8, not in this chapter.

7.1 False Target Echo Signal

Estimated intercepted radar signal parameters ($\hat{\mu}$, $\hat{f}_c$) from the ES model are used as signal parameters, for the false signal simulation. False target parameters such as time delay "t_o^f" (corresponding to range "R_o^f"), Doppler frequency "f_d^f" and elevation angle "ψ^f" are also entered into the signal model. Cross-eye jamming uses an "out of phase" copy of the entire intercepted radar signal, in addition to the other false target parameters.

The DBR receiver models discussed in subsequent chapters then simulate the receiving and processing of both true and false signals.

7.1.1 False Stationary Target Echo:

The false target signal model for a stationary target *as transmitted by the jammer* is shown in equation (195). A stationary target is defined as a target without any velocity (hence Doppler shift) at a range "R_o" from the DBR. This signal model is a notational construct used to introduce the complete false signal model with all of its parts.

The complete signal is made up of the amplitude function term, false target complex envelope and intercepted radar carrier frequency term:

$$\underset{\text{False Analytic Signal}}{x_{rs}^{f}(t)} = \underbrace{A_j(t)}_{\text{Amplitude Function}} \cdot \underbrace{\tilde{x}_{rs}{}^{f}(t)}_{\text{False Envelope Signal}} \cdot \underbrace{e^{j2\pi \hat{f}_c t}}_{\substack{\text{Intercepted Carrier} \\ \text{Frequency Term}}} \tag{195}$$

The amplitude of the false target signal as transmitted by the jammer is defined as:

$$A_j(t) = 10\sqrt{\frac{P_{tx}^{r}\, G_{tx}^{r}\, L_{jammer}^{pol}\left(JSR\,\sigma\right)}{4\pi\left(R_j(t)\right)^2 G_{tx}^{j}\beta^2}} \tag{196}$$

The equation above has been derived from D. Schleher's textbook, reference [4]. The false target signal amplitude is set by adjusting the Jamming to Signal Ratio "*JSR*" at the Jammer and was also defined in section 4.2.4. It is:

$$\sigma_f = JSR\,\sigma \tag{197}$$

A "rule of thumb" provided by D. Schleher in reference [4], for the false target power level was that the *JSR* should be between 7 to 10 dBW relative to the true target echo power, in order to "capture the radar's tracking gates", D. Schleher reference [4].

In equation (196), the independent variable "R_j" was made a function of time to ensure that a jammer "track" with varying range could be entered into the model to update the received amplitude per time step.

However, once the false signal has arrived at the radar and travelled the return distance from the jammer to the radar, its amplitude function is defined as:

$$A_{rj}(t) = 10\sqrt{\frac{P_{tx}^{r}\, G_{tx}^{r}\, G_{rx}^{r}\, P_{tx}^{j}\, G_{PC}\, G_{DOP}\,\lambda^4}{\left(4\pi\, R_j(t)\right)^4 L_{radar} L_{jammer}^{pol}}} \tag{198}$$

The false target signal amplitude at the Jammer Receiver was derived from the "Repeater Jamming Equations" in Schleher [4]. These system-level equations were presented in section 4.2.4. It was shown in section 4.2.4, that the jammer transmitter can operate in an unsaturated capability over the entire detection range of the DBR in X and L-Bands. The dynamic range of the jammer transmitters would therefore be sufficient to mask the three

target types over the whole DBR detection range. For this reason, the false target signal power received at the radar was set to be similar to the true target RCS echo power.

The amplitude function was developed to be a function of time by ensuring the independent variable "R_j" is a function of time. This allowed the capability of ensuring that a jammer "track" with varying range could be entered into the model to update the received amplitude *per time step.*

Noise power is not taken into account in the amplitude models, since it is added to the signals separately per time step as indicated in equation (15). In the power form ("System Models") of these equations, from which the amplitude functions are derived, noise power is included.

The false signal transmitted by the jammer and received at the radar is therefore defined as shown in equation (199):

$$\underbrace{x_{rs}^{f}(t)}_{\text{False Analytic Signal}} = \underbrace{A_{rj}(t)}_{\text{Amplitude Function}} \cdot \underbrace{\tilde{x}_{rs}{}^{f}(t)}_{\text{False Envelope Signal}} \cdot \underbrace{e^{j2\pi \hat{f}_c t}}_{\substack{\text{Intercepted Carrier} \\ \text{Frequency Term}}} \tag{199}$$

The false target signal model received at the radar is similar to the false target signal transmitted by the jammer (equation (195)), except that the amplitude functions are different. The correct amplitude for the false signal received at the radar is shown in red in equation (199). In this signal, the estimate of the intercepted carrier signal by the ES system is used as the false target carrier. This carrier frequency is also shown in red font in equation (199).

The complex envelope of the false target signal can be broken down further as shown in equation (200):

$$\underbrace{\tilde{x}_{rs}{}^{f}(t)}_{\text{False Envelope Signal}} = \underbrace{\text{Rect}\left(\frac{t-t_o^f}{\tau}\right)}_{\text{Rectangular Envelope}} \cdot \underbrace{e^{j\pi\hat{\mu}\left(t-t_o{}^{f}\right)2}}_{\text{Time Delayed Term}} \cdot \underbrace{e^{-j2\pi \hat{f}_c t_o^f}}_{\text{Phase Shifted Term}} \tag{200}$$

The complex envelope is made of a "rectangular envelope" term, used to limit the envelope signal to a pulse-width duration. It is shown in equation(201):

$$\text{Rect}\left(\frac{t-t_o^f}{\tau}\right)\cdot = \begin{Bmatrix} 1, 0 \le t \le \tau + t_o^f \\ 0, otherwise \end{Bmatrix} \tag{201}$$

The second term in the complex envelope is a time-delayed version of the LFM signal. The chirp rate of the intercepted signal "$\hat{\mu}$" is estimated by the ES system. A false time delay "$t_o{}^{f}$" corresponding to the desired false target range is selected by the jammer and inserted into the signal. Finally, the last term in the complex envelope is a phase-shifted term, whose phase

shift is an effect, induced by time delay of a target at a range from the radar. The phase shift term is shown in terms of the false target range in equation (202):

$$\delta_0{}^f = -2\pi \hat{f}_c t_o{}^f = -2\pi \hat{f}_c \left(\frac{2R_o{}^f}{c} \right) = -4\pi \frac{R_o{}^f}{\hat{\lambda}} \tag{202}$$

Finally, the complete analytic false target signal for a stationary target with complex envelope terms expanded is shown in equation (203):

$$x_{rs}^f(t) = A_{rj}(t)\,\mathrm{Rect}\left(\frac{t - t_o^f}{\tau} \right) e^{j\pi\hat{\mu}(t-t_o)^2}\; e^{-j2\pi \hat{f}_c t_o^f}\; e^{j2\pi \hat{f}_c t} \tag{203}$$

Equation (203) is identical to equation (195), except that the false target complex envelope signal is expanded.

7.1.2 False Moving Target Echo

The false moving target signal, in "compact form" is shown in equation (204):

$$\underbrace{x_{rm}^f(t)}_{\text{False Analytic Signal}} = \underbrace{A_j(t)}_{\text{Amplitude Function}} \cdot \underbrace{\tilde{x}_{rm}{}^f(t)}_{\text{False Envelope Signal}} \cdot \underbrace{e^{j2\pi \hat{f}_c t}}_{\substack{\text{Estimated Carrier} \\ \text{Frequency Term}}} \tag{204}$$

By comparing the above equation to the "False Stationary Target Case", (equation (195)), it can be seen that the compact forms of these equations are similar.

However, the false *moving* target complex envelope has an additional Doppler frequency term, to simulate the effect of Doppler shift on a target, which is selected by the jammer to the required value. The additional terms are shown in equation (205) below:

$$\underbrace{\tilde{x}_{rm}{}^f(t)}_{\text{False Envelope Signal}} = \underbrace{\mathrm{Rect}\left(\frac{t - t_o^f}{\tau} \right)}_{\text{Rectangular Envelope}} \cdot \underbrace{e^{j\pi\hat{\mu}\left(t-t_o^f\right)^2}}_{\text{Time Delayed Term}} \cdot \underbrace{e^{j\cdot 2\pi\cdot f_d^f \cdot t}}_{\text{Doppler Term}} \cdot \underbrace{e^{-j\cdot 2\pi\cdot\left(\hat{f}_c + f_d^f\right)\cdot t_o^f}}_{\text{Phase Shifted Term}} \tag{205}$$

The complete false target analytic signal with complex envelope expanded is shown in equation (206):

$$x_{rm}^f(t) = A_{rj}(t)\,\mathrm{Rect}\left(\frac{t - t_o^f}{\tau} \right) e^{j\pi\hat{\mu}\left(t-t_o^f\right)^2}\; e^{j\cdot 2\pi\cdot f_d^f \cdot t}\; e^{-j\cdot 2\pi\cdot\left(\hat{f}_c + f_d^f\right)\cdot t_o^f}\; e^{j2\pi \hat{f}_c t} \tag{206}$$

This is the false moving target echo signal received at the DBR receiver.

7.1.3 False Moving Target Echo with Elevation Angle term:

Finally, the complete moving target signal of a false target at a height relative to the radar, is shown below, in compact form, in equation (207):

$$\underbrace{x_{rh}^{f}(t)}_{\text{False Analytic Signal}} = \underbrace{A_j(t)}_{\text{Amplitude Function}} \cdot \underbrace{\tilde{x}_{rh}{}^{f}(t)}_{\text{False Envelope Signal}} \cdot \underbrace{e^{j2\pi \hat{f}_c t}}_{\substack{\text{Estimated Carrier} \\ \text{Frequency Term}}} \tag{207}$$

The complex envelope with a phase shifted term caused by the target signal at an elevation angle relative to the radar is shown in red in equation (208):

$$\underbrace{\tilde{x}_{rh}{}^{f}(t)}_{\text{False Envelope Signal}} = \underbrace{\text{Rect}\left(\frac{t-t_o^f}{\tau}\right)}_{\text{Rectangular Envelope}} \cdot \underbrace{e^{j\pi\hat{\mu}\left(t-t_o^f\right)^2}}_{\text{Time Delayed Term}} \cdot \underbrace{e^{j\cdot 2\pi\cdot f_d^f \cdot t}}_{\text{Doppler Term}} \cdot \underbrace{e^{-j\cdot 2\pi\cdot\left(\hat{f}_c+f_d^f\right)\cdot t_o^f}}_{\text{Phase Shifted Term}} \cdot \underbrace{e^{j\psi^f(d)}}_{\substack{\text{Elevation Angle} \\ \text{Phase Shifted Term}}} \tag{208}$$

In a hypothetical situation, the jammer would select a phase shift function "$\psi^f(d)$" corresponding to the desired false target elevation angle. However, the DBR "Digital Beam-forming on Receive" processing would still be able determine the true elevation angle of the signal regardless of the modulation imparted on it by the jammer, unless the jammer could transmit a signal with a specific phase shift per antenna element, but this scenario could only be tested in a laboratory.

An alternative method of jamming the DBR elevation angle estimator was then investigated, called "Cross Eye Jamming".

7.1.4 False Moving Target Echo with Cross-Eye Jamming

The "Cross-Eye Repeater Jammer" is typically used against monopulse tracking radars. It uses two or more "coherent sources" that transmit signals that are out of phase with one another to distort the phase front of the EM wave. A fundamental assumption in phased interferometry as applied in the DBR is that the phase front of the target echo is uniform. A distorted phase front degrades the "Digital Beam-forming on Receive" function, for elevation angle estimation. A particular cross-eye repeater jammer described by D. Schleher in reference [4] is shown in Figure 136. This type of cross-eye jammer has two separate repeater paths, each with its own receiving and transmitting antenna and amplifiers to transmit the jamming signals. The intercepted radar signal is received in channel A and B. In the cross-eye configuration proposed by D. Schleher in reference [4], the false signals are transmitted back to the victim radar, without any other modulations except for the 180° Channel B phase shift. The advantage of using this cross-eye jammer configuration, is that "the signals radiated by the two coherent jamming sources arrive at the victim radar matched in amplitude and

180 degrees out of phase, independent of the AoA of the victim radar's signal at the jammer", D. Schleher (reference [4]). The phase front of the EM wave is therefore distorted when it arrives at the radar receive antenna, which prevents any angular measurements through phase interferometry. In this study, it is proposed that the repeater control logic and phase shifter is replaced by a DRFM. This will allow other signal modulations (time delay, Doppler shift etc.) to be inserted into the false signal together with the "cross-eye" phase shift term. Alternatively, the cross-eye jammer can be built as a separate configuration from the deception jammer, if the ES subsystem response time in estimating radar parameters is not sufficient. However, regardless of the configuration selected, the DBR Jammer would be able to deceive the radar in range and velocity estimation and simultaneously deny elevation angle measurement, if cross-eye jamming is used. It is quite likely that the radar would still be able to perform target azimuth estimation, but would not be able to designate the target in "radar track mode" for fire control of effectors (anti-aircraft guns or missiles).

Nevertheless, if more than one DBR is deployed, the radars would be able to triangulate the true target position based on target azimuth angle only, if the radars are operating in a network. On the other hand, if more than one DBR Jammer is deployed, azimuth angle jamming techniques could be used against the radar, if the jammers are in separate azimuth bins and are able to coordinate their jamming.

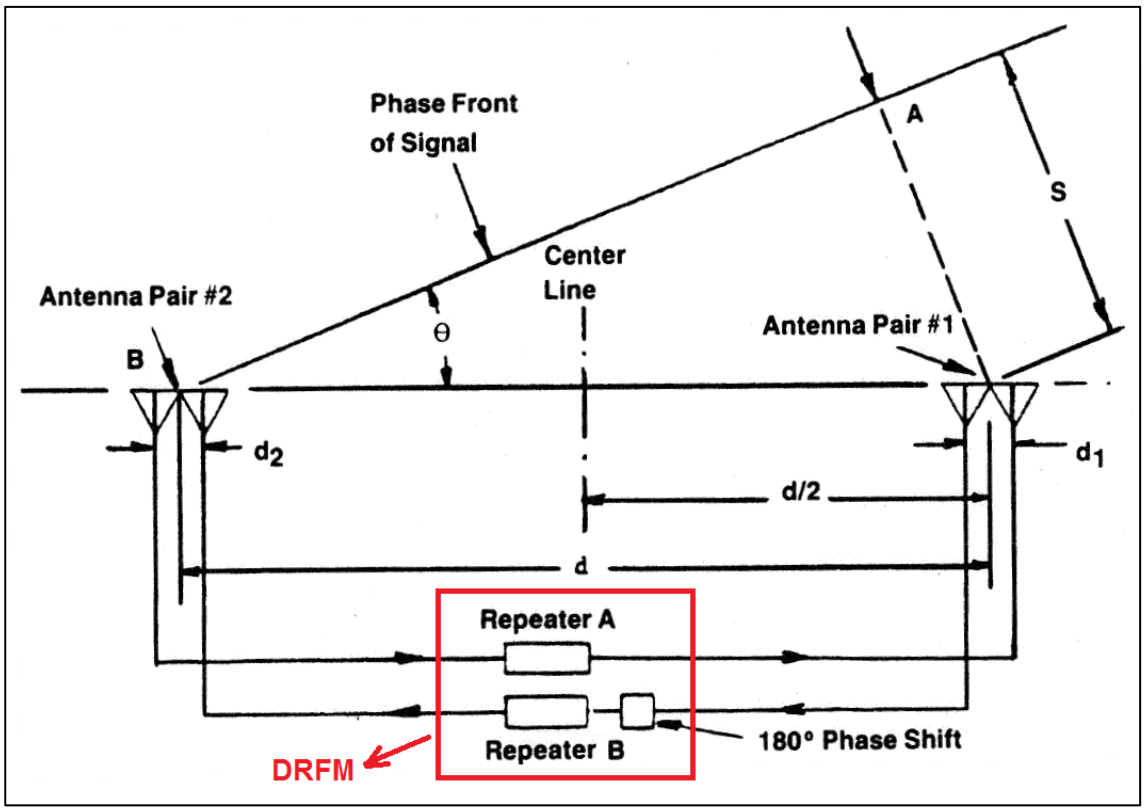

Figure 136: Cross-Eye Repeater Jammer (reference [4])

To simulate the cross eye jamming effect, a false moving target signal (equation (204)) is used. An arbitrary phase "ψ^c" is applied to it as shown by the term highlighted in red in the false moving target signal shown in equation (209):

$$\underbrace{\tilde{x}^f_{rc,0}(t)}_{\substack{\text{In Phase}\\ \text{False Envelope Signal}}} = \underbrace{\text{Rect}\left(\frac{t-t_o^f}{\tau}\right)}_{\text{Rectangular Envelope}} \cdot \underbrace{e^{j\pi\hat{\mu}\left(t-t_o^f\right)^2}}_{\text{Time Delayed Term}} \cdot \underbrace{e^{j\cdot 2\pi\cdot f_d^f\cdot t}}_{\text{Doppler Term}} \cdot \underbrace{e^{-j\cdot 2\pi\cdot\left(\hat{f}_c+f_d^f\right)\cdot t_o^f}}_{\text{Phase Shifted Term}} \cdot \underbrace{e^{j\psi^c(t)}}_{\substack{\text{In Phase Term}}} \quad (209)$$

Then a second signal similar, to the first one is simulated. However, the phase of the second signal is 180° out of synchronization with the first one. The "Out-of-Phase" moving false target signal with the a phase of "$\psi^c(t)+\pi$" is shown in equation (210):

$$\underbrace{\tilde{x}^f_{rc,180}(t)}_{\substack{\text{Out of Phase}\\ \text{False Envelope Signal}}} = \underbrace{\text{Rect}\left(\frac{t-t_o^f}{\tau}\right)}_{\text{Rectangular Envelope}} \cdot \underbrace{e^{j\pi\hat{\mu}\left(t-t_o^f\right)^2}}_{\text{Time Delayed Term}} \cdot \underbrace{e^{j\cdot 2\pi\cdot f_d^f\cdot t}}_{\text{Doppler Term}} \cdot \underbrace{e^{-j\cdot 2\pi\cdot\left(\hat{f}_c+f_d^f\right)\cdot t_o^f}}_{\text{Phase Shifted Term}} \cdot \underbrace{e^{j\psi^c(t)+\pi}}_{\text{Out of Phase Term}} \quad (210)$$

Finally, the two signals are added as shown in equation (211):

$$\underbrace{x^f_{rc}(t)}_{\text{False Analytic Signal}} = \underbrace{A_{rj}(t)}_{\text{Amplitude Function}} \cdot \underbrace{\tilde{x}_{rc,0}{}^f(t)}_{\substack{\text{In Phase}\\ \text{False Envelope Signal}}} \cdot \underbrace{e^{j2\pi\hat{f}_c t}}_{\substack{\text{Estimated Carrier}\\ \text{Frequency Term}}} + \underbrace{A_{rj}(t)}_{\text{Amplitude Function}} \cdot \underbrace{\tilde{x}_{rc,180}{}^f(t)}_{\substack{\text{Out of Phase}\\ \text{False Envelope Signal}}} \cdot \underbrace{e^{j2\pi\hat{f}_c t}}_{\substack{\text{Estimated Carrier}\\ \text{Frequency Term}}} \quad (211)$$

7.2 Human Intelligence (HUMINT)

HUMINT on a radar antenna is very informative, to an EW operator. For example if the antenna diameter is known for a circular antenna, "θ_{3dB}" and "G" can be calculated using the following equations from Barton [2]:

$$\theta_{3dB} \approx 70\frac{\lambda}{D_{circular}} \quad (212)$$

$$G \approx \frac{2}{3}\left(\frac{\pi D_{circular}}{\lambda}\right)^2 \quad (213)$$

Antenna parameters, if known "a priori", would improve jamming effectiveness of a radar. Substantial information with respect to antenna parameters can be obtained from the shape of the antenna, number of elements etc.

It is therefore entirely plausible that a potential adversary could obtain pictures of a radar antenna (trade show, brochure etc.) and use the data to obtain the necessary radar parameters.

For this reason it is important, to ensure that even basic general information such as a picture of the antenna, be controlled.

7.3 Jammer Signal Function, Simulation Flow

If the "False Target" switch is activated in the higher-level "calling" program, the jammer signal model, described in this section is activated. It loads the processed intercepted signal parameters from the "es_param.mat" file, applies amplitude to the false target signal and "passes" the discretized signal to the calling program. The SFD showing the jammer signal implementation in Matlab is shown in Figure 137. A description of the functions and programs in the "jammer_signals.m" SFD shown below, as well as their role in the simulation are listed in Appendix 14.1.

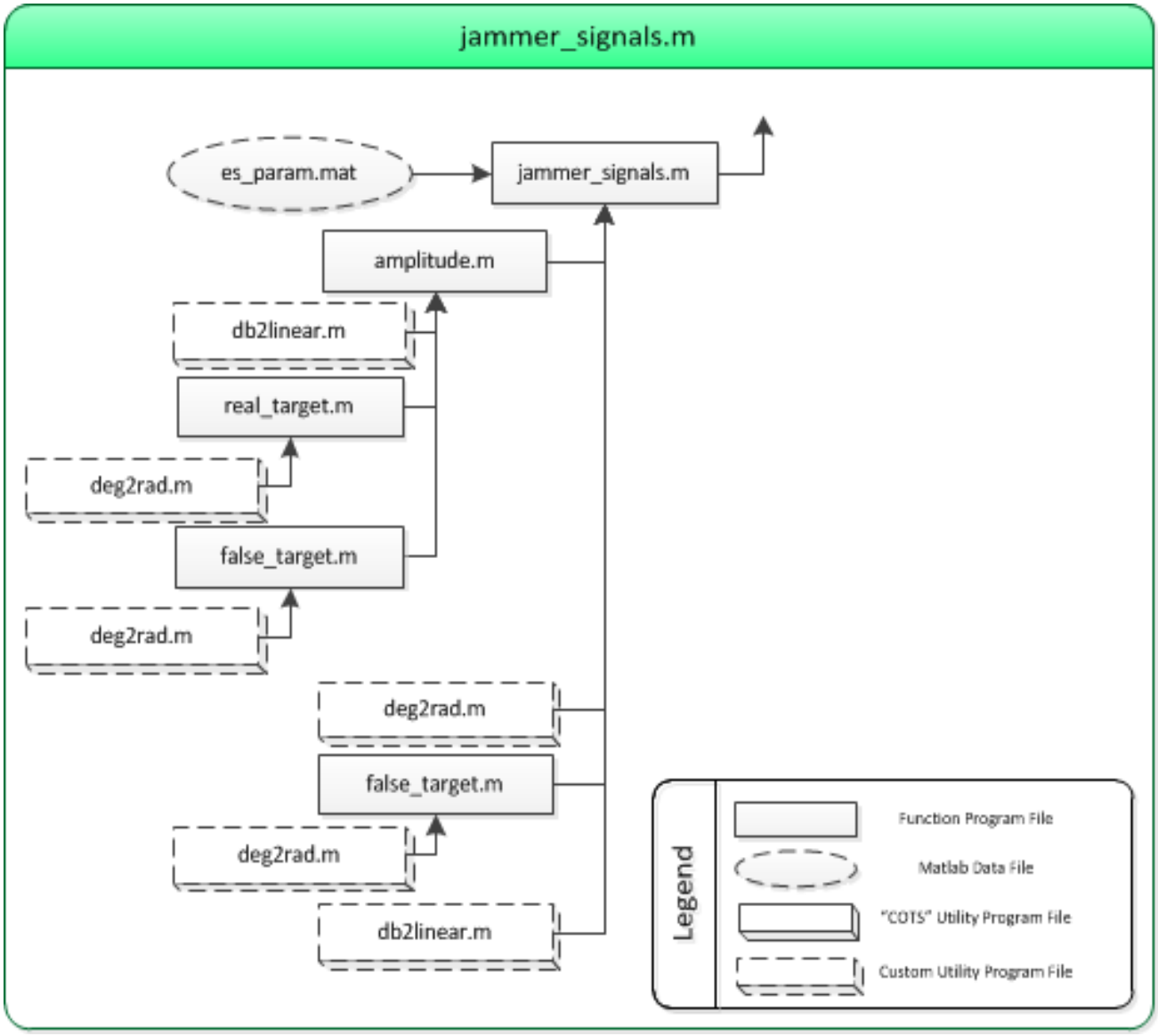

Figure 137: SFD, Jammer Signals

7.4 Electronic Attack Model, Results

Results from the electronic attack model simulation are presented in this section. The reader is advised to inspect the figures and refer to discussion *after all of the figures are presented*, for observations and conclusions on this section.

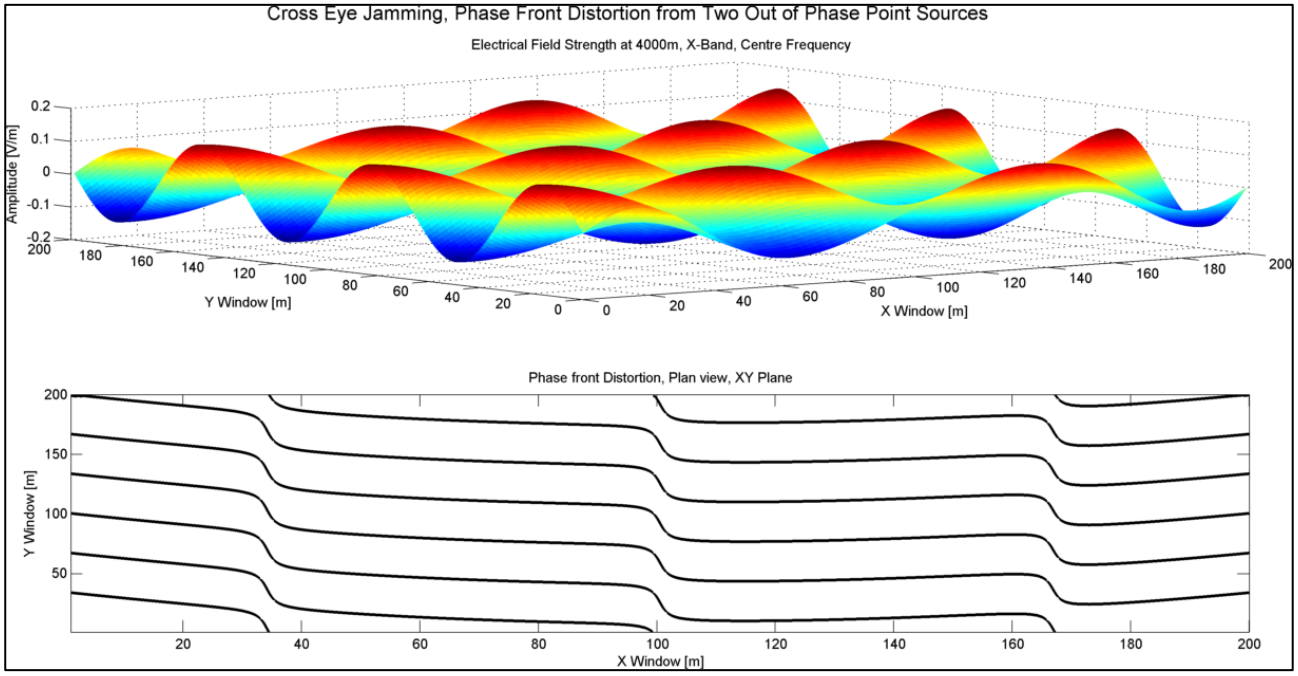

Figure 138: Electromagnetic Wave Phase Front Distortion due to Cross Eye Jamming

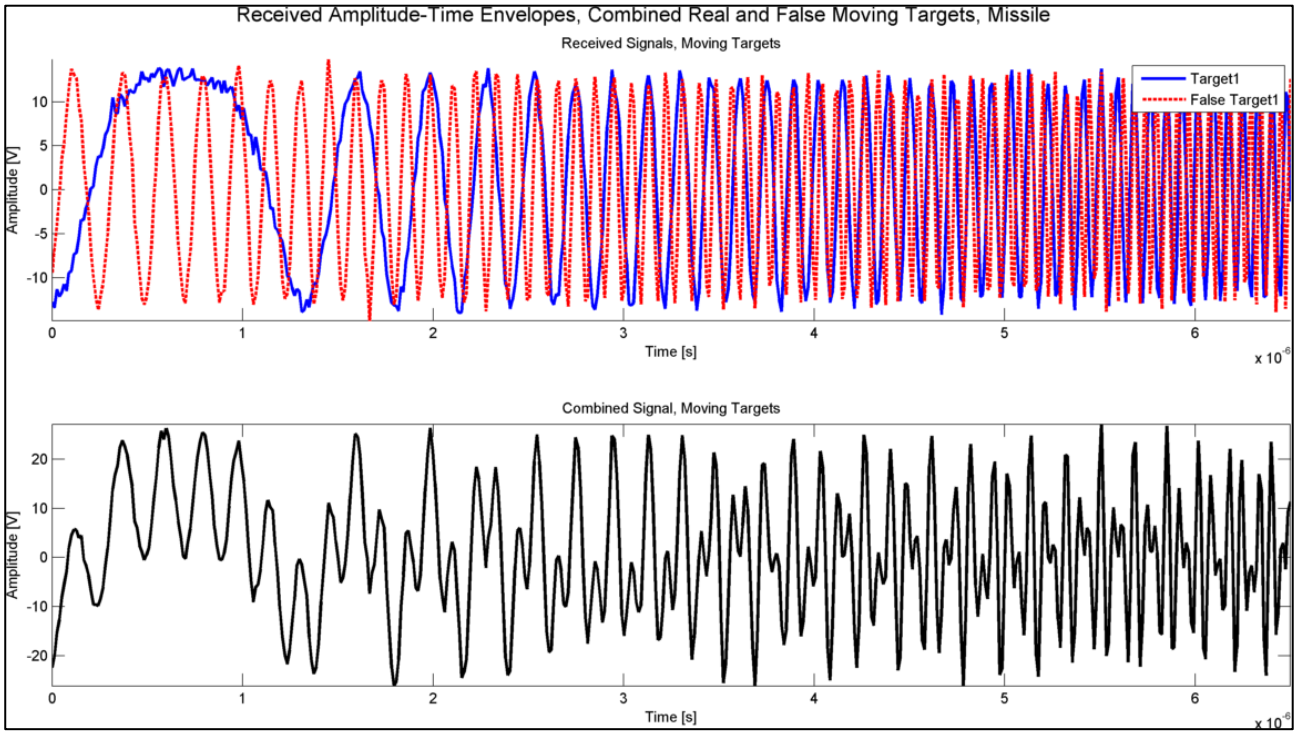

Figure 139: True Target Echo signal and False Jammer Signal

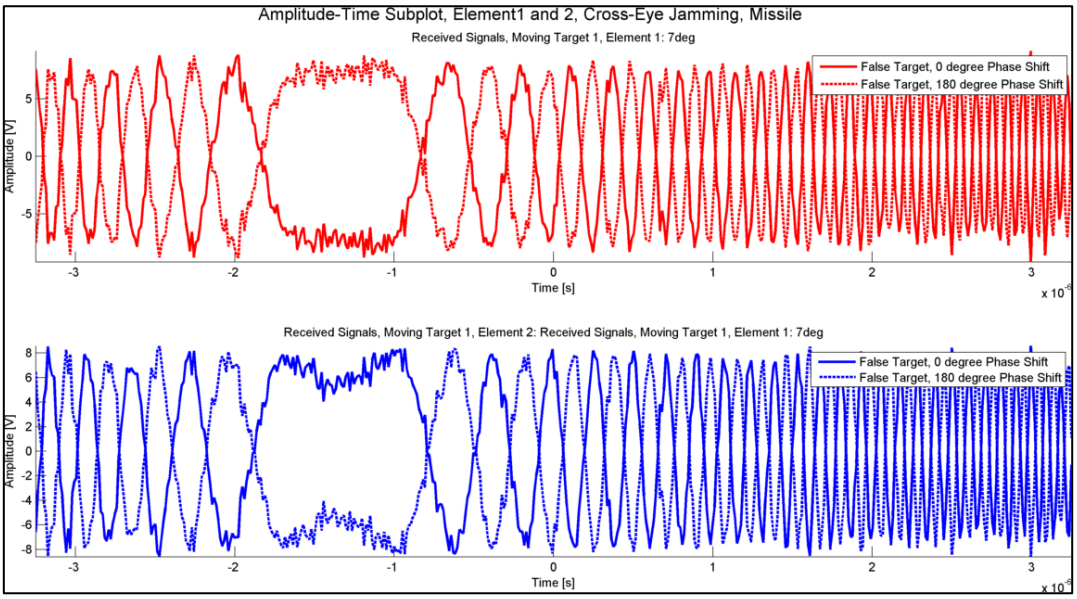

Figure 140: Cross Eye Jamming Signals at the Radar Receiver

7.5 Electronic Attack Model, Discussion of Results

A "commercial-off-the-shelf (COTS)" simulation called "CROSSEYE.m" written by D. Schleher as described in reference [4], was used to plot the EM field pattern of two coherent out of phase source emitters. This EM field pattern is shown in upper subplot of Figure 138. The pattern is plotted at the DBR centre frequency at a distance of 4km from the jammer for a rectangular "region" in space where the "region" is defined by "X Window" and "Y-Window" lengths. In the upper plot of Figure 138, the electric field intensity is plotted in a window of 200m by 200m, at a distance of 4000m from the jammer. The two out of phase point source antennas, induce constructive and destructive interference in the combined signal, which gives the EM wave its peculiar shape, as shown in Figure 138. The bottom subplot shows the phase front of the wave, as it would be viewed from above and the distorted shape of the phase front is clearly shown. The concept of phased interferometry used on the DBR, requires a *distinct linear phase front* to accurately estimate the elevation angle. However, cross-eye jamming *distorts the phase front* as shown, which is why it is able to jam the DBR elevation angle estimator.

Figure 139 shows the false Doppler shifted and time delayed signal transmitted by the Jammer, relative to the true target echo in the upper subplot. The lower subplot shows the combined signal at the radar. In this result, the false signal amplitude was set to be equal to the true target return. In practice, it would be 7 to 10dbW higher as stated in section 4.2.4.

In Figure 140, the two out of phase signals, received from the cross-eye jammer at the DBR receive antenna is shown. The upper subplot shows the signals at the first receive element of the antenna, while the lower subplot shows the signal at the second element. The jammer is at an angle of 5° to the radar in this scenario. From this plot, it can be seen that the two signals are matched in amplitude and exactly 180° out of phase.

8 Signal Models, Radar Receiver, Single Plot Mode

8.1 Radar Receiver, Single Plot Mode, Overview

In this chapter the estimation of "*single-plot*" target parameters for true and false target detection by the radar receiver are discussed and analysed. Chapter 9 is the second chapter on radar receiver operation, but the estimation of true and false target parameters from "*multiple-plots" (or "tracks")* is discussed there. A "plot" is a single radar measurement point, containing target coordinates in range, Doppler, azimuth and elevation angle. However, in this simulation the targets are assumed to approach along a single azimuthal direction. This assumption has been explained in section 1.2.2.

In other words, the analysis of target information from a single "*Range-Doppler-Elevation Angle"* bin is discussed in this chapter, while the analysis of *"Range-Doppler-Elevation Angle"* information over multiple bins is discussed in Chapter 9.

Within the overall simulation, the work described in this chapter can be placed into context by referring to Figure 141. The portion of the scenario definition, shown encircled in red is the subject of discussion in this chapter.

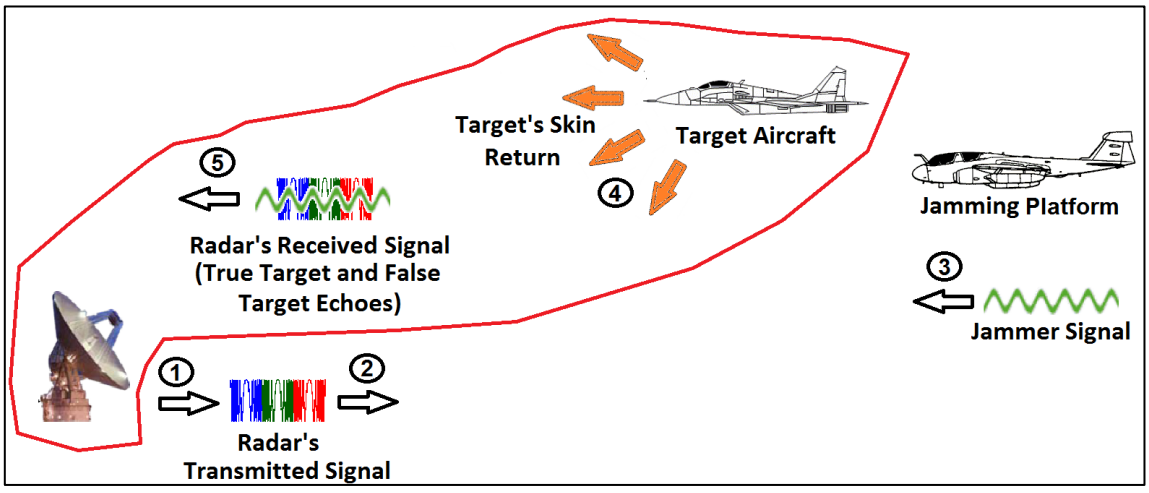

Figure 141: Scenario Definition, "Radar Receives Signals"

Target echoes from the true target metallic surface and synthetic false signals from the DBR Jammer on the Jammer Platform are received at the radar and processed. The aim in this portion of the simulation is to determine target range, velocity and elevation angle at a fixed azimuthal angle relative to the radar. Mathematics describing the signal models is discussed initially followed by the SFD and simulation results. Then a *detailed discussion* of the results obtained is included.

8.2 True Target Echo Signal

The equations describing the signal reflected from the surface of a target at a range "R_o", elevation angle "ϕ" and travelling at a velocity "v" are described in this section. The signal model equations are presented in the order of increasing complexity, with the "stationary target" described initially, following by the moving target. Finally, elevation angle is included in the moving target signal model. The simulation uses the specified radar parameters listed in Table 6 and Table 7 of section 3.1.1.

8.2.1 True Stationary Target Echo

A stationary target is defined as a target without any velocity (hence Doppler shift) at a range "R_o" from the DBR. This signal model is a notational construct used to introduce the complete signal model with all of its components. It is also used in the simulation of the DBR range match filter signal processing but this is discussed in detail, later in this chapter.

The complete LFM pulse received from a stationary target as defined in Mahafza [1] is:

$$\underset{\text{Analytic Signal}}{x_{rs}(t)} = \underbrace{A_{rr}(t)}_{\text{Amplitude Function}} \cdot \underset{\text{Envelope Signal}}{\tilde{x}_{rs}(t)} \cdot \underbrace{e^{j2\pi f_c t}}_{\text{Carrier Frequency Term}} \tag{214}$$

Where:

$$\underset{\text{Envelope Signal}}{\tilde{x}_{rs}(t)} = \underbrace{\text{Rect}\left(\frac{t-t_o}{\tau}\right)}_{\text{Rectangular Envelope}} \cdot \underbrace{e^{j\pi\mu(t-t_o)^2}}_{\text{Time Delayed Term}} \cdot \underbrace{e^{-j2\pi f_c t_o}}_{\text{Phase Shifted Term}} \tag{215}$$

$$\text{Rect}\left(\frac{t-t_o}{\tau}\right) = \begin{Bmatrix} 1, & 0 \le t \le \tau + t_o \\ 0, & otherwise \end{Bmatrix} \tag{216}$$

$$\delta_0 = -2\pi f_c t_o = -2\pi f_c \left(\frac{2R_o}{c}\right) = -4\pi \frac{R_o}{\lambda} \tag{217}$$

From equation (214), it can be seen that the complete signal model is made up of three parts; the amplitude function "$A_{rr}(t)$", the complex envelope and the carrier frequency term.

To derive the equation for "$A_{rr}(t)$" as shown in equation (218) below, the radar range equation as defined in equation (2.8) in reference [6] was used. The relationship between signal-level amplitude and system-level RF power was described in detail in section 1.2.3.

$$A_{rr}(t) = 10\sqrt{\frac{P_{tx}^r G_{tx}^r G_{rx}^r G_{PC} G_{DOP} \lambda^2 \sigma(t)}{(4\pi)^3 R_o^4(t) L_{other}^r}} \tag{218}$$

From equation (214) it can be seen that the dependent variable "A_{rr}" is a function of time, as well as the independent random variables "σ" and "R_o". Defining the independent variables in this manner allows random values from corresponding Swerling target model probability distributions and target ranges per time step to be used, in the NRT simulation. The instantaneous target RCS per time step "$\sigma(t)$" was generated randomly from an "Exponential" or "Chi-Square" distribution. The Swerling model selected controls the choice of the probability distribution for modelling of the stochastic target RCS fluctuation.

The complex envelope term shown in equation (215) can be broken down further, as indicated in the equation.

The rectangular envelope term bounds the "continuous" LFM signal to a pulse-width length to simulate the effect of pulsing of the signal.

A time-delayed version of the transmitted LFM signal is one of the components of the complex envelope. The time delay "t_o" is caused by a delay in the transmitted signal when it is reflected signal from the target. A phase shift term proportional to the target range "R_o" also forms part of the complex envelope.

8.2.2 True Moving Target Echo

A moving target LFM echo (with a velocity and Doppler shift at a range "R_o"), is described in Mahafza [1] as:

$$\underbrace{x_{rm}(t)}_{\text{Analytic Signal}} = \underbrace{A_{rr}(t)}_{\text{Amplitude Function}} \cdot \underbrace{\tilde{x}_{rm}(t)}_{\text{Envelope Signal}} \cdot \underbrace{e^{j2\pi f_c t}}_{\text{Carrier Frequency Term}} \tag{219}$$

$$\underbrace{\tilde{x}_{rm}(t)}_{\text{Envelope Signal}} = \underbrace{\text{Rect}\left(\frac{t-t_o}{\tau}\right)}_{\text{Rectangular Envelope}} \underbrace{e^{j\pi\mu(t-t_o)^2}}_{\text{Time Delayed Term}} \cdot \underbrace{e^{j2\pi f_d t}}_{\text{Doppler Term}} \cdot \underbrace{e^{-j2\pi(f_c+f_d)t_o}}_{\text{Phase Shifted Term}} \tag{220}$$

From equation (220), the effect of the Doppler frequency shift caused by the moving target is indicated by the terms highlighted in red. Compared to the "stationary target" complex envelope signal shown in equation (215), it can be seen that an additional Doppler frequency complex sinusoid is inserted into the signal model. The phase of the "Phase shifted term" is also translated by the target's Doppler frequency shift.

Nevertheless, the general structure of the signal model remains the same to the stationary target signal model.

8.2.3 True Moving Target Echo with Elevation Angle Term

Finally, the target elevation angle is inserted into the signal model as an additional complex sinusoid over and above the moving target complex envelope signal definition of equation (220).

A target echo signal arriving at an elevation angle "$\hat{\phi}$" can be modelled as a plane wave arriving at the antenna as described by R McAulay [33]. The wave arrives at an elevation angle "ϕ" relative to the radar antenna. This occurrence is depicted in Figure 142.

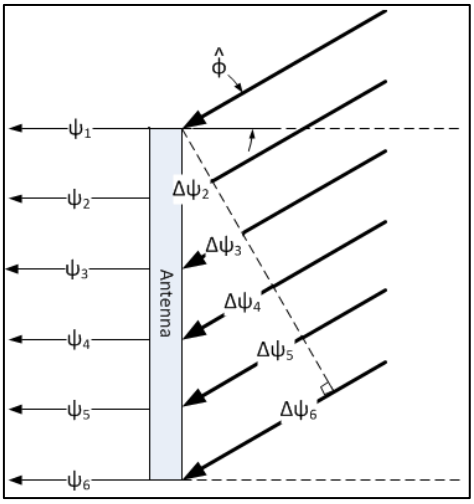

Figure 142: DBR Phased Interferometry

The component of the wave at element 1 has an arbitrary phase shift. The first element relative phase shift "$\Delta\psi_1$" is zero. However, relative to element 1, the subsequent waves experience a phase shift due to the increased path length, they travel to the antenna's receiving elements. This is shown in R McAulay [33] as:

$$\psi(d) = \psi_i + \Delta\psi_i, \quad i = 1,2,\ldots Q \tag{221}$$

$$\Delta\psi = \frac{2\pi}{\lambda} d \sin\phi \tag{222}$$

The absolute phase shift is combined with other target signal components as follows:

$$\tilde{x}_{rh}(t) = \tilde{x}_{rm}(t) e^{j\psi(d)} \tag{223}$$

$$\underset{\text{Analytic Signal}}{x_{rh}(t)} = \underbrace{A_{rj}(t)}_{\text{Amplitude Function}} \cdot \underset{\text{Envelope Signal}}{\tilde{x}_{rh}(t)} \cdot \underbrace{e^{j2\pi f_c t}}_{\text{Carrier Frequency Term}} \tag{224}$$

$$\underset{\text{Envelope Signal}}{\tilde{x}_{rh}(t)} = \underbrace{\text{Rect}\left(\frac{t-t_o}{\tau}\right)}_{\text{Rectangular Envelope}} \cdot \underbrace{e^{j\pi\mu(t-t_o)^2}}_{\text{Time Delayed Term}} \cdot \underbrace{e^{j2\pi f_d t}}_{\text{Doppler Term}} \cdot \underbrace{e^{-j2\pi(f_c+f_d)t_o}}_{\text{Phase Shifted Term}} \cdot \underbrace{e^{j\psi(d)}}_{\substack{\text{Elevation Angle} \\ \text{Phase Shifted Term}}} \tag{225}$$

The elevation angle complex sinusoid term is inserted into the moving target signal as indicated by the term in red, in equation (225).

Thereafter the receiver noise modelled using equation (15) is added to the signal per step as shown in equation (226):

$$x_{rh}^{f}(t) = \text{Rect}\left(\frac{t-t_o}{\tau}\right) e^{j\pi\mu(t-t_o)^2}\ e^{j2\pi f_d t}\ e^{-j2\pi(f_c+f_d)t_o}\ e^{j\psi(d)} e^{j2\pi f_c t} + noise(t) \qquad (226)$$

Equation (226) finally defines the complete true target signal model as simulated.

8.3 Radar Receiver Signal Processing

After the target signals (both true and false) are simulated, they are passed to the radar receiver models for range, velocity and elevation angle estimation. In this section, match filtering for range estimation is discussed initially, followed by the Doppler filtering for velocity estimation. Finally the "phased interferometry spatial FFT" is applied to estimate target elevation angles.

8.3.1 Range Estimation

The match filter is applied to the received samples for target range estimation because the algorithm maximizes the signal power at a time delay corresponding to the range of the target relative to the range bin. Range bin size corresponds to the distance travelled by the signal in a "pulse-width's" time duration.

The matched filtered signal of a target for the continuous case is defined as ([6]):

$$y(t) = \int_{-\infty}^{\infty} \tilde{x}_r(t)\,\tilde{x}^*(t-t_d)\,dt \qquad (227)$$

The integral above, can be also be calculated, using the "Inverse Fast Fourier Transform" (IFFT) of the FFT's of the complex envelope signal and the "replica". The replica is copy of the "complex conjugate" of the transmitted complex envelope.

$$y(t) = IFFT\left\{FFT\left(\tilde{x}_r(t)\right) FFT\left(\tilde{x}^*(t)\right)\right\} \qquad (228)$$

The discrete "IFFT" is defined as ([3]):

$$x(n) = IFFT\left\{X(k)\right\} = \frac{1}{N}\sum_{k=1}^{N} X(k)\, e^{j2\pi\frac{(n-1)(k-1)}{N}}, \quad n = 1,2,\ldots,N-1 \qquad (229)$$

The above method of calculating the matched filter response is called the "IFFT of the FFT's". Alternatively the cross correlation of the complex envelope and replica can be calculated to determine the matched filtered response. It is ([6]):

$$y(t) = \hat{R}_{xy}(m) = \sum_{n=0}^{M-m-1} \tilde{x}_r(n+m)\,\tilde{x}^*(m), \quad m = 1,2,\ldots,2M-1 \qquad (230)$$

The cross correlation method is directly applied to the time domain signal, while the IFFT based match-filtering method converts the signal and operates on it, in the frequency domain. Both methods were used to estimate target range.

It was assumed that the Doppler frequency term (equation (220)) was removed before match filtering for range. The presence of an uncompensated Doppler term in the return signal causes "range-Doppler coupling", which degrades the match filtered estimation accuracy. This is a general problem with LFM waveforms. Nevertheless, the problem can be overcome using the signal-processing techniques described by B. Mahafza [1].

8.3.2 Velocity Estimation

The "Doppler Processing" technique was used to determine the target velocity as described in Richards [6]. If a target is moving, it will have a Doppler frequency shift in proportion to its velocity. The Doppler frequency shift or "Doppler shift" was estimated, by calculating the DFT of the moving target envelope signal ($\tilde{X}_{rm}$). It was found using the equation shown below ([3]):

$$\tilde{X}_{rm}(k) = FFT\left\{\tilde{x}_{rm}(n)\right\} = \sum_{n=1}^{N} \tilde{x}_{rm}(n) e^{-j2\pi\frac{(n-1)(k-1)}{N}}, \quad k = 1, 2, \ldots, N-1 \qquad (231)$$

This spectrum was calculated over the "slow time" of one CPI in order to obtain the resolution necessary to detect the target Doppler shift from the received signal spectrum. The spectrum was also normalised by "n_p".

Every point in the calculated spectrum is shifted by the Doppler shift. However, the amount translated by the spectrum cannot be found easily, by estimating the translation between maximums or minimums, or other unique reference points in the spectrum. This is because these characteristic "reference points" are difficult to identify uniquely between the un-shifted spectrum and the shifted spectrum. Therefore, a "Pseudo Match Filtering" technique was used to determine the amount of shift between un-shifted spectrum and its Doppler shifted target echo spectrum. The "Spectrum of Spectrums" was calculated which maximised the spectrum energy at the Doppler Shifted frequency as shown in Figure 162 and Figure 163. The "Spectrum of Spectrums" was calculated using the following equation:

$$\tilde{XX}_{rm}(k) = IFFT\left\{FFT\left(\tilde{X}_{rm}(k)\right) FFT\left(\tilde{X}(k)\right)\right\} \qquad (232)$$

The technique worked reliably and did not require any characteristic reference points for calculation of the translation (or "Doppler shift") between the two waveforms (spectrums in this case).

A window function is typically applied to the time domain signal prior to Doppler filtering to reduce side lobes which increasing velocity estimation accuracy with Doppler filtering. Two negative consequences of windowing are that the main lobe of the target Doppler spectrum is broadened and attenuated in amplitude. These two effects degrade the Doppler filtering accuracy. Nevertheless, "Kaiser" and "Chebyshev" windows were applied to the time domain signals prior to Doppler filtering. The Kaiser window was selected for its low side lobes over other window types, while the Chebyshev window was selected because it allows the narrowest possible main lobe for a specified sidelobe level.

8.3.3 Elevation Angle Estimation

Once the complete target signal (either true or false) "$x_{rh}(t)$" (equation (225)) or "$x_{rh}^{f}(t)$ (equation (207))" or "$x_{rc}^{f}(t)$ (equation (211))" is received, the carrier frequency term is removed (through coherent demodulation) leaving only, the complex envelope of the received target signal.

A "spatial FFT" is then formed across the elements of the antenna array per time step, in order to determine the AoA of the signal. In this case, the AoA is the elevation angle "ϕ".

Usually an FFT is used to filter the signal for target Doppler frequencies. In this case, the time domain signal consists of samples *separated in time* and the output of the FFT are samples *separated in frequency*. The spatial FFT on the other hand, operates on a signal composed of samples that are *separated in distance* and outputs samples that are *separated in AoA.*

To illustrate the relationship amongst antenna distance samples, signal time samples and spectrum FFT points, an example is given:

- If Q=6, M=128, N=256, the spatial FFT is performed over the [M(128) x Q(6)] matrix over N (256) FFT points.
- Then the squared magnitude of the matrix is calculated. The result is a [M(128) x N(256)] matrix <u>per</u> frequency. In this application each signal at X or L Bands has three distinct frequency components.
- The M (128) columns are added to generate a [1 x N (256)] vector, which, when plotted has a peak at the target elevation angle.
- Then the [M(128) x N(256)] spatial FFT is calculated using the formula below:

$$\tilde{X}_{rh}(k) = \left| FFT\left\{\tilde{x}_{rh}(n)\right\}\right|^2 = \left|\sum_{n=1}^{N} \tilde{x}_{rh}(n)\, e^{-j2\pi\frac{(n-1)(k-1)}{N}}, \quad k = 1, 2, \ldots, N-1\right|^2 \qquad (233)$$

Because a sum is performed over the array, the FFT is termed “Cumulative FFT”. The SFD for the Radar Elevation Angle Estimator is shown in Figure 146. The implementation of the elevation angle estimation algorithms described in this section, was implemented in Matlab according to this SFD.

8.4 Radar Receiver, Simulation Flow

The Radar Receiver simulation model is the *main* simulation model developed for the radar. It integrates and controls the range, velocity and elevation angle estimator modules. The Radar Receiver SFD for the radar receiver, is shown in Figure 143.

Program controls listed in section 3.3 are set in the “radar.m” program, depicted by Figure 143. This model calls the three primary radar functions “myrange.m (Figure 144), mydoppler_filter.m (Figure 145), my_height.m (Figure 146)” as shown in Figure 143.

Radar setup parameters and jammer parameters are loaded from file and passed to these functions and their outputs are integrated in the Radar Model.

The Radar Receiver model also integrates the “Single Plot Mode” and “Multiple Plot Mode” controls, inputs and outputs. Any of the desired radar receiver outputs in the range, velocity estimator or elevation angle estimators can be controlled and output through the “radar.m” function. The program inputs, outputs and controls were discussed in detail in chapter 3.

A description of all the functions and programs in the DBR Receiver SFD’s as well as their role in the simulation are listed in Appendix 14.1.

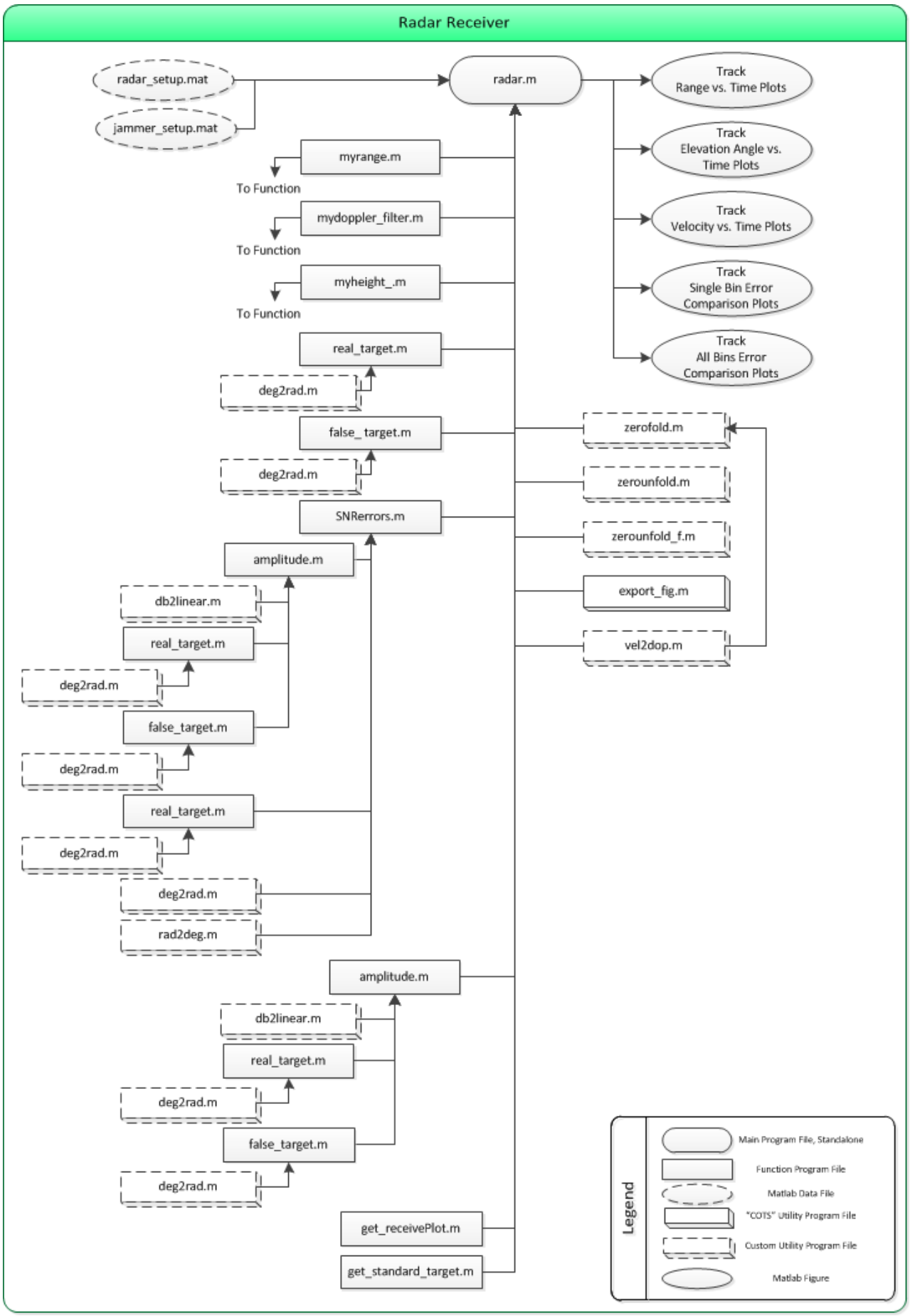

Figure 143: SFD, Radar Receiver

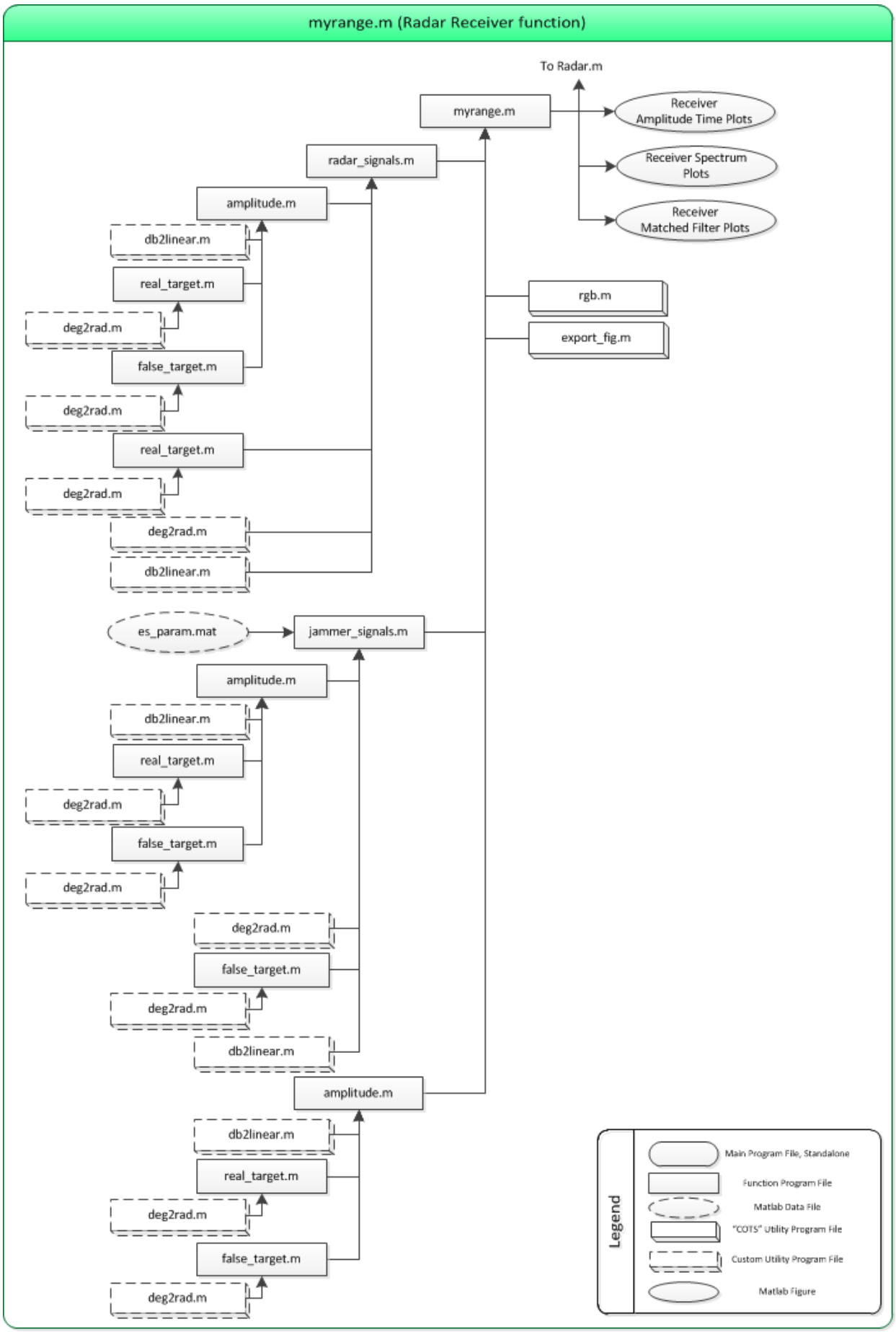

Figure 144: SFD, Range Estimator

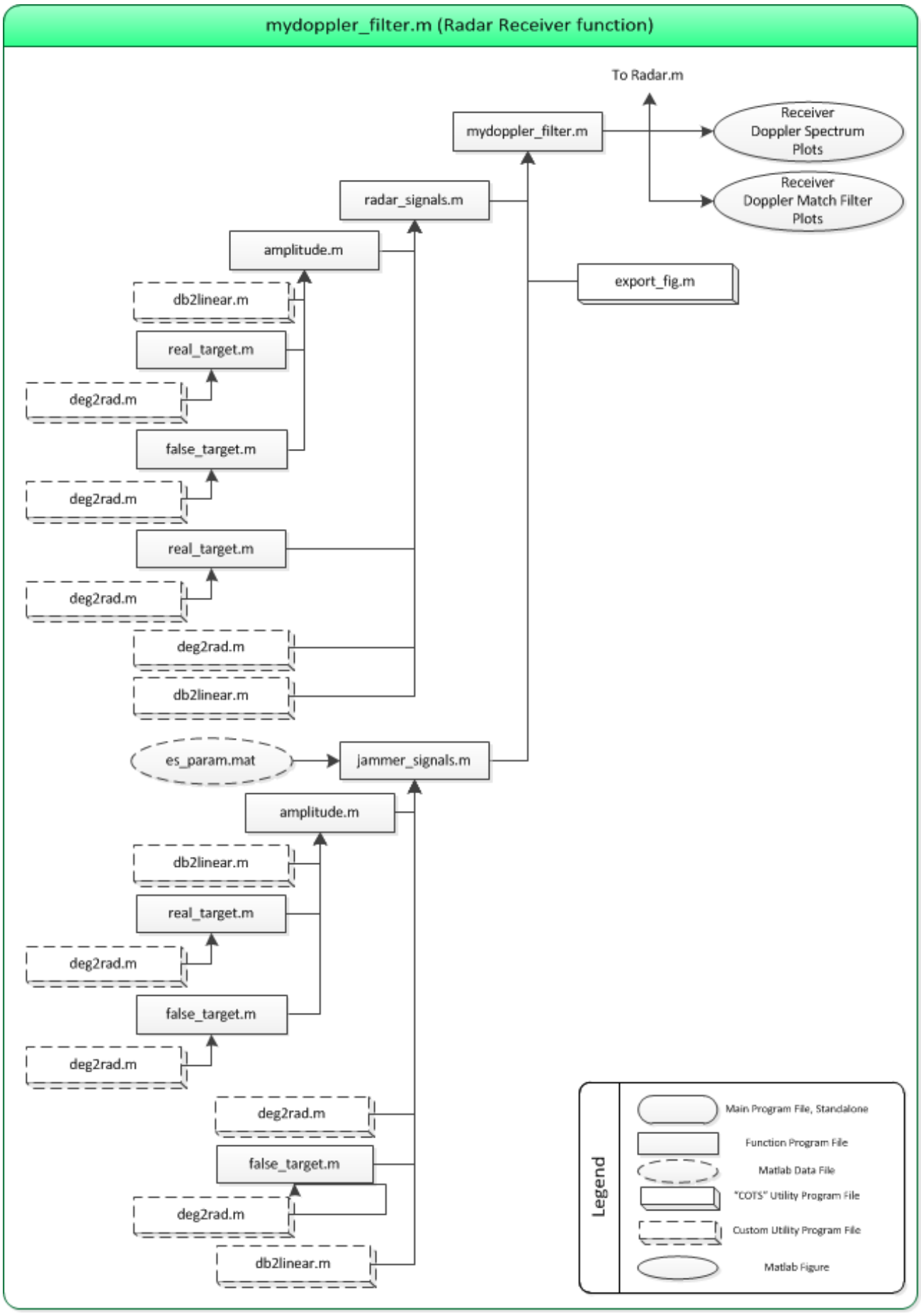

Figure 145: SFD, Velocity Estimator

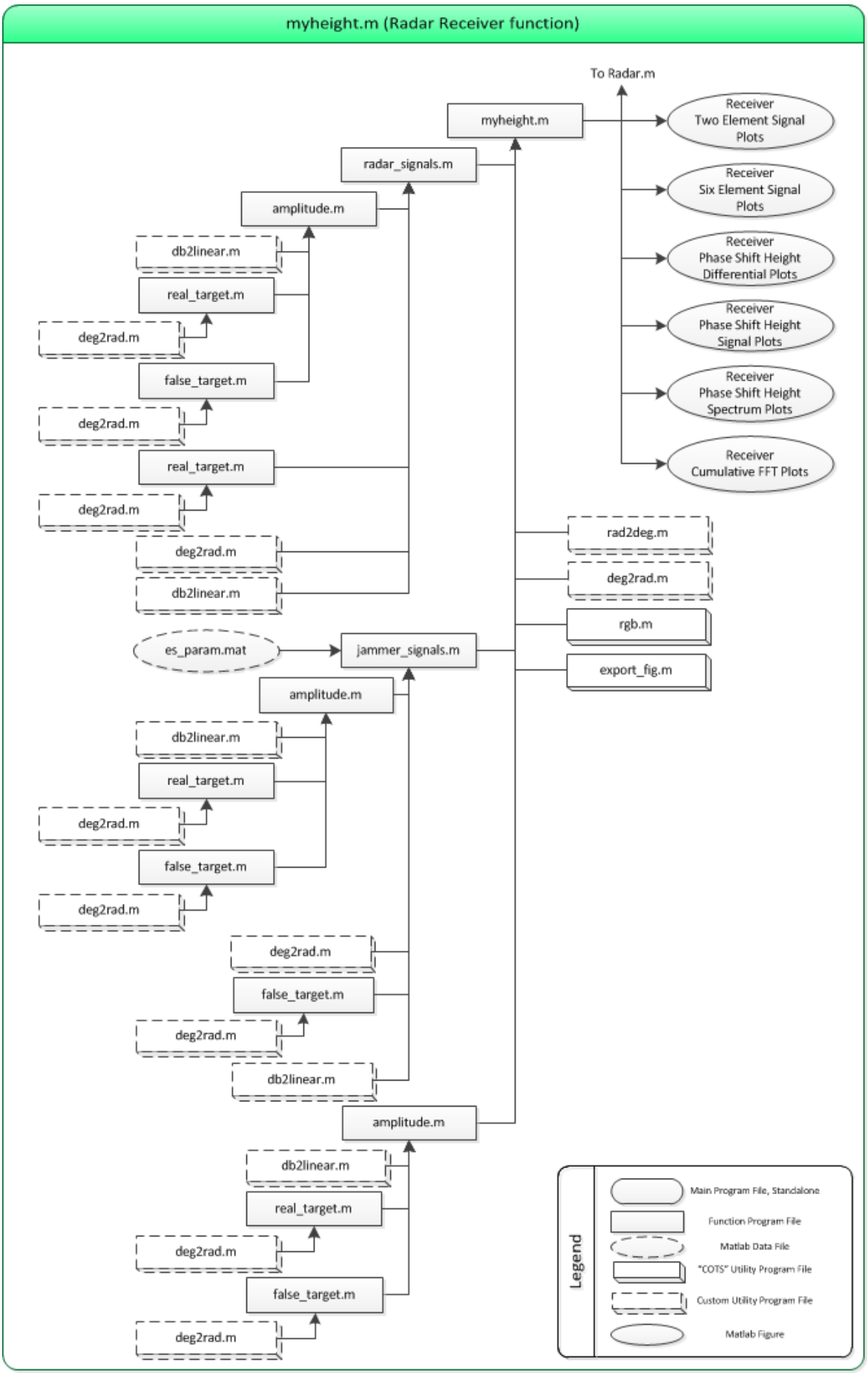

Figure 146: SFD, Elevation Angle Estimator

8.5 Radar Receiver, Single Plot Mode, Scenario Description

The two scenarios used to test the DBR range, velocity and elevation angle estimators in "single-plot" mode is discussed in this section.

In the first scenario, a missile and fixed wing target are detected in a range bin located 44.025 km from the radar. The range of the two targets relative to the *range bin coordinate system* is then selected, at a single point. The targets are also travelling at true unfolded velocities of 102.5m/s and 432.5 m/s and elevation angles of 2° and 7°, respectively. The DBR X-Band system is tested using scenario 1 while the L-Band subsystem is tested using scenario 2.

The second scenario simulates a helicopter and missile at "Range to Bin + Bin Range" from the radar. In other words, the helicopter is at a range of 100km + 4km =104 km from the radar. These ranges were selected to ensure that the *SNR* is small (i.e. large range), which implies a small signal amplitude, thereby challenging the radar's target parameter estimators.
Scenario 2 also investigates the behaviour of the radar receiver outputs when two false targets are injected into the radar, in order to mask the true targets. The scenarios tested in the entire simulation have already been discussed in detail in section 1.2.1.

	Target Type	Range to Bin [m]	Bin Range [m]	Unfolded Velocity [m/s]	Folded Velocity [m/s]	Unwrapped Elevation Angle [deg	Wrapped Elevation Angle [deg]
True Target 1	Fixed Wing	44025	200	102.5	20	23.2	7
True Target 2	Missile	44025	-100	432.5	20	18.2	2
False Target 1	Missile	44025	200	240	20	21.2	5

Table 19: X-Band, Single Plot Mode Scenarios

	Target Type	Range to Bin [m]	Bin Range [m]	Unfolded Velocity [m/s]	Folded Velocity [m/s]	Unwrapped Elevation Angle [deg	Wrapped Elevation Angle [deg]
True Target 1	Rotary Wing	100000	4000	124	15	19.2	3
True Target 2	Missile	100000	15	471	35	28.3	4
False Target 1	Rotary Wing	100000	3900	119	10	21.2	5
False Target 2	Missile	100000	0	466	30	31.3	7

Table 20: L-Band, Single Plot Mode Scenarios

8.6 Single Plot Mode Range Estimator, Results

The Radar Target Range Estimator output plots are presented and discussed in this section. The reader is advised to inspect the figures and refer to discussion after the figures for observations and conclusions for this section.

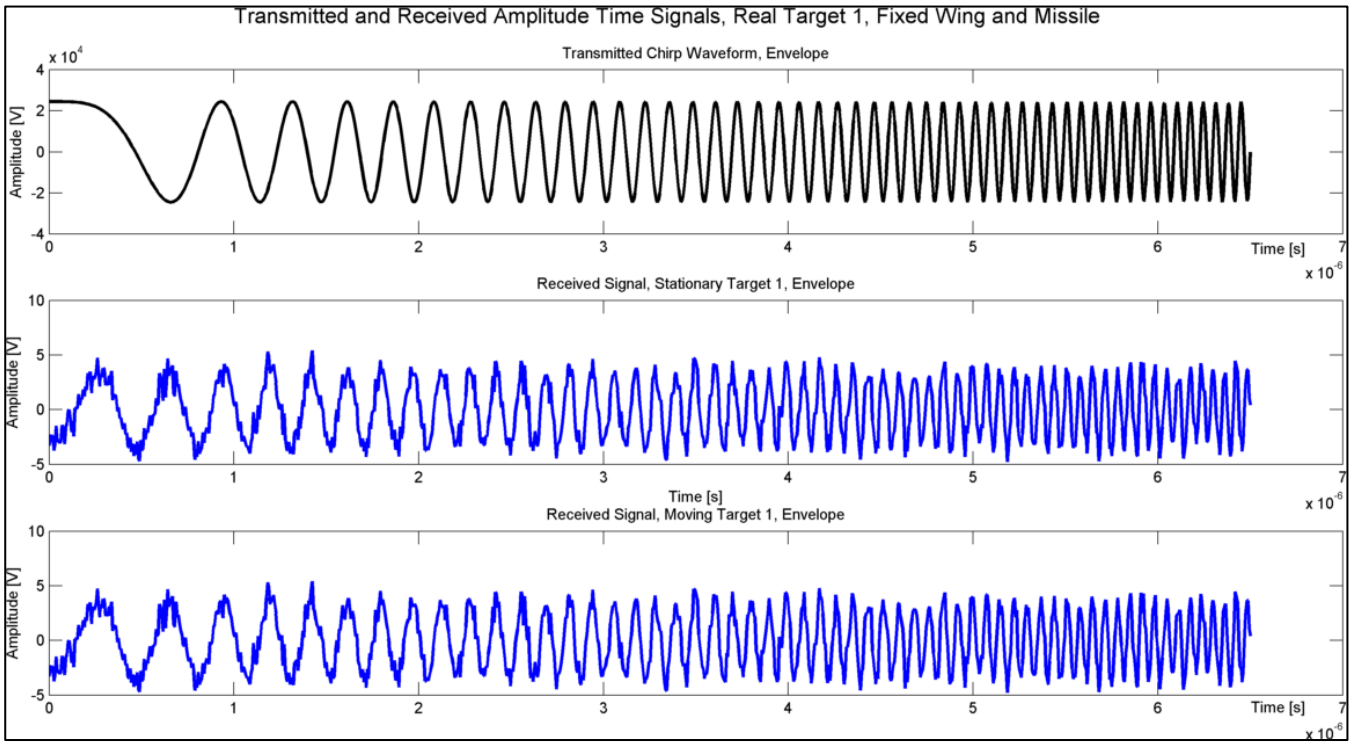

Figure 147: X-Band Radar Signals for Fixed Wing Target, Noise and Amplitude

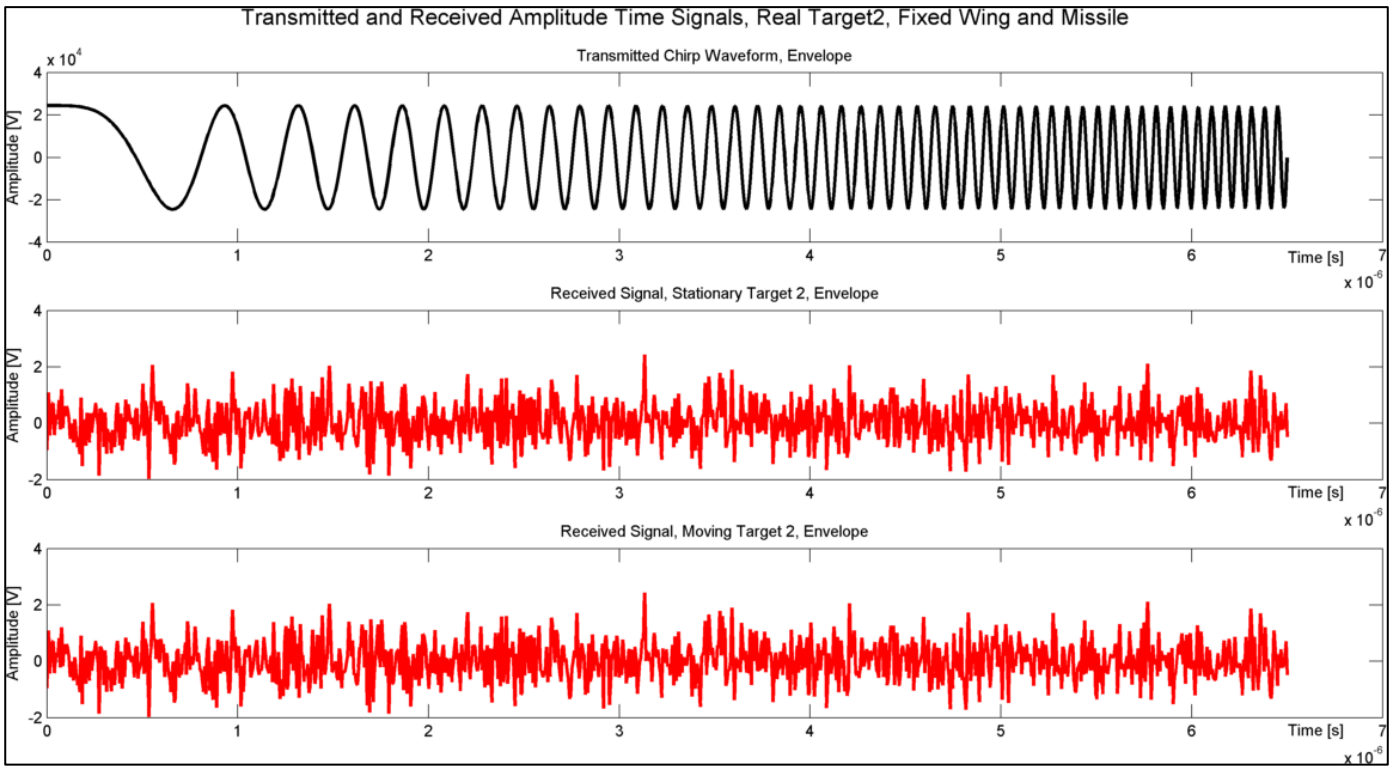

Figure 148: X-Band Radar Signals for Missile, Noise and Amplitude

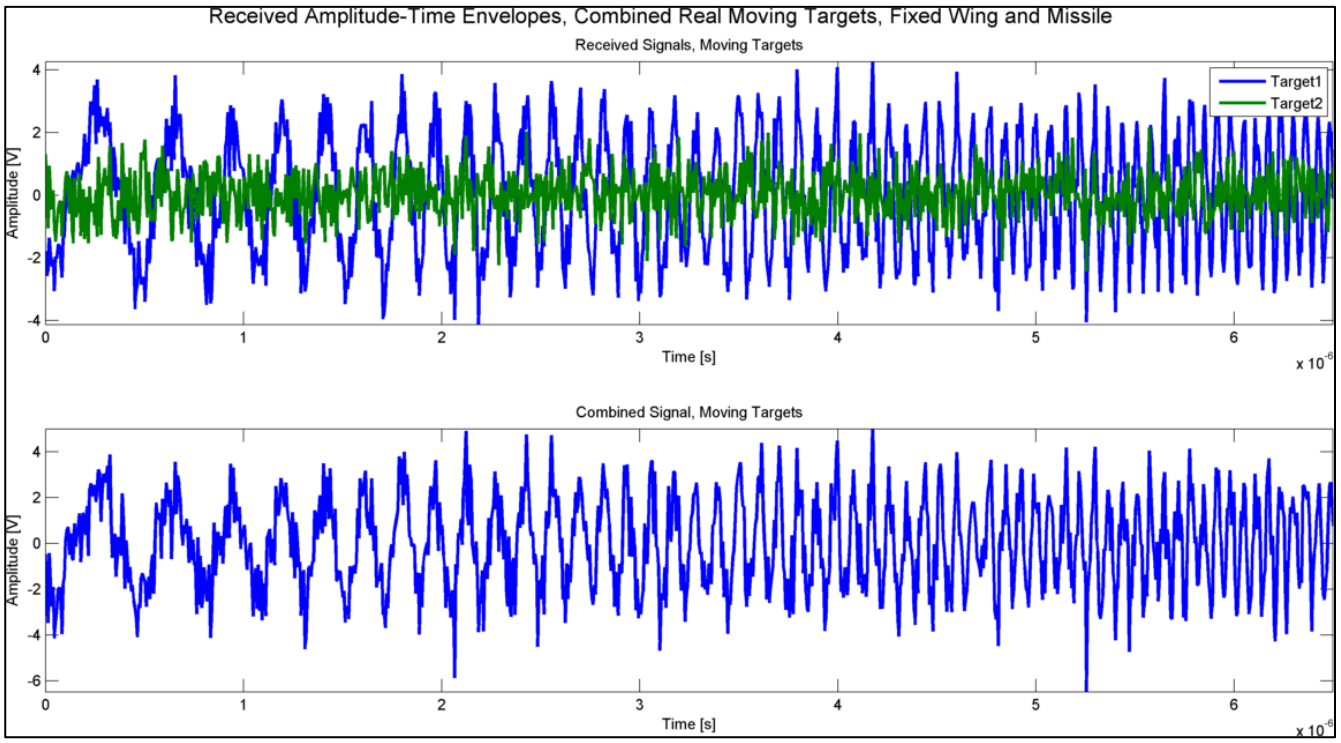

Figure 149: Combined Target Signals at X-Band for a Missile and Fixed Wing Target

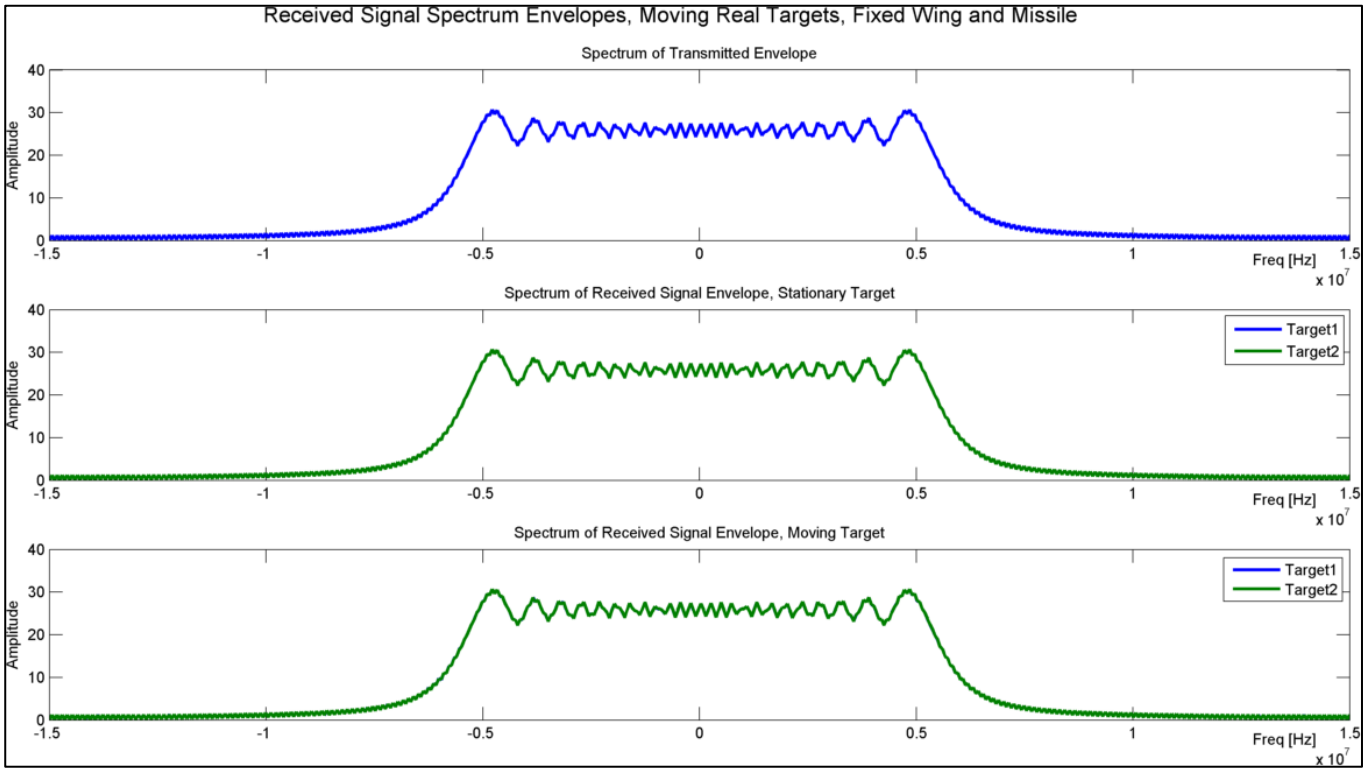

Figure 150: X-Band Target Spectrums, Fixed Wing and Missile, Zero Time Delay

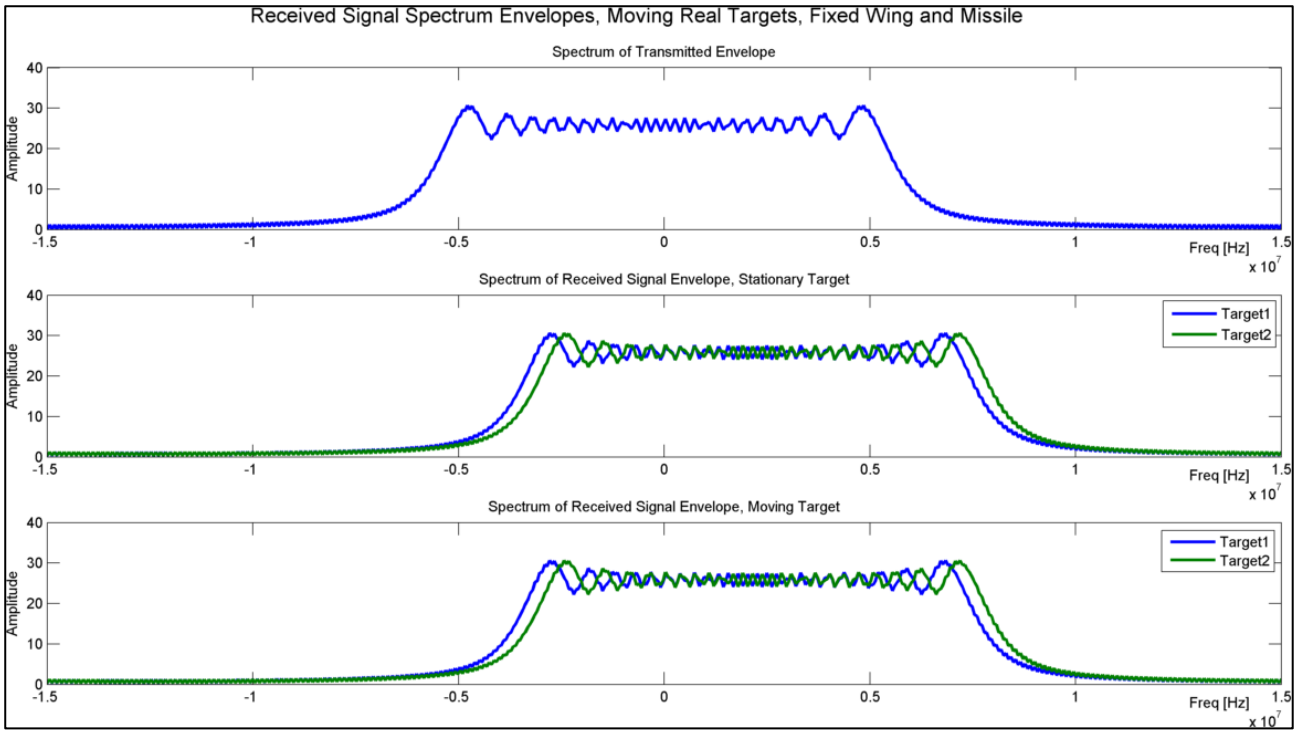

Figure 151: Fixed Wing and Missile, Target 1 at 170m, Target 2 at 200m, X-Band

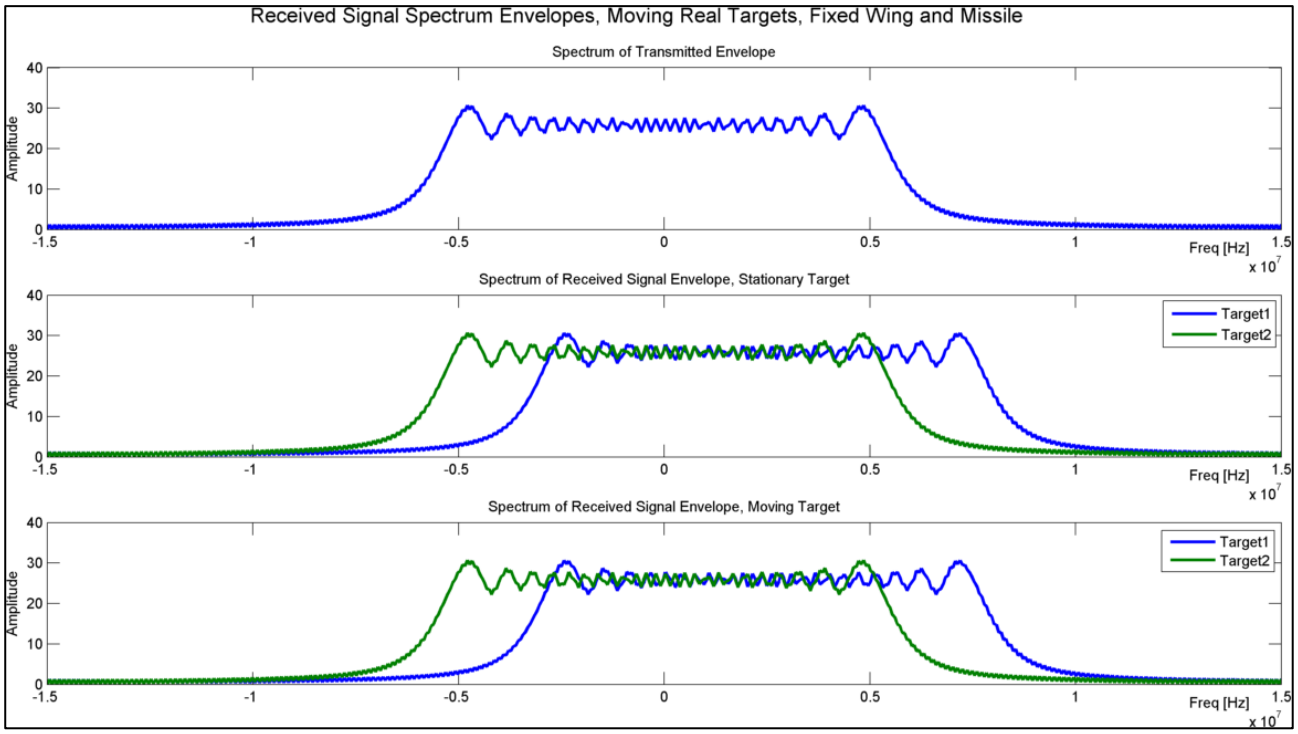

Figure 152: Fixed Wing and Missile, Target 1 at 200m, Target 2 at 0m

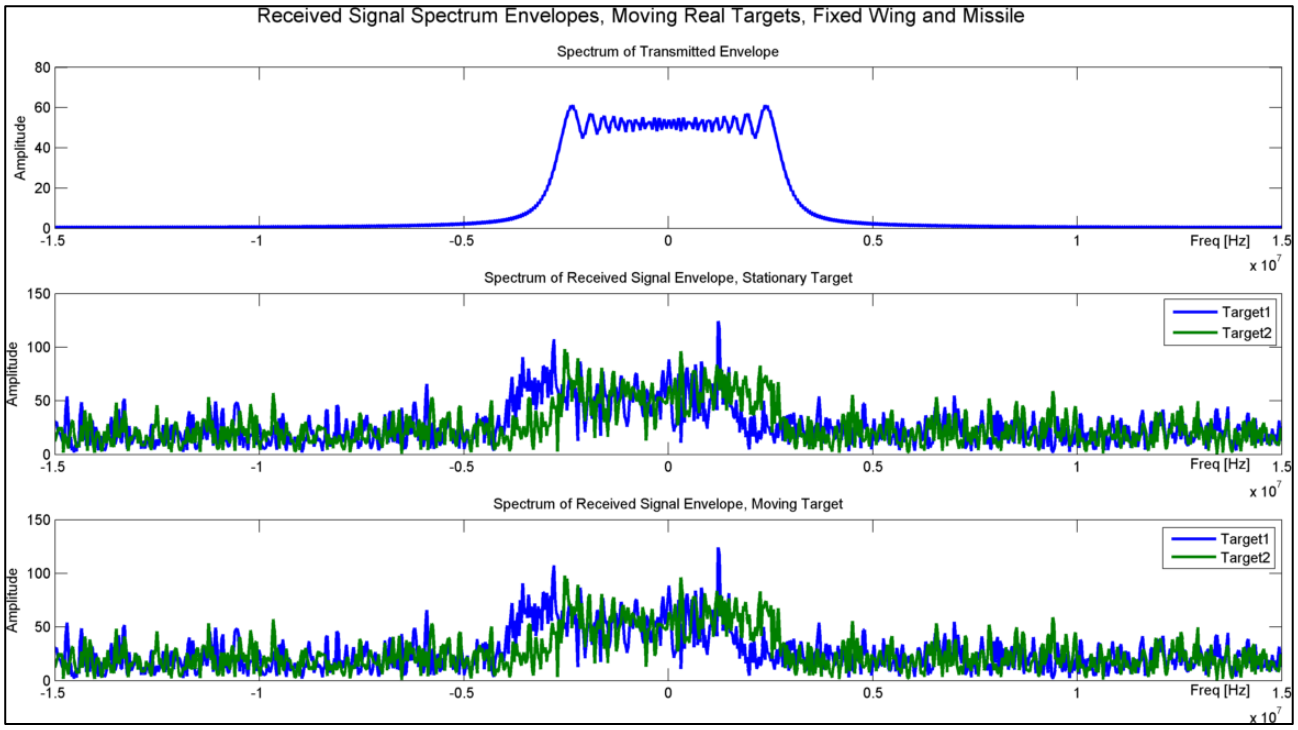

Figure 153: Noise Distortion of Received Target Spectrums

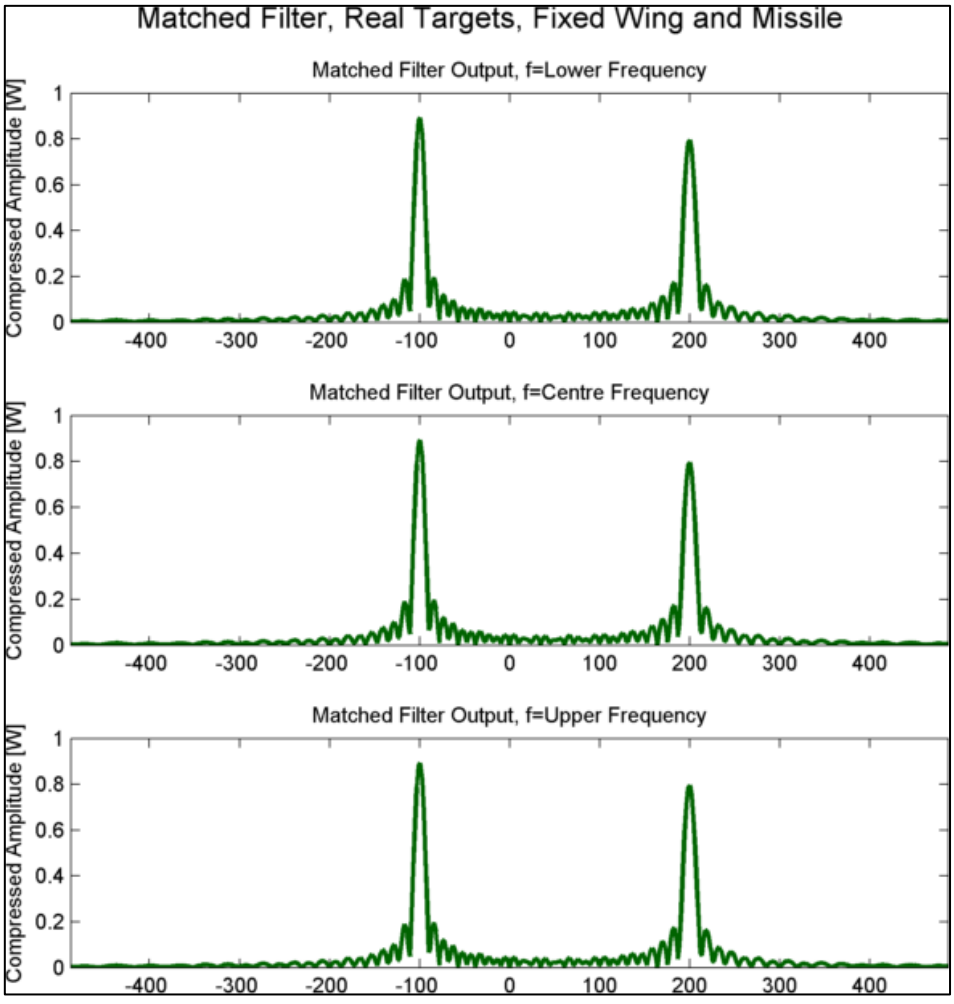

Figure 154: X-Band Range Estimator Matched Filter, Fixed Wing and Missile

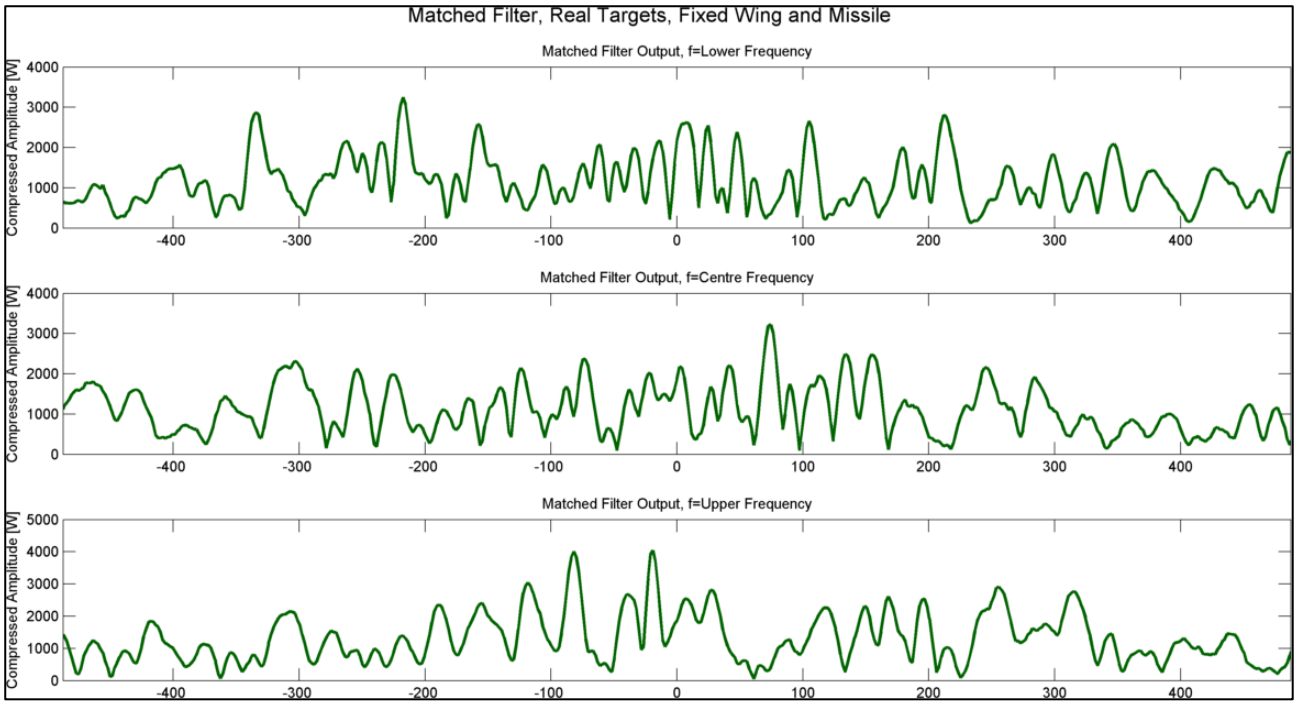

Figure 155: X Band Range Estimator Matched Filter with Noise and Amplitude

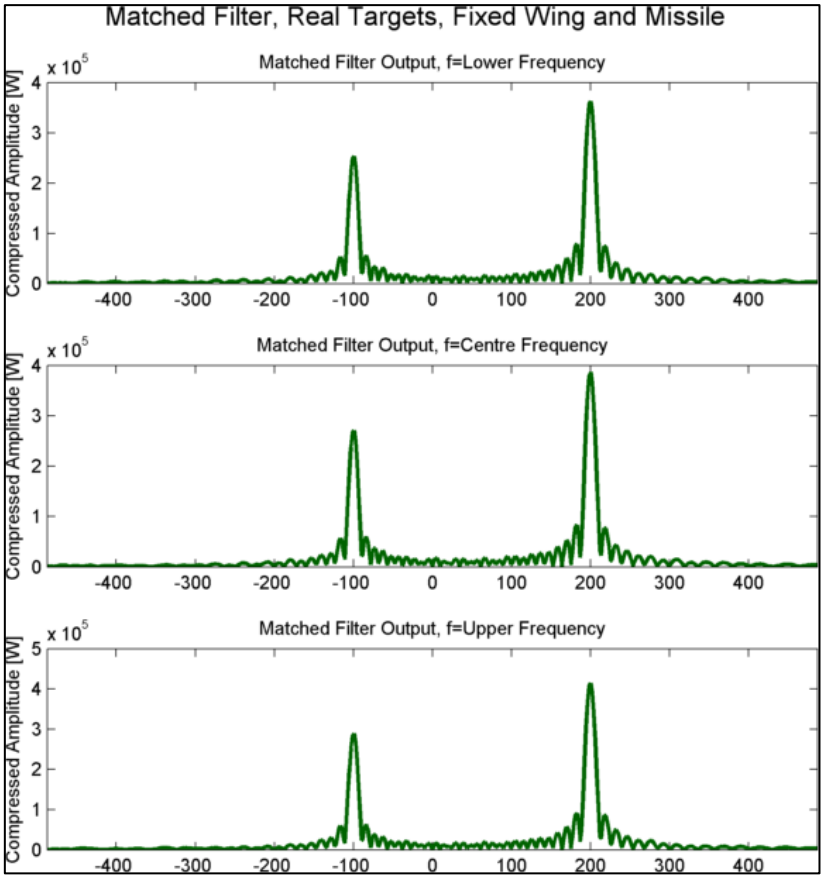

Figure 156: X Band Range Estimator Matched Filter with RF Processing Gain

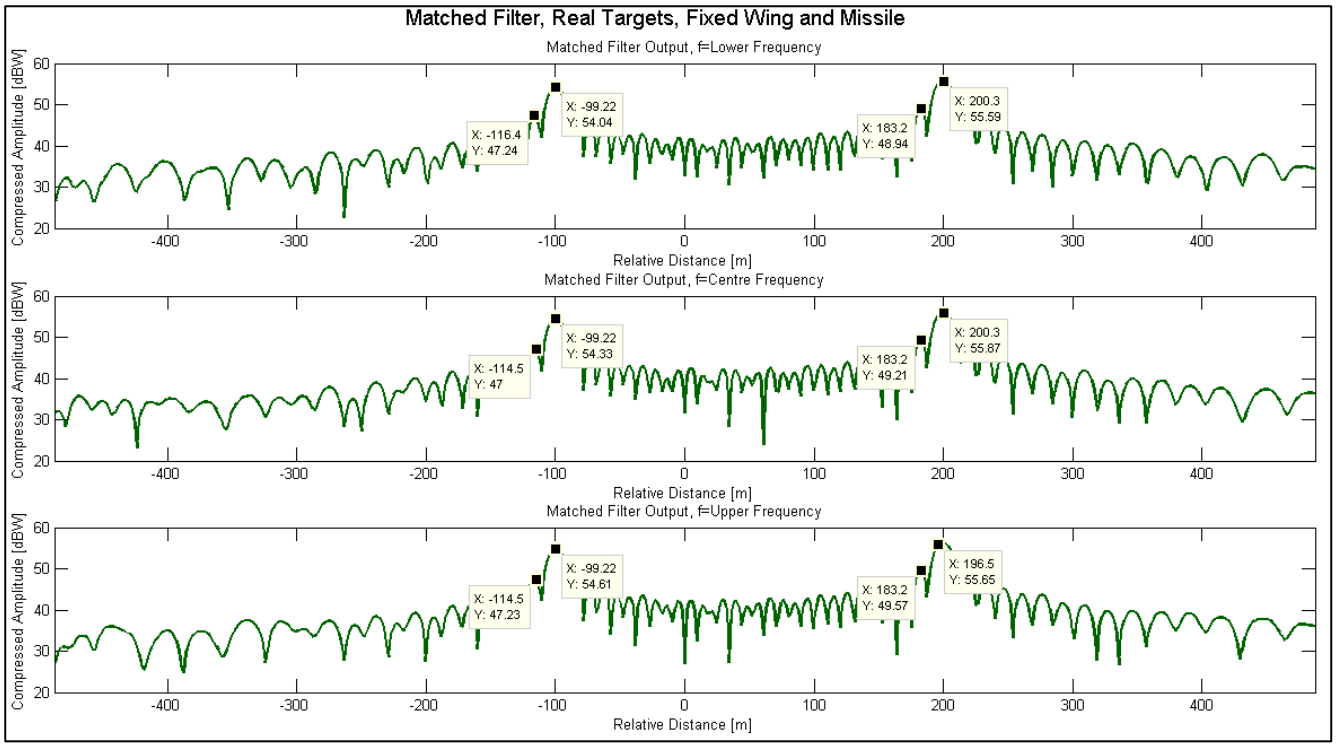

Figure 157: X Band Range Estimator Matched Filter, Correlation Processor dBW Scale

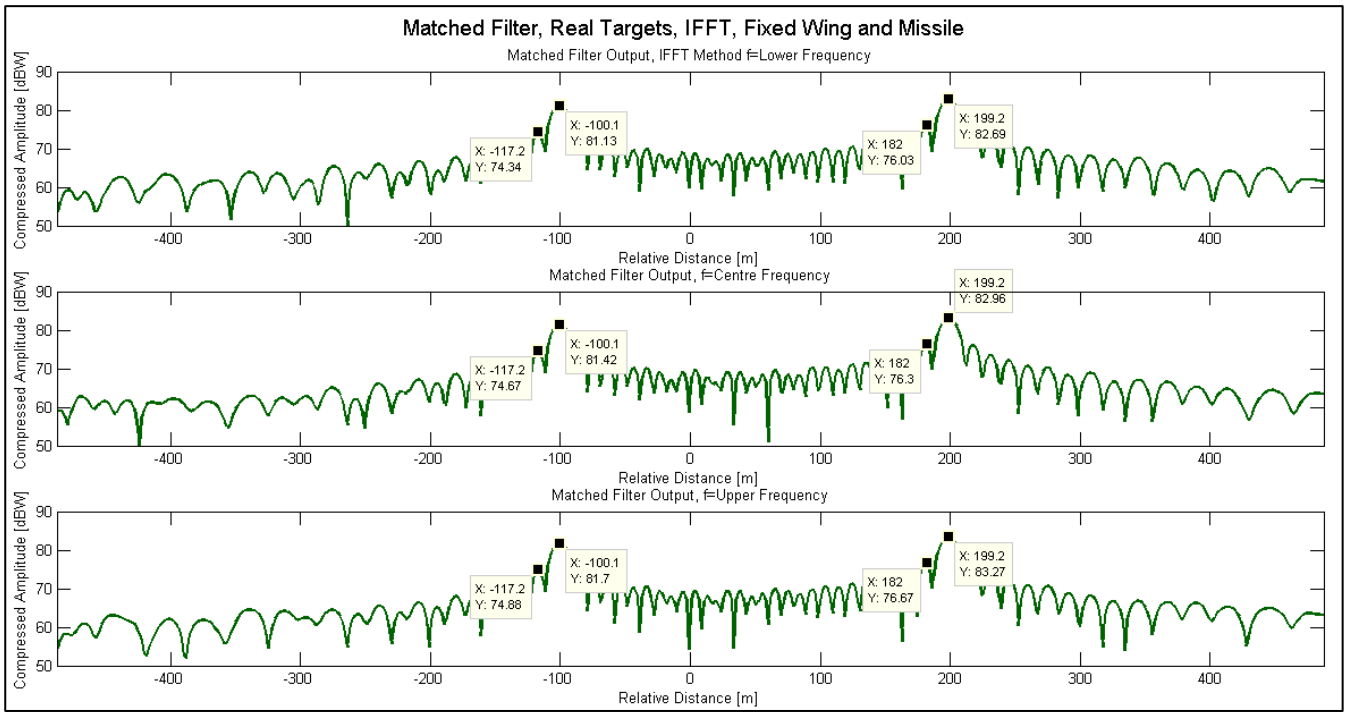

Figure 158: X Band Range Estimator Matched Filter, IFFT Processing, dBW Scale

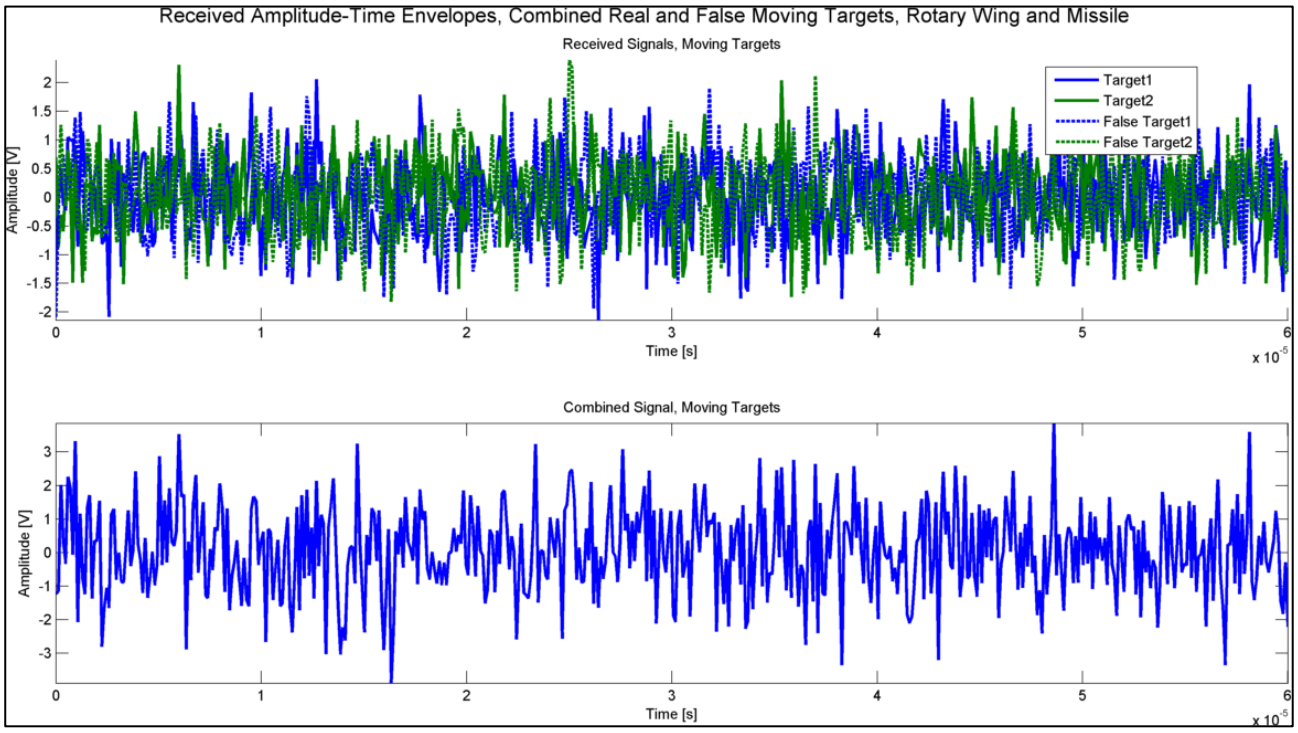

Figure 159: L Band Received Signals with True and False Targets

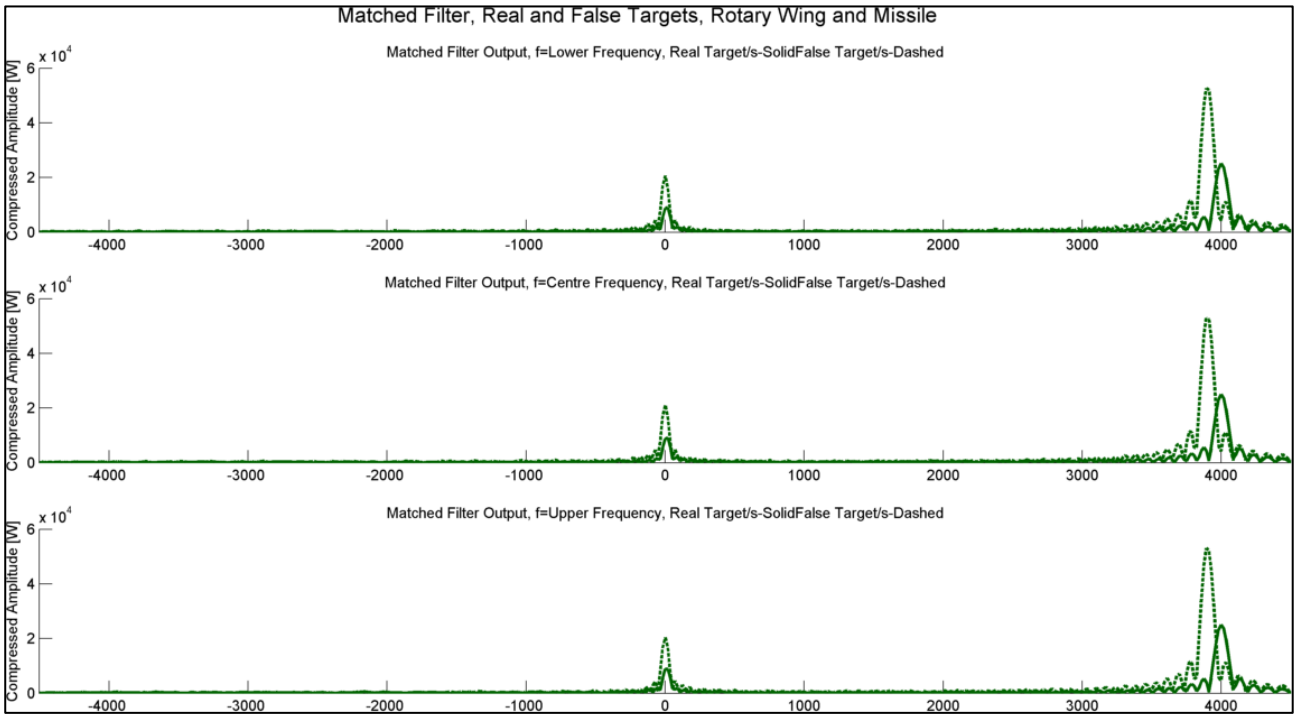

Figure 160: L-Band Range Match Filtered Response, Cover Pulse Jamming

The *real* part of the complex envelopes of the transmitted signal "$\tilde{x}(t)$", true stationary target echo signal $\tilde{x}_{rs}(t)$" and true moving target echo "$\tilde{x}_{rm}(t)$" for the fixed wing target defined in section 8.5 is shown in Figure 147. In this scenario, both fixed wing target and missile are detected in the same range bin. The distance to the start of the range bin was simulated to be 44025m from the radar. In all of these signal plots, the complex envelope of the LFM signal is shifted to start at zero to simplify visualisation of the signal to reduce complexity in understanding. The exact definition displayed in equation (153) is repeated in equation (234) and shown below:

$$\tilde{x}(t) = A_t \cdot \text{Rect}\left(\frac{t}{\tau}\right) e^{j\pi\mu t^2} \tag{234}$$

However shifting the LFM signal to commence at zero is described by:

$$\tilde{x}(t) = A_t \cdot \text{Rect}\left(\frac{t-\tau/2}{\tau}\right) e^{j\pi\mu(t-\tau/2)^2} \tag{235}$$

Inspecting equation (235) shows that the LFM signal is shifted to the right by "$\tau/2$" seconds, which also corresponds to the result shown in Figure 147.

Another observation from Figure 147, is that the Doppler term caused by the Doppler shift effect cannot be noticed at the scale shown by comparing stationary and moving target signal models. This is because the Doppler term is small in comparison to the other terms in the signal definition. In all of these results, the signal as it would actually be measured at the radar antenna is shown, since amplitude effects and receiver noise were included in the signals.

The echo signal from the *missile* target in the same range bin as the fixed wing target, is shown in Figure 148 (noise and amplitude, included). Target parameters (range, Doppler shift) were set differently for the missile compared to the fixed wing target, which explains the shorter signal period in the missile echo signal compared to the fixed wing target. The smaller RCS of the missile is the cause for the smaller signal voltage compared to the fixed wing target shown in Figure 147. The effect of the smaller missile RCS can be seen in Figure 148, by the smaller returned signal voltage, compared to the fixed wing target.

A comparison of the two returned signals highlighting the differences in signal amplitudes between the fixed wing target and missile is shown in the top subplot of Figure 149. The bottom subplot shows the combined signal as received by the radar if the two targets were in the same Range-Doppler-Elevation angle bin.

The signal spectrums for the fixed wing target and missile are shown in Figure 150, Figure 151 and Figure 152. The missile is travelling at a much higher velocity compared to the fixed wing target and thus experiences a larger Doppler shift. However, the shift is still too small relative to the bandwidth of the spectrum shown in Figure 150, to be noticed.
The range-Doppler coupling effect can be observed by inspection of Figure 151 and Figure 152. Applying a time delay to the target signals cause the spectrums to shift as shown. This is an effect also caused by range-Doppler coupling effects of the LFM signal.
In Figure 153, the distortion of the fixed wing and missile spectrums is shown, when noise is added to the signal.
These series of spectrum plots visually show why Doppler filtering requires the calculation of the signal spectrum over the "slow time" dimension (per CPI), since the shift in the "fast time" dimension (per range bin) is too small to be measured accurately.

The range matched filter processor output of the combined received target signals for the fixed wing target and missile is shown in Figure 154, when a 1V (or 0dBW) signal amplitude is applied to the signal and no noise is added. Under these conditions, the peaks of the match filter clearly indicate the missile target at -100m and the fixed wing target at 200m, relative to the range bin coordinate system. However, if noise and signal amplitude are applied to the signal, SNR is not high enough to ensure the targets are detectable above the noise. This effect is noticeable in Figure 155, which shows that the match filter output is completely degraded, because of the low SNR. This result provides justification for a radar requiring RF pre-processing of the signal in order to amplify the raw received signals. When RF processing gain is applied to signal, *with* noise and amplitude applied, the match filter output is displayed in Figure 156. RF processing gains for both the X-Band and L-Band DBR Subsystems were discussed in section 1.2.2.

The match filter output with RF processing gain, amplitude and noise shown in Figure 156 is displayed in units of "dBW" in Figure 157. The average of the target peaks over the three frequency signals was 54.33dBW for the missile at -100m and 55.7dBW for the fixed wing target at 200m. The side-lobe levels were 7.17dBW for the missile and 6.46dBW for the fixed wing target.

In Figure 158, the match filter output of the same scenario used to generate in Figure 157 was calculated using the "IFFT" method as opposed to the "Time Correlation" method discussed in

section 8.3.1. The peak amplitude was larger than that calculated using the correlation method of in Figure 157, however the sidelobe levels for the targets were similar. A average sidelobe level of 6.79dBW was measured for the missile and 6.55dBW was measured for the fixed wing target. The simulation runs for the two range match-filter outputs (Time Correlation and IFFT methods) were different. Therefore, a different RCS fluctuation, noise level and amplitude would be generated for either run. This is why the sidelobe levels are not identical, yet similar. It can therefore be concluded that the IFFT method does not offer any clear advantage over the time correlation method, for calculating a matched filter output of a signal.

Figure 159 shows *L-Band* signals returned to the radar for two true targets (rotary wing and missile) and two false targets (rotary wing and missile). The two false targets are in the same "range-Doppler-elevation-angle" bin as the two true targets. From the top subplot of Figure 159, it can be deduced that there are no distinguishing features inherent to the false targets that can be used to classify them as false, from the time domain signals. This conclusion is based on the assumption that the ES system has accurately estimated the DBR's signal parameters and used those parameters to mimic the true target echo return. The bottom subplot of Figure 159 shows the combined target signal formed by adding returns from all four targets. From the combined signal in the time domain, it can be seen that it is impossible to determine whether true or false target signals are received. However, it is important for the jammer to coordinate range jamming with Doppler frequency jamming *as well as* angle jamming to ensure the radar cannot detect the false target by using any one of the false target coordinates (range, velocity or angle).
Some radar's also perform consistency checks between the velocity estimated from the Doppler frequency measurement and the velocity measured by calculating the rate of change of target range i.e. target velocity. If the target velocity measurement obtained using both methods is not similar, the radar is able to identify the false measurement.

The signals in Figure 159 are shown after match filter processing in Figure 160. Range and amplitudes of the false targets were selected to ensure that they mask or obscure the true target match filter outputs in order to deceive the radar into tracking the false target. This can clearly be seen in Figure 160. The radar detector would therefore erroneously select the incorrect target and be "led off" the true target. Increasing the number of false targets could deceive the radar to an even greater degree.

8.7 Single Plot Mode Velocity Estimator, Results

The Radar's Target Velocity Estimator output plots are presented and discussed in this section. The reader is advised to inspect the figures and refer to discussion after the velocity estimator figures, for observations and conclusions.

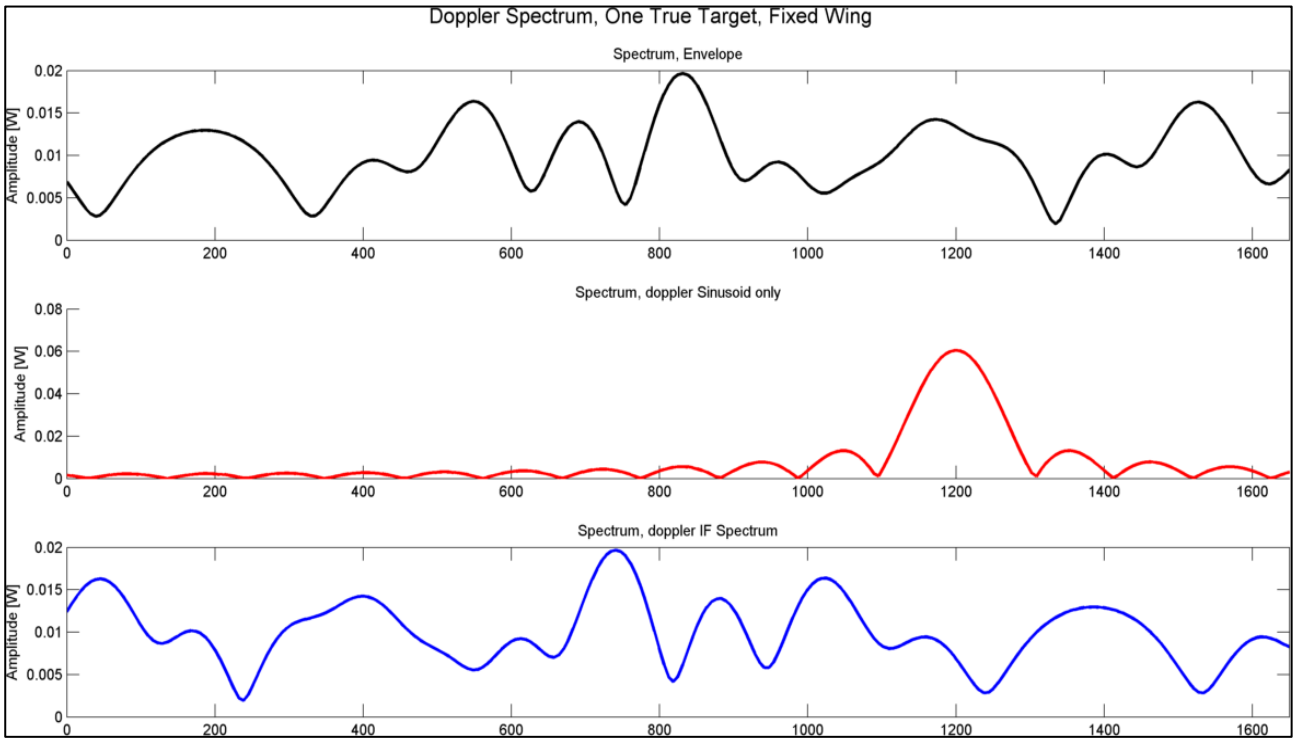

Figure 161: X-Band Doppler Spectrum, One Target

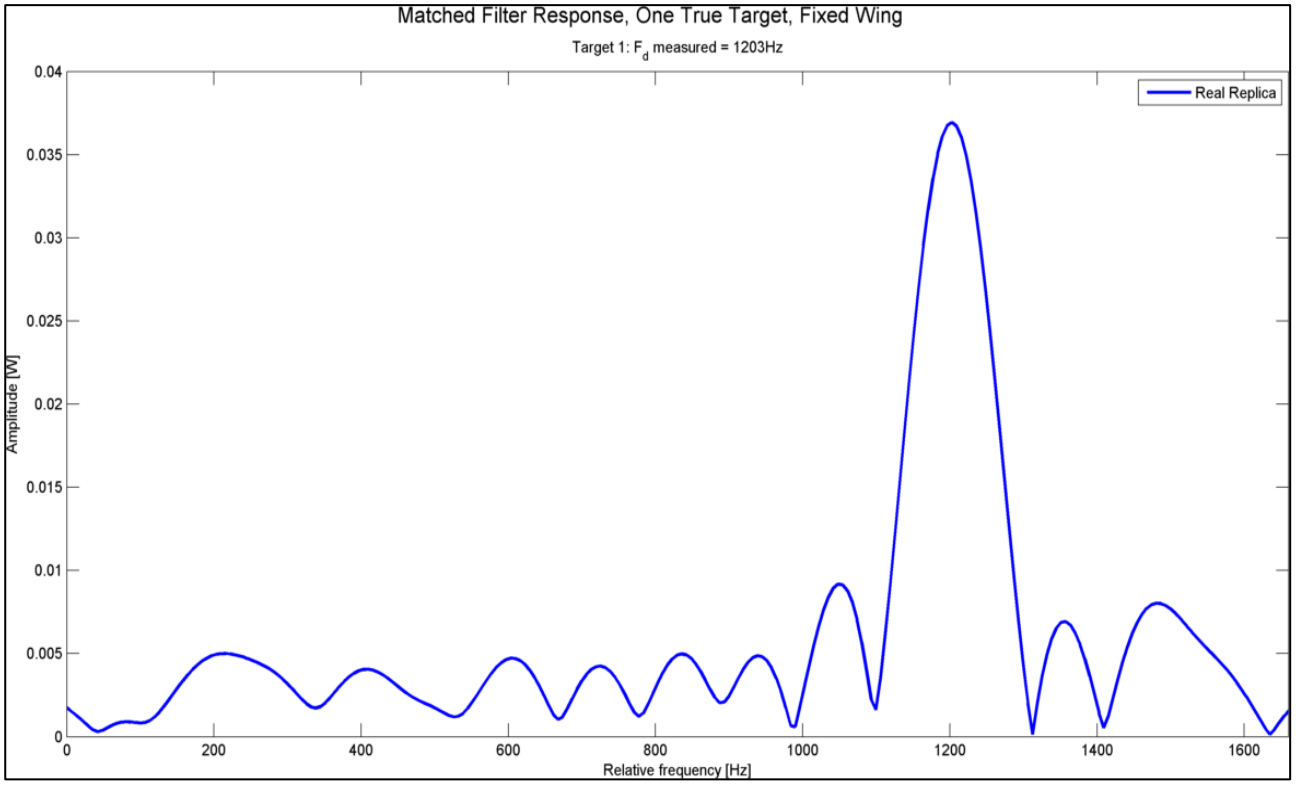

Figure 162: X-Band Doppler Match Filtered Response

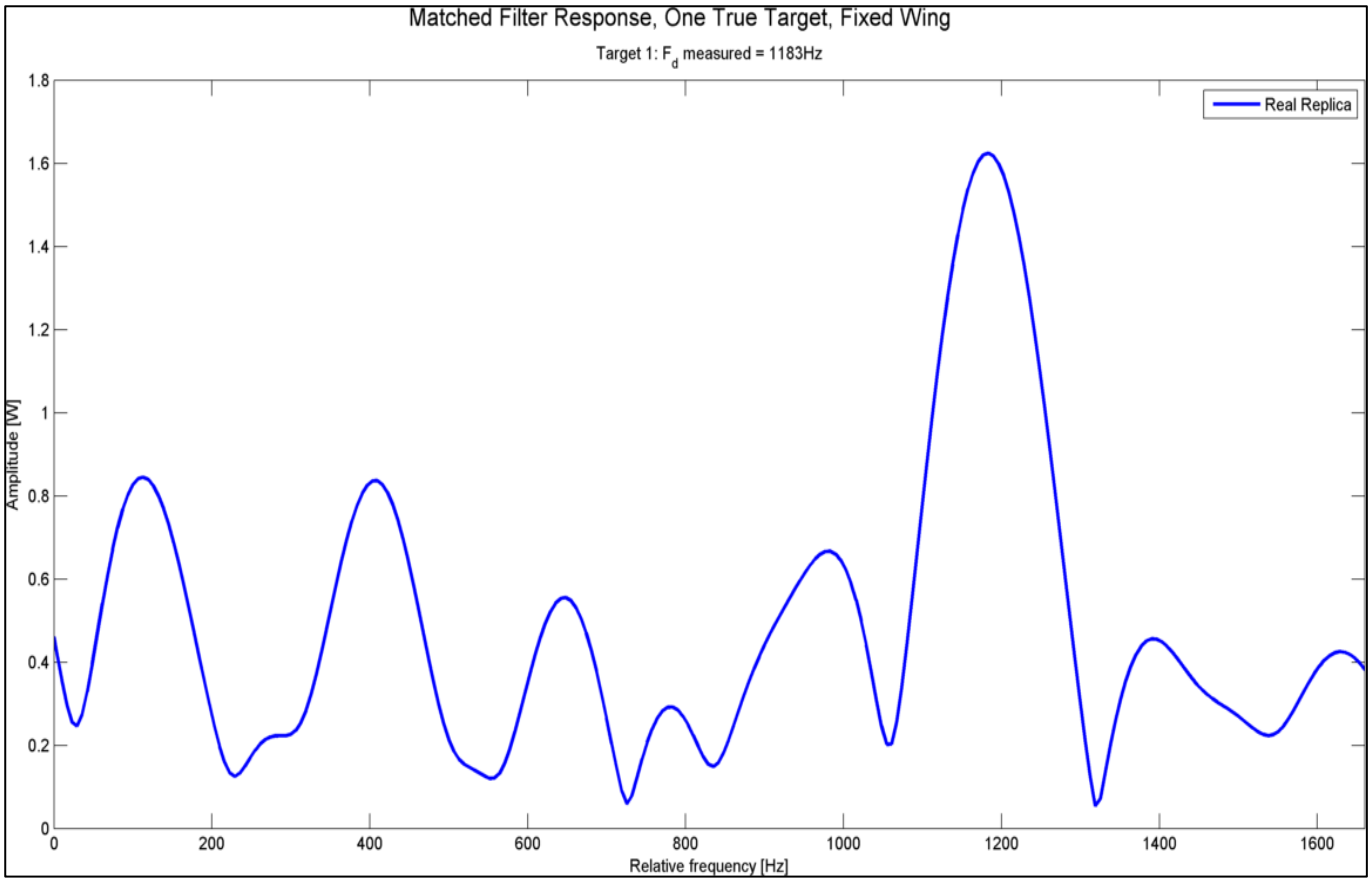

Figure 163: X-Band Doppler Match Filter, Amplitude and Noise effects, Kaiser Window

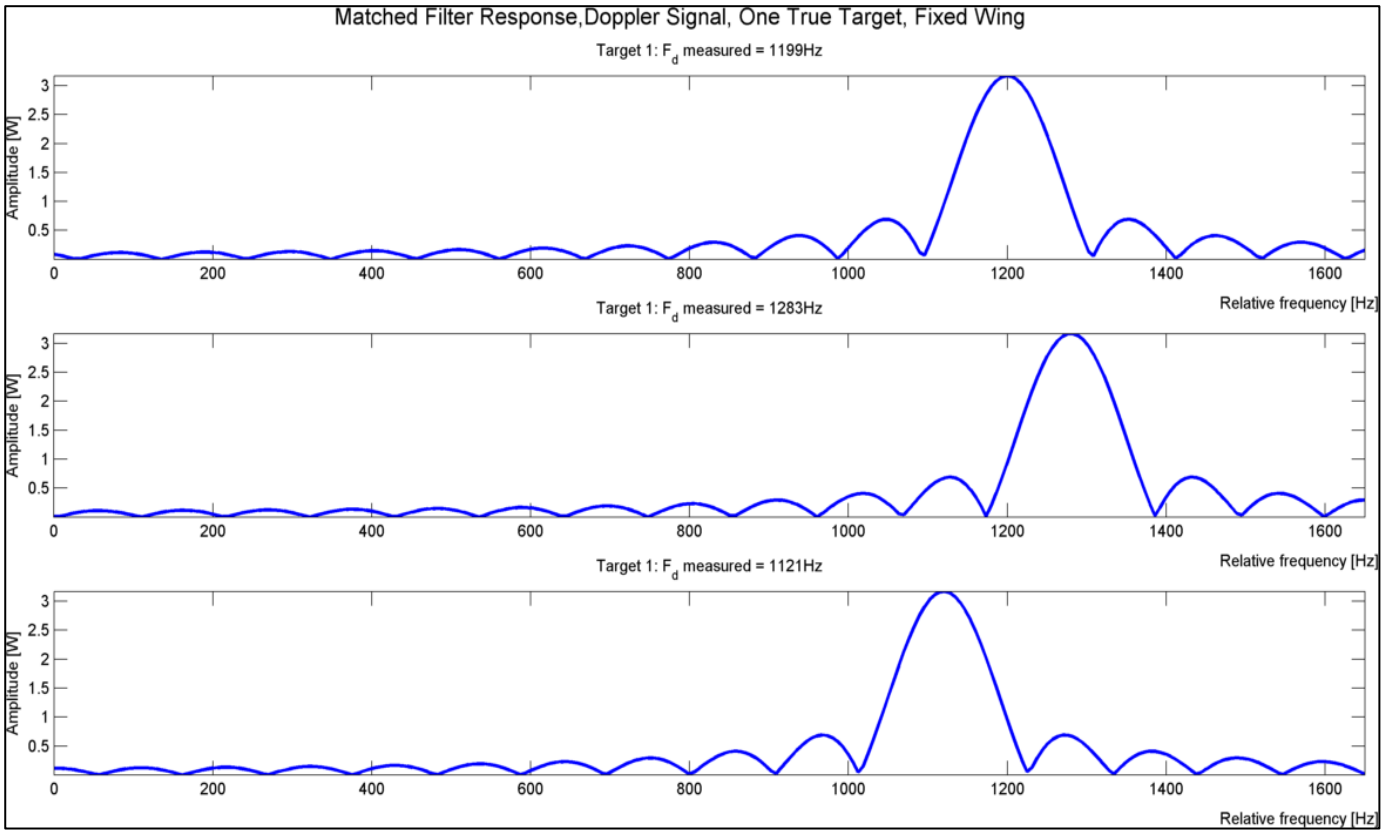

Figure 164: X-Band Doppler Exponential Signal for a Fixed Wing Target

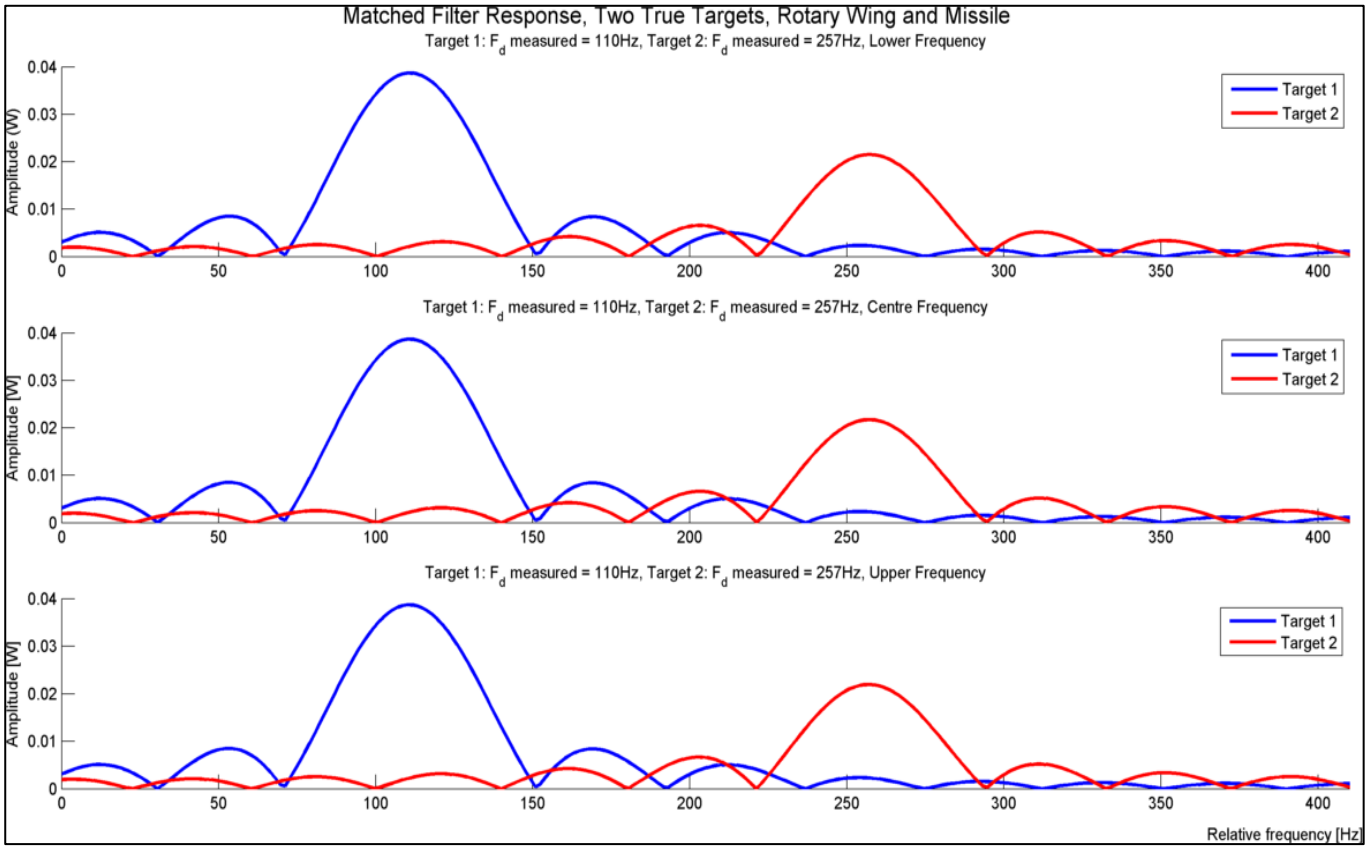

Figure 165: L-Band Doppler Spectrums with two true targets

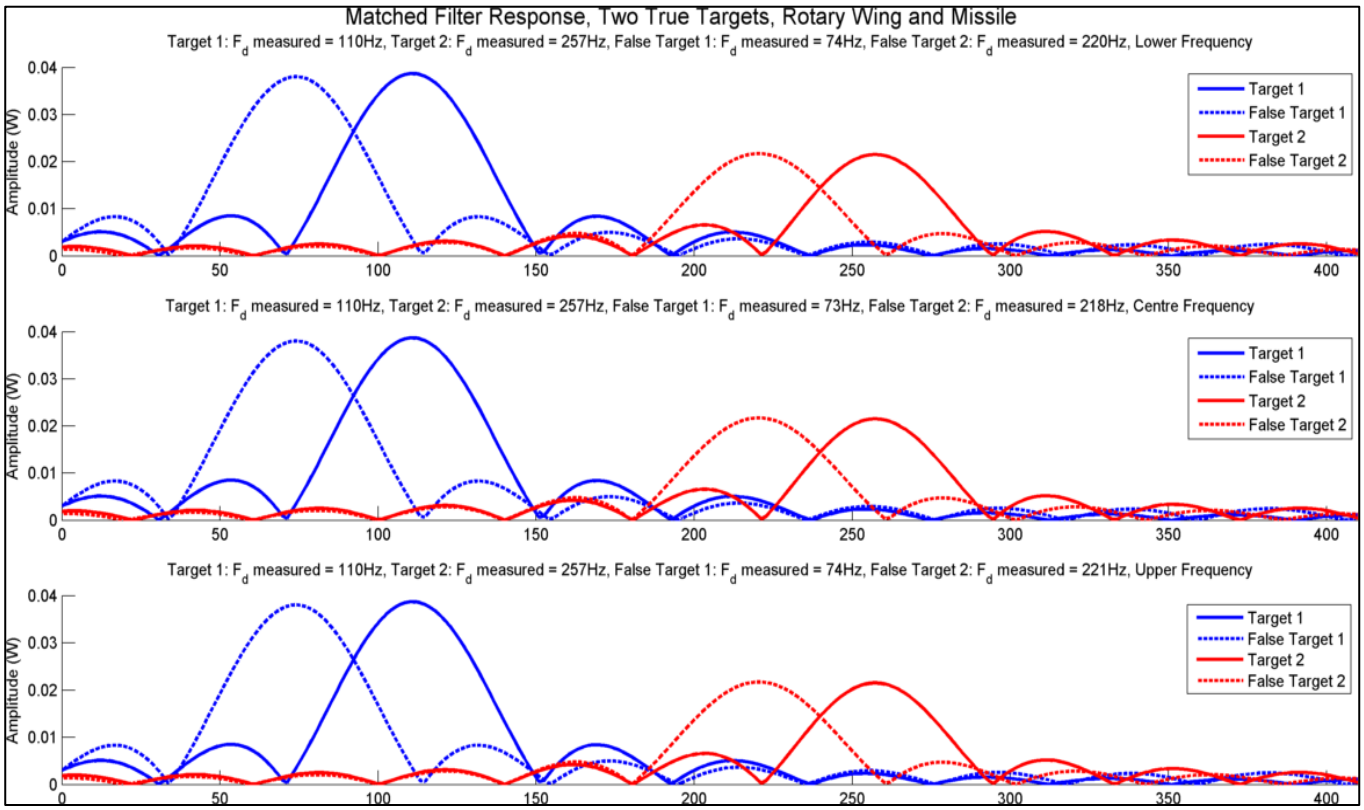

Figure 166: L-Band Doppler Spectrums with two false targets

The spectrum of the transmitted signal processed over all Doppler bins per range bin ("slow time") is shown in Figure 161. The rectangular envelope, time delayed term, phase shifted term, elevation angle term *and* Doppler term are applied to the transmitted signal, to simulate the actual target echo. The middle subplot of Figure 161 shows the spectrum of the Doppler term only, while the bottom subplot shows the Doppler shifted and time delayed spectrum of the target echo. These spectrums were generated for signals with a 1 V amplitude and no noise.

In order to determine the Doppler shift of the target echo, the complex envelope of the received moving target signal "$\tilde{x}_{rm}(t)$" was "Doppler-processed" according the "Spectrum of Spectrums" method described in section 8.3.2. The result is shown in Figure 162. A peak at a frequency corresponding to the target's Doppler shift is clearly visible at 1200Hz in Figure 162. It can be seen that the sidelobe structure of the Doppler matched response shown in Figure 162 is not uniform. This effect becomes a problem when noise and amplitude are applied to the signal as shown in Figure 163. The side-lobes of the Doppler match-filtered response degrade even further, when amplitude and noise are applied. This degradation might even compromise the detection of the true target peak, and was noticeable even when a windowing function was applied to reduce side-lobes in the FFT. In this particular case, a "Kaiser" window was applied.

The cause for the degradation in side-lobes is range-Doppler coupling of the LFM waveform. For this reason, it was assumed that these effects could be removed through specific processing for removal of the range-Doppler coupling effects. Some processing techniques mentioned by M.A. Richards et. al in reference [6] to remove these effects are:

- The use of banks of matched filters for measuring Doppler, each tuned to a particular Doppler shift.
- Estimate targets velocity from the range rate measurement and use it to compensate for the expected Doppler shift.

From this point forward, it was assumed that effects of Doppler shift on range-Doppler coupling for the LFM waveform were compensated for. Then, the target Doppler shift can be simulated by a complex sinusoid formed at the target Doppler shift, if the signals are processed over the "slow time" (multiple Doppler bins over the CPI, per range bin) dimension. This observation was made by M.A. Richards in section 8.7.1 of reference [6].

The spectrum of the Doppler term for all three frequencies *with* noise and amplitude applied to the signal is shown in Figure 164. It can be seen that the target velocity is very accurately estimated, since clear peaks form at the target's Doppler frequency, despite the addition of receiver noise and amplitude effects.

In Figure 165, the Doppler spectrums for a rotary wing and missile target, calculated at the *L-Band frequency* is shown. The maximum positive Doppler frequency that can be measured is also shown in Figure 165 and this frequency is defined as:

$$f_{d,\max} = \pm\frac{PRF}{2} \tag{236}$$

Since the PRF for the L-Band DBR subsystem is 800Hz, the maximum positive Doppler frequency that can be measured is 400Hz. At X-Band, this was $3300/2 = 1650$Hz.

Figure 166 shows the Doppler filtered responses for two true targets and two false targets. The false target Doppler frequency was inserted into the false replica of the intercepted radar signal, in order to deceive the radar. It is important to note that no distinction in Doppler frequency can be made, by the radar between the true and false targets. Therefore, it can be concluded that the false target can easily be mistaken for the true target by the radar, *if Doppler frequency were the only target coordinate* being measured. However, coordinated range, Doppler and angle deception jamming is necessary in order to deceive the DBR completely.

8.8 Single Plot Mode Elevation Angle Estimator, Results

The Elevation Angle estimator output plots are presented and discussed in this section. The reader is advised to inspect the figures and refer to discussion after the figures for observations and conclusions for this section.

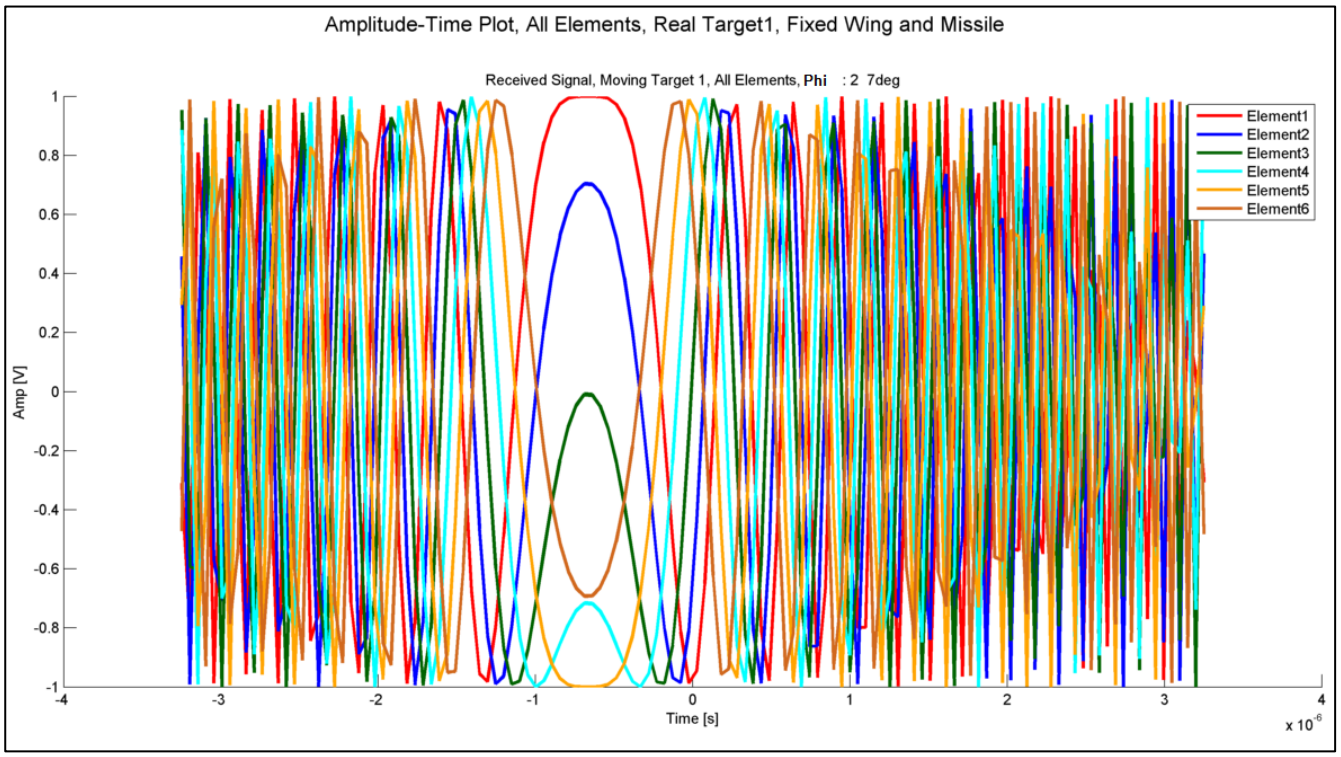

Figure 167: Phase shifted Target Signals, Combined, all Elements

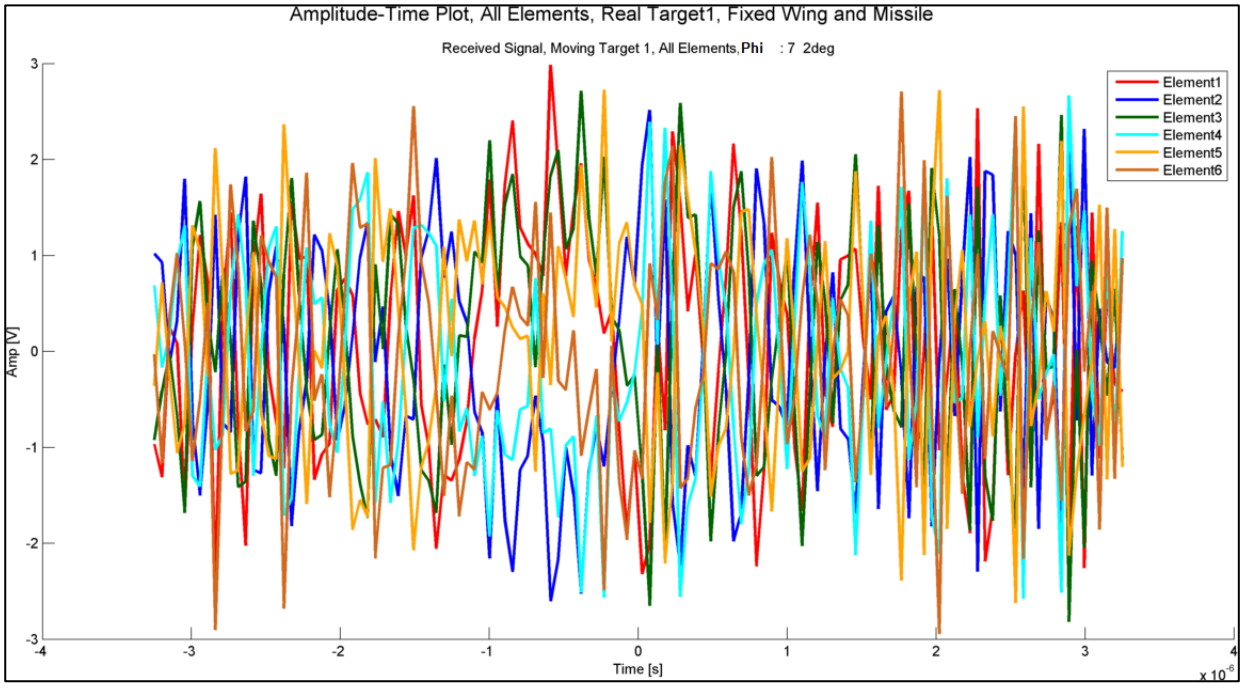

Figure 168: Phase shifted Target Signals, Combined, all Elements, Noise and Amplitude

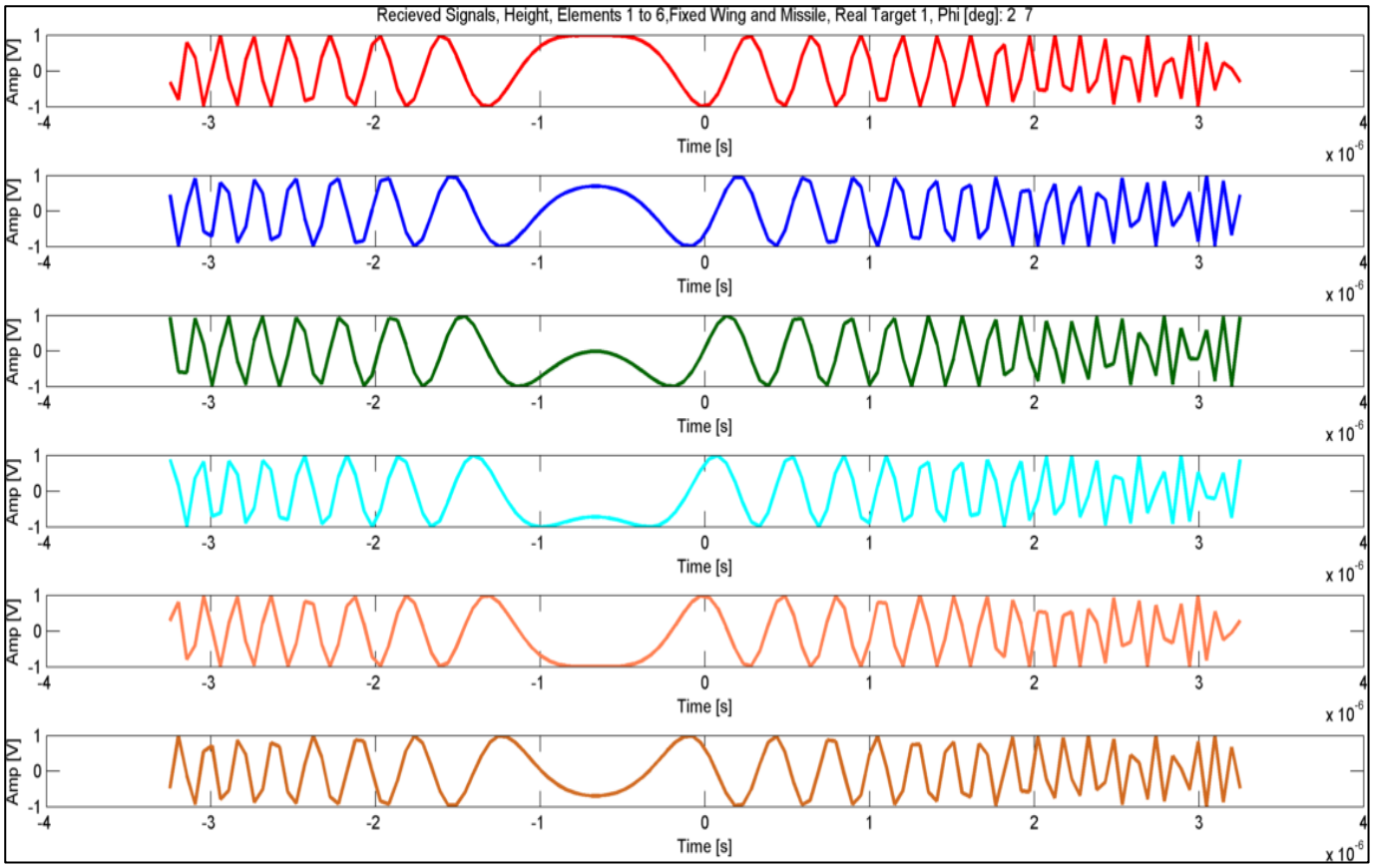

Figure 169: Phase shifted Target Signals, all Elements

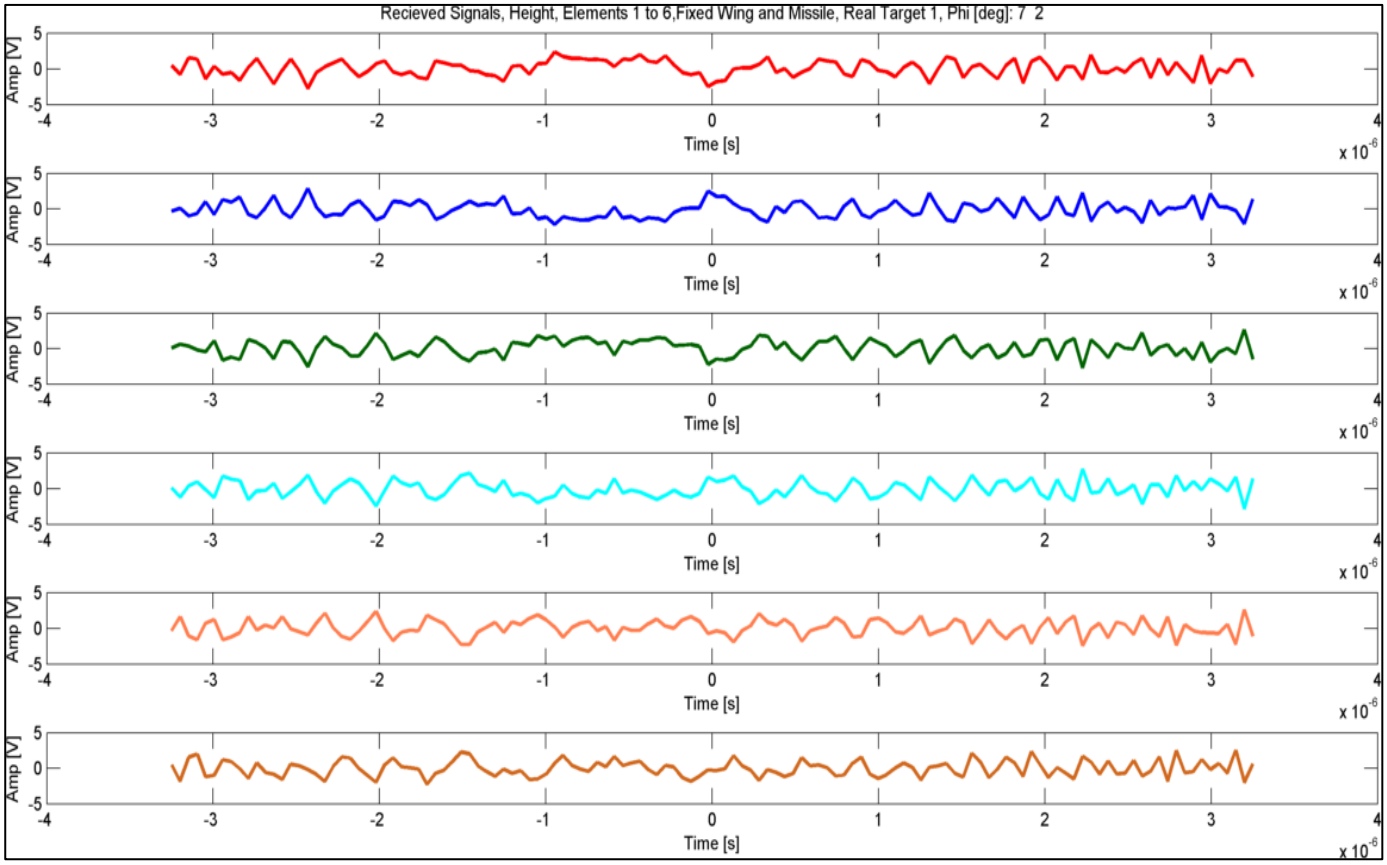

Figure 170: Phase shifted Target Signals, all Elements, Noise and Amplitude

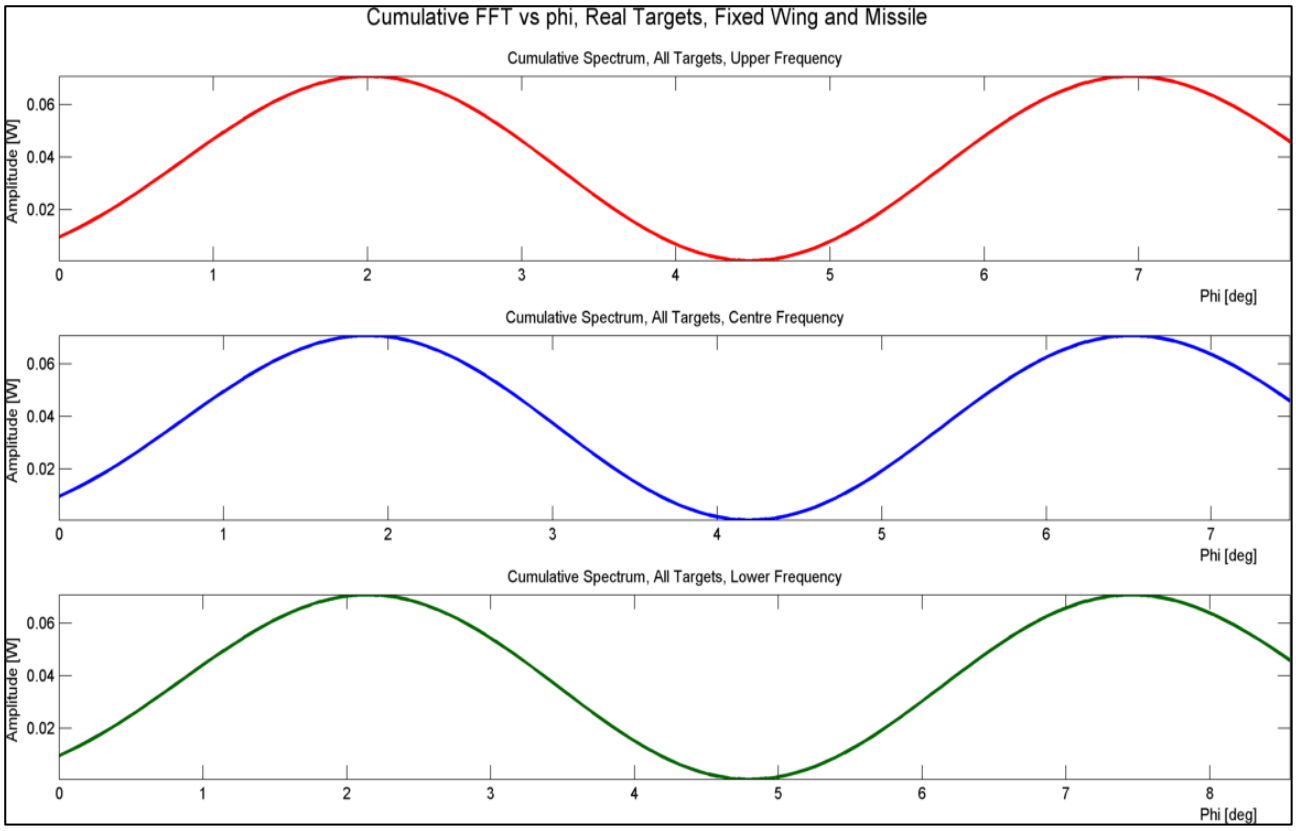

Figure 171: Phase Shifted Signal, Cumulative FFT

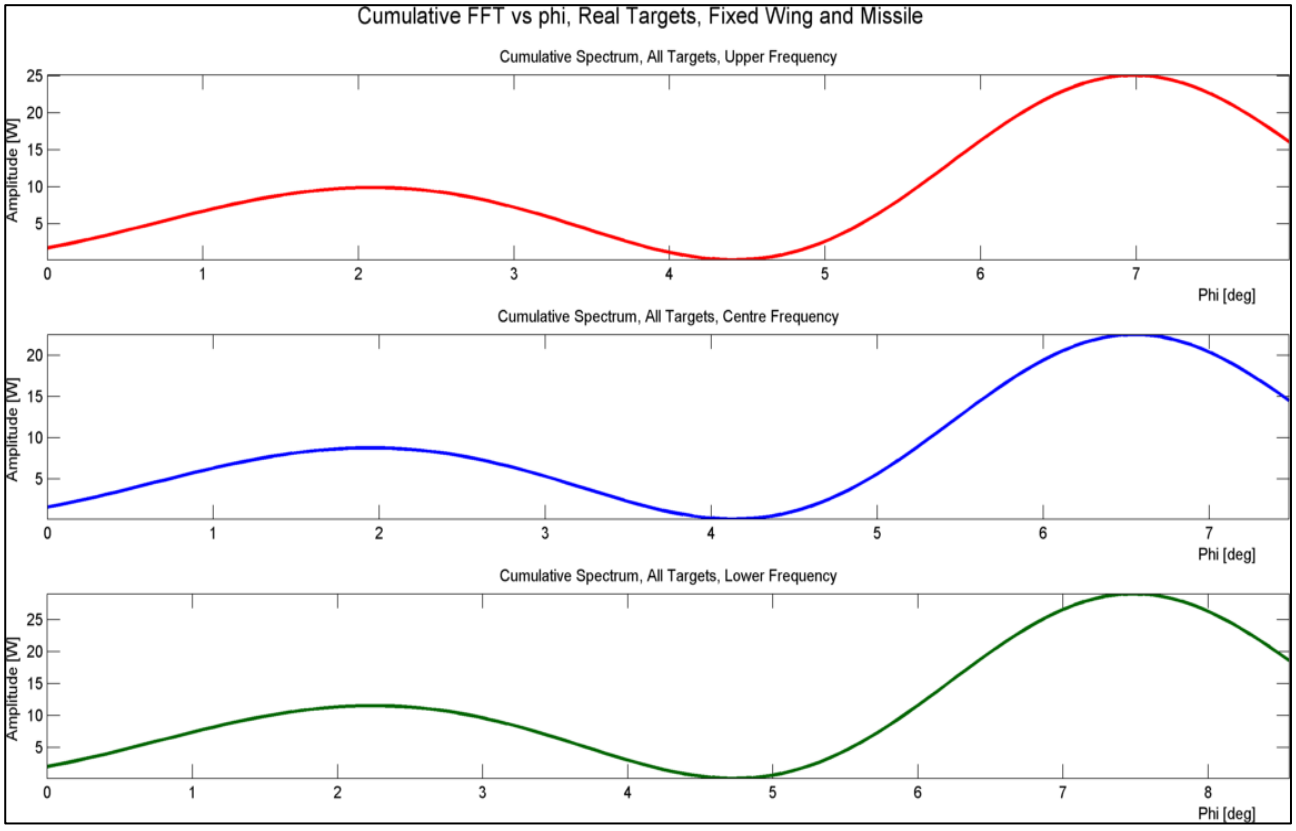

Figure 172: Phase Shifted Signal, Cumulative FFT, Noise and Amplitude

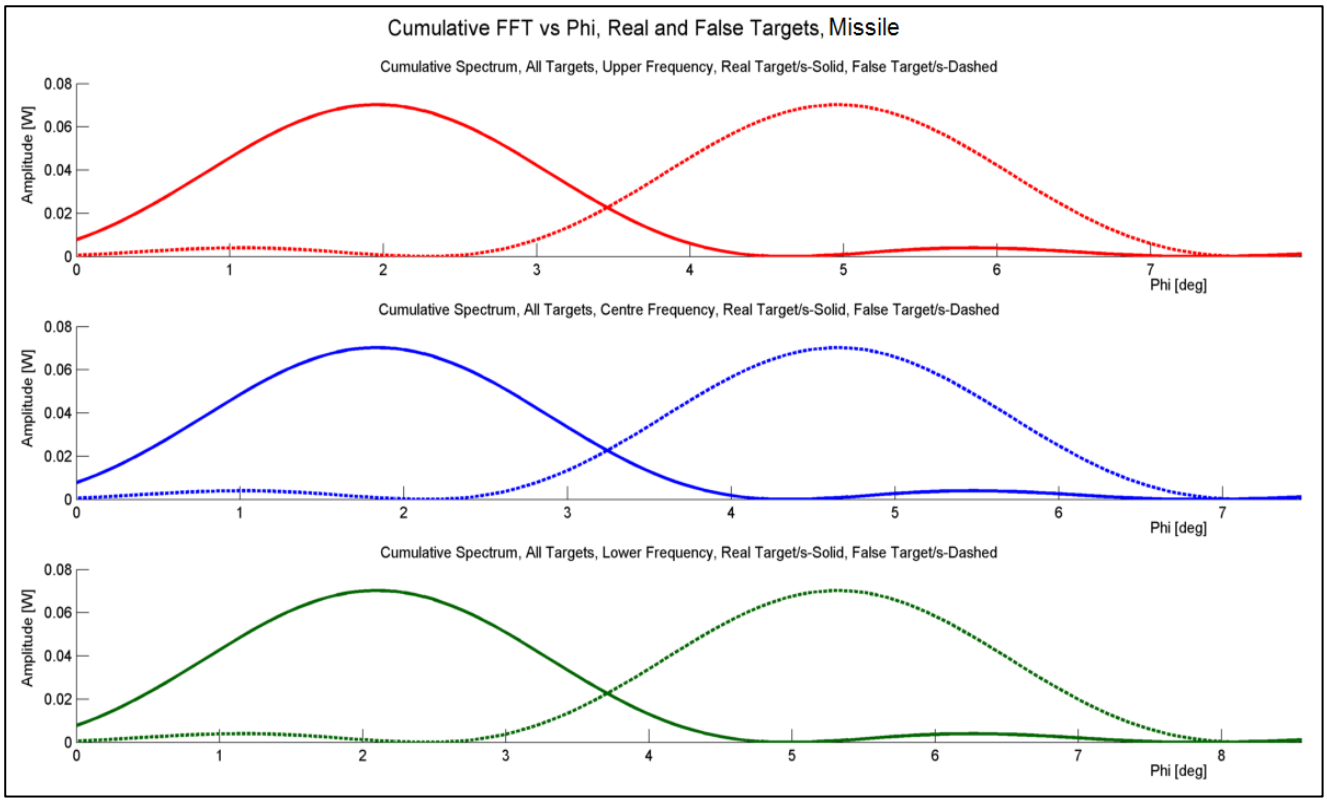

Figure 173: Phase Shifted Signal with False Target, Cumulative FFT

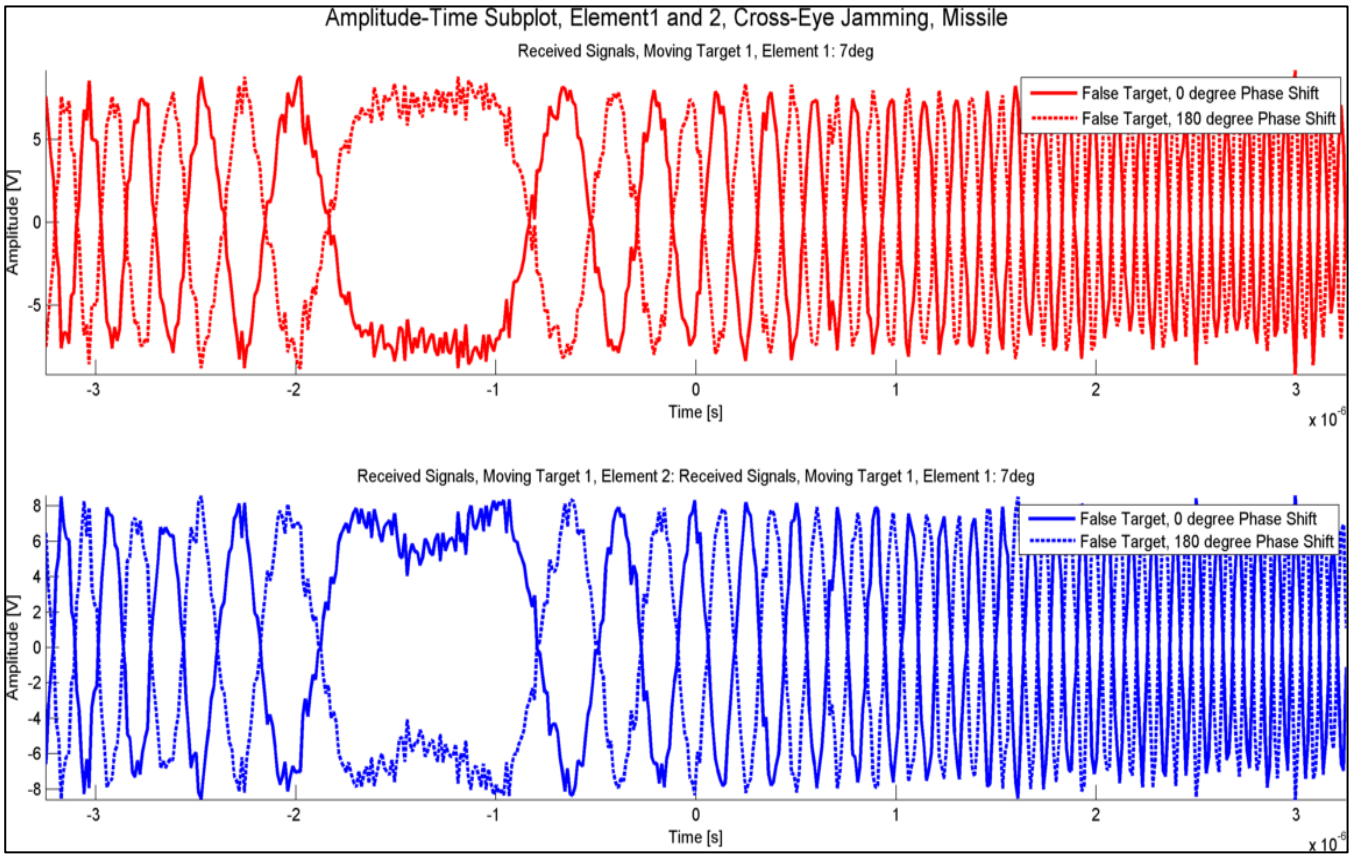

Figure 174: Cross-Eye Jamming Signals at Radar Receiver, Element 1 and 2

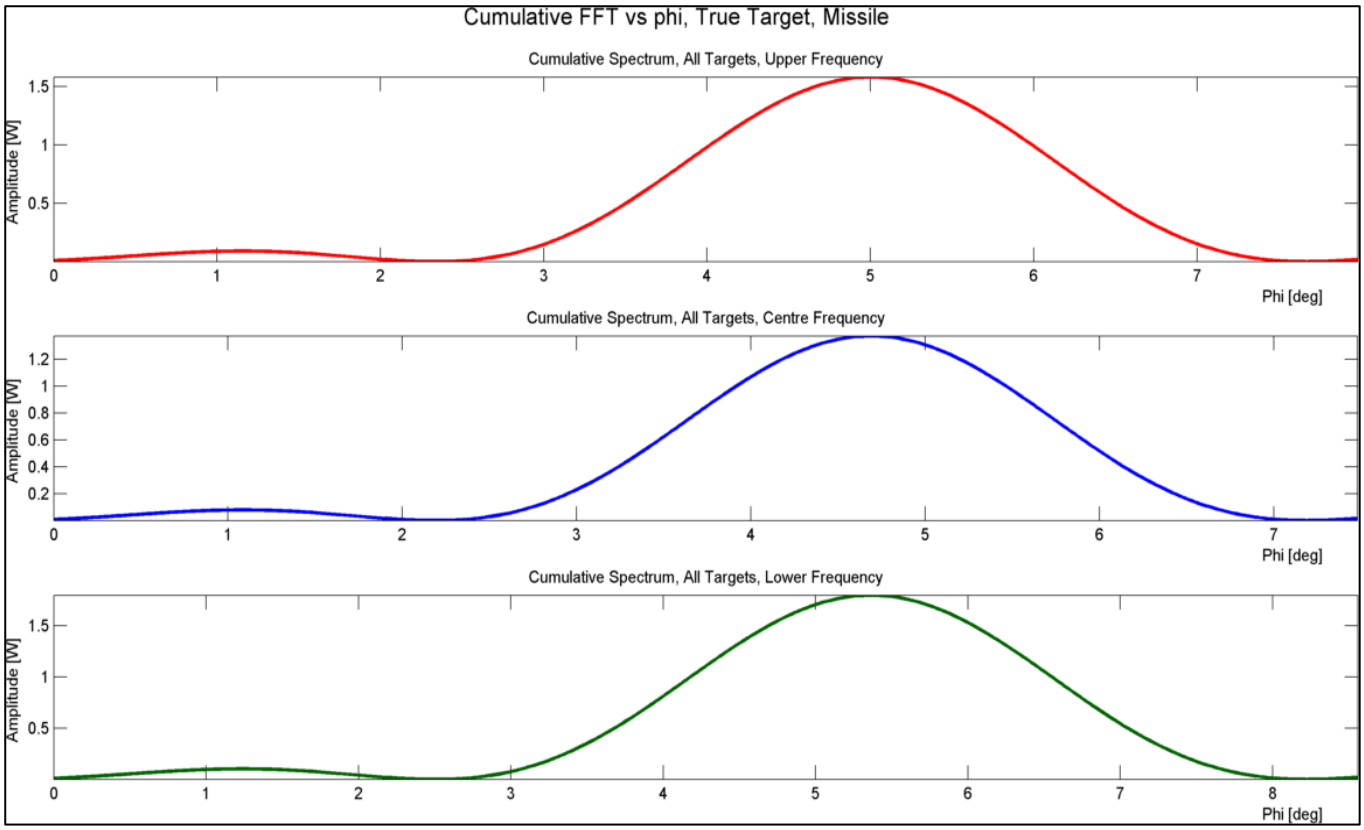

Figure 175: Cumulative FFT output for a Missile

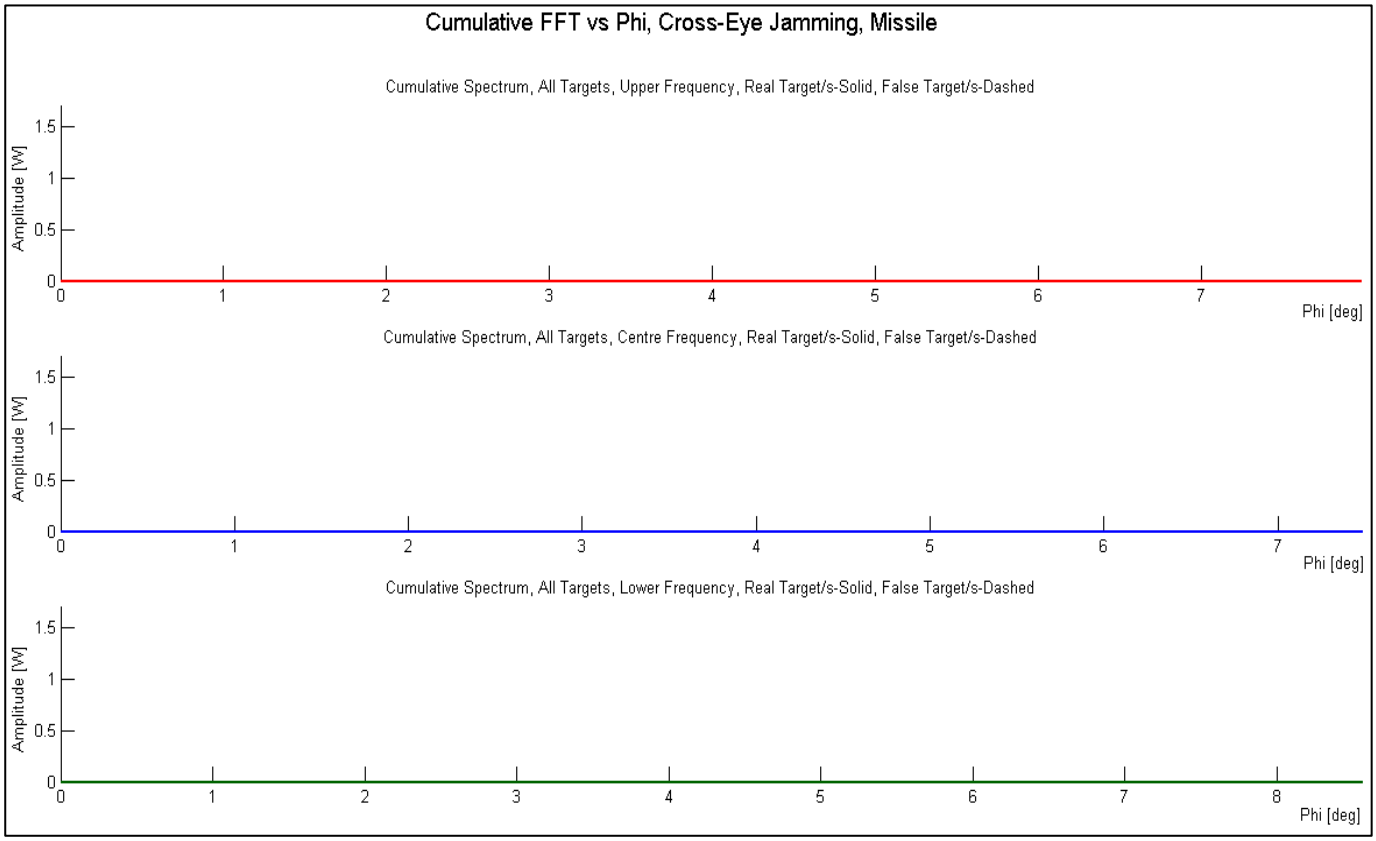

Figure 176: Cumulative FFT output with Cross Eye Jamming, Missile

This analysis is applicable to the X-Band portion of the DBR only, since the L-Band signal is not suited to measure target elevation angle as already explained in section 1.2.2. Recall that the L-Band DBR sub system is to be used primarily for long-range target detection and the X-Band is used for elevation angle measurement as well as high resolution tracking of the target. In this section, a large emphasis was placed on visualizing the phenomena present at the antenna when the signal is received over the elements. For this reason, numerous "views" or plot combinations were used to obtain a clear understanding of the elevation angle estimation process. This was done in order to understand and propose techniques to jam the DBR elevation angle estimator.

Figure 167 shows the combined received signals across the six-element antenna array for a fixed wing target and a missile. The elevation angles, at which these two target signals were simulated, was listed in Table 19. In Figure 167, the phase shift across the aperture caused by the path length difference of the target's echo arriving as a plane wave at an elevation angle "ϕ" can clearly be seen. The phase shift effect can be seen by comparing the change in shape of the LFM waveform across the antenna aperture starting at element 1 and ending at element 6. The differential phase shift was defined as "$\Delta\psi$" in equation (222). In Figure 168, the same signals are shown, as in Figure 167, however noise has been added to the signal and amplitude, "$A_{rr}(t)$" is applied.

The signals per element, with and without noise and amplitude are then displayed separately in Figure 169 and Figure 170. The phase shift is more visible in these figures compared to Figure 167 and Figure 168.

Figure 171 and Figure 172 show the output of the cumulative FFT algorithm. Peaks at the target elevation angles can clearly be seen in Figure 171. However, once noise and amplitude are included, detection of either target's elevation angle, in the same Range-Doppler-Elevation angle bin becomes problematic, as shown in Figure 172. It is quite probable that one target could be masked by the other, it they appear closely spaced in the same bin. However, other radar measurements of the target (range, velocity, azimuthal angle) could still be used to discriminate between the two targets.

If an exact phase differential over every receive element of the DBR radar could injected independently of the other elements, the elevation angle match filter or "Cumulative FFT" output of the elevation angle estimator would be as shown Figure 173. However, it would be very difficult in practice to isolate the return signal *per* receive element to inject a false signal with a differential phase shift corresponding to the false target elevation angle, in an actual EW engagement. Practically, despite any modulation imparted to the false signal by inserting an *absolute phase shift* corresponding to the false elevation angle, the DBR "digital beam-

forming-on receive" phased interferometry method (described in section 8.2.3), would still allow the true elevation angle of the jammer to be estimated. This is because the method measures *relative phase shift* regardless of the modulation applied to the signal.

For this reason, it is recommended that "Cross-Eye Jamming" instead, is used to disrupt the "phase front" across the receive antenna, so that no target elevation angle measurement is possible. For this reason, the two coherent out of phase signals from the DBR cross-eye jammer is shown in Figure 174 as received at DBR antenna elements 1 and 2. The false signals are transmitted simulateously but are 180° out of phase. As stated in section 7.1, two coherent sources repeating the radar's signal, disrupt the phase front and thus deny elevation angle estimation at the DBR.

The output of the DBR elevation angle estimator for estimation of the elevation angle of a true missile target is shown in Figure 175. The target's elevation "wrapped" angle is estimated as 5°. In Figure 176, the Cumulative FFT for the same target is shown, however the out-of-phase Cross Eye Jamming Signal was added to the true target return echo, at the radar receiver. From Figure 176, *no elevation angle measurement* is made by the radar.
It can therefore be concluded that cross-eye jamming can be used to deny target elevation angle measurement at the radar under ideal conditions. However, practical jammer specific considerations such as maintaining signal coherency, and required JSR, place limitations on cross-eye jamming effectiveness. An additional constraint in this application of cross-eye jamming, is that the received wavefront should be distorted in vertical polarisation to jam the DBR elevation angle estimation. This is discussed in detail in Chapter 10.

9 Signal Models, Radar Receiver, Multiple Plot Mode

The Radar Model in "Multiple Plot" or "Track Mode" is discussed in this chapter. Radar receiver models for simulating the measurement and estimation of target range, velocity and elevation angle as described in Chapter 8 are used in this section of the simulation. However, in "multiple-plot" mode, the radar receiver "single-plot" estimation models are "called" repeatedly over the entire vector of target ranges, velocities and elevation angles. Simulating the radar operation in this manner provides an estimated target coordinate per simulation time step. One major advantage of simulating the radar operation in this manner is that any error in the single-plot implementation is made apparent over the numerous simulation cycles necessary to generate the entire target track. Another feature of the "multiple-plot" mode simulation is that the single-plot mode figures can be dynamically run, as the track is generated. For example if the range match filter switch is activated in multiple-plot mode as the track is being generated and estimated, the functioning of the match filter per plot is visible. The user can therefore dynamically visualise the exact process at the single-plot level in NRT. This multiple-plot mode or capability can already be used in its current form to utilize actual target trajectories.

In this chapter, the mathematical foundation to the simulation multiple-plot mode is initially described, followed by presentation of results. Finally, a discussion of the results for this chapter is included. The results are interpreted and *conclusions are drawn*.

9.1 Radar Receiver Model, Multiple Plot Mode

9.1.1 Number of Bins

The receive window of the radar, during which time, the radar receives and processes signal information is given by:

$$R_{receive} = R_{\max} - R_{\min} = \frac{c\,PRI}{2} - \frac{c\,3\tau}{2} = \frac{c}{2}\left(PRI - 3\tau\right) \tag{237}$$

$$R_{\max} = \frac{c\,PRI}{2} \tag{238}$$

$$R_{\min} = \frac{c\,3\tau}{2} \tag{239}$$

$$t_{recieve} = PRI - 3\tau \tag{240}$$

The number of range bins is calculated using:

$$n_{Bin} = \frac{R_{\max}}{R_{\min}} \tag{241}$$

The range bin vector is generated using "n_{Bin}"and "dR" (which is the range vector sampling differential and not "range resolution"). Every time step corresponds to a single "dR" range increment. In that period the range, velocity and elevation angle estimates are generated for a single "Range-Doppler-Elevation angle" bin. The process is then repeated for the next "Range-Doppler-Elevation angle" bin.

9.1.2 Range Estimator

A target trajectory is selected based on target type. The model simulates the full range of the target trajectory. Then the range to the start of the range bin being processed, is randomized using the range measurement uncertainty, calculated using (16). This is done by assuming the measured range to the range bin is the mean of a standard Gaussian distribution with a standard deviation given by equation (16). The "randomization" process is shown mathematically in equations (242) and (243) for true and false target ranges.

$$R^{r}_{bin,\sigma} = R^{r}_{bin}(t) + U^{r}_{R}(t) \tag{242}$$

$$R^{f}_{bin,\sigma} = R^{f}_{bin}(t) + U^{j}_{R}(t) \tag{243}$$

In the above equations, the variables "U^{r}_{R}" and "U^{j}_{R}" are normally distributed random variables with means of "R^{r}_{bin}" and "R^{j}_{bin}" and standard deviations of "σ_R" and "$\sigma_R{}^{f}$". Measurement uncertainties for the true and false targets are generated independently to ensure that their respective measurement errors are uncorrelated.

The true target range "$R_o(t)$" is then folded to the ambiguous range within the range bin currently being processed. The following equation from Richards [6] was used to fold the randomized ranges "$R^{r}_{bin,\sigma}$" and "$R^{f}_{bin,\sigma}$" to the appropriate range bin:

$$R^{a}(t) = R(t) - k_R \frac{c\tau}{2} \tag{244}$$

The "appropriate" range bin is defined as the bin in which the true target detection should occur. Thereafter the folded, randomized range is converted to a time delay "t_o" for use in the signal models. The custom developed range match filter module "myrange.m" is then used to estimate the target range per plot. Thereafter, the estimated target range is obtained after unfolding the range to its correct bin and adding the randomized range to the start of that bin. The unfolding process is done using equation:

$$R(t) = R^{a}(t) + k_R \frac{c\tau}{2} \tag{245}$$

Thereafter, the randomized range to the range bin is added to the estimated range using the following equations:

$$R_{est}^{r}(t) = R_{bin,\sigma}^{r}(t) + R_{est}^{r}(t) \tag{246}$$

$$R_{est}^{f}(t) = R_{bin,\sigma}^{f}(t) + R_{est}^{f}(t) \tag{247}$$

The range error is then then difference between true and measured ranges:

$$R_{error}^{r} = R_{o} - R_{est}^{r} \tag{248}$$

$$R_{error}^{j} = R_{o}^{\ f} - R_{est}^{j} \tag{249}$$

Finally the range measurement uncertainty standard deviation is converted to a variance and compared to the variance of the theoretical range errors shown in equations (248) and (249).

9.1.3 Velocity Estimator

As stated earlier the target trajectory is selected based on target type. The track or multiple-plot model then generates all the required velocities in the target trajectory. It is assumed that the target is accelerating uniformly throughout the target trajectory and the time for the target to accelerate from its slowest velocity "$v_{\min}$" to its fastest "$v_{\max}$" is calculated using a "one dimensional equation of motion" from reference [9]:

$$t = \frac{v_{\max} - v_{\min}}{a_o} \tag{250}$$

The distance travelled by the target is calculated using another "one dimensional equation of motion" from reference [9]:

$$R = v_{\min} t + \frac{1}{2} a_o t^2 \tag{251}$$

The time calculated using equation (250) and range calculated using equation (251) are then used to set the maximum values of the time, range and velocity vectors for this simulation. Thereafter, the range to the target is randomized, folded (if necessary), estimated and unfolded in exactly the same manner as discussed in section 9.1.2.

The target velocity to the *Doppler* bin is also randomized using a similar method, as described in the previous section. The unfolded velocity relative to the start of the Doppler bin is randomized using the velocity measurement uncertainty equations (equations (17), (18) and (19)). The randomized velocity variable is added as indicated in equations (252) and (253):

$$v_{bin,\sigma}^{r} = v_{bin}^{r}(t) + U_{v}^{r}(t) \tag{252}$$

$$v_{bin,\sigma}^{f} = v_{bin}^{f}(t) + U_{v}^{j}(t) \tag{253}$$

The variables "U_v^r" and "U_v^j" are normally distributed random variables with means of "v_{bin}^r" and "v_{bin}^j" and standard deviations of "σ_V^{centre}, σ_V^{lower} and σ_V^{upper}". The randomized velocities are thereafter converted to Doppler frequency using equation (113).

Target Doppler frequencies are then folded to the zero Doppler bin at every simulation time step prior to estimation. The following equation from Richards [6] was used:

$$f_d{}^a = f_d - k_f\, PRF \tag{254}$$

The Doppler filter ("mydoppler.m") as described in "Single Plot" mode (section 8.3.2) is used to calculate the target Doppler frequency estimate per time step. This velocity estimate is then unfolded:

$$f_d = f_d{}^a + k_f PRF \tag{255}$$

The estimated Doppler frequencies are then converted to velocities once again and the velocity estimation errors were calculated using following set of equations:

$$v_{error}^r = v_o - v_{est}^r \tag{256}$$

$$v_{error}^j = v_o - v_{est}^j \tag{257}$$

9.1.4 Elevation Angle Estimator

Target elevation angle is simulated between the minimum and maximum elevation angles that are detectable by the DBR. The elevation angle vector is randomized using the elevation angle measurement uncertainty (equation (23)) as discussed in section 1.2.3.

A random measurement uncertainty value is then added to the estimate as shown:

$$\phi_{bin,\sigma}^r = \phi_{bin}^r(t) + U_\phi^r(t) \tag{258}$$

$$\phi_{bin,\sigma}^j = \phi_{bin}^j(t) + U_\phi^r(t) \tag{259}$$

In equations (258) and (259), the random variables "U_ϕ^r" and "U_ϕ^j" are normally distributed with means of "ϕ_{bin}^r" and "ϕ_{bin}^j" and a standard deviation "σ_ϕ". Then the elevation angles are unwrapped to the zero elevation angle bin, using the following equations

$$\phi_{amb} = k_\phi \sin^{-1}\left(\frac{\hat{\lambda}}{d}\right) \tag{260}$$

The elevation angles are then estimated using the DBR Single Plot "Elevation Angle Estimator" (myheight.m) and unwrapped using the elevation angle unwrapping factor "k_ϕ". Thereafter the measurement errors are calculated using:

$$\phi_{error}^r = \phi_o - \phi_{est}^r \tag{261}$$

$$\phi_{error}^j = \phi_o - \phi_{est}^j \tag{262}$$

9.2 Radar Receiver in Multiple Plot Mode, Scenario Description

Multiple plot mode for the radar receiver model, was developed to test whether a true or false target *trajectory* that is changing in range, velocity and elevation angle could be estimated. The next priority for the multiple-plot mode development was to simulate the effects of false target injection into the radar receiver, to determine whether the radar could distinguish between true and false target tracks. In multiple-plot mode, the capability to inject various types of false target profiles ("Range Gate Pull Off/Range Gate Pull in etc.") has been "built-in" to the simulation. Therefore, in order to test the full capability of the multiple-plot mode over all possible ranges, velocities and elevation angles, in X and L-Band, the scenarios listed in Table 21 and Table 22 were developed. In general, the missile target was selected in the majority of multiple-plot scenarios, since the missile travels over a larger distance at a higher velocity than the other targets. The radar target estimators are therefore tested over a larger sequence of range, velocity and elevation angle values.

	Target Type	Range to Target [m]	Velocity [m/s]	Acceleration [m/s^2]	Elevation Angle [deg]
True Target 1	Rotary Wing	0 - 45000	60	9.81	0
False Target 1	-	-	-	-	-
True Target 2	Missile	0 - 5000	150-1000	98.1	0-40
False Target 2	Missile	0 - 5000	150-1000	98.1	1-41

Table 21: X-Band, Multiple Plot Mode Scenarios

	Target Type	Range to Target [m]	Velocity [m/s]	Acceleration [m/s^2]	Elevation Angle [deg]
True Target 1	Missile	0 - 187000	800	98.1	0
False Target 1	Missile	15 -187015	800	98.1	0
True Target 2	Missile	0 - 5000	150-1000	98.1	0
False Target 2	Missile	0 - 5000	160-1010	98.1	0

Table 22: L-Band, Multiple Plot Mode Scenarios

It was found that testing the model in multiple-plot mode according to the scenarios listed above, robustly tested the range match filter, Doppler filter and Elevation angle Spatial FFT estimator, together with folding and unfolding of true values into the bin of interest. Any errors that would not be detected in "Single Plot" mode became clearly apparent in "Multiple Plot" mode, because an error is propagated hundreds of times, over multiple "single-plot" mode, simulation runs.

9.3 Radar Receiver Track Model, Results

Results from the Radar Receiver Model in Track Mode are displayed in this section. The X and L-Band range estimator and velocity estimator results as well as the X-Band Elevation angle estimator, output plots are presented and discussed in this section. The reader is advised to inspect the figures and refer to the discussion after *all of the figures* (range, velocity and elevation angle) are presented, for collective observations and conclusions on this section.

9.3.1 Range Measurement and Estimation, Results, X-Band

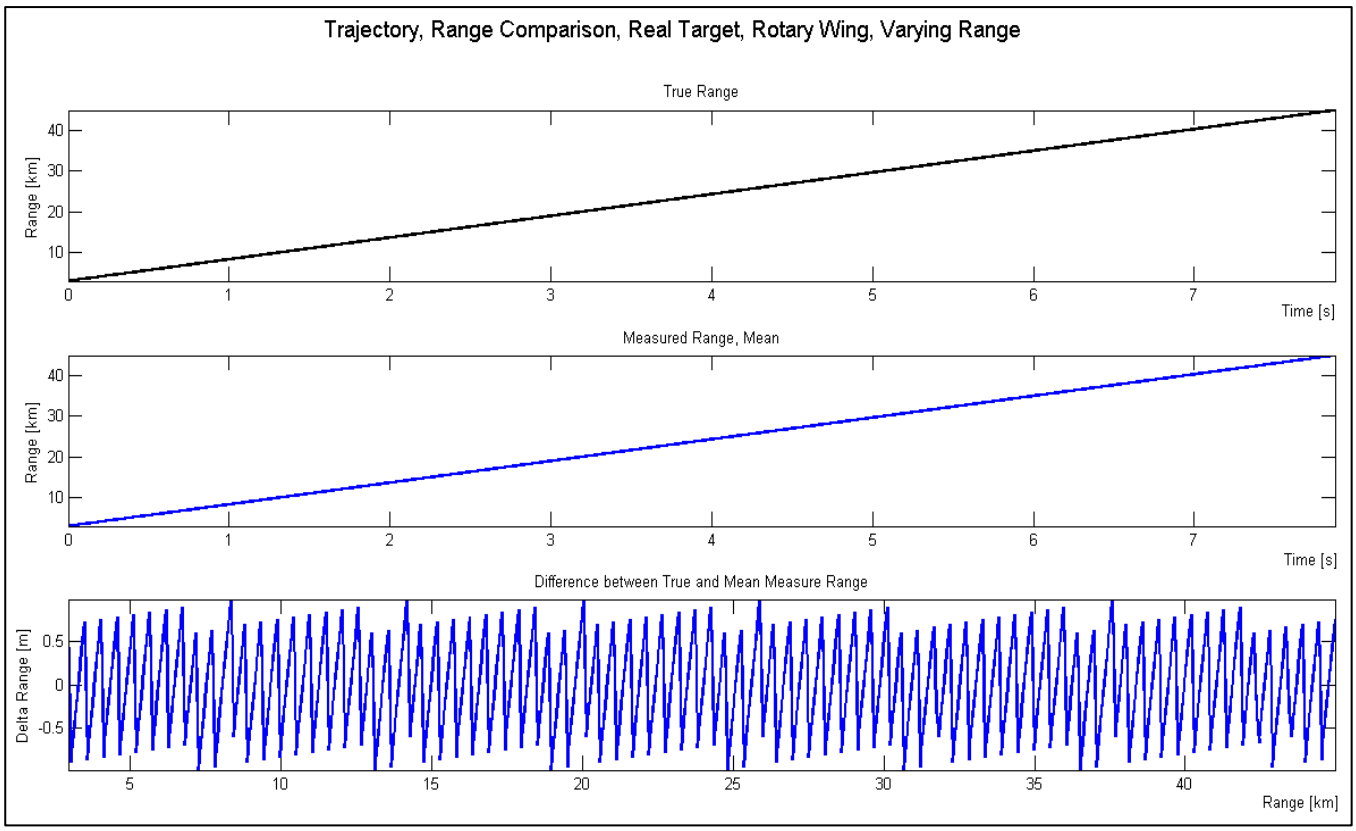

Figure 177: X-Band Range Estimation Track

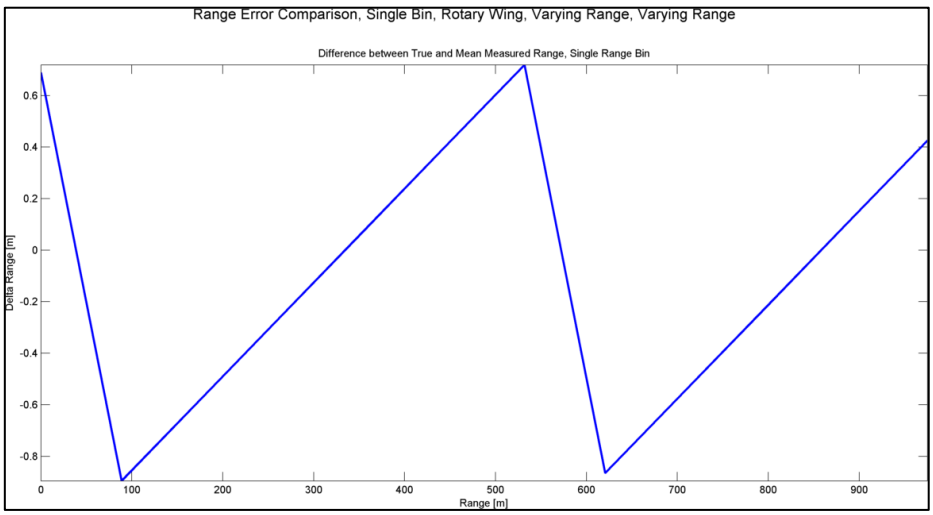

Figure 178: X-Band Range Estimation Error, Single Bin, 0dBW Amplitude

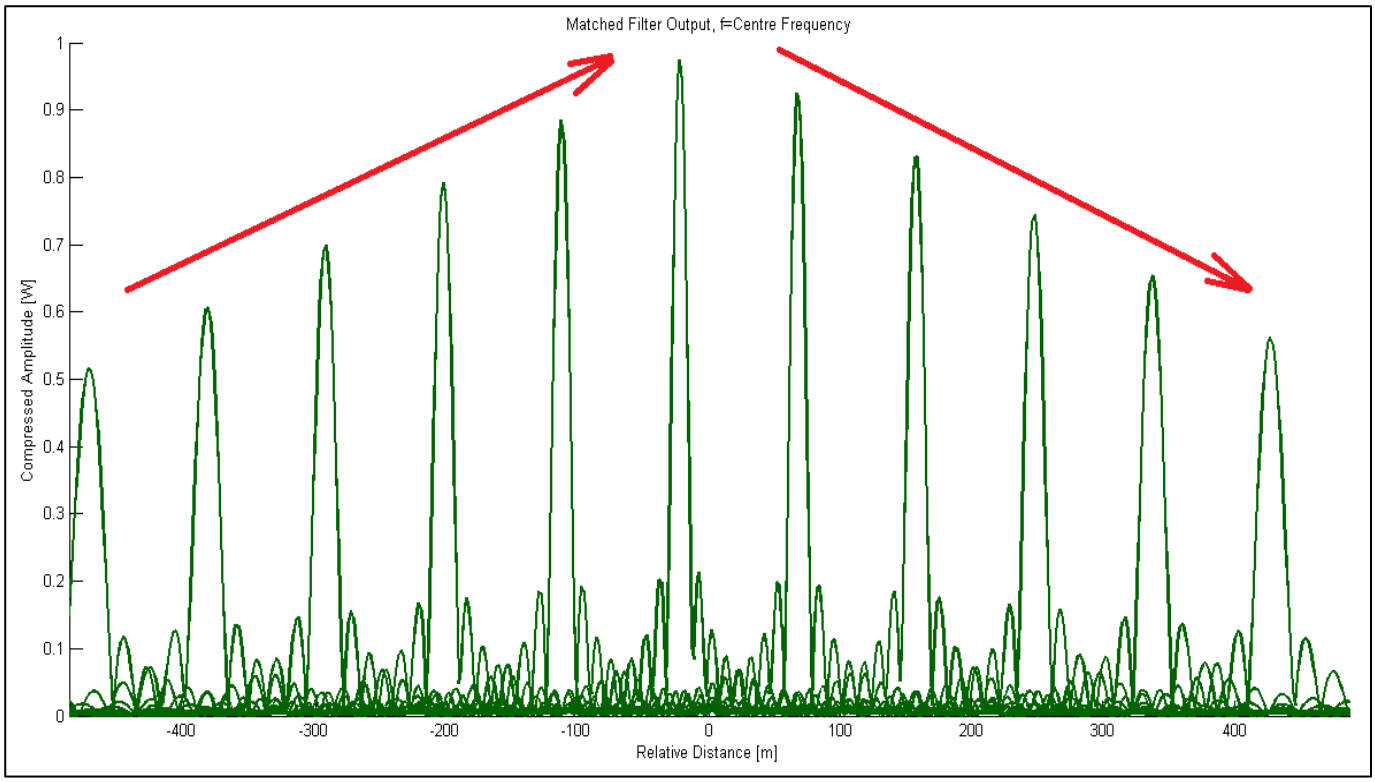

Figure 179: Degradation in range Match Filter estimation accuracy

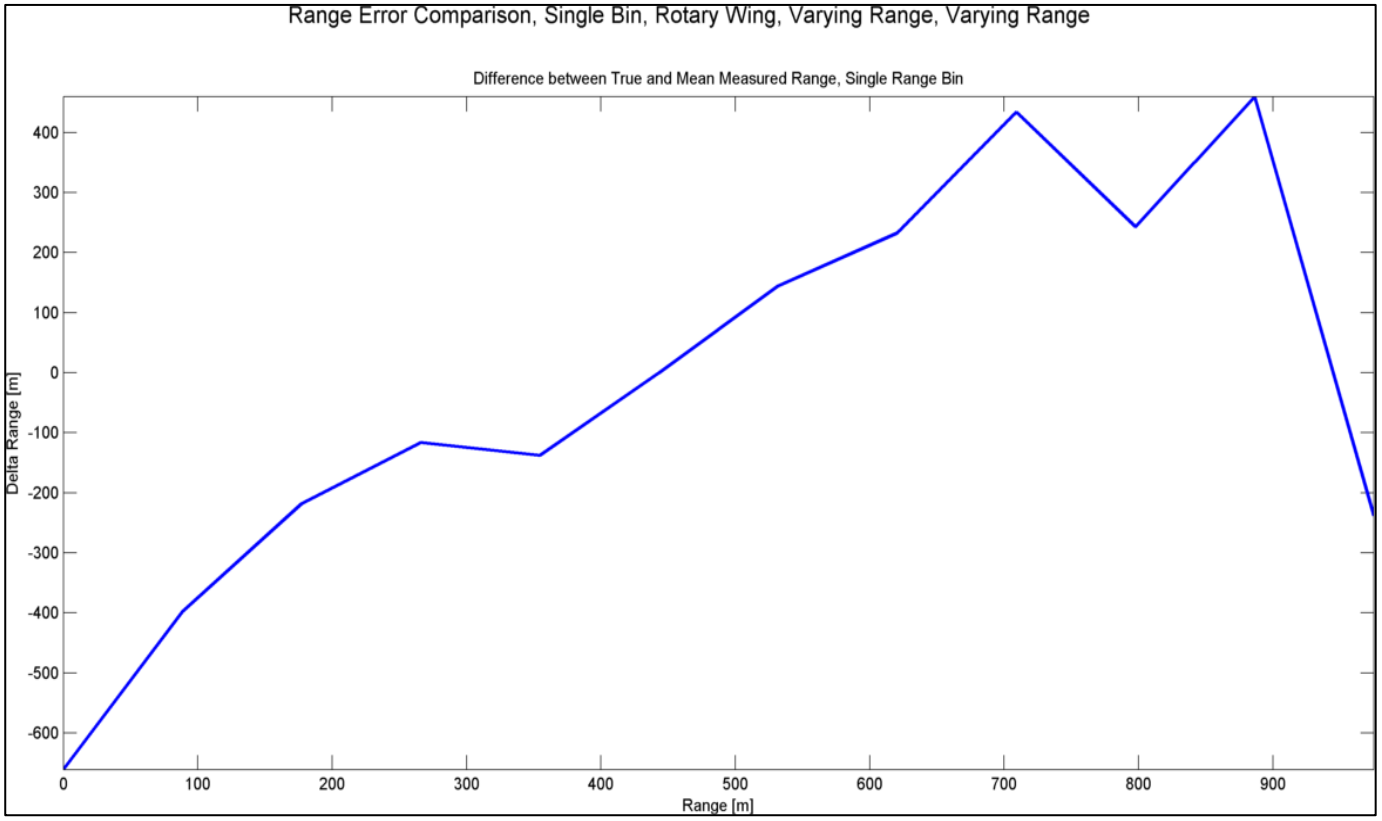

Figure 180: X-Band Range Estimation Error, Single Bin, Amplitude and Noise

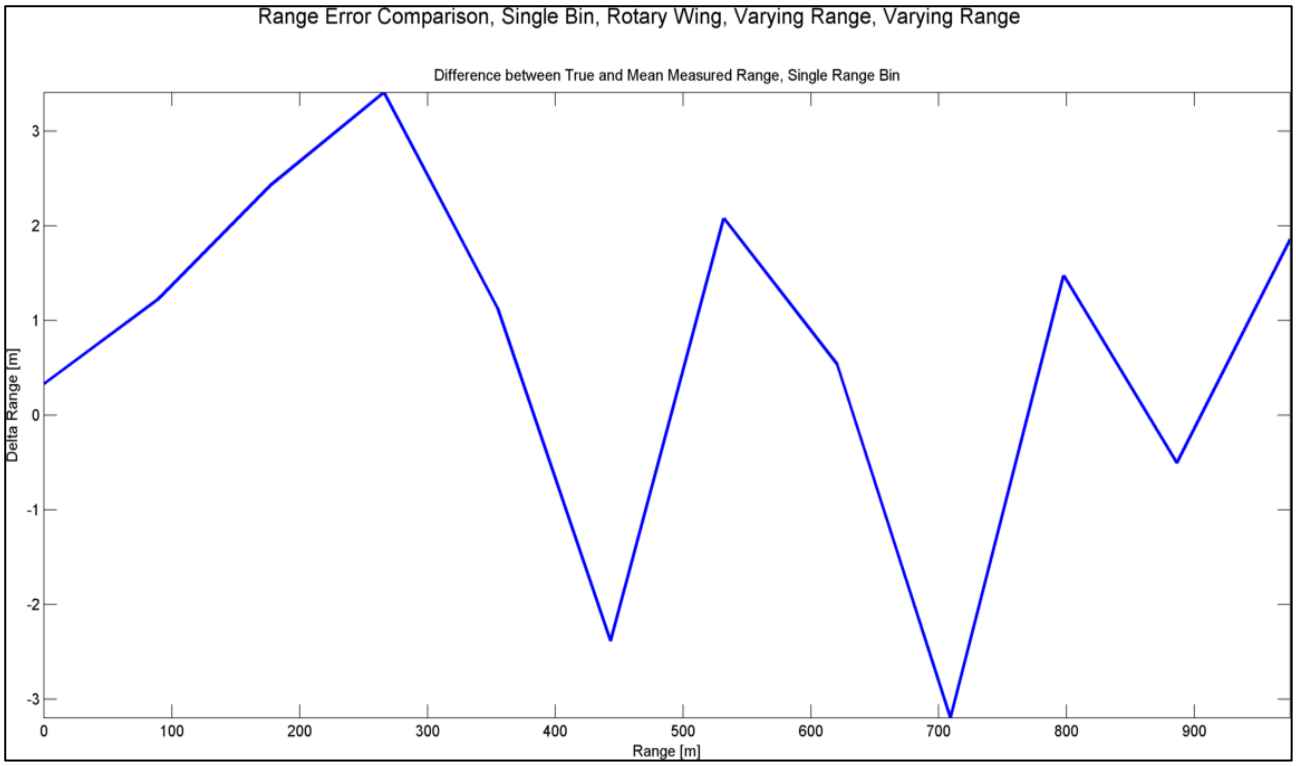

Figure 181: X-Band Range Estimation Error, Single Bin, with RF Gain

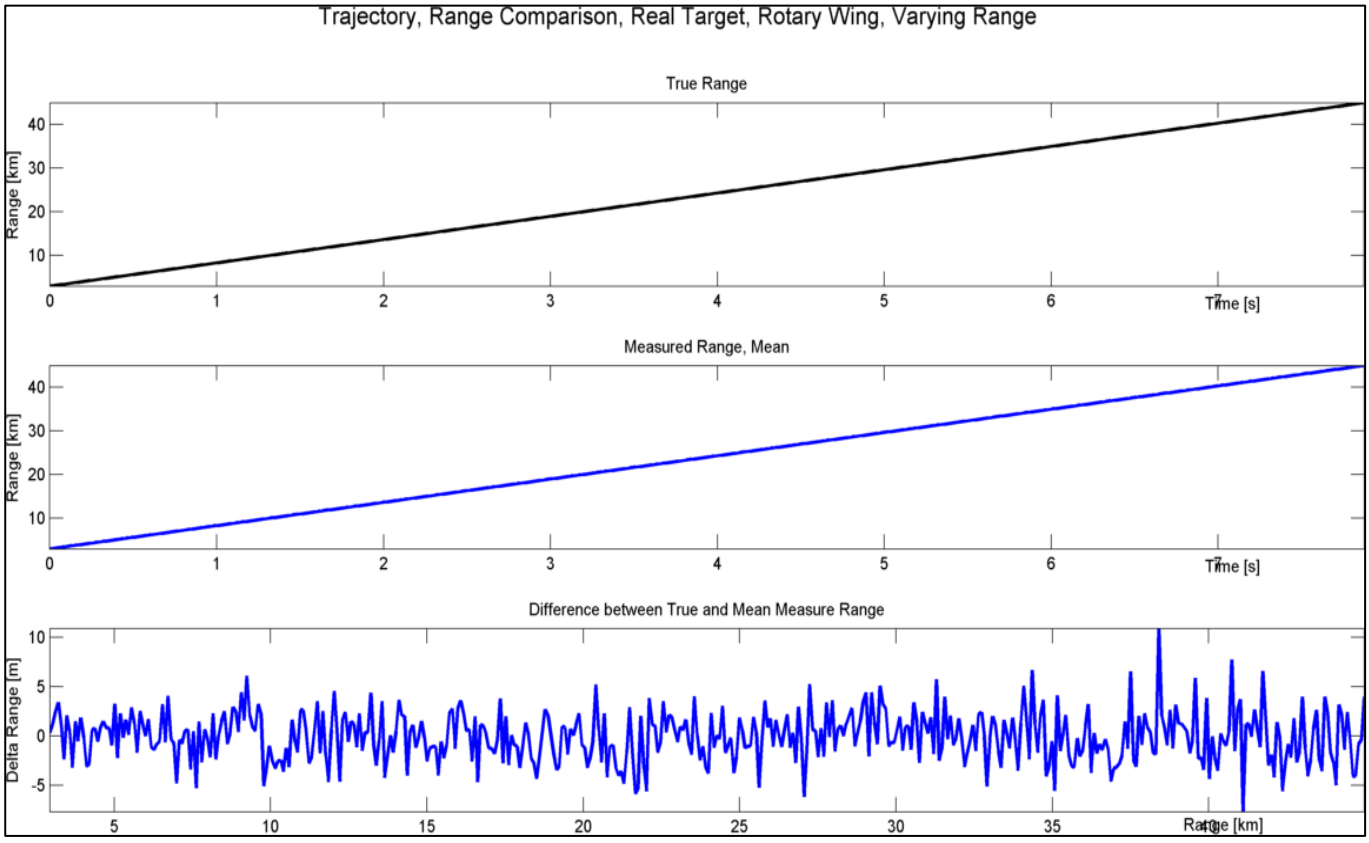

Figure 182: X-Band Range Estimation with Amplitude, Noise and RF Processing Gain

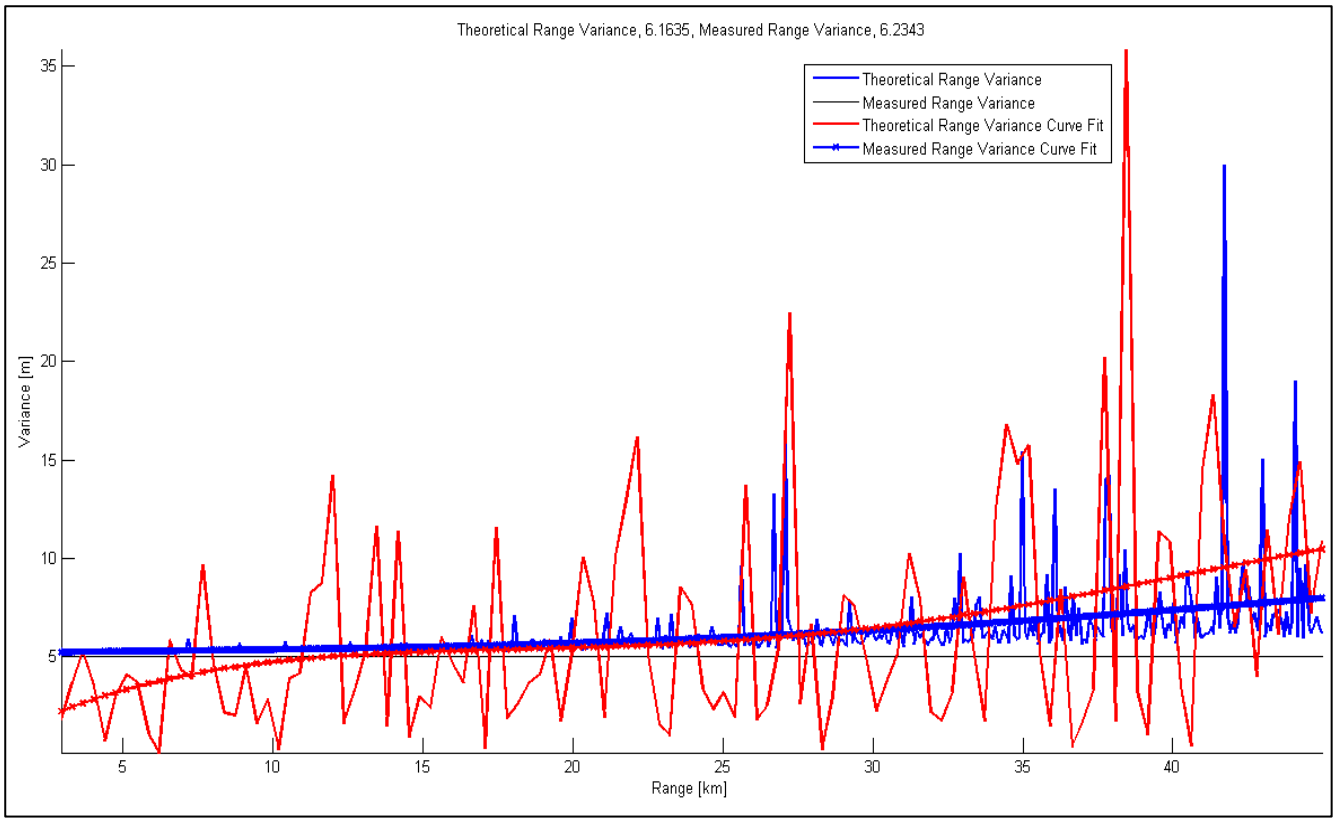

Figure 183: X-Band Theoretical Range Measurement Variance

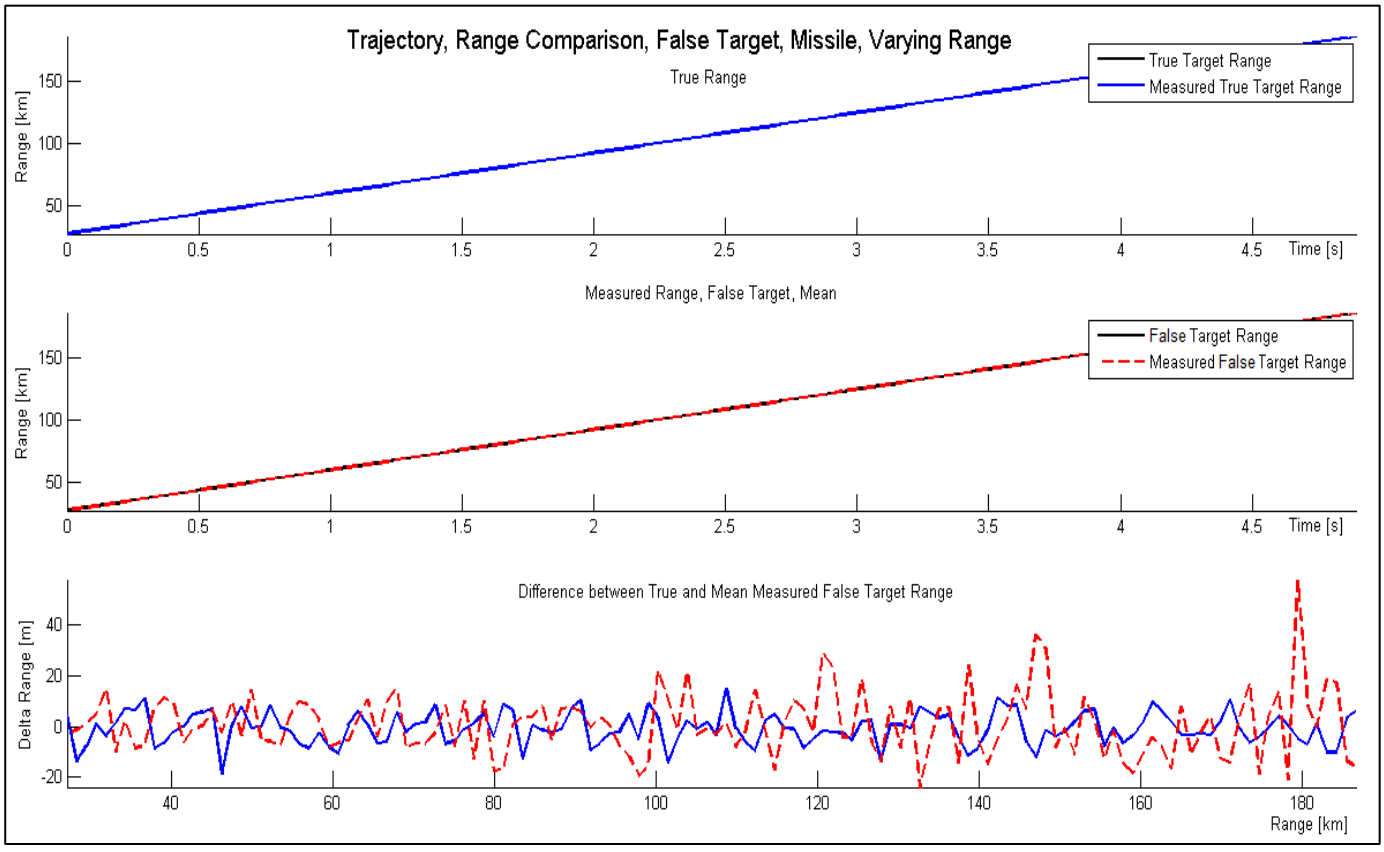

Figure 184: L-Band Range Track, with false target

9.3.2 Velocity Measurement and Estimation, Results

Target velocity estimation results from the Radar Receiver Model in "Track" mode are displayed in this section.

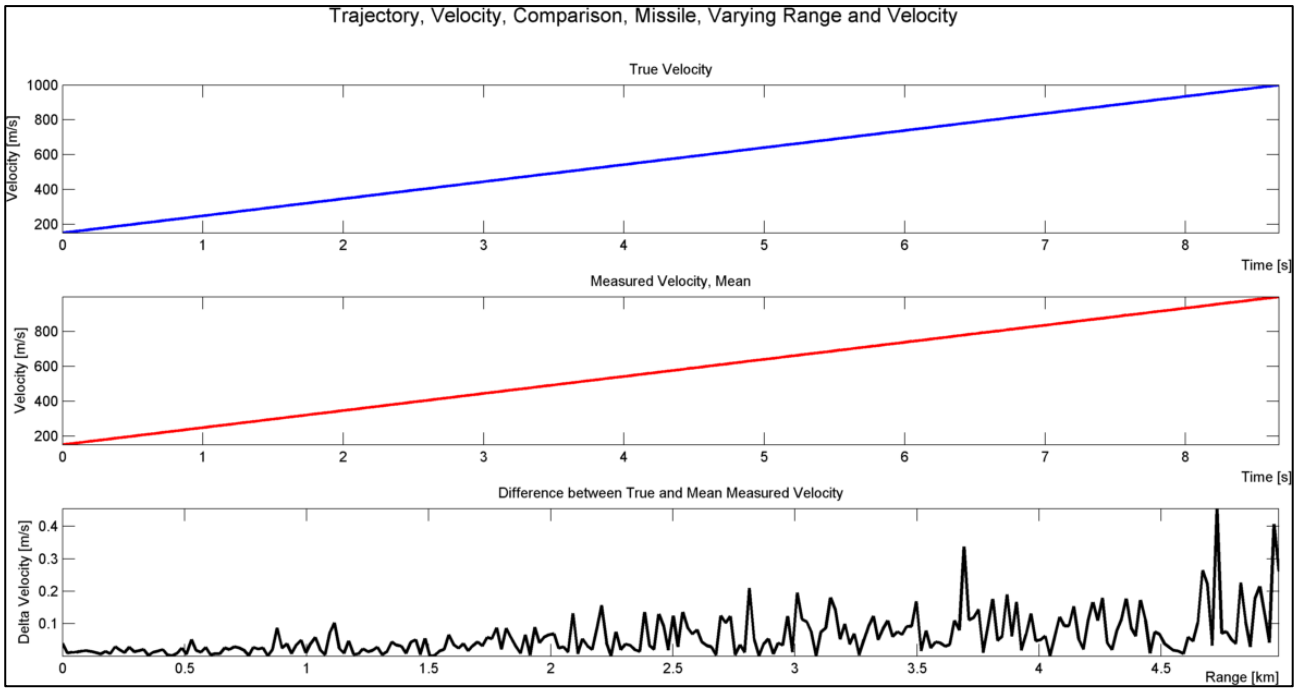

Figure 185: X-Band Velocity Estimation, Track

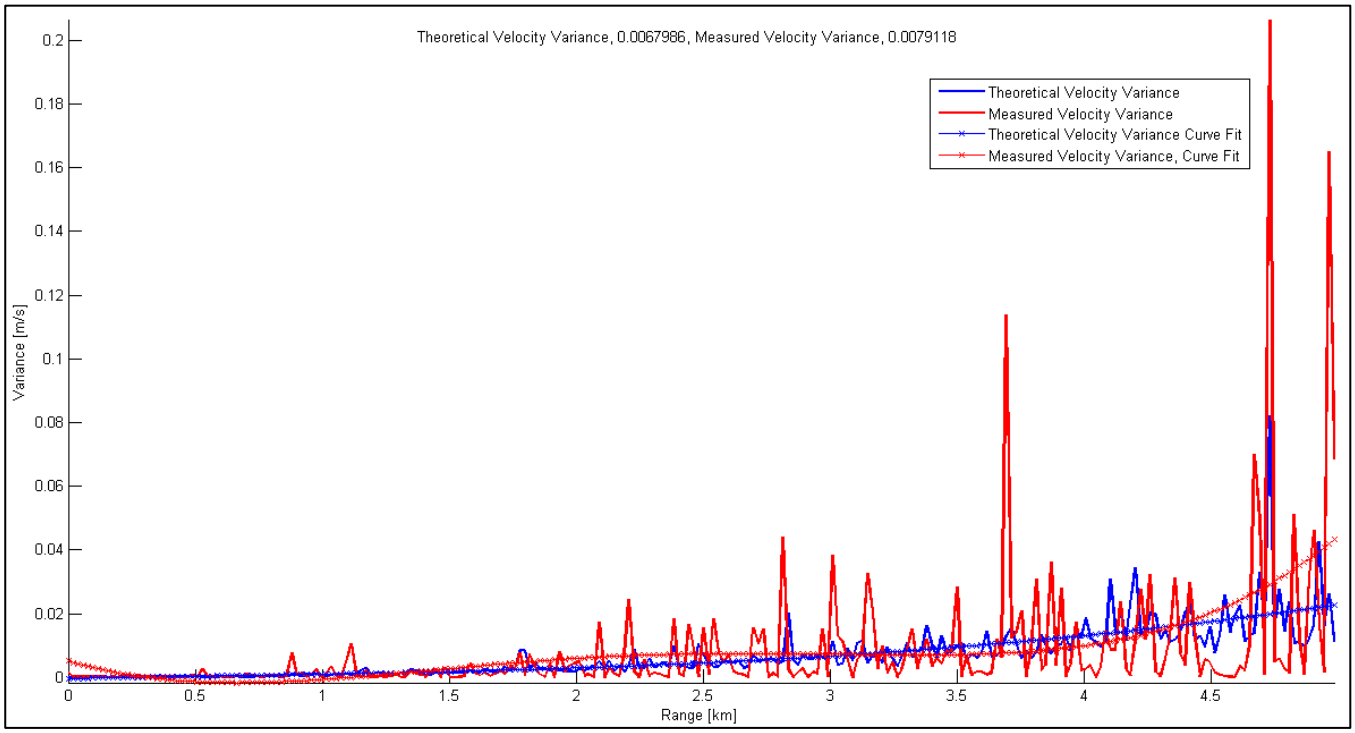

Figure 186: X-Band Velocity Variance, Comparison

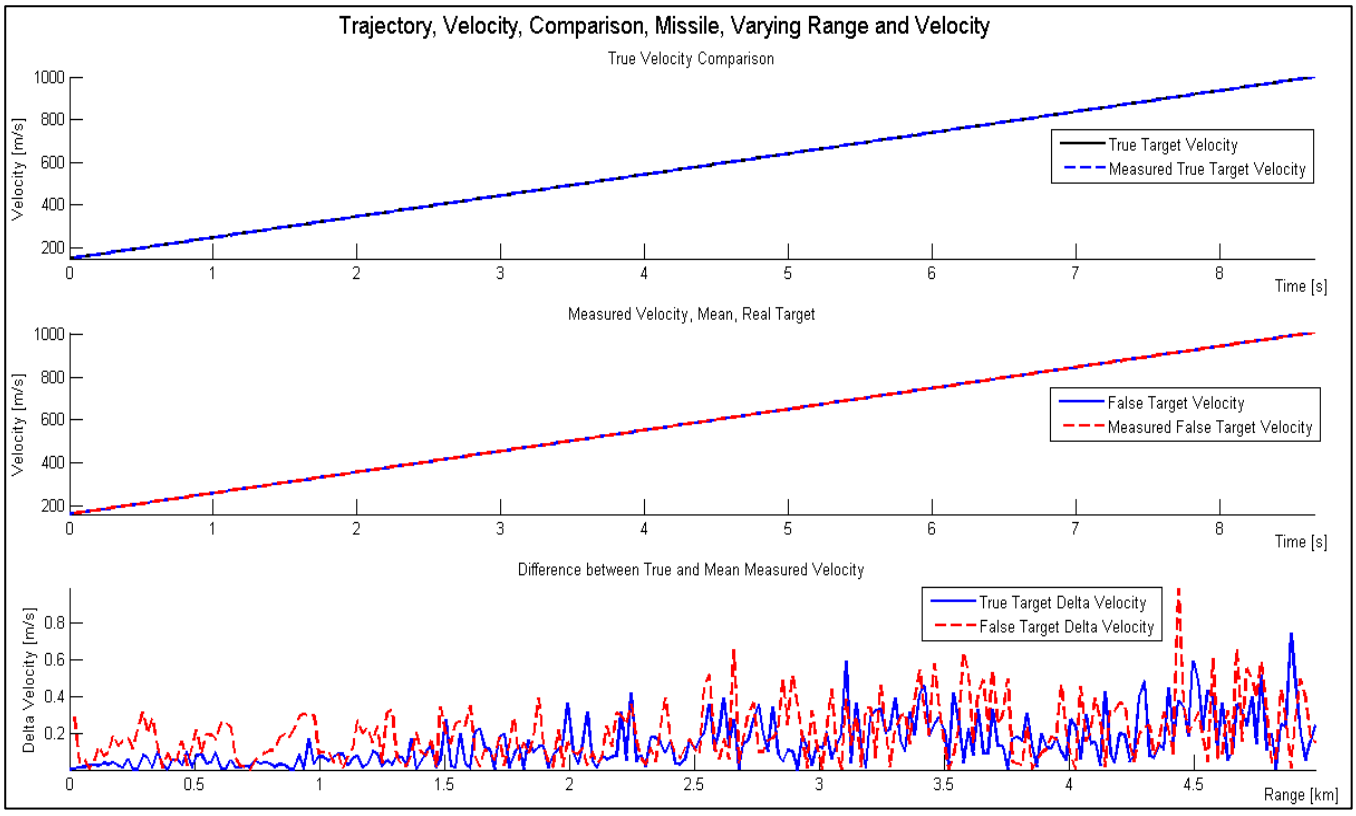

Figure 187: L-Band Velocity Estimation with False Target

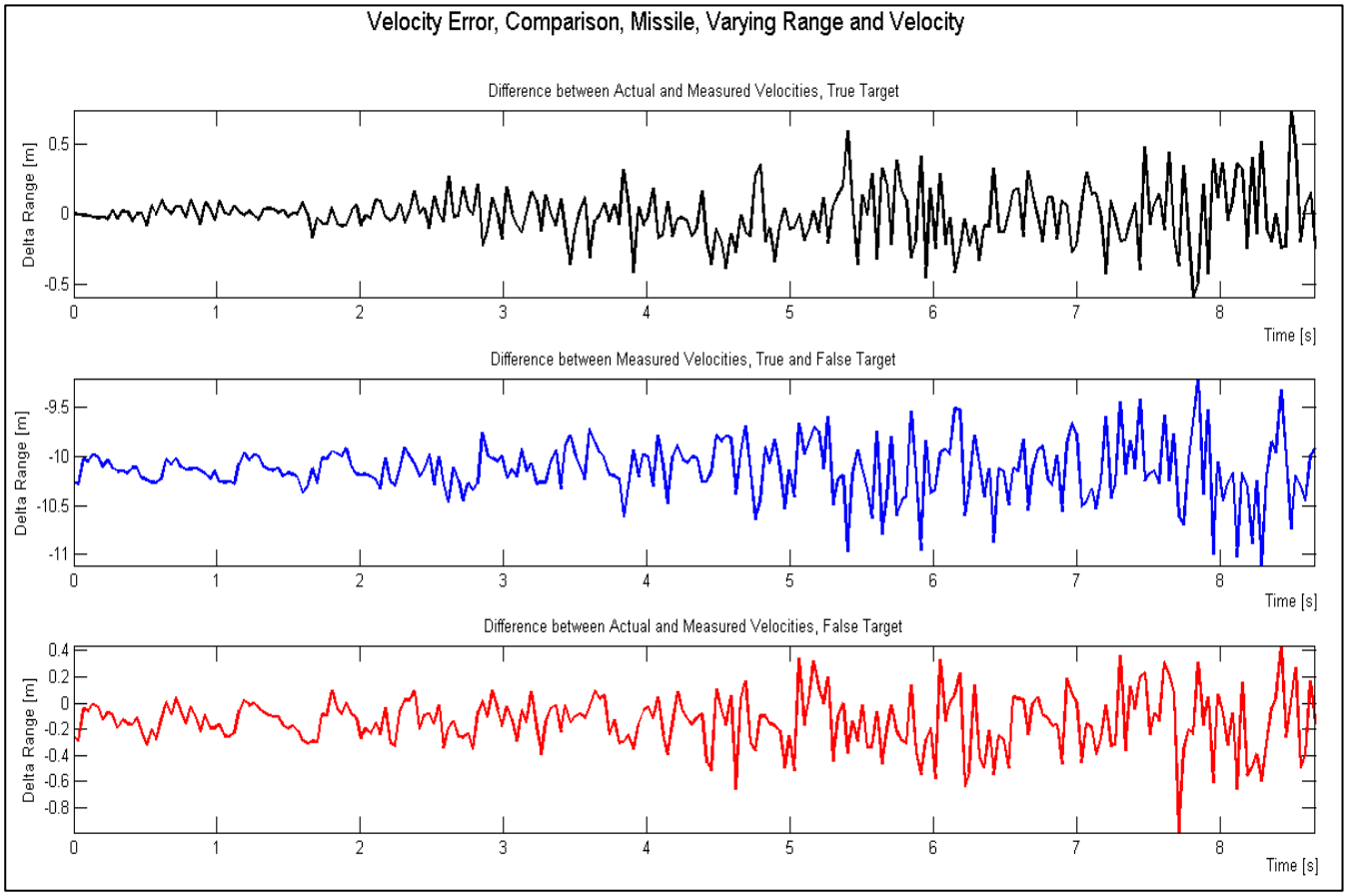

Figure 188: L-Band Velocity Estimation Errors for a True and False Target

9.3.3 Elevation Angle Measurement and Estimation, Results

Elevation angle estimation results, from the Radar Receiver Model in "Track" mode are shown in this section.

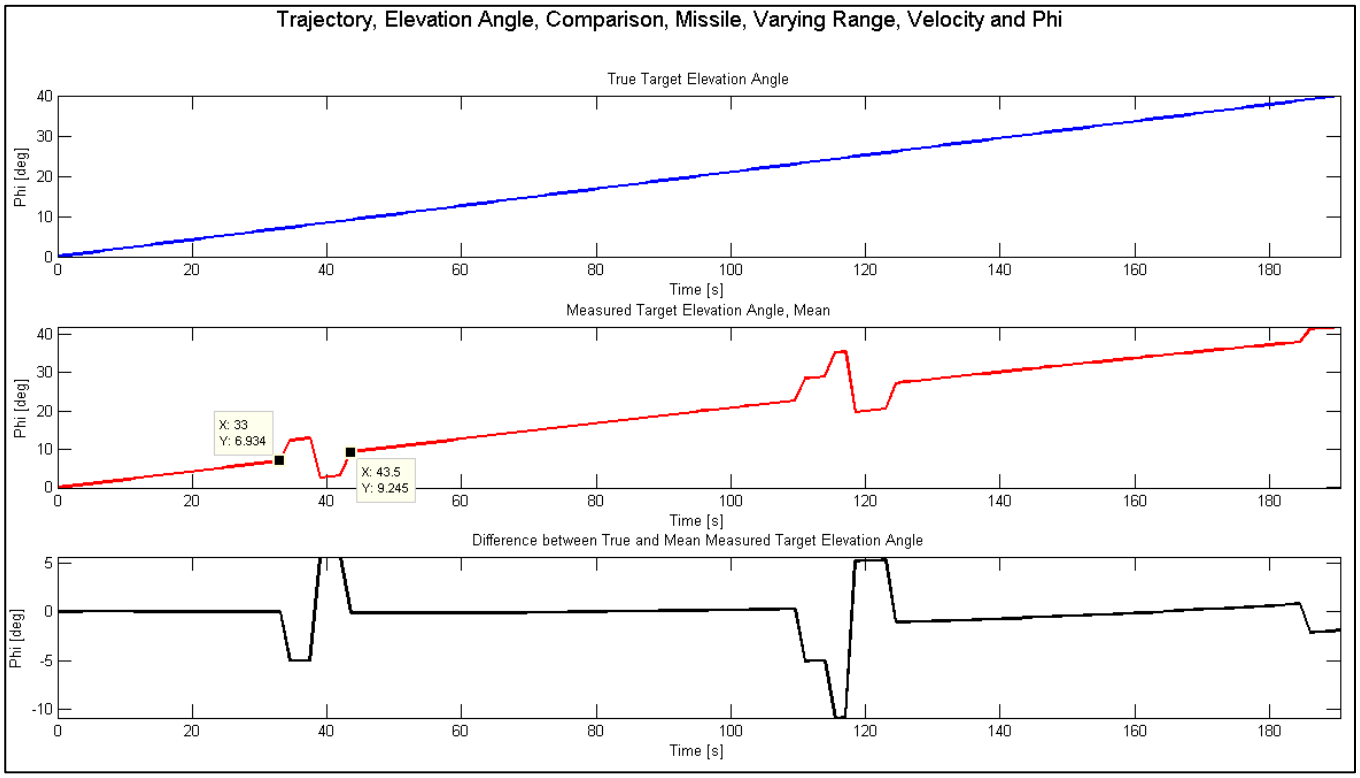

Figure 189: Elevation Angle Estimation, Track

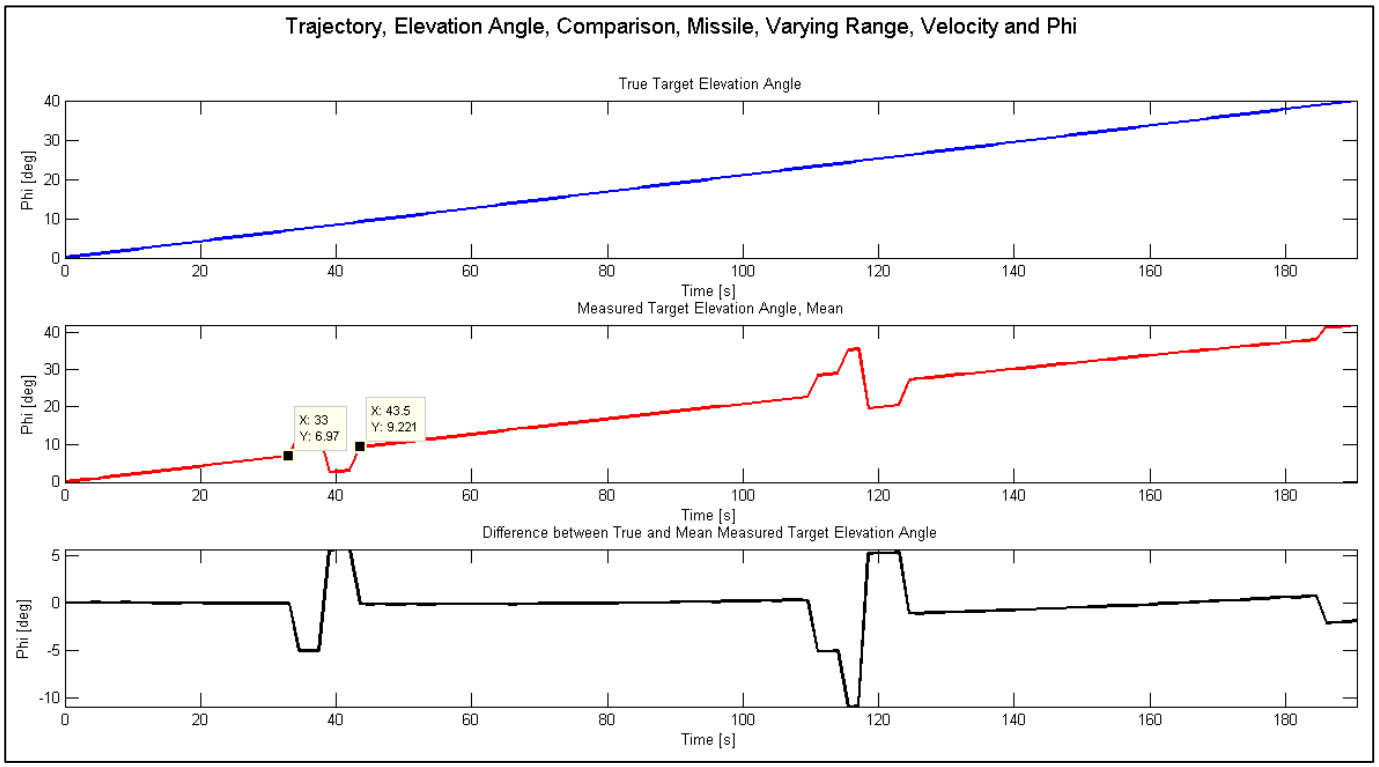

Figure 190: Elevation Angle Estimation, Track, Noise, Amplitude and Variance

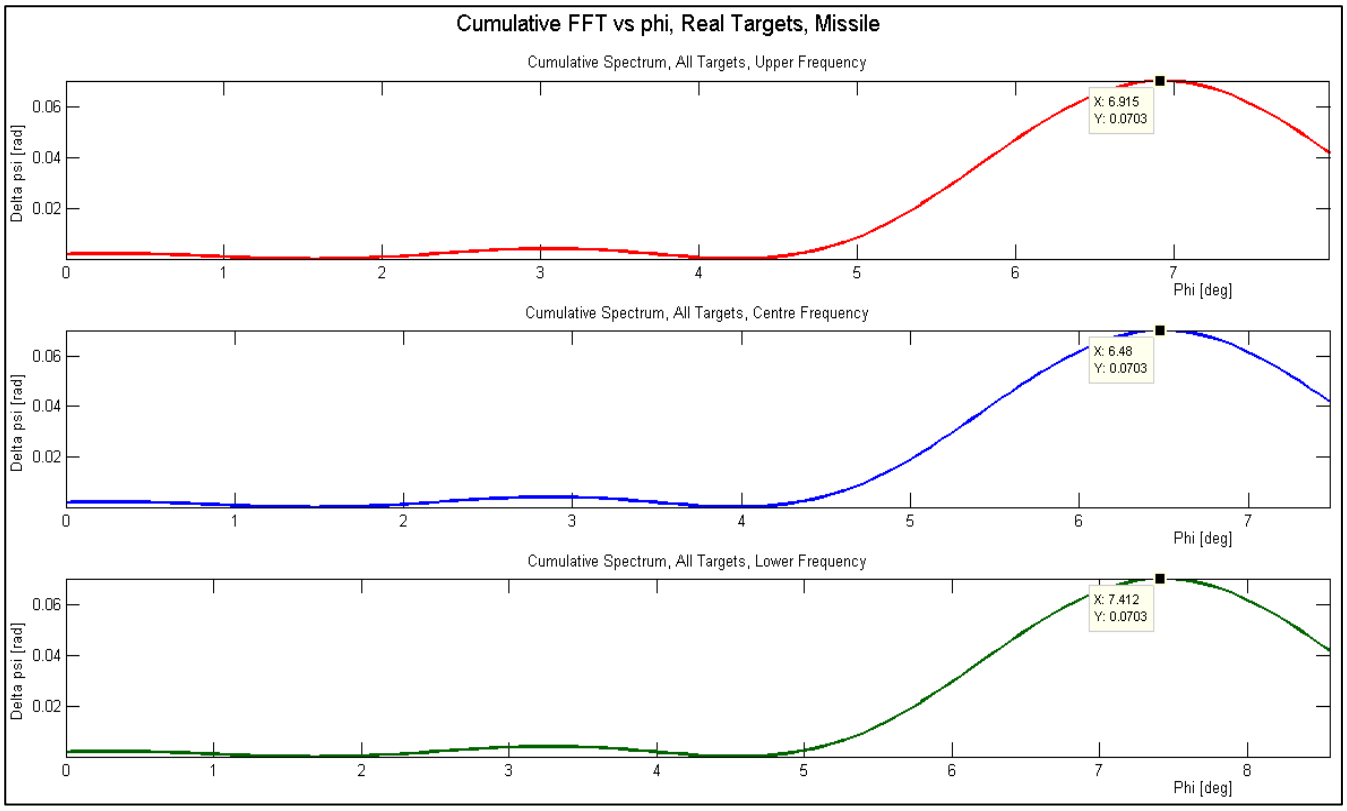

Figure 191: Maximum unambiguous Elevation Angle

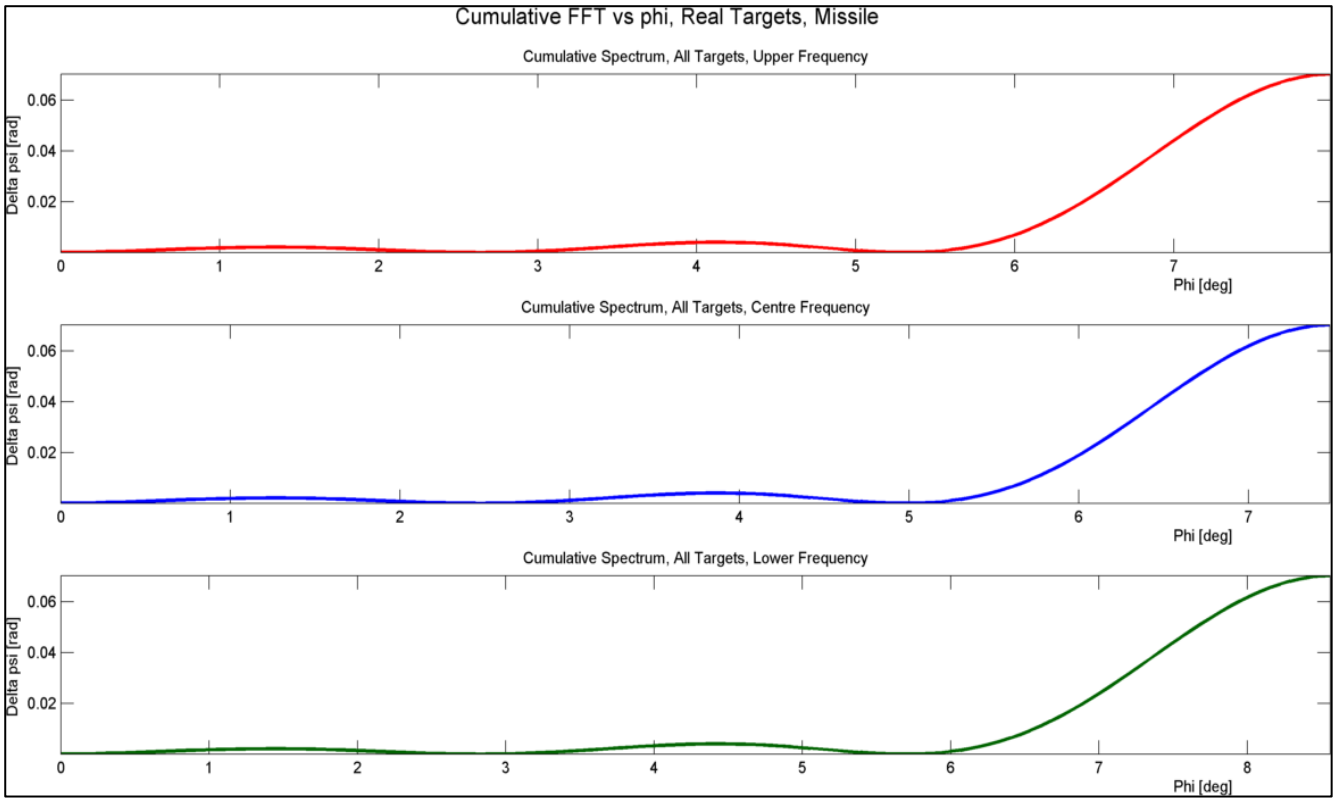

Figure 192: Degradation in Elevation Angle measurement

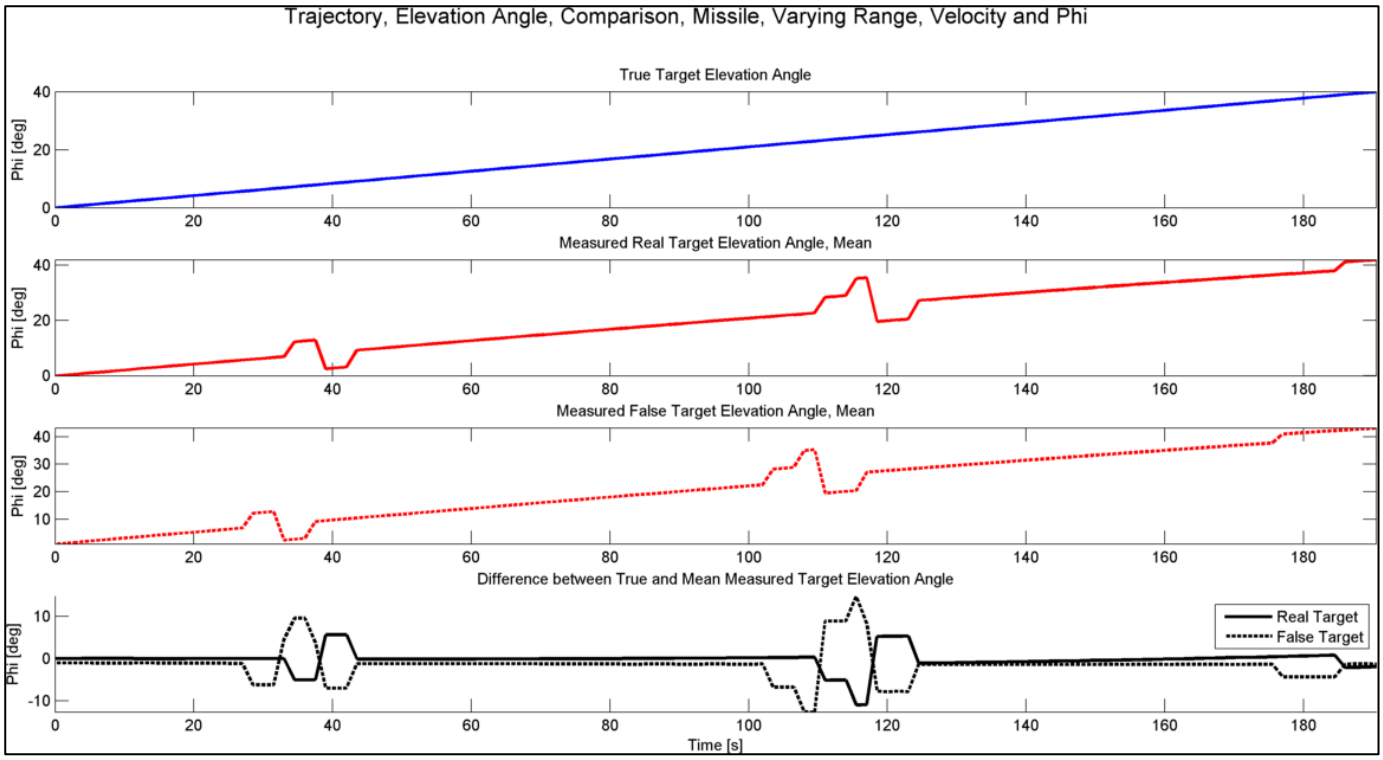

Figure 193: Elevation Angle Estimation, with False Target, Track

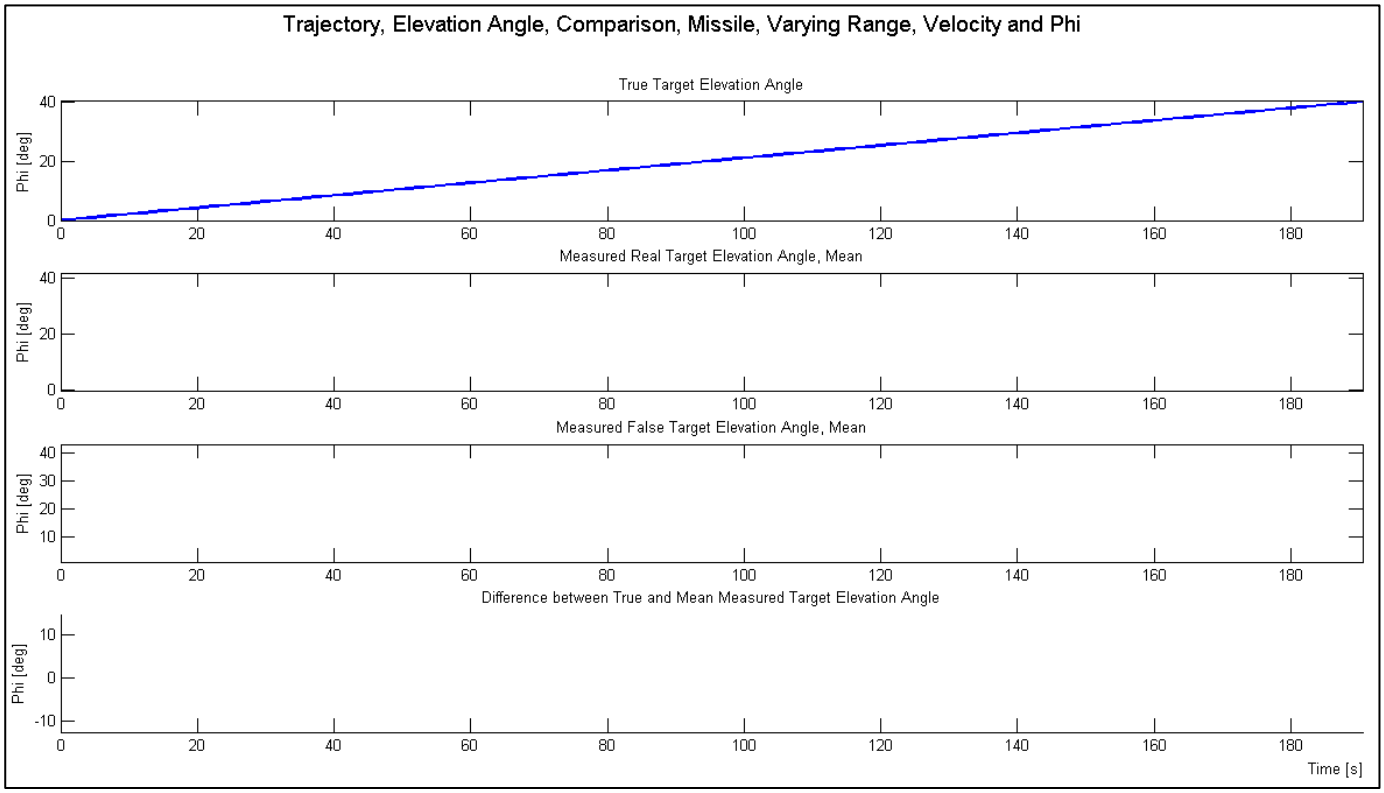

Figure 194: Elevation Angle Estimation, Cross Eye Jamming

9.4 Radar Receiver Track Model, Discussion of Results

The results obtained from the range, velocity and elevation angle estimators operating in "multiple-plot" mode are discussed collectively in this section.

Range Estimator, Multiple Plot Mode, Discussion of Results

The estimation of a rotary wing target as it moves across the entire detection range of the DBR X-Band subsystem was simulated and this result is displayed in Figure 177. The true target range trajectory is shown in the upper subplot of Figure 177.

The helicopter travels at a constant speed of 60m/s across the 45km DBR, X-Band theoretical detection range. During this time, the DBR is repeatedly processing the received target echoes per plot, using the range match filter in "Single Plot mode". The output of the range match filter, which is the estimated or "measured" target range is shown in the middle subplot of Figure 177. In the bottom subplot of Figure 177, the difference between true range and estimated target range, " R_{error}^{r} " is shown. An estimation error with a regular pattern is noted across the detection range in this subplot.. This scenario was selected to investigate the shape and magnitude of the error " R_{error}^{r} " that directly results from the match-filter.For this reason, no noise or measurement uncertainty were applied to the signal and the amplitude of the target echo was 1V.

The same error shown over the entire detection range in Figure 177 is shown for a single range bin in Figure 178. The shape of the error is caused by the periodic estimation error imparted to the estimate by the range match filter as the target moves to the edges of the range bin. This effect is shown in Figure 179, which is an example of a "dynamic plot" output, generated while the simulation is running in "Multiple Plot" mode "building" the tracks. The peak of the match filtered response decreases at the edges of the range bin as can be seen in Figure 179.

In Figure 180, single bin range error is shown when amplitude, noise and measurement uncertainty are inserted into the signals *without including RF processing gain*. The size of the error grows substantially to approximately 800m which is caused by the fact that insufficient SNR is available for match filter operation. The range match filter response degrades substantially in this case as was shown in Figure 155. Nevertheless, when RF processing gain is applied, with amplitude, noise and measurement uncertainty, measurement errors decrease to approximately 6 m, as shown in Figure 181.

In Figure 182 the same scenario shown in Figure 178 was tested, except, noise, amplitude, RF gain and measurement uncertainty were applied to the signal. This particular simulation result most accurately represents actual range estimation by the DBR. Target RCS scintillation effects, range bin estimation errors and receiver noise were all taken into consideration. In addition, use of the range measurement standard deviation to randomize the range to the start of the range bin, takes into account *errors* caused by false detections in clutter, even though clutter was not simulated.

The increase in the range estimation error as the target range from the radar is increased, can be seen from the lower subplot of Figure 182. This is the result of a decrease in SNR as range increases according to the "$1/R^4$" relationship between SNR and Range "R". This trend is also visible in Figure 183, which compares the theoretical range variance (equation (16)) with the simulated or measured range error variance. A trendline fitted to both sets of data show that the measured variance is generally higher than the theoretical range error. Both error variances increase with range (or decrease in SNR). This result proves that the simulation errors are within theoretical limits and thus provides an improved "level confidence" with respect to the simulation fidelity.

Figure 184 depicts an important result generated at L-Band over the 187.5km theoretical detection range. A false missile target was simulated at a range of 15m behind the true target. By comparing the size and shape of the range measurement error for both the true target and false target as shown in the lower subplot of Figure 184, it can be concluded that no difference between true and false targets would be discernible by the DBR. However, this is based on the assumption that the intercepted radar signal parameters are accurately estimated by the ES subsytem, in the first place.

Velocity Estimator, Multiple Plot Mode, Discussion of Results

The velocity profile of a missile accelerating at 10g's from 150m/s to 1000m/s is shown in Figure 185. The set of velocities in this scenario, test the DBR target Doppler estimation module as per the full DBR capability requirement for a missile target.

The true target velocity "v_o" is shown in blue in the upper subplot of Figure 185. Every velocity-time point of the true target trajectory was input into the simulated DBR Doppler Filter. The output of the filter was the estimated target velocity "v_{est}^r" per plot, which is shown in the middle subplot of Figure 185.The difference between the two velocity profiles, "v_{error}^r"

is shown in the bottom subplot. Noise, amplitude, RF processing gain and measurement uncertainty were all simulated in this scenario.

Theoretical velocity estimation variance (equations (17), (18) (19)) was compared to estimated velocity estimation variance as shown in Figure 186. The estimated variance compared closely to the theoretical variance, which imply the DBR velocity estimator is sufficiently accurate. The increase in variance as *SNR* decreases is clearly visible in this figure.

A deception jamming scenario where a false target with false Doppler shift was injected into the DBR receiver, together with a true target echo was simulated at L-Band. The false target travels at velocity 10m/s faster, than the true missile target at every time step.

The results are shown in Figure 187 and Figure 188. The true velocity track and its measurement is shown in the first subplot of Figure 187, while the false target velocity track and its radar measurement is shown in the second subplot. The bottom subplot compares the *absolute value* of the velocity estimation errors for the true and false targets. It can be seen that the magnitude of the maximum error for both targets are similar (6 - 8m/s) and the basic shape of the errors are similar.

A more in depth analysis of the velocity estimation errors calculated by comparing differences between true and false target velocities is depicted in Figure 188. The upper subplot shows the difference between actual and measured velocity for the true target (this error was also shown in the bottom subplot of Figure 187). The middle subplot shows the difference between true and false *measured* velocities. The 10m/s offset of the false target from the true one, can be observed in this subplot. In the lower subplot of Figure 188, the velocity estimation error between false target profile and its measured profile are shown (this error was also shown in the bottom subplot of Figure 187). From the velocity error analysis just presented, it can be concluded that there are no distinguishing features allowing the radar to discriminate between the true and false targets. This conclusion is obviously based on the proviso, that the ES subsystem has correctly estimated intercepted radar signal parameters.

Elevation Angle Estimator, Multiple Plot Mode, Discussion of Results

The upper subplot of Figure 189 shows a true target elevation angle changing over time. The target is a missile flying from an elevation angle of 0° to 40°. As previously mentioned, the maximum elevation angle measurable by the DBR is 40°, which is bounded by the elevation 3dBW beam width. The missile thus flies through the full range of elevation angles measurable by the radar, while simultaneously moving at constant velocity away from the

radar. The elevation angle measured by the radar is shown in the middle subplot, in red. The difference between the actual and measured target elevations are shown in black in the third subplot of Figure 189.

Large discontinuities are noticeable at two points in the measured elevation angle subplot (middle subplot). The start of the first discontinuity occurs at an angle of 6.934°, and ends at an angle of 9.245°. The elevation estimation accuracy begins to degrade at angles greater than 6.934° and less than 9.245°. The elevation angle cumulative FFT peak used to estimate the target elevation angle begins to move close to its unambiguous limit as shown in Figure 191. The theoretical maximum positive angle, is defined as:

$$\phi_{\max} = \frac{\sin^{-1}\dfrac{\lambda}{d}}{2} \tag{263}$$

The average maximum angle calculated for all three X-Band frequencies is 8.1°, with the total elevation angle calculated from the average value of the peaks estimated at the three frequencies as shown in Figure 191. If the target elevation peak occurs past this point, the elevation angle measurement, begins to degrade. The measurement at the maximum elevation angle limit of 8.1°, is shown in Figure 192.

Generally, ambiguous angles occur as defined in the equation below:

$$\phi_{amb} = \sin^{-1}\left(k_\phi \frac{\lambda}{d}\right) = \sin^{-1}\left(k_\phi \frac{\lambda}{d}\right) = \sin^{-1}\left(k_\phi \lambda f_s{}^d\right) \tag{264}$$

Where the "spatial sampling frequency" is defined as:

$$f_s{}^d = \frac{1}{d} \tag{265}$$

In equation (264) "k_ϕ" is an integer representing the "k^{th}" ambiguous angle. In this simulation, a correction factor was applied if the angle was in one of the unambiguous regions. A method to resolve the angle ambiguity was presented by R. McAulay in reference [33].

The elevation angle result obtained when noise, amplitude and variance are applied to the target signal is shown in Figure 190. It can be seen that estimation accuracy is marginally affected, but the general accuracy of the method is unaffected when compared to Figure 189. This can be seen by comparing the value at first degradation of the angle at 6.934° (middle subplot of Figure 189) to 6.97° (middle subplot of Figure 190).

It can therefore be concluded that the cumulative FFT method is robust against noise, amplitude and measurement uncertainty variations, but suffers a loss in estimation accuracy at multiples of the maximum unambiguous angle.

The results under *hypothetical* jamming conditions are shown in Figure 193. A false target signal with a false elevation angle phase shift is injected into the model per receiver element. As mentioned in section 7.1, this situation would only occur under laboratory testing conditions. Nevertheless, it can be seen that the false target elevation angle varied in a similar manner to the actual elevation angle profile.

In order to jam the DBR elevation angle estimator, it is proposed that a multiple antenna jammer such as the DBR Jammer (shown in Figure 10) be used with the cross-eye jamming technique to induce a phase shift distortion across the antenna. Under these jamming conditions, the DBR elevation estimator is completely compromised. The radar is therefore "denied" elevation angle measurement and not "deceived" by a false elevation angle measurement. The DBR is therefore *unable* to perform any elevation angle measurement as depicted by Figure 194.

Please note that the L-Band portion of the DBR is not intended to be used for height estimation as explained in section 1.2.2, therefore no L-Band results are presented for the elevation angle estimator.

Summary of Results, Range, Velocity and Elevation Angle, Multiple-plot mode.

A summary of all the track estimation errors (range, velocity and elevation angle) for all three target types are discussed in this section. X-Band results are shown in Table 23 while the L-Band results are shown in Table 24.

Target Type	Error Type	Maximum Error [Amplitude, RF Gain, Noise, Measurement Uncertainty]
Fixed Wing	Range Estimation [m]	1.075
Fixed Wing	Velocity Estimation [m/s]	0.050
Fixed Wing	Elevation Angle Estimation [°]	N/A, Cross Eye
Rotary Wing	Range Estimation [m]	1.112
Rotary Wing	Velocity Estimation [m/s]	0.496
Rotary Wing	Elevation Angle Estimation [°]	N/A, Cross Eye
Missile	Range Estimation [m]	1.100
Missile	Velocity Estimation [m/s]	0.049
Missile	Elevation Angle Estimation [°]	N/A, Cross Eye

Table 23: X-Band "Multiple Plot Mode", Summary of Results

Target Type	Error Type	Maximum Error [Amplitude, RF Gain, Noise, Measurement Uncertainty]
Fixed Wing	Range Estimation [m]	9.166
Fixed Wing	Velocity Estimation [m/s]	0.057
Rotary Wing	Range Estimation [m]	9.275
Rotary Wing	Velocity Estimation [m/s]	0.096
Missile	Range Estimation [m]	9.091
Missile	Velocity Estimation [m/s]	0.099

Table 24: L-Band "Multiple Plot Mode", Summary of Results

In Table 23, it can be seen that the maximum errors for all three target types was similar. However, the error at X-Band for range estimation was much smaller than at L-Band. The finer wavelength at X-Band reduces estimation error compared to L-Band, but the X-Band maximum detection range is smaller than at L-Band. It can also be deduced that if cross eye jamming is utilized by the DBR Jammer, no elevation measurement is possible by the X-Band system as shown in Table 23.

10 Conclusions and Recommendations

10.1 Conclusions

The primary conclusion from this study is that the DBR can be effectively electronically attacked, if a modern EA system is used. Modern in this context, is classified as "digital EA", with a particular focus on digital "Deception Jamming" and "Cross Eye Jamming" using a DRFM. DRFM's can be built from COTS hardware that is available commercially. The digital receivers, microwave lenses, antennas etc. are all commercially available. In other words, the conclusion is that the ease at which a custom-built DBR Jammer could be developed by a foe is high.

An important pre-condition to the claim made above: *"attacked effectively electronically*"; is that the DBR signals are accurately estimated in NRT. The sensitivity of Microwave Receivers on the market as well as their quick digital processing capabilities indicates that this is entirely plausible. In particular, the Digital Channelizing Receiver, in my opinion would be the most suitable candidate for an anti-DBR, ES system. This type of receiver offers wideband operation in both the DBR's operating bands and allows an appropriate sampling rate for effective ES algorithm operation. The architecture proposed in Figure 10 would allow simultaneously intercept of the signals in either of the DBR transmission bands. False signals could also be re-transmitted simultaneously in both bands using this configuration.

The wideband "non-stationary" signal used on the DBR also pose challenges to its parameter estimation, by an EA system. Despite this, some algorithms are capable of detecting and interpreting this type of intercepted signal. The WVD and its many variants have been used in actual EW systems for this purpose, as shown in the papers by J. Hu et al. [24]. However, ES systems that use IFM receivers would not be effective against the DBR if multiple DBR's are deployed that transmit in the same frequency band. Interference received from any other emitter in the X or L bands would render any IFM estimate of signal parameters, ineffective. A statement by F. Auger [12] explains why: *"The fundamental notion of instantaneous frequency implicitly assumes that at each time instant there exists only a single frequency component"*. Even though the standard WVD would not perform robustly, if pulses from multiple DBR's are received at the ES receiver portion of the DBR Jammer, because of the "cross term interference"; further processing using the HT suppresses the interference peak. The multi-component IFM signal cannot be improved by HT processing however.

The “SPWVD” or “Spectrogram” algorithms are much less susceptible to interference and can also be used to estimate a multi-component signal. The Spectrogram algorithm, runs faster than the SPWVD. However, both the SPWVD or spectrogram algorithms still have poor resolution relative to RSPWVD. Overall, the RSPWVD was on par with the Spectrogram in terms of processing speed, offers better resolution than either the WVD, SPWVD or Spectrogram and is not susceptible to interference like the IFM algorithms. By far, the biggest advantage of the RSPWVD is that one ES algorithm can be used to estimate multiple signal parameters. Intercepted signal carrier frequency, chirp rate, PRI, bandwidth and number of pulses can all be estimated using a single TF representation. Older methods require the use of different algorithms to estimate signal parameters. A particular advantage of the RSPWVD is the excellent resolution compared to other ES algorithms. This is important when a radar pulse with pulse diversity, is intercepted. The waveform coding applied to the pulse can be determined if the TF image resolution is high enough, with the RSPWVD. In addition, if the TF image is processed over the whole radar bandwidth, the sequence of frequencies or PRF’s used by the radar when it is in “frequency agility”, “frequency hopping” or “PRF agility” mode can be determined by the ES system. These measures are typically used by the radar to “protect” the radar’s signal parameters from being intercepted.

If signal preprocessing techniques based on “Blind Source Separation” are used, the IFM and WVD algorithms could still be used, since signal components are separated using the “Blind Source Separation” based methods, before application of the ES algorithms. However, these pre-processing algorithms consume response time and jammer signal processing resources. On the other hand, the RSPWVD would still be able to operate on the intercepted signal even without Blind Source Separation pre-processing.

However, a problem with the RSPWVD and most ES algorithms, is that the chirp rate estimation error at low SNRs (<-2dBW), grows very large, very quickly. This is also a problem for any of the typical “Energy Based” ES algorithms such as the WVD or Spectrogram. The IFM also suffers from this problem.

Nevertheless, under the critical assumption that the radar parameters have been accurately estimated by the *ES* subsystem, the DBR Jammer, *EA* subsystem can mimic a true target response, accurately. Target range and velocity as well as false amplitude modulations to simulate false RCS’s can be generated and retransmitted, by the EA subsystem. However, inducing false ranges and false Doppler frequencies (i.e. false velocities) would be far easier than inducing a false elevation angle and hence, height. This is because the “digital beam-

forming on receive" processing done by the DBR uses the signal's "relative phase" to determine its elevation angle and hence its height. Any false "*absolute phase"* modulated onto the false signal would therefore have no effect, since the radar measures "*relative phase".* For this reason, it would be impossible practically to *deceive* the radar in elevation angle, but it would certainly be possible to *deny* the radar, in elevation angle measurement.
An EW technique, simulated in this study, called "Cross-Eye Jamming" would be effective to jam the DBR height finding "digital beam-forming on receive" technology. In this case, no "a-priori" information is required on the radar antenna in order to induce a false phase shift across the aperture. The combination of signals from the cross-eye jammer are "coherently out of phase" and are also replica's of the true radar signal, which cause the phase front of the received signal to be "disrupted" at the DBR antenna. This prevents the DBR from measuring relative phase for determining target elevation angle.

However, a unique Cross Eye Jammer requirement for jamming the DBR is that the false signals be transmitted using cross-eye jammer antennas, which are vertically orientated since the phase front should be disrupted across the vertically orientated beam-forming elements on the DBR. A vertical baseline cross-eye jammer is certainly not yet a common configuration for most airborne jammers. It is possible that the traditional horizontal baseline cross-eye jammer be used against the DBR, with "horizontal to vertical"polarizers at the jammer antennas. Some loss in false signal power would result because of this modification, however.
Another physical design complication faced by the cross-eye jammer, is the difficulty in maintaining phase and amplitude coherency between the two coherent false signals.

Because of the advanced nature of the cross-eye jammer required to jam the DBR, it is quite reasonable to conclude that the DBR elevation angle estimator, is protected against elevation angle jamming, since it is unlikely that an advanced cross-eye jammer of the type described above, be deployed against the DBR in the African Battle space.
As shown in the "System Level" analysis, the dual detection range of the DBR L and X-Band subsystems, places different design constraints on the DBR Jammer, in terms of ES sensitivity, response time and POI, which would complicate the Jammer design.
If noise jamming were used against the DBR without any EP, then the noise jammers certainly have the advantage if the "Burn-Through" range performance is considered. However, noise jammers would not be very effective against a DBR, if EP measures such as Jam Strobe

Detection, Jammer Strobe Excision and Side-lobe Cancellation as well as radar processing techniques such as Coherent Integration, Doppler Processing are used.

To summarize, it is stated that the DBR Jammer proposed can effectively jam the DBR's range, velocity and elevation angle estimators, *in theory*. The azimuth angle estimator cannot be jammed using only one DBR jammer. However target azimuth angle information alone, cannot be used by the radar to track the target, in order to engage it with anti-aircraft weapons. Practical design constraints on the jammer would reduce its effectiveness in jamming the DBR.

10.2 Recommendations

The recommendations from this study are divided into sections; those related to DBR specific improvements and those related to simulation improvements.

10.2.1 Electronic Protection

The following measures are suggested for improved Electronic Protection:

1. There are currently, established waveforms in use on Air Surveillance, Acquisition and Tracking Radars that use better electronically protected waveforms than the LFM. "Non-Linear Frequency Modulation (NLFM)" waveforms and "Pulse Coded" waveforms are some examples that provide greater challenges to an ES system. It is recommended that a more complex waveform be used in both Bands compared to the LFM.
2. Investigate the use of "Orthogonal Frequency Division Multiplexing (OFDM)" Waveforms ([25]) or temporal pulse diversity with the LFM ([20]). Both techniques allow identification of the Deception Jammer's false target by the radar.
3. Radar measurement uncertainties are difficult for a DRFM to process, without "a priori" victim radar knowledge. This is because measurement uncertainties depend on specific radar parameters. See equations (16), (17) and (23) that are dependent on radar parameters, "ΔR", "ΔV" and ϕ_{3dB}". The true target would therefore have measurement uncertainties within known limits, while the false target might not. This fact could be used to discriminate between true and false targets.
4. Improved jamming requires "HUMINT" on the Radar. The DDS based EA system uses radar waveforms stored in memory in order to jam effectively. The development information surrounding any radar must be strictly controlled. In particular, marketing material should not include pictures of the antenna that would be accurate in dimension.

10.2.2 Simulation Model Improvements

5. If an actual radar signal processor were provided for use in the simulation, actual radar performance in an EW scenario can be estimated. This would be done using:
   a. Simulation of the detection process, including the Constant False Alarm Rate (CFAR) process. Target detection statistics in an EW encounter can be thereafter, be measured.
   b. Tracking filter performance analyses using actual target trajectory data. The simulation would be extended to simulate targets approaching at any azimuthal angle.
6. Low SNR ES algorithms, in particular the FrFT and its variants are proven to operate effectively at low SNR. The Fast ICA with FrFT [42] promises good performance at SNR's as low as -15dBW. This algorithm should be simulated and tested.
7. Simulation of environmental effects, such as ground, sea and volume clutter, multipath effects, multiple emitter interference and target glint, can be modelled to improve simulation fidelity.
8. Substantial scope for software optimisation is possible in this simulation. The various models and functions were developed, as the individual algorithms were validated. These standalone functions were then integrated. The effect of this approach is that inefficient programming techniques were sometimes employed. The recommendation is therefore to consider redesigning the simulation from a "Top-Down" perspective, as opposed to "Bottom Up", to streamline and optimise the simulation operation.
9. In particular, much optimisation of the ES parameter estimation algorithm can be done for NRT processing. NRT operation of the ES Model with the inherent limitations of processing power on a commercial Personal Computer might be efficiently mitigated by porting the simulation to an efficient programming language such as C++.
10. The impact on the DBR from a greater range of EA techniques can be simulated to determine a greater array of performance impacts on radar and jammer. For example, two deception-based jamming techniques that can be considered were presented by Z. Bin, in reference ([46]):
    a. Smart Noise Jamming

$$J_1(t) = U_n(t) \cdot \cos\left(2\pi \cdot f_j \cdot t + \varphi(t)\right) \tag{266}$$

    Where

$$\varphi(t) \in [0\,;\,2\pi] \tag{267}$$

    b. Cover Pulse Jamming

$$J_2(t) = A_{cp} \cdot \cos\left(2\pi \cdot f_c \cdot t\right) \tag{268}$$

11 List of Abbreviations

A/D or ADC	Analog-Digital Converter
ABADS	Airborne Air Defence System
AESA	Active Electronically Scanned Array
AoA	Angle of Arrival
AOC	Association of Old Crows
ARM	Anti-Radiation Missile
C&I	Chopping and Interleaving
CA-CFAR	Cell Averaging Constant False Alarm Rate
CFAR	Constant False Alarm Rate
COBRA	Counter Battery Radar
COHO	Coherent Local Oscillator
CPI	Coherent Processing Interval
C-RAM	Counter Rockets, Artillery Mortars
CSIR	Council for Scientific and Industrial Research
CWT	Continuous Wavelet Transform
C4I	Command, Control, Computers and Intelligence
DBR	Dual Band Radar
D/A or DAC	Digital-Analog Converter
DDS	Direct Digital Synthesizer
DFT	Discrete Fourier Transform
DP	Doppler Processing
DPSS	Defence, Peace, Safety and Security
DRFM	Digital Radio Frequency Memory
DSP	Digital Signal Processor
DWVD	Discrete Wigner Ville Distribution
EA	Electronic Attack
ECM	Electronic Countermeasures
ECCM	Electronic Counter-Countermeasures
ED	Electronic Defence

ELINT	Electronic Intelligence
EM	Electromagnetic Spectrum
EMP	Electromagnetic Pulse
EO	Electro-optic
EP	Electronic Protection
ES	Electronic Support
EW	Electronic Warfare
FA	Fractional Autocorrelation
(FastICA)	Fast Independent Component Analysis
FFT	Fast Fourier Transform
FH	Frequency Hopping
FPGA	Field Programmable Gate Array
FrRT	Fractional Fourier Transform
GA	Genetic Algorithm
GaAs	Gallium Arsenide
GBADS	Ground Based Air Defence
GLRT	Generalized Likelihood Ratio Test
GST	Generalized S Transform
HMI	Human Machine Interface
HPM	High Power Microwave
HT	Hough Transform
IC	Integrated Circuit
ICA	Independent Component Analysis
IEEE	Institute for Electrical and Electronics Engineers
IF	Intermediate Frequency
IFM	Instantaneous Frequency Measurement
IFFT	Inverse Fast Fourier Transform
IR	Infrared
JAD	Joint Air Defence

JEM	Jet Engine Modulation
LFM	Linear Frequency Modulation
LO	Local Oscillator
LNA	Low Noise Amplifier
MIC	Microwave Integrated Circuits
MMIC	Monolithic MIC
MT	Multi-Tone
NLFM	Non-Linear Frequency Modulation
NRT	Near Real Time
OFDM	Orthogonal Frequency Division Multiplexing
PC	Pulse Compression
PCB	Printed Circuit Board
PDF	Probability Distribution Function
PIN	Positive-Intrinsic-Negative
PM	Phase Modulated
POI	Probability of Intercept
PSF	Point Spread Function
RBM	Helicopter Rotor Blade Modulation
RCS	Radar Cross Section
RF	Radio Frequency
RGPI	Range Gate Pull In
RGPO	Range Gate Pull Off
RSPWVD	Reassigned Smoothed Psuedo-Wigner-Ville Distribution
RSPWVD1	Single figure RSPWVD contour plot
RT	Radon Transform
RWT	Radon-Wigner Transform
SAFIRE	Software Based Simulator for Advanced Fighter Radar
SAR	Synthetic Aperture Radar
SBADS	Surface Based Air Defence System
SFD	Simulation Flow Diagram

SFDR	Spurious Free Dynamic Range
SHORAD	Short Range Air Defence Missile
SIJ	Stand-in Jamming
SJ	Support Jamming
SMSP	Smeared Spectrum
SOJ	Stand-off Jamming
SPJ	Self-Protection Jamming
SPWHT1	Single figure HT Plot
SPWHT4	Four figure HT Plot
SPWVD	Smoothed Psuedo Wigner-Ville Distribution
SPWVD1	Single figure Smoothed Psuedo Wigner-Hough Transform contour Plot
SPWVD4	Four figure Smoothed Psuedo Wigner-Hough Transform Plot
STALO	Stable Local Oscillator
STAP	Space Time Adaptive Processing
STFT	Short Time Fourier Transform
SV	Slope Varying
TF	Time-Frequency
T/R	Transmit/Receive
TWTA	Traveling Wave Tube Amplifier
UAV	Unmanned Aerial Vehicle
UWB	Velocity Gate Pull In
VGPO	Velocity Gate Pull Off
vs.	versus
VSHORAD	Very Short Range Air Defence Missile
WHT	Wigner-Hough Transform
WHT1	Single figure HT contour Plot
WHT4	Four figure HT surface and contour Plot
WVD	Wigner-Ville Distribution
WVD1	Single figure WVD contour Plot
WVD4	Four figure WVD surface and contour Plot

12 List of Symbols

12.1 English Symbols

a_o	True target acceleration	[m/s²]
$a_0{}^f$	False target acceleration	[m/s²]
$\bar{a}$	Antenna taper coefficients	[ ]
a_i	Digital beam-former relative amplitude of weight	[ ]
a_n	OFDM signal amplitude	[V]
$a(t)$	Amplitude as function of time	[V]
A	Amplitude	[V]
A_{cp}	Amplitude of cover pulse jamming signal	[V]
A_{jr}	Amplitude of false target signal from jammer	[V]
A_{jr}	Amplitude of intercepted radar signal at ES system	[V]
$A_{rj}(t)$	False target signal from jammer received at radar	[V]
$A_{rr}(t)$	Target signal amplitude	[V]
A_t	Transmit signal amplitude	[V]
B_r	Bandwidth of radar receiver	[Hz]
B_j	Bandwidth of jammer	[Hz]
c	Speed of Light	[299 792 458 m/s]
c_{line}	y intercept of straight line	[depends on x, y units]
C	"x" co-ordinate of centre point of TF LFM plot	[ ]
C_x	Cohen's class of TF energy distributions	[W]
$C(z)$	Fresnel Cosine integral as function of discrete frequency z	[N/A]
dR	Range Vector Time Step	[m]
D	Detectability Factor	[W]
D_f	Sampling Decimation Factor	[W]
$D_{circular}$	Circular antenna diameter	[m]

d	True antenna element spacing	[m]
d^f	Estimated antenna element spacing	[m]
dt	Sampling interval	[s]
dv	Target velocity increment of velocity vector	[m/s]
D	"y" co-ordinate of centre point of TF LFM plot	[ ]
f	Frequency/Normalised frequency axis in TF Plot	[Hz]
$f(t)$	Instantaneous Frequency	[Hz]
f'	Normalised HT frequency axis in TF Plot/RSPWVD frequency	[Hz]
Δf	Frequency separation between OFDM sub carriers	[Hz]
f_c	Carrier frequency	[Hz]
f_{centre}	Signal centre frequency component	[Hz]
$\hat{f}_c$	Estimated carrier frequency	[Hz]
$f_{c,error}$	Carrier frequency estimation error	[%]
$\overline{f}_c$	Normalised estimated carrier frequency	[Hz]
f_d	Doppler frequency of true target	[Hz]
f_d^f	Doppler frequency of false target	[Hz]
$\hat{f}_d$	Estimated Doppler frequency	[Hz]
f_d^a	Ambiguous (folded) Doppler frequency	[Hz]
$\hat{f}_d^a$	Estimated ambiguous (folded) Doppler frequency	[Hz]
$f_{d,\max}$	Maximum unambiguous Doppler Frequency	[Hz]
Δf_d	Doppler frequency resolution	[Hz]
f_j	Induced false frequency	[Hz]
f_{jc}	Induced false frequency for multiple cover jamming	[Hz]
f_{jm}	Induced false frequency multiple false target jamming	[Hz]
f_{jo}	First target false induced frequency	[Hz]
$f_{jo}(t)$	Initial false induced frequency of LFM pulse	[Hz]
Δf_j	Induced false frequency component difference	[Hz]
f_s	Sampling frequency	[Hz]

f_s^d	Spatial FFT, sampling frequency	[rad]
$f_{line}(x,y)$	Function of a straight line	[depends on x, y units]
f_{lower}	Lower signal frequency component	[Hz]
f_{osc}	Oscillator frequency	[Hz]
$f_{\max}$	Maximum LFM frequency per carrier frequency	[Hz]
$\overline{f}_{\max}$	Normalised maximum LFM frequency per carrier frequency	[Hz]
$f_{\min}$	Minimum LFM frequency per carrier frequency	[Hz]
$\overline{f}_{\min}$	Normalised minimum LFM frequency per carrier frequency	[Hz]
f_o	Initial Frequency	[Hz]
f_s	Sampling frequency	[Hz]
f_{upper}	Upper signal frequency component	[Hz]
F_x	Short Time Fourier Transform	[V.s]
F^{α}	Fractional Fourier Transform Operator	[ ]
g	SPWVD, time smoothing window in time domain	[ ]
$g_{line}(\rho,\hat{\theta})$	HT function of ρ and $\hat{\theta}$	[depends on ρ, $\hat{\theta}$ units]
G	General antenna Gain	[W]
G_{DOP}	Radar, Doppler processing gain	[W]
G_{LNA}	Low Noise Amplifier Gain	[dBW]
G_{PC}	Radar, pulse compression processing gain	[W]
G_{REP}^j	Repeater jammer gain	[W]
$G_{r,proc}$	Radar Receiver, RF Processing Gain	[dBW]
G_{rx}^j	Jammer, receive antenna gain	[W]
G_{rx}^r	Radar, transmit antenna gain	[W]
G_{sl}^r	Radar side-lobe ratio gain	[W]
G_{tx}^j	Jammer, transmit antenna gain	[W]
G_{tx}^r	Radar, transmit antenna gain	[W]
GS_x	Generalized S-Transform of signal x	[W]

h	TF smoothing window	[ ]
$h(t)$	Low pass finite impulse response filter	[ ]
$J_1(t)$	Deception jamming noise signal	[V]
$J_2(t)$	Cover pulse jamming noise signal	[V]
JSR	Jamming to Signal Ratio	[W]
k	Summation index	[ ]
k_b	Boltzmann's constant	[1.38E-23 J/K]
k_f	Doppler fold index	[ ]
k_R	Range fold index	[ ]
k_ϕ	Elevation angle "fold" index/Ambiguous angle fold index	[ ]
K	Kernel (or Core) function	[function dependent]
l	Window function index	[ ]
L	Window function length	[ ]
L_{Filter}	Filter Insertion Loss	[W]
L_r	Range glint component	[m]
L_{ant}^{r}	Radar antenna losses	[W]
L_{jammer}^{pol}	ES polarisation losses	[W]
L_{jammer}	Total jammer losses	[W]
L_{Mixer}	Radar receiver mixer conversion loss	[W]
L_{other}^{r}	Radar losses, besides antenna losses	[W]
L_{radar}	Total radar losses	[W]
$L(\alpha)$	FrFT based detection statistic	[ ]
m	Signal time index	[ ]
m_{line}	Gradient of straight line	[depends on x, y units]
m_n	Modulated signal	[V]
M	Total number of samples	[ ]
MDS	ES Receiver minimum detectable signal power	[W]

n	Summation index	[ ]
n_{Bin}	Number of range bins	[ ]
n_e	Number of Degree of freedom in	[ ]
n_p	Number of transmitted pulses	[ ]
n_s	Number of components in false induced signal	[ ]
$noise_{jammer}$	Jammer noise power	[W]
$noise_{radar}$	Radar noise power	[W]
N	Number of DFT samples/Number of FFT "Points"	[ ]
p_1	Generalized S-Transform window adjustment parameter 1	[ ]
p_2	Generalized S-Transform window adjustment parameter 2	[ ]
P	Power	[W]
P_D^{pulse}	Probability of Detection for a single pulse	[ ]
P_D^{burst}	Probability of Detection for multiple pulses	[ ]
P_{FA}	Probability of False Alarm for multiple pulses	[ ]
P_{tx}^{j}	Jammer transmit signal power	[W]
P_{tx}^{r}	Radar transmit signal power	[W]
POI	Overall Probability of Intercept (POI) of radar signal at ES receiver	[%]
POI_{BW}	Bandwidth POI of radar signal at ES Receiver	[%]
POI_{θ}^{AOA}	Azimuth Angle of Arrival POI of radar signal at ES Receiver	[%]
POI_{ϕ}^{AOA}	Elevation Angle of Arrival POI of radar signal at ES Receiver	[%]
PRI	Pulse repetition interval	[s]
$\hat{PRI}$	Estimate of pulse repetition interval	[s]
PRI_{error}	Difference between PRI and $\hat{PRI}$	[%]
PW_x	Psuedo Wigner Ville Distribution [W]	
Q	Number of lateral receive elements in antenna	[ ]
r	Binomial Theorem index	[ ]
R	Miscellaneous range to target	[m]

R^a	Ambiguous range/folded range	[m]
R_{bin}	Range to current range bin	[m]
R_{burn}	Radar "burn-through" range to jammer	[m]
R_{ES}	Range at which ES system can detect Radar	[m]
R_{est}^j	Estimated false target range, relative to current range bin	[m]
R_{est}^r	Estimated true target range, relative to current range bin	[m]
R_{error}^j	Difference between True Range and Estimated False Range	[m]
R_{error}^r	Difference between True Range and Estimated True Range	[m]
R_j	Radar to jammer range	[m]
$R_{\max}$	Maximum radar detection range	[m]
$R_{\min}$	Minimum radar detection range	[m]
R_o	True target range, vector in track model	[m]
R_{bin}^r	True target range to start of range bin	[m]
$R_{bin,\sigma}^r$	Randomized true target range to start of range bin	[m]
R_{bin}^f	False target range to start of range bin	[m]
$R_{bin,\sigma}^f$	Randomized false target range to start of range bin	[m]
R_o^f	False target range	[m]
R_{rec}	Radar receive window	[m]
$\hat{R}_{xy}(m)$	Cross correlation of two signals as function of sample index m	[V²]
$R_\alpha(\rho)$	Fractional Autocorrelation of radial distance ρ	[V²]
$RSPWV_x$	RSPWVD of signal x	[W]
ΔR	Range resolution	[m]
s	Binomial Theorem index/SPWVD integration variable	[ ]
Sc_x	Scalogram of signal	[W]
S_x	Spectrogram of signal	[W]
$S(Z)$	Fresnel Sine integral as function of discrete frequency z	[N/A]
$Samples_\tau^X$	Number of samples to represent τ at X-Band	[m]

$Samples_{\tau}^{L}$	Number of samples to represent τ at L-Band	[m]
$Samples_{PRI}^{X}$	Number of samples to represent the PRI at X-Band	[ ]
$Samples_{PRI}^{L}$	Number of samples to represent the PRI at L-Band	[ ]
$Samples_{CPI}^{X}$	Number of samples to represent the CPI at X-Band	[ ]
$Samples_{CPI}^{L}$	Number of samples to represent the CPI at L-Band	[ ]
SJR	Signal to jammer power ratio	[W]
SNR_{jr}	Signal to noise power ratio of radar signal at jammer	[W]
SNR_{rj}	Signal to noise power ratio of jammer signal at radar	[W]
SNR_{rj}^{side}	Signal to noise power side-lobe ratio of jammer signal at radar	[W]
SNR_{burst}	Signal to noise power ratio of a burst of pulses	[W]
SNR_{in}	Input signal to noise power ratio	[W]
SNR_{out}	Output signal to noise power ratio	[W]
SNR_{pulse}	Signal to noise power ratio of a single pulse	[W]
S_x	S-Transform of signal x	[W]
$SPWV_x$	SPWVD of signal x	[W]
t	Time/Time axis in TF plot	[s]
t'	HT time axis in TF Plot/RSPWVD time	[s]
$\hat{t}_c$	Estimate of "Centre Time" of LFM Pulse	[s]
$\overline{t_c}$	Normalised estimate of "Centre Time" of LFM Pulse	[s]
t_d	Time Delay	[s]
t_g	Group Delay	[s]
$t_i^{\,f}$	Initial time for RGPO/start time of RGPO	[s]
t_o	Time to true target at R_o	[s]
t_o^f	Time to false target at R_o^f	[s]
T	Total sampling time interval	[s]
T_{ca}	False target "pull-off" duration	[s]
$T_s^{\,j}$	Jammer system Noise Temperature	[K]
$T_s^{\,r}$	Radar system Noise Temperature	[K]

T_{scan}	Antenna scan time	[s]
T_x	Continuous Wavelet Transform of signal	[V.s]
u	FrFT independent variable	[ ]
$U_{NR}(t)$	Real Normally Distributed Random Variable, function of t	[ ]
$U_{NC}(t)$	Complex Normally Distributed Random Variable, function of t	[ ]
$U_r(t)$	Rayleigh Distributed Random Variable, function of t	[ ]
$U_R^r(t)$	Normally Distributed Random Variable, function of t , true target σ_R	[ ]
$U_v^r(t)$	Normally Distributed Random Variable, function of t , true target σ_v	[ ]
$U_R^j(t)$	Normally Distributed Random Variable, function of t , false target σ_R	[ ]
$U_v^j(t)$	Normally Distributed Random Variable, function of t , false target σ_v	[ ]
$U_\phi^r(t)$	Normally Distributed Random Variable, function of t , true target σ_ϕ	[ ]
$U_\phi^j(t)$	Normally Distributed Random Variable, function of t , false target σ_ϕ	[ ]
v	Target velocity	[m/s]
v_{bin}^r	Unfolded true target velocity relative to start of Doppler bin	[m/s]
$v_{bin,\sigma}^r$	Randomized unfolded true target velocity to start of Doppler bin	[m/s]
v_{bin}^f	Unfolded false target velocity relative to start of Doppler bin	[m/s]
$v_{bin,\sigma}^f$	Randomized unfolded false target velocity to start of Doppler bin	[m/s]
v_{est}^r	Estimated true target velocity	[m/s]
v_{est}^r	Estimated true target velocity	[m/s]
v_{est}^j	Estimated false target velocity	[m/s]
v_{error}^j	Difference between True Velocity and Estimated False Velocity	[m/s]
v_{error}^r	Difference between True Velocity and Estimated True Velocity	[m/s]
v_o	Target velocity at range R_o , vector in track model	[m/s]
v_o^f	False target velocity at range R_o , vector in track model	[m/s]
v_t^f	False target terminal velocity	[m/s]
$v_{\max}$	Maximum target velocity	[m/s]

$v_{\min}$	Minimum target velocity	[m/s]
Δv_{centre}	Velocity resolution for centre frequency component	[m/s]
Δv_{lower}	Velocity resolution for lower frequency component	[m/s]
Δv_{upper}	Velocity resolution for upper frequency component	[m/s]
V	Voltage	[V]
V_{peak}	Peak signal voltage	[V]
V_{rms}	Root mean square signal voltage	[V]
w	Wavelet scale parameter	[ ]
$w(l)$	Window Function (Hamming, Blackman, etc.)	[ ]
w_i	Digital beam-former weight at antenna element "i"	[ ]
W_x	WVD of signal $x(t)$	[W]
WH_x	WHT of signal $x(t)$	[W]
x	x coordinate	[depends on x, units]
x_i	"i^{th}" x coordinate	[depends on x, units]
$x(n)$	Discrete form of $x(t)$	[N/A]
$x(t)$	True analytic signal transmitted by radar as a function of time t	[V]
$x^f(t)$	False copy of radar's transmitted signal	[V]
$x_I(t)$	In-Phase component of analytic signal "$x(t)$"	[V]
$x_Q(t)$	Quadrature component of analytic signal "$x(t)$"	[V]
$\tilde{x}(t)$	Complex envelope of signal transmitted by radar, function of time t	[V]
$\tilde{x}_h(t)$	Complex envelope true target signal term with ϕ estimate	[V]
$\tilde{x}_h^f(t)$	Complex envelope false target signal term with ϕ^f estimate	[V]
$x_{rh}(t)$	Analytic signal of true moving target with elevation, $\phi(t)$	[V]
$x_{rh}^f(t)$	Analytic signal of false moving target with elevation, $\phi(t)$	[V]
$x_{rs}(t)$	Analytic signal of true stationary target as a function of time t	[V]
$x_{rs}^f(t)$	Analytic signal of false stationary target as a function of time t	[V]
$x_{rm}(t)$	Analytic signal of true moving target as a function of time t	[V]

$x_{rm}^{f}(t)$	Analytic signal of false moving target as a function of time t	[V]
$\tilde{x}(t)$	Complex envelope of transmitted radar signal as a function of time t	[V]
$\tilde{x}_h(t)$	Complex envelope term of phase shifted target signal due to ϕ	[rad]
$\tilde{x}_r(t)$	Complex envelope of stationary or moving target signal	[V]
$\tilde{x}_{rs}(t)$	Complex envelope of true stationary target as a function of time t	[V]
$\tilde{x}_{rs}{}^{f}(t)$	Complex envelope of false stationary target as a function of time t	[V]
$\tilde{x}_{rh}(t)$	Complex envelope term of ϕ phase shifted moving true target	[V]
$\tilde{x}_{rh}{}^{f}(t)$	Complex envelope term of ϕ phase shifted moving false target	[V]
$\tilde{x}_{rm}(t)$	Complex envelope of true moving target signal	[V]
$\tilde{x}_{rm}{}^{f}(t)$	Complex envelope of false moving target signal	[V]
$\tilde{X}(k)$	DFT of $\tilde{x}(t)$	[W]
$\tilde{X}_{rh}(k)$	Spatial squared magnitude of DFT of $\tilde{x}_{rh}(t)$	[W^2]
$\tilde{X}_{rm}(k)$	DFT of $\tilde{x}_{rm}(t)$	[V.s]
$\tilde{\tilde{X}}_{rm}(k)$	DFT spectrum of spectrums of $\tilde{X}_{rm}(k)$	[W]
$X(k)$	Fourier transform of $x(n)$	[V.s]
$X(t)$	Fourier transform of $x(t)$	[V.s]
X_{α}	Fractional Fourier Transform	[V.s]
y	y coordinate	[depends on y, units]
y_i	"j^{th}" y coordinate	[depends on y, units]
$y(t)$	Matched filtered $\tilde{X}_{rm}(k)$ target signal as a function of time t	[V]
z_1	Maximum Frequency of LFM waveform	[Hz]
z_2	Minimum Frequency of LFM waveform	[Hz]
Z_o	Impedance	[Ω]

12.2 Greek symbols

α	FrFT angle parameter	[rad]
$\hat{\alpha}$	Angle of normal line in HT of TF Plot	[rad]
$\hat{\alpha}_1$	Angle of normal line in HT of TF Plot, HT conversion Cases 5 and 6	[rad]
$\hat{\alpha}_2$	Angle of normal line in HT of TF Plot, HT conversion Cases 5 and 6	[rad]
β	Jammer duty cycle	[ ]
δ	RSPWVD integration function	[V]
δ_p	Interferometer antenna "Passband" parameter	[ ]
δ_s	Interferometer antenna "Stopband" parameter	[ ]
δ_0	Phase shift due to time delay t_o of target at range R_o	[rad]
${\delta_0}^f$	Phase shift due to false time delay ${t_o}^f$ of target at range ${R_o}^f$	[rad]
γ	Instantaneous Auto Correlation, kernel function	[ ]
θ	Azimuth angle	[rad]
$\hat{\theta}$	HT angle	[rad]
$\hat{\theta}_1$	HT angle, HT conversion Cases 5 and 6	[rad]
$\hat{\theta}_2$	HT angle, HT conversion Cases 5 and 6	[rad]
θ_T	Azimuth angle area of interest, radar signal intercept at ES receiver	[rad]
θ_{3dB}	Azimuth "3dBW" beam-width of radar or ES receiver antenna	[deg]
$\dot{\theta}_{scan}$	Antenna scan rate	[rad/s]
λ	Wavelength	[m]
$\hat{\lambda}$	Estimated wavelength	[m]
λ_{centre}	Wavelength corresponding to centre signal carrier frequency	[m]
λ_{lower}	Wavelength corresponding to lower signal carrier frequency	[m]
λ_{upper}	Wavelength corresponding to upper signal carrier frequency	[m]
μ	LFM rate/Chirp rate	[1/s^2]
$\hat{\mu}$	Estimated LFM rate/Chirp rate	[1/s^2]

μ_{error}	Estimated LFM rate/Chirp rate	[1/s^2]
$\bar{\mu}$	Normalised Estimated LFM rate/Chirp rate	[1/s^2]
μ'	Modified LFM rate/Chirp rate	[1/s^2]
ρ	HT distance	[m]
ρ_m	Multipath coefficient	[ ]
ρ_1	HT distance, HT conversion Cases 5 and 6	[m]
ρ_2	HT distance, HT conversion Cases 5 and 6	[m]
$p_\sigma(\sigma)$	RCS target fluctuation probability as a function of σ	[ ]
σ	True target RCS	[m^2]
$\sigma_{average}$	Average target RCS	[m^2]
σ_f	False target RCS	[m^2]
$\sigma_{f_c}^2$	WVD estimation variance for carrier frequency	[Hz]
σ_R	True target range estimation standard deviation	[m]
$\sigma_R{}^f$	False target range estimation standard deviation	[m]
σ_V^{centre}	Velocity estimation standard deviation for centre frequency	[m/s]
σ_V^{lower}	Velocity estimation standard deviation for lower frequency	[m/s]
σ_V^{upper}	Velocity estimation standard deviation for upper frequency	[m/s]
σ_ϕ	Elevation angle standard deviation	[rad]
σ_μ^2	WVD estimation variance for LFM rate/Chirp rate	[1/s^2]
$\sigma_\psi{}^2$	Phase noise variance	[rad^2]
τ	Pulse width	[s]
τ_d	WVD, integration variable	[s]
$\varphi(t)$	Uniformly distributed random variable as a function of time t	[ ]
ϕ	Elevation angle, true target	[rad]
$\phi_{\min}$	Minimum elevation angle	[rad]
$\phi_{\max}$	Minimum elevation angle	[rad]
ϕ_o	Elevation angle at range R_o , vector in track model	[rad]

ϕ^f	Elevation angle, false target	[rad]
ϕ_{amb}	Ambiguous elevation angle	[rad]
ϕ_{est}^j	Estimated false target elevation angle vector	[N/A]
$\phi_{est}^j(t)$	Estimated false target elevation angle	[rad]
ϕ_{est}^r	Estimated true target elevation angle vector	[N/A]
$\phi_{est}^r(t)$	Estimated true target elevation angle	[rad]
ϕ_{error}^j	Difference between True ϕ and estimated false ϕ	[rad]
ϕ_{error}^r	Difference between True ϕ and estimated true ϕ	[rad]
ϕ_{error}^{rj}	Difference between estimated true ϕ and estimated false ϕ	[rad]
ϕ_{unamb}	Unambiguous elevation angle limit	[rad]
ϕ_T	Elevation angle area of interest, radar signal intercept at ES receiver	[rad]
ϕ_{3dB}	Elevation "3dBW" radar beam-width, radar or ES receiver antenna	[deg]
ψ	Phase of signal	[rad]
$\psi(d)$	Phase shift as a function of element spacing d, true target	[rad]
$\psi^f(d^f)$	Phase shift as a function of element spacing d^f false target	[rad]
ψ_i	Phase at element "i" in antenna array for true target	[rad]
ψ_i^f	Phase at element "i" in antenna array for false target	[rad]
$\Delta\psi_i$	Change in signal phase between elements for true target	[rad]
$\Delta\psi_i^f$	Change in signal phase between elements for false target	[rad]
$\Psi_{t,a}$	Wavelet transform as a function of time and scale	[ ]
Ω	Phase of Instantaneous Autocorrelation	[rad]

12.3 Superscripts

*	Complex Conjugate
^	Estimate or angle, depends on context in which variable is used
~	Complex envelope portion of signal
r	Radar
j	Jammer

13 List of References

13.1 Books

[1] B. Mahafza, *Radar Signal Analysis and Processing using Matlab*, Second Edition, CRC Press, 2009.

[2] D.K. Barton, *Modern Radar Systems Analysis*, First Edition, Artech House Publishers Inc., 1988

[3] D. Hanselman, B. Littlefield, *Mastering Matlab 7*, International Edition, Pearson Prentice Hall Publishers, 2005

[4] D. Schleher, *Electronic Warfare in the Information Age*, Third Edition, Artech House Publishers Inc., 1999.

[5] J.B. Tsui, *Microwave Receivers with Electronic Warfare Applications*, First Edition, Scitech Publishing Inc., 2005.

[6] M. A. Richards *et al.*, *Principles of Modern Radar*, First Edition, Scitech Publishing Inc., 2010.

[7] L. Blake, M. Long, *Antennas, Fundamentals, Design, Measurement*, Third Edition, Scitech Publishing Inc., 2009

[8] R. M. O'Donnell, *A Course in Radar Systems Engineering*, IEEE New Hampshire Section, 2009

[9] P. Fishbane, S. Gasiorowicz, S. Thornton, *Physics for Scientists and Engineers*, Prentice-Hall Publishers Inc., 1996

13.2 Standards and Handbooks

[10] *Electronic Warfare and Radar Systems Engineering Handbook*, Naval Air Systems Command, Avionics Department AIR-4.5, NAWCWPNS TP 8347, April 1999

[11] *System Engineering Handbook,* Version 3.2, International Council of Systems Engineers

13.3 Toolboxes

[12] F. Auger *et al.*, "*Time-Frequency Toolbox*", Version 1.2, Centre National De La Recherche Scientifique (CNRS) and Rice University, 1996

13.4 Technical Papers

[13] A.V. Essop, *"Local Warning Segment, Effective, Interoperable and Flexible Ground Based Air Defence System"*, South African Joint Air Defence Symposium, 2009

[14] A. Madni, H. M. Endler, *"Solid-state Multiple Deception Jamming System For ECM Applications"*, IEEE Aerospace Conference, 1998

[15] B. Boashash, P. Black, *"An Efficient Real Time Implementation of the Wigner-Ville Distribution"*, IEEE Transactions on Acoustics, Speech and Signal Processing, Volume ASSP-35, No. 11, November 1987

[16] D. DiFilippo, et al., *"Simulator for advanced fighter radar EPM development"*, IEEE Proceedings on Radar, Sonar and Navigation, Volume148, Issue: 3, 2001

[17] D. Gupta et al., *"Digital Channelizing Radio Frequency Receiver"*, IEEE Transactions on Applied Superconductivity, Volume 17, Issue 2, 2007

[18] D. K. Barton, *"Universal Equations for Radar Target Detection"*, IEEE Transactions on Aerospace and Electronic Systems, Volume 41, Issue 3

[19] D. Wang et al., "*A Detection and Parameter Estimation Algorithm of Multi-component Chirp Signals Based on Generalized S-Transform"* , International Journal of Signal Processing, Image Processing and Pattern Recognition, Volume 5, No. 2, June, 2012

[20] G. Lu et al., *"Cancellation of Complicated DRFM Range False Targets via Temporal Pulse Diversity",* Progress In Electromagnetics Research, Volume 16, Pages 69-84, 2010

[21] J. Jensen, *"Hough Transform for Straight Lines*", Mini-Project in Image Processing, 7th Semester 2007, Group 721

[22] J. E. Wilhjelm, *"Target Velocity Estimation with FM and PW Echo Ranging Doppler Systems Part I: Signal Analysis"* , IEEE Transactions on Ultrasonics, Ferroelectrics and Frequency Control, Volume 40, No. 4, July 1993

[23] J. E. Wilhjelm, *"Target Velocity Estimation with FM and PW Echo Ranging Doppler Systems Part II: Systems Analysis"* , IEEE Transactions on Ultrasonics, Ferroelectrics and Frequency Control, Volume 40, No. 4, July 1993

[24] J. Hu et al. ,*"A Smart Repeater for Weapon Location Radar Based on Time-frequency Analysis"*, Annual Conference of IEEE Industrial Electronics (IECON), 2009

[25] J. Schuerger, D Garmatyuk, "*Deception Jamming Modelling in Radar Sensor Networks"*, Military Communications Conference, 2008

[26] K. Olivier, *"Advances in DRFM technology during the past decade and its importance as part of an EW suite"*, Aardvark Roost AOC Conference, September, 2011

[27] K. Olivier et al., *"Design and performance of wideband DRFM for radar test and evaluation"*, Electronics Letters, Volume 47, Issue: 14, 2011

[28] L. Dai, *"A Blanket Deception Jamming Rejection Approach Based on Jamming Sample Recognition"*, International Conference on Microwave and Millimeter Wave Technology (ICMMT), 2007.

[29] M. Soumekh, "*SAR-ECCM using Phase Perturbed LFM Chirp Signals and DRFM Repeat Jammer Penalization*", IEEE Transactions on Aerospace and Electronic Systems, Volume 42, Issue 1, January, 2006

[30] P. M. Oliviera, V. Barroso, "*On the Concept of Instantaneous Frequency*", IEEE International Conference on Acoustics, Speech and Signal Processing, Volume 4, 1998

[31] PCJ. Pring et al., *"Phase Performance of DRFM's"*, Second International Conference on Advanced A/D and D/A Conversion Techniques and their Applications, 1994.

[32] P. West, B.J. Slocomb, *"ECM Modeling for Assessment of Target Tracking Algorithms"*, Proceedings of the Twenty-Ninth South-Eastern Symposium on System Theory, 1997

[33] R. McAulay, *"Interferometer Design for Elevation Angle Estimation"*, IEEE Transactions on Aerospace and Electronic Systems, Volume AES-13, No. 5, September1977.

[34] S. Barbarossa, *"Analysis of Multi-component LFM Signals by a Combined Wigner-Hough Transform",* IEEE Transactions on Signal Processing, Volume 43, No.6, June, 1995

[35] S. Barbarossa, A. Zanalda, *"A Combined Wigner-Ville and Hough Transform for Cross Term Suppression and Optimal Detection and Parameter Estimation"*, IEEE International Conference on Acoustics, Speech and Signal Processing, 1992.

[36] S. D. Berger , *"DRFM Linear Range Gate Stealer Spectrum"*, IEEE Transactions on Aerospace and Electronic Systems, Volume 39, Issue 2

[37] S. Kristoffersen, H. J. F. Meon, *"Denial Jamming Technique Development against Pulse-Doppler Radars using the Genetic Algorithm"*, IEEE International Conference on Radar, September 2008

[38] S. Verwey, "*Air Defence in Africa"*, South African Joint Air Defence Symposium, 2003

[39] S. Z. K. Sajib, A. Mostayed, *"A Parameter Estimation Method for Linear Amplitude Modulated Chirp Signals Based on Discrete Fractional Fourier Transform",* 5th International Conference on Electrical and Computer Engineering (ICECE), December 2008.

[40] T. Haynes, *"A Primer on Digital Beam-forming", Spectrum Signal Processing",* March 1998.

[41] P. Tang, et al., "*Design and Simulation of DRFM System Based on Digital Channelized Receiver and Transmitter"*, School of Electronic Science and Engineering, National University of Defence Technology, International Conference on Mechatronic Science, 2011

[42] P. Wang et al., "*A Fast Algorithm for Parameter Estimation of Multi-Component LFM Signal at Low SNR"*, School of Electronic Engineering, University of Electronic Science and Technology of China, 2005

[43] Q Guo et al., *"A New Method of Detecting Multi-component LFM Signals Based on Blind Signal Processing",* Journal of Computers, Volume 6, No.9, September 2011

[44] W.D. Blair et al., "*Benchmark Problem for Beam Pointing Control of Phased Array Radar Against Maneuvering Targets in the Presence of ECM and False Alarms"*, Proceedings of the American Control Conference, Volume 4, 1995

[45] Y. Yang, "*Study on Frequency-shifting Jamming to Linear Frequency Modulation Pulse Compression Radars"*, International Conference on Wireless Communications & Signal Processing (WCSP), 2009.

[46] Z. Bin, *"Simulated Study of Jamming of LFM PC Radar Signal"* , Jiangsu University of Science and Technology, School of Electronic Information, Jiangsu Zhenjiang, 2008

13.5 Datasheets and Journals

[47] Delphi Digital Receiver, ADC3295

[48] Sinuous Antennas, 07-S-1147, Randtron Antenna Systems, L3 Communications

[49] Journal of Electronic Defence, March 2013, Volume 36, No. 3

[50] Journal of Electronic Defence, October 2013, Volume 36, No. 10

[51] Journal of Electronic Defence, November 2013, Volume 36, No. 11

[52] Submarine Tactical ESM and ELINT Systems UME-100/200, Saab Electronic Defence Systems, Cape Town, South Africa

[53] World Defence Almanac 2012, Issue 1, Volume XXXVI

14 Appendices

14.1 DBR Simulation, Files and Functions

File Name	Type	Purpose
es.m	Standalone Program	Processes intercepted Radar signal
jammer_setup.m	Standalone Program	Sets Jammer parameters
jammer_sys.m	Standalone Program	Calculates Jammer System performance metrics
proc_es_param.m	Standalone Program	Processes estimated Radar signal data
radar.m	Standalone Program	Simulates Radar Signal Processor
radar_setup.m	Standalone Program	Sets Radar parameters
radar_sys.m	Standalone Program	Calculates Radar System performance
radar_transmit.m	Standalone Program	Simulates Radar transmitter
amplitude.m	Function Program	Generates amplitudes for signal models
false_target.m	Function Program	Sets false target parameters
jammer_signals.m	Function Program	Generates jammer false signal models
get_ReceivePlot.m	Function Program	Iterates through all radar receiver plots for automatic collection of results
get_standard_target.m	Function Program	Iterates through standard targets for automatic collection of results
get_targetsignals.m	Function Program	Iterates through intercepted radar signals for automatic collection of results
get_transmitPlot.m	Function Program	Steps through radar receiver plots for automatic collection of results
mydoppler_filter.m	Function Program	Simulates target doppler frequency measurement in radar signal processor
myheight.m	Function Program	Simulates target elevation angle measurement in radar signal processor
myrange.m	Function Program	Simulates target range measurement in radar signal processor
radar_signals.m	Function Program	Generates target true signal models
true_target.m	Function Program	Sets true target parameters
SNRerrors.m	Function Program	Generates radar measurement errors from SNR's
radar_setup.mat	Data File	Stores radar parameters
jammer_setup.mat	Data File	Stores jammer parameters
es_param_raw.mat	Data File	Stores raw intercepted Radar signal parameters
es_param.mat	Data File	Stores processed intercepted Radar signal parameters
fmlin.m	COTS Utility Program	Generates LFM signal model

File Name	Type	Purpose
export_fig.m	COTS Utility Program	Crops and saves Matlab Figures for use in documents
htl.m	COTS Utility Program	Calculates HT of WVD of intercepted LFM signals
tfrwv.m	COTS Utility Program	Calculates WVD of intercepted LFM signals
tfrwspwv.m	COTS Utility Program	Calculates SPWVD of intercepted LFM signals
rgb.m	COTS Utility Program	Allows 256 colours to be set in Matlab 2D Plots
quant.m	COTS Utility Program	Rounds number to selected number of digits
db2linear.m	Utility Program	Converts RF Powers from watts to decibels
deg2rad.m	Utility Program	Converts angles from degrees to radians
linear2db.m	Utility Program	Converts RF Powers from decibels to watts
hough1convert.m	Utility Program	Converts HT estimates to LFM signal parameter estimates (Centre Frequency and Chirp Rate)
hough2convert.m	Utility Program	Converts HT estimates to LFM signal parameter estimates (PRI)
rad2degm	Utility Program	Converts angles from radians to degrees
zerofold.m	Utility Program	Calculates target velocities zero folds
zerounfold.m	Utility Program	Calculates true target measured velocities from zero folds to actual target velocities
zerounfold_f.m	Utility Program	Calculates false target measured velocities from zero folds to actual false target velocities
vel2dop.m	Utility Program	Converts target velocities to doppler frequencies

14.2 Hough Transform Conversions

The TF toolbox ([12]), HT function positions its reference axes, in the centre of the figure/image under analysis. It also rotates the co-ordinate axes by 90°. In Figure 195, for example, the TF axes are shown in blue. It is translated and rotated, relative to the figure reference axis (shown in red).

The green line represents the LFM time frequency plot whose centre point ("$\hat{f}_c$") and gradient ("$\hat{\mu}$") must be estimated using the HT.

The point C coordinate in Figure 132 is the "centre time ("$\hat{t}_c$")" estimate (time at which centre frequency of LFM pulse is received). The point D coordinate is the "centre frequency ("$\hat{f}_c$")" estimate, while the chirp rate ("$\hat{\mu}$") is found by finding the angle "$\hat{\theta}$" or the "gradient of the line. The HT coordinates are in a "$\rho, \hat{\theta}$" axis.

The relationship of the HT estimated parameters "$\hat{\theta}$" and "ρ" to the LFM "$\hat{f}_c$" and "$\hat{\mu}$" was found using trigonometric relationships indicated in Figure 195, Figure 196, Figure 197, Figure 198, Figure 199 and Figure 200.

The signal frequencies must be normalised for use with the TF toolbox. They are normalised using the following equation:

$$\overline{f}_{\max} = \frac{f_{\max} - f_{osc}}{f_s} \tag{269}$$

$$\overline{f}_{\min} = \frac{f_{\min} - f_{osc}}{f_s} \tag{270}$$

Upon estimation by the TF toolbox, the normalised parameters must be "de-normalised" to obtain actual estimates using the following equations:

$$\hat{f}_c = \overline{f}_c \cdot f_s + f_{osc} \tag{271}$$

$$\hat{\mu} = \overline{\mu} \cdot \frac{f_s}{\tau} \tag{272}$$

The HT conversion per TF quadrant, for a single pulse is mathematically described in sections 14.2.1, 14.2.2, 14.2.3 and 14.2.4. Two-pulse HT conversions are presented in sections 14.2.5 and 14.2.6.

14.2.1 Case 1: 0° < θ ≤ 90°

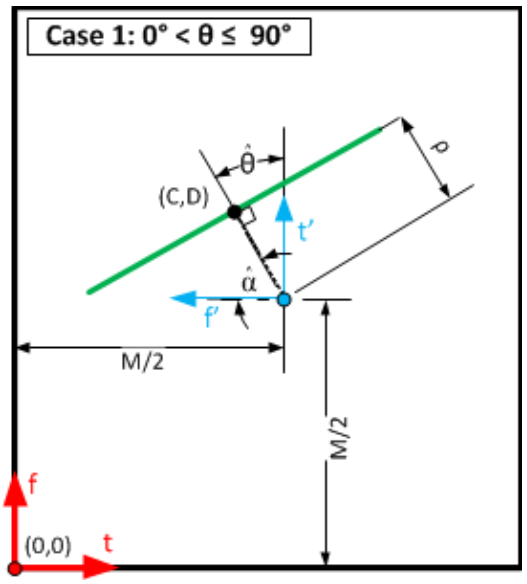

Figure 195: Hough Transform Conversion, Case 1

$$\hat{\alpha} = 90° - \hat{\theta} \tag{273}$$

$$\bar{f}_c = \rho \cdot \cos\hat{\theta} + \frac{M}{2} \tag{274}$$

$$\bar{t}_c = \frac{M}{2} - \rho \cdot \sin\hat{\theta} \tag{275}$$

$$\bar{\mu} = \tan\hat{\theta} \tag{276}$$

14.2.2 Case 2: 90° < θ ≤ 180°

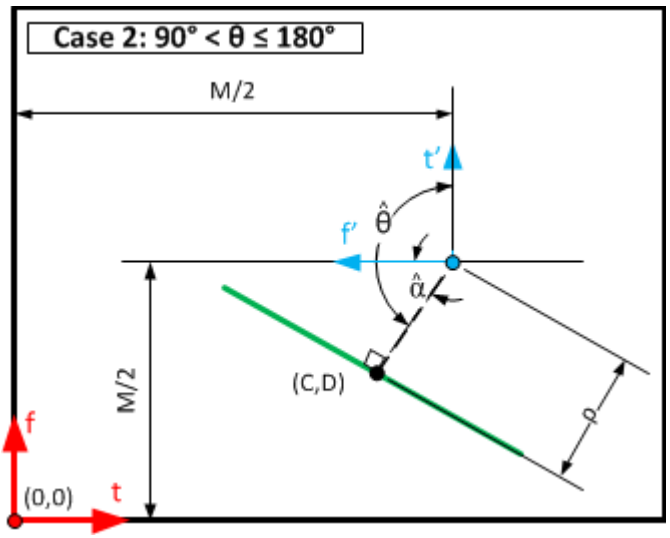

Figure 196: Hough Transform Conversion, Case 2

$$\hat{\alpha} = \hat{\theta} - 90° \tag{277}$$

$$\bar{f}_c = \frac{M}{2} - \rho \cdot \sin\left(\hat{\theta} - 90°\right) \tag{278}$$

$$\bar{t}_c = \frac{M}{2} - \rho \cdot \cos\left(\hat{\theta} - 90°\right) \tag{279}$$

$$\bar{\mu} = \tan\hat{\theta} \tag{280}$$

14.2.3 Case 3: 180° < θ ≤ 270°

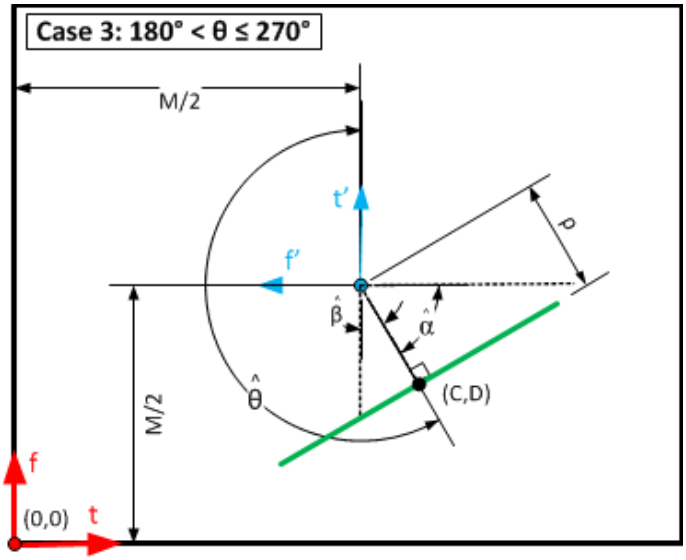

Figure 197: Hough Transform Conversion, Case 3

$$\hat{\alpha} = 270° - \hat{\theta} \tag{281}$$

$$\bar{f}_c = \frac{M}{2} - \rho \cdot \sin\left(270° - \hat{\theta}\right) \tag{282}$$

$$\bar{t}_c = \frac{M}{2} + \rho \cdot \cos\left(270° - \hat{\theta}\right) \tag{283}$$

$$\bar{\mu} = \tan\hat{\theta} \tag{284}$$

14.2.4 Case 4: 270° < θ ≤ 360°

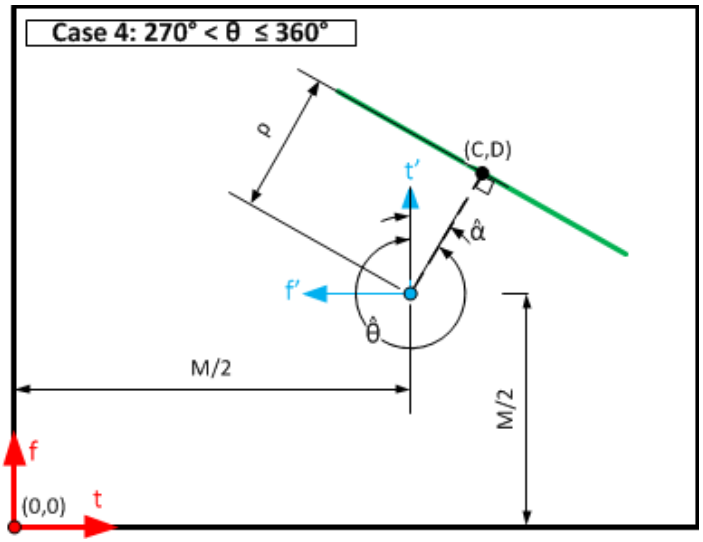

Figure 198: Hough Transform Conversion, Case 4

$$\hat{\alpha} = 360° - \hat{\theta} \tag{285}$$

$$\bar{f}_c = \rho \cdot \cos\left(360° - \hat{\theta}\right) + \frac{M}{2} \tag{286}$$

$$\bar{t}_c = \frac{M}{2} + \rho \cdot \sin\left(360° - \hat{\theta}\right) \tag{287}$$

$$\bar{\mu} = \tan\hat{\theta} \tag{288}$$

14.2.5 Case 5 0° < θ ≤ 90° and 180° < θ ≤ 270°

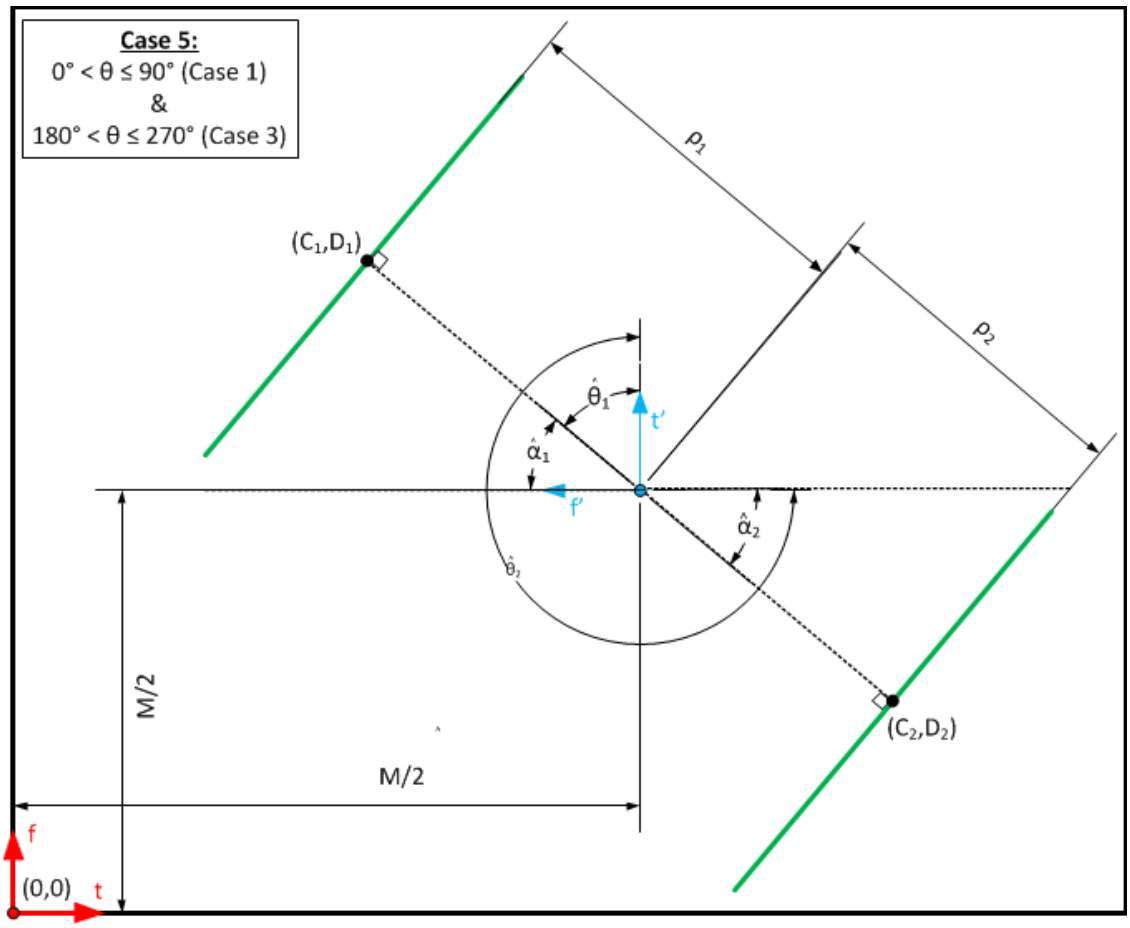

Figure 199: Hough Transform Conversion, Case 5

The two-pulse definitions are used to estimate the intercepted signal PRI estimation error. In the actual system the two pulses would be separated by larger number of samples (if 2GHz sampling used) than can be simulated on a corporate laptop (as described in section 6.2). For this reason, the PRI error is estimated and not the PRI since the error can be scaled to the actual system.

$$\hat{\alpha}_1 = 90° - \hat{\theta}_1 \tag{289}$$

$$\hat{\alpha}_2 = 270° - \hat{\theta}_2 \tag{290}$$

$$\hat{PRI} = \frac{\rho_1}{\sin\hat{\theta}_1} + \frac{\rho_2}{\cos\left(270° - \hat{\theta}_2\right)} \tag{291}$$

The simulated "PRI" is given in units of "number of samples", while the estimated "$\hat{PRI}$" is also in "number of samples". The "PRI_{error}" is then:

$$PRI_{error} = \frac{PRI - \hat{PRI}}{PRI} \cdot 100\% \tag{292}$$

14.2.6 Case 6: 90° < θ ≤ 180° and 270° < θ ≤ 360°

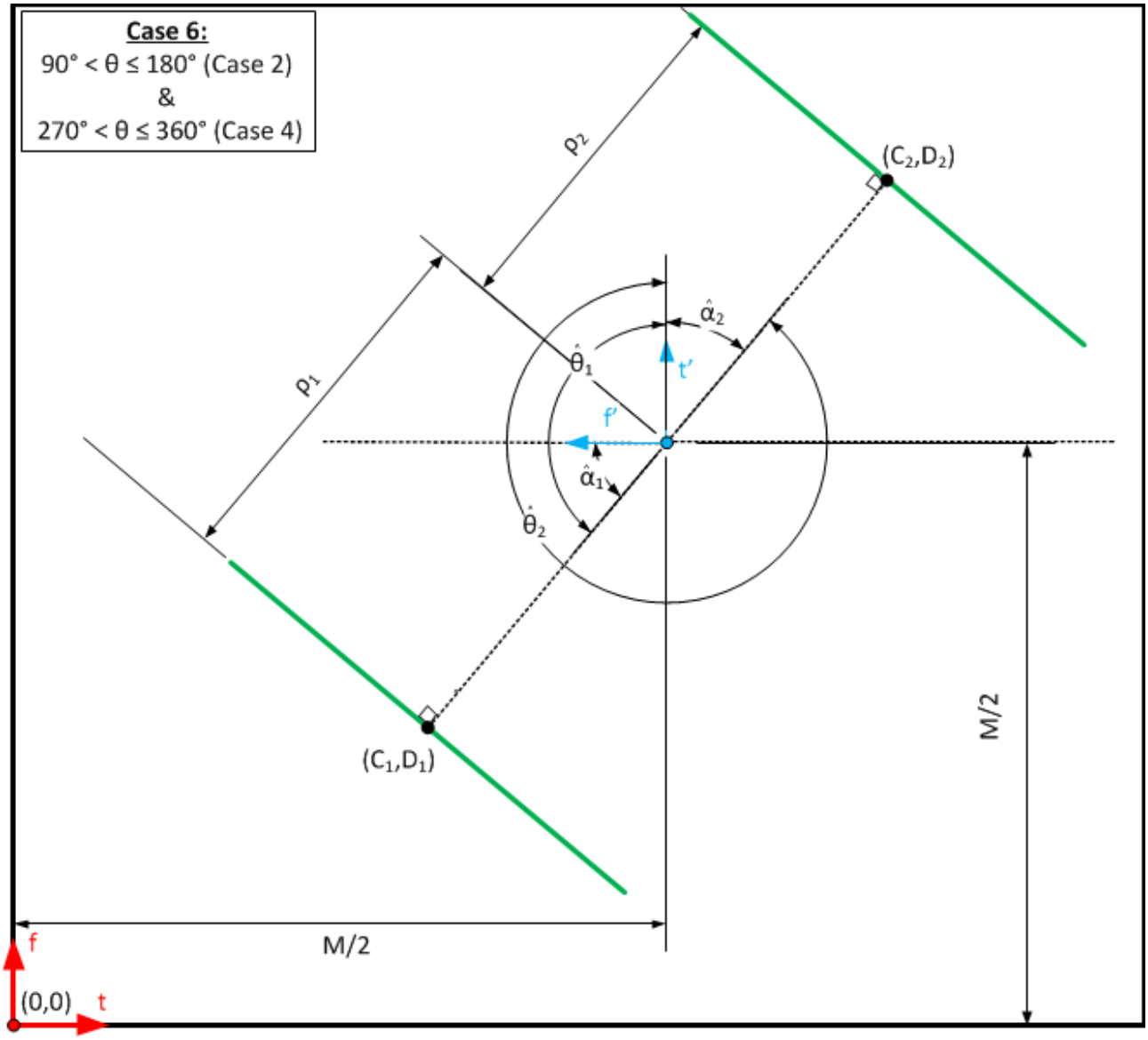

Figure 200: Hough Transform Conversion, Case 6

$$\hat{\alpha}_1 = \hat{\theta}_1 - 90° \tag{293}$$

$$\hat{\alpha}_2 = 360° - \hat{\theta}_2 \tag{294}$$

$$\hat{PRI} = \frac{\rho_1}{\cos\left(\hat{\theta}_1 - 90°\right)} + \frac{\rho_2}{\cos\left(\hat{\theta}_2 - 270°\right)} \tag{295}$$

14.3 Delphi Digital Receiver Datasheet ([47])

DELPHI
Engineering Group, Inc.

High Performance, Real-Time Acquisition Solutions for the Aerospace, Defense and Communication Industries.

2 Gsps 10-Bit ADC Module

ADC3295 With Virtex 5

Features

General

- 384 MB SDRAM Buffer (256 MSamples)
- Xilinx Virtex 5 FPGA XC5VSX95T
- Programmable Sampling Delay/Length
- VITA-35 Compliant Pn4 Interface With 32 LVDS Pairs
- AC or DC Coupling
- Onboard PLL Option
- VxWorks, Linux, Windows Software Drivers
- 32/64-bit Up to 100 MHz, 3.3V, PCI 2.2 or PCI-X Compliant Bus
- Onboard DMA Engine
- Industry Standard PMC Format
- Conduction/Convection Cooled
- Available Temperature Versions:
  - Commercial
  - Industrial

Performance

- Analog Input: 100 KHz to 3.0 GHz
- Sampling Rate: 200 Msps to 2 Gsps
- ENOB = 7.5 Effective Bits, F_{IN} = 2 GHz
- SNR = 50 dBc, SFDR = -54 dBc, F_{IN} = 2

Applications

- RADAR
- LiDAR/LADAR
- SATCOM
- Data Analysis Systems
- Preprocessing Systems
- Direct RF Down-Conversion
- Multi-Carrier Power Amplifiers
- High-Speed Test and Instrumentation

Description

Delphi Engineering Group's ADC3295 is a PMC, analog to digital converter module designed for digitizing wide bandwidth analog signals at 10 bits, at sampling rates of up to 2 Gsps. Buffering of the digitized data samples is provided onboard. Samples can be transferred to the host board via the PCI-X bus at a high rate using the built-in DMA controller.

A Xilinx Virtex 5 FPGA provides continuous sampling, buffering, and timing. Delphi also offers an FPGA design kit which allows custom development of the onboard FPGA. FPGA design can be customized for specific applications such as digital filtering, data preprocessing and DSP functions such as FFT.

For systems running Microsoft Windows, Delphi offers ADCView, a signal visualization application which displays sampled data graphically. Through ADCView's graphical user interface, users can configure sampling parameters such as: start/stop vectors, IRQ operation, and triggering options. Sample data exportable to analysis applications such as Matlab.

The ADC3295 is a PMC based technology that has been rigorously tested to operate on leading PowerPC, PC, and DSP host processor systems. Delphi has a proven track-record of delivering high-performance PMC modules for mission-critical applications.

DELPHI
Engineering Group, Inc.

Interfaces

Analog Input

An analog single-ended input signal is accepted through an SMA female type connector on the front edge of the module.

Clock Input

An analog single-ended clock input of -10 dBm to +10 dBm is accepted through an SMA female type connector on the front edge of the module.

Trigger Input

Trigger input is provided through an SMA female type connector on the front of the module.

All SMA inputs are 50 ohm terminated.

PCI Interface

Processed sample data is transferred to the host system through the PCI bus. Data collection timing and duration are fully programmable through the PCI bus. PCI interface is implemented in an onboard FPGA.

Onboard FPGA

The board's Xilinx Virtex 5 FPGA implements processing, buffering, timing, DRAM control, and the PCI interface.

Contact factory for custom FPGA design.

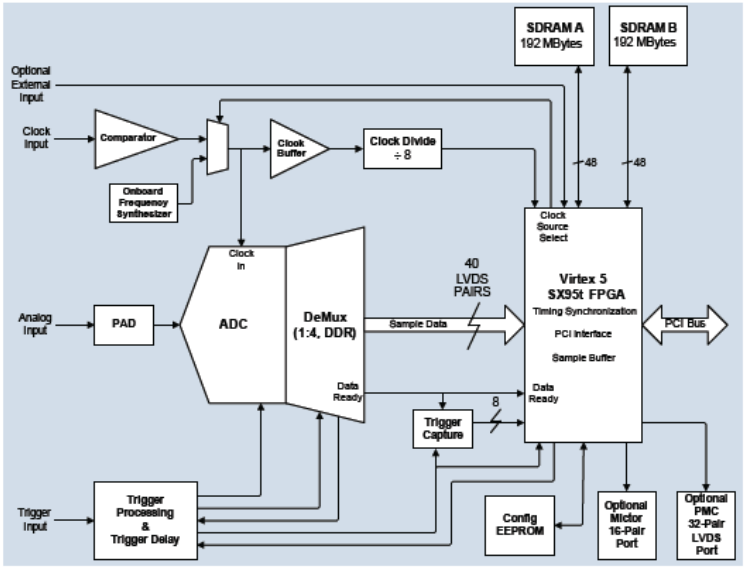

Top Level Block Diagram

Analog ADC Performance

- Full Power Analog Input Bandwidth: 3.0 GHz (-3 dBm)
- ENOB = 7.8 Effective Bits, F_{IN} = 1000 MHz
- SNR = 51 dBc, SFDR = -55 dBc, F_{IN} = 1000 MHz
- ENOB = 7.5 Effective Bits, F_{IN} = 2 GHz
- SNR = 50 dBc, SFDR = -54 dBc, F_{IN} = 2 GHz
- Sampling Rate: 200 Msps to 2 Gsps

Environmental Requirements

- Convection Cooled
  - Minimum Airflow: 400 LFM
  - Ambient Air Temp (Commercial): 0°C to +50°C
  - Ambient Air Temp (Industrial): -40°C to +70°C
- Conduction Cooled
  - Cold Wall Temp (Commercial): 0°C to +65°C
  - Cold Wall Temp (Industrial): -40°C to +70°C

Physical Characteristics

- Dimensions: 2.91" x 5.66"
- Weight: 4.5 oz.

Delphi Engineering Group, Inc.
485 East 17th Street, Suite 400
Costa Mesa, CA 92627
www.delphieng.com

For more detailed specifications contact us at:
Telephone: (949)515-1490
Fax: (949)515-1491
EMail: sales@delphieng.com

ADC3295 Brochure Ver 1.1 02/02/2009

14.4 RWR/ESM Systems, Survey (Extracted from reference [49])

RWR/ESM SYSTEMS

MODEL	REC TYPE	OP FREQ	INST BWIDTH	TYP INST SENS	DYN RANGE	SUPPORT DF	PWR (W)
Aeronix, Inc.; Melbourne, FL, USA; +1-321-984-1671; www.aeronix.com**							
FinderPlus	Hybrid	2-18 GHz	2-18 GHz	*	>100 dB	Yes	<400 W
Copperfield II	Hybrid	0.5-40 GHz	8 GHz	*	>70 dB	Yes	<175 W
Argon ST; Fairfax, VA, USA; +1-703-995-4200; www.argonst.com							
WBR-2000 ESM System	IFM	2-18 GHz	16 GHz	-65 dBm	60 dB	Yes	<350 W
WBR-3000 ESM and ELINT System	Combined IFM and superhet	2-18 GHz	16 GHz	-65 dBm	60 dB	Yes	<500 W
BAE Systems Australia; Edinburgh Parks, SA, Australia; +61 3 9918 4000; www.baesystems.com***							
Lightweight ESM Payload	*	2-18 GHz	*	-60 dBm	*	Yes	*
PRISM	*	2-18 GHz	*	-60 dBm	*	Yes	*
BAE Systems Electronic Solutions; Nashua, NH, USA; +1-603-885-6065; www.baesystems.com							
AN/ALR-56M	Superhet	C-J bands	*	*	*	*	*
Cassidian Electronics; Ulm, Germany; +49-0-731-392-0; www.cassidian.com							
ASIS	Digital	*	6 GHz	-80 dBm	+10 dBm	Yes	<700 W
Elbit Systems EW and SIGINT - Elisra; Bene Beraq, Israel; +972-3-6175111; www.elisra.com							
AES 210/E, AES 210V, GES 210/E	Superhet, Wideband DIFM	0.5-40 GHz; 1 - 18 GHz; 0.5-40 GHz	0.5-40 GHz	-65 dBm	>60 dB	Yes	300-500 W
Aqua Marine - ESM	Superhet, DIFM and channalizer	0.5-40 GHz	0.5-40 GHz	-65 dBm	>60 dB	Yes	1,500 W
Spectrolite SPS-65 V5	Digital	0.5-18 GHz	*	*	*	Yes	*
CV-RWR	CVR	8-18 GHz	*	*	*	Yes	*
SPS-3000/1000V5	Superhet, DIFM ,CVR	0.5-18 GHz	*	*	*	Yes	*
ELETTRONICA S.p.A.; Rome, Italy; +39-0641541; www.elt-roma.com							
ELT/741 Family	IFM	C-J + K	Wide open	High	*	Yes	*
SEAL	DIFM and superhet	C-J + K (option)	Wide open	High	*	Yes	*
ELT/160 Family	IFM	E-J + K	Wide open	Medium	*	Yes	*
ELT/800 Family	DIFM and superhet	C-J + K (option)	Wide open	High	*	Yes	*
VIRGILIUS Family (in RX only configurations)	Wband superhet	C-J + K	Wide open	Very high	*	Yes	*
Elta Systems Ltd.; Ashdod, Israel; +972-8-857-2312; www.elta-iai.com**							
EL/L-8388 3D Ground-Based Multi-Mission ESM/ELINT	Channelizer and digital	0.5-18 GHz	*	*	*	Yes	*
EL/L-8385 ESM/ELINT UAV Payload	Digital	2-18 GHz	*	*	*	Yes	*
EL/L-8382N 3D Naval ESM/ ELINT	Channelizer and digital	0.5-18 GHz	*	*	*	Yes	*
EL/L-8265 RWL- Radar Warning & Threat Location	Digital	2-18 GHz	*	*	*	Yes	*
EL/L-8382 MPA ESM/ELINT for Maritime Patrol Aircraft	Channelizer, superhet and digital	0.5-18 GHz	*	*	*	Yes	*

** Product data from February 2009 JED survey *** Product data from company literature

RWR/ESM SYSTEMS

MODEL	REC TYPE	OP FREQ	INST BWIDTH	TYP INST SENS	DYN RANGE	SUPPORT DF	PWR (W)
INDRA; Madrid, Spain; +34-914-806-032; www.indra.es**							
ALR-400 RWR	Digital	0.5-42 GHz	4 GHz	-65 dBm	60 dB	Yes	200 W
AMES-C ESM/ELINT	DIFM and superhet	0.5-18 GHz	16 GHz	-90 dBm	60 dB	Yes	1,000 W
AMES-800 ESM/ELINT	Digital	0.5-42 GHz	16 GHz	-90 dBm	*	Yes	200-800 W
MRSR-800/MRGR-800 ESM	Digital	0.5-18 GHz	17.5 GHz	-85 dBm	60 dB	Yes	<3,500 W
MRGR-ELINT-FD	Digital and superhet	0.5-18 GHz	>500 MHz	-90 dBm	55 dB	Yes	2,000 W
ITT Exelis; Clifton, NJ, USA; +1-973-284-4543; www.exelisinc.com							
ALQ-211 (V) 8 AIDEWS Radar Warning Receiver	Digital	C-J	*	*	*	Yes	*
ALQ-211 (V) 4 AIDEWS Radar Warning Receiver	Digital	C-J	*	*	*	Yes	*
ES-3701	Circular Array Phase Interferometer	2-18 GHz	16 GH	-65 dBm	>60 dB	Yes	<1 kW
ES-3601	Amplitude Comparison DF	2-18 GHz	16 GHz	-65 dBm	>60 dB	Yes	<1 kW
ALR-95/97/98 family	Wideband DIFM and superhet channel	0.5-18 GHz	16 GHz	*	*	Yes	<500 W
Lockheed Martin MST; Owego, NY, USA; +1-607-751-3135; www.lockheedmartin.com							
AN/ALQ-210	*	*	*	*	*	Yes	400W
MiKES Microwave Electronic Systems Inc.; Ankara, Turkey; +90-312-847-51-00; www.mikes.com.tr							
AN/ALQ 178 V(5)+	Superhet, channelizer and digital.	C-J	*	*	*	*	~4 kW
AN/ALQ 178 V(3)	Superhet, channelizer and digital	C-J	*	*	*	*	~5 kW
Northrop Grumman Corp.; Rolling Meadows, IL, USA; +1-224-625-6777***							
AN/ALR-93	CVR, IFM and digital	0.5-20 GHz	*	*	*	Yes	198W
AN/ALQ-218	Digital	*	*	*	*	*	*
LR-100	Superhet	2-18 GHz	*	*	*	*	219
Rafael Advanced Defense Systems Ltd; Haifa, Israel; +972-4-8795143; www.rafael.com							
Top Scan	Digital	0.5-40 GHz	32 GHz	-65 dBm	90 dB	Yes	850 W
C-Pearl	Digital	0.5-40 GHz	Wide open	-65 dBm	90 dB	Yes	1,100 W
Raytheon Company; Goleta, CA, USA; +1-310-647-1000; www.raytheon.com							
ALR-67(V)3 Radar Warning Receiver	Superhet, channelizer and digital	0.65-18 GHz, 28-40 GHz	*	*	*	Yes	600 W
ALR-69A Radar Warning Receiver	Digital channelizer	C-J	*	*	*	Yes	500 W

** Product data from February 2009 JED survey *** Product data from company literature

RWR/ESM SYSTEMS

MODEL	REC TYPE	OP FREQ	INST BWIDTH	TYP INST SENS	DYN RANGE	SUPPORT DF	PWR (W)
Aeronix, Inc.; Melbourne, FL, USA; +1-321-984-1671; www.aeronix.com**							
FinderPlus	Hybrid	2-18 GHz	2-18 GHz	*	>100 dB	Yes	<400 W
Copperfield II	Hybrid	0.5-40 GHz	8 GHz	*	>70 dB	Yes	<175 W
Argon ST; Fairfax, VA, USA; +1-703-995-4200; www.argonst.com							
WBR-2000 ESM System	IFM	2-18 GHz	16 GHz	-65 dBm	60 dB	Yes	<350 W
WBR-3000 ESM and ELINT System	Combined IFM and superhet	2-18 GHz	16 GHz	-65 dBm	60 dB	Yes	<500 W
BAE Systems Australia; Edinburgh Parks, SA, Australia; +61 3 9918 4000; www.baesystems.com***							
Lightweight ESM Payload	*	2-18 GHz	*	-60 dBm	*	Yes	*
PRISM	*	2-18 GHz	*	-60 dBm	*	Yes	*
BAE Systems Electronic Solutions; Nashua, NH, USA; +1-603-885-6065; www.baesystems.com							
AN/ALR-56M	Superhet	C-J bands	*	*	*	*	*
Cassidian Electronics; Ulm, Germany; +49-0-731-392-0; www.cassidian.com							
ASIS	Digital	*	6 GHz	-80 dBm	+10 dBm	Yes	<700 W
Elbit Systems EW and SIGINT - Elisra; Bene Beraq, Israel; +972-3-6175111; www.elisra.com							
AES 210/E, AES 210V, GES 210/E	Superhet, Wideband DIFM	0.5-40 GHz; 1 - 18 GHz; 0.5-40 GHz	0.5-40 GHz	-65 dBm	>60 dB	Yes	300-500 W
Aqua Marine - ESM	Superhet, DIFM and channalizer	0.5-40 GHz	0.5-40 GHz	-65 dBm	>60 dB	Yes	1,500 W
Spectrolite SPS-65 V5	Digital	0.5-18 GHz	*	*	*	Yes	*
CV-RWR	CVR	8-18 GHz	*	*	*	Yes	*
SPS-3000/1000V5	Superhet, DIFM ,CVR	0.5-18 GHz	*	*	*	Yes	*
ELETTRONICA S.p.A.; Rome, Italy; +39-0641541; www.elt-roma.com							
ELT/741 Family	IFM	C-J + K	Wide open	High	*	Yes	*
SEAL	DIFM and superhet	C-J + K (option)	Wide open	High	*	Yes	*
ELT/160 Family	IFM	E-J + K	Wide open	Medium	*	Yes	*
ELT/800 Family	DIFM and superhet	C-J + K (option)	Wide open	High	*	Yes	*
VIRGILIUS Family (in RX only configurations)	Wband superhet	C-J + K	Wide open	Very high	*	Yes	*
Elta Systems Ltd.; Ashdod, Israel; +972-8-857-2312; www.elta-iai.com**							
EL/L-8388 3D Ground-Based Multi-Mission ESM/ELINT	Channelizer and digital	0.5-18 GHz	*	*	*	Yes	*
EL/L-8385 ESM/ELINT UAV Payload	Digital	2-18 GHz	*	*	*	Yes	*
EL/L-8382N 3D Naval ESM/ ELINT	Channelizer and digital	0.5-18 GHz	*	*	*	Yes	*
EL/L-8265 RWL- Radar Warning & Threat Location	Digital	2-18 GHz	*	*	*	Yes	*
EL/L-8382 MPA ESM/ELINT for Maritime Patrol Aircraft	Channelizer, superhet and digital	0.5-18 GHz	*	*	*	Yes	*

** Product data from February 2009 JED survey *** Product data from company literature

Survey Key – RWR/ESM Systems

MODEL

Product name or model number

REC TYPE

Receiver type

- *superhet = superheterodyne*
- *IFM = instantaneous frequency measurement*
- *CVR = crystal video receiver*
- *DF = direction finding*
- *DIFM = digital instantaneous frequency measurement*
- *SAW = surface acoustic wave*
- *LPI = low probability of intercept*
- *FFT = Fast Fourier Transform*

OP FREQ

Operating frequency

- *VHF = very high frequency*

INST BWIDTH

Instantaneous bandwidth (if different from operating frequency)

TYP INST SENS

Typical installed sensitivity

DYN RANGE

Total dynamic range

SUPPORT DF

Does it support direction finding?

PWR (in W)

Power dissipated in Watts per channel

SIZE (in inches)

Size by height x weight x length, or diameter, in inches

- *ATR = air transport rack*

PLATFORM

Platform

- *air = airborne*
- *grd mob = ground, mobile*
- *grd fix = ground, fixed*
- *shp = shipboard*
- *sub = submarine*

WEIGHT

Weight in lb/kg

FEATURES

Additional features

- *AIS = automatic identification system*
- *CW = continuous wave*
- *ECM = electronic countermeasure*
- *GPS = global positioning system*
- *HOS = Head of State*
- *LBI = long baseline interferometer*
- *LWS = laser warning system*
- *MDF = monopulse direction finder*
- *NTISP = National Transportation Communications for ITS Protocol*
- *POI = probability of intercept*
- *SBI = short baseline interferometer*
- *UAV = unmanned aerial vehicle*

OTHER ABBREVIATIONS USED

- *< = greater than*
- *> = less than*
- *config = configuration*
- *deg = degree*
- *dep = dependent*
- *freq = frequency*
- *max = maximum*
- *min = minimum*
- *nband = narrowband*
- *opt = option/optional*
- *wband = wideband*

** Indicates answer is classified, not releasable or no answer was given.*

MAY 2013 PRODUCT SURVEY:
Signal Generators

This survey, JED's first on this topic in more than five years, will cover Signal Generators that can be used in testing and integration of EW systems. Please e-mail JEDeditor@naylor.com to request a survey questionnaire.

OTHER COMPANIES

This reference list includes websites for additional companies in the field that were unable to provide survey information due to security constraints or publication deadlines, or that declined to participate.

Company Name	Website
BAE Systems ES	www.baesystems.com
Era Corporation	www.erabeyondradar.com
Lockheed Martin MS2	www.lockheedmartin.com

14.5 CTT Incorporated Low Noise Amplifier Datasheet

CTT INC. Low-Noise and High-Power Microwave Amplifiers and Subassemblies

MODEL NUMBER	Freq. (GHz)	(dB) Min	(±dB) Max	(dB) Max	(dBm) Min	In/Out Max	Volts	(mA) Typ	Case	For Quote
AMM/020-1015	0.5-2.0	15	1.00	1.0	8	2.0:1	12~15	80	M4	RFQ
AMM/020-1022	0.5-2.0	22	1.00	1.0	10	2.0:1	12~15	120	M5	RFQ
AMM/020-1030	0.5-2.0	30	1.25	1.0	10	2.0:1	12~15	200	M5	RFQ
AMM/020-1515	0.5-2.0	15	1.00	1.5	8	2.0:1	12~15	80	M4	RFQ
AMM/020-1522	0.5-2.0	22	1.00	1.5	10	2.0:1	12~15	120	M5	RFQ
AMM/020-1530	0.5-2.0	30	1.25	1.5	10	2.0:1	12~15	200	M5	RFQ
AMX/00510-2516	0.5-10.0	16	1.00	2.5	8	2.0:1	12~15	80	M4	RFQ
AMX/00510-2524	0.5-10.0	24	1.25	2.5	8	2.0:1	12~15	120	M5	RFQ
AMX/00510-2532	0.5-10.0	32	1.50	2.5	10	2.0:1	12~15	200	M5	RFQ
AMX/00518-3515	0.5-18.0	15	2.00	3.5	8	2.5:1	12~15	80	M4	RFQ
AMX/00518-3522	0.5-18.0	22	2.00	3.5	8	2.5:1	12~15	140	M5	RFQ
AMX/00518-3530	0.5-18.0	30	2.50	3.5	10	2.5:1	12~15	200	M5	RFQ
AMO/040-1516	2.0-4.0	16	1.00	1.5	8	2.0:1	12~15	80	M4	RFQ
AMO/040-1524	2.0-4.0	24	1.25	1.5	8	2.0:1	12~15	120	M5	RFQ
AMO/040-1532	2.0-4.0	32	1.50	1.5	10	2.0:1	12~15	200	M5	RFQ
AMO/040-1816	2.0-4.0	16	1.00	1.8	8	2.0:1	12~15	80	M4	RFQ
AMO/040-1824	2.0-4.0	24	1.25	1.8	8	2.0:1	12~15	120	M5	RFQ
AMO/040-1832	2.0-4.0	32	1.50	1.8	10	2.0:1	12~15	200	M5	RFQ
AMM/080-2216	2.0-8.0	16	1.00	2.2	8	2.0:1	12~15	80	M4	RFQ
AMM/080-2224	2.0-8.0	24	1.25	2.2	8	2.0:1	12~15	120	M5	RFQ
AMM/080-2232	2.0-8.0	32	1.50	2.2	10	2.0:1	12~15	200	M5	RFQ
AMX/0218-3515	2.0-18.0	15	2.00	3.5	8	2.5:1	12~15	80	M4	RFQ
AMX/0218-3522	2.0-18.0	22	2.00	3.5	8	2.5:1	12~15	140	M5	RFQ
AMX/0218-3530	2.0-18.0	30	2.50	3.5	10	2.5:1	12~15	200	M5	RFQ
AMX/0220-4510	2.0-20.0	10	2.00	4.5	8	2.5:1	12~15	80	M4	RFQ
AMX/0220-4520	2.0-20.0	20	2.00	4.5	8	2.5:1	12~15	140	M5	RFQ
AMX/0220-4530	2.0-20.0	30	2.50	4.5	10	2.5:1	12~15	200	M5	RFQ
AMO/080-1518	4.0-8.0	18	1.00	1.5	6	2.0:1	12~15	80	M4	RFQ
AMO/080-1526	4.0-8.0	26	1.00	1.5	8	2.0:1	12~15	120	M5	RFQ
AMO/080-1534	4.0-8.0	34	1.25	1.5	10	2.0:1	12~15	180	M5	RFQ

14.6 Hittite Microwave Corporation X-Band Mixer Datasheet

Hittite MICROWAVE CORPORATION v04.0504

HMC141C8

GaAs MMIC SMT DOUBLE-BALANCED MIXER, 6 - 15 GHz

Typical Applications

The HMC141C8 is ideal for:

- Microwave Point-to-Point Radios
- VSAT Ground Equipment

Features

Input IP3: +21 dBm

Conversion Loss: 8.5 dB

LO to RF Isolation: 35 dB

Functional Diagram

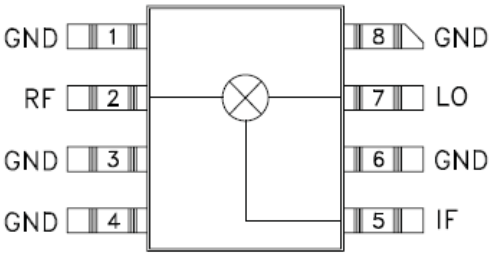

General Description

The HMC141C8 is a miniature passive double-balanced mixer in a non-hermetic ceramic surface mount package that can be used as an upconverter or downconverter. The device is a passive diode/balun type mixer with high dynamic range. The mixer can handle larger signal levels than most active mixers due to the high third order intercept of 20 dBm. MMIC implementation provides exceptional balance in the circuit resulting in high LO/RF and LO/IF isolations and unit-to-unit consistency. This mixer has applications where small size and surface mount compatibility are important.

Electrical Specifications, T_A = +25° C, LO Drive = +15 dBm

Parameter	Min.	Typ.	Max.	Min.	Typ.	Max.	Units
Frequency Range, RF & LO		7 - 10			6 - 14.4		GHz
Frequency Range, IF		DC - 2			DC - 2		GHz
Conversion Loss		8.5	10		10.5	12.5	dB
Noise Figure (SSB)		8.5	10		10.5	12.5	dB
LO to RF Isolation	28	35		23	30		dB
LO to IF Isolation	17	25		10	17		dB
IP3 (Input)		20			20		dBm
IP2 (Input)		45			45		dBm
1 dB Gain Compression (Input)		10			10		dBm

For price, delivery, and to place orders, please contact Hittite Microwave Corporation:
20 Alpha Road, Chelmsford, MA 01824 Phone: 978-250-3343 Fax: 978-250-3373
Order On-line at www.hittite.com

14.7 Hittite Microwave Corporation L-Band Mixer Datasheet

Hittite MICROWAVE CORPORATION v02.0705

HMC423MS8 / 423MS8E

GaAs MMIC MIXER w/ INTEGRATED LO AMPLIFIER, 0.6 - 1.3 GHz

Typical Applications

The HMC423MS8 / HMC423MS8E is ideal for:

- Base Stations
- Portable Wireless
- CATV/DBS
- ISM

Features

Integrated LO Amplifier w/ Pdiss <50 mW

Conversion Loss / Noise Figure: 8 dB

Low LO Drive: 0 dBm

Input IP3: +15 dBm

Single Positive Supply: 3V, 15 mA

Functional Diagram

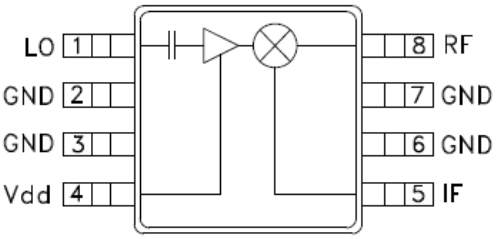

General Description

The HMC423MS8 & HMC423MS8E are double balanced mixer ICs with integrated LO amplifiers. This mixer can operate as an upconverter or downconverter between 0.6 GHz and 1.3 GHz. With the integrated LO amplifier, the mixer requires an LO drive level of only 0 dBm, and requires only 15mA from a single positive +3V rail. The mixer has 8 dB of conversion loss, an input P1dB of +8 dBm and an input third order intercept point of +15 dBm at 1.3 GHz.

Electrical Specifications, T_A = +25° C

Parameter	IF = 100 MHz LO = 0 dBm, Vdd = 3V			Units
	Min.	Typ.	Max.	
Frequency Range, RF & LO		0.6 - 1.3		GHz
Frequency Range, IF		DC - 0.4		GHz
Conversion Loss		8	11	dB
Noise Figure (SSB)		8	11	dB
LO to RF Isolation	25	35		dB
LO to IF Isolation	15	25		dB
RF to IF Isolation	12	20		dB
IP3 (Input)	13	15		dBm
1 dB Compression (Idd)	6.5	8		dBm
Supply Current (Idd)		15		mA

** Unless otherwise noted, all measurements performed as downconverter, IF= 100 MHz.*

For price, delivery, and to place orders, please contact Hittite Microwave Corporation:
20 Alpha Road, Chelmsford, MA 01824 Phone: 978-250-3343 Fax: 978-250-3373
Order On-line at www.hittite.com

14.8 Saab Submarine Tactical ELINT and ESM Systems, Product Specification

SAAB

SUBMARINE
TACTICAL ESM AND ELINT SYSTEMS

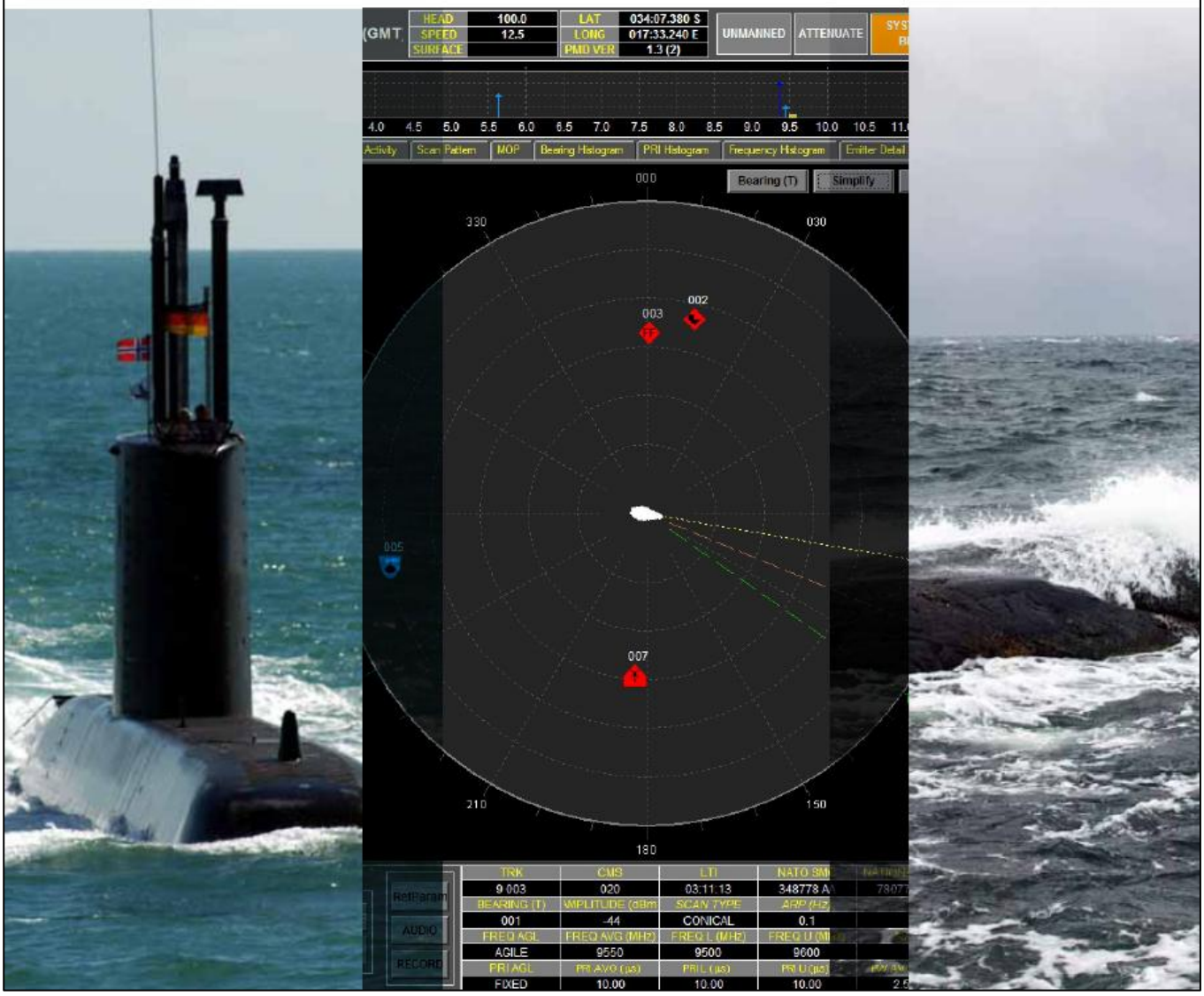

SAAB

SUPPORT EQUIPMENT

Integrated Test Bench, ITB

The purpose of the ITB is to facilitate system testing of UME systems in a controlled environment. The system testing philosophy is aimed at system level verification, and diagnostic testing dependant on the system level test outcomes.

The ITB provides the functionality required to emulate radar signals, and measure the ESM system-under-test response to the emulated signals, evaluate system interfaces, provide test bench assisted fault finding capability, and generate system failure reports in response to the test outcomes.

Integrated Test Bench (ITB)

Threat Data Management Systems, TDMS

The TDMS consist of hardware and software components, it is a collection of tools that enable the user to capture threat emitter data, prepare pre-mission data, playback and extensively analyse recorded information.

The information can be transferred to the platform prior to a mission, it can be utilized to define pre-mission data files as well as be utilized for pre-mission training. On completion of a mission all post mission data can be downloaded onto the existing database.

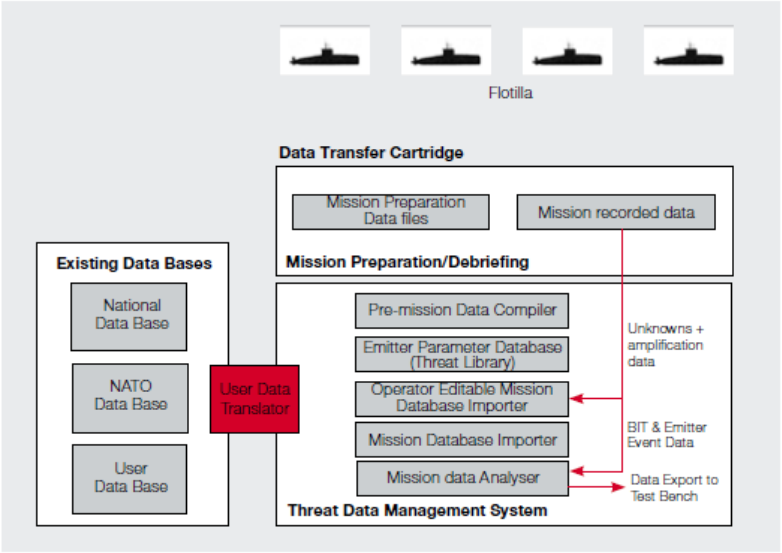

Threat Data Management Systems (TDMS)

TECHNICAL DATA

KEY PARAMETER	UME-100	UME-200
Architecture	ESM with ELINT functionality and comprising parallel: • Acquisition Receiver • ESM Receiver	Simultaneous ESM and ELINT System with parallel: • Acquisition Receiver • ESM Receiver • ELINT Receiver • Integrated LPI Receiver
Frequency range: Standard Options	 2 – 18 GHz 0.6 – 2.0 and 18 – 40 GHz	 2 – 18 GHz 0.6 – 2.0 and 18 – 40 GHz
Probability of Intercept	100 %	100 %
Direction finding: Method Accuracy	 Amplitude 5 degrees rms	 Phase and Amplitude 2 degrees rms

Specifications subject to change without notice

www.saabgroup.com

Saab
Electronic Defence Systems
PO Box 39347

Tel +27 21 709 9000
Fax +27 21 709 9031

15 EBE Faculty: Assessment of Ethics in Research Projects

Any person planning to undertake research in the Faculty of Engineering and the Built Environment at the University of Cape Town is required to complete this form before collecting or analysing data. When completed it should be submitted to the supervisor (where applicable) and from there to the Head of Department. If any of the questions below have been answered YES, and the applicant is NOT a fourth year student, the Head should forward this form for approval by the Faculty EIR committee: submit to Ms Zulpha Geyer (Zulpha.Geyer@uct.ac.za; Chem Eng Building, Ph 021 650 4791).Students must include a copy of the completed form with the final year project when it is submitted for examination.

Name of Principal Researcher/Student: AADIL VALLI ESSOP **Department:** ELECTRICAL ENGINEERING

If a Student: YES **Degree:** MASTERS **Supervisor:** PROFESSOR MICHAEL INGGS

If a Research Contract indicate source of funding/sponsorship: DENEL

Research Project Title: ELECTRONIC ATTACK OF A DUAL BAND RADAR

Overview of ethics issues in your research project:

Question 1: Is there a possibility that your research could cause harm to a third party (i.e. a person not involved in your project)?	YES	NO
Question 2: Is your research making use of human subjects as sources of data? If your answer is YES, please complete Addendum 2.	YES	NO
Question 3: Does your research involve the participation of or provision of services to communities? If your answer is YES, please complete Addendum 3.	YES	NO
Question 4: If your research is sponsored, is there any potential for conflicts of interest? If your answer is YES, please complete Addendum 4.	YES	NO

If you have answered YES to any of the above questions, please append a copy of your research proposal, as well as any interview schedules or questionnaires (Addendum 1) and please complete further addenda as appropriate.

I hereby undertake to carry out my research in such a way that

- there is no apparent legal objection to the nature or the method of research; and
- the research will not compromise staff or students or the other responsibilities of the University;
- the stated objective will be achieved, and the findings will have a high degree of validity;
- limitations and alternative interpretations will be considered;
- the findings could be subject to peer review and publicly available; and
- I will comply with the conventions of copyright and avoid any practice that would constitute plagiarism.

Signed by:

	Full name and signature	**Date**
Principal Researcher/Student:	***AADIL VALLI ESSOP***	14 February 2014

This application is approved by:

Supervisor (if applicable):	*****PROFESSOR MICHAEL INGGS*****	14 February 2014
HOD (or delegated nominee): Final authority for all assessments with NO to all questions and for all undergraduate research.	**Janine Buxey**	14 February 2014
Chair : Faculty EIR Committee For applicants other than undergraduate students who have answered YES to any of the above questions.		